frontiers | Research Topics

Methods in vaccines and molecular therapeutics 2022

Edited by
Nargis Khan, P. Bernard Fourie, Mrinmoy Sanyal and Ernesto T. A. Marques

Published in
Frontiers in Immunology

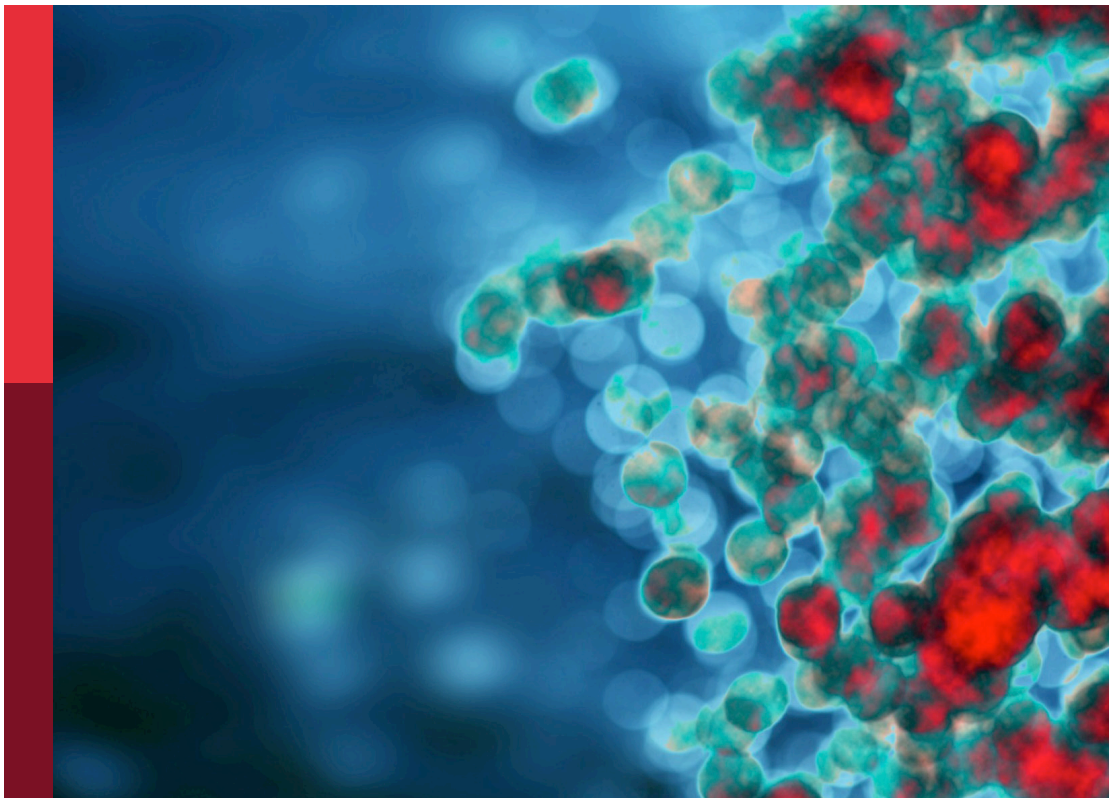

FRONTIERS EBOOK COPYRIGHT STATEMENT

The copyright in the text of individual articles in this ebook is the property of their respective authors or their respective institutions or funders. The copyright in graphics and images within each article may be subject to copyright of other parties. In both cases this is subject to a license granted to Frontiers.

The compilation of articles constituting this ebook is the property of Frontiers.

Each article within this ebook, and the ebook itself, are published under the most recent version of the Creative Commons CC-BY licence. The version current at the date of publication of this ebook is CC-BY 4.0. If the CC-BY licence is updated, the licence granted by Frontiers is automatically updated to the new version.

When exercising any right under the CC-BY licence, Frontiers must be attributed as the original publisher of the article or ebook, as applicable.

Authors have the responsibility of ensuring that any graphics or other materials which are the property of others may be included in the CC-BY licence, but this should be checked before relying on the CC-BY licence to reproduce those materials. Any copyright notices relating to those materials must be complied with.

Copyright and source acknowledgement notices may not be removed and must be displayed in any copy, derivative work or partial copy which includes the elements in question.

All copyright, and all rights therein, are protected by national and international copyright laws. The above represents a summary only. For further information please read Frontiers' Conditions for Website Use and Copyright Statement, and the applicable CC-BY licence.

ISSN 1664-8714
ISBN 978-2-8325-4528-7
DOI 10.3389/978-2-8325-4528-7

About Frontiers

Frontiers is more than just an open access publisher of scholarly articles: it is a pioneering approach to the world of academia, radically improving the way scholarly research is managed. The grand vision of Frontiers is a world where all people have an equal opportunity to seek, share and generate knowledge. Frontiers provides immediate and permanent online open access to all its publications, but this alone is not enough to realize our grand goals.

Frontiers journal series

The Frontiers journal series is a multi-tier and interdisciplinary set of open-access, online journals, promising a paradigm shift from the current review, selection and dissemination processes in academic publishing. All Frontiers journals are driven by researchers for researchers; therefore, they constitute a service to the scholarly community. At the same time, the *Frontiers journal series* operates on a revolutionary invention, the tiered publishing system, initially addressing specific communities of scholars, and gradually climbing up to broader public understanding, thus serving the interests of the lay society, too.

Dedication to quality

Each Frontiers article is a landmark of the highest quality, thanks to genuinely collaborative interactions between authors and review editors, who include some of the world's best academicians. Research must be certified by peers before entering a stream of knowledge that may eventually reach the public - and shape society; therefore, Frontiers only applies the most rigorous and unbiased reviews. Frontiers revolutionizes research publishing by freely delivering the most outstanding research, evaluated with no bias from both the academic and social point of view. By applying the most advanced information technologies, Frontiers is catapulting scholarly publishing into a new generation.

What are Frontiers Research Topics?

Frontiers Research Topics are very popular trademarks of the *Frontiers journals series*: they are collections of at least ten articles, all centered on a particular subject. With their unique mix of varied contributions from Original Research to Review Articles, Frontiers Research Topics unify the most influential researchers, the latest key findings and historical advances in a hot research area.

Find out more on how to host your own Frontiers Research Topic or contribute to one as an author by contacting the Frontiers editorial office: frontiersin.org/about/contact

Methods in vaccines and molecular therapeutics: 2022

Topic editors

Nargis Khan – University of Calgary, Canada
P. Bernard Fourie – University of Pretoria, South Africa
Mrinmoy Sanyal – Stanford University, United States
Ernesto T. A. Marques – University of Pittsburgh, United States

Citation

Khan, N., Fourie, P. B., Sanyal, M., Marques, E. T. A., eds. (2024). *Methods in vaccines and molecular therapeutics: 2022*. Lausanne: Frontiers Media SA. doi: 10.3389/978-2-8325-4528-7

Table of contents

05 Strategies in developing dimethyl sulfoxide (DMSO)-free cryopreservation protocols for biotherapeutics
Marlene Davis Ekpo, George Frimpong Boafo, Jingxian Xie, Xiangjian Liu, Chuanpin Chen and Songwen Tan

12 Actin depolymerizing factor-based nanomaterials: A novel strategy to enhance *E. mitis*-specific immunity
ZhengQing Yu, LiXin Xu, Ke He, MingMin Lu, RuoFeng Yan, XiaoKai Song and XiangRui Li

30 Hcp1-loaded staphylococcal membrane vesicle vaccine protects against acute melioidosis
Keting Zhu, Gang Li, Jia Li, Mingxia Zheng, Xiaohui Peng, Yifan Rao, Ming Li, Renjie Zhou and Xiancai Rao

43 Heterodimeric IL-15 (hetIL-15) reduces circulating tumor cells and metastasis formation improving chemotherapy and surgery in 4T1 mouse model of TNBC
Vasiliki Stravokefalou, Dimitris Stellas, Sevasti Karaliota, Bethany A. Nagy, Antonio Valentin, Cristina Bergamaschi, Konstantinos Dimas and George N. Pavlakis

59 Design of a multi-epitope vaccine against six Nocardia species based on reverse vaccinology combined with immunoinformatics
Fei Zhu, Caixia Tan, Chunhui Li, Shiyang Ma, Haicheng Wen, Hang Yang, Mingjun Rao, Peipei Zhang, Wenzhong Peng, Yanhui Cui, Jie Chen and Pinhua Pan

80 Specific *in situ* immuno-imaging of pulmonary-resident memory lymphocytes in human lungs
Duncan C. Humphries, Richard A. O'Connor, Hazel L. Stewart, Tom M. Quinn, Erin E. Gaughan, Beth Mills, Gareth O.S. Williams, James M. Stone, Keith Finlayson, Martine Chabaud-Riou, Florence Boudet, Kevin Dhaliwal and Vincent Pavot

93 A tool for evaluating heterogeneity in avidity of polyclonal antibodies
Kan Li, Michael Dodds, Rachel L. Spreng, Milite Abraha, Richard H. C. Huntwork, Lindsay C. Dahora, Tinashe Nyanhete, Sheetij Dutta, Ulrike Wille-Reece, Erik Jongert, Katie J. Ewer, Adrian V. S. Hill, Celina Jin, Jennifer Hill, Andrew J. Pollard, S. Munir Alam, Georgia D. Tomaras and S. Moses Dennison

107 Development of multi-epitope vaccines against the monkeypox virus based on envelope proteins using immunoinformatics approaches
Caixia Tan, Fei Zhu, Pinhua Pan, Anhua Wu and Chunhui Li

131 Challenges and opportunities in analyzing and modeling peptide presentation by HLA-II proteins
Hesham ElAbd, Petra Bacher, Andreas Tholey, Tobias L. Lenz and Andre Franke

138 rAAV expressing recombinant antibody for emergency prevention and long-term prophylaxis of COVID-19
Ilias B. Esmagambetov, Ekaterina I. Ryabova, Artem A. Derkaev, Dmitry V. Shcheblyakov, Inna V. Dolzhikova, Irina A. Favorskaya, Daria M. Grousova, Mikhail A. Dovgiy, Vladimir V. Prokofiev, Andrey I. Gosudarev, Daria V. Byrikhina, Ilia D. Zorkov, Anna A. Iliukhina, Anna V. Kovyrshina, Artem Y. Shelkov, Boris S. Naroditsky, Denis Y. Logunov and Alexander L. Gintsburg

151 Rational strategies for enhancing mAb binding to SARS-CoV-2 variants through CDR diversification and antibody-escape prediction
Masaud Shah, Ji-Yon Shin and Hyun Goo Woo

164 Multiparametric flow cytometry to characterize vaccine-induced polyfunctional T cell responses and T cell/NK cell exhaustion and memory phenotypes in mouse immuno-oncology models
Davide Moi, Bijun Zeng, Simone A. Minnie, Rituparna Bhatt, Jack Wood, David P. Sester, Roberta Mazzieri and Riccardo Dolcetti

184 Multiplexed bead-based assay for the simultaneous quantification of human serum IgG antibodies to tetanus, diphtheria, pertussis toxin, filamentous hemagglutinin, and pertactin
Vishal Rathod, Laxmikant Kadam, Manish Gautam, Prabhu Dasu Gumma, Kevin Marke, Cathy Asokanathan, Alex Douglas-Bardsley, Laura Hassell, Sachin Bhandare, Sumit Gupta, Sameer Parekh, Pramod Pujari, Harish Rao, Hitt Sharma, Umesh Shaligram and Sunil Gairola

204 Protection against tuberculosis achieved by dissolving microneedle patches loaded with live *Mycobacterium paragordonae* in a BCG prime-boost strategy
Mi-Hyun Lee, Hyejun Seo, Moon-Su Lee, Byoung Jun Kim, Hye Lin Kim, Du Hyung Lee, Jaehun Oh, Ju Yeop Shin, Ju Young Jin, Do Hyeon Jeong and Bum-Joon Kim

217 Development and optimization of an in-house heterologous ELISA for detection of prednisolone drug in enzyme conjugates using spacers
Dinesh Kumar, Harinder Singh Oberoi, Harpal Singh, Tulsidas G. Shrivastav, Prudhvi Lal Bhukya, Mansi Kumari, Bidhan Chandra Koner and Subash Chandra Sonkar

233 Appropriate intradeltoid muscle needle penetration depth in vaccine administration: an MRI study in Thailand
Teeranan Laohawiriyakamol, Pattira Boonsri, Khetnathee Phutphithak, Thamonchanok Niyomkarn, Prapakorn Klabklay and Chaiwat Chuaychoosakoon

243 Integrated control strategies for dengue, Zika, and Chikungunya virus infections
Nelson Côrtes, Aline Lira, Wasim Prates-Syed, Jaqueline Dinis Silva, Larissa Vuitika, William Cabral-Miranda, Ricardo Durães-Carvalho, Andrea Balan, Otavio Cabral-Marques and Gustavo Cabral-Miranda

frontiers | Frontiers in Immunology

TYPE Opinion
PUBLISHED 05 October 2022
DOI 10.3389/fimmu.2022.1030965

Check for updates

OPEN ACCESS

EDITED BY
Mrinmoy Sanyal,
Stanford University, United States

REVIEWED BY
Xavier Lafarge,
Établissement Français du Sang (EFS), France

*CORRESPONDENCE
Songwen Tan
songwen.tan@csu.edu.cn

SPECIALTY SECTION
This article was submitted to Vaccines and Molecular Therapeutics, a section of the journal Frontiers in Immunology

RECEIVED 29 August 2022
ACCEPTED 20 September 2022
PUBLISHED 05 October 2022

CITATION
Ekpo MD, Boafo GF, Xie J, Liu X, Chen C and Tan S (2022) Strategies in developing dimethyl sulfoxide (DMSO)-free cryopreservation protocols for biotherapeutics. *Front. Immunol.* 13:1030965. doi: 10.3389/fimmu.2022.1030965

COPYRIGHT
© 2022 Ekpo, Boafo, Xie, Liu, Chen and Tan. This is an open-access article distributed under the terms of the Creative Commons Attribution License (CC BY). The use, distribution or reproduction in other forums is permitted, provided the original author(s) and the copyright owner(s) are credited and that the original publication in this journal is cited, in accordance with accepted academic practice. No use, distribution or reproduction is permitted which does not comply with these terms.

Strategies in developing dimethyl sulfoxide (DMSO)-free cryopreservation protocols for biotherapeutics

Marlene Davis Ekpo, George Frimpong Boafo, Jingxian Xie, Xiangjian Liu, Chuanpin Chen and Songwen Tan*

Xiangya School of Pharmaceutical Sciences, Central South University, Changsha, China

KEYWORDS

cryopreservation, cryoprotectants, biobanking, dimethyl sulfoxide, DMSO-free, biotherapeutics

Introduction

Cryopreservation is a technology employed in long-term storage of biologics achieved by cooling to cryogenic temperatures (1, 2). This preservation technique has become increasingly relevant especially in the development and commercialization of cellular therapeutic products (3, 4). Conventional cryopreservation protocols involve the application of the permeating cryoprotectant; dimethyl sulfoxide (DMSO) due its ability to restrict ice nucleation and promote post-thaw viability (4). Although DMSO effectively preserves biologics, it can impair functional recovery (5–7) and induce a variety of mild to severe toxic effects in patients which must be avoided at all cost when administering immunotherapeutic products (8, 9).

The situation is considerably more critical during vitrification; a freezing method that has attracted heightened recognition as a faster and economic substitute to slow freezing as the unorganized liquid state of water is rapidly transformed to a glassy solid state without ice crystallization (10). In vitrification, high cooling rates and high concentrations (4–8 M) of cryoprotectants are usually required (11); enforcing on the exigency of using non-toxic cryoprotectants because increasing DMSO concentration is not advisable.

Efficacious cryopreservation and biobanking requires the development of safe and consistent storage protocols (12, 13). Favorably, such procedures should be devoid of xenogeneic or toxic components and to this effect, many scientists have put forward for the replacement of DMSO. Several groups have discovered/developed safer alternative cryoprotectants with a range of potential cryoprotection mechanisms like ice

recrystallization inhibition, osmolality control, cell membrane stabilization and vitrification (14).

Numerous methods have since emerged to lessen the quantity of DMSO used (mostly by supplementation with other cryoprotectants) (15–20) or to completely eliminate DMSO application and these methods may also require special adjunct treatments, reagents or freezing protocols as would be discussed here in specifics. Attempts have also been made at preserving cellular products at non-freezing temperatures (21–25), advanceable by hypoxia and hypercapnia induced cytoprotection (26–28). Although highly beneficial to low-income countries where biobanking facilities are not obtainable, hypothermic storage is however limited to a few days thus fueling the need for safer freezing protocols.

But for the review by Weng et al. (29), studies on replacing DMSO are yet to be critically analyzed; a process that would track research accomplishments, expose novel supplementary techniques applied and encourage further research aimed at improving DMSO-free cryopreservation protocols for different biologicals. Through this article, we wish to draw the attention of researchers to possibility of a DMSO-free preservation era which is achievable in the nearest future. We provide prove of total exclusion of DMSO from cryopreservation solutions and summarize some of the supplementary techniques that have been applied to improve post-thaw viability and function. Our survey has also revealed the commercial availability of DMSO-free cryoprotectant solutions especially those used for cellular therapeutics, but there are limited studies to scrutinize or validate the potency of these products; which might be why most researchers are yet to largely patronizing products without DMSO as there is little to no evidence to back up these product claims. We therefore urge researchers to extend the application of these products to a wider range of biotherapeutics so as to speed up the availability of clinically approved products especially immunotherapeutics which is the answer to many complicated diseases like cancers.

Challenges in cryopreservation with DMSO

Cryopreservation is an important determinant of the stability and activity of biopharmaceutical formulations. Several studies have proven the hypothesis that the application of DMSO can induce temperature-, time-, and concentration-dependent toxicities (7, 30). DMSO causes mitochondrial damage to astrocytes (31), and impacts negatively on cellular membrane/cytoskeleton structure and integrity by interacting with proteins and dehydrating lipids (32) as evident in the increased membrane permeability of erythrocytes (33) and altered chromatin conformation in fibroblasts (30). Also, the presence of DMSO in culture medium can induce unwanted stem cell differentiation (34).

Furthermore, repeated DMSO use even at sub-toxic levels can affect cellular epigenetic profile resulting in undesirable phenotypic disturbances (35). For instance, DMSO interferes with DNA methyltransferases and histone modification enzymes of human pluripotent stem cells causing epigenetic variations and reduction in their pluripotency (36, 37). Similarly, murine embryonic stem cells display disrupted mRNA expression levels of several markers following DMSO treatment (38).

Adverse reactions from cardiac, neurological, and gastrointestinal systems have been reported in patients receiving DMSO-containing cellular products (39, 40). These discoveries have led to the design of several washing procedures to ensure complete DMSO removal. However, the washing protocol usually involves agitation and osmotic/mechanical stresses which are to be avoided due to the fragile and sensitive nature of biologics post-thaw (40). The washing step can also be time consuming, expensive and resource wasting since a significant number of cells are loss in the process.

Strategies in DMSO-free cryopreservation of biotherapeutics

Potent and safe alternative cryoprotectants to DMSO are highly desirable in order to meet the demands in the development and manufacturing of cellular and genetic therapies. In numerous instances, the observed cryoprotective effect is derived from a combination of two or more strategies as discussed below. These strategies and their outcome are also summarized in Table 1.

Alternative cryoprotectants to DMSO

Replacing DMSO with other cryoprotectants is the typical approach in eradicating the use of DMSO in cryopreservation. Kuleshova et al. vitrified neural stem cells using a combination of ethylene glycol (EG) and sucrose. Post-storage evaluations revealed no substantial differences between fresh and vitrified cells in cell markers expression, proliferation or multipotent differentiation (51).

Osmolyte-based freezing solutions containing varying blends of sucrose, glycerol, creatine, isoleucine and mannitol have supported the recovery and survival of mesenchymal stromal cells when compared to conventional preservation with DMSO. These solutions conferred cryoprotection, retained cell differentiation capacity and modulated the cytosine-phosphate-guanine epigenome (54). StemCell Keep™ has been proven effective for the cryopreservation of human induced pluripotent stem cells

TABLE 1 Methods/Techniques used in DMSO-free cryopreservation of biotherapeutics.

Material	Cryoprotectant	Additional strategy	Outcome/Conclusion	Ref
Human umbilical cord matrix MSCs	1,2-propanediol and 1.0 M EG	Thawing *via* magnetic induction heating of magnetic extracellular Fe_3O_4 nanoparticles	Suppressed devitrification and recrystallization with improved cell survival	(41)
Mesenchymal stromal cells	100–300 mM sucrose	Addition of using 10% platelet lysate to expansion medium	Improved cryopreservation	(42)
Human dermal MSCs	Mannitol, lactose, sucrose, trehalose or raffinose	24-hour sugar pretreatment prior to cryopreservation	Cryopreserved MSCs has retained attachment, proliferation and multilineage differentiation	(43)
Human umbilical cord MSCs	Sucrose, trehalose and raffinose	Electroporation-assisted pre-freeze delivery of cryoprotectants	Improved cryopreservation of MSCs	(44)
HiPSCs	StemCell Keep™	Nano-warming	Improved cryopreservation of HiPSCs	(45)
HESCs	StemCell Keep™	N/A	Higher recovery rates and cell attachment	(46)
Human bone marrow-derived MSCs	Polyampholyte cryoprotectant	N/A	High viability and do not affect the biological properties of the cells even after 24 months of cryopreservation at 80°C.	(47)
HiPSCs	EG	-Dissociation of iPSCs with Accutase in the presence of a ROCK inhibitor -Programmed freezing	Up to 6-fold improvement in comparison to the standard freezing in clumps without ROCK inhibitor.	(48)
Wharton' s Jelly Tissue	0.05 M glucose, 0.05 M sucrose, and 1.5 M EG in PBS	Programmed freezing	Higher post-thaw cell survivability	(49)
PDL cells and dental pulp tissues.	N/A	Programmed freezing using alternating magnetic field; "Cells Alive System"	Acceptable immediate autotransplantation results	(50)
Neural stem and progenitor cells	40% v/v EG and 0.6 M sucrose	N/A	Preserved expression of cell markers, proliferation and multipotent differentiation	(51)
HiPSCs	Sucrose, glycerol, isoleucine, and poloxamer 188	Controlled-rate freezing in a liquid nitrogen-based controlled-rate freezer	Improved cryopreservation of hiPSCs	(52)
Erythrocytes	0.1 wt% PVA	N/A	Significantly high post-thaw cell recovery	(53)
Mesenchymal Stromal Cells	Osmolyte-based freezing solutions	N/A	Comparable post-thaw recovery and improved post-thaw attachment	(54, 55)
MSCs	Amphiphilic Block Copolymer	N/A	Excellent MSC proliferation and multilineage differentiation properties	(56)
Human bone marrow-derived MSCs	2 M 1,2-EG, 2 M 1,2- propyl alcohol, and 0.5 M trehalose	Nano-warming with synthetic Pluronic F127-liquid metal nanoparticles (PLM NPs)	Threefold increase in viability, and maintained attachment, proliferation, surface marker expression, and multilineage differentiation	(57)
Human MSC monolayers	6.5 M EG, 0.5 M sucrose, and 10% w/w COOH-PLL	Slow vitrification at rates of 4.9 and 10.8°C/min	Significantly improved viability with less apoptosis	(58)
Natural killer cells	Poly-L-lysine, Ectoine, dextran and sucrose	N/A	Maintained cells viability, morphology and cytotoxic activity following long-term cryopreservation up to 2 months.	(59)
Erythrocytes	Biomimetic Block Copolymer Worms with PVA	N/A	Improved cell recovery with no evidence of hemagglutination or abnormal cell morphologies.	(60)
Human ADSCs	1.0 M Trehalose and 20% glycerol	N/A	High preservation efficiency with acceptable outcomes	(12)
Human ADSCs	Trehalose	Nanoparticle-mediated intracellular delivery of trehalose	Eliminates multistep washing of the cryopreserved cells to remove toxic/penetrating cryoprotectants	(61)
HiPSCs	Trehalose-based cryosolutions containing EG or glycerol	N/A	High cell viability and high stability with retained their morphology, self-renewal, pluripotency and differentiation.	(36)
HSCs	HP01 (Macopharma)	N/A	Conserved full short- and long-term post-thaw cellular activity	(62)
HiPSCs	Sucrose, glycerol, L-isoleucine, poloxamer 188 (P188)	N/A	Highly viable and functional HiPSCs	(5, 63)

(Continued)

TABLE 1 Continued

Material	Cryoprotectant	Additional strategy	Outcome/Conclusion	Ref
HSCs	Antifreeze protein mimetics produced by X-Therma Inc. (Richmond, CA), XT-Thrive A™ and XT-Thrive B™	N/A	X-Therma formulations may offer clinically safer alternative to DMSO-based solutions.	(64)
HSCs, T-cells, $CD34^+$ cells	Pentaisomaltose™, CryoScarless™, CryoNovo P24™, CryoProtectPureSTEM™	N/A	Comparable results to those cryopreserved with DMSO	(9, 65–67)

N/A, Not Applicable; HiPSCs, Human induced pluripotent stem cells; Human embryonic stem cells, hESCs; EG, Ethylene glycol; DMSO, Dimethyl sulfoxide; PDL, Periodontal ligament; PVA, Polyvinyl alcohol; COOH-PLL, carboxylated poly-L-lysine; HSCs, Hematopoietic stem cells; MSCs, Mesenchymal stem cells; ADSCs, Adipose-derived stem cells.

(hiPSCs) (68), human embryonic stem cells (hESCs) (46) and mesenchymal stem cells (MSCs) (47). Further investigation on the mechanism of cryoprotection showed that the polyampholyte is adsorbed on to the cell membrane suggesting that it can confer protection on cell surface and eliminate the use of proteins and DMSO (47). Other polyampholytes have also shown great potential as DMSO substitutes in storage of murine L929 cells and rat MSCs (69), natural killer cells (59) and other mammalian cell types (70).

A cocktail of non-toxic and Food and Drug Administration (US-FDA)-approved infusible substances including sucrose, glycerol, isoleucine, human serum albumin, and poloxamer 188, have been applied for preservation of hiPSCs (52). In a recent study by Park et al., a block copolymer; PEG–PA (5000 –500) has been presented as an excellent cryoprotectant where the recovered stem cells exhibited acceptable survival, proliferation and multilineage differentiation post-thaw (56).

These studies and more presented in Table 1 portray the synergistic activity of several biocompatible cryoprotectants and suggests that this approach may be an innovative paradigm for safe cryopreservation. Presently, commercially manufactured DMSO-free cryosolutions like Pentaisomaltose™, CryoScarless™, CryoNovo P24™, StemCell Keep™, CryoSOfree™ and XT-Thrive™ are available but their quality and capacity to protect a wide range of therapeutics is under-investigated. Further research would involve testing the compatibility of these cryoprotectants with other biotherapeutics. In addition to substituting cryoprotectants, supporting techniques used to improve on solvent-free cryopreservation are discussed below.

Pre-cryopreservation treatment

The pretreatment of biotherapeutics with cryoprotective and stabilizing agents prior to cryopreservation is largely becoming a viable approach to ensuring safe storage. Sugar pretreatment, supplementation of expansion medium with 10% platelet lysate and slow freezing is reportedly an effective protocol in DMSO-less cryopreservation of adipose-derived stromal cells (42). Similarly, sugar pretreatment increased survival, metabolic activity, attachment, proliferation and multilineage differentiation after recultivation of dermal MSCs (43). Improved results are also obtained when the sugars are positioned intracellularly as performed by Mutsenko and coworkers who explored electroporation-aided delivery of cryoprotective sugars in human umbilical cord MSCs (44). Also, pre-incubation of MSCs with osmolyte-based freezing solutions could foster effective cryopreservation (54). These results corroborate the potential advantages of pre-cryopreservation treatment(s).

Programmed freezing methods

Programmed freezing offers improved control over ice nucleation parameters. A technique involving a magnetic field driven freezer termed “Cells Alive System” has been used to prevent formation of intracellular ice for up to three months. The magnetic field vibration function prohibits water molecules from creating clusters during freezing. Although the optimal conditions needed for survival and viability of isolated human periodontal ligament cells (PDL), pulp tissue and tooth using CAS freezers were determined previously (71) (72) with DMSO, the technique proved equally effective without DMSO, promoting greater survival rates over that obtained with conventional freezers (50). Programmed freezing has also been used for cryopreservation of human Wharton’s Jelly Tissue, showing higher post-thaw cell survivability when used in conjunction with a freezing solution consisting of 0.05 M glucose, 0.05 M sucrose and 1.5 M EG in PBS (49).

Matsumura et al. reports a simple, novel slow vitrification method at 4.9 and 10.8°C/min for the cryopreservation of MSC monolayers using a polyampholyte based vitrification solution. Thermal analysis confirmed stable vitrification and post-thaw assessment revealed significantly improved viability and retained differentiation capacity (58).

Thawing protocol

Due to the low thermal conductivity of biological samples, the conventional approach of rewarming large-volume cryopreserved samples in a water bath heated at 37°C is associated with non-uniform distribution of temperature,

which can induce thermal stress (41). Preferably, a high heating rate is desirable during thawing, because devitrification and recrystallization may occur if the temperature cannot be elevated rapidly above the sample's melting point (73). Therefore, both the heating rate and uniformity of heating during rewarming are important to cryopreservation especially vitrification. Nevertheless, attaining the optimal rewarming rate remains a major factor complicating effective vitrification.

Wang et al. proposes magnetic induction heating (MIH) of extracellular Fe_3O_4 magnetic nanoparticles also called nano-warming technology as a method to amplify rewarming. This technique was successfully applied to rewarming vitrified MSCs where the sample was thawed by plunging the straw into a 0.2 M trehalose supplemented culture medium heated to 37°C. Then, the system was subjected to MIH under alternating magnetic field at a medium frequency for a duration of 10 s. Results obtained reveals the prospective benefits this technique holds as it significantly hindered ice recrystallization/devitrification during rewarming and improved cell viability (41). More recently, Ito et al. also employed the nano-warming technology for thawing of hiPSC using StemCell Keep as cryoprotectant. Similarly, nano-warming showed more uniform and rapid rewarming of vitrified samples, prevented devitrification/recrystallization and improved viability (45).

Another nanotechnology assisted thawing approach involves the utilization of soft liquid metal nanoparticles possessing reproducible photothermal stability, high photothermal conversion efficiency, low cytotoxicity and the ability to suppress ice formation. This technique promotes less ice nucleation during freezing and ultrarapid rewarming while thawing. Human bone marrow stromal cells have been successfully rewarmed with this technique (57).

These studies reveal that the advantages of nanotechnology can be capitalized on to promote safe rewarming post-cryopreservation after verifying the biocompatibility of the nanoparticles.

Conclusion

A critical step prior to the clinical application of biotherapeutics is the optimization of cryopreservation protocols that minimize post-thaw alterations in the stability and potency of preserved materials. Cryosolutions containing 10% of DMSO is a widely used cryopreservative but there is an increasing amount of evidence showing inconsistent results on its impact on post-cryopreservation performance of biologicals. This drawback forms the basis for the development of safer preservation protocols. DMSO-free strategies have the potential to alleviate the aforementioned obstacles as demonstrated by studies discussed in this article. The application of other cryoprotectants, combined with other techniques like programmed freezing, pretreatments and modified thawing protocols have shown good prospects.

In conclusion, the development of effective DMSO-free cryopreservation techniques that will provide high post-thaw viability and preserve original morphology and functioning remains key because this is essential to hastening the industrialization and clinical application of biotherapeutics. We are of the opinion that more research efforts should be put into the development and performance validation of trademarked DMSO-free products. In cases where DMSO elimination is unavoidable, only confirmed safe concentrations should be applied preferably in combination with non-toxic cryoprotectants and other potent strategies.

Author contributions

Conceptualization: ME, CC, ST. Writing—original draft preparation: ME, JX, XL, GB. Writing—review and editing: ME, XL, GB, CC and ST. Supervision and approval: ST. All authors contributed to the article and approved the submitted version.

Conflict of interest

The authors declare that the research was conducted in the absence of any commercial or financial relationships that could be construed as a potential conflict of interest.

Publisher's note

All claims expressed in this article are solely those of the authors and do not necessarily represent those of their affiliated organizations, or those of the publisher, the editors and the reviewers. Any product that may be evaluated in this article, or claim that may be made by its manufacturer, is not guaranteed or endorsed by the publisher.

References

1. Pomeroy KO, Comizzoli P, Rushing JS, Lersten IL, Nel-Themaat L. The ART of cryopreservation and its changing landscape. *Fertil Steril* (2022) 117(3):469–76. doi: 10.1016/j.fertnstert.2022.01.018

2. Betsy J, Kumar S. Cryopreservation: History and development. In: Betsy J, Kumar S, editors. *Cryopreservation of fish gametes*. Singapore: Springer Singapore (2020). p. 135–49.

3. Hunt CJ. Technical considerations in the freezing, low-temperature storage and thawing of stem cells for cellular therapies. *Transfus Med Hemother* (2019) 46 (3):134–50. doi: 10.1159/000497289

4. Whaley D, Damyar K, Witek RP, Mendoza A, Alexander M, Lakey JR. Cryopreservation: An overview of principles and cell-specific considerations. *Cell Transplant* (2021) 30:963689721999617. doi: 10.1177/0963689721999617

5. Li R, Walsh P, Truong V, Petersen A, Dutton JR, Hubel A. Differentiation of human iPS cells into sensory neurons exhibits developmental stage-specific cryopreservation challenges. *Front Cell Dev Biol* (2021) 9:796960. doi: 10.3389/fcell.2021.796960

6. Mizuno M, Matsuzaki T, Ozeki N, Katano H, Koga H, Takebe T, et al. Cell membrane fluidity and ROS resistance define DMSO tolerance of cryopreserved synovial MSCs and HUVECs. *Stem Cell Res Ther* (2022) 13(1):177. doi: 10.1186/s13287-022-02850-y

7. Awan M, Buriak I, Fleck R, Fuller B, Goltsev A, Kerby J, et al. Dimethyl sulfoxide: a central player since the dawn of cryobiology, is efficacy balanced by toxicity? *Regener Med* (2020) 15(3):1463–91. doi: 10.2217/rme-2019-0145

8. Ock SA, Rho GJ. Effect of dimethyl sulfoxide (DMSO) on cryopreservation of porcine mesenchymal stem cells (pMSCs). *Cell Transplant* (2011) 20(8):1231–9. doi: 10.3727/096368910x552835

9. Svalgaard JD, Talkhoncheh MS, Haastrup EK, Munthe-Fog L, Clausen C, Hansen MB, et al. Pentaisomaltose, an alternative to DMSO. engraftment of cryopreserved human CD34(+) cells in immunodeficient NSG mice. *Cell Transplant* (2018) 27(9):1407–12. doi: 10.1177/0963689718786226

10. Sharma A, Rao JS, Han Z, Gangwar L, Namsrai B, Gao Z, et al. Vitrification and nanowarming of kidneys. *Adv Sci (Weinh)* (2021) 8(19):e2101691. doi: 10.1002/advs.202101691

11. Murray KA, Gibson MI. Chemical approaches to cryopreservation. *Nat Rev Chem* (2022) 6(8):579–93. doi: 10.1038/s41570-022-00407-4

12. Zhang TY, Tan PC, Xie Y, Zhang XJ, Zhang PQ, Gao YM, et al. The combination of trehalose and glycerol: An effective and non-toxic recipe for cryopreservation of human adipose-derived stem cells. *Stem Cell Res Ther* (2020) 11(1):460. doi: 10.1186/s13287-020-01969-0

13. Raju R, Bryant SJ, Wilkinson BL, Bryant G. The need for novel cryoprotectants and cryopreservation protocols: Insights into the importance of biophysical investigation and cell permeability. *Biochim Biophys Acta Gen Subj* (2021) 1865(1):129749. doi: 10.1016/j.bbagen.2020.129749

14. Arutyunyan IV, Kananykhina EY, Elchaninov AV, Fatkhudinov TK. Influence of sucrose on the efficiency of cryopreservation of human umbilical cord-derived multipotent stromal cells with the use of various penetrating cryoprotectants. *Bull Exp Biol Med* (2021) 171(1):150–5. doi: 10.1007/s10517-021-05187-3

15. Kaiser D, Otto NM, McCallion O, Hoffmann H, Zarrinrad G, Stein M, et al. Freezing medium containing 5% DMSO enhances the cell viability and recovery rate after cryopreservation of regulatory T cell products ex vivo and in vivo. *Front Cell Dev Biol* (2021) 9:750286. doi: 10.3389/fcell.2021.750286

16. Tuten Sevim E, Arat S. Combining dimethyl sulphoxide (DMSO) with different cryoprotectants ensures better cartilage cell cryopreservation. *Cryo Lett* (2021) 42(4):220–6.

17. Gilfanova R, Auclair KM, Hui A, Norris PJ, Muench MO. Reduced dimethyl sulfoxide concentrations successfully cryopreserve human hematopoietic stem cells with multi-lineage long-term engraftment ability in mice. *Cytotherapy* (2021) 23 (12):1053–9. doi: 10.1016/j.jcyt.2021.07.007

18. Jahan S, Kaushal R, Pasha R, Pineault N. Current and future perspectives for the cryopreservation of cord blood stem cells. *Transfus Med Rev* (2021) 35(2):95–102. doi: 10.1016/j.tmrv.2021.01.003

19. Trummer T, Fox R, Koç JR, de Lima M, Otegbeye F. Cryopreservation of hematopoietic cells using a pre-constituted, protein-free cryopreservative solution with 5% dimethyl sulfoxide. *Cytotherapy* (2020) 22(11):613–6. doi: 10.1016/j.jcyt.2020.05.006

20. Duchez P, Chevaleyre J, Brunet de la Grange P, Vlaski M, Boiron JM, Wouters G, et al. Cryopreservation of hematopoietic stem and progenitor cells amplified ex vivo from cord blood CD34+ cells. *Transfusion* (2013) 53(9):2012–9. doi: 10.1111/trf.12015

21. Bekadja MA, Boumendil A, Blaise D, Chevallier P, Peggs KS, Salles G, et al. Non-cryopreserved hematopoietic stem cells in autograft patients with lymphoma: a matched-pair analysis comparing a single center experience with the use of cryopreserved stem cells reported to the European society for blood and marrow transplantation registry. *Cytotherapy* (2021) 23(6):483–7. doi: 10.1016/j.jcyt.2020.12.016

22. Araújo AB, Soares TB, Schmalfuss T, Angeli MH, Furlan JM, Salton GD, et al. Non-cryopreserved peripheral blood stem cells as a safe and effective alternative for autologous transplantation in multiple myeloma. *Transfusion* (2022). doi: 10.1111/trf.17090

23. Jennane S, Hasnaoui N, Mahtat EM, Merimi F, Bougar S, El Maaroufi H, et al. Non-cryopreserved peripheral blood stem cells autologous transplantation in multiple myeloma: Bicentric study. *Transfus Clin Biol* (2020) 27(3):152–6. doi: 10.1016/j.tracli.2020.03.006

24. Piriyakhuntorn P, Tantiworawit A, Rattanathammethee T, Hantrakool S, Chai-Adisaksopha C, Rattarittamrong E, et al. Outcomes of non-cryopreserved versus cryopreserved peripheral blood stem cells for autologous stem cell transplantation in multiple myeloma. *Ann Transplant* (2020) 25:e927084. doi: 10.12659/aot.927084

25. Bittencourt MCB, Mariano L, Moreira F, Schmidt-Filho J, Mendrone-Jr A, Rocha V. Cryopreserved versus non-cryopreserved peripheral blood stem cells for autologous transplantation after high-dose melphalan in multiple myeloma: comparative analysis. *Bone Marrow Transplant* (2019) 54(1):138–41. doi: 10.1038/s41409-018-0250-1

26. Jeanne M, Kovacevic-Filipovic M, Szyporta M, Vlaski M, Hermitte F, Lafarge X, et al. Low-oxygen and high-carbon-dioxide atmosphere improves the conservation of hematopoietic progenitors in hypothermia. *Transfusion* (2009) 49 (8):1738–46. doi: 10.1111/j.1537-2995.2009.02191.x

27. Vlaski M, Negroni L, Kovacevic-Filipovic M, Guibert C, Brunet de la Grange P, Rossignol R, et al. Hypoxia/hypercapnia-induced adaptation maintains functional capacity of cord blood stem and progenitor cells at 4°C. *J Cell Physiol* (2014) 229(12):2153–65. doi: 10.1002/jcp.24678

28. Gerby S, Simplicien M, Duchez P, Chevaleyre J, Ivanovic Z, Vlaski-Lafarge M. Hypoxia/hypercapnia prevents iron-dependent cold injuries in cord blood stem and progenitor cells. *Cytotherapy* (2019) 21(4):460–7. doi: 10.1016/j.jcyt.2019.02.006

29. Weng L, Beauchesne PR. Dimethyl sulfoxide-free cryopreservation for cell therapy: A review. *Cryobiology* (2020) 94:9–17. doi: 10.1016/j.cryobiol.2020.03.012

30. Verheijen M, Lienhard M, Schrooders Y, Clayton O, Nudischer R, Boerno S, et al. DMSO induces drastic changes in human cellular processes and epigenetic landscape in vitro. *Sci Rep* (2019) 9(1):4641. doi: 10.1038/s41598-019-40660-0

31. Yuan C, Gao J, Guo J, Bai L, Marshall C, Cai Z, et al. Dimethyl sulfoxide damages mitochondrial integrity and membrane potential in cultured astrocytes. *PloS One* (2014) 9(9):e107447. doi: 10.1371/journal.pone.0107447

32. Cheng CY, Song J, Pas J, Meijer LH, Han S. DMSO induces dehydration near lipid membrane surfaces. *Biophys J* (2015) 109(2):330–9. doi: 10.1016/j.bpj.2015.06.011

33. Gironi B, Kahveci Z, McGill B, Lechner BD, Pagliara S, Metz J, et al. Effect of DMSO on the mechanical and structural properties of model and biological membranes. *Biophys J* (2020) 119(2):274–86. doi: 10.1016/j.bpj.2020.05.037

34. Sambo D, Li J, Brickler T, Chetty S. Transient treatment of human pluripotent stem cells with DMSO to promote differentiation. *J Vis Exp* (2019) 149:1–11. doi: 10.3791/59833

35. Cheng H, Han Y, Zhang J, Zhang S, Zhai Y, An X, et al. Effects of dimethyl sulfoxide (DMSO) on DNA methylation and histone modification in parthenogenetically activated porcine embryos. Reproduction. *Fertil Dev* (2022) 34(8):598–607. doi: 10.1071/RD21083

36. Ntai A, La Spada A, De Blasio P, Biunno I. Trehalose to cryopreserve human pluripotent stem cells. *Stem Cell Res* (2018) 31:102–12. doi: 10.1016/j.scr.2018.07.021

37. Fu K, Bonora G, Pellegrini M. Interactions between core histone marks and DNA methyltransferases predict DNA methylation patterns observed in human cells and tissues. *Epigenetics* (2020) 15(3):272–82. doi: 10.1080/15592294.2019.1666649

38. Yi JK, Park S, Ha JJ, Kim DH, Huang H, Park SJ, et al. Effects of dimethyl sulfoxide on the pluripotency and differentiation capacity of mouse embryonic stem cells. *Cell Reprogram* (2020) 22(5):244–53. doi: 10.1089/cell.2020.0006

39. Kollerup Madsen B, Hilscher M, Zetner D, Rosenberg J. Adverse reactions of dimethyl sulfoxide in humans: A systematic review. *F1000Res* (2018) 7:1746. doi: 10.12688/f1000research.16642.2

40. Xie J, Ekpo MD, Xiao J, Zhao H, Bai X, Liang Y, et al. Principles and protocols for post-cryopreservation quality evaluation of stem cells in novel biomedicine. *Front Pharmacol* (2022) 13:907943. doi: 10.3389/fphar.2022.907943

41. Wang J, Zhao G, Zhang Z, Xu X, He X. Magnetic induction heating of superparamagnetic nanoparticles during rewarming augments the recovery of hUCM-MSCs cryopreserved by vitrification. *Acta Biomater* (2016) 33:264–74. doi: 10.1016/j.actbio.2016.01.026

42. Rogulska O, Petrenko Y, Petrenko A. DMSO-free cryopreservation of adipose-derived mesenchymal stromal cells: expansion medium affects post-thaw survival. *Cytotechnology* (2017) 69(2):265–76. doi: 10.1007/s10616-016-0055-2

43. Petrenko YA, Rogulska OY, Mutsenko VV, Petrenko AY. A sugar pretreatment as a new approach to the Me2SO- and xeno-free cryopreservation of human mesenchymal stromal cells. *Cryo Lett* (2014) 35(3):239–46.

44. Mutsenko V, Barlič A, Pezić T, Dermol-Černe J, Dovgan B, Sydykov B, et al. Me2SO- and serum-free cryopreservation of human umbilical cord mesenchymal stem cells using electroporation-assisted delivery of sugars. *Cryobiology* (2019) 91:104–14. doi: 10.1016/j.cryobiol.2019.10.002

45. Ito A, Yoshioka K, Masumoto S, Sato K, Hatae Y, Nakai T, et al. Magnetic heating of nanoparticles as a scalable cryopreservation technology for human induced pluripotent stem cells. *Sci Rep* (2020) 10(1):13605. doi: 10.1038/s41598-020-70707-6

46. Ota A, Matsumura K, Lee JJ, Sumi S, Hyon SH. StemCell keep™ is effective for cryopreservation of human embryonic stem cells by vitrification. *Cell Transplant* (2017) 26(5):773–87. doi: 10.3727/096368916x692654

47. Matsumura K, Hayashi F, Nagashima T, Hyon SH. Long-term cryopreservation of human mesenchymal stem cells using carboxylated poly-l-lysine without the addition of proteins or dimethyl sulfoxide. *J Biomater Sci Polym Ed* (2013) 24(12):1484–97. doi: 10.1080/09205063.2013.771318

48. Katkov I, Kan N, Cimadamore F, Nelson B, Snyder E, Terskikh A. DMSO-free programmed cryopreservation of fully dissociated and adherent human induced pluripotent stem cells. *Stem Cells Int* (2011) 981606:8. doi: 10.4061/2011/981606

49. Shivakumar SB, Bharti D, Subbarao RB, Jang SJ, Park JS, Ullah I, et al. DMSO- and serum-free cryopreservation of wharton's jelly tissue isolated from human umbilical cord. *J Cell Biochem* (2016) 117(10):2397–412. doi: 10.1002/jcb.25563

50. Kawata T, Abedini S, Kaku M, Koseki H, Kojima S, Sumi H, et al. Effects of DMSO (Dimethyl sulfoxide) free cryopreservation with program freezing using a magnetic field on periodontal ligament cells and dental pulp tissues. *Biomed Res* (2012) 23(3):438–43.

51. Kuleshova LL, Tan FCK, Magalhães R, Gouk SS, Lee KH, Dawe GS. Effective cryopreservation of neural stem or progenitor cells without serum or proteins by vitrification. *Cell Transplant* (2009) 18(2):135–44. doi: 10.3727/096368909788341298

52. Li R, Hornberger K, Dutton JR, Hubel A. Cryopreservation of human iPS cell aggregates in a DMSO-free solution-an optimization and comparative study. *Front Bioeng Biotechnol* (2020) 8:1. doi: 10.3389/fbioe.2020.00001

53. Deller RC, Vatish M, Mitchell DA, Gibson MI. Synthetic polymers enable non-vitreous cellular cryopreservation by reducing ice crystal growth during thawing. *Nat Commun* (2014) 5:3244. doi: 10.1038/ncomms4244

54. Pollock K, Samsonraj RM, Dudakovic A, Thaler R, Stumbras A, McKenna DH, et al. Improved post-thaw function and epigenetic changes in mesenchymal stromal cells cryopreserved using multicomponent osmolyte solutions. *Stem Cells Dev* (2017) 26(11):828–42. doi: 10.1089/scd.2016.0347

55. Pollock K, Yu G, Moller-Trane R, Koran M, Dosa PI, McKenna DH, et al. Combinations of osmolytes, including monosaccharides, disaccharides, and sugar alcohols act in concert during cryopreservation to improve mesenchymal stromal cell survival. *Tissue Eng Part C Methods* (2016) 22(11):999–1008. doi: 10.1089/ten.TEC.2016.0284

56. Park JK, Patel M, Piao Z, Park S-J, Jeong B. Size and shape control of ice crystals by amphiphilic block copolymers and their implication in the cryoprotection of mesenchymal stem cells. *ACS Appl Mater Interfaces* (2021) 13(29):33969–80. doi: 10.1021/acsami.1c09933

57. Hou Y, Lu C, Dou M, Zhang C, Chang H, Liu J, et al. Soft liquid metal nanoparticles achieve reduced crystal nucleation and ultrarapid rewarming for human bone marrow stromal cell and blood vessel cryopreservation. *Acta Biomater* (2020) 102:403–15. doi: 10.1016/j.actbio.2019.11.023

58. Matsumura K, Kawamoto K, Takeuchi M, Yoshimura S, Tanaka D, Hyon SH. Cryopreservation of a two-dimensional monolayer using a slow vitrification method with polyampholyte to inhibit ice crystal formation. *ACS Biomater Sci Eng* (2016) 2(6):1023–9. doi: 10.1021/acsbiomaterials.6b00150

59. Pasley S, Zylberberg C, Matosevic S. Natural killer-92 cells maintain cytotoxic activity after long-term cryopreservation in novel DMSO-free media. *Immunol Lett* (2017) 192:35–41. doi: 10.1016/j.imlet.2017.09.012

60. Mitchell DE, Lovett JR, Armes SP, Gibson MI. Combining biomimetic block copolymer worms with an ice-inhibiting polymer for the solvent-free cryopreservation of red blood cells. *Angew Chem Int Ed Engl* (2016) 55(8):2801–4. doi: 10.1002/anie.201511454

61. Rao W, Huang H, Wang H, Zhao S, Dumbleton J, Zhao G, et al. Nanoparticle-mediated intracellular delivery enables cryopreservation of human adipose-derived stem cells using trehalose as the sole cryoprotectant. *ACS Appl Mater Interfaces* (2015) 7(8):5017–28. doi: 10.1021/acsami.5b00655

62. Duchez P, Rodriguez L, Chevaleyre J, de la Grange PB, Ivanovic Z. Clinical-scale validation of a new efficient procedure for cryopreservation of ex vivo expanded cord blood hematopoietic stem and progenitor cells. *Cytotherapy* (2016) 18(12):1543–7. doi: 10.1016/j.jcyt.2016.08.004

63. Li R, Hornberger K, Dutton JR, Hubel A. Cryopreservation of human iPS cell aggregates in a DMSO-free solution–an optimization and comparative study. *Front Bioeng Biotechnol* (2020) 8:1. doi: 10.3389/fbioe.2020.00001

64. Gilfanova R, Callegari A, Childs A, Yang G, Luarca M, Gutierrez AG, et al. A bioinspired and chemically defined alternative to dimethyl sulfoxide for the cryopreservation of human hematopoietic stem cells. *Bone Marrow Transplant* (2021) 56(11):2644–50. doi: 10.1038/s41409-021-01368-w

65. Kaushal R, Jahan S, McGregor C, Pineault N. Dimethyl sulfoxide-free cryopreservation solutions for hematopoietic stem cell grafts. *Cytotherapy* (2022) 24(3):272–81. doi: 10.1016/j.jcyt.2021.09.002

66. Svalgaard JD, Haastrup EK, Reckzeh K, Holst B, Glovinski PV, Gørløv JS, et al. Low-molecular-weight carbohydrate pentaisomaltose may replace dimethyl sulfoxide as a safer cryoprotectant for cryopreservation of peripheral blood stem cells. *Transfusion* (2016) 56(5):1088–95. doi: 10.1111/trf.13543

67. Vanichapol T, Pongsakul N, Srisala S, Apiwattanakul N, Chutipongtanate S, Hongeng S. Suppressive characteristics of umbilical cord blood-derived regulatory T cells after ex vivo expansion on autologous and allogeneic T effectors and various lymphoblastic cells. *J Immunother* (2019) 42(4):110–8. doi: 10.1097/cji.0000000000000262

68. Matsumura K, Bae JY, Kim HH, Hyon SH. Effective vitrification of human induced pluripotent stem cells using carboxylated ϵ-poly-l-lysine. *Cryobiology* (2011) 63(2):76–83. doi: 10.1016/j.cryobiol.2011.05.003

69. Matsumura K, Hyon S-H. Polyampholytes as low toxic efficient cryoprotective agents with antifreeze protein properties. *Biomaterials* (2009) 30(27):4842–9. doi: 10.1016/j.biomaterials.2009.05.025

70. Matsumura K, Bae JY, Hyon SH. Polyampholytes as cryoprotective agents for mammalian cell cryopreservation. *Cell Transplant* (2010) 19(6):691–9. doi: 10.3727/096368910x508780

71. Abedini S, Kaku M, Kawata T, Koseki H, Kojima S, Sumi H, et al. Effects of cryopreservation with a newly-developed magnetic field programmed freezer on periodontal ligament cells and pulp tissues. *Cryobiology* (2011) 62(3):181–7. doi: 10.1016/j.cryobiol.2011.03.001

72. Kaku M, Kamada H, Kawata T, Koseki H, Abedini S, Kojima S, et al. Cryopreservation of periodontal ligament cells with magnetic field for tooth banking. *Cryobiology* (2010) 61(1):73–8. doi: 10.1016/j.cryobiol.2010.05.003

73. Baboo J, Kilbride P, Delahaye M, Milne S, Fonseca F, Blanco M, et al. The impact of varying cooling and thawing rates on the quality of cryopreserved human peripheral blood T cells. *Sci Rep* (2019) 9(1):3417. doi: 10.1038/s41598-019-39957-x

frontiers | Frontiers in Immunology

TYPE Original Research
PUBLISHED 21 December 2022
DOI 10.3389/fimmu.2022.1080630

Check for updates

OPEN ACCESS

EDITED BY
Nargis Khan,
University of Calgary, Canada

REVIEWED BY
Tarek A. Ahmad,
Bibliotheca Alexandrina, Egypt
Maria Agallou,
Pasteur Hellenic Institute, Greece

*CORRESPONDENCE
XiangRui Li
lixiangrui@njau.edu.cn

†These authors have contributed equally to this work

SPECIALTY SECTION
This article was submitted to Vaccines and Molecular Therapeutics, a section of the journal Frontiers in Immunology

RECEIVED 26 October 2022
ACCEPTED 06 December 2022
PUBLISHED 21 December 2022

CITATION
Yu Z, Xu L, He K, Lu M, Yan R, Song X and Li X (2022) Actin depolymerizing factor-based nanomaterials: A novel strategy to enhance *E. mitis*-specific immunity. *Front. Immunol.* 13:1080630. doi: 10.3389/fimmu.2022.1080630

COPYRIGHT
© 2022 Yu, Xu, He, Lu, Yan, Song and Li. This is an open-access article distributed under the terms of the Creative Commons Attribution License (CC BY). The use, distribution or reproduction in other forums is permitted, provided the original author(s) and the copyright owner(s) are credited and that the original publication in this journal is cited, in accordance with accepted academic practice. No use, distribution or reproduction is permitted which does not comply with these terms.

Actin depolymerizing factor-based nanomaterials: A novel strategy to enhance *E. mitis*-specific immunity

ZhengQing Yu[1,2†], LiXin Xu[2†], Ke He[2], MingMin Lu[2], RuoFeng Yan[2], XiaoKai Song[2] and XiangRui Li[2*]

[1]School of Agriculture, Ningxia University, Yinchuan, Ningxia, China, [2]Ministry of Education (MOE) Joint International Research Laboratory of Animal Health and Food Safety, College of Veterinary Medicine, Nanjing Agricultural University, Nanjing, Jiangsu, China

The epidemic of avian coccidiosis seriously threatens the animals' welfare and the economic gains of the poultry industry. Widespread in avian coccidiosis, *Eimeria mitis* (*E. mitis*) could obviously impair the production performance of the infected chickens. So far, few effective vaccines targeting *E. mitis* have been reported, and the nanovaccines composed of nanospheres captured our particular attention. At the present study, we construct two kinds of nanospheres carrying the recombinant *E. mitis* actin depolymerizing factor (rEmADF), then the characterization was then analyzed. After safety evaluation, the protective efficacy of rEmADF along with its nanospheres were investigated in chickens. The promoted secretions of antibodies and cytokines, as well as the enhanced percentages of $CD4^+$ and $CD8^+$ T cells were evaluated by the ELISA and flow cytometry assay. In addition, the absolute quantitative real-time PCR (qPCR) assay implied that vaccinations with rEmADF-entrapped nanospheres could significantly reduce the replications of *E. mitis* in feces. Compared with the rEmADF-loaded chitosan (EmADF-CS) nanospheres, the PLGA nanospheres carrying rEmADF (EmADF-PLGA nanosphers) were more effective in up-regulating weight efficiency of animals and generated equally ability in controlling *E. mitis* burdens in feces, suggesting the PLGA and CS nanospheres loaded with rEmADF were the satisfactory nanovaccines for *E. mitis* defense. Collectively, nanomaterials may be an effective antigen delivery system that could help recombinant *E. mitis* actin depolymerizing factor to enhance immunoprotections in chicken against the infections of *E. mitis*.

KEYWORDS

Eimeria mitis, actin depolymerizing factor, nanomaterial, nanosphere, immune protection

1 Introduction

As a parasitic enteric disease mainly induced by one or more *Eimeria* species, avian coccidiosis can cause malabsorption, reduction in growth, even increased mortality (1). As estimated, the property losses caused by chicken coccidiosis exceed USD 3 billion yearly (2). Normally, there is consensus that seven *Eimeria* species are considered to be infectious to the chicken (3), and these *Eimeria* species can be grouped into those leading to hemorrhagic enteritis (*E. tenella*, *E. necatrix*, and *E. brunetti*) and those leading to deficiency in nutrient's absorption (*E. mitis*, *E. acervulina*, *E. praecox*, and *E. maxima*) (4). Interestingly, each *Eimeria* specie revealed a predilection for certain part of the chicken gut. Although it is considered to be less-pathogenic in chickens, *E. mitis* and *E. praecox* could obviously inhabit the productivity of animals (5, 6), posing a serious threat to the poultry husbandry worldwide (7, 8). According to the previously published papers, *E. mitis* has been proved to be related to low growth efficiency and poor laying performance (5, 7). Nowadays, the prevention strategies against avian coccidiosis primarily depends on the anticoccidial drugs or live attenuated vaccines (9). The sulphonamides are used as the main drugs for avian coccidiosis since 1940s, no new efficient ingredients are close to the market, except for the introduction of Diclazuril in 1990 (10). Furthermore, constraints such as the drug resistance and cost of live vaccines are of main issues that holds the progress of poultry husbandry (11). Under these circumstances, control of avian coccidiosis has become a main concern in poultry industry (11, 12).

Safe and reliable anticoccidial vaccines may be the best approach to reduce the burdens of *Eimeria* species (13, 14). Nowadays, anticoccidial vaccines have gained a considerable development, but the vaccines which could provide full protection against *Eimeria* species are still unavailable (15). As an actin-binding protein, the actin-depolymerizing factor (ADF) possesses high conservatism in eukaryotes, and could depolymerize filamentous actin to monomeric actin (16).The genomes of apicomplexan parasites contain few actin-binding proteins including ADF and which modulates motility processes of parasites (17). In addition, the movement of intracellular parasites rely on the rapid turnover of actin filaments (18), and the critical role of *E. tenella* ADF in the invasion of parasite has been proved (19). According to a previously published paper, the DNA vaccines expressing *E. tenella* ADF with 3-1E protein could improve host immunity against coccidiosis in chickens (20). These publications lent credit to the idea that a critical role played by *E. mitis* ADF (EmADF) in the invasion of avian coccidiosis, and development of anticoccidial vaccines targeting the EmADF seems to be practical in inducing robust immunity against *E. mitis* infections.

Currently, commercial vaccine strategies against avian coccidiosis are intensively concentrated in the live attenuated and inactivated vaccines (2).However, live attenuated anticoccidial vaccines allows the duplications of *Eimeria* species *in vivo* to generate adequate immunoprotections against coccidiosis, such strategy may lead to virulence recovery after vaccine immunizations (21, 22). Moreover, inactivated coccidiosis is more likely to induce strongly nonspecific immunity, and can bring on side effects (23). The occurrence of DNA and recombinant subunit vaccines can effectively make up these problems, and the two types of vaccines are proved to be effective in resisting avian coccidiosis in the previous publications (14). Even so, limitations also occurred in DNA vaccines as the risk of foreign DNA integration in host genomes (23), while the recombinant subunit vaccines are easy to be degraded by enzyme *in vivo* (24). Collectively, an effective vaccine resisting avian coccidiosis is still unavailable. Recently, nanomaterials served as the biodegradable delivery system have appeared in vaccines (25, 26), it can prevent antigens from undesirable degradation and enhance the immunogenic characteristics of entrapped antigens (27, 28). As a bio-based and fully biodegradable polymer, poly lactic-co-glycolic acid (PLGA) has been licensed by FDA and EMA in the manufacturing process of vaccines and drugs (29). With the nature characteristics of biocompatibility, biodegradability, and non-toxicity, PLGA has been widely used in vaccine synthesis and considered to be effective in antigen delivery (30). However, PLGA also exhibited many weaknesses in antigen delivery, when loading negative molecules. Chitosan (CS), a cationic polysaccharide, could solve this problem. CS is an attractive nanomaterial because of its good biocompatibility, biodegradable, and non-toxic (31, 32), and is proved to be safe in wound dressings and biomedical materials, even in partial food industry (33).

Followed by the views mentioned, the *E. mitis* actin depolymerizing factor (EmADF) was first expressed by prokaryotic expression system, the obtained recombinant EmADF protein (rEmADF) was then entrapped in PLGA and CS to synthesize the nanovaccines (EmADF-PLGA and EmADF-CS nanospheres). The immunoprotections of synthesized nanospheres was investigated in chickens. These observations highlighted the novel nanospheres in inducing *E. mitis*-specific immunity, and it should be an effective strategy with high-priority to prevent *E. mitis*.

2 Materials and methods

2.1 Animals and parasites

Used to provide a relevant model in this study, newborn Hy-Line (breed W-36) chickens were purchased from Tegeili Hatchery, Nanjing, China. All chickens were kept in a coccidia-free condition without administration of any coccidia vaccine, and had free access to sterilized food and clean water

without anti-coccidia drugs. The specific pathogen-free (SPF) BALB/c mice (weighed 18-22 g) were obtained from the Model Animal Research Center, Nanjing University, Nanjing, China, and were reared in the isolators under the room temperature. The management of the animals, test operations, and sample gathering in the study were strictly followed the Ethics Procedures and Guidelines of the People's Republic of China, and were supervised by the Animal Ethics Committee, Nanjing Agriculture University, Nanjing, China.

The purified *E. mitis* oocysts were stored in 2.5% potassium dichromate at 4°C at the MOE Joint International Research Laboratory of Animal Health and Food Safety, College of Veterinary Medicine, Nanjing Agricultural University, Nanjing, China. Followed the instructions of the previous paper (34), the *E. mitis* oocysts were large-scaled propagated, accumulated, and sporulated ten days prior to animals infections.

2.2 Cloning, expression and purification of recombinant EmADF protein

Based on the introductions of Trizol® reagent (Vazyme Biotech Co., Ltd, Nanjing, China), extraction of 10^7 purified *E. mitis* oocysts RNA were conducted, and cDNA was synthesized by using the reverse transcription kit (Vazyme Biotech Co., Ltd, Nanjing, China). The conserved domain sequences (CDS) of EmADF (GeneBank: XM_013496771.1) was amplified from the obtained cDNA using the primers as follows. The forward primers, 5'- CGC GGATCC ATGGCGAGCGGAATGC-3', and the reverse primers, 5'- CCC AAGCTT TTAGGTA AGCACGCTGAGGTC-3'. High-Fidelity Master Mix (Tsingke Biological Technology, Nanjing, China) was used for PCR reaction with the recommended protocol in the instructions. The PCR products were purified by the Gel Extraction Kit (Omega Bio-Tek, Norcross, GA, USA), digested by *Bam*HI and *Hind*III restriction endonuclease (Takara Biotechnology, Dalian, China), and subcloned to a linearized pET-32a prokaryotic vector (Invitrogen Biotechnology, Carlsbad, CA, USA) by using the DNA Ligation Kit (Takara Biotechnology, Dalian, China). Then the recombinant plasmid was transferred into the *Escherichia coli* (*E. coli*) BL21 (DE3) cells (Tsingke Biological Technology, Nanjing, China), and propagated in Luria Bertani (LB) medium containing 100 μg/ml ampicillin. A Plasmid Mini Kit (Omega Bio-Tek, Norcross, GA, USA) was used to extract the recombinant plasmid, then double restriction enzyme digestion and the ABI PRISM™ 3730 XL DNA Analyzer (Applied Biosystems, Waltham, MA, USA) were conducted to determine the recombinant plasmid. After sequencing of the recombinant plasmid, the sequence analysis was conducted by the online Blast program (https://blast.ncbi.nlm.nih.gov/Blast.cgi).

The expression and purification procedures for recombinant EmADF (rEmADF) were carried out by a chelating column (HisTrap™ FF, Cytiva, Marlborough, MA, USA) following the manufacturer's protocol. Briefly, the chemical competent cells carrying the correct plasmid were grown in LB medium containing 100 μg/ml ampicillin at 37°C (180 rpm) until the OD600 reached approximately 0.5. Induced for 4 h under the same condition with 1.0 mM isopropyl β-D-thiogalactoside (IPTG, Sigma, Saint Louis, MO, USA), the chemical competent cells were harvested and broken by supersonic technique. Then rEmADF was purified by a chelating column (HisTrap™ FF, Cytiva, Marlborough, MA, USA), and the ToxinEraser™ Endotoxin Removal Kit (GeneScript, Piscataway, NJ, USA) was used to eradicate the endotoxin. To analyze the endotoxin level and purity of rEmADF, the ToxinSensor™ Chromogenic LAL Endotoxin Assay Kit (GeneScript, Piscataway, NJ, USA) and 12% (*w*/*v*) sodium dodecyl sulfate-polyacrylamide gel electrophoresis (SDS-PAGE) were conducted. The obtained rEmADF was stored at -80°C until use. The concentrations of rEmADF were investigated by Pierce™ BCA Protein Assay Kit (Thermo Scientific, Waltham, MA, USA) before subsequent analysis.

2.3 Sera collections and immunoblot analysis

Negative sera were harvested from coccidia-free chickens. To obtain the positive sera against *E. mitis*, coccidia-free chickens at the age of fourteen days were first orally challenged with 5×10^4 sporulated oocysts, four times in total at an interval of seven days. Seven days after the last challenge, blood samples were collected from wing vein of the challenged chickens. The collected sera were kept at -20°C until use.

Recombinant EmADF were analyzed by Western blot assays with sera to determine the recognition of rEmADF. In brief, rEmADF was first analyzed in 12% SDS-PAGE gel, subsequently transferred to polyvinylidene fluoride (PVDF) membranes (Millipore Ltd., Tullagreen, Carrigtwohill, Co. Cork, IRL) *via* the Trans-Blot Turbo (Bio-rad, Hercules, CA, USA). Then membranes were treated with TBST (tris buffered saline containing 0.5% (*v*/*v*) Tween 20) containing 5% (*w*/*v*) skimmed milk powder and incubated with chicken sera against *E. mitis* (1:100 dilutions) overnight at 4°C on a rotary shaker (30 rpm). Rinsed in TBST at room temperature for 5 min, membranes were incubated with HRP-conjugated goat anti-chicken IgY (1: 5,000 dilutions, eBioscience, San Diego, USA) for 1 h at 37°C. Finally, the proteins were visualized by Electro-Chemi Luminescence (ECL) system (Tanon, Shanghai, China). The sera harvested from coccidia-free chickens were used as a control.

2.4 Vaccine formulation

As published previously (35), the PLGA nanospheres were synthesized by double emulsion solvent evaporation technique

(*w*/*o*/*w*) with minor alterations. Briefly, 50 mg PLGA (MW: 40,000-75,000 Da, LA/GA: 65/35, Sigma, Saint Louis, MO, USA) was first dissolved in 1.0 ml dichloromethane (DCM, Sigma, Saint Louis, MO, USA) at room temperature. 2.0 ml of 5.0% (*w*/*v*) polyvinyl alcohol (PVA, MW: 31,000-75,000 Da, Sigma, Saint Louis, MO, USA) was subsequently dropwise added. Fully mixed by a vortex at maximum speed, the liquid was kept in an ice bath and tip sonication was immediately performed in a continuous mode (durative time 2 s, interval time 2 s) under the output power of 40 W until the liquid transferred into milky white. Then 4.0 ml of rEmADF at 1.0 mg/ml concentration was dropwise added. Fully mixed again by a vortex at room temperature, the mixture was then sonicated using the same criteria mentioned above. To develop *w*/*o*/*w* emulsions, 2.0 ml of 5.0% PVA was dropwise added and tip sonication was again conducted. After passing through the 0.22 μm filtering membrane (Millipore, Billerica, MA, USA), the developed emulsions were centrifugated at 35,000 rpm for 40 min at 4°C. The supernatants were collected and stored at -20°C, and the precipitates were also collected and resuspended in double distilled water. The resuspended solution was kept at -80°C until it was fully frozen, and was completely freeze-dried (Labconco, Kansas City, MO, USA) to remove DCM. The EmADF-PLGA nanospheres were then stored at -20°C in powder form, and diluted by 1 × PBS before use.

The ionic gelation technique was utilized as described previously to synthesize chitosan nanospheres (36). To obtain 2.0 mg/ml chitosan solution, 20.0 mg of chitosan (MW: 50-190 kDa, Sigma, Saint Louis, MO, USA) was dissolved in 10.0 ml of 1.0% (*v*/*v*) aqueous solution of acetic acid, then the pH value was regulated to 5.0 by NaOH solution. Then 4.0 ml of rEmADF at 1.0 mg/ml concentration and 2.0 ml of 2.0 mg/ml sodium tripolyphosphate (TPP, Aladdin, Shanghai, China) solution were respectively dropwise mixed with 10 ml of chitosan solution through stirring. Subsequently, the mixture was kept in an ice bath, and tip sonication was conducted in a continuous mode (durative time 4 s, interval time 2 s) under the output power of 50 W for 3 min. After passing through the 0.22 μm filtering membrane, the mixture was then centrifuged at 35,000 rpm for 40 min at 4°C. The supernatants were harvested and stored at -20°C while the precipitates were dissolved in double distill water and stored at -80°C until the liquids were completely frozen. After fully freeze-dried by the same criteria mentioned above, The EmADF-CS nanospheres were stored at -20°C in powder form, and diluted by 1 × PBS before use.

2.5 Nanospheres characterization

To characterize the surface morphology of prepared nanospheres, EmADF-PLGA and EmADF-CS nanospheres were sent to College of science, Nanjing Agriculture University for scanning electron microscope (SEM) observation (SU8010, Hitachi, Tokyo, Japan). Nanospheres in SEM images were randomly measured by ImageJ software (version 1.8.0, NIH, Bethesda, MD, USA) to access the average diameter of prepared nanospheres. The loading capacity (LC) and encapsulation efficiency (EE) of rEmADF were investigated as described previously with slight modification (37), the concentration of uncombined proteins in the supernatant collected in section 2.4 were evaluated by BCA method, and the total volume of collected supernatant was also measured. Then LC and EE can be calculated based on the Formula (2) and (3).

$$\begin{aligned}&\text{Uncombined protein (mg)}\\&= \text{uncombined protein concentration}\\&\times \text{ Supernatant volume}\end{aligned} \quad (1)$$

$$\text{LC (\%)} = \frac{\text{Weight of nanospheres} - \text{uncombined protein}}{\text{Weight of nanospheres}} \times 100\,\% \quad (2)$$

$$\text{EE (\%)} = \frac{\text{Total protein} - \text{uncombined protein}}{\text{Total protein}} \times 100\,\% \quad (3)$$

The *in vitro* cumulative release of antigen from synthesized nanospheres was determined by the previously described method with minor modification (38). Nanospheres in power form were first dissolved in 1 × PBS (pH7.4) at placed in a shaker (37°C, 180 rpm). At an interval of 12 h, samples were taken out and centrifuged at 15,000 rpm for 10 min, and 20 μl of supernatant was harvested and kept at -20°C until use. Samples were resuspended and replaced, and the total volume of nanosphere solutions was recorded. After the last collection, the amount of free antigen in the supernatant was evaluated by Pierce™ BCA Protein Assay Kit. The *in vitro* cumulative release (CR) profile was evaluated by Formula (4).

$$\text{CR (\%)} = \frac{\text{Total volume} \times \text{Protein concentration}}{\text{Total loaded proteins}} \times 100\,\% \quad (4)$$

To analyze the toxicity of formulated nanospheres, BALB/c mice were randomly divided into seven groups with five replicates in each group: Blank (vaccinated with equal volume of 1 × PBS), Control (vaccinated with pET-32a vector protein), EmADF (vaccinated with rEmADF), EmADF-PLGA (vaccinated with EmADF-PLGA nanospheres), and EmADF-CS (vaccinated with EmADF-CS nanospheres) groups. Each animal was intramuscularly injected with a dose containing 300 μg of antigen, and the dosage was three times the usual (5 mg/kg body weight). A booster immunization was also carried out by using the same strategy three days later. One day after the booster immunization, sera were collected from mice's eye sockets, and the levels of blood urea nitrogen (BUN) and creatinine (Cr) were detected by the commercially available

kits (Solarbio, Beijing, China). Throughout the process, the clinical status of animals was kept under constant surveillance.

2.6 Animal immunization and challenge

Newborn chickens were randomly allocated into seven groups with forty replicates in each group. Fourteen-day-old chickens were immunized in the leg muscles with multipoint, and the maximum dosage for single immunization was controlled within 500 µl. Detailed administration dosages were shown in Table 1. Seven days later, primary immunization was followed by a booster dose of immunization using the same vaccination strategy as referenced to the previous studies (39, 40). To demonstrate the protective efficacy elicited by the nanospheres, ten chickens of 22 days old from each group were orally challenged with 5×10^4 *E. mitis* sporulated oocysts (high-dose challenge), while another ten chickens at the same age were orally challenged with 3×10^3 *E. mitis* sporulated oocysts (low-dose challenge, Table 1). Seven days later, all animals were sacrificed under the supervision of Animal Ethics Committee, Nanjing Agriculture University, China. During the seven days after challenge, feces excreted by each low-dose challenged chicken were collected, fully mixed, and kept at 4°C. To investigate the body weight changes, ten of high-dose challenged chickens from each group were weighted at age of 14 day (one day before the first vaccination), 28 days (seven days after the booster vaccination), and 35 days (seven days after the challenge), and the body weight changes of each chicken were calculated following the Formula (5).

$$\text{Coefficient of growth (\%)} = \frac{\text{Final weight} - \text{Initial weight}}{\text{Initial weight}} \times 100\,\% \quad (5)$$

2.7 Detection of antibody and cytokine secretion

At age of 15 (before first vaccination), 22 (seven days after the first vaccination), and 29 day (seven days after the booster vaccination and before challenge), chickens were anesthetized and sera were collected from the heart, and the sera were kept at -20°C until use. According to the previous study (40), enzyme linked immunosorbent (ELISA) assays were carried out to assess the EmADF-specific serum antibody levels. In brief, the 96-well microtiter plate (Corning Costar, Cambridge, USA) was coated with rEmADF (1 µg/well) overnight at 4°C. The sera samples were diluted 1: 100 in TBST with 5% (*w*/*v*) skimmed milk powder. After being rinsed in TBST for 5 min, plates were incubated with 100 µl of the sera for 1 h at 37°C. Rinsed again in TBST, plates were incubated with 1:8,000 dilutions (100 µl each well) of the HRP-conjugated anti-chicken IgY (Abcam, Cambridge, UK) at 37°C for 1 h. After being washed in TBST, 100 µl of 3,3',5,5'-tetramethylbenzidine (TMB, Tiangen, Beijing, China) were added to each well of the plates to develop colors at room temperature. To stop the reactions, 100 µl of 2 M newly prepared H_2SO_4 solutions were added to each well. The absorbance at OD450 was measured on a microplate photometer (Thermo Scientific, Waltham, USA) within 30

TABLE 1 Group assignment and immune procedure.

Group	Treatment (each chicken)	Time for vaccination	Infection dose (each chicken)
Blank (PBS)	Equal volume of 1 × PBS	At 15 and 22 days old	Equal volume of PBS (0 oocyst) at 29 days old
Blank (Coccidia)	Equal volume of 1 × PBS		For high-dose challenge: 5×10^4 oocysts of purified *E. mitis* for each chicken at 29 days old; for low-dose challenge: 3×10^3 oocysts of purified *E. mitis* for each chicken at 29 days old
Control	200 µg pET-32a vector protein		
PLGA	Equal volume of PLGA nanosphere loading 1 × PBS		
CS	Equal volume of CS nanosphere loading 1 × PBS		
EmADF	200 µg rEmADF		
EmADF-PLGA	EmADF-PLGA nanospheres containing 200 µg rEmADF		
EmADF-CS	EmADF-CS nanospheres containing 200 µg rEmADF		

min. Each group involved five biological replicates, and each replication was detected once.

The concentrations of interferon-gamma (IFN-γ), interleukin (IL) 4 (IL-4), transforming growth factor (TGF) β (TGF-β), IL-6, IL-10, and IL-17 in the collected sera were analyzed by commercially available ELISA kits (Enzyme-linked Biotechnology, Shanghai, China) according to the manufacturer's protocol. Each group involved five biological replicates, and each replication was detected once.

2.8 Lymphocytes proliferation assay

At the age of 22 (seven days after the first vaccination) and 29 days (seven days after the booster vaccination and before challenge), five chickens from each group were euthanized to isolate splenic lymphocytes using the commercially available separation solution (TBD, Tianjin, China) in line with the previous report (41). The splenic lymphocytes proliferation assay was conducted using newly separated lymphocytes as reported previously with slight modifications (42). Briefly, splenic lymphocytes were diluted in Dulbecco's Modified Eagle's Medium (DMEM, Invitrogen Biotechnology, Carlsbad, CA, USA) containing 20% (*v*/*v*) fetal bovine serum (FBS) and 20 μg/ml recombinant EmADF proteins. Then 100 μl medium containing 10^5 cells was added into each well of a 96-well plates. Incubated for 72 h at 37°C in a 5% (*v*/*v*) CO_2 atmosphere, each well of the plates was added with 10 μl of Cell Counting Kit 8 reagent (CCK-8, Beyotime Biotech, Shanghai, China). After a four-hour incubation according to the manufacturer's instructions, the absorbance at OD450 was investigated by a microplate photometer. Each group involved five biological replicates, and each replication was detected once.

2.9 Investigation of $CD4^+$ and $CD8^+$ T lymphocytes

As described in section 2.8, splenic lymphocytes were collected and resuspended in 1 × PBS. To evaluate the proportions of $CD4^+$ T lymphocytes subsets, 100 μl medium containing 10^6 lymphocytes were dually stained with FITC-conjugated anti-chicken CD3 (Southern Biotech, Birmingham, AL, USA) and APC-conjugated anti-chicken CD4 (Southern Biotech, Birmingham, AL, USA) for 30 min at 4°C in the dark. As for the percentages of $CD8^+$ T lymphocytes subsets, 10^6 lymphocytes were suspended in 100 μl PBS, and stained with FITC-conjugated anti-chicken CD3 and PE-conjugated anti-chicken CD8 (Southern Biotech, Birmingham, AL, USA) by the same strategy. After being washed in 1 × PBS, cells were sorted by a flow cytometry (Beckman Coulter Inc, Brea, CA, USA), and the populations were determined by CytExpert software (Beckman Coulter Inc, Brea, CA, USA). Noticeably, fluorescence compensation was performed based on the fluorescence minus one (FMO) control before cell sorting. Each group involved five biological replicates, and each replication was detected once.

2.10 *E. mitis* burdens in animals

To evaluate the immune protective efficacy generated by nanospheres, 200 mg feces collected in section 2.6 were lysed to extract genomic DNA by using Stool DNA kit (Omega Bio-Tek, Norcross, GA, USA). According to the unique sequence derived from sequence characterized amplified region (SCAR) markers, absolute quantitative real-time (qPCR) was conducted to demonstrate the parasite burdens in the feces from low-dose challenged chickens (43). To construct the reference standards, the sequence of SCAR markers (GeneBank: AY571506.1) was amplified from the DNA extracts by using the following primers. The forward primer: 5'-GCAGGGCAGGCAGGGTAG-3', and the reverse primer: 5'-GCACGGCAGGCTCAGAAA-3'. High-Fidelity Master Mix was used for PCR reaction according to the instructions. The PCR amplicons of SCAR markers were then subcloned to a linearized pMD-19T vector (Takara Biotechnology, Dalian, China). To evaluate *E. mitis* burdens, PerfectStart® Green qPCR SuperMix (TransGen Biotech, Beijing, China) was used for qPCR amplification with the guidelines of instruction. Furthermore, the melt-curve analysis was also carried out at the end of amplifications, and one uniform peak of the melting curve in each reaction was determined. Each group involved ten biological replicates, and each replication was detected once.

2.11 Statistical analysis

Statistical analysis was evaluated by GraphPad Prism (version 8.0, GraphPad Software, San Diego, CA, USA). Groups were evaluated by using a one-way analysis of variance (ANOVA) followed by Dunnett's test. Comparisons among EmADF, EmADF-PLGA, and EmADF-CS group were conducted by ANOVA following Bonferroni's correction. Values were presented as mean ± standard deviation (SD), and significance was considered at $p< 0.05$.

3 Results

3.1 Production of rEmADF and immunoblot analysis

The vector of pET-32a-EmADF was successfully established, and the results of double enzyme digestion yielded two fragments, approximately 360 bp and 6,000 bp (Figure 1A),

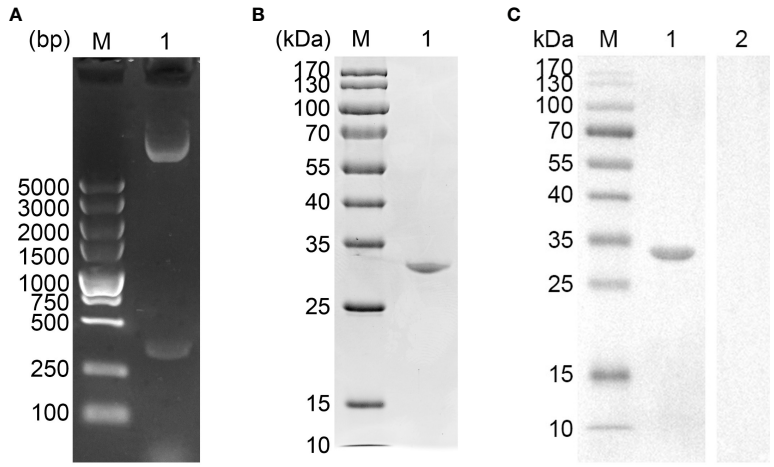

FIGURE 1
(A) Double digestion analysis. Line M: DL5,000 marker; Line 1: Double digestion of the constructed pET-32a-EmADF vector by *Bam*HI and *Hind*III. **(B)** SDS-PAGE analysis. Line M: MW marker proteins. Line 1: purified recombinant EmADF proteins. **(C)** Western blot analysis of purified rEmADF. Line M: MW marker proteins. Line 1: Purified rEmADF were detected by sera from *E. mitis*-infected chickens; Line 2: Purified rEmADF were detected by sera from coccidia-free chickens.

which was in accordance with the theory calculation (363 bp and 5,875 bp). Moreover, sequence analysis also demonstrated the pET-32a-EmADF vector was correctly constructed (Figure S1). Based on the guidelines of pET-32a vector, the recombinant EmADF protein expressed by the constructed vector consisted of his-tag protein (17.7 kDa) and EmADF protein (13.21 kDa). Thus, in theory, the molecular weight of the rEmADF was 30.91 kDa, which matched the result (Figure 1B). Furthermore, the endotoxin level in purified rEmADF felled to 0.1 EU/ml after endotoxin eradication. Demonstrated by western blot assay (Figure 1C), rEmADF could be identified by the chicken sera against *E. mitis*, indicating a satisfactory antigenicity of rEmADF which could elicit the host immunity.

3.2 Characteristics of synthesized nanospheres

The SEM results displayed that EmADF-PLGA (Figure 2A) and EmADF-CS nanospheres (Figure 2B) were uniforms, spherical, and rough surface. According to the SEM results, the diameter of EmADF-PLGA nanospheres was about 94.75 ± 10.41 nm (n = 5) in average, while the mean diameter of EmADF-CS nanospheres sized 79.55 ± 16.51 nm (n = 5). Furthermore, the LC and EE of synthesized nanospheres were also investigated. By using 5.0% PVA and 1.0 mg/ml rEmADF, the LC of EmADF-PLGA nanospheres reached 1.14% (n = 3), while the LC of EmADF-CS nanospheres reached 4.60% (n = 3) using 2.0 mg/ml TPP and 1.0 mg/ml rEmADF. According to the results of three independent trials, the EE of EmADF-PLGA and EmADF-CS nanospheres were 73.39% and 54.31%, respectively.

The release profile of EmADF-PLGA and EmADF-CS nanospheres were investigated by a continuously slow release over a seven-day duration. As illustrated in Figure 3, a burst release indicated with around 27.61% of rEmADF was combined on the surface of PLGA nanospheres, and the initial release of EmADF-CS nanospheres demonstrated that approximately 43.48% rEmADF unbound from CS nanospheres. When compared with the Em1a-CS nanospheres within the first two days, the EmADF-PLGA nanosphere elicited a steadier release. At the fifth day, the CR curve of EmADF-PLGA nanospheres turned to be smooth, while the release profile of EmADF-CS nanospheres became flat after the fourth day.

As the main point of preclinical research, the repeated dose toxicity test plays an important role in evaluating the safety of vaccines before clinical experiments. Thus, the toxicity of EmADF-PLGA and EmADF-CS nanospheres against mice was evaluated (Figure 4), and the levels of BUN and Cr in animals maintained in consistent with the control groups ($p > 0.05$), evaluating the health status of animals could not be affected by the synthesized nanospheres. Moreover, all mice were in good state of clinical health without adverse reaction after immunizations. All these obtained findings indicated that the recombinant EmADF and its nanospheres were harmless to the health of animals.

3.3 Level of antibodies and cytokines

To determine the humoral immunity induced by nanospheres, animals were immunized with 200 μg of purified rEmADF or the formulated nanospheres containing equivalent

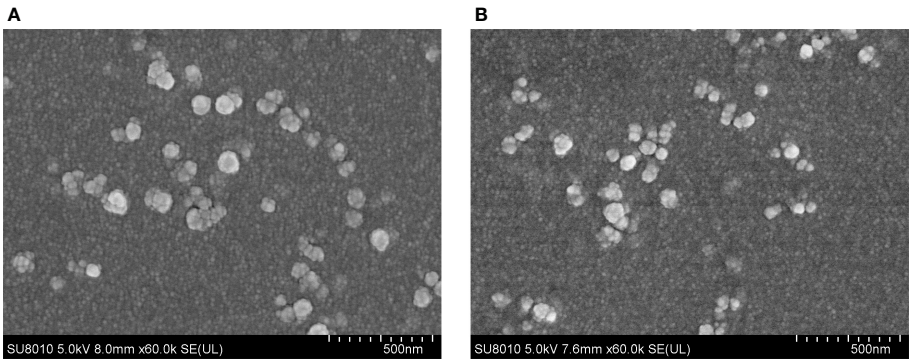

FIGURE 2
The SEM observation of EmADF-PLGA **(A)** and EmADF-CS **(B)** nanospheres. Double emulsion solvent evaporation technique was conducted to formulate EmADF-PLGA nanospheres, while the ionic technique was carried out to synthesize EmADF-CS nanospheres. Bar represented 500 nm.

rEmADF. Sera were collected at age of 15 (before the first immunization), 22 (seven days after the first immunization), and 29 day (seven days after the booster immunization), and the capacity of nanospheres to potentiate antibody immunity in chickens was evaluated by quantifying rEmADF-specific antibodies *via* standard ELISA. As illustrated in Figure 5, animals in EmADF, EmADF-PLGA, and EmADF-CS secreted remarkably higher levels of IgY when compared with the animals in negative groups seven days after the first and booster immunizations ($p< 0.001$). Furthermore, immunizations with EmADF-PLGA and EmADF-CS generated significantly higher IgY than that of rEmADF immunized animals at the age of 22 (seven days after the first immunization) and 29 day (seven days after the booster immunization, $p< 0.01$). When compared with the blank or control group, no rEmADF-specific antibody was detected in the chickens from the PLGA and CS group ($p > 0.05$).

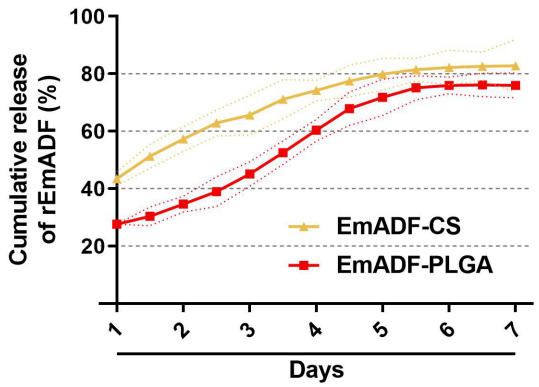

FIGURE 3
In vitro release of recombinant EmADF proteins from EmADF-PLGA and EmADF-CS nanospheres. The concentrations of uncombined proteins in the supernatant were investigated by BCA assay, and the CR profiles were evaluated by the concentrations and the total volumes. Three independent experiments were conducted, and each sample was measured once. Values were presented as the mean of the mean ± SD (n = 3), and SD were represented by the dotted lines.

To further detect the results of T lymphocytes activation, sera were collected from five chickens and the secretions of cytokines were determined by the double-antibody sandwich ELISA. As exhibited in Figure 6A, statistically higher levels of IFN-γ could be detected in EmADF, EmADF-PLGA, and EmADF-CS group ($p< 0.001$), when compared with the negative group. Furthermore, sera from the EmADF-PLGA and EmADF-CS group showed significantly higher levels of IFN-γ than those from EmADF group ($p< 0.001$). As for the TGF-β illustrated in Figure 6B, no statistical difference was indicated between the rEmADF-loaded nanospheres and the EmADF group ($p > 0.05$) at the age of 22 day (seven days after the first immunization). However, the secretions of TGF-β in animals immunized with rEmADF and its nanospheres were promoted after the booster immunization ($p< 0.05$). Chickens from the rEmADF-loaded nanospheres could induce statistically higher levels of IL-4 after the first and booster immunizations ($p< 0.001$, Figure 6C), while at the age of 29 day (seven days after the booster immunization), sera isolated from EmADF-PLGA group were detected with significantly higher levels of IL-4 than those from the EmADF group ($p< 0.001$). Furthermore, rEmADF and its nanospheres could statistically up-regulate the secretions of IL-6 (Figure 6D), IL-10 (Figure 6E), and IL-17 (Figure 6F) after the first and booster immunizations. After the booster vaccination, EmADF-PLGA nanospheres could stimulate the secretions of IL-10 in chickens ($p< 0.001$, Figure 6E), while EmADF-CS nanospheres increased the secretions of IL-17 ($p< 0.01$, Figure 6F). Noticeably, comparisons between the blank and control group revealed consistency in statistics ($p > 0.05$).

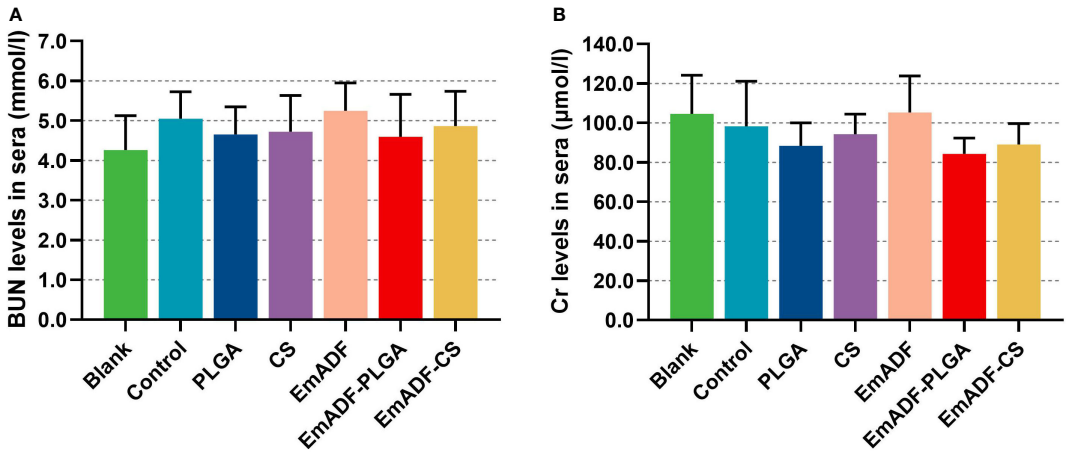

FIGURE 4
The toxicity of recombinant EmADF proteins and its nanospheres. Based on the urease-indophenol and sarcosine oxidase method, the levels of BUN **(A)** and Cr **(B)** were investigated by the commercially available kits. Each group involved five biological replicates, and each replication was detected once. Values were estimated using one-way ANOVA analysis followed by Dunnett's test. Comparisons among EmADF, EmADF-PLGA, and EmADF-CS group were conducted by ANOVA following Bonferroni's correction. Values were presented as the mean of the mean ± SD.

3.4 The proliferation of lymphocytes

The matured dendritic cells could activate T lymphocytes, then the activated T lymphocytes initiated cell proliferation. Thus, the effects of rEmADF and its nanospheres in promoting T cell proliferation was investigated. As illustrated in Figure 7, vaccinations of EmADF, EmADF-PLGA nanospheres, and EmADF-CS nanospheres promoted the lymphocyte proliferation when compared with the negative groups ($p< 0.05$). In addition, the promoting effects were also evaluated in EmADF-PLGA and EmADF-CS nanospheres when compared with rEmADF at the age of 29 day (seven days after the booster immunization, $p< 0.01$).

3.5 Identification the proportions of $CD4^+$ and $CD8^+$ T lymphocytes

Seven days after the first and booster vaccination (at age of 22 and 29 day), lymphocytes were separated by using the

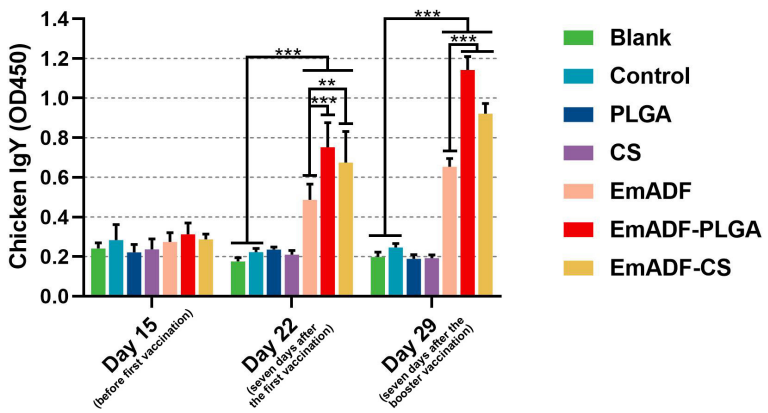

FIGURE 5
Determination of EmADF-specific antibody in the chickens' sera. Each group involved five biological replicates, and each replication was detected once. Values were estimated using one-way ANOVA analysis followed by Dunnett's test. Comparisons among EmADF, EmADF-PLGA, and EmADF-CS group were conducted by ANOVA following Bonferroni's correction. Values were presented as the mean of the mean ± SD. $^{**}p< 0.01$ and $^{***}p< 0.001$.

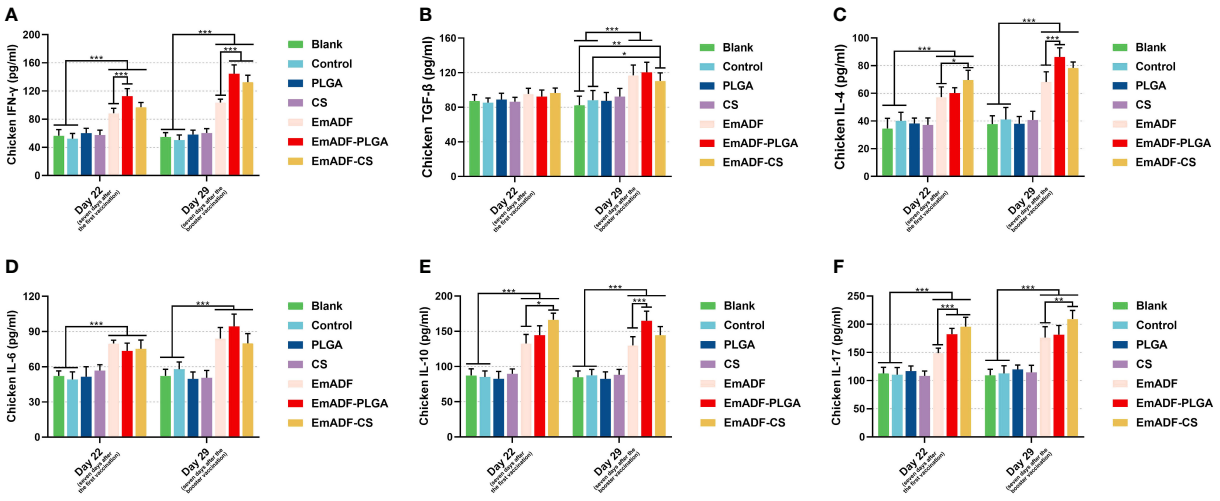

FIGURE 6
Determination of cytokines in chickens' sera. The concentrations of IFN-γ **(A)**, TGF-β **(B)**, IL-4 **(C)**, IL-6 **(D)**, IL-10 **(E)**, and IL-17 **(F)** were illustrated by commercial ELISA kits. Each group involved five biological replicates, and each replication was detected once. Values were estimated using one-way ANOVA analysis followed by Dunnett's test. Comparisons among EmADF, EmADF-PLGA, and EmADF-CS group were conducted by ANOVA following Bonferroni's correction. Values were presented as the mean of the mean ± SD. *$p< 0.05$, **$p< 0.01$, and ***$p< 0.001$.

previously described method. After incubation with the antibodies, lymphocytes were sorted by a flow cytometry. As evaluated in Figure 8A, EmADF-PLGA and EmADF-CS nanospheres could induce significantly higher proportions of $CD4^+$ T cells at the age of 22 (seven days after the first immunization) and 29 day (seven days after the booster immunization, $p< 0.001$). As for the $CD8^+$ T cells showed in Figure 8B, rEmADF and its encapsulations could statistically increase the expression of CD8 molecules on the surface of $CD3^+$ T lymphocytes after the first and second immunizations. Furthermore, EmADF-PLGA nanospheres exhibited the capacity in inducing the differentiation of lymphocytes into $CD8^+$ T cells when compared with rEmADF at the age of 22 (seven days after the first immunization) and 29 day (seven days

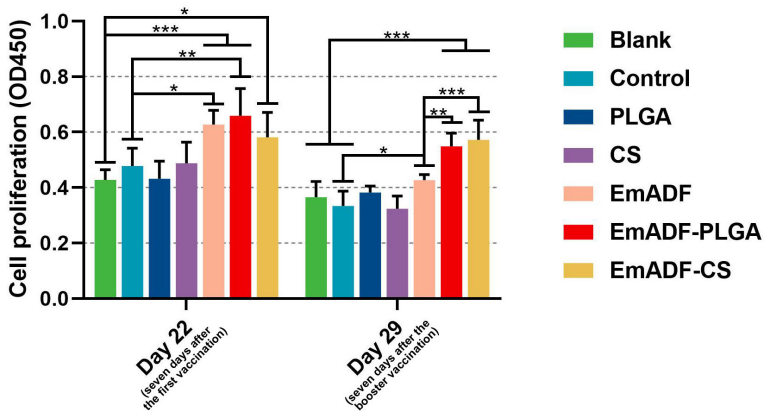

FIGURE 7
The proliferation of chickens' lymphocytes. Chickens in each group were sacrificed, and the lymphocytes was collected. The proliferation of lymphocytes was then determined by CCK-8 reagent. Each group involved five biological replicates, and each replication was detected once. Values were estimated using one-way ANOVA analysis followed by Dunnett's test. Comparisons among EmADF, EmADF-PLGA, and EmADF-CS group were conducted by ANOVA following Bonferroni's correction. Values were presented as the mean of the mean ± SD. *$p< 0.05$, **$p< 0.01$, and ***$p< 0.001$.

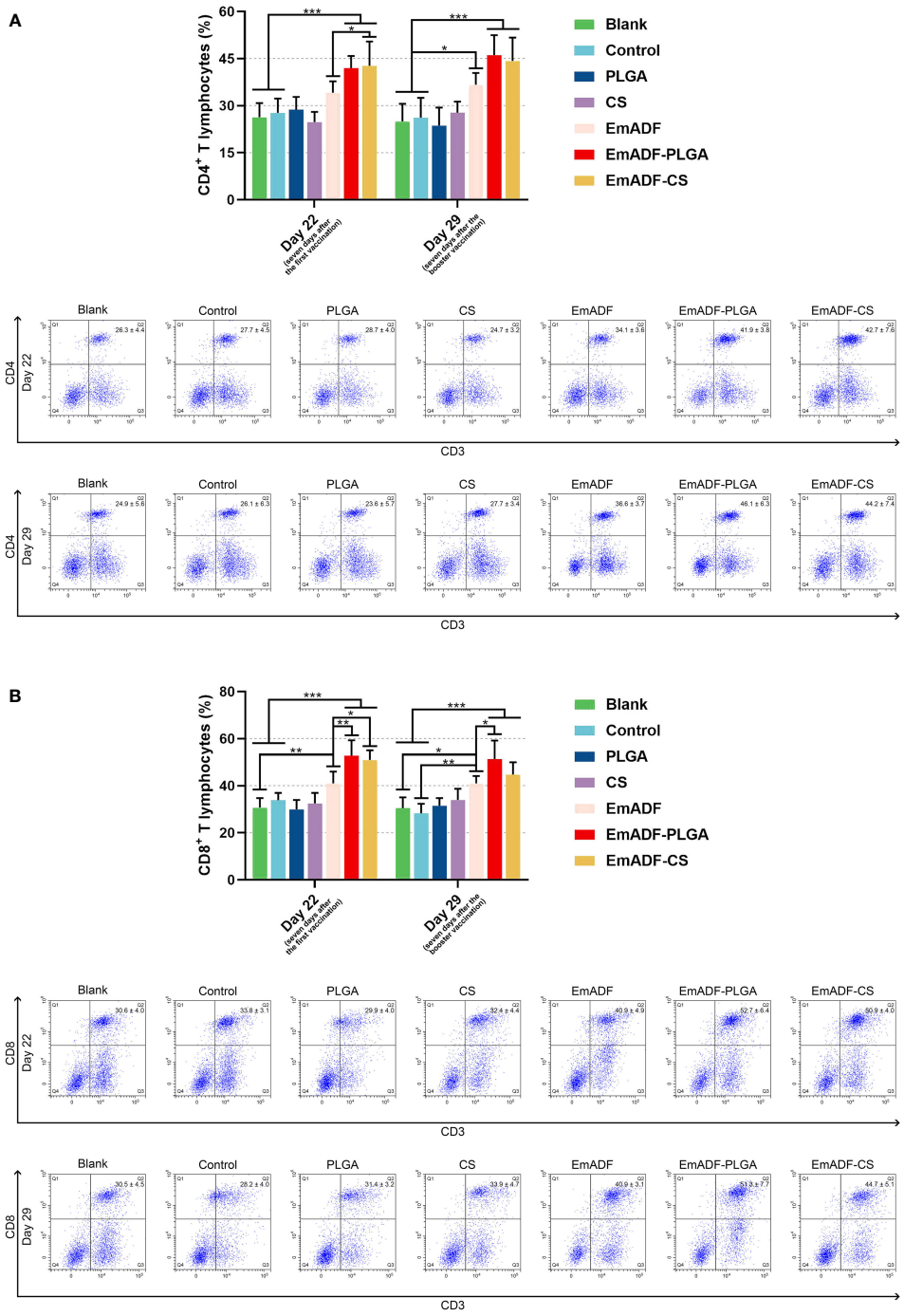

FIGURE 8
Flow cytometry analysis of $CD4^+$ **(A)** and $CD8^+$ T lymphocytes **(B)** in splenocytes at the age of 22 and 29 day. Chickens in each group were sacrificed, and the lymphocytes was collected. Adequate compensation was conducted before cell sorting, and the lymphocytes were analyzed by flow cytometry. Each group involved five biological replicates, and each replication was detected once. Values were estimated using one-way ANOVA analysis followed by Dunnett's test. Comparisons among EmADF, EmADF-PLGA, and EmADF-CS group were conducted by ANOVA following Bonferroni's correction. Values were presented as the mean of the mean ± SD. *p< 0.05, **p< 0.01, and ***p< 0.001.

after the booster immunization, $p< 0.05$). It is noteworthy that no significance was detected in the lymphocytes across any negative group ($p > 0.05$).

3.6 Weight analysis and protective efficacy

In order to study the synthesized nanospheres on weight changes of infected animals, ten chickens from each group were high-dose challenged. All chickens were weighted at the age of 14 (before the first immunization), 28 (seven days after the first immunization), and 35 day (seven days after the booster immunization), and the growth efficiency was calculated. Furthermore, all infected chickens survived during the experimental period. As illustrated in Figure 9, all challenged chickens exhibited significantly inhibition in growth efficiency as compared to the chickens challenged with 1 × PBS (50.94 ± 10.63%, $p< 0.001$). When compared with the challenged animals in negative group (9.11 ± 4.93% in Blank (Coccidia) group, while 10.64 ± 3.86% in control group), animals immunized with rEmADF-loaded nanospheres (19.28 ± 4.9%) showed higher growth efficiency ($p< 0.001$). In addition, among all challenged groups, EmADF-PLGA group (29.56 ± 11.46%) generated significantly higher growth efficiency than EmADF group (25.48 ± 5.84%, $p< 0.01$), while no significant difference evaluated in rEmADF-loaded nanoshperes ($p > 0.05$). All these obtained results highlight the significance of EmADF-PLGA nanospheres in up-regulating the growth efficiency after the infections of *E. mitis*.

To investigate the immunoprotection of the prepared nanospheres, chickens were low-dose challenged. All vaccinated animals survived after *E. mitis* infections, and the oocyst burdens of each chickens were analyzed by qPCR seven days after challenge. When compared with the blank (326.80 ± 38.69 copies) or control group (315.60 ± 36.82 copies), significantly inhabited levels of SCAR markers were evaluated in EmADF (163.07 ± 34.69 copies), EmADF-PLGA (86.52 ± 26.03 copies), and EmADF-CS groups (116.98 ± 21.51 copies, $p< 0.001$, Figure 10), indicating rEmADF enhanced host immunity against *E. mitis*. Moreover, compared with chickens in EmADF group, chickens in EmADF-PLGA ($p< 0.001$) and EmADF-CS group ($p< 0.001$) were detected with lower burdens of *E. mitis*, emphasizing nano-material could boost the immune response. Noticeably, EmADF-PLGA nanospheres showed fewest parasite burdens in the collected feces, demonstrating the strongest anti-*E. mitis* effect. All these findings suggested the efficiency of synthesized nanospheres in eliciting stronger immunity against *E. mitis*.

4 Discussion

As the intracellular protozoan parasite, individual or several *Eimeria* species could cause intestinal coccidiosis in chickens (2, 44), and cause huge economic losses to the poultry industry (12, 45). Compared with medical treatment, poultry immunization has been thought to be critical in reducing occurrence of coccidiosis (15). In recent years, minimal components from *Eimeria* spp. are used as a novel approach to elicit avian coccidiosis resistance (15). Such approaches are designed

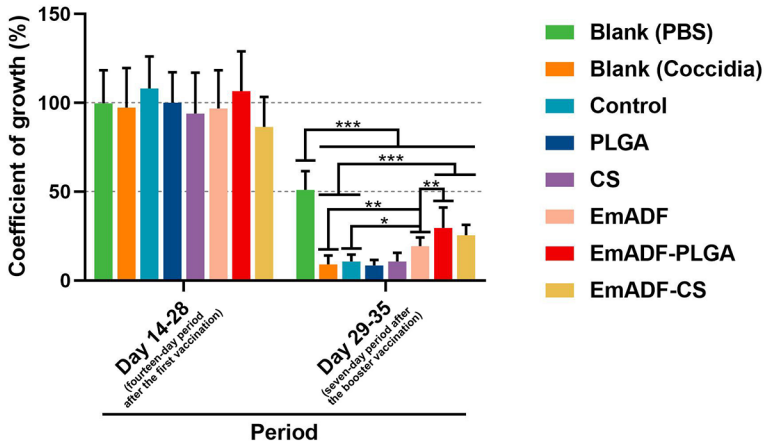

FIGURE 9
The coefficient of growth in immunized chickens. Each chicken was orally challenged with 5×10^4 purified *E. mitis* oocysts seven days after the second vaccination. Chickens were weighted at the age of 14, 28, and 35 days, and the coefficient of growth was calculated. Each group involved ten biological replicates, and each replication was detected once. Values were estimated using one-way ANOVA analysis followed by Dunnett's test. Comparisons among EmADF, EmADF-PLGA, and EmADF-CS group were conducted by ANOVA following Bonferroni's correction. Values were presented as the mean of the mean ± SD. *$p< 0.05$, **$p< 0.01$, and ***$p< 0.001$.

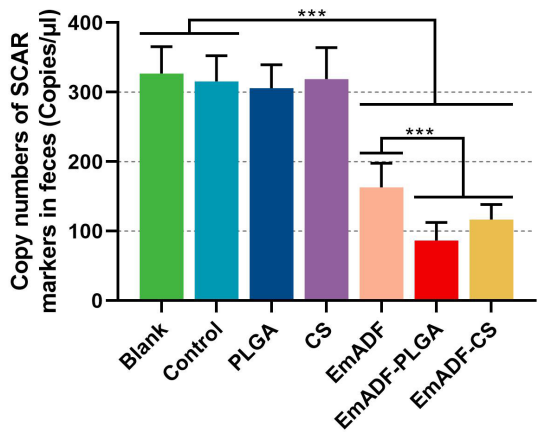

FIGURE 10
E. mitis oocyst burdens in the excreted feces from low-dose challenged chickens. Each chicken was orally challenged with 3,000 purified *E. mitis* oocysts seven days after the booster immunization. Seven days after challenge, feces of each chicken were collected for DNA extractions. Each group involved ten biological replicates, and each replication was detected three times. Values were estimated using one-way ANOVA analysis followed by Dunnett's test. Comparisons among EmADF, EmADF-PLGA, and EmADF-CS group were conducted by ANOVA following Bonferroni's correction. Values were presented as the mean of the mean ± SD. ***$p < 0.001$.

according to parasites' antigens, and the immunogenicity of parasites remained (46). Detailed studies in *Eimeria* genomics with novel tools have revealed many microbial proteins that are considered as the candidates of vaccine antigens (47, 48). Many *Eimeria* antigens are utilized to construct the anticoccidial vaccines, such as surface antigen (49), apical membrane antigen (11, 50), microneme (51, 52), rhoptry, profilin (53) etc. Although the antigens mentioned above have been proved to be effective in eliciting host immunity against the *Eimeria* species, these antigens could not provide fully immunoprotections against coccidiosis. In addition, different antigens could induce *E. mitis*-specific immunity through different immune effector mechanisms, and the immune effects were mainly evaluated by parasite-challenge (14). The present study focused on the *E. mitis* actin-depolymerizing factor, which intimately participated in the modification of the cytoskeleton and motility of *Eimeria* species (54). The recombinant EmADF protein was first expressed by the prokaryotic expression system, and the immunogenicity was investigated by western blot. Then rEmADF was entrapped in nanospheres to protect protease-antigens from degradation, and the immunoprotection of synthesized nanospheres was subsequently analyzed in animals. The results indicated that EmADF-PLGA and EmADF-CS nanospheres were spherical in shape and nontoxic with satisfactory immunogenicity. *In vivo*, rEmADF-loaded nanospheres exhibited potent immune enhancement in inducing humoral and cellular immune response, and were capable of evoking growth efficiency and inhabiting *E. mitis* burdens in feces. All these obtained findings suggested that EmADF-PLGA and EmADF-CS nanospheres could be an efficient approach to prevent the infections of *E. mitis*.

Nanosphere-based vaccines offer the chances as highly safe and effective alternatives to traditional subunit vaccines (55, 56). Currently, many techniques have been exhibited much advantage in nanosphere formulation (40, 57). Under such circumstances, we successfully prepared rEmADF-loaded PLGA and CS nanospheres by double emulsion solvent evaporation and ionic gelation technique, respectively. The obtained EmADF-PLGA and EmADF-CS nanospheres were nanosized with spherical shape that was considered as easier to be absorbed by cells (58). As reported previously (59), nanospheres sized approximately 100 nm were easier to go through cell membrane in Hela cell lines when compared with those sized about 1,000 nm in diameter. The published studies also showed that the CS nanospheres sized about 300 nm in diameter gained better absorption compared with the nanospheres sized 1,000 and 3,000 nm in diameter (60). All these results imply that our prepared nanospheres may have more advantages in inducting host immunity. Notably, LC and EE of nanospheres vary in the published studies. Followed by the similar procedures, the EE and LC reached 82.40 ± 0.06% and 2.00 ± 0.01% respectively in PLGA-rEtTA4 nanospheres (40). Reported in another paper, the EE was 89.35 ± 1.18% in PLGA-rEm14-3-3 nanospheres, and in CS-rEm14-3-3 nanospheres reaches 83.46% (61). However, by using similar procedures with minor modifications, the EE reached 55% in the formulation of CS-PLGA-rOmp22 nanospheres, while the LC was about 0.94% (62). Such phenomena may be caused by the encapsulated antigens and synthesized methods, and furthermore affect LC and EE (36, 57). The subsequent studies should focus on the effects of loaded antigens and synthesized procedures on LC and EE in formulating nanospheres.

Due to the slow diffusion of the loaded antigens into the medium, nanospheres can decrease the times of immunity and improve the antigen-presenting in APCs (63, 64). In the current research, the slow-release profile of EmADF-PLGA and EmADF-CS nanospheres was observed, and a more stable release was also detected in EmADF-CS nanospheres when compared with the EmADF-PLGA nanospheres. Moreover, the synthesized nanospheres were spherical in appearance, which seems play an important role in inhabiting obvious burst release. As a polyester that is nontoxic, PLGA could combine with lipid monolayers, and then promote the slow release of antigens (64). Similarly, chitosan, served as a cation polysaccharide, can bind to the cell membranes, leading to a long-term residence (65). However, the burst release of formulated nanospheres occurred at the first day, and such characteristic may be driven by the unbound antigens. In addition, the diameter, polarity, molecular weight, even the encapsulations of the nanospheres can affect the burst release (66). Noticeably, the prospect of nanospheres in vaccines is

usually limited by their toxicity for mammals (67). In all reagents used in nanosphere formulations, only DCM was regarded as toxic and hard to erase by evaporation (68). Therefore, the EmADF-PLGA nanospheres were fully freeze-fried to fully remove the toxicity. Unsurprisingly, no toxic side effect occurred and all experimental animals were kept in good clinical status, demonstrating the synthesized nanospheres could be applied to animal immunization.

By preventing the parasites from attaching to the surface of host cells (69), largely produced IgY plays an crucial role in resisting the infection of *Eimeria* species (70). Based on the results of standard ELISA, high titers of EmADF-specific IgY antibody were illustrated in chickens vaccinated with rEmADF-loaded nanospheres. These findings implied the qualified immunogenicity of expressed rEmADF, and the enhanced humoral immunity induced by the rEmADF-loaded nanospheres.

Cytokines are the essential factors in modulating naïve T cells differentiation into either Th1 or Th2 type cells (71, 72), and play a crucial role in the process against avian coccidiosis (1, 8). By augmenting the production of IFN-γ, the pro-inflammatory cytokines enhance the Th1 immune response, which is considered to be predominant in resisting the replications of *Eimeria* species (72–74). Based on the results of double antibody sandwich ELISA, promoted levels of IFN-γ were confirmed in animals' sera vaccinated with EmADF-PLGA and EmADF-CS nanospheres, emphasizing the Th1-related immune response was induced. Additionally, driven by IL-4 cytokine, Th2 immunity also plays an important role in resisting the coccidiosis (72). Secreted by the $CD4^+$ follicular helper T (Tfh) cells and $CD4^+$ Th2 cells (75), IL-4 cytokines mediate humoral immunity in the interface of host and parasite (76). Significant high levels of IL-4 cytokine were evaluated in the animals vaccinated with rEmADF and its nanospheres in the current study, demonstrating the Th2 cell mediated and Tfh-related immunity was activated. With the existence of TGF-β, $CD4^+$ Th2 cells can differentiate to $CD4^+$ Th9 cells as previously reported (77, 78). Participated in the immunity against *Eimeria* species, the activated $CD4^+$ Th9 cells could release IL-10, an anti-inflammatory cytokine, which related to the maintenance and reestablishment of host immune system (79). However, as a double-edged sword largely released by inducible regulatory T (iTreg) cells, TGF-β cytokines are mainly involved in host immunosuppression (80). At the present study, animals vaccinated with rEmADF-loaded nanospheres were observed with enhanced TGF-β and IL-10 at the age of 29 day, indicating the Th9 cell mediated immunity was activated in host immune response against avian coccidiosis, and the slight immunosuppression was also induced. By inducing the specific differentiation of naïve T cells to $CD4^+$ Th17 cells (81), IL-6 cytokines play an important role in connecting innate to the adaptive immunity (82). In addition, IL-6 cytokines are also proved to be essential in induction of cytotoxic T cells (83). Morevoer, the mRNA levels of chicken IL-17 cytokines are up-regulated in intestinal intraepithelial lymphocytes (IELs) after *Eimeria* infections, suggesting the IL-17 cytokine is related to the immunity against the invasion of parasites (84, 85). As a symbolic cytokine generated by $CD4^+$ Th17 cells, IL-17 also participated in the secretion of IL-6 (86), and exerts a pro-inflammatory effect in inhabiting the infections of *Eimeria* species (87, 88). In our study, the secretions of IL-6 and IL-17 were statistically promoted in the animals vaccinated with rEmADF and its nanospheres, indicating the adaptive immune response was induced in anti-*E. mitis* defense.

With the participation of both $CD4^+$ and $CD8^+$ T lymphocytes, cell-mediated immunity exhibits a dominant role in inducing an antigen-specific immunoprotection against *Eimeria* species (1, 72, 89). Acted as the effector cells, $CD8^+$ T cells could generate cytokines to generate cytotoxic effect in anticoccidial immunity, while $CD4^+$ T cells were of great assistance in the formulation of $CD8^+$ T cells (72, 76). Furthermore, the activation of $CD4^+$ T cells requires two signals, major histocompatibility complex II (MHC-II) and costimulatory molecules (90, 91), while $CD4^+$ T cells as well as the antigen-presenting cells (APC) play an important role in $CD8^+$ T cell activation (92, 93). The activated $CD8^+$ T cells will go through two phases: proliferation and differentiation (94). Different Th lymphocytes can be polarized by T lymphocytes, and determine the type of host immunoprotection (95). In the current study, CCK-8 assay was recruited to illustrate the effects of rEmADF on the lymphocyte proliferation *in vivo*. Compared with the rEmADF-immunized group, groups immunized with rEmADF-loaded nanospheres displayed greater proliferation after the booster immunization, suggesting EmADF-PLGA and EmADF-CS nanospheres were essential in promoting the proliferation of splenic lymphocytes in chicken. In addition, the flow cytometry was recruited to evaluate the proportions of $CD4^+$ and $CD8^+$ T cells, and all positive groups were illustrated with higher levels compared with the negative groups, indicating that rEmADF as well as its encapsulations were mainly responsible for the percentages of $CD4^+$ and $CD8^+$ T cells in animals. According to results, rEmADF and its encapsulations could induce the generation of cellular immunity against coccidiosis, and the encapsulations in nanospheres could further confer the cellular resistance.

Many researches indicate that encapsulations in nanospheres could strengthen the entrapped antigens in host immunity against specific pathogens (96). Entrapped in a novel adjuvant, named QCDC, the recombinant *E. acervulina* profilin proteins could better up-regulate weight gains and reduce the oocysts in feces excreted by the challenged animals (97). Encapsulated in the nanospheres formulated by Xu et al., *E. mitis* 1a protein exhibited higher immune response in resisting parasites (98). Similar findings also confirmed by Huang et al. in Hy-Line chickens vaccinated with PLGA nanospheres loaded with recombinant *E. tenella* TA4 proteins (40). To analyze the best encapsulation in the current study, the weight changes and parasites burdens of immunized chickens after challenge were investigated. Chickens

were high-dose challenged to evaluate the impact of synthesized nanospheres on animals' growth efficiency, and only the EmADF-PLGA nanospheres induced statistically higher growth efficiency compared with the naked antigens. To demonstrate the effects of nanospheres in inhabiting *E. mitis* oocysts, animals were low-dose challenged and the copy number of SCAR markers in feces were investigated by qPCR. The results showed chickens immunized with EmADF-PLGA or EmADF-CS nanospheres received a lower parasites burden in feces. Highlighted its advantages in promoting the growth efficiency and resisting the infections of *E. mitis*, all these obtained findings lent credit to the idea that both EmADF-PLGA and EmADF-CS nanospheres could induce a satisfactorily protective immunity.

Conclusion

Collectively, our research first prepared rEmADF by prokaryotic expression. Entrapped in PLGA and CS nanospheres *via* double emulsion solvent evaporation technique and ionic technique, the protective efficiency of rEmADF and its encapsulations were then evaluated in chickens. The obtained results ratified that rEmADF-loaded nanospheres could elicit strongly humoral and cellular immunity against the infections of *E. mitis*. Compared with naked antigens, EmADF-PLGA and EmADF-CS nanospheres could significantly increase host immunity against *E. mitis*, and were regarded as the superior vaccines in the present research. Despite its strongly protective efficiency, both EmADF-PLGA and EmADF-CS nanospheres could not provide fully protections against the infections of *E. mitis*. Consequently, future studies on the novel nanospheres should optimize the administration strategy, dose, and route to enhance host immune protections as well as the animals' growth efficiency.

Data availability statement

The original contributions presented in the study are included in the article/Supplementary Material. Further inquiries can be directed to the corresponding author.

Ethics statement

The animal study was reviewed and approved by Animal Ethics Committee, Nanjing Agriculture University, Nanjing, China.

Author contributions

LX and XL designed the research. ZY, LX and KH conducted the research. ZY, KH, and ML analyzed the data. ZY and LX wrote the manuscript. RY and XS participated in the revision of the manuscript. All authors contributed to the article and approved the submitted version.

Funding

This work was supported by Joint Research Project between National Natural Science Foundation of China and Pakistan Science Foundation (NSFCPSF, 31661143017).

Acknowledgments

With the help on data analysis, we would greatly thank vice prof. Yanli Yu in School of Economics and Management, Ningxia University, Yinchuan, China. Furthermore, we would give our thanks to Dr. HaiFeng Sun in MOA key laboratory of Animal Bacteriology, Nanjing Agricultural University, Nanjing, China, with the technical assistance in flow cytometry.

Conflict of interest

The authors declare that the research was conducted in the absence of any commercial or financial relationships that could be construed as a potential conflict of interest.

Publisher's note

All claims expressed in this article are solely those of the authors and do not necessarily represent those of their affiliated organizations, or those of the publisher, the editors and the reviewers. Any product that may be evaluated in this article, or claim that may be made by its manufacturer, is not guaranteed or endorsed by the publisher.

Publisher's note

All claims expressed in this article are solely those of the authors and do not necessarily represent those of their affiliated organizations, or those of the publisher, the editors and the reviewers. Any product that may be evaluated in this article, or claim that may be made by its manufacturer, is not guaranteed or endorsed by the publisher.

Supplementary material

The Supplementary Material for this article can be found online at: https://www.frontiersin.org/articles/10.3389/fimmu.2022.1080630/full#supplementary-material

References

1. Chapman HD. Milestones in avian coccidiosis research: A review. *Poult Sci* (2014) 93(3):501–11. doi: 10.3382/ps.2013-03634

2. Venkatas J, Adeleke MA. A review of *Eimeria* antigen identification for the development of novel anticoccidial vaccines. *Parasitol Res* (2019) 118(6):1701–10. doi: 10.1007/s00436-019-06338-2

3. Vrba V, Poplstein M, Pakandl M. The discovery of the two types of small subunit ribosomal rna gene in eimeria mitis contests the existence of *E. mivati* as an independent species. *Vet Parasitol* (2011) 183(1-2):47–53. doi: 10.1016/j.vetpar.2011.06.020

4. Reid AJ, Blake DP, Ansari HR, Billington K, Browne HP, Bryant J, et al. Genomic analysis of the causative agents of coccidiosis in domestic chickens. *Genome Res* (2014) 24(10):1676–85. doi: 10.1101/gr.168955.113

5. Fitz-Coy SH, Edgar SA. Pathogenicity and control of *Eimeria mitis* infections in broiler chickens. *Avian Dis* (1992) 36(1):44–8. doi: 10.2307/1591713

6. López-Osorio S, Chaparro-Gutiérrez JJ, Gómez-Osorio LM. Overview of poultry *Eimeria* life cycle and host-parasite interactions. *Front Vet Sci* (2020) 7:384. doi: 10.3389/fvets.2020.00384

7. Fitz-Coy SH, Edgar SA. Effects of *Eimeria mitis* on egg production of single-comb white leghorn hens. *Avian Dis* (1992) 36(3):718–21. doi: 10.2307/1591771

8. Dalloul RA, Lillehoj HS. Poultry coccidiosis: Recent advancements in control measures and vaccine development. *Expert Rev Vaccines* (2006) 5(1):143–63. doi: 10.1586/14760584.5.1.143

9. Mesa-Pineda C, Navarro-Ruíz JL, López-Osorio S, Chaparro-Gutiérrez JJ, Gómez-Osorio LM. Chicken coccidiosis: From the parasite lifecycle to control of the disease. *Front Vet Sci* (2021) 8:787653. doi: 10.3389/fvets.2021.787653

10. Blake DP, Marugan-Hernandez V, Tomley FM. Spotlight on avian pathology: Eimeria and the disease coccidiosis. *Avian Pathol* (2021) 20:1–5. doi: 10.1080/03079457.2021.1912288

11. Fatoba AJ, Adeleke MA. Transgenic *Eimeria* parasite: A potential control strategy for chicken coccidiosis. *Acta Trop* (2020) 205:105417. doi: 10.1016/j.actatropica.2020.105417

12. Blake DP, Tomley FM. Securing poultry production from the ever-present *Eimeria* challenge. *Trends Parasitol* (2014) 30(1):12–9. doi: 10.1016/j.pt.2013.10.003

13. Ahmad TA, El-Sayed BA, El-Sayed LH. Development of immunization trials against *Eimeria* spp. *Trials Vaccinol* (2016) 5:38–47. doi: 10.1016/j.trivac.2016.02.001

14. Soutter F, Werling D, Tomley FM, Blake DP. Poultry coccidiosis: Design and interpretation of vaccine studies. *Front Vet Sci* (2020) 7:101. doi: 10.3389/fvets.2020.00101

15. Zaheer T, Abbas RZ, Imran M, Abbas A, Butt A, Aslam S, et al. Vaccines against chicken coccidiosis with particular reference to previous decade: Progress, challenges, and opportunities. *Parasitol Res* (2022) 121(10):2749–63. doi: 10.1007/s00436-022-07612-6

16. Bernstein BW, Bamburg JR. Adf/Cofilin: A functional node in cell biology. *Trends Cell Biol* (2010) 20(4):187–95. doi: 10.1016/j.tcb.2010.01.001

17. Santos JM, Lebrun M, Daher W, Soldati D, Dubremetz JF. Apicomplexan cytoskeleton and motors: Key regulators in morphogenesis, cell division, transport and motility. *Int J Parasitol* (2009) 39(2):153–62. doi: 10.1016/j.ijpara.2008.10.007

18. Fuhrmann J, Käs J, Stevens A. Initiation of cytoskeletal asymmetry for cell polarization and movement. *J Theor Biol* (2007) 249(2):278–88. doi: 10.1016/j.jtbi.2007.08.013

19. Zhou BH, Wang HW, Xue FQ, Wang XY, Yang FK, Ban MM, et al. Actin-depolymerizing factor of second-generation merozoite in *Eimeria tenella*: Clone, prokaryotic expression, and diclazuril-induced mrna expression. *Parasitol Res* (2010) 106(3):571–6. doi: 10.1007/s00436-009-1699-z

20. Zhao Y, Xu R, Zhang Y, Ji X, Zhang J, Liu Y, et al. Protective efficacy in chickens of recombinant plasmid Pet32a(+)-Adf-3-1e of *Eimeria acervulina*. *Parasitol Res* (2014) 113(8):3007–14. doi: 10.1007/s00436-014-3963-0

21. Lai L, Bumstead J, Liu Y, Garnett J, Campanero-Rhodes MA, Blake DP, et al. The role of sialyl glycan recognition in host tissue tropism of the avian parasite *Eimeria tenella*. *PloS Pathog* (2011) 7(10):e1002296. doi: 10.1371/journal.ppat.1002296

22. Tan L, Li Y, Yang X, Ke Q, Lei W, Mughal MN, et al. Genetic diversity and drug sensitivity studies on *Eimeria tenella* field isolates from hubei province of China. *Parasit Vectors* (2017) 10(1):137. doi: 10.1186/s13071-017-2067-y

23. Francis MJ. Recent advances in vaccine technologies. *Vet Clin North Am Small Anim Pract* (2018) 48(2):231–41. doi: 10.1016/j.cvsm.2017.10.002

24. Blake DP, Pastor-Fernández I, Nolan MJ, Tomley FM. Recombinant anticoccidial vaccines - a cup half full? *Infect Genet Evol* (2017) 55:358–65. doi: 10.1016/j.meegid.2017.10.009

25. Kwon YJ, James E, Shastri N, Fréchet JM. *In vivo* targeting of dendritic cells for activation of cellular immunity using vaccine carriers based on ph-responsive microparticles. *Proc Natl Acad Sci U.S.A.* (2005) 102(51):18264–8. doi: 10.1073/pnas.0509541102

26. Reddy ST, van der Vlies AJ, Simeoni E, Angeli V, Randolph GJ, O'Neil CP, et al. Exploiting lymphatic transport and complement activation in nanoparticle vaccines. *Nat Biotechnol* (2007) 25(10):1159–64. doi: 10.1038/nbt1332

27. van Riet E, Ainai A, Suzuki T, Kersten G, Hasegawa H. Combatting infectious diseases; nanotechnology as a platform for rational vaccine design. *Adv Drug Delivery Rev* (2014) 74:28–34. doi: 10.1016/j.addr.2014.05.011

28. Skwarczynski M, Toth I. Peptide-based synthetic vaccines. *Chem Sci* (2016) 7(2):842–54. doi: 10.1039/c5sc03892h

29. Chavan YR, Tambe SM, Jain DD, Khairnar SV, Amin PD. Redefining the importance of polylactide-Co-Glycolide acid (Plga) in drug delivery. *Ann Pharm Fr* (2022) 80(5):603–16. doi: 10.1016/j.pharma.2021.11.009

30. Chereddy KK, Vandermeulen G, Préat V. Plga based drug delivery systems: Promising carriers for wound healing activity. *Wound Repair Regener* (2016) 24(2):223–36. doi: 10.1111/wrr.12404

31. Shariatinia Z. Pharmaceutical applications of chitosan. *Adv Colloid Interface Sci* (2019) 263:131–94. doi: 10.1016/j.cis.2018.11.008

32. Li X, Xing R, Xu C, Liu S, Qin Y, Li K, et al. Immunostimulatory effect of chitosan and quaternary chitosan: A review of potential vaccine adjuvants. *Carbohydr Polym* (2021) 264:118050. doi: 10.1016/j.carbpol.2021.118050

33. Illum L. Chitosan and its use as a pharmaceutical excipient. *Pharm Res* (1998) 15(9):1326–31. doi: 10.1023/a:1011929016601

34. Tomley F. Techniques for isolation and characterization of apical organelles from *Eimeria tenella* sporozoites. *Methods* (1997) 13(2):171–6. doi: 10.1006/meth.1997.0509

35. Salari F, Varasteh AR, Vahedi F, Hashemi M, Sankian M. Down-regulation of Th2 immune responses by sublingual administration of poly (Lactic-Co-Glycolic) acid (Plga)-encapsulated allergen in Balb/C mice. *Int Immunopharmacol* (2015) 29(2):672–8. doi: 10.1016/j.intimp.2015.09.011

36. Fan W, Yan W, Xu Z, Ni H. Formation mechanism of monodisperse, low molecular weight chitosan nanoparticles by ionic gelation technique. *Colloids Surf B Biointer* (2012) 90:21–7. doi: 10.1016/j.colsurfb.2011.09.042

37. Zhao K, Zhang Y, Zhang X, Li W, Shi C, Guo C, et al. Preparation and efficacy of Newcastle disease virus DNA vaccine encapsulated in chitosan nanoparticles. *Int J Nanomed* (2014) 9:389–402. doi: 10.2147/ijn.S54226

38. Derman S, Mustafaeva ZA, Abamor ES, Bagirova M, Allahverdiyev A. Preparation, characterization and immunological evaluation: Canine parvovirus synthetic peptide loaded plga nanoparticles. *J BioMed Sci* (2015) 22:89. doi: 10.1186/s12929-015-0195-2

39. Zhang B, Yuan C, Song X, Xu L, Yan R, Shah MAA, et al. Optimization of immunization procedure for *Eimeria tenella* DNA vaccine Pvax1-Petk2-Il-2 and its stability. *Acta Parasitol* (2019) 64(4):745–52. doi: 10.2478/s11686-019-00090-4

40. Huang J, Chen S, Zhou Z, Sun X, Haseeb M, Lakho SA, et al. Poly (D, l-Lactide-Co-Glycolide) delivery system improve the protective efficacy of recombinant antigen Ta4 against *Eimeria tenella* infection. *Poult Sci* (2021) 100(5):101083. doi: 10.1016/j.psj.2021.101083

41. Sasai K, Aita M, Lillehoj HS, Miyamoto T, Fukata T, Baba E. Dynamics of lymphocyte subpopulation changes in the cecal tonsils of chickens infected with *Salmonella enteritidis*. *Vet Microbiol* (2000) 74(4):345–51. doi: 10.1016/s0378-1135(00)00193-0

42. Nikbakht M, Pakbin B, Nikbakht Brujeni G. Evaluation of a new lymphocyte proliferation assay based on cyclic voltammetry; an alternative method. *Sci Rep* (2019) 9(1):4503. doi: 10.1038/s41598-019-41171-8

43. Vrba V, Blake DP, Poplstein M. Quantitative real-time pcr assays for detection and quantification of all seven eimeria species that infect the chicken. *Vet Parasitol* (2010) 174(3-4):183–90. doi: 10.1016/j.vetpar.2010.09.006

44. Madlala T, Okpeku M, Adeleke MA. Understanding the interactions between *Eimeria* infection and gut microbiota, towards the control of chicken coccidiosis: A review. *Parasite* (2021) 28:48. doi: 10.1051/parasite/2021047

45. Witcombe DM, Smith NC. Strategies for anti-coccidial prophylaxis. *Parasitology* (2014) 141(11):1379–89. doi: 10.1017/s0031182014000195

46. Parvizpour S, Pourseif MM, Razmara J, Rafi MA, Omidi Y. Epitope-based vaccine design: A comprehensive overview of bioinformatics approaches. *Drug Discovery Today* (2020) 25(6):1034–42. doi: 10.1016/j.drudis.2020.03.006

47. Blake DP, Billington KJ, Copestake SL, Oakes RD, Quail MA, Wan KL, et al. Genetic mapping identifies novel highly protective antigens for an apicomplexan parasite. *PloS Pathog* (2011) 7(2):e1001279. doi: 10.1371/journal.ppat.1001279

48. Blake DP. *Eimeria* genomics: Where are we now and where are we going? *Vet Parasitol* (2015) 212(1-2):68–74. doi: 10.1016/j.vetpar.2015.05.007

49. Geng T, Luo L, Wang Y, Shen B, Fang R, Hu M, et al. Evaluation of immunoprotective effects of recombinant proteins and DNA vaccines derived from *Eimeria tenella* surface antigen 6 and 15 in vivo. *Parasitol Res* (2022) 121(1):235–43. doi: 10.1007/s00436-021-07364-9

50. Ma C, Li G, Chen W, Jia Z, Yang X, Pan X, et al. *Eimeria tenella*: Imp1 protein delivered by lactococcus lactis induces immune responses against homologous challenge in chickens. *Veterinary Parasitol* (2021) 289:109320. doi: 10.1016/j.vetpar.2020.109320

51. Zhang Z, Huang J, Li M, Sui Y, Wang S, Liu L, et al. Identification and molecular characterization of microneme 5 of *Eimeria acervulina*. *PloS One* (2014) 9(12):e115411. doi: 10.1371/journal.pone.0115411

52. Chen W, Ma C, Li G, Jia Z, Yang X, Pan X, et al. Specific Etmic3-binding peptides inhibit *Eimeria tenella* sporozoites entry into host cells. *Vet Res* (2021) 52 (1):24. doi: 10.1186/s13567-020-00873-y

53. Tang X, Suo J, Li C, Du M, Wang C, Hu D, et al. Transgenic *Eimeria tenella* expressing profilin of *Eimeria maxima* elicits enhanced protective immunity and alters gut microbiome of chickens. *Infect Immun* (2018) 86(9):e00888-17. doi: 10.1128/iai.00888-17

54. Fowler RE, Margos G, Mitchell GH. The cytoskeleton and motility in apicomplexan invasion. *Adv Parasitol* (2004) 56:213–63. doi: 10.1016/s0065-308x (03)56004-3

55. Peek LJ, Middaugh CR, Berkland C. Nanotechnology in vaccine delivery. *Adv Drug Delivery Rev* (2008) 60(8):915–28. doi: 10.1016/j.addr.2007.05.017

56. Xing L, Fan YT, Zhou TJ, Gong JH, Cui LH, Cho KH, et al. Chemical modification of chitosan for efficient vaccine delivery. *Molecules* (2018) 23(2):229. doi: 10.3390/molecules23020229

57. Allahyari M, Mohit E. Peptide/Protein vaccine delivery system based on plga particles. *Hum Vaccin Immunother* (2016) 12(3):806–28. doi: 10.1080/21645515.2015.1102804

58. Vasir JK, Labhasetwar V. Quantification of the force of nanoparticle-cell membrane interactions and its influence on intracellular trafficking of nanoparticles. *Biomaterials* (2008) 29(31):4244–52. doi: 10.1016/j.biomaterials.2008.07.020

59. Gratton SE, Ropp PA, Pohlhaus PD, Luft JC, Madden VJ, Napier ME, et al. The effect of particle design on cellular internalization pathways. *Proc Natl Acad Sci U.S.A.* (2008) 105(33):11613–8. doi: 10.1073/pnas.0801763105

60. Koppolu B, Zaharoff DA. The effect of antigen encapsulation in chitosan particles on uptake, activation and presentation by antigen presenting cells. *Biomaterials* (2013) 34(9):2359–69. doi: 10.1016/j.biomaterials.2012.11.066

61. Haseeb M, Huang J, Lakho SA, Yang Z, Hasan MW, Ehsan M, et al. Em14-3-3 delivered by plga and chitosan nanoparticles conferred improved protection in chicken against *Eimeria maxima*. *Parasitol Res* (2022) 121(2):675–89. doi: 10.1007/s00436-021-07420-4

62. Du X, Xue J, Jiang M, Lin S, Huang Y, Deng K, et al. A multiepitope peptide, Romp22, encapsulated in chitosan-plga nanoparticles as a candidate vaccine against *Acinetobacter baumannii* infection. *Int J Nanomed* (2021) 16:1819–36. doi: 10.2147/ijn.S296527

63. Silva AL, Soema PC, Slütter B, Ossendorp F, Jiskoot W. Plga particulate delivery systems for subunit vaccines: Linking particle properties to immunogenicity. *Hum Vaccin Immunother* (2016) 12(4):1056–69. doi: 10.1080/21645515.2015.1117714

64. Yan X, Zhou M, Yu S, Jin Z, Zhao K. An overview of biodegradable nanomaterials and applications in vaccines. *Vaccine* (2020) 38(5):1096–104. doi: 10.1016/j.vaccine.2019.11.031

65. Koppolu BP, Smith SG, Ravindranathan S, Jayanthi S, Suresh Kumar TK, Zaharoff DA. Controlling chitosan-based encapsulation for protein and vaccine delivery. *Biomaterials* (2014) 35(14):4382–9. doi: 10.1016/j.biomaterials.2014.01.078

66. Herdiana Y, Wathoni N, Shamsuddin S, Muchtaridi M. Drug release study of the chitosan-based nanoparticles. *Heliyon* (2022) 8(1):e08674. doi: 10.1016/j.heliyon.2021.e08674

67. Kheirollahpour M, Mehrabi M, Dounighi NM, Mohammadi M, Masoudi A. Nanoparticles and vaccine development. *Pharm Nanotechnol* (2020) 8(1):6–21. doi: 10.2174/2211738507666191024162042

68. Schlosser PM, Bale AS, Gibbons CF, Wilkins A, Cooper GS. Human health effects of dichloromethane: Key findings and scientific issues. *Environ Health Perspect* (2015) 123(2):114–9. doi: 10.1289/ehp.1308030

69. Wang Y, Zhou X, Wang H, Sun L, Wang B, Jiang Y, et al. The role of *Eimeria tenella* etcab protein in the attachment and invasion of host cells. *Vet Parasitol* (2021) 292:109415. doi: 10.1016/j.vetpar.2021.109415

70. Wallach M. Role of antibody in immunity and control of chicken coccidiosis. *Trends Parasitol* (2010) 26(8):382–7. doi: 10.1016/j.pt.2010.04.004

71. Zhang Y, Zhang Y, Gu W, Sun B. Th1/Th2 cell differentiation and molecular signals. *Adv Exp Med Biol* (2014) 841:15–44. doi: 10.1007/978-94-017-9487-9_2

72. Kim WH, Chaudhari AA, Lillehoj HS. Involvement of T cell immunity in avian coccidiosis. *Front Immunol* (2019) 10:2732. doi: 10.3389/fimmu.2019.02732

73. Rose ME, Wakelin D, Hesketh P. Interferon-Gamma-Mediated effects upon immunity to coccidial infections in the mouse. *Parasite Immunol* (1991) 13(1):63–74. doi: 10.1111/j.1365-3024.1991.tb00263.x

74. Ogedengbe JD, Hunter DB, Barta JR. Molecular identification of eimeria species infecting market-age meat chickens in commercial flocks in Ontario. *Vet Parasitol* (2011) 178(3-4):350–4. doi: 10.1016/j.vetpar.2011.01.009

75. Iwaszko M, Biały S, Bogunia-Kubik K. Significance of interleukin (Il)-4 and il-13 in inflammatory arthritis. *Cells* (2021) 10(11):3000. doi: 10.3390/cells10113000

76. Laidlaw BJ, Craft JE, Kaech SM. The multifaceted role of Cd4(+) T cells in Cd8(+) T cell memory. *Nat Rev Immunol* (2016) 16(2):102–11. doi: 10.1038/nri.2015.10

77. Veldhoen M, Uyttenhove C, van Snick J, Helmby H, Westendorf A, Buer J, et al. Transforming growth factor-beta 'Reprograms' the differentiation of T helper 2 cells and promotes an interleukin 9-producing subset. *Nat Immunol* (2008) 9 (12):1341–6. doi: 10.1038/ni.1659

78. Dardalhon V, Awasthi A, Kwon H, Galileos G, Gao W, Sobel RA, et al. Il-4 inhibits tgf-Beta-Induced Foxp3+ T cells and, together with tgf-beta, generates il-9 + il-10+ Foxp3(-) effector T cells. *Nat Immunol* (2008) 9(12):1347–55. doi: 10.1038/ni.1677

79. Bedke T, Muscate F, Soukou S, Gagliani N, Huber S. Il-10-Producing T cells and their dual functions. *Semin Immunol* (2019) 44:101335. doi: 10.1016/j.smim.2019.101335

80. Liu M, Li S, Li MO. Tgf-B control of adaptive immune tolerance: A break from treg cells. *Bioessays* (2018) 40(11):e1800063. doi: 10.1002/bies.201800063

81. Korn T, Bettelli E, Oukka M, Kuchroo VK. Il-17 and Th17 cells. *Annu Rev Immunol* (2009) 27:485–517. doi: 10.1146/annurev.immunol.021908.132710

82. Tanaka T, Narazaki M, Kishimoto T. Il-6 in inflammation, immunity, and disease. *Cold Spring Harb Perspect Biol* (2014) 6(10):a016295. doi: 10.1101/cshperspect.a016295

83. Quentmeier H, Klaucke J, Mühlradt PF, Drexler HG. Role of il-6, il-2, and il-4 in the in vitro induction of cytotoxic T cells. *J Immunol* (1992) 149(10):3316–20. doi: 10.4049/jimmunol.149.10.3316

84. Hong YH, Lillehoj HS, Dalloul RA, Min W, Miska KB, Tuo W, et al. Molecular cloning and characterization of chicken nk-lysin. *Vet Immunol Immunopathol* (2006) 110(3-4):339–47. doi: 10.1016/j.vetimm.2005.11.002

85. Hong YH, Lillehoj HS, Lee SH, Dalloul RA, Lillehoj EP. Analysis of chicken cytokine and chemokine gene expression following eimeria acervulina and *Eimeria tenella* infections. *Vet Immunol Immunopathol* (2006) 114(3-4):209–23. doi: 10.1016/j.vetimm.2006.07.007

86. Hwang SY, Kim JY, Kim KW, Park MK, Moon Y, Kim WU, et al. Il-17 induces production of il-6 and il-8 in rheumatoid arthritis synovial fibroblasts *Via* nf-kappab- and Pi3-Kinase/Akt-Dependent pathways. *Arthritis Res Ther* (2004) 6 (2):R120–8. doi: 10.1186/ar1038

87. Zhang L, Liu R, Song M, Hu Y, Pan B, Cai J, et al. *Eimeria tenella*: Interleukin 17 contributes to host immunopathology in the gut during experimental infection. *Exp Parasitol* (2013) 133(2):121–30. doi: 10.1016/j.exppara.2012.11.009

88. Min W, Kim WH, Lillehoj EP, Lillehoj HS. Recent progress in host immunity to avian coccidiosis: Il-17 family cytokines as sentinels of the intestinal mucosa. *Dev Comp Immunol* (2013) 41(3):418–28. doi: 10.1016/j.dci.2013.04.003

89. Subramanian BM, Sriraman R, Rao NH, Raghul J, Thiagarajan D, Srinivasan VA. Cloning, expression and evaluation of the efficacy of a recombinant eimeria tenella sporozoite antigen in birds. *Vaccine* (2008) 26(27-28):3489–96. doi: 10.1016/j.vaccine.2008.04.024

90. Gaud G, Lesourne R, Love PE. Regulatory mechanisms in T cell receptor signalling. *Nat Rev Immunol* (2018) 18(8):485–97. doi: 10.1038/s41577-018-0020-8

91. Bretscher PA. The history of the two-signal model of lymphocyte activation: A personal perspective. *Scand J Immunol* (2019) 89(6):e12762. doi: 10.1111/sji.12762

92. Mittrücker HW, Visekruna A, Huber M. Heterogeneity in the differentiation and function of $Cd8^+$ T cells. *Arch Immunol Ther Exp (Warsz)* (2014) 62(6):449–58. doi: 10.1007/s00005-014-0293-y

93. Verdon DJ, Mulazzani M, Jenkins MR. Cellular and molecular mechanisms of Cd8(+) T cell differentiation, dysfunction and exhaustion. *Int J Mol Sci* (2020) 21 (19):7357. doi: 10.3390/ijms21197357

94. Dimeloe S, Burgener AV, Grählert J, Hess C. T-Cell metabolism governing activation, proliferation and differentiation; a modular view. *Immunology* (2017) 150(1):35–44. doi: 10.1111/imm.12655

95. Zhu J, Yamane H, Paul WE. Differentiation of effector Cd4 T cell populations (*). *Annu Rev Immunol* (2010) 28:445–89. doi: 10.1146/annurev-immunol-030409-101212

96. Li J, Wang F, Ma C, Huang Y, Wang D, Ma D. Recombinant lactococcus lactis expressing *Eimeria tenella* Ama1 protein and its immunological effects against homologous challenge. *Exp Parasitol* (2018) 191:1–8. doi: 10.1016/j.exppara.2018.05.003

97. Lee SH, Lillehoj HS, Jang SI, Lee KW, Yancey RJ, Dominowski P. The effects of a novel adjuvant Complex/*Eimeria* profilin vaccine on the intestinal host immune response against live e. acervulina challenge infection. *Vaccine* (2010) 28(39):6498–504. doi: 10.1016/j.vaccine.2010.06.116

98. Xu L, Yu Z, He K, Wen Z, Aleem MT, Yan R, et al. Plga nanospheres as delivery platforms for *Eimeria mitis* 1a protein: A novel strategy to improve specific immunity. *Front Immunol* (2022) 13:901758. doi: 10.3389/fimmu.2022.901758

frontiers | Frontiers in Immunology

TYPE Original Research
PUBLISHED 23 December 2022
DOI 10.3389/fimmu.2022.1089225

Check for updates

OPEN ACCESS

EDITED BY
Nargis Khan,
University of Calgary, Canada

REVIEWED BY
Ming-Hsien Chiang,
National Defense Medical Center, Taiwan
Andrés Corral Lugo,
Carlos III Health Institute (ISCIII), Spain

*CORRESPONDENCE
Ming Li
sotx7080@163.com
Renjie Zhou
zhou_rj@aliyun.com
Xiancai Rao
raoxiancai@126.com

†These authors have contributed equally to this work and share first authorship

‡These authors have contributed equally to this work and share last authorship

SPECIALTY SECTION
This article was submitted to Vaccines and Molecular Therapeutics, a section of the journal Frontiers in Immunology

RECEIVED 04 November 2022
ACCEPTED 13 December 2022
PUBLISHED 23 December 2022

CITATION
Zhu K, Li G, Li J, Zheng M, Peng X, Rao Y, Li M, Zhou R and Rao X (2022) Hcp1-loaded staphylococcal membrane vesicle vaccine protects against acute melioidosis. *Front. Immunol.* 13:1089225. doi: 10.3389/fimmu.2022.1089225

COPYRIGHT
© 2022 Zhu, Li, Li, Zheng, Peng, Rao, Li, Zhou and Rao. This is an open-access article distributed under the terms of the Creative Commons Attribution License (CC BY). The use, distribution or reproduction in other forums is permitted, provided the original author(s) and the copyright owner(s) are credited and that the original publication in this journal is cited, in accordance with accepted academic practice. No use, distribution or reproduction is permitted which does not comply with these terms.

Hcp1-loaded staphylococcal membrane vesicle vaccine protects against acute melioidosis

Keting Zhu[1†], Gang Li[2†], Jia Li[1], Mingxia Zheng[1], Xiaohui Peng[1], Yifan Rao[1], Ming Li[2*‡], Renjie Zhou[1*‡] and Xiancai Rao[2*‡]

[1]Department of Emergency Medicine, Xinqiao Hospital, Army Medical University, Chongqing, China, [2]Department of Microbiology, College of Basic Medical Sciences, Army Medical University, Chongqing, China

Burkholderia pseudomallei is the causal agent of melioidosis, a deadly tropical infectious disease that lacks a vaccine. On the basis of the attenuated *Staphylococcus aureus* RN4220-Δ*agr* (RN), we engineered the RN4220-Δ*agr*/*pdhB-hcp1* strain (RN-Hcp1) to generate *B. pseudomallei* hemolysin-coregulated protein 1 (Hcp1)-loaded membrane vesicles (^{hcp1}MVs). The immunization of BALB/c mice with ^{hcp1}MVs mixed with adjuvant by a three-dose regimen increased the serum specific IgG production. The serum levels of inflammatory factors, including TNF-α and IL-6, in ^{hcp1}MV-vaccinated mice were comparable with those in PBS-challenged mice. The partial adjuvant effect of staphylococcal MVs was observed with the elevation of specific antibody titer in ^{hcp1}MV-vaccinated mice relative to those that received the recombinant Hcp1 protein (rHcp1) or MVs derived from RN strain ($^{\Delta agr}$MVs). The ^{hcp1}MVs/adjuvant vaccine protected 70% of mice from lethal *B. pseudomallei* challenge. Immunization with ^{hcp1}MVs only protected 60% of mice, whereas vaccination with rHcp1 or $^{\Delta agr}$MVs conferred no protection. Moreover, mice that received ^{hcp1}MVs/adjuvant and ^{hcp1}MVs immunization had low serum TNF-α and IL-6 levels and no inflammatory infiltration in comparison with other groups. In addition, all surviving mice in ^{hcp1}MVs/adjuvant and ^{hcp1}MVs groups exhibited no culturable bacteria in their lungs, livers, and spleens five days postinfection. Overall, our data highlighted a new strategy for developing *B. pseudomallei* vaccine and showed that Hcp1-incorporated staphylococcal MV is a promising candidate for the prevention of acute melioidosis.

KEYWORDS

***Burkholderia pseudomallei*, vaccine, membrane vesicles, Hcp1, melioidosis, protection**

Introduction

Burkholderia pseudomallei is a dangerous pathogen that causes melioidosis, a tropical infectious disease with clinical manifestation varying from local abscess to systemic sepsis (1). Human melioidosis was first described in 1911 by Dr. Alfred Whitmore in Yangon, Myanmar, and this disease has been neglected until 1985 when the Infectious Disease Association of Thailand has enabled people to recognize melioidosis as a remarkable public health problem (2, 3). The worldwide distribution of *B. pseudomallei* especially in tropical areas such as South America and the Caribbean, Southeast Asia, Northern Australia, and the Indian subcontinent, results in an estimate of 165,000 human melioidosis cases per year and a high mortality of 53.9% (2–5). *B. pseudomallei* can colonize and invade multiple organs of the body, including brain, lung, liver, kidney, and skin, and the extensive tissue tropism of *B. pseudomallei* contributes to the development of melioidosis (6, 7) and complicates the diagnosis due to the variable clinical presentations of the disease (2). Moreover, *B. pseudomallei* is intrinsically resistant to a variety of antibiotics (2, 8), and insufficient antibacterial treatment can lead to a fatality rate of more than 70% (9, 10). In addition, *B. pseudomallei* has been recognized as a category B biological agent by the US Centers for Disease Control and Prevention (11). The high prevalence and potential biological threat of *B. pseudomallei* calls for effective vaccines. However, commercial vaccines against melioidosis are still unavailable.

Substantial effort has been given to the development of melioidosis vaccines in recent years. Preclinical studies showed that inactivated whole-cell (such as paraformaldehyde-killed *B. pseudomallei* A2 (12)) and live attenuated (like the auxotrophic mutant Δ*ilvI* (13)) vaccines can protect 20%–80% of vaccinated mice from lethal bacterial challenge. However, sterilizing immunity is not achieved (8). By contrast, subunit vaccines with one or several antigens are considered safe and protective. Therefore, the selection and assessment of potential antigen candidates from *B. pseudomallei* have attracted the attention of the research community. Many antigens, such as the lipoprotein export system component LolC (14), outer membrane protein OmpW (15), heat shock protein GroEL (16), trimeric autotransporter adhesin PSL2063 (17), type III secreted protein BopA (18), and the type VI secretion system (T6SS)-associated hemolysin-coregulated proteins (Hcp; including Hcp1, Hcp2, Hcp3, and Hcp6) (19), have been identified as good vaccine candidates for further investigation. However, these subunit vaccine candidates have not advanced to clinical trials due to lack of suitable delivery systems.

Bacterial membrane vesicles (MVs) are nanoscale structures naturally secreted by Gram-positive bacteria and Gram-negative ones (also termed outer membrane vesicles, OMVs) during their growth (20). MVs can incorporate bacterial proteins, which may effectively stimulate specific humoral and cellular immune responses, and grant remarkable protection against subsequent bacterial infections (21). The innate characteristics of bacterial MVs support vaccine candidates and provide excellent vaccine delivery systems (22, 23). Examples of the successful bacterial MV vaccines are two licensed meningococcal serogroup B (MenB) MV vaccines designated as MenB-4C and MenB-FHbp, which can protect against infections caused by all 14 pathogenic meningococcal strains tested (24). A safe staphylococcal platform has been constructed previously by deleting the whole *agr* locus in the genome of *Staphylococcus aureus* strain RN4220, and at least four dominant components in the RN4220-Δ*agr* mutant are capable of delivering the antigens of dengue virus to MVs, which can induce specific antibodies against all four serotypes of the dengue virus (25).

As one of the subunit vaccine candidates against melioidosis, Hcp1 is a structural protein forming the secretion tube of T6SS and an important effector involving in *B. pseudomallei* pathogenesis (26). Anti-Hcp1 specific antibodies, including IgM and IgG, exist in the sera of patients with melioidosis, indicating the development of humoral response against Hcp1 (26, 27). In the present study, the *hcp1* gene is genetically in-frame fused to the gene encoding pyruvate dehydrogenase E1 component subunit beta (PdhB), one of the aforementioned major vesicular components in *S. aureus* RN4220-Δ*agr*. The immunization of BALB/c mice with Hcp1-loaded MVs derived from RN4220-Δ*agr/pdhB-hcp1* (^{hcp1}MVs) induces a high titer of specific antibodies and protects about 70% of vaccinated mice from acute intraperitoneal challenge with lethal *B. pseudomallei*, highlighting a technical advancement in developing melioidosis vaccines.

Materials and methods

Plasmids, bacterial strains, and their growth conditions

The plasmids and bacterial strains used in this study were listed in Supplementary Table 1. *S. aureus* strains were cultured from a freezer stock and streaked on tryptic soy broth (TSB; Oxoid, UK) agar for 16 h at 37°C. The colonies of bacteria were inoculated into 2 mL of TSB and incubated for 16 h at 37°C with agitation. *Escherichia coli* strains were grown in Luria Broth (LB) medium or plated on LB agar for 16 h at 37°C. *B. pseudomallei* strains were cultured from a freezer stock and spread on LB agar supplemented with 200 μM $FeSO_4{\cdot}7H_2O$ for 48 h at 37°C. Bacterial colonies were then inoculated into 2 mL of LB broth and cultured at 37°C for 16 h with agitation. When required, cultures were supplemented with 100 μg/mL of kanamycin (Kan) or 50 μg/mL of ampicillin (Amp) for *E. coli* and 10 μg/mL of chloramphenicol (Cm) for *S. aureus* harboring recombinant plasmids.

The plasmid pBT2 and *S. aureus* RN4220 were kindly provided by Prof. Baolin Sun (University of Science and Technology of China). *B. pseudomallei* strain BPC006 was isolated from the clinical specimen of a patient hospitalized in Hainan People's Hospital (28), and kindly provided by Prof. Xu-hu Mao (Army Medical University).

Construction of *S. aureus* strain producing Hcp1-loaded MVs

To construct *S. aureus* RN4220-Δ*agr/pdhB-hcp1*, the *hcp1* gene was amplified from *B. pseudomallei* BPC006 genomic DNA using primer pair hcp1-F/R (Supplementary Table 2). For homologous recombination, the left region (Up-pdhB) and right region (Down-pdhB) across the stop codon of the *pdhB* gene of *S. aureus* RN4220-Δ*agr* were amplified from the genomic DNA using primers uppdhB-F/R and downpdhB-F/R (Supplementary Table 2), respectively. A fusion fragment was generated by overlap PCR using the *hcp1* gene fragment, Up-pdhB, and Down-pdhB as templates. The fusion DNA was digested with *Bam*H I/*Sac* I restriction enzymes and ligated into the temperature-sensitive shuttle vector pBT2 *via* Gibson assembly master mix (NEB, USA). The resultant vector pBT2-hcp1 was firstly transformed into *E. coli* DH5α and subsequently electroporated into *S. aureus* strain RN4220-Δ*agr*. The seamless *hcp1* insertion mutant designated as RN4220-Δ*agr/pdhB-hcp1* (RN-Hcp1) was screened as previously described (29), and confirmed through PCR amplification and DNA sequencing.

Preparation of bacterial MVs

Bacterial MVs were prepared from *S. aureus* culture supernatants as described previously (25). Briefly, overnight culture of *S. aureus* strains of interest was inoculated into 1 L TSB (1:100), and incubated for 20 h at 37°C with shaking (200 rpm). Culture supernatants were collected by centrifugation at 5,000 × *g* at 4°C for 30 min to remove bacterial cells, and then filtered through 0.45 μm Millex syringe filters (Beyotime) to remove any remaining cell debris. The filtrate was concentrated about 60 times with an ultrafiltration system with an interception molecular weight of 100 kDa (Shenchen, China). Culture supernatants were then centrifuged at 200,000 × *g* for 3 h at 4°C, and the MV pellets were resuspended in phosphate-buffered saline (PBS, pH 7.2) after two washes with PBS. The protein concentration of MV samples was determined using an enhanced BCA Protein Assay Kit according to the instruction provided by the Company (Beyotime). MVs were stored as aliquots at -80°C.

Transmission electron microscope (TEM) observation

The purified Hcp1-loaded MVs were added to 230-mesh formvar/carbon-coated copper grids (Zhongjingkeji Tech., China), and negatively stained with 2% (m/v) uranylacetate for 30 sec. For immunogold labeling, Hcp1-loaded MVs was 1:20 diluted in NTE buffer (10 mM Tris-Cl, pH 7.0, 100 mM NaCl) and adsorbed onto 230-mesh formvar/carbon-coated nickel grids. After 5 min wash with TBS buffer (50 mM Tris-HCl, 150 mM NaCl, pH 7.5), the specimen was blocked with 3% (m/v) bovine serum albumin (BSA) in TBS for 45 min. Mouse-anti-Hcp1 antibody was 1:500 diluted in 1% (m/v) BSA/TBS and applied to the nickel grids for 1.0 h at room temperature. After washed three times with TBS, gold-conjugated goat-anti-mouse IgG (Sigma, USA) was added and incubated for 1.0 h at room temperature. Next, the grids were washed twice with TBS, once with water and followed by negatively stained with 2% (m/v) uranylacetate for 15 sec. Electron micrographs were recorded with a JEM1011 microscope (JEOL, Japan) at 100 kV acceleration voltage.

Expression and purification of recombinant Hcp1

Recombinant Hcp1 (rHcp1) was expressed and purified as described previously with minor modifications (25). Briefly, the *hcp1* gene was amplified from genomic DNA of *B. pseudomallei* BPC006 using primer pair pET28a-F/R (Supplementary Table 2), and cloned into the expression vector pET28a to generate pET28a-*hcp1*. *E. coli* strain BL21 (DE3) harbouring the resulting plasmid pET28a-*hcp1* was grown in 1.0 L fresh LB broth at 37°C to an OD600 of 0.5 and induced with 0.5 mM IPTG at 37°C for 6 h. For protein purification, bacterial cells were harvested by centrifugation at 5,000 × g at 4°C for 30 min and lysed by sonication in buffer A (50 mM Tris-HCl and 200 mM NaCl, pH 8.0). After centrifugation at 16,000 × g at 4°C for 30 min to remove cell debris, the supernatant was collected and centrifuged again at 10,000 × g for 30 min, filtered through a 0.22 mm filter unit (Beyotime), and applied to an Ni-NTA resin column (GE, USA) pre-equilibrated with buffer A. The column was washed with buffer A, followed by buffer A mixed with a linear gradient of 5%–100% (v/v) buffer B (buffer A containing 500 mM imidazole) to remove the nonspecifically bound proteins and elute the target proteins. Protein purity was analyzed by sodium dodecyl sulfate polyacrylamide gel electrophoresis (SDS-PAGE), and the major fractions containing target proteins were collected and dialyzed five times against buffer

A to remove imidazole. The concentration of rHcp1 proteins was determined using a BCA protein assay kit (Pierce). Aliquots of the purified rHcp1 proteins were stored at -80°C.

SDS-PAGE and Western blot

Protein samples were solubilized in 5 × SDS-PAGE sample buffer and heated to 100°C for 10 min. After centrifugation, the sample supernatants were loaded and proteins were separated on 12% SDS-PAGE. Proteins were visualized *via* staining with Coomassie blue R-250. For Western blot, proteins on the PAGE gel were electrotransferred onto a PVDF membrane (Beyotime). The membrane was blocked with 5% skim milk in high-salt Tris-buffered saline (HS-TBS; 20 mM Tris, 500 mM NaCl, pH 7.5) for 60 min at room temperature. Then, the membrane was incubated overnight at 4°C with a 1:10,000 dilution of the *B. pseudomallei* Hcp1-specific polyclonal antibody. After washed five times with PBS-T (PBS containing 0.05% Tween-20), the membrane was incubated for 1.0 h at 37°C with 1:5,000 of goat-anti-mouse IgG-horseradish peroxidase conjugate (Solarbio). Blot was visualized using the Pierce ECL Western blotting substrate (Thermo Scientific) and a ChemiDoc XRS imaging system (Bio-Rad).

Median lethal dose (LD50) determination

Female BALB/c mice (aged 6–8 weeks) were purchased from the Animal Center of Army Medical University (Third Military Medical University) and acclimated in an ABLS-2^+ laboratory for five days before experiments. All mice were fed an autoclaved pellet diet and sterile water under the following housing conditions: 23°, 50% humidity, half-day light/dark periods, and quiet surroundings with minimal disturbance. The experimental procedures for animals were performed according to the Regulations for Administration of Affairs Concerning Experimental Animals approved by Chinese State Council. Cervical dislocation was applied as euthanasia way of the experimental animals.

For LD50 determination, 50 female mice were challenged through intraperitoneal route with different concentrations of *B. pseudomallei* strain BPC006 (3.0×10^5, 6.0×10^5, 1.0×10^6, 3.0×10^6, and 6.0×10^6 CFU, $n = 10$ per group). Infected mice were monitored for survival over 21 days, and the LD50 was calculated using Bliss method by SPSS software.

Mouse vaccination and infection

Anesthetized BALB/c mice were grouped and administered in multisite routes (i.e., subcutaneous, intramuscular, and intraperitoneal) by three-dose vaccination regimens with (i) 100 μL PBS, (ii) 50 μg $^{\Delta agr}$MVs (in 100 μL PBS) prepared from *S. aureus* RN4220-Δ*agr* (RN), (iii) 50 μg ^{hcp1}MVs derived from *S. aureus* RN-Hcp1, (iv) 50 μg ^{hcp1}MVs emulsified with 50% Freund's adjuvant (Sigma, USA), and (v) 0.2 μg rHcp1 proteins (equal to the amount of Hcp1 in 50 μg ^{hcp1}MVs) on days -30, -20 and -10 prechallenge. Ten days after the third boost (day 0), the vaccinated mice were infected *via* intraperitoneal with lethal dose (5 × LD50) of *B. pseudomallei* BPC006. Challenged mice were monitored for behavior changes and survival time over 21 days.

Detection of *B. pseudomallei* specific antibodies

During the process of mouse vaccination, sera from immunized mice ($n = 3$) seven days after the last vaccination (day -3 prechallenge) were collected, and antibodies against *B. pseudomallei* Hcp1 were determined by enzyme-linked immunosorbent assay (ELISA) as described (30). Briefly, 96-well Maxisorp plates (Nunc) were coated overnight at 4°C with rHcp1 (50 ng/mL) solubilized in carbonate buffer (pH 9.6). The plates were blocked at room temperature for 1.0 h with StartingBlock T20 blocking buffer (Pierce). After blocking, plates were washed three times with TBS-T (Tris-buffered saline supplemented 10% StartingBlock T20 and 0.05% Tween 20, pH 7.5). Then, twofold dilutions of serum samples were made with TBS-T, added in triplicate to wells, and incubated for 2.0 h at 37°C. After washed three times with TBS-T, the plates were incubated for 1.0 h at 37°C with goat anti-mouse IgG-horseradish peroxidase conjugate (1:5,000 dilution, Solarbio). After incubation, the plates were washed three times with TBS-T and developed by the EL-ABTS Chromogenic Reagent kit (Sangon Biotech) and read at 405 nm by using a FLUOstar Omega microplate reader (BMG Labtech). The reciprocals of the highest dilutions exhibiting optical densities (OD) that were 2.1 times relative to the normal mouse serum levels were used to determine the endpoint titers of antibodies for individual vaccinated mice.

Detection of inflammatory factors

Serum samples were collected from individual vaccinated mice at 6 h after prime vaccination (day -30), days -20, -10, and -3 prechallenge, and days 0.5, 1, 2, and 5 postchallenge ($n = 3$ per time point). Then, the levels of inflammatory factors TNF-α and IL-6 in each serum samples were determined with an ELISA kit according to the manufacturer's instructions (R&D Systems, USA). Results were examined with an ELISA reader Multiskan Mk3 (Thermo Fisher Scientific) at 450 nm, and inflammatory factor levels were determined according to the standard curve.

Bacterial burden in organs of infected mice

The organs, including lungs, livers, and spleens, were collected from vaccinated mice on day 0.5 and 5 postchallenge, and subjected to colony forming unit (CFU) enumeration with a plate dilution method. Briefly, vaccinated mice (n = 50 for PBS group, n = 25 per other groups) were infected *via* intraperitoneal with lethal dose (5 × LD50) of *B. pseudomallei* BPC006 on day 0. Twelve infected mice on day 0.5 were sacrificed for organ bacterial counting (n = 10) and histological evaluation (n = 2). The remained mice were sacrificed on day 5 postchallenge. For bacterial counting, mouse organs were harvested, weighed, and homogenized in PBS using Covidien Precision tissue grinders (Fisher Scientific). Tissue homogenates were tenfold diluted in PBS, plated on LB agar, and incubated for 48 h at 37°C. Colonies were counted.

Histological evaluation of mouse organs

The lungs, livers, and spleens collected from vaccinated mice (n = 2) on day 0.5 and 5 postchallenge were used for histological evaluation. Individual organ was fixed with 10% normal buffered formalin. The fixed tissues were embedded in paraffin and sectioned prior to staining with hematoxylin-eosin (HE). Tissue sections were observed under a microscope (Olympus BX53, Japan) and photographed.

Statistical analysis

All experiments were conducted at least three times. Statistical analysis was performed using GraphPad Prism 8.0 software. The one-way analysis of variance (ANOVA), or two-way ANOVA method was used to compare the means from multiple groups and assess the statistical significance. All values were expressed as the mean ± standard derivations (SD) or standard error of the means (SEM). Significant difference was expressed as $^{*}P < 0.05$, $^{**}P < 0.01$, or $^{***}P < 0.001$.

Results

Construction of *S. aureus* strain producing Hcp1-loaded membrane vesicles

The *hcp1* gene of *B. pseudomallei* strain BPC006 was amplified with PCR and genetically fused to the 3′-terminus of the *pdhB* gene in *S. aureus* mutant RN4220-Δ*agr* (RN) to load Hcp1 into staphylococcal MVs. The in-frame fusion of target genes was verified by PCR amplification and DNA sequencing (Supplementary Figure 1), and the resultant strain was designated as RN4220-Δ*agr*/*pdhB-hcp1* (RN-Hcp1).

The MVs produced by engineered *S. aureus* RN-Hcp1 (^{hcp1}MVs) were prepared, and Western blot revealed the existence of a successful fusion protein with molecular weight of approximately 57 kDa in the total cell lysates of RN-Hcp1 and ^{hcp1}MVs by using PdhB polyclonal antibodies as probe. *S. aureus* mutant RN and its derived $^{\Delta agr}$MVs presented wild-type PdhB with a low molecular weight (37 kDa, Figure 1A and Supplementary Figure 2). When polyclonal antibodies against Hcp1 were used, the protein of interest was only detected in the total cell lysates of RN-Hcp1 and ^{hcp1}MVs but not in the RN mutant and $^{\Delta agr}$MVs (Figure 1B). TEM revealed the varied sizes of the purified MVs (Supplementary Figure 3A), and immuno-electron microscopy showed the membrane location of Hcp1 proteins (Supplementary Figures 3B, C). These data indicated that the engineered *S. aureus* RN-Hcp1 could successfully produce Hcp1-loaded MVs.

General manifestation and humoral immune response in mice after Hcp1-loaded MV immunization

BALB/c mice were immunized with PBS, $^{\Delta agr}$MVs, ^{hcp1}MVs, ^{hcp1}MVs/adjuvant, and recombinant Hcp1 (rHcp1, n = 10 per group) by a three-dose regimen at 10-day intervals *via* multiple routes (i.e., subcutaneous, intramuscular, and intraperitoneal) to assess the effects of Hcp1-loaded MVs on tested animals (Figure 2A). The body weights of MVs- or rHcp1-challenged mice showed no difference during the immunization process compared with those of the PBS-challenged mice (Figure 2B). All vaccinated mice exhibited good mental state, smooth fur, normal food and water intake, normal posture and gait, and comparable nutrition. Sera from vaccinated mice (n = 3 per group) on day -3 prechallenge were used to determine antibody responses to rHcp1 by using indirect ELISA. Results revealed that the titer of the total serum IgG antibodies from ^{hcp1}MVs/adjuvant-immunized mice was highest among all groups (Figure 2C). The sera from mice that received a prime and two boosts of ^{hcp1}MVs vaccination demonstrated higher IgG titers than those from rHcp1- and $^{\Delta agr}$MVs-vaccinated mice (Figure 2C), suggesting a partial adjuvant effect of staphylococcal MVs.

Inflammatory factor production following Hcp1-loaded MV immunization

The levels of inflammatory factor production present the systemic inflammation of body caused by bacteria or toxins (31).

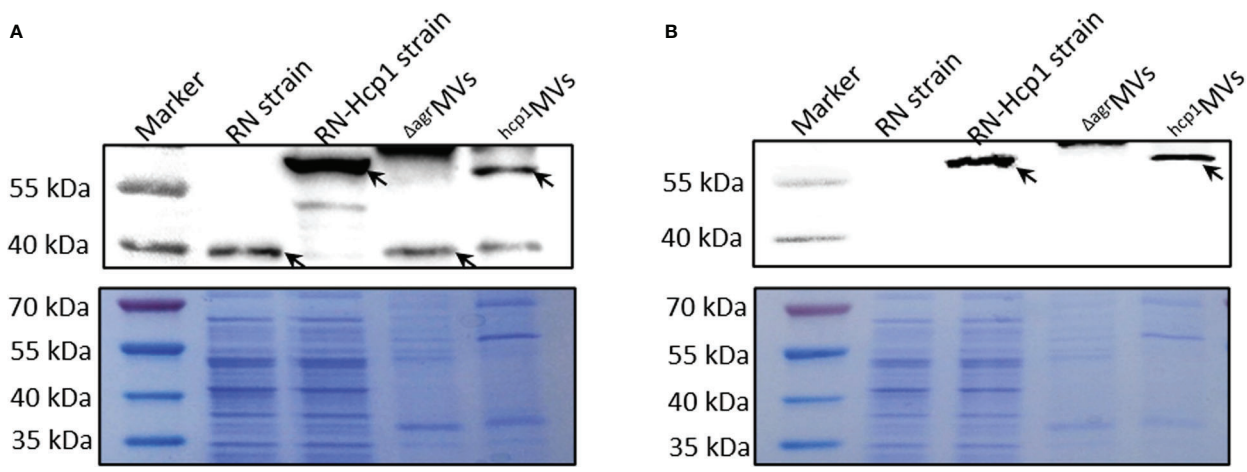

FIGURE 1
Characterization of PdhB-Hcp1 fusion proteins in *S. aureus* RN-Hcp1 strain and its MVs. Western blot with anti-PdhB **(A)** and anti-Hcp1 **(B)** antibodies, respectively. The top panels showed the blots of target proteins (indicated by black arrows) in bacterial cell lysates of *S. aureus* RN and RN-Hcp1 strains and their MVs, including $^{\Delta agr}$MVs and ^{hcp1}MVs. The proteins in samples of interest were separated by 12% SDS-PAGE, stained with Coomassie blue R-250 and served as loading controls (bottom panels). The sizes of the protein Marker were indicated on the left.

However, certain antigens or adjuvants can activate immune cells to secrete cytokines, such as TNF-α, IL-6, and IL-12, that are involved in the promotion of Th1 immune responses (32). Sera from BALB/c mice vaccinated with PBS, $^{\Delta agr}$MVs, ^{hcp1}MVs, ^{hcp1}MVs/adjuvant, and rHcp1 (n = 3 per time point) were collected at 6 h after prime vaccination (day -30) and days -20, -10, and -3 preinfection, and subjected to quantification of IL-6 and TNF-α levels by using ELISA. As shown in Figure 3A, the IL-6 levels in mice 6 h after prime vaccination (day -30) with $^{\Delta agr}$MVs, ^{hcp1}MVs, and ^{hcp1}MVs/adjuvant were significantly increased compared with those in PBS- and rHcp1-vaccinated mice ($P < 0.001$). The TNF-α level in immunized mice 6 h after prime vaccination of ^{hcp1}MVs/adjuvant and $^{\Delta agr}$MVs remarkably increased relative to that in PBS-challenged mice, whereas comparable TNF-α level was observed in mice 6 h after prime vaccination of ^{hcp1}MVs and rHcp1. Furthermore, the IL-6 and TNF-α levels of $^{\Delta agr}$MVs-, ^{hcp1}MVs-, ^{hcp1}MVs/adjuvant-, and rHcp1-injected group on days -20, -10, and -3 were low and comparable with those of PBS-injected group (Figure 3B). These data indicated that the Hcp1-loaded MV vaccine was safe and only elicited increased inflammatory factor production during early stage of prime immunization.

Protective capacity of Hcp1-loaded MV vaccine against *B. pseudomallei* infection

The median lethal dose (LD50) was determined to evaluate the protective repertoire of Hcp1-loaded MV against *B. pseudomallei* challenge. Female BALB/c mice were challenged intraperitoneally with various dosages of *B. pseudomallei* BPC006 (3.0×10^5, 6.0×10^5, 1.0×10^6, 3.0×10^6, and 6.0×10^6 CFU). Mouse survival was monitored for 21 days postinfection, and the Bliss method of SPSS software showed that the LD50 was 5.75×10^5 CFU (Supplementary Figure 4). BALB/c mice were vaccinated with PBS, $^{\Delta agr}$MVs, ^{hcp1}MVs, ^{hcp1}MVs/adjuvant, or rHcp1 (n = 10 per group) by a three-dose regimen at 10-day intervals and then infected with lethal dose of *B. pseudomallei* BPC006 (5 × LD50) 10 days after the final boost to evaluate the protective capacity of the MV vaccine. All infected mice in the PBS-treated group succumbed rapidly to the lethal challenge of *B. pseudomallei* BPC006 (< 7 days). $^{\Delta agr}$MVs- or rHcp1-vaccinated mice survived less than 20 days after *B. pseudomallei* infection. By contrast, immunization with ^{hcp1}MVs and ^{hcp1}MVs/adjuvant protected 60% and 70% of mice, respectively, from lethal bacterial challenge with surviving time exceeding 21 days (Figure 4).

Inflammatory cytokine production in vaccinated mice after *B. pseudomallei* infection

Serum samples of vaccinated mice on days 0.5, 1, 2, and 5 postinfection of *B. pseudomallei* BPC006 were collected and subjected to the determination of inflammatory cytokine levels. As shown in Figure 5, the levels of TNF-α and IL-6 in PBS-treated mice five days after lethal bacterial exposure were significantly elevated than those in other groups and increased over time. By contrast, the TNF-α and IL-6 levels in ^{hcp1}MVs- and ^{hcp1}MVs/adjuvant-immunized mice five days postchallenge decreased continuously after day 0.5 of infection (except TNF-α). Notably, inflammatory cytokine levels in the ^{hcp1}MVs/

10.3389/fimmu.2022.1089225

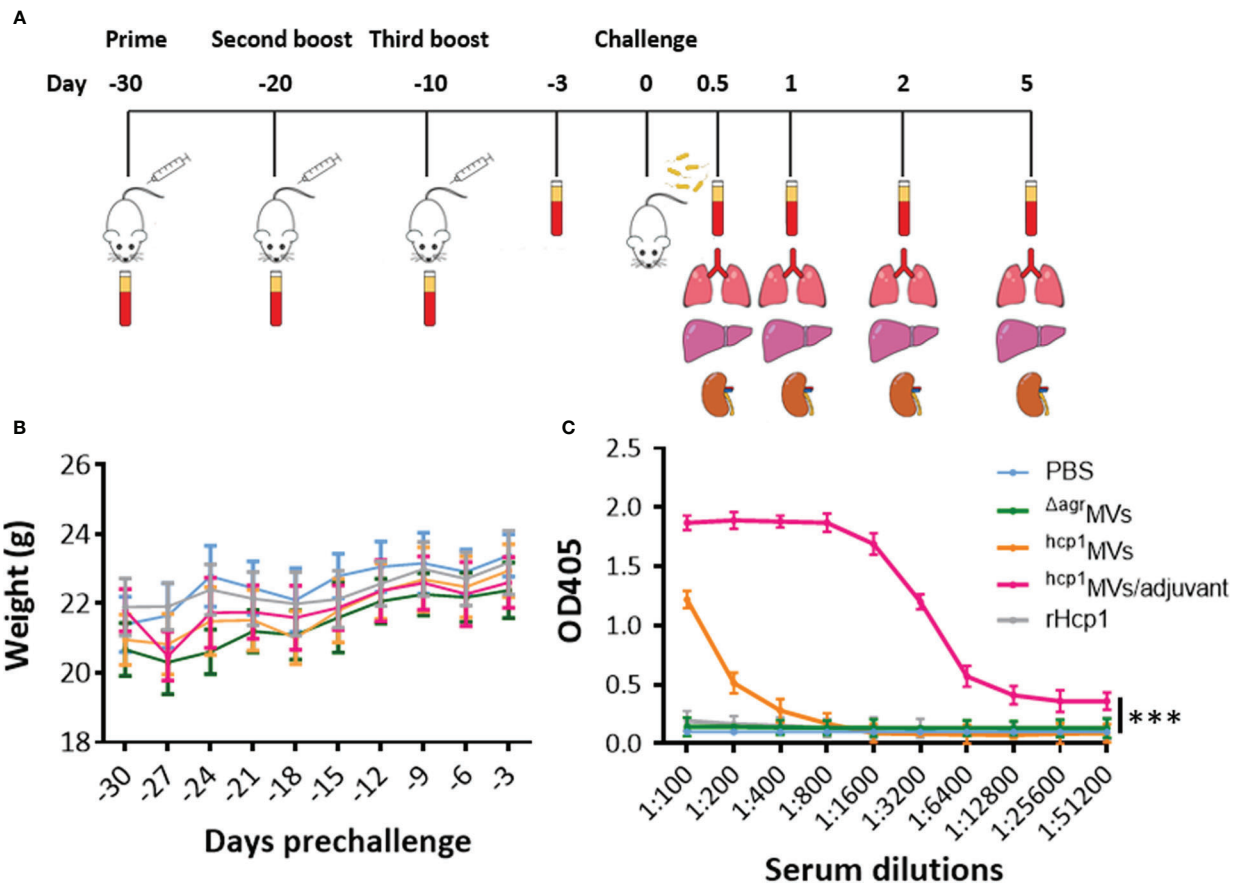

FIGURE 2
Body weight dynamics and serum antibody response of the vaccinated mice. **(A)** Experimental design and timeline of the regimen of PBS, $^{\Delta agr}$MVs, ^{hcp1}MVs, ^{hcp1}MVs/adjuvant, and rHcp1 vaccination, bacterial challenge, and sample collection. **(B)** Body weight dynamics of the vaccinated mice. Immunized BALB/c mice (*n* = 10 per group) were weighed every three days, and the weight of all groups increased gradually during vaccination. **(C)** Quantitation of serum antibody titers raised against rHcp1. The serum IgG antibody titers of immunized mice (*n* = 3 per group) on day -3 prechallenge were determined by ELISA and defined as the highest serum dilution that exhibited an optical density (OD) value of 2.1 times relative to the negative control (PBS group serum). Statistical significance was calculated by two-way ANOVA, ***P < 0.001.

adjuvant-vaccinated mice increased remarkably after day 0.5 of exposure, decreased rapidly, and then maintained at a low level. The increased inflammatory cytokine levels during early period after *B. pseudomallei* exposure may contribute to bacterial clearance (32).

Bacterial burden in vaccinated mice after bacterial challenge

Powerful vaccines resulted in bacterial clearance *in vivo*. BALB/c mice were vaccinated with PBS, $^{\Delta agr}$MVs, ^{hcp1}MVs, ^{hcp1}MVs/adjuvant, or rHcp1 (*n* = 9 per group), and tissue samples of lungs, livers, and spleens were obtained from immunized mice on day 0.5 and 5 postchallenge with lethal *B. pseudomallei*. Bacterial enumeration revealed that the viable bacteria in collected organs of the ^{hcp1}MVs- and ^{hcp1}MVs/adjuvant-immunized mice on day 0.5 postchallenge were decreased than those of other groups (Figure 6A). Moreover, ^{hcp1}MVs- and ^{hcp1}MVs/adjuvant- immunized mice demonstrated undetectable viable bacteria in the three tissues on day 5 postinfection (Figure 6B). Results also showed that all mice immunized with ^{hcp1}MVs or ^{hcp1}MVs/adjuvant exhibited no detectable bacteria in their tissues on day 5 postinfection (Figure 6B). These data indicated that Hcp1-loaded MV vaccine is a promising candidate for *B. pseudomallei* clearance and protects against acute melioidosis.

Histopathological analysis of infected mouse tissues

The lungs, livers, and spleens of mice immunized with PBS, $^{\Delta agr}$MVs, ^{hcp1}MVs, ^{hcp1}MVs/adjuvant, or rHcp1 (*n* = 2 per

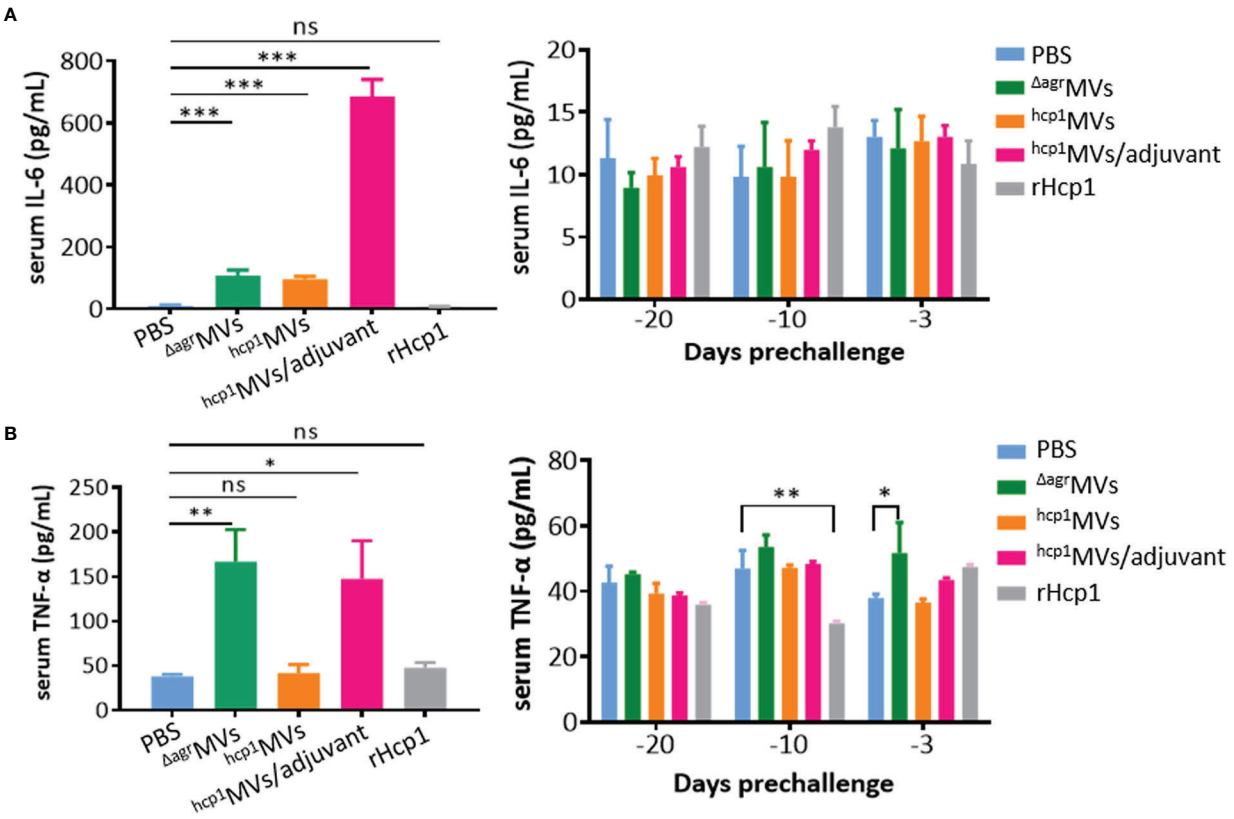

FIGURE 3
Inflammatory factor production determined by ELISA. BALB/c mice (n = 3 per group) were each vaccinated with PBS, $^{\Delta agr}$MVs, ^{hcp1}MVs, ^{hcp1}MVs/adjuvant, or rHcp1 on days -30, -20, and -10. Serum samples were collected at 6 h after prime vaccination (day -30, left panels) and days -20, -10 and -3 preinfection (right panels). ELISA was performed to quantitate serum IL-6 **(A)** and TNF-α **(B)** levels with commercial kits (R&D Systems). The assay was repeated in triplicate. Statistical significances were calculated by one-way ANOVA; ns indicates no statistical significance, $^{*}P < 0.05$, $^{**}P < 0.01$, and $^{***}P < 0.001$.

group) were collected on day 0.5, 1, 2, and 5 postchallenge with *B. pseudomallei* BPC006 and subjected to histopathological analysis. In the gross view, the normal morphologies of livers, spleens, and lungs were maintained in ^{hcp1}MVs/adjuvant-vaccinated mice after five days of infection. However, small white abscesses formed in the livers, spleens, and lungs of PBS-immunized mice five days postinfection and enlarged spleens and lungs with mucinous exudate on the surface were also observed (Supplementary Figure 5).

Tissue sections, including lungs, livers, and spleens, were prepared, stained with hematoxylin and eosin (HE), and examined in a blind manner by a pathologist. Histopathological analysis revealed that the lungs, livers, and spleens from ^{hcp1}MVs/adjuvant-immunized mice on day 5 postinfection exhibited normal tissue architecture (Figure 7). By contrast, the lungs, livers, and spleens of animals vaccinated with ^{hcp1}MVs were almost normal except for some areas of mild interstitial inflammation. The bronchovascular inflammatory infiltrations were observed in lungs of $^{\Delta agr}$MVs- or rHcp1-vaccinated mice on the indicated days postchallenge (Supplementary Figure 6). Bronchovascular infiltration was a prevalent characteristic in the lungs of mice vaccinated with PBS. In addition, frequent interstitial inflammation and multinucleated giant cell infiltration were also observed in the spleens of PBS-vaccinated mice five days after bacterial challenge (Figure 7). Overall, these data demonstrated the vaccinogenic potential of Hcp1-loaded staphylococcal MVs.

Discussion

Despite the fact that licensed vaccines are unavailable, many vaccine candidates against melioidosis, including inactivated whole-cell (32, 33), live attenuated (13, 34), subunit (14, 15), glycoconjugate (35, 36), DNA (37, 38), and viral vector-based (39) vaccines, have been studied in recent years. However, these vaccines only have partial protection probably because *B. pseudomallei* is an intracellular organism that survives in

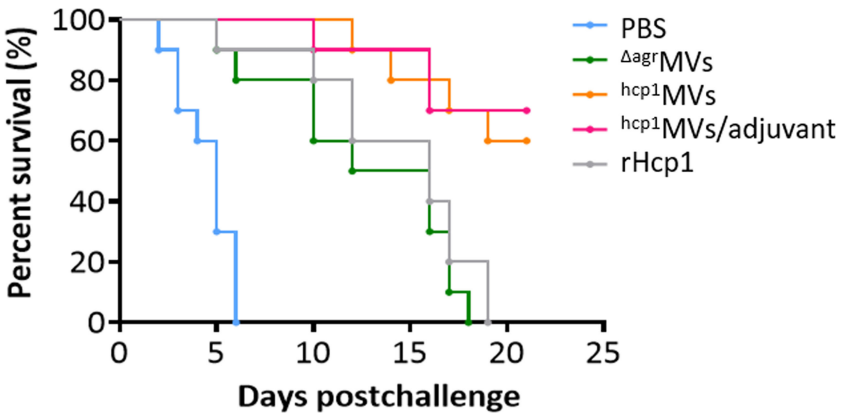

FIGURE 4
Hcp1-loaded MV vaccination protects mice from acute melioidosis. BALB/c mice (n = 10 per group) were vaccinated with PBS, $^{\Delta agr}$MVs, ^{hcp1}MVs, ^{hcp1}MVs/adjuvant, or rHcp1 by a three-dose regimen at 10-day intervals. Then, mice were infected with 5 × LD50 of *B. pseudomallei* BPC006 (lethal dose) 10 days after the final boost. Mouse mortality was evaluated daily for 21 days and the percent survival (%) was indicated.

macrophages, neutrophils, and monocytes, thus avoiding the induction of protective immune responses (40–43). Nieves et al. prepared MVs naturally derived from *B. pseudomallei* strain 1026b (44) and showed that the vaccination of BALB/c mice with MVs provides considerable protection against septic (100%) and pneumonic (60%) melioidosis (44, 45). However, natural MVs are commonly enriched with virulence factors, such as lipopolysaccharide (21, 25), and the application of MVs produced by wild-type *B. pseudomallei* strains raises safety concerns. In a previous study, a whole gene locus deletion of *agr* system is used to generate an *S. aureus* strain RN4220-Δ*agr* (25). MVs prepared from RN4220-Δagr ($^{\Delta agr}$MVs) are remarkably attenuated, and PdhB is the most abundant component among $^{\Delta agr}$MVs that is suitable for the delivery of heterogeneous antigens from bacteria to the secreted MVs. On the basis of this safe protein delivery platform, the gene of *B. pseudomallei* protective antigen Hcp1 is genetically fused with *pdhB* in *S. aureus* RN4220-Δ*agr*, and the protective immune responses generated by ^{hcp1}MVs vaccination against acute melioidosis are evaluated in the present study.

Recent studies showed that antibody responses play a critical role in the protection of live attenuated vaccine-vaccinated mice from *B. pseudomallei* infection and that bacterium-specific cellular responses make a minor contribution (34, 46). In this

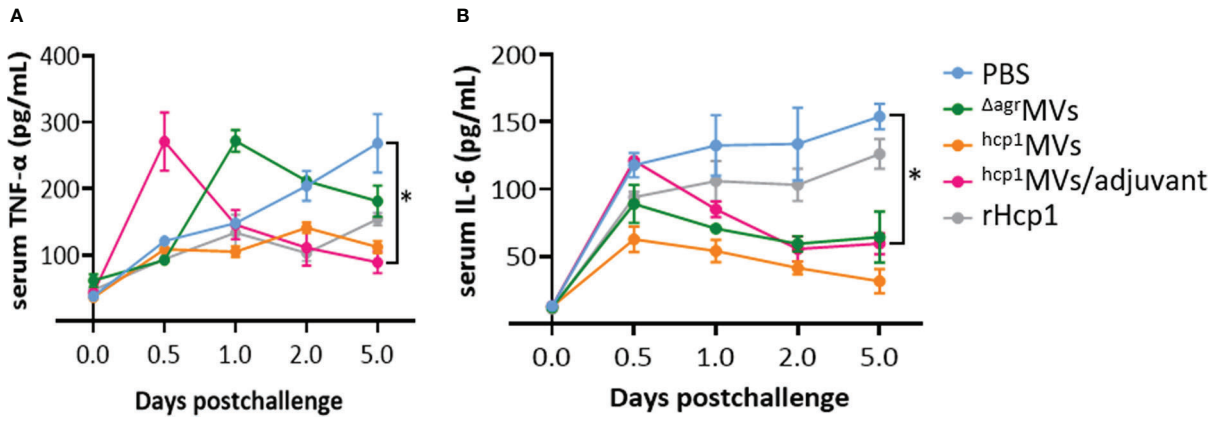

FIGURE 5
The inflammatory cytokine levels in sera of vaccinated mice after *B. pseudomallei* challenge. Mice (n = 3 per group) were vaccinated with PBS, $^{\Delta agr}$MVs, ^{hcp1}MVs, ^{hcp1}MVs/adjuvant, or rHcp1 by three inoculations at 10-day intervals. Ten days after the final boost, mice were infected with lethal dose of *B. pseudomallei* BPC006 (5 × LD50) *via* intraperitoneal injection. Serum samples were harvested on days 0.5, 1, 2, and 5 postinfection and the levels of inflammatory cytokines, including TNF-α **(A)** and IL-6 **(B)**, were determined by ELISA. Data are presented as mean ± SD. Statistical significance was calculated by two-way ANOVA, $^*P < 0.05$.

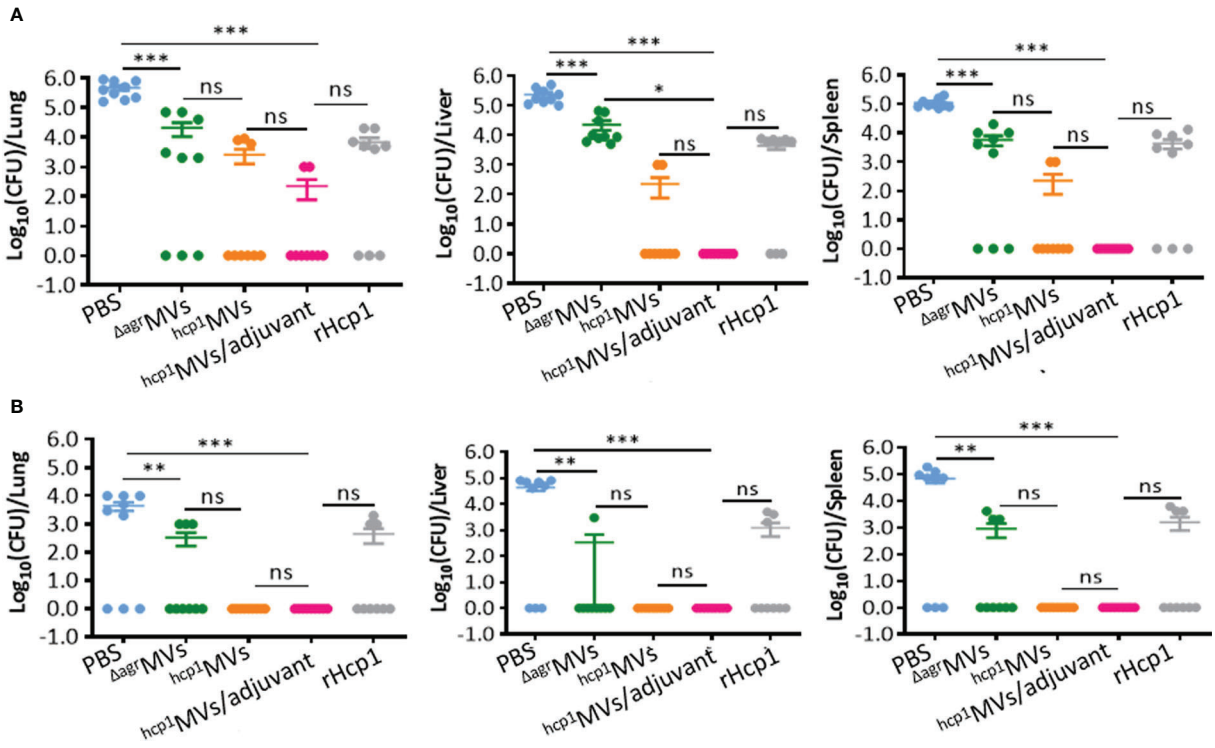

FIGURE 6
Bacterial enumeration in vaccinated mice challenged with *B. pseudomallei*. Viable bacteria in lungs, livers, and spleens of immunized mice (n = 9 per group) on day 0.5 **(A)** and 5 **(B)** postinfection. Tissues were weighed and homogenized in PBS. Viable bacteria were counted using the plate dilution method and calculated as CFU. Data are presented as mean ± standard error of the mean (SEM). Significant differences were analyzed by one-way ANOVA, ns indicates no difference, $^{*}P < 0.05$, $^{**}P < 0.01$, and $^{***}P < 0.001$.

study, vaccination with rHcp1 proteins without adjuvants in a three-dose regimen has produced indistinguishable level of antibodies compared with the PBS control (Figure 2C), suggesting the requirement of immune adjuvants, such as Freund's adjuvant (47), Sigma adjuvant system (19), and CpG DNA (37), in subunit vaccine immunization. By contrast, the vaccination of mice with Hcp1-loaded MVs (^{hcp1}MVs) in the absence of adjuvants produces considerable humoral responses (serum IgG titer > 1:400) compared with the vaccination of mice with $^{\Delta agr}$MVs that do not encapsulate Hcp1 (Figure 2C), indicating an adjuvant effect of staphylococcal $^{\Delta agr}$MVs for Hcp1. However, the adjuvant effect of $^{\Delta agr}$MVs remains partial because the immunization of mice with a formulation of ^{hcp1}MVs/adjuvant induces high specific antibodies (IgG titer > 1:51,200, Figure 2C). The self-adjuvant activity of MVs is probably due to the presence of vesicle-related pathogen-associated molecular patterns (PAMPs), which can bind pathogen recognition receptors on innate immune cells to enhance antigen-presenting functions (48). The MV adjuvant activity is remarkably correlated with the type and amount of PAMPs incorporated in vesicles (48, 49). As heterogeneous MVs for *B. pseudomallei* Hcp1, PAMPs and their functions in staphylococcal $^{\Delta agr}$MVs deserve further investigation.

As a subunit vaccine, rHcp1 is previously prepared and mixed with Sigma adjuvant, and BALB/c mice are vaccinated by three inoculations of 10 μg rHcp1 proteins at 2-week intervals and infected with *B. pseudomallei* K96243 strain three weeks after the final boost. Results showed that the rHcp1/adjuvant can protect 50% of mice from lethal dose challenge but fails to prevent chronic colonization (19). In this study, the inability to prevent acute melioidosis is observed after vaccination of BALB/c mice with $^{\Delta agr}$MVs or rHcp1 protein only (Figure 4). Notably, a similar post-challenge survival pattern was observed between rHcp1- and $^{\Delta agr}$MVs- immunized mice. Vaccination of rHcp1 without adjuvant formulation can enhance the post-challenge survival of BALB/c mice against *B. pseudomallei*. *S. aureus* derived $^{\Delta agr}$MVs do not have specific antigens of *B. pseudomallei*, however, $^{\Delta agr}$MVs can exhibit intrinsic adjuvant activity (25). The PAMPs involved in $^{\Delta agr}$MVs may activate innate immune cells, such as dendritic cells and monocytes/macrophages, to provide certain roles in pathogen inactivation (48). By contrast, engineered ^{hcp1}MVs protects 60% of BALB/c mice against lethal challenge with BPC006, and the

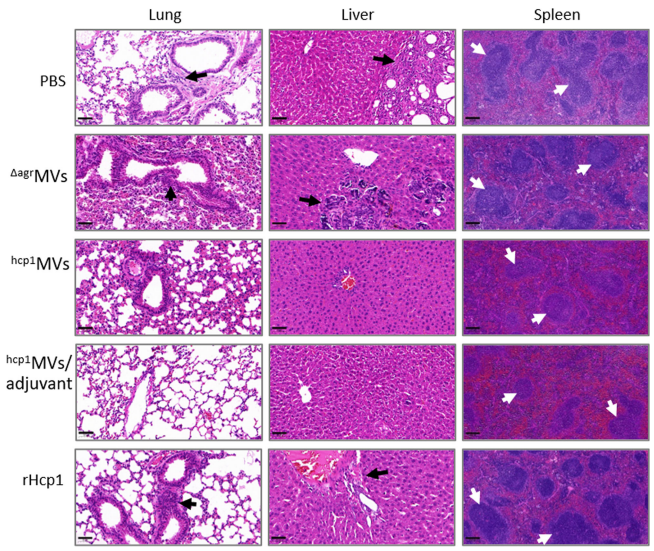

FIGURE 7
Reduced organ inflammations in vaccinated mice after exposure to *B. pseudomallei*. The lungs, livers, and spleens (n = 2 per group) of vaccinated mice on day 5 postchallenge were collected and fixed in 10% formalin. Then, tissues were paraffin-embedded, sectioned, stained with hematoxylin and eosin, and subjected to pathological examination. The representative field for certain tissues was observed at 20× (bar = 50 μm, lung and liver) and 10× (bar = 200 μm, spleen) magnifications under a microscope. White arrows indicated multinucleated giant cells, whereas black arrows showed inflammatory infiltrations.

formulation of ^{hcp1}MVs/adjuvant protects 70% of mice against acute melioidosis. Compared with the rHcp1 protein/adjuvant formulation (19), the elevated protective ability of ^{hcp1}MVs may be ascribed to the intrinsic adjuvanticity of staphylococcal MVs. PAMPs encapsulated in bacterial MVs can also activate immune cells to secrete cytokines and promote a Th1 immune response (32). Consistently, the serum levels of TNF-α and IL-6 in mice 6 h after prime vaccination (day -30) with ^{hcp1}MVs/adjuvant are significantly increased compared with those in the PBS control group. The serum TNF-α and IL-6 levels in mice vaccinated with $^{\Delta agr}$MVs are also remarkably increased and then gradually decreased to normal levels on days -20, -10, and -3 prechallenge (Figure 3). This result is consistent with the finding in the previous study that $^{\Delta agr}$MVs inoculation induces lower level of inflammatory factor production than MVs derived from the wild-type *S. aureus* strain (25). However, the inflammatory cytokine levels, especially TNF-α, in the ^{hcp1}MVs/adjuvant-vaccinated mice increased remarkably on day 0.5 after *B. pseudomallei* exposure (Figure 5). The increased inflammatory cytokine levels during early period after infection may contribute to bacterial clearance (32), which is partially confirmed by the bacterial counting from infected mouse organs (Figure 6A). By contrast, ^{hcp1}MVs-vaccinated animals have low serum TNF-α and IL-6 levels throughout the experimental period. The reason behind this phenomenon is unclear, and the association between ^{hcp1}MV-stimulated inflammatory factor level and its protective potential is of interest and worthy of further study.

A major challenge in developing vaccines against diseases caused by facultative intracellular pathogens is the ability of the host to achieve sterilizing immunity (50). Importantly, vaccination with ^{hcp1}MVs or ^{hcp1}MVs/adjuvant can achieve sterilizing immunity. Culturable bacteria are not determined in lungs, livers, and spleens of ^{hcp1}MVs- or ^{hcp1}MVs/adjuvant-vaccinated mice on day 5 postinfection of *B. pseudomallei* BPC006, whereas most PBS-inoculated mice (66.7%) have bacterial burden in their organs (Figure 6B). In addition, the organ tissue histopathology of vaccinated mice after challenge with *B. pseudomallei* was assessed, and data showed decreased histopathological changes, reduced interstitial inflammation foci, and declined multinucleated giant cell numbers in ^{hcp1}MVs- and ^{hcp1}MVs/adjuvant- vaccinated mice compared with those in PBS-injected mice (Figure 7). These discrete organ bacterial burdens and histopathological observations indicate that the vaccination of Hcp1-loaded MVs contributes to the induction of specific immune responses that control the infection and prevent disseminated melioidosis disease in various organs. Our observations correlate well with the previous finding that pathogen clearance is observed in *B. mallei* live attenuated vaccine-vaccinated mice after challenge with bacteria (88% clearance) (34).

In conclusion, our data demonstrate that Hcp1, a tube component and secreted effector of T6SS in *B. pseudomallei*, is an effective vaccine candidate and that engineered *S. aureus* RN4220-*Δagr/pdhB-hcp1* can successfully produce ^{hcp1}MVs that have protection potential against *B. pseudomallei* acute infections. We have reached an interesting partial adjuvant activity of staphylococcal MVs. The addition of an adjuvant to ^{hcp1}MVs will further improve the protection ability and stimulate an enhanced

sterilizing immunity for complete bacterial clearance. Overall, our results present a new way to develop melioidosis vaccines and provide valuable insights into the development of an antigenically defined, safe, and effective MV vaccine.

Data availability statement

The original contributions presented in the study are included in the article/Supplementary Material. Further inquiries can be directed to the corresponding authors.

Ethics statement

The animal study was reviewed and approved by Third Military Medical University.

Author contributions

XR, RZ, and ML designed experiments, and revised manuscript. KZ, GL, MZ, XP, and JL performed experiments and interpreted data. KZ, GL, and YR investigated data and drew figures. XR and YR edited manuscript. All authors reviewed drafts and approved the submitted version.

Funding

This work was supported by the National Natural Science Foundation of China (82071857 and 81971565).

Acknowledgments

We thank Xu-hu Mao and Cheng-long Rao (Department of Clinical Microbiology and Immunology, College of Medical Laboratory, Army Medical University) for performance of animal experiment.

Conflict of interest

The authors declare that the research was conducted in the absence of any commercial or financial relationships that could be construed as a potential conflict of interest.

Publisher's note

All claims expressed in this article are solely those of the authors and do not necessarily represent those of their affiliated organizations, or those of the publisher, the editors and the reviewers. Any product that may be evaluated in this article, or claim that may be made by its manufacturer, is not guaranteed or endorsed by the publisher.

Supplementary material

The Supplementary Material for this article can be found online at: https://www.frontiersin.org/articles/10.3389/fimmu.2022.1089225/full#supplementary-material

References

1. Birnie E, Virk HS, Savelkoel J, Spijker R, Bertherat E, Dance DAB, et al. Global burden of melioidosis in 2015: a systematic review and data synthesis. *Lancet Infect Dis* (2019) 19(8):892902. doi: 10.1016/S1473-3099(19)30157-4

2. Limmathurotsakul D, Golding N, Dance DA, Messina JP, Pigott DM, Moyes CL, et al. Predicted global distribution of *Burkholderia pseudomallei* and burden of melioidosis. *Nat Microbiol* (2016) 1:15008. doi: 10.1038/nmicrobiol.2015.8

3. Dance DA, Limmathurotsakul D. Global burden and challenges of melioidosis. *Trop Med Infect Dis* (2018) 3(1):13. doi: 10.3390/tropicalmed3010013

4. Suputtamongkol Y, Chaowagul W, Chetchotisakd P, Lertpatanasuwun N, Intaranongpai S, Ruchutrakool T, et al. Risk factors for melioidosis and bacteremic melioidosis. *Clin Infect Dis* (1999) 29(2):408413. doi: 10.1086/520223

5. Trinh TT, Nguyen LDN, Nguyen TV, Tran CX, Le AV, Nguyen HV, et al. Melioidosis in Vietnam: Recently improved recognition but still an uncertain disease burden after almost a century of reporting. *Trop Med Infect Dis* (2018) 3 (2):39. doi: 10.3390/tropicalmed3020039

6. Wiersinga WJ, Virk HS, Torres AG, Currie BJ, Peacock SJ, Dance DAB, et al. Melioidosis. *Nat Rev Dis Primers* (2018) 4:17107. doi: 10.1038/nrdp.2017.107

7. Aziz A, Currie BJ, Mayo M, Sarovich DS, Price EP. Comparative genomics confirms a rare melioidosis human-to-human transmission event and reveals incorrect phylogenomic reconstruction due to polyclonality. *Microb Genom* (2020) 6(2):e000326. doi: 10.1099/mgen.0.000326

8. Wang G, Zarodkiewicz P, Valvano MA. Current advances in *Burkholderia* vaccines development. *Cells* (2020) 9(12):2671. doi: 10.3390/cells9122671

9. Hinjoy S, Hantrakun V, Kongyu S, Kaewrakmuk J, Wangrangsimakul T, Jitsuronk S, et al. Melioidosis in Thailand: Present and future. *Trop Med Infect Dis* (2018) 3(2):38. doi: 10.3390/tropicalmed3020038

10. Hatcher CL, Muruato LA, Torres AG. Recent advances in *Burkholderia mallei* and b. *pseudomallei Res Curr Trop Med Rep* (2015) 2(2):629. doi: 10.1007/s40475-015-0042-2

11. Limmathurotsakul D, Funnell SG, Torres AG, Morici LA, Brett PJ, Dunachie S, et al. Consensus on the development of vaccines against naturally acquired melioidosis. *Emerg Infect Dis* (2015) 21(6):e141480. doi: 10.3201/eid2106.141480

12. Breitbach K, Köhler J, Steinmetz I. Induction of protective immunity against *Burkholderia pseudomallei* using attenuated mutants with defects in the intracellular life cycle. *Trans R Soc Trop Med Hyg* (2008) 102($^{Suppl\ 1}$):S8994. doi: 10.1016/S0035-9203(08)70022-1

13. Atkins T, Prior RG, Mack K, Russell P, Nelson M, Oyston PC, et al. A mutant *of burkholderia pseudomallei*, auxotrophic in the branched chain amino acid biosynthetic pathway, is attenuated and protective in a murine model of melioidosis. *Infect Immun* (2002) 70(9):5290–4. doi: 10.1128/IAI.70.9.5290-5294.2002

14. Harland DN, Chu K, Haque A, Nelson M, Walker NJ, Sarkar-Tyson M, et al. Identification of a LolC homologue in *Burkholderia pseudomallei*, a novel protective antigen for melioidosis. *Infect Immun* (2007) 75(8):4173–80. doi: 10.1128/IAI.00404-07

15. Casey WT, Spink N, Cia F, Collins C, Romano M, Berisio R, et al. Identification of an OmpW homologue in *Burkholderia pseudomallei*, a protective vaccine antigen against melioidosis. *Vaccine* (2016) 34(23):2616–21. doi: 10.1016/j.vaccine.2016.03.088

16. Yi J, Simpanya MF, Settles EW, Shannon AB, Hernandez K, Pristo L, et al. Caprine humoral response to *Burkholderia pseudomallei* antigens during acute melioidosis from aerosol exposure. *PloS Negl Trop Dis* (2019) 13(2):e0006851. doi: 10.1371/journal.pntd.0006851

17. Gourlay LJ, Peano C, Deantonio C, Perletti L, Pietrelli A, Villa R, et al. Selecting soluble/foldable protein domains through single-gene or genomic ORF filtering: Structure of the head domain of burkholderia pseudomallei antigen BPSL2063. *Acta Crystallogr Sect D Biol Crystallogr* (2015) 71(Pt 11):2227–35. doi: 10.1107/S1399004715015680

18. Whitlock GC, Deeraksa A, Qazi O, Judy BM, Taylor K, Propst KL, et al. Protective response to subunit vaccination against intranasal *Burkholderia mallei* and b. *pseudomallei challenge Proc Vaccinol* (2010) 2(1):73–7. doi: 10.1016/j.provac.2010.03.013

19. Burtnick MN, Brett PJ, Harding SV, Ngugi SA, Ribot WJ, Chantratita N, et al. The cluster 1 type VI secretion system is a major virulence determinant in. *Burkholderia pseudomallei Infect Immun* (2011) 79(4):1512–25. doi: 10.1128/IAI.01218-10

20. Nagakubo T, Nomura N, Toyofuku M. Cracking open bacterial membrane vesicles. *Front Microbiol* (2019) 10:3026. doi: 10.3389/fmicb.2019.03026

21. Qiao L, Rao Y, Zhu K, Rao X, Zhou R. Engineered remolding and application of bacterial membrane vesicles. *Front Microbiol* (2021) 12:729369. doi: 10.3389/fmicb.2021.729369

22. Zhao X, Zhao R, Nie G. Nanocarriers based on bacterial membrane materials for cancer vaccine delivery. *Nat Protoc* (2022) 17(10):2240–74. doi: 10.1038/s41596-022-00713-7

23. Xie J, Li Q, Haesebrouck F, Van Hoecke L, Vandenbroucke RE. The tremendous biomedical potential of bacterial extracellular vesicles. *Trends Biotechnol* (2022) 40(10):1173–94. doi: 10.1016/j.tibtech.2022.03.005

24. Findlow J, Bayliss CD, Beernink PT, Borrow R, Liberator P, Balmer P. Broad vaccine protection against *Neisseria meningitidis* using factor h binding protein. *Vaccine* (2020) 38(49):7716–27. doi: 10.1016/j.vaccine.2020.08.031

25. Yuan J, Yang J, Hu Z, Yang Y, Shang W, Hu Q. Safe staphylococcal platform for the development of multivalent nanoscale vesicles against viral infections. *Nano Lett* (2018) 18(2):725–33. doi: 10.1021/acs.nanolett.7b03893

26. Lim YT, Jobichen C, Wong J, Limmathurotsakul D, Li S, Chen Y, et al. Extended loop region of Hcp1 is critical for the assembly and function of type VI secretion system in. *Burkholderia pseudomallei Sci Rep* (2015) 5:8235. doi: 10.1038/srep08235

27. Chieng S, Mohamed R, Nathan S. Transcriptome analysis of *Burkholderia pseudomallei* T6SS identifies Hcp1 as a potential serodiagnostic marker. *Microb Pathog* (2015) 79:47–56. doi: 10.1016/j.micpath.2015.01.006

28. Fang Y, Huang Y, Li Q, Chen H, Yao Z, Pan J, et al. First genome sequence of a *Burkholderia pseudomallei* isolate in China, strain BPC006, obtained from a melioidosis patient in hainan. *J Bacteriol* (2012) 194(23):6604–5. doi: 10.1128/JB.01577-12

29. Rao Y, Peng H, Shang W, Hu Z, Yang Y, Tan L, et al. A vancomycin resistance-associated WalK(S221P) mutation attenuates the virulence of vancomycin-intermediate. *Staphylococcus aureus J Adv Res* (2022) 40:167–78. doi: 10.1016/j.jare.2021.11.015

30. Burtnick MN, Heiss C, Schuler AM, Azadi P, Brett PJ. Development of novel O-polysaccharide based glycoconjugates for immunization against glanders. *Front Cell Infect Microbiol* (2012) 2:148. doi: 10.3389/fcimb.2012.00148

31. Kim OY, Choi SJ, Jang SC, Park KS, Kim SR, Choi JP, et al. Bacterial protoplast-derived nanovesicles as vaccine delivery system against bacterial infection. *Nano Lett* (2015) 15(1):26674. doi: 10.1021/nl503508h

32. Puangpetch A, Anderson R, Huang YY, Saengsot R, Sermswan RW, Wongratanacheewin S. Comparison of the protective effects of killed *Burkholderia pseudomallei* and CpG oligodeoxynucleotide against live challenge. *Vaccine* (2014) 32(45):5983–8. doi: 10.1016/j.vaccine.2014.08.035

33. Sarkar-Tyson M, Smither SJ, Harding SV, Atkins TP, Titball RW. Protective efficacy of heat-inactivated b. thailandensis, *B. mallei* or *B. pseudomallei* against experimental melioidosis and glanders. *Vaccine* (2009) 27(33):4447–51. doi: 10.1016/j.vaccine.2009.05.040

34. Khakhum N, Bharaj P, Myers JN, Tapia D, Walker DH, Endsley JJ, et al. Evaluation of *Burkholderia mallei* ΔtonB Δhcp1 (CLH001) as a live attenuated vaccine in murine models of glanders and melioidosis. *PloS Negl Trop Dis* (2019) 13:e0007578. doi: 10.1371/journal.pntd.0007578

35. Burtnick MN, Shaffer TL, Ross BN, Muruato LA, Sbrana E, DeShazer D, et al. Development of subunit vaccines that provide high-level protection and sterilizing immunity against acute inhalational melioidosis. *Infect Immun* (2017) 86 (1):e00724–17. doi: 10.1128/IAI.00724-17

36. Garcia-Quintanilla F, Iwashkiw JA, Price NL, Stratilo C, Feldman MF. Production of a recombinant vaccine candidate against *Burkholderia pseudomallei* exploiting the bacterial n-glycosylation machinery. *Front Microbiol* (2014) 5:381. doi: 10.3389/fmicb.2014.00381

37. Chen YS, Hsiao YS, Lin HH, Liu Y, Chen YL. CpG-modified plasmid DNA encoding flagellin improves immunogenicity and provides protection against *Burkholderia pseudomallei* infection in BALB/c mice. *Infect Immun* (2006) 74 (3):1699–705. doi: 10.1128/IAI.74.3.1699-1705.2006

38. Lankelma JM, Wagemakers A, Birnie E, Haak BW, Trentelman JJA, Weehuizen TAF, et al. Rapid DNA vaccination against *Burkholderia pseudomallei* flagellin by tattoo or intranasal application. *Virulence* (2017) 8 (8):1683–94. doi: 10.1080/21505594.2017.1307485

39. Lafontaine ER, Chen Z, Huertas-Diaz MC, Dyke JS, Jelesijevic TP, Michel F, et al. The autotransporter protein BatA is a protective antigen against lethal aerosol infection with. *Burkholderia mallei Burkholderia pseudomallei Vaccine X* (2018) 1:100002. doi: 10.1016/j.jvacx.2018.100002

40. Willcocks SJ, Denman CC, Atkins HS, Wren BW. Intracellular replication of the well-armed pathogen. *Burkholderia pseudomallei Curr Opin Microbiol* (2016) 29:94–103. doi: 10.1016/j.mib.2015.11.007

41. Khakhum N, Bharaj P, Walker DH, Torres AG, Endsley JJ. Antigen-specific antibody and polyfunctional T cells generated by respiratory immunization with protective *Burkholderia* ΔtonB Δhcp1 live attenuated vaccines. *NPJ Vaccines* (2021) 6(1):72. doi: 10.1038/s41541-021-00333-4

42. Klimko CP, Shoe JL, Rill NO, Hunter M, Dankmeyer JL, Talyansky Y, et al. Layered and integrated medical countermeasures against *Burkholderia pseudomallei* infections in C57BL/6 mice. *Front Microbiol* (2022) 13:965572. doi: 10.3389/fmicb.2022.965572

43. Morici L, Torres AG, Titball RW. Novel multi-component vaccine approaches for. *Burkholderia pseudomallei Clin Exp Immunol* (2019) 196(2):178–88. doi: 10.1111/cei.13286

44. Nieves W, Asakrah S, Qazi O, Brown KA, Kurtz J, Aucoin DP, et al. A naturally derived outermembrane vesicle vaccine protects against lethal pulmonary *Burkholderia pseudomallei* infection. *Vaccine* (2011) 29(46):8381–9. doi: 10.1016/j.vaccine.2011.08.058

45. Nieves W, Petersen H, Judy BM, Blumentritt CA, Russell-Lodrigue K, Roy CJ, et al. A *Burkholderia pseudomallei* outer membrane vesicle vaccine provides protection against lethal sepsis. *Clin Vaccine Immunol* (2014) 21(5):747–54. doi: 10.1128/CVI.00119-14

46. Khakhum N, Bharaj P, Myers JN, Tapia D, Kilgore PB, Ross BN, et al. *Burkholderia pseudomallei* ΔtonB Δhcp1 live attenuated vaccine strain elicits full protective immunity against aerosolized melioidosis infection. *mSphere* (2019) 4 (1):e00570–18. doi: 10.1128/mSphere.00570-18

47. Su YC, Wan KL, Mohamed R, Nathan S. Immunization with the recombinant *Burkholderia pseudomallei* outer membrane protein Omp85 induces protective immunity in mice. *Vaccine* (2010) 28(31):5005–11. doi: 10.1016/j.vaccine.2010.05.022

48. Sanders H, Feavers IM. Adjuvant properties of meningococcal outer membrane vesicles and the use of adjuvants in *Neisseria meningitidis* protein vaccines. *Expert Rev Vaccines* (2011) 10(3):323–34. doi: 10.1586/erv.11.10

49. Park KS, Svennerholm K, Crescitelli R, Lässer C, Gribonika I, Lötvall J. Synthetic bacterial vesicles combined with tumour extracellular vesicles as cancer immunotherapy. *J Extracell Vesicles* (2021) 10(9):e12120. doi: 10.1002/jev2.12120

50. Titball RW. Vaccines against intracellular bacterial pathogens. *Drug Discovery Today* (2008) 13(13-14):596–600. doi: 10.1016/j.drudis.2008.04.010

frontiers | Frontiers in Immunology

TYPE Original Research
PUBLISHED 13 January 2023
DOI 10.3389/fimmu.2022.1014802

Check for updates

OPEN ACCESS

EDITED BY
Ernesto T. A. Marques,
University of Pittsburgh, United States

REVIEWED BY
Samir N. Khleif,
Georgetown University, United States
Rafael Dhalia,
Fiocruz Pernambuco, Brazil

*CORRESPONDENCE
Konstantinos Dimas
kdimas@uth.gr
George N. Pavlakis
George.pavlakis@nih.gov

SPECIALTY SECTION
This article was submitted to Vaccines and Molecular Therapeutics, a section of the journal Frontiers in Immunology

RECEIVED 09 August 2022
ACCEPTED 23 December 2022
PUBLISHED 13 January 2023

CITATION
Stravokefalou V, Stellas D, Karaliota S, Nagy BA, Valentin A, Bergamaschi C, Dimas K and Pavlakis GN (2023) Heterodimeric IL-15 (hetIL-15) reduces circulating tumor cells and metastasis formation improving chemotherapy and surgery in 4T1 mouse model of TNBC.
Front. Immunol. 13:1014802.
doi: 10.3389/fimmu.2022.1014802

COPYRIGHT
© 2023 Stravokefalou, Stellas, Karaliota, Nagy, Valentin, Bergamaschi, Dimas and Pavlakis. This is an open-access article distributed under the terms of the Creative Commons Attribution License (CC BY). The use, distribution or reproduction in other forums is permitted, provided the original author(s) and the copyright owner(s) are credited and that the original publication in this journal is cited, in accordance with accepted academic practice. No use, distribution or reproduction is permitted which does not comply with these terms.

Heterodimeric IL-15 (hetIL-15) reduces circulating tumor cells and metastasis formation improving chemotherapy and surgery in 4T1 mouse model of TNBC

Vasiliki Stravokefalou[1,2], Dimitris Stellas[1,3], Sevasti Karaliota[1,4], Bethany A. Nagy[5], Antonio Valentin[1], Cristina Bergamaschi[6], Konstantinos Dimas[2*] and George N. Pavlakis[1*]

[1]Human Retrovirus Section, Vaccine Branch, Center for Cancer Research, National Cancer Institute at Frederick, Frederick, MD, United States, [2]Department of Pharmacology, Faculty of Medicine, University of Thessaly, Larissa, Greece, [3]Department of Chemical Biology, National Hellenic Research Foundation, Athens, Greece, [4]Basic Science Program, Frederick National Laboratory for Cancer Research, Leidos Biomedical Research, Frederick, MD, United States, [5]Laboratory Animal Sciences Program, Frederick National Laboratory for Cancer Research, Leidos Biomedical Research, Frederick, MD, United States, [6]Human Retrovirus Pathogenesis Section, Vaccine Branch, Center for Cancer Research, National Cancer Institute at Frederick, Frederick, MD, United States

Immunotherapy has emerged as a viable approach in cancer therapy, with cytokines being of great interest. Interleukin IL-15 (IL-15), a cytokine that supports cytotoxic immune cells, has been successfully tested as an anti-cancer and anti-metastatic agent, but combinations with conventional chemotherapy and surgery protocols have not been extensively studied. We have produced heterodimeric IL-15 (hetIL-15), which has shown anti-tumor efficacy in several murine cancer models and is being evaluated in clinical trials for metastatic cancers. In this study, we examined the therapeutic effects of hetIL-15 in combination with chemotherapy and surgery in the 4T1 mouse model of metastatic triple negative breast cancer (TNBC). hetIL-15 monotherapy exhibited potent anti-metastatic effects by diminishing the number of circulating tumor cells (CTCs) and by controlling tumor cells colonization of the lungs. hetIL-15 treatment in combination with doxorubicin resulted in enhanced anti-metastatic activity and extended animal survival. Systemic immune phenotype analysis showed that the chemoimmunotherapeutic regimen shifted the tumor-induced imbalance of polymorphonuclear myeloid-derived suppressor cells (PMN-MDSCs) in favor of cytotoxic effector cells, by simultaneously decreasing PMN-MDSCs and increasing the frequency and activation of effector ($CD8^+$T and NK) cells. Tumor resection supported by neoadjuvant and adjuvant administration of hetIL-15, either alone or in combination with doxorubicin, resulted in the cure

of approximately half of the treated animals and the development of anti-4T1 tumor immunity. Our findings demonstrate a significant anti-metastatic potential of hetIL-15 in combination with chemotherapy and surgery and suggest exploring the use of this regimen for the treatment of TNBC.

KEYWORDS

heterodimeric IL-15 (hetIL-15), doxorubicin, chemoimmunotherapy, circulating tumor cells (CTCs), metastasis, surgery, triple negative breast cancer (TNBC)

Introduction

Breast cancer is the leading cause of cancer-related deaths in women globally, according to CLOBOCAN (1). One of the most challenging breast cancer subtypes is the triple-negative breast cancer (TNBC), which is characterized by the lack of estrogen receptor, progesterone receptor and human epidermal growth factor receptor 2 (HER2) expression (2). TNBC accounts for 10% to 20% of all breast carcinomas and has a poor prognosis (3). TNBC is more likely to show metastatic recurrence and patients with metastatic TNBC have higher mortality compared to patients with other breast cancer types (42.2% vs 28%, respectively) (4). This is attributed mostly to the lack of therapeutic targets and to the acquired resistance of tumor cells from previous chemotherapeutic treatments (5, 6), which support the need for additional therapeutic strategies.

The recent introduction of immunotherapeutic interventions has resulted in favorable outcomes in several human cancers (7) and provides additional opportunities for new therapeutic combinations. IL-15 is a cytokine of great interest to the cancer immunotherapy field (8); it enhances anti-tumor responses through the stimulation of several leukocyte populations, including cytotoxic $CD8^+$ T lymphocytes and NK (Natural Killer) cells (9–11). Early studies showed that recombinant single chain IL-15 (rhIL-15) produced in *Escherichia coli* has substantial anti-tumor activity (12). Additional efforts to improve IL-15 *in vivo* properties led to the generation of several more stable variants that combine IL-15 with IL-15Rα. The promising results of these variants in several preclinical cancer models have advanced them to clinical trials for safety and efficacy evaluation [reviewed in (13, 14)]. Studies by our group revealed that IL-15 is produced together with IL-15Rα, forming a heterodimeric protein that is the *in vivo* active form of the cytokine in mice and humans (15–18). IL-15Rα is therefore part of the cytokine and does not have any receptor function (13). The complex is termed heterodimeric IL-15 (hetIL-15) and has an extended half-life and better efficacy compared to rhIL-15 (15, 17). Our studies have shown that hetIL-15 exhibits significant anti-cancer activity as monotherapy in several preclinical cancer models including B16 melanoma, MC38 colon carcinoma, EO771 breast adenocarcinoma and TC-1 carcinoma (19–21). Additionally, we have reported that hetIL-15 enhances adoptive cell transfer (ACT) in immunocompetent hosts promoting T lymphocyte infiltration into the tumor (19). hetIL-15 (NIZ985) has been tested as a single agent in a first-in-human study (22), and is currently being evaluated in combination with anti-PD-1 antibodies (Spartalizumab and Tislelizumab) for the treatment of metastatic or unresectable tumors (NCT02452268) and solid tumors or lymphoma (NCT04261439). Results from the phase I NCT02452268 clinical trial showed that hetIL-15 as a single agent is well tolerated and induces IFN-γ production and expansion of cytotoxic lymphocytes in patients with several advanced cancers (22).

Several preclinical studies have demonstrated the important role of IL-15 in controlling metastatic disease (23–29), and combinations with immune checkpoint inhibitors (ICIs) have been proven beneficial (27, 30). In spite of initial supportive evidence (31), IL-15 anti-metastatic activity has not been extensively tested in combination with chemotherapeutic agents. It has been shown that low-dose chemotherapy can enhance anti-tumor immune responses by inducing immunogenic cell death (32), providing the rationale for combining chemotherapy with immunotherapy. To explore novel and more effective therapeutic interventions against metastatic TNBC, we studied the anti-cancer effects of hetIL-15 in combination with the chemotherapeutic agent doxorubicin in the 4T1 murine model of TNBC. Doxorubicin is a broadly used chemotherapeutic agent of the anthracyclines class and the foremost standard of care for TNBC (33). In the present study, we examined the anti-metastatic effects of the treatment by monitoring the presence of metastatic tumor cells in both blood and lungs. To study the mechanism of action of this chemo-immunotherapeutic regimen, we further analyzed the immune cell landscape in the blood, spleen, lung and tumor focusing on the cytotoxic effector cells ($CD8^+$T and NK cells) and immunosuppressive populations (MDSCs). Finally, following standard protocols applicable in clinical settings, we evaluated the efficacy of hetIL-15 alone or together with doxorubicin as neoadjuvants and adjuvants in combination with surgery. Our study evaluates for the first time the therapeutic effect of hetIL-15 in combination with

10.3389/fimmu.2022.1014802

doxorubicin, with or without surgery, demonstrating a significant anti-metastatic potential of this regimen.

Materials and methods

Cells and mice

4T1 cell line (ATCC) was tested for mycoplasma (by PCR using standard mycoplasma testing protocol) and cultured in RPMI-1640 [+] L-glutamine medium (Gibco, #11875-093) supplemented with 100 IU/ml penicillin and 100 µg/ml streptomycin (Lonza, # DE17-602E) and 10% heat-inactivated fetal bovine serum (FBS, Sigma, #F2442). Female Balb/c mice were purchased from Charles River Laboratories (Wilmington, MA, USA) and kept under pathogen-free conditions at the National Cancer Institute Animal Facility in Frederick.

The studies were approved by the National Cancer Institute-Frederick Animal Care and Use Committee. NCI-Frederick is accredited by AAALAC International and follows the Public Health Service Policy for the Care and Use of Laboratory Animals. Animal care was provided in accordance with the procedures outlined in the "Guide for Care and Use of Laboratory Animals (National Research Council; 1996; National Academy Press; Washington, D.C.).

Animal studies and treatment

4T1 tumor cells (0.35-1x10^6) were orthotopically inoculated in the fourth mammary fat pad or injected (10^4) in the lateral tail-vein (intravenously, IV) of 6-8 weeks old Balb/c mice. For the orthotopic inoculation, the cells were resuspended in Dulbecco's PBS (DPBS, Gibco, # 14190-144), and Matrigel (Corning, #354234) was added at 1:3 dilution. Matrigel is a soluble and sterile extract of basement membrane proteins that forms a 3D gel at 37°C (34) preventing cell leakage to adjacent tissues upon inoculation. Tumor size was measured by a digital caliper and tumor volume was calculated by the equation L*W*H*π/6. The treatment started when the tumors reached a size of 30-80mm^3. In both orthotopic and IV models, the mice were randomized into four therapeutic groups: untreated (PBS) (eight IP injections), doxorubicin [(Doxorubicin Hydrochloride injection solution (Dox), Pfizer, #NDC 0069-4037)] (three IV injections - 5mg/kg), hetIL-15 (eight IP injections - 3ug/mouse) and doxorubicin+hetIL-15 (combined schedule of monotherapies). hetIL-15 was purified from HEK293 cells (Admune Therapeutic LLC/Novartis). The study endpoints were: (i) day 22 and (ii) day 18, post tumor cell inoculation, in the orthotopic and IV model, respectively. In the survival studies, mice were sacrificed when the primary tumor reached a 2cm diameter or any other humane endpoints listed in the ACUC-approved animal protocol, such as 20% weight loss or acute morbidity.

Metastasis evaluation

Metastasis evaluation in the blood and lungs was performed by clonogenic assays according to Pulaski and Ostrand-Rosenberg protocol (35). Briefly, RBC-lysed blood and lung cell suspensions were placed in a petri dish (100 mm) and cultured in a selection medium: complete RPMI-1640 [+] L-glutamine supplemented with 60µg/ml of 6-thioguanine (6-TG, Sigma, #A4882) for 14 days. Lung cell suspensions were obtained by enzymatic digestion (Lung Dissociation Kit, mouse, Miltenyi Biotec, #130-095-927) and mechanical dissociation (GentleMACS dissociator, Miltenyi Biotec) according to the manufacturer's protocol. At the end of the 14 days, colonies were fixed with 50% ice-cold trichloroacetic acid (TCA, Sigma, #T6399) and stained with sulforhodamine B (0.04% SRB, Sigma, #S1402) according to Orellana and Kasinski protocol (36). The evaluation was performed macroscopically under the stereoscope counting the individual colonies and assigning the animals in one of the following ranges: 0, 1-50, 50-500 and >500 number of colonies. For the India Ink staining, India Ink (15%, Speedball, #3378) was injected into the trachea of the animal and the lungs were washed in PBS. Lungs were then stored overnight in Fekete's solution containing 300ml of 70% ethanol (Pharmco, #111000200), 30ml of 37% formaldehyde (Sigma, #252549) and 5ml of glacial acetic acid (Sigma, #A6283). The next day, the white pulmonary tumor nodules were counted macroscopically.

Histological analysis

Lungs were fixed in 10% neutral buffered formalin (NBF, Sigma, #HT501128) and paraffin embedded. Sections were stained with hematoxylin/eosin (H&E) or processed for immunohistochemistry (IHC). IHC automated staining was performed on Leica Biosystems' Bond RX with the following conditions: Epitope Retrieval 1 (Citrate) 20' for CD8a (eBioscience, #14-0808-82, 1:50) and Ly6G/GR1 Granulocyte Marker (Origene, #DM3589P, 1:100). The Bond Polymer Refine Detection Kit (Leica Biosystems, #DS9800) with the omission of the Post Primary Reagent was used, and an anti-rat secondary antibody (Vector Labs, #BA-4001) was included. Isotype rat IgG2a antibody (BD Bioscience, #559073) was used in place of the primary antibodies for the negative controls. H&E and IHC slides were scanned using an Aperio AT2 scanner (Leica Biosystems, Buffalo Grove, IL) into whole slide digital images (one section was used for the analysis). Image analysis of positive-stained cells in lung tissue was performed using HALO image analysis software (v3.3.2541.300; Indica Labs,

Corrales, NM). Positive-stained cells located in vessels or areas of artifact such as folds and tears were excluded from the analysis.

Flow cytometry

Tumors and lungs were processed by enzymatic digestion and mechanical dissociation as mentioned above, and spleens were homogenized mechanically. Single-cell suspensions were obtained by filtering the homogenates using 100 µm cell strainers (Corning, #352360). Red blood cells were lysed using ACK lysis buffer (Lonza, #10-548E). Single cells were washed with PBS and stained (except blood) with a fixable aqua dead cell stain kit (ThermoFisher Scientific, #L34957) for 30 min at 4°C. Next, the samples were surface stained with the following antibodies: CD45 (clone 30-F11, Biolegend, #103108 or BD Biosciences, #557659), CD3 (clone 145-2C11, Biolegend, #100310), CD8a (clone 53-6.7, BD Biosciences, #563234), CD69 (clone H1.2F3, Biolegend, #104545), KLRG1 (clone 2F1, BD Biosciences, #563595), PD-1 (clone 29F.1A12, Biolegend, #135220), B220 (clone RA3-6B2, BD Biosciences, #553091), Ly6G (clone 1A8, BD Biosciences, #562700), CD49b (clone DX5, BD Biosciences, #562453) and Ly6C (clone AL-21, BD Biosciences, #560593), CD19 (clone 6D5, Biolegend, #115540 or clone 1D3, ThermoFisher Scientific, #15-0193-83), CD11b (clone M1/70, ThermoFisher Scientific, #45-0112-82). For intracellular staining, cells were fixed and permeabilized using the Foxp3 staining buffer (ThermoFisher Scientific, #00-5523-00), following the manufacturer's instructions. After permeabilization, the cells were stained with Ki67 (clone B56, BD Biosciences, # 561277), granzyme B (clone GB12, ThermoFisher Scientific, #MHGB05) and bcl-2 (clone BCL/10C4, Biolegend, #633508). Samples were acquired in a Fortessa flow cytometer (BD Biosciences), and the data were analyzed using FlowJo software (Version 10.8.0, Becton Dickinson and Company, Ashland, OR). PMN-MDSCs were characterized as $CD45^+lin^{neg}$(CD3/CD49b/CD19/B220)/$CD11b^+/Ly6G^+/Ly6C^{low}$ and M-MDSCs as $CD45^+lin^{neg}$(CD3/CD49b/CD19/B220)/$CD11b^+/Ly6G^-/Ly6C^{high}$. Some of the tumors were excluded from the report of intratumoral cell populations because of an unusually high percentage of B cells (> 4.5% of $CD45^+$) that was attributed to contamination with cells from the draining lymph node. All the animals were included in the tumor growth and survival analyses.

Tumor surgeries and pre- and post-treatment

Tumor resections were performed one week post 4T1 cells (0.35×10^6) inoculation (tumor volume $130mm^3$). The treatments started before and continued after surgery following a neoadjuvant and adjuvant setting. On day 4 (tumor size $60mm^3$), the mice were randomized into five groups: (1) untreated (PBS) without tumor resection, (2) untreated (PBS) with resection only, (3) doxorubicin-treated with resection, (4) hetIL-15-treated with resection (5) combination-treated with resection. The dosing schedule was the same as mentioned above except for the additional hetIL-15 administration on day 4 (total of nine injections). The study endpoint was either on day 22, or the mice were evaluated for their survival. Mice showing local tumor regrowth after surgery were excluded from the analysis.

Rechallenge experiment

4T1 tumor cells ($5x10^4$) were subcutaneously injected in the flanks of 18-20 weeks old naïve Balb/c mice (not previously challenged with 4T1 cells, control group) or survivors after tumor resection and hetIL-15 or combination therapy (considered as one group). Cells were resuspended in PBS and Matrigel was added at 1:3 dilution. The rechallenge was performed 90 days after the first challenge. The animals were monitored, and the tumors were measured for 19 days post-inoculation.

Statistical analysis

Statistical analyses were performed using Prism 9.2.0 (GraphPad) Software (San Diego, CA, USA). Ordinary one-way ANOVA (analysis of variance) and Tukey's multiple comparisons tests analysis was used to compare the different groups or Dunette's multiple comparisons test analysis to compare each experimental group to tumor-free group only. Two-way ANOVA or mixed-effects analysis model and Tukey's multiple comparisons test were used to compare the tumor growths among the groups overtime. Survival analysis was done using Log-rank (Mantel-Cox) test. Significant p values were annotated as follows *p<0.05, **p<0.01, ***p<0.001, ****p<0.0001.

Results

hetIL-15 improves the therapeutic benefit of doxorubicin by reducing metastatic burden in lungs and blood

The anti-cancer activity of hetIL-15, as a single agent or in combination with doxorubicin, was evaluated in the 4T1 murine model of TNBC. 4T1 tumor cells were orthotopically inoculated in Balb/c mice and, when the tumors became palpable, the mice were randomized into four therapeutic groups: untreated (vehicle), doxorubicin, hetIL-15 and combination group. The treatment was performed according to the schedule shown in Figure 1A.

The efficacy of the different treatments was initially evaluated by monitoring the growth of the primary tumor and by animal survival. Mice in the three groups that received therapy showed a significant delay in tumor growth compared to the untreated animals (Figure 1B) (data pooled from 6 individual studies - Supplementary Figure S1). The most prominent effect on tumor delay was observed among mice treated with the combination therapy. However, compared to doxorubicin monotherapy, the two agents together result in a marginal improvement in the control of the primary tumor. When the different treatments were evaluated for animal survival, doxorubicin-treated mice showed a moderate benefit, whereas mice in the combination group had significantly extended survival compared to all the other groups (Figure 1C). Although hetIL-15 monotherapy did not show any benefit in survival, when the mice were evaluated for the presence of pulmonary metastatic foci (measured as tumor areas at their individual endpoint), it was found that hetIL-15 exerted a strong anti-metastatic effect (Figure 1D). Following the NIH guidelines, animals were euthanized when the primary tumors approached 2cm in one dimension, despite the fact that the mice were not showing any signs of distress or respiratory discomfort. hetIL-15 co-administration with doxorubicin resulted in an even better control of metastasis. The tumor areas covering the lung tissue in untreated and doxorubicin-treated groups were found to be approximately 16%, whereas these areas were reduced to approximately 5.5% and 2.5% in the hetIL-15- and combination-treated mice, respectively (Figure 1D).

To evaluate this observation in more depth, the anti-metastatic effect in the lungs was further examined by clonogenic assays. On day 22, whole lung homogenates from each animal were cultured in a selection medium to allow for tumor colony formation. Based on the number of tumor colonies per mouse (represented by each plate), the mice were classified into 4 groups: (i) 0 (no colonies), (ii) 1-50, (iii) 50-500 and (iv) >500 colonies. We found that 62.5% (10/16) of the untreated control mice had more than 500 metastatic colonies, and we observed a decrease in these numbers in the therapeutic groups: 2/16 in the doxorubicin group (12.5%), 2/16 in the hetIL-15 group (12.5%) and 1/16 in the combination group (6.25%) (Figure 1E). Importantly, only mice in the hetIL-15 (1 mouse) and combination group (4 mice) were found to have lungs completely free of metastatic cells, revealing the strong anti-metastatic effects of these treatments (Figure 1E).

Next, we sought to evaluate the effect of the treatments on CTCs, which are cells capable of initiating metastatic lesions (37). The evaluation was performed by clonogenic assays in blood collected on day 22. The mice were classified into four groups based on the number of tumor colonies, as described above. Of the 19 untreated 4T1 tumor-bearing animals, 7 (36.84%) developed CTC colonies with 4 of these having more than 500 colonies (Figure 1F). In contrast, none of the animals in hetIL-15 and combination groups had more than 500 CTC colonies. Interestingly, only 4 out of 18 mice (22.2%) developed CTC colonies in the hetIL-15 group, which however were minimal, as 2 of these animals developed only 15 CTC colonies and the other 2, only 2 colonies. The most prominent effect though was observed in the combination group, where only 2 out of 19 mice (10.53%) were positive for CTC colonies with very low numbers (20 and 1 colonies, respectively). The rest of the mice in both hetIL-15 and combination groups did not develop any colony. Mice in the doxorubicin group also showed a reduction in the number of CTCs, however it was not as effective as in the other treated groups.

Taken together, these data indicate that hetIL-15 shows anti-tumor activity in the 4T1 breast cancer model, mainly by reducing the metastatic burden. hetIL-15 was found to exert its anti-metastatic activity by both decreasing the number of CTCs and by preventing metastasis formation in the lungs. This activity was found to improve the efficacy of doxorubicin, leading ultimately to the extended survival of the combination-treated mice.

hetIL-15 and combination therapy show local anti-metastatic effect in the lungs

Given the observation that the treatments decreased the CTCs in the blood, we aimed to study whether the observed anti-metastatic effect in the lungs is a result of fewer cells reaching the tissue. For this purpose, we injected 4T1 tumor cells intravenously into the lateral tail-vein making the lungs the main site of tumor cells seeding. The treatment started 24 hours post cells injection following the schedule shown in Figure 2A. On day 18, mice were sacrificed, and their lungs were analyzed by histology for the presence of metastatic foci (expressed as tumor areas). Mice in the untreated and doxorubicin groups showed approximately 30% of the lung area occupied by tumor cells. hetIL-15 treatment decreased the area to 7% and combination therapy to 4% (5-fold and 8-fold decrease, respectively) (Figure 2B). Of note, two mice in the combination group had less than 1% of lung surface occupied by tumor. This finding provides evidence that hetIL-15, in addition to CTCs reduction, exerts its anti-metastatic effect by inhibiting the colonization of tumor cells locally in the lung metastatic site. Combination with chemotherapy enhanced this effect.

hetIL-15 synergizes with doxorubicin to increase $CD8^+$T and NK cells and reduce PMN-MDSCs systemically

To identify the mechanisms of the observed anti-cancer effects, we sought to evaluate the immune profile of the 4T1 tumor-bearing mice upon treatment. We have previously

10.3389/fimmu.2022.1014802

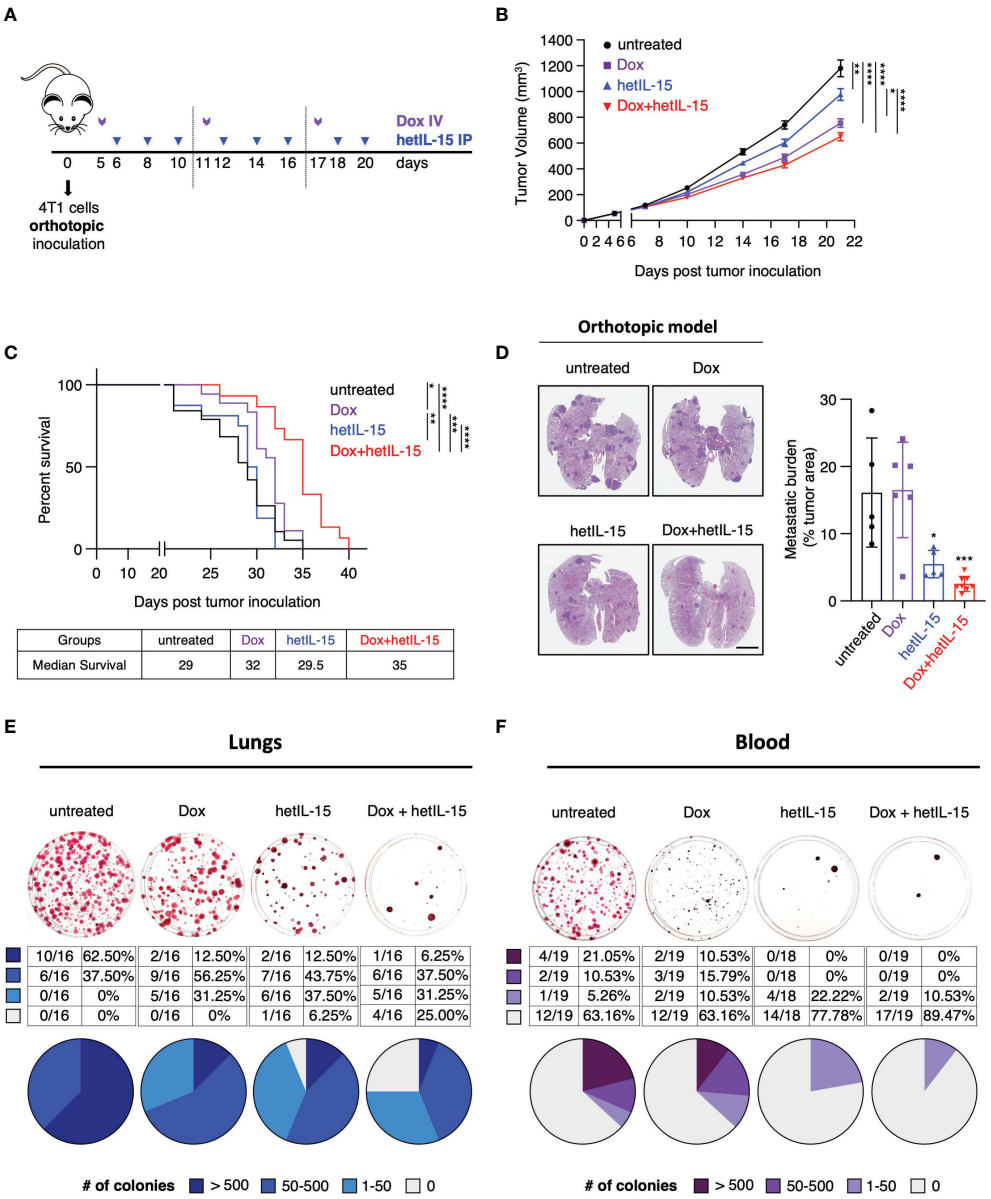

FIGURE 1
hetIL-15 improves doxorubicin efficacy in extending survival by inhibiting metastatic formation in the lungs and CTCs dissemination in the blood. **(A)** Cartoon showing the treatment design. 0.35-1x10^6 4T1 cells were orthotopically inoculated in Balb/c mice and the animals were randomized in four groups: (i) untreated (PBS), (ii) Dox (Doxorubicin)-treated, (iii) hetIL-15-treated and (iv) Dox+hetIL-15-treated. Treatment started on day 5 post tumor inoculation with Dox (5mg/kg IV, purple arrows) once per week, followed by hetIL-15 (3 μg/mouse IP, blue arrows) every other day until day 20. **(B)** Tumor growth curves for each group overtime until day 21. Data were merged from 6 independent studies (n=54-60). Tumor volume (mm^3) ± SEM for each time point is shown. Statistical analysis was done by mixed effects analysis model and Tukey's multiple comparisons test. **(C)** Percent survival of the mice in each group. Statistical analysis was performed by Log-rank (Mantel-Cox) test and data merged from two independent experiments (n=15-19). **(D)** Representative images from H&E-stained lung sections (left panel), and the percentage of tumor areas present in each mouse lungs (right panel, asterisks show the significance of difference from the untreated group) presented as mean ± SD for each group. Data derived from one survival study (n=5-8) of **(C)**. Scale bar, 4mm. Statistical analysis was done by one-way ANOVA and Tukey's multiple comparisons test. **(E, F)** Representative images (upper panels) from clonogenic assays showing SRB-stained tumor colonies derived from lungs **(E)** and blood **(F)**, and tables with the number and the percentage (plotted in pies) of mice with different number of tumor colonies (lower panels) in each group on day 22. Data were merged from 3 independent experiments (n=16) for the lungs and 2 independent experiments (n=18-19) for the blood. Legend shows number of tumor colonies in 4 different ranges. *p < 0.05, **p < 0.01, ***p <0.001, ****p < 0.0001, SD, standard deviation; SEM, standard error of the mean. Image Credit: vector.me.

10.3389/fimmu.2022.1014802

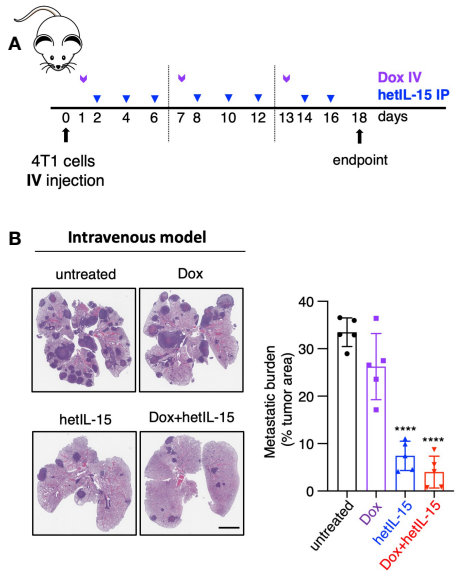

FIGURE 2
hetIL-15 alone and in combination with doxorubicin exerts local anti-metastatic effect in the lungs. **(A)** Cartoon showing the treatment design. 10^4 4T1 cells were injected IV in Balb/c mice and the animals were randomized in four groups: (i) untreated (PBS), (iii) Dox-treated, (iii) hetIL-15-treated and (iv) Dox+hetIL-15-treated. Treatment started one day post tumor cell injection with Dox (5mg/kg IV, purple arrows) once per week, followed by hetIL-15 (3 µg/mouse IP, blue arrows) every other day until day 16. **(B)** Representative images of H&E-stained lung sections (left panel) and the metastatic burden expressed as percentage of tumor area (right panel) in each group on day 18. Percentages presented as mean ± SD for each group. Scale bar, 4mm. Results are from one experiment (n= 5). Statistical analysis was done by one-way ANOVA and Tukey's multiple comparisons test. Asterisks show the significance of difference from the untreated group, ****$p < 0.0001$. Image Credit: vector.me.

reported the role of hetIL-15 on expanding $CD8^+$T and NK cells in tumor-bearing mice (19, 20), while others have shown that doxorubicin decreases the myeloid-derived suppressor cells (MDSCs) (38). For these reasons, we analyzed by flow cytometry the blood, spleens, lungs and tumors of tumor-bearing and age-matched tumor-free mice, to monitor changes in the frequencies of $CD8^+$T, NK, PMN (polymorphonuclear) - and M (monocytic) -MDSC cells. All tissues were collected two days after the last hetIL-15 dose (day 16).

Comparison between tumor-bearing mice and tumor-free mice revealed that the disease causes a systemic reduction in the frequencies of both $CD8^+$T and NK cells, as revealed by flow cytometry (Figure 3A; Supplementary Figure S2A, D). This reduction was prevented by hetIL-15 monotherapy, as the mice showed increased $CD8^+$T and NK cell frequencies in their lungs (Figure 3A), blood and spleen (Supplementary Figure S2A, D). Interestingly, co-administration of hetIL-15 with doxorubicin increased both populations to significantly higher levels also in the lungs (Figure 3A), blood and spleen (Supplementary Figure S2A, D). The increase was statistically significant compared to untreated and both monotherapy groups with $p < 0.0001$ (except the $CD8^+$T cells frequencies in the lungs compared to hetIL-15 monotherapy with $p=0.0014$), which indicated that the two agents synergize to increase $CD8^+$T and NK cell frequencies. Both hetIL-15 and combination treatment promoted $CD8^+$T and NK cells proliferation (measured by Ki67 expression) in the same tissues (Figure 3B; Supplementary Figure S2B, E). These data suggest that the observed increased cell frequencies are a result of increased proliferation within the tissues. The lymphocytes phenotype was further evaluated in the lung tissue by measuring the expression of granzyme B, CD69 and bcl-2 (B-cell lymphoma 2) and the immune checkpoint molecules KLRG1 (killer cell lectin-like receptor G1) and PD-1 (Programmed cell death protein 1) (Supplementary Figure S3). $CD8^+$ T cells from animals treated with hetIL-15 (monotherapy and combination therapy groups) expressed increased levels of CD69 and contained more granzyme B, indicating an activated cytotoxic phenotype. In addition, the cells expressed higher levels of the antiapoptotic molecule bcl-2, suggesting not only enhanced cytotoxicity but also extended survival of these effector cells within the tissue. The expression of these markers on NK cells were particularly increased in mice of the combination group, whereas the expression of granzyme B was also elevated in NKs of the animals treated with hetIL-15 monotherapy. The expression of KLRG1 was also increased in both cell types in animals treated with hetIL-15 (monotherapy and combination therapy groups), and immune checkpoint inhibitor PD-1 was increased in $CD8^+$T cells and in animals treated with combination therapy only (PD-1 expression data in NKs are not shown as the percentage of NKs expressing the marker was below 1%). Within tumors, hetIL-15 treatment resulted in enhanced accumulation of NK cells, while the combination therapy increased both $CD8^+$T and NK cells, revealing that the treatments trigger the intratumoral infiltration of effector cells (Supplementary Figure S4A). The increase of $CD8^+$T cells upon combination treatment was significant not only compared to untreated group, but also to both monotherapy groups ($p=0.008$ and 0.039 to doxorubicin and hetIL-15-monotherapy groups, respectively). In contrast, doxorubicin as monotherapy did not affect either the frequency or the Ki67 expression in these two cell subsets, in any of the tissues (Figures 3A, B; Supplementary Figures S2A-B, D-E, 4A).

Next, we examined the frequencies of MDSCs as these cells are characterized by the ability to suppress T and NK cell functions (39). Flow cytometry analysis revealed that tumor-bearing animals had increased frequencies of MDSCs compared to tumor-free counterparts. The population of PMN-MDSCs was found to be significantly expanded in the lungs (Figure 3D), blood and spleen (Supplementary Figures S2C, F), whereas M-MDSCs were found to be increased mostly in the spleen (Supplementary Figure S2F). Mice treated with hetIL-15 and combination therapy were found with significantly reduced PMN-MDSCs systemically (Figures 3C, D; Supplementary Figure S2C, F). Combination therapy showed the most effective reduction, reducing the PMN-MDSCs frequencies

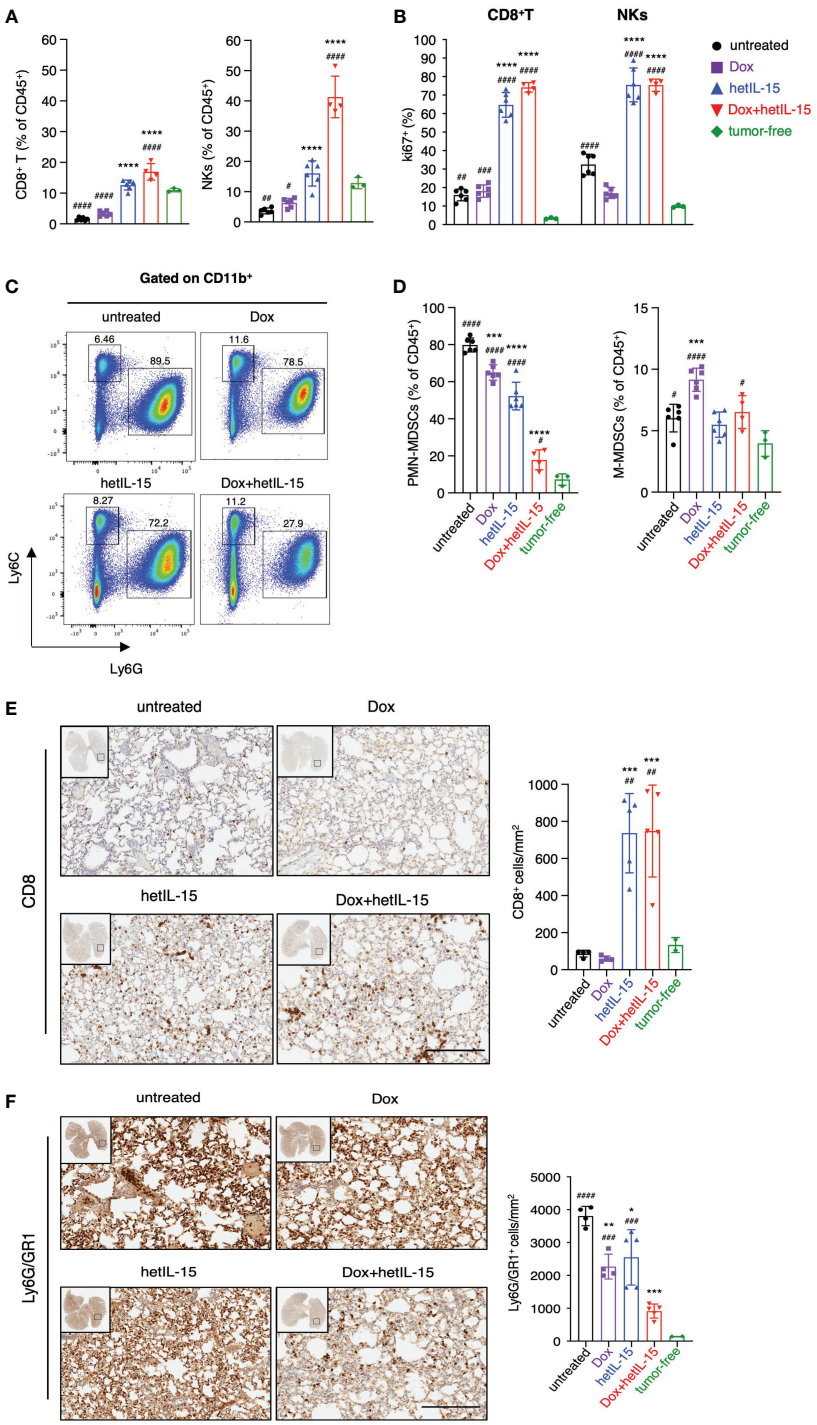

FIGURE 3
hetIL-15 synergizes with doxorubicin to increase CD8$^+$T and NK cells and to reduce PMN-MDSCs in lungs. Mice were treated following the scheme shown in Figure 1A and the tissues were harvested on day 16. **(A)** Frequencies and **(B)** Ki67 expression of CD8$^+$T and NK cells in the lungs of each group. Data are representative of two independent experiments and bars show the mean ± SD for each group (n= 4-6). **(C)** Dot plots from a representative animal from each group showing the percentages of PMN-MDSCs and M-MDSCs in lungs gated in CD11b$^+$. **(D)** PMN-MDSCs and M-MDSCs frequencies in the lungs of each group expressed as percentage of CD45$^+$ cells. Data are representative of two independent experiments and bars show the mean ± SD for each group (n= 4-6). **(E, F)** Representative IHC images of lung slides stained with anti-CD8 **(E)** and anti-Ly6G/GR1 **(F)** for each group. The bar graphs show the absolute numbers of CD8$^+$ cells/mm^2 (**E**, right panel) and Ly6G/GR1$^+$ cells/mm^2 (**F**, right panel) of the whole lung area in each group. Scale bar, 200μm. Results were obtained from one experiment; bars show the mean ± SD for each group (n=4-5). Data obtained from lungs of tumor-free mice are also included [n=3 in **(A–D)** and n=2 in **(E, F)**]. Statistical analysis was done by one-way ANOVA and Tukey's or Dunnette's multiple comparisons test. Asterisks show the significance of difference from the untreated group and hashtags from the tumor-free group, *or $^{\#}p < 0.05$, ** or $^{\#\#}p < 0.01$, *** or $^{\#\#\#}$ $p < 0.001$, **** or $^{\#\#\#\#}p < 0.0001$. SD, standard deviation.

close to normal levels, especially in the lungs. This group showed statistically significant decrease of PMN-MDSCs in comparison to the untreated and both monotherapy groups with $p<0.0001$ (Figure 3D). This effect was also prominent in blood ($p<0.0001$) (Supplementary Figure S2C) and spleen ($p<0.0001$) (Supplementary Figure S2F) revealing significant differences in comparison to either monotherapy group. Our results indicate that the two agents have additive effects also in decreasing PMN-MDSCs. Mice treated with doxorubicin monotherapy also had a lower frequency of PMN-MDSCs, although to a lesser extent as compared to the other two treated groups and only in lungs (Figure 3D). Interestingly, mice treated with doxorubicin monotherapy showed an increase in the frequency of M-MDSCs (Figure 3D; Supplementary Figures S2C, F). Finally, mice from all the groups that received therapy showed a reduction in the tumor-infiltrating PMN-MDSC population, which however reached statistical significance only in the mice from the combination group (Supplementary Figure S4B). In contrast, the tumor-infiltrating M-MDSC population was increased in all the therapeutic groups (Supplementary Figure S4B).

To confirm the findings from the flow cytometry analysis, the absolute number of $CD8^+$ and PMN-MDSC cells in the lungs was also evaluated by immunohistochemistry (IHC). Indeed, the numbers of $CD8^+$ cells were higher in mice from the hetIL-15 and combination groups (Figure 3E), while the number of PMN-MDSC cells was significantly reduced in all the therapeutic groups (Figure 3F). These results suggest that the treatments not only affect the relative frequency of these two cell subsets, but also their absolute numbers.

Overall, these data suggest that hetIL-15 and doxorubicin synergize towards an effective antitumor immunity by increasing the $CD8^+$T and NK cells and decreasing the PMN-MDSCs in the lungs, blood, and spleen. The intratumoral populations were found to be similarly affected, although to a lesser extent.

hetIL-15 and combination therapies restore the imbalance of suppressive to effector cell populations in the tumor-bearing mice

To further evaluate the impact of the different treatments on the immune population landscape, we calculated the ratios of MDSCs (both PMN-MDSCs and M-MDSCs) to $CD8^+$T and NK cells in blood, spleen, lungs, and tumors from the mice in the therapeutic groups and contrasted the results with data obtained from age-matched tumor-free mice.

All the ratios were found to be significantly increased in the examined tissues of the 4T1 tumor-bearing mice compared to tumor-free animals. Notably, the ratios of PMN-MDSCs to both $CD8^+$T and NK cells were more elevated compared to the ratios of M-MDSCs (Figures 4A, B; Supplementary Figures S5A–F). Combination treatment was the most effective at restoring the ratios back to the levels measured in tumor-free mice, in lungs (Figure 4A, B), blood and spleen (Supplementary Figures S5A–D). hetIL-15 monotherapy showed a similar trend, although of lower magnitude, in reducing the ratios, but it was as efficient at reducing the M-MDSCs to effector ratios in lungs (Figure 4B) and blood (Supplementary Figure S5B). Intratumorally, PMN-MDSCs to $CD8^+$T ratios were also significantly reduced in the tumor-bearing mice that received the combination therapy while hetIL-15 decreased only the PMN-MDSCs to NKs ratios

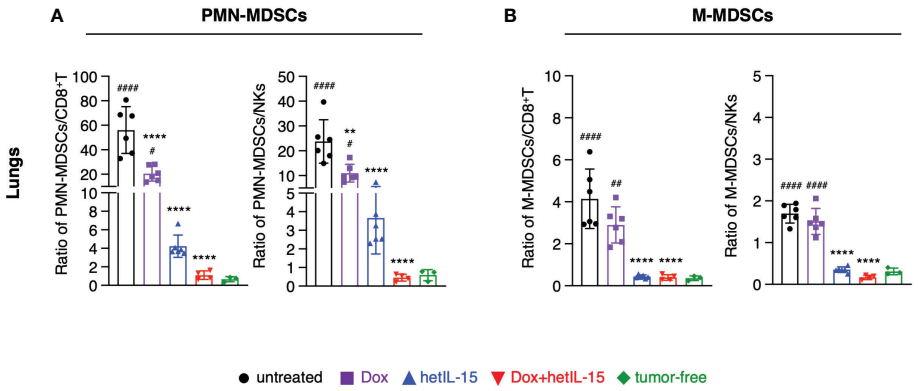

FIGURE 4
hetIL-15 alone and in combination with doxorubicin decreases the suppressor/effector ratios in the lungs. Ratio of **(A)** PMN-MDSCs to $CD8^+$T (left) or NKs (right) and **(B)** M-MDSCs to $CD8^+$T (left) or NKs (right) in the lungs of each group. Mice were treated following the treatment schedule shown in Figure 1A. The treatment was given for two cycles and the tissues were harvested on day 16. Ratios obtained from tumor-free mice are also included (n=3). Similar results were obtained in two different experiments; bars show the mean ± SD for each group (n=4-6). Statistical analysis was done by one-way ANOVA and Tukey's or Dunette's multiple comparisons test. Asterisks show the significance of difference from the untreated group and hashtags from the tumor-free group, ** or $^{\#\#}p < 0.01$, **** or $^{\#\#\#\#}p < 0.0001$. SD, standard deviation.

(Supplementary Figure S5E). No significant changes were observed in any treated mice for the M-MDSCs to effector ratios within the tumors (Supplementary Figure S5F). Mice treated with doxorubicin alone had also decreased ratios, mostly of PMN-MDSCs to effectors in lungs and blood (Figure 4A; Supplementary Figure S5A). However, an increase in M-MDSCs to effector ratios was observed as a trend in the spleen (Supplementary Figure S5D) and tumors (Supplementary Figure S5F) of doxorubicin-treated mice.

Taken together, these data show that hetIL-15 treatment decreases the suppressor to effector cell ratio. This effect is further augmented by the combination with doxorubicin restoring the imbalance induced by the disease and enhancing the antitumor response.

The pre- and post-surgery administration of hetIL-15 monotherapy or combination therapy eradicate metastatic burden curing the animals

It has been previously reported that 4T1 tumor resection reduces MDSCs in the lungs leading to a better control of metastasis (40). Taking this into account and given the observed effects in PMN-MDSCs reduction and metastatic control upon hetIL-15 monotherapy or combination with doxorubicin, we explored the effects of the treatments together with tumor resection. 4T1 tumor cells were orthotopically inoculated in Balb/c mice and the formed tumors were resected one week later. To imitate the neoadjuvant and adjuvant settings (pre- and post-surgery) of the clinical therapeutic schemes (5), the treatments started before surgery and continued afterwards following the administration schedule shown in Figure 5A.

The frequency of circulating PMN-MDSCs was analyzed by flow cytometry on day 16 (Figure 5B). Mice in the groups that underwent surgery showed approximately 2.5 – 3.5-fold reduction of PMN-MDSCs compared to mice from the unresected group, regardless of the treatment type (Figure 5B). Additionally, in all the mice that underwent surgery we found a decrease in the number of Ly6G/GR1 positive cells in their lungs on day 22, indicating a reduction in the absolute numbers of PMN-MDSCs that was again independent of the treatment (Figure 5C). These results show that surgery alone results in the depletion of PMN-MDSCs in blood and lungs.

Metastatic disease was evaluated by India Ink staining of the lungs for the detection of pulmonary nodules on day 22 (Figure 5D). Primary tumor resection alone was effective in decreasing the number of metastatic nodules in comparison to no resection (mean of 21±3 and 78±4 nodules, respectively) (Figure 5D). Remarkably, no metastatic foci were found in the lungs of the mice that underwent surgery and received hetIL-15, either alone or in combination with doxorubicin, revealing that the treatments can eradicate the metastatic disease in the absence of the primary tumor. Mice treated with doxorubicin showed significant foci reduction compared to both non-resected and resected only mice. Similar results were obtained with H&E staining of the lungs (Figure 5D).

We next evaluated the effects of our therapeutic surgery intervention on the overall survival of the mice (Figure 6A). Pre- and post-surgery administration of hetIL-15 monotherapy led to 70% (9 out of 13) cures as the mice did not show any signs of morbidity up to day 80 when the studies were terminated. Similarly, combination treatment led to 45% (4 out of 9) cures of the resected mice, while doxorubicin monotherapy resulted in just 1 cure and marginally extended the median survival to 33 days. None of the non-resected or resected-only mice were cured, and the median survival was similar for both groups (approximately 28 days). Mice that were considered long-term survivors from hetIL-15 (n=7) and combination (n=2) groups were rechallenged with the 4T1 tumor cells. The rechallenge was performed 90 days after the first challenge and the tumor growth was monitored up to day 19 in the absence of any treatment. Survivor animals significantly controlled tumor growth compared to age-matched control animals (challenged for the first time) (Figure 6B), indicating the presence of anti-tumor immunity elicited during the first challenge.

Taken together, these data show that pre- and post-surgery administration of hetIL-15 as monotherapy or in combination with doxorubicin can eradicate the metastatic disease which leads to complete cures and allows the development of effective immunological memory against 4T1 tumor cells.

Discussion

In the present study, we used the immunotherapeutic drug candidate hetIL-15 which has advanced in clinical trials either alone or in combination with the anti-PD-1 antibodies Spartalizumab or Tislelizumab (NCT02452268, NCT04261439). Results from the first-in-human study were recently published reporting that hetIL-15 monotherapy showed stable disease as the best clinical response in 21% of the patients with metastatic or unresectable cancer (22). The data agree with the results obtained in clinical studies using other IL-15 variants (41, 42) and also suggest that combinations should be explored for enhancing IL-15 anti-cancer effects in humans. In this study, we provide supporting evidence that hetIL-15 not only reduces the metastatic disease in the lungs, but also diminishes the number of circulating tumor cells (CTCs). Our findings show the strong anti-metastatic effect of hetIL-15 when administered in combination with doxorubicin and the additive benefits of the two agents in systemically expanding $CD8^+$T and NK cells and reducing PMN-MDSCs. Finally, our data also show that tumor resection together with neoadjuvant and adjuvant administration of hetIL-15, either alone or in combination with doxorubicin, results in the cure of approximately half of the treated animals and the development of immunological memory against 4T1 tumor cells.

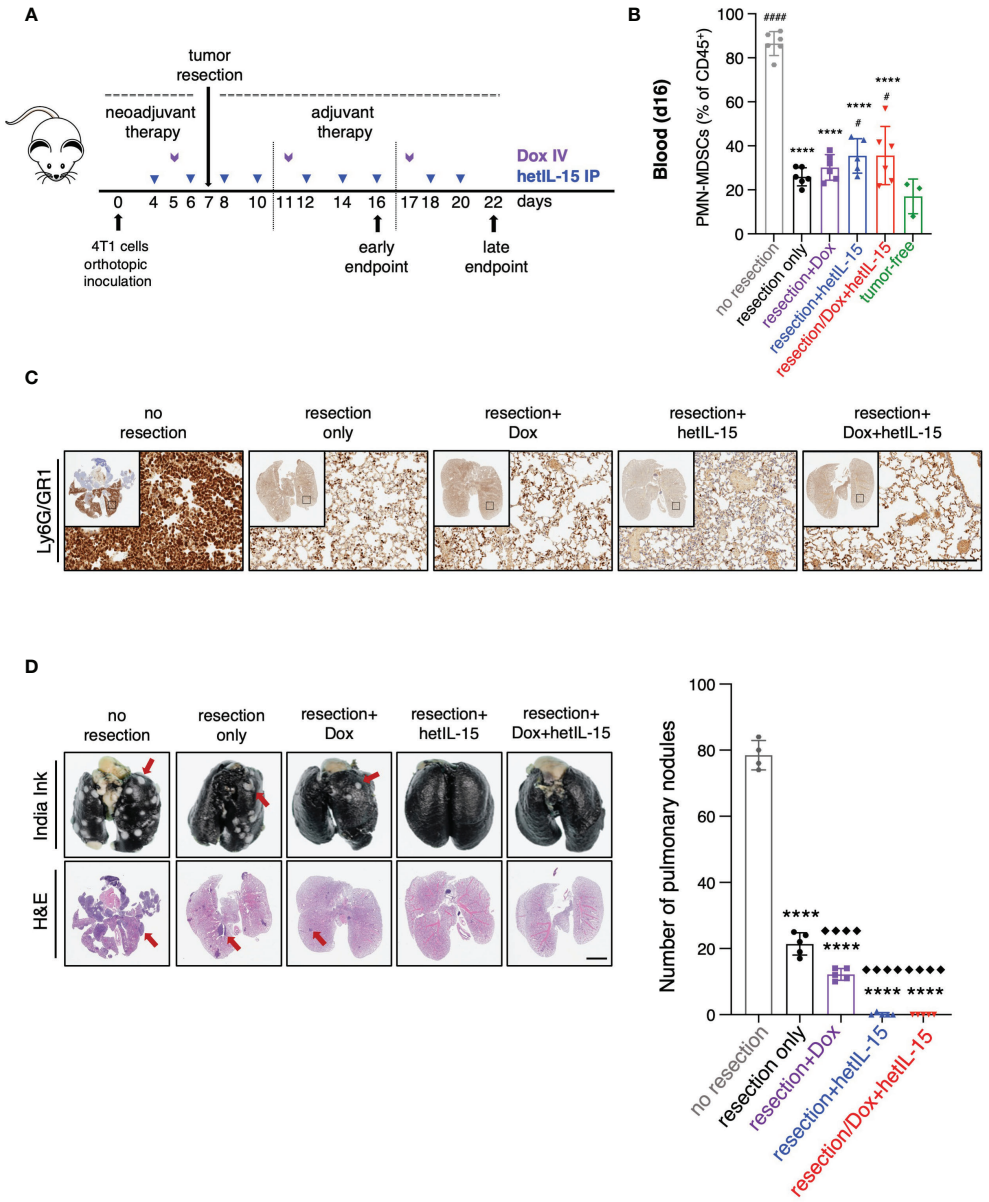

FIGURE 5
Tumor resection reduces PMN-MDSCs and together with hetIL-15, either alone or in combination with doxorubicin, eradicates metastatic disease. **(A)** Cartoon showing the experimental design with the time of tumor resection and the treatments in neoadjuvant and adjuvant setting. 0.35-1x10^6 4T1 cells were orthotopically inoculated in Balb/c mice and tumors were resected one week later. The mice randomized in five groups: (i) no resection, (ii) resection only, (iii) resection+Dox, (iv) resection+hetIL-15 and (v) resection+combinatorial treatment. Treatment started 3 days before surgery with hetIL-15 (3 μg/mouse IP, blue arrows) every other day, followed by doxorubicin (5mg/kg IV, purple arrows) once per week. Treatment endpoints were day 16 (early) or day 22 (late). **(B)** PMN-MDSCs frequencies in blood of each group on day 16. Data obtained from tumor-free mice are also included (n=3). Data are from one experiment; bars shown the mean ± SD for each group (n=5-6). Asterisks show the significance of difference from the non-resected group and hashtags from the tumor-free group $^{\#}p < 0.05$, **** or $^{\#\#\#\#}p < 0.0001$. **(C)** Representative IHC images of Ly6G/GR1-stained lungs from one mouse in each group on day 22. Scale bar, 200μm. Similar results were observed in two independent experiments. **(D)** Representative images from India ink- and H&E-stained lungs (left panels) and number of white tumor nodules (from India ink staining evaluation) in lungs (right panel) are shown as mean ± SD for each group (n=4-5). Results were obtained from two independent experiments. Scale bar, 4mm. Statistical analysis was done by one-way ANOVA and Tukey's or Dunette's multiple comparisons test. Asterisks show the significance of difference from the non-resected group and rhombuses from the resection-only group, **** or $^{◆◆◆◆}p < 0.0001$. SD, standard deviation. Image Credit: vector.me.

IL-15 anti-metastatic activity has been reported in preclinical studies, as single agent [rhIL-15 (27, 28), N-803 (23) and RLI (Receptor-Linker-IL-15) (24, 26)] and in combination (N-803 with PD-L1) (30) or fusion with ICIs [N-809 (N-803 fused to two αPD-L1 domains)] (43). In these studies, the use of IL-15 variants as single agents reduced the pulmonary metastatic foci (23, 24, 26–28) and co-administration or fusion with the ICIs increased the anti-metastatic efficacy of IL-15 (30, 43). Here, we show that hetIL-15 monotherapy significantly reduces metastatic disease in the lungs and co-administration with doxorubicin enhances the efficacy. Combination therapy is also more effective in delaying the growth of the primary 4T1 tumor, while hetIL-15 monotherapy shows a moderate effect. Other IL-15 monotherapy variants have not shown any effect on delaying the primary tumor growth (23, 24, 30). This difference could be attributed to the different treatment schemes (routes of delivery and the total amount of the IL-15 given in the different studies). Further improvements that include alternative delivery routes (such as peritumoral administration) or drug delivery systems, could improve the anti-tumor effect (44).

A main finding of the present study is that hetIL-15 diminishes CTCs. CTCs are the precursors of metastatic lesions (37) and there is an increasing interest in their biology and in therapeutic strategies to target them (45). However, CTCs detection is challenging as they are present in low numbers in the blood (46). Here, using clonogenic assays, we detected CTCs in 36.84% of the untreated mice, with more than half of them forming more than 500 CTC colonies. In contrast, the frequency of mice with detectable CTCs was reduced in both hetIL-15- and combination-treated groups, and these mice showed less than 20 CTC colonies. This finding could be the result of several effects targeting different steps of the metastatic process. Reduction of the shedding from the primary site and increased immunosurveillance in the parenchyma or vasculature of the target organs may independently contribute to this protection. It has been suggested that NK cells patrol the circulation in search of malignant cells (47, 48). In this study we show that NKs are increased in animals receiving hetIL-15 or combination treatment. Furthermore, the reduction of PMN-MDSCs upon

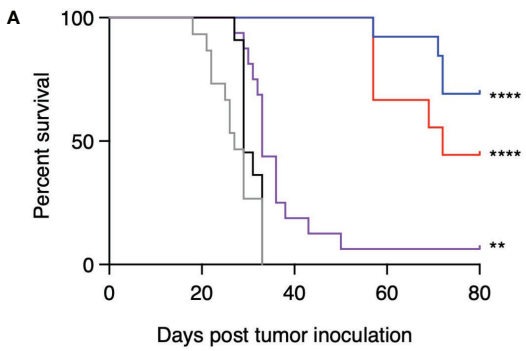

Groups	Median survival
no resection	27
resection only	29
resection+Dox	33
resection+hetIL-15	undefined
resection+Dox +hetIL-15	72

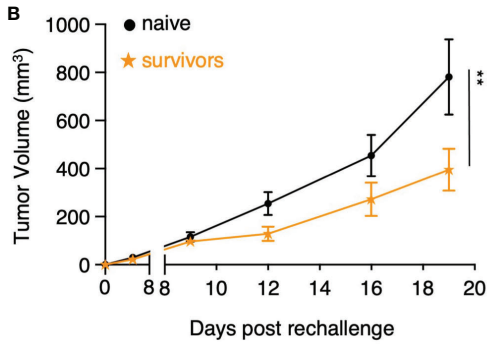

FIGURE 6
hetIL-15 alone or in combination with doxorubicin cures the resected mice and facilitates the development of tumor-specific immunological memory. **(A)** Survival curves for the animals in each experimental group. Mice were resected and treated following the therapeutic schedule shown in Figure 5A. Data merged from two independent studies (n=9-16). Statistical analysis was done by Log-rank (Mantel-Cox) test. **(B)** Tumor growth curves of naive and survivor animals [hetIL-15 and combination group mice merged from (A)] after rechallenge with $5x10^4$ 4T1 cells without any treatment until day 19. Tumor volume (mm^3) ± SEM for each time point is shown. Statistical analysis was done by two-way ANOVA (n=9-10). $^{**}p < 0.01$, $^{****}p < 0.0001$, SEM, standard error of the mean.

these treatments may also contribute to the protection as a study has shown that they inhibit NK cytotoxic activity against tumor cells trapped in pulmonary microvessels (49). Additionally, it was recently reported that IL-15 renders NK cells less susceptible to the oxidative stress induced by myeloid cells in the tumor microenvironment (50). Thus, it is possible that hetIL-15 not only expands NKs but also shields them against PMN-MDSCs, helping them to maintain their cytotoxic activity. Further studies are needed to unfold these mechanisms.

Our study suggests that the anti-metastatic effect of hetIL-15 operates not only through diminishing CTCs but also by exerting local effects in the metastatic site, in this case the lungs. This effect could be related to the higher frequencies of activated $CD8^+$T and NK cells and the reduced PMN-MDSC frequencies found in the tissue upon hetIL-15 treatment. Increased lung-infiltrating $CD8^+$T and NK cells after IL-15 treatment have also been reported in previous studies by our group (15) and others (24). Reduced frequencies of PMN-MDSCs in blood, spleen and lungs could contribute to the anti-metastatic effect as studies have shown that PMN-MDSCs are key regulators of metastasis (51). Others have also reported that MDSC frequencies are reduced upon IL-15/IL-15Ra administration in the Her2/neu+ mammary carcinoma (52). We also show that hetIL-15 decreases the absolute number (not only the frequency) of $Ly6G/GR1^+$ cells in the lungs, suggesting that their infiltration is prevented by the cytokine treatment. In agreement with these data, Desbois et al. reported that the $CD11b^+$ $Ly6G^+$ Ly6Clow cells in the lungs (frequency and absolute counts) were reduced in the 4T1 model upon IL-15-based treatment (24). In line with other studies (30), we did not find major changes in M-MDSCs frequencies, but the M-MDSCs to effectors ratios were restored to normal levels upon hetIL-15 treatment.

Co-administration of hetIL-15 with doxorubicin showed beneficial anti-tumoral effects by increasing the effector populations ($CD8^+$T and NK cells) and by reducing the immunosuppressive PMN-MDSCs in all the tissues analyzed. Doxorubicin induces immunogenic cell death facilitating cytotoxic T cells stimulation (53), and also depletes MDSCs (38). This dual function of Doxorubicin helps the immune system to mount effective anti-tumor responses and provides the rationale for combining doxorubicin with IL-15. In our study, the combination of these two agents successfully controlled metastatic disease in the lungs and blood resulting in better animal survival. In earlier studies, IL-15 combined with cyclophosphamide showed better survival and control of metastatic disease in an IV model of rhabdomyosarcoma (31) providing the initial supportive findings of these therapeutic modalities. PMN-MDSCs depletion by doxorubicin may facilitate the expansion of effectors cells mediated by hetIL-15, suggesting a mechanism for the observed enhanced anti-metastatic activity. Although we did not observe a reduction in the frequency of PMN-MDSCs in the blood or spleen of doxorubicin-treated mice, the reduction in the lungs (frequency and absolute numbers) was significant. Moreover, the combination treatment increased the cytotoxicity and proliferation of lymphocytes, which also expressed anti-apoptotic signals. This observation is in line with the strong anti-metastatic effect observed in the lungs of these animals. The lymphocytes also expressed the marker KLRG1 which is expressed in highly differentiated NK and T cells and is related to senescence (54). Nevertheless, there is evidence that $KLRG1^+CD8^+$ T cells are not impaired in effector functions (55), and $KLRG1^+$NKs have been shown to protect against lung metastasis (56). Furthermore, the effector cells expressed high levels of the Ki67 marker after combination treatment, indicating that doxorubicin does not negatively affect them even if they actively proliferate upon hetIL-15 administration and also that they are not in exhaustion state. Overall, these findings support the notion of combining doxorubicin, and potentially other anthracyclines, with cytokines like hetIL-15 that stimulate the activation and proliferation of cytotoxic immune cells to improve the treatment outcome.

In an effort to develop an additional clinically relevant approach, we surgically removed the orthotopically implanted 4T1 tumors and treated the animals pre- and post-surgery. Lumpectomy or mastectomy is the standard treatment of TNBC upon clinical detection, and this is followed by chemotherapy. In our experimental model, tumor resection supported by neoadjuvant and adjuvant administration of hetIL-15, either alone or combined with doxorubicin, resulted in the cure of approximately half of the treated mice. The hetIL-15 monotherapy group had a higher percentage of cured mice compared to the combination group, but this difference was not statistically significant. Thus, we do not think that hetIL-15 monotherapy has benefit compared to the combination treatment. Other studies have shown that adjuvant administration of the IL-15 agonist N-803 significantly prolongs animal survival (23, 30). Interestingly, Liu et al. demonstrated that neoadjuvant immunotherapy is superior to adjuvant in controlling metastatic disease in two different murine models of TNBC (including the 4T1 model) (57). We hypothesize that hetIL-15 administration as neoadjuvant (in addition to adjuvant) increases the effector cells and systemically protects the tissues from the cancer cells dissemination associated with surgery. A therapeutic scheme that combines pembrolizumab (anti-PD-1) as neoadjuvant therapy with chemotherapy has been already approved by the FDA for early-stage patients with TNBC (58). Additionally, our data indicate that hetIL-15 treatment facilitates the development of tumor-specific immunological memory. This could represent an effective defense against future relapse caused by dormant cancer cells resistant to chemotherapy (59). Based on the limited number of mice with detectable CTCs when the primary tumor was present, we did not evaluate the CTCs in the resected mice upon the different treatments.

It has been shown that tumor resection leads to decreased metastatic burden in the lungs by depleting MDSCs (40). Although mice in resected-only group had fewer PMN-MDSCs in the periphery and lungs, they did not show benefit in survival compared to the non-resected group. This could be related to the establishment of metastasis prior to tumor resection. In support to this, Bosiljcic et al. (40) reported that although surgery decreases

MDSCs, mice are still prone to immunosuppressive functions of PMN-MDSCs for at least 2 weeks after 4T1 tumor resection. In the case of hetIL-15-treated groups, the reduced numbers of PMN-MDSCs in the system of the mice after surgery provided survival benefit, suggesting that hetIL-15 can cure the metastatic disease when the primary tumor is removed and, thus, the tumor-derived factors are heavily decreased. Interestingly, MDSCs have been reported to differentiate into macrophages and mature DCs in the absence of tumor-derived factors (60). The phenotypic analysis of MDSCs upon surgery and treatment would be of interest for future studies.

In summary, our study shows that hetIL-15 exhibits potent anti-metastatic effects in the lungs and reduces the dissemination of tumor cells in peripheral blood, resulting in improved therapeutic benefit in combination with chemotherapy and surgery. Our data suggest that this anti-cancer response is achieved by the expansion of $CD8^+$T and NK cells and the reduction of the immunosuppressive PMN-MDSCs caused by hetIL-15 combination with chemotherapy. Importantly, tumor resection accompanied by the pre- and post-surgery administration of hetIL-15 alone or in combination with doxorubicin leads to the cure of the animals and the establishment of immunological memory. Overall, the data presented herein propose that incorporating hetIL-15 in clinical regimens based on doxorubicin and surgery to treat TNBC could control metastasis and thus reduce the disease recurrence rates.

Data availability statement

The original contributions presented in the study are included in the article/Supplementary Material. Further inquiries can be directed to the corresponding authors.

Ethics statement

The animal study was reviewed and approved by the National Cancer Institute-Frederick Animal Care and Use Committee. NCI-Frederick is accredited by AAALAC International and follows the Public Health Service Policy for the Care and Use of Laboratory Animals. Animal care was provided in accordance with the procedures outlined in the "Guide for Care and Use of Laboratory Animals (National Research Council; 1996; National Academy Press; Washington, D.C.).

Author contributions

VS, DS, SK, AV and KD performed experiments and analyzed data. BN performed experiments. VS, DS, KD and GP conceived the study and designed the experiments. VS wrote the manuscript. VS, DS, SK, AV, CB, KD and GP reviewed all data and finalized the manuscript. All co-authors reviewed the final manuscript.

Funding

This work was funded by the Intramural Research Program of the National Cancer Institute, National Institutes of Health (NCI/NIH) to GP. This project has been funded in part with Federal funds from the National Cancer Institute, National Institutes of Health, under Contract No. HHSN261201500003I. The content of this publication does not necessarily reflect the views or policies of the Department of Health and Human Services, nor does mention of trade names, commercial products, or organizations imply endorsement by the U.S. Government. This contract number represents work performed within the scope of work of the non-severable IDIQ contract (SK, BAN).

Acknowledgments

We thank Breana Myers from the Laboratory Animal Sciences Program, Frederick National Laboratory for Cancer Research (FNLCR); Batiar Karim, Tammy Beachley and Donna Butcher from the Molecular Histopathology Laboratory, FNLCR for technical assistance; Dr. Barbara K. Felber for discussions and support; Drs. Pavlakis and Felber's lab members for discussions and support; Katherine C. Goldfarbmuren for discussions and T. Jones for editorial assistance.

Conflict of interest

GP and CB are inventors of US Government-owned patents related to hetIL-15. Authors SK and BN are employed by Leidos Biomedical Research, Inc.

The remaining authors declare that the research was conducted in the absence of any commercial or financial relationships that could be construed as a potential conflict of interest.

Publisher's note

All claims expressed in this article are solely those of the authors and do not necessarily represent those of their affiliated organizations, or those of the publisher, the editors and the reviewers. Any product that may be evaluated in this article, or claim that may be made by its manufacturer, is not guaranteed or endorsed by the publisher.

Supplementary material

The Supplementary Material for this article can be found online at: https://www.frontiersin.org/articles/10.3389/fimmu.2022.1014802/full#supplementary-material

References

1. Sung H, Ferlay J, Siegel RL, Laversanne M, Soerjomataram I, Jemal A, et al. Global cancer statistics 2020: GLOBOCAN estimates of incidence and mortality worldwide for 36 cancers in 185 countries. *CA: A Cancer J Clin* (2021) 71(3):209–49. doi: 10.3322/caac.21660

2. Rakha EA, Reis-Filho JS, Ellis IO. Basal-like breast cancer: A critical review. *J Clin Oncol* (2008) 26(15):2568–81. doi: 10.1200/JCO.2007.13.1748

3. Kumar P, Aggarwal R. An overview of triple-negative breast cancer. *Arch Gynecol Obstet* (2016) 293(2):247–69. doi: 10.1007/s00404-015-3859-y

4. Dent R, Trudeau M, Pritchard KI, Hanna WM, Kahn HK, Sawka CA, et al. Triple-negative breast cancer: clinical features and patterns of recurrence. *Clin Cancer Res* (2007) 13(15 Pt 1):4429–34. doi: 10.1158/1078-0432.CCR-06-3045

5. Bianchini G, Balko JM, Mayer IA, Sanders ME, Gianni L. Triple-negative breast cancer: challenges and opportunities of a heterogeneous disease. *Nat Rev Clin Oncol* (2016) 13(11):674–90. doi: 10.1038/nrclinonc.2016.66

6. Balko JM, Giltnane JM, Wang K, Schwarz LJ, Young CD, Cook RS, et al. Molecular profiling of the residual disease of triple-negative breast cancers after neoadjuvant chemotherapy identifies actionable therapeutic targets. *Cancer Discovery* (2014) 4(2):232–45. doi: 10.1158/2159-8290.CD-13-0286

7. Mellman I, Coukos G, Dranoff G. Cancer immunotherapy comes of age. *Nature* (2011) 480(7378):480–9. doi: 10.1038/nature10673

8. Cheever MA. Twelve immunotherapy drugs that could cure cancers. *Immunol Rev* (2008) 222:357–68. doi: 10.1111/j.1600-065X.2008.00604.x

9. Carson WE, Giri JG, Lindemann MJ, Linett ML, Ahdieh M, Paxton R, et al. Interleukin (IL) 15 is a novel cytokine that activates human natural killer cells via components of the IL-2 receptor. *J Exp Med* (1994) 180(4):1395–403. doi: 10.1084/jem.180.4.1395

10. Zhang X, Sun S, Hwang I, Tough DF, Sprent J. Potent and selective stimulation of memory-phenotype CD8+ T cells in vivo by IL-15. *Immunity* (1998) 8(5):591–9. doi: 10.1016/S1074-7613(00)80564-6

11. Klebanoff CA, Finkelstein SE, Surman DR, Lichtman MK, Gattinoni L, Theoret MR, et al. IL-15 enhances the in vivo antitumor activity of tumor-reactive CD8+ T cells. *Proc Natl Acad Sci U.S.A.* (2004) 101(7):1969–74. doi: 10.1073/pnas.0307298101

12. Munger W, Dejoy SQ, Jeyaseelan R, Torley LW, Grabstein KH, Eisenmann J, et al. Studies evaluating the antitumor activity and toxicity of interleukin-15, a new T cell growth factor: Comparison with interleukin-2. *Cell Immunol* (1995) 165(2):289–93. doi: 10.1006/cimm.1995.1216

13. Bergamaschi C, Stravokefalou V, Stellas D, Karaliota S, Felber BK, Pavlakis GN. Heterodimeric IL-15 in cancer immunotherapy. *Cancers (Basel)* (2021) 13(4):837. doi: 10.3390/cancers13040837

14. Robinson TO, Schluns KS. The potential and promise of IL-15 in immuno-oncogenic therapies. *Immunol Lett* (2017) 190:159–68. doi: 10.1016/j.imlet.2017.08.010

15. Bergamaschi C, Rosati M, Jalah R, Valentin A, Kulkarni V, Alicea C, et al. Intracellular interaction of interleukin-15 with its receptor alpha during production leads to mutual stabilization and increased bioactivity. *J Biol Chem* (2008) 283(7):4189–99. doi: 10.1074/jbc.M705725200

16. Bergamaschi C, Jalah R, Kulkarni V, Rosati M, Zhang GM, Alicea C, et al. Secretion and biological activity of short signal peptide IL-15 is chaperoned by IL-15 receptor alpha in vivo. *J Immunol* (2009) 183(5):3064–72. doi: 10.4049/jimmunol.0900693

17. Chertova E, Bergamaschi C, Chertov O, Sowder R, Bear J, Roser JD, et al. Characterization and favorable in vivo properties of heterodimeric soluble IL-15.IL-15Ralpha cytokine compared to IL-15 monomer. *J Biol Chem* (2013) 288(25):18093–103. doi: 10.1074/jbc.M113.461756

18. Bergamaschi C, Bear J, Rosati M, Beach RK, Alicea C, Sowder R, et al. Circulating IL-15 exists as heterodimeric complex with soluble IL-15Ralpha in human and mouse serum. *Blood* (2012) 120(1):e1–8. doi: 10.1182/blood-2011-10-384362

19. Ng SSM, Nagy BA, Jensen SM, Hu X, Alicea C, Fox BA, et al. Heterodimeric IL15 treatment enhances tumor infiltration, persistence, and effector functions of adoptively transferred tumor-specific T cells in the absence of lymphodepletion. *Clin Cancer Res* (2017) 23(11):2817–30. doi: 10.1158/1078-0432.CCR-16-1808

20. Bergamaschi C, Pandit H, Nagy BA, Stellas D, Jensen SM, Bear J, et al. Heterodimeric IL-15 delays tumor growth and promotes intratumoral CTL and dendritic cell accumulation by a cytokine network involving XCL1, IFN-γ, CXCL9 and CXCL10. *J Immunother Cancer* (2020) 8(1). doi: 10.1136/jitc-2020-000599

21. Stellas D, Karaliota S, Stravokefalou V, Nagy BA, Felber BK, Pavlakis GN. Abstract 3259: heterodimeric IL-15 monotherapy results in complete regression of EO771 murine breast tumors through cDC1-lymphocyte interactions and induction of antitumor immunity. *Cancer Res* (2019) 79(13_Supplement):3259–9. doi: 10.1158/1538-7445.AM2019-3259

22. Conlon K, Watson DC, Waldmann TA, Valentin A, Bergamaschi C, Felber BK, et al. Phase I study of single agent NIZ985, a recombinant heterodimeric IL-15 agonist, in adult patients with metastatic or unresectable solid tumors. *J ImmunoTher Cancer* (2021) 9(11):e003388. doi: 10.1136/jitc-2021-003388

23. Kim PS, Kwilas AR, Xu W, Alter S, Jeng EK, Wong HC, et al. IL-15 superagonist/IL-15RαSushi-Fc fusion complex (IL-15SA/IL-15RαSu-Fc; ALT-803) markedly enhances specific subpopulations of NK and memory CD8+ T cells, and mediates potent anti-tumor activity against murine breast and colon carcinomas. *Oncotarget* (2016) 7(13):16130–45. doi: 10.18632/oncotarget.7470

24. Desbois M, Béal C, Charrier M, Besse B, Meurice G, Cagnard N, et al. IL-15 superagonist RLI has potent immunostimulatory properties on NK cells: implications for antimetastatic treatment. *J ImmunoTher Cancer* (2020) 8(1):e000632. doi: 10.1136/jitc-2020-000632

25. Kobayashi H, Dubois S, Sato N, Sabzevari H, Sakai Y, Waldmann TA, et al. Role of trans-cellular IL-15 presentation in the activation of NK cell-mediated killing, which leads to enhanced tumor immunosurveillance. *Blood* (2005) 105(2):721–7. doi: 10.1182/blood-2003-12-4187

26. Bessard A, Solé V, Bouchaud G, Quéméner A, Jacques Y. High antitumor activity of RLI, an interleukin-15 (IL-15)–IL-15 receptor α fusion protein, in metastatic melanoma and colorectal cancer. *Mol Cancer Ther* (2009) 8(9):2736–45. doi: 10.1158/1535-7163.MCT-09-0275

27. Yu P, Steel JC, Zhang M, Morris JC, Waldmann TA. Simultaneous blockade of multiple immune system inhibitory checkpoints enhances antitumor activity mediated by interleukin-15 in a murine metastatic colon carcinoma model. *Clin Cancer Res* (2010) 16(24):6019–28. doi: 10.1158/1078-0432.CCR-10-1966

28. Tang F, Zhao L, Jiang Y, Ba D, Cui L, He W. Activity of recombinant human interleukin-15 against tumor recurrence and metastasis in mice. *Cell Mol Immunol* (2008) 5(3):189–96. doi: 10.1038/cmi.2008.23

29. Gillgrass A, Gill N, Babian A, Ashkar AA. The absence or overexpression of IL-15 drastically alters breast cancer metastasis via effects on NK cells, CD4 T cells, and macrophages. *J Immunol* (2014) 193(12):6184–91. doi: 10.4049/jimmunol.1303175

30. Knudson KM, Hicks KC, Alter S, Schlom J, Gameiro SR. Mechanisms involved in IL-15 superagonist enhancement of anti-PD-L1 therapy. *J Immunother Cancer* (2019) 7(1):82. doi: 10.1186/s40425-019-0551-y

31. Chapoval AI, Fuller JA, Kremlev SG, Kamdar SJ, Evans R. Combination chemotherapy and IL-15 administration induce permanent tumor regression in a mouse lung tumor model: NK and T cell-mediated effects antagonized by b cells. *J Immunol* (1998) 161(12):6977–84.

32. Chen G, Emens LA. Chemoimmunotherapy: reengineering tumor immunity. *Cancer Immunol Immunother* (2013) 62(2):203–16. doi: 10.1007/s00262-012-1388-0

33. von Minckwitz G, Martin M. Neoadjuvant treatments for triple-negative breast cancer (TNBC). *Ann Oncol* (2012) 23:vi35–9. doi: 10.1093/annonc/mds193

34. Kleinman HK, Martin GR. Matrigel: basement membrane matrix with biological activity. *Semin Cancer Biol* (2005) 15(5):378–86. doi: 10.1016/j.semcancer.2005.05.004

35. Pulaski BA, Ostrand-Rosenberg S. Mouse 4T1 breast tumor model. *Curr Protoc Immunol* (2001). doi: 10.1002/0471142735.im2002s39

36. Orellana EA, Kasinski AL. Sulforhodamine b (SRB) assay in cell culture to investigate cell proliferation. *Bio-protocol* (2016) 6(21). doi: 10.21769/BioProtoc.1984

37. Baccelli I, Schneeweiss A, Riethdorf S, Stenzinger A, Schillert A, Vogel V, et al. Identification of a population of blood circulating tumor cells from breast cancer patients that initiates metastasis in a xenograft assay. *Nat Biotechnol* (2013) 31(6):539–44. doi: 10.1038/nbt.2576

38. Alizadeh D, Trad M, Hanke NT, Larmonier CB, Janikashvili N, Bonnotte B, et al. Doxorubicin eliminates myeloid-derived suppressor cells and enhances the efficacy of adoptive T-cell transfer in breast cancer. *Cancer Res* (2014) 74(1):104–18. doi: 10.1158/0008-5472.CAN-13-1545

39. Veglia F, Sanseviero E, Gabrilovich DI. Myeloid-derived suppressor cells in the era of increasing myeloid cell diversity. *Nat Rev Immunol* (2021) 21(8):485–98. doi: 10.1038/s41577-020-00490-y

40. Bosiljcic M, Cederberg RA, Hamilton MJ, LePard NE, Harbourne BT, Collier JL, et al. Targeting myeloid-derived suppressor cells in combination with primary mammary tumor resection reduces metastatic growth in the lungs. *Breast Cancer Res* (2019) 21(1):103. doi: 10.1186/s13058-019-1189-x

41. Miller JS, Morishima C, McNeel DG, Patel MR, Kohrt HEK, Thompson JA, et al. A first-in-Human phase I study of subcutaneous outpatient recombinant

human IL15 (rhIL15) in adults with advanced solid tumors. *Clin Cancer Res* (2018) 24(7):1525–35. doi: 10.1158/1078-0432.CCR-17-2451

42. Margolin K, Morishima C, Velcheti V, Miller JS, Lee SM, Silk AW, et al. Phase I trial of ALT-803, a novel recombinant IL15 complex, in patients with advanced solid tumors. *Clin Cancer Res* (2018) 24(22):5552–61. doi: 10.1158/1078-0432.CCR-18-0945

43. Knudson KM, Hicks KC, Ozawa Y, Schlom J, Gameiro SR. Functional and mechanistic advantage of the use of a bifunctional anti-PD-L1/IL-15 superagonist. *J ImmunoTher Cancer* (2020) 8(1):e000493. doi: 10.1136/jitc-2019-000493

44. Stravokefalou V, Stellas D, Karaliota S, Nagy B, Guerin T, Kozlov S, et al. Abstract 2727: Heterodimeric IL-15 (hetIL-15) affects conventional dendritic cells and a distinct novel dendritic cell population in different mouse cancer models of breast and pancreatic cancer. *Cancer Res* (2021) 81(13_Supplement):2727–7. doi: 10.1158/1538-7445.AM2021-2727

45. Zhong X, Zhang H, Zhu Y, Liang Y, Yuan Z, Li J, et al. Circulating tumor cells in cancer patients: developments and clinical applications for immunotherapy. *Mol Cancer* (2020) 19(1):15. doi: 10.1186/s12943-020-1141-9

46. Hattori M, Nakanishi H, Yoshimura M, Iwase M, Yoshimura A, Adachi Y, et al. Circulating tumor cells detection in tumor draining vein of breast cancer patients. *Sci Rep* (2019) 9(1):18195. doi: 10.1038/s41598-019-54839-y

47. Barlozzari T, Reynolds CW, Herberman RB. In vivo role of natural killer cells: involvement of large granular lymphocytes in the clearance of tumor cells in anti-asialo GM1-treated rats. *J Immunol* (1983) 131(2):1024–7.

48. Lambert AW, Pattabiraman DR, Weinberg RA. Emerging biological principles of metastasis. *Cell* (2017) 168(4):670–91. doi: 10.1016/j.cell.2016.11.037

49. Spiegel A, Brooks MW, Houshyar S, Reinhardt F, Ardolino M, Fessler E, et al. Neutrophils suppress intraluminal NK cell-mediated tumor cell clearance and enhance extravasation of disseminated carcinoma cells. *Cancer Discov* (2016) 6 (6):630–49. doi: 10.1158/2159-8290.CD-15-1157

50. Yang Y, Neo SY, Chen Z, Cui W, Chen Y, Guo M, et al. Thioredoxin activity confers resistance against oxidative stress in tumor-infiltrating NK cells. *J Clin Invest* (2020) 130(10):5508–22. doi: 10.1172/JCI137585

51. Ouzounova M, Lee E, Piranlioglu R, El Andaloussi A, Kolhe R, Demirci MF, et al. Monocytic and granulocytic myeloid derived suppressor cells differentially regulate spatiotemporal tumour plasticity during metastatic cascade. *Nat Commun* (2017) 8:14979. doi: 10.1038/ncomms14979

52. Guo S, Smeltz RB, Nanajian A, Heller R. IL-15/IL-15Rα heterodimeric complex as cancer immunotherapy in murine breast cancer models. *Front Immunol* (2021) 11(3712). doi: 10.3389/fimmu.2020.614667

53. Casares N, Pequignot MO, Tesniere A, Ghiringhelli F, Roux S, Chaput N, et al. Caspase-dependent immunogenicity of doxorubicin-induced tumor cell death. *J Exp Med* (2005) 202(12):1691–701. doi: 10.1084/jem.20050915

54. Borys SM, Bag AK, Brossay L, Adeegbe DO. The yin and yang of targeting KLRG1(+) tregs and effector cells. *Front Immunol* (2022) 13:894508. doi: 10.3389/fimmu.2022.894508

55. Sarkar S, Kalia V, Haining WN, Konieczny BT, Subramaniam S, Ahmed R. Functional and genomic profiling of effector CD8 T cell subsets with distinct memory fates. *J Exp Med* (2008) 205(3):625–40. doi: 10.1084/jem.20071641

56. Malaisé M, Rovira J, Renner P, Eggenhofer E, Sabet-Baktach M, Lantow M, et al. KLRG1+ NK cells protect T-bet-deficient mice from pulmonary metastatic colorectal carcinoma. *J Immunol* (2014) 192(4):1954–61. doi: 10.4049/jimmunol.1300876

57. Liu J, Blake SJ, Yong MC, Harjunpää H, Ngiow SF, Takeda K, et al. Improved efficacy of neoadjuvant compared to adjuvant immunotherapy to eradicate metastatic disease. *Cancer Discov* (2016) 6(12):1382–99. doi: 10.1158/2159-8290.CD-16-0577

58. Schmid P, Cortes J, Pusztai L, McArthur H, Kümmel S, Bergh J, et al. Pembrolizumab for early triple-negative breast cancer. *New Engl J Med* (2020) 382 (9):810–21. doi: 10.1056/NEJMoa1910549

59. Sosa MS, Bragado P, Aguirre-Ghiso JA. Mechanisms of disseminated cancer cell dormancy: an awakening field. *Nat Rev Cancer* (2014) 14(9):611–22. doi: 10.1038/nrc3793

60. Narita Y, Wakita D, Ohkur T, Chamoto K, Nishimura T. Potential differentiation of tumor bearing mouse CD11b+Gr-1+ immature myeloid cells into both suppressor macrophages and immunostimulatory dendritic cells. *BioMed Res* (2009) 30(1):7–15. doi: 10.2220/biomedres.30.7

frontiers | Frontiers in Immunology

TYPE Original Research
PUBLISHED 02 February 2023
DOI 10.3389/fimmu.2023.1100188

Check for updates

OPEN ACCESS

EDITED BY
Mrinmoy Sanyal,
Stanford University, United States

REVIEWED BY
Thanh Binh Nguyen,
The University of Queensland, Australia
Aiswarya Sethumadhavan,
Stanford University, United States

*CORRESPONDENCE
Jie Chen
chenjie869@163.com
Pinhua Pan
pinhuapan668@csu.edu.cn

SPECIALTY SECTION
This article was submitted to Vaccines and Molecular Therapeutics, a section of the journal Frontiers in Immunology

RECEIVED 16 November 2022
ACCEPTED 13 January 2023
PUBLISHED 02 February 2023

CITATION
Zhu F, Tan C, Li C, Ma S, Wen H, Yang H, Rao M, Zhang P, Peng W, Cui Y, Chen J and Pan P (2023) Design of a multi-epitope vaccine against six Nocardia species based on reverse vaccinology combined with immunoinformatics.
Front. Immunol. 14:1100188.
doi: 10.3389/fimmu.2023.1100188

COPYRIGHT
© 2023 Zhu, Tan, Li, Ma, Wen, Yang, Rao, Zhang, Peng, Cui, Chen and Pan. This is an open-access article distributed under the terms of the Creative Commons Attribution License (CC BY). The use, distribution or reproduction in other forums is permitted, provided the original author(s) and the copyright owner(s) are credited and that the original publication in this journal is cited, in accordance with accepted academic practice. No use, distribution or reproduction is permitted which does not comply with these terms.

Design of a multi-epitope vaccine against six Nocardia species based on reverse vaccinology combined with immunoinformatics

Fei Zhu[1,2,3,4,5], Caixia Tan[5,6], Chunhui Li[5,6], Shiyang Ma[1,2,3,4,5], Haicheng Wen[5], Hang Yang[1,2,3,4,5], Mingjun Rao[1,2,3,4,5], Peipei Zhang[1,2,3,4,5], Wenzhong Peng[1,2,3,4,5], Yanhui Cui[1,2,3,4,5], Jie Chen[1,2,3,4,5]* and Pinhua Pan[1,2,3,4,5]*

[1]Department of Respiratory Medicine, National Key Clinical Specialty, Branch of National Clinical Research Center for Respiratory Disease, Xiangya Hospital, Central South University, Changsha, Hunan, China, [2]Center of Respiratory Medicine, Xiangya Hospital, Central South University, Changsha, Hunan, China, [3]Clinical Research Center for Respiratory Diseases in Hunan Province, Changsha, Hunan, China, [4]Hunan Engineering Research Center for Intelligent Diagnosis and Treatment of Respiratory Disease, Changsha, Hunan, China, [5]National Clinical Research Center for Geriatric Disorders, Xiangya Hospital, Changsha, Hunan, China, [6]Department of Infection Control Center of Xiangya Hospital, Central South University, Changsha, Hunan, China

Background: *Nocardia* genus, a complex group of species classified to be aerobic actinomycete, can lead to severe concurrent infection as well as disseminated infection, typically in immunocompromised patients. With the expansion of the susceptible population, the incidence of Nocardia has been gradually growing, accompanied by increased resistance of the pathogen to existing therapeutics. However, there is no effective vaccine against this pathogen yet. In this study, a multi-epitope vaccine was designed against the Nocardia infection using reverse vaccinology combined with immunoinformatics approaches.

Methods: First, the proteomes of 6 Nocardia subspecies Nocardia subspecies (Nocardia farcinica, Nocardia cyriacigeorgica, Nocardia abscessus, Nocardia otitidiscaviarum, Nocardia brasiliensis and Nocardia nova) were download NCBI (National Center for Biotechnology Information) database on May 1st, 2022 for the target proteins selection. The essential, virulent-associated or resistant-associated, surface-exposed, antigenic, non-toxic, and non-homologous with the human proteome proteins were selected for epitope identification. The shortlisted T-cell and B-cell epitopes were fused with appropriate adjuvants and linkers to construct vaccines. The physicochemical properties of the designed vaccine were predicted using multiple online servers. The Molecular docking and molecular dynamics (MD) simulation were performed to understand the binding pattern and binding stability between the vaccine candidate and Toll-like receptors (TLRs). The immunogenicity of the designed vaccines was evaluated via immune simulation.

Results: 3 proteins that are essential, virulent-associated or resistant-associated, surface-exposed, antigenic, non-toxic, and non-homologous with the human proteome were selected from 218 complete proteome sequences of the 6 Nocardia subspecies epitope identification. After screening, only 4 cytotoxic T lymphocyte (CTL) epitopes, 6 helper T lymphocyte (HTL) epitopes, and 8 B cell

epitopes that were antigenic, non-allergenic, and non-toxic were included in the final vaccine construct. The results of molecular docking and MD simulation showed that the vaccine candidate has a strong affinity for TLR2 and TLR4 of the host and the vaccine-TLR complexes were dynamically stable in the natural environment. The results of the immune simulation indicated that the designed vaccine had the potential to induce strong protective immune responses in the host. The codon optimization and cloned analysis showed that the vaccine was available for mass production.

Conclusion: The designed vaccine has the potential to stimulate long-lasting immunity in the host, but further studies are required to validate its safety and efficacy.

KEYWORDS

Nocardia, immunoinformatics, reverse vaccinology (RV), multi-epitope vaccine, molecular docking, molecular dynamics (MD) simulation

1 Introduction

The genus *Nocardia*, a group of obligate aerobic gram-positive actinomycetes, is a common etiological agent of nocardiosis that widely exists in the soil, decaying plants, and other organic organisms (1). In 1888, Edmond Nocard isolated an acid-resistant filamentous pathogen from the diseased cattle with symptoms of primary suppurative pulmonary infection and granulomatous abscess (2). In 1889, Trevisan dubbed this strain "*Nocardia farcinica*" and introduced the *Nocardia* genus in detail (2). To date, 120 strains have been identified, of which 54 can cause nocardiosis, and based on the widely accepted Brown-Elliott classification, the *Nocardia* genus has been divided into 9 groups (3, 4). When immunity is significantly compromised, *Nocardia* can invade the body *via* trauma and the respiratory tract, leading to suppurative skin infection and lung infection, or even spreading to organs such as brain and kidney through hematogenous dissemination to result in a systemic infection (5). Notably, the case fatality rate of patients with disseminated infection is 16.2%-38.2% and may be over 50% if the central nervous system (CNS) is affected (6, 7). In recent years, with the increase in the usage of immunosuppressive drugs, organ transplantation, and the incidence of chronic lung diseases, the incidence of *Nocardia* infection has shown an upward trend.

Nocardia has been reported to be capable of surviving as a facultative intracellular parasite within macrophages and evading damage by host neutrophils and monocytes (8, 9). Some *Nocardia* infections are asymptomatic, combined with a long incubation period, making them difficult to identify in clinical specimens (10, 11). Moreover, the co-occurrence of bacterial and fungal infections will further complicate the diagnosis (12). In addition to immune escape and diagnostic difficulty, another issue worth noting is the heterogeneity in the genome size (ranging from 6 to 10 million base pairs (bps) among distinct *Nocardia* species (13, 14). *Nocardia* varies from different species in antimicrobial susceptibility patterns and virulence. Currently, clinically relevant *Nocardia* species have been categorized into 13 antimicrobial susceptibility patterns (15). Nevertheless, the identification of *Nocardia* species necessitates cutting-edge equipment and extensive professional expertise, which is generally difficult to achieve in clinical practice (16, 17). At present, antibiotic therapy is the mainstay of treatment for *Nocardia*, but its duration of treatment is very lengthy. It is generally recommended that patients with normal immune function should receive 6–12 months of antimicrobial therapy, but those with weakened immune systems or CNS dissemination should be treated for at least 12 months (18). Notably, the development of resistance in *Nocardia* to preferred antibiotics, such as trimethoprim-sulfamethoxazole (TMP–SMX), amikacin, and third-generation cephalosporins, is becoming highly common (19, 20). Thus, it is important to develop effective prevention strategies as quickly as possible.

Vaccination is one of the most cost-effective ways to protect people and communities against infectious diseases. However, no vaccine study on human nocardiosis has been reported yet. Traditional vaccine development is a costly and time-consuming procedure, and is fraught with uncertainty regarding the vaccine's specificity, allergenicity, and toxicity, especially for pathogens with complex species and strains (21). Owing to developments in structural biology, genomics, proteomics, and computational science, the field of vaccines has undergone revolutionary changes during the past decades. Reverse vaccinology (RV), as a new technique, is able to locate immunogenic antigens from the pathogen's entire genome sequence (22). It has many advantages over traditional vaccination methods (23, 24). First, convenience – the whole process starts with the analysis of genome sequence, with no need to cultivate microorganisms. Second, safety – it can avoid the spread of pathogenic microorganisms. Third, comprehensiveness – all protein antigens expressed by the pathogens in different periods and environments can be analyzed and used as candidate antigens, even when little is known about the pathogenic mechanism and immune response of the microorganisms. Moreover, RV can be combined with other methods such as immunoinformatics or various biophysical analyses to construct a novel multi-epitope vaccine. It is worth mentioning that the vaccines developed using this approach against several additional infections, including *Brucella melitensis* and *Acinetobacter baumannii*, had been tested in animal experiments, and encouraging experimental results were obtained (25, 26).

In this study, we developed a multi-epitope vaccine against *Nocardia* infection by combining RV with immunoinformatics techniques. All the

proteomes of 6 *Nocardia* subspecies (i.e., *Nocardia farcinica*, *Nocardia cyriacigeorgica*, *Nocardia abscessus*, *Nocardia otitidiscaviarum*, *Nocardia brasiliensis* and *Nocardia nova*) that have a much wider range of popularity were employed to identify the ideal T-cell (CTL and HTL) and B-cell epitopes to be used in the final vaccine construct. The binding mode with immune receptors, the immune effect, the population coverage, and the potential for mass production of the designed vaccine were then assessed using immunoinformatics methods. This study not only gives theoretical reference and data for future research on the *Nocardia* vaccine but also offers new ideas for vaccine development against other similar pathogens.

2 Methodology

2.1 Target proteins screening

2.1.1 Proteome retrieval and core proteins screening

A total of 218 complete proteome sequences of the 6 *Nocardia* subspecies (i.e., *Nocardia farcinica*, *Nocardia cyriacigeorgica*, *Nocardia abscessus*, *Nocardia otitidiscaviarum*, *Nocardia brasiliensis*, and *Nocardia nova*) were obtained from the NCBI (National Center for Biotechnology Information) database on May 1st, 2022. The Bacterial Pan Genome Analysis (BPGA) tool v1.3, which utilizes USEARCH to cluster proteins with a sequence identity threshold of 0.5, was employed to identify core proteins (27, 28).

2.1.2 Screening of essential proteins, virulence proteins and resistance-related proteins

To identify the essential proteins, all selected proteins were submitted to the BLAST v2.12.0+ software to perform sequence alignment between selected proteins and proteins in the Database of Essential Genes 10 (DEG 10) based on the filtering criteria of E-value<10-4, bit score>100 and sequence identity>30% (29). The DEG 10 (http://origin.tubic.org/deg/public/index.php) is a database containing frequently updated essential proteins of prokaryotes (30). Moreover, the virulence proteins and resistance-related proteins were identified *via* BLASTp from the Virulence Factor database (VFDB) (http://www.mgc.ac.cn/VFs/) and The Comprehensive Antibiotic Resistance Database (CARD) (https://card.mcmaster.ca/), respectively, with the filtering criteria set to E-value<10-4, bit score>100 and sequence identity >30% in both cases (31, 32). All of the above sequence data was downloaded from DEG, VFDB and CARD on May 1st, 2022.

2.1.3 Screening of human non-homologous proteins

To avoid inducing autoimmune reactions, we checked the homology between the chosen proteins and the human proteome. First, we obtained the Homo species reference proteome (taxid: 9606) from the NCBI database and then built a local database using the local BLAST v2.12.0+ software based on the obtained data. Then, sequence alignment between selected essential proteins and the established local database was performed using BLASTp. Following the exclusion criteria of E-value<10-4 and bit score>100, the essential proteins with homology to the human proteome were excluded.

2.1.4 Analysis of antigenicity and subcellular localization

VaxiJen2.0 (http://www.ddg-pharmfac.net/vaxijen/VaxiJen/VaxiJen.html) was utilized to assess the antigenicity of the chosen proteins based on the physicochemical properties of protein amino acids (33). To ensure that the final epitopes included in the vaccine construct have better binding ability to lymphocyte receptors or antibodies, we increased the screening threshold for antigenicity to 0.5. Moreover, to validate the results, ANTIGENpro (http://scratch.proteomics.ics.uci.edu/) was also used to predict the antigenicity of chosen proteins (34). The membrane and secretory proteins are easily accessible to lymphocyte receptors and antibodies, indicating that they may serve the ideal vaccine targets. Hence, two web servers, PSORTb v3.0.2 (https://www.psort.org/psortb/) and Cell-PLoc 2.0 (http://www.csbio.sjtu.edu.cn/bioinf/Cell-PLoc-2/) were employed to predict the subcellular localization of the selected proteins. PSORTb v3.0.2, a bacterial localization prediction program, can be used to predict the cytoplasmic membrane, outer membrane, periplasm, extracellular and other subcellular localizations (35), and Cell-PLoc 2.0 can also be used to predict subcellular localizations of proteins in many organisms (36).

2.1.5 Prediction of transmembrane helix, peptide signal and physicochemical properties

The DeepTMHMM server (https://dtu.biolib.com/DeepTMHMM) was employed to predict the transmembrane helix, and the results suggested that its performance was superior to that of previous versions (37). Only the selected proteins with transmembrane helix ≤1 would proceed to the next screening step. The SignalIP 6.0 server (https://services.healthtech.dtu.dk/service.php?SignalP-6.0), which can predict 5 types of signal peptides and their cleavage sites in bacterial and archaeal proteins, was used to predict the signal sequence of selected proteins, and only the proteins without signal sequence were considered for vaccine construction (38). Physicochemical properties such as molecular weight and instability index were calculated *via* the ProtParam server (https://web.expasy.org/protparam/) (39). To facilitate protein purification during vaccine development, only proteins with appropriate molecular weight (<110KDa) and ideal stability (instability index<40) were selected for epitope identification. Further, the toxicity and allergenicity of proteins were predicted by ToxinPred2 and AllerTOP v.2.0 servers, respectively (40, 41). Finally, the models of selected proteins were predicted *via* Robetta server (42), the quality of which was validated through PROCHECK (https://saves.mbi.ucla.edu/) (43), ERRAT (https://saves.mbi.ucla.edu/) (44) and the ProSA-web (https://prosa.services.came.sbg.ac.at/prosa.php) (45) servers.

2.2 Epitopes screening

2.2.1 Prediction of cytotoxic T lymphocyte epitopes

The CTL epitopes were restrictive in binding to MHC class I molecules. To design vaccines with a wide population coverage, we selected human leukocyte antigen (HLA) class I alleles with a high frequency of expression in this study. Each HLA-I allele covered more than 5% of the global population, which was calculated by the Population Coverage tool in the Immune Epitope Database (IEDB) (http://tools.iedb.org/mhci/). There were high frequency HLA-I alleles (HLA-A*01:01,

HLA-A*02:01, HLA-A*03:01, HLA-A*11:01, HLA-A*23:01, HLA-A*24:02, HLA-A*26:01, HLA-A*31:01, HLA-A*68:01, HLA-B*07:02, HLA-B*08:01, HLA-B*18:01, HLA-B*35:01, HLA-B*40:01, HLA-B*44:02, HLA-B*44:03, HLA-B*51:01, HLA-C*01:02, HLA-C*02:02, HLA-C*03:03, HLA-C*04:01, HLA-C*03:04, HLA-C*05:01, HLA-C*06:02, HLA-C*07:01, HLA-*C07:02). The NetCTLpan1.1 server (https://services.healthtech.dtu.dk/service.php?NetCTLpan-1.1) was utilized to predict CTL epitopes by combining MHC-binding peptide prediction, proteasome cleavage site prediction and TAP transport efficiency prediction (46). In this server, the threshold for epitope identification was set to 1%, which indicated that CTL epitopes had good binding to HLA-I alleles.

2.2.2 Prediction of helper T lymphocytes epitopes

NetMHCIIpan 4.0 (https://services.healthtech.dtu.dk/service.php?NetMHCIIpan-4.0), which predicts peptide binding to any major histocompatibility complex (MHC) II molecules of the known sequence using Artificial Neural Networks (ANNs), was employed to predict HTL epitopes, with the 14 most prevalent HLA II alleles (HLA-DRB1*01:01, HLA-DRB1*03:01, HLA-DRB1*04:01, HLA-DRB1*04:04, HLA-DRB1*04:05, HLA-DRB1*07:01, HLA-DRB1*08:02, HLA-DRB1*09:01, HLA-DRB1*11:01, HLA-DRB1*13:02, HLA-DRB1*15:01, HLA-DRB3*01:01, HLA-DRB4*01:01, HLA-DRB5*01:01) in human selected as the binding targets (47). In this study, the epitopes with a percentile rank<1%, which are considered stronger binders, were chosen for further analysis.

2.2.3 Prediction of B-cell epitopes

B-cell epitopes are essential for eliciting humoral immune responses and neutralizing antibody responses. In this study, we utilized three servers to identify B-cell epitopes, and only overlapping epitopes were chosen for further analysis. The first server is ABCpred (https://webs.iiitd.edu.in/raghava/abcpred/), which uses the artificial neural network (ANN) to predict epitopes with an accuracy of 65.3% (48, 49). The second server is Bepipred2.0 (http://tools.iedb.org/bcell/), which employs a random forest method to predict B-cell epitopes from antigen sequences (50). The third server is ElliPro (http://tools.iedb.org/ellipro/), which was used to predict potential B-cell epitopes based on the 3D structure of proteins (51).

2.2.4 Antigenicity, toxicity, allergenicity, and surface accessibility of selected epitopes

The antigenicity of selected epitopes was predicted using the VaxiJen 2.0 server, and the epitopes with antigenicity>0.5 were further submitted to the ToxinPred2 (https://webs.iiitd.edu.in/raghava/toxinpred2/algo.html) and AllerTOP v.2.0 (https://www.ddg-pharmfac.net/AllerTOP/) servers to check for their toxicity and allergenicity, respectively. The screening threshold of the ToxinPred2 server was set to 0.6, and its performance appeared to be superior to that of other servers. AllerTOP v.2.0 predicts the antigenicity of epitopes using the k closest neighbors (kNN) algorithm with an accuracy of 88.7% (41). The accessibility of epitopes on protein surfaces was observed by the surface mode of the PyMOL v2.4 software (52). Based on the above prediction results, all epitopes located in signal peptides, transmembrane helices, and intramembrane regions were excluded.

2.2.5 Immunogenicity analysis of CTL epitopes and validation of the binding of HLA class I alleles

Immunogenicity is the capacity of an agent, such as an epitope or antigen, to stimulate an immune response within the body. In this study, the Class I Immunogenicity tool (http://tools.iedb.org/immunogenicity/) in the IEDB was employed to evaluate the immunogenicity of CTL (the higher the immunogenicity score, the greater the probability of triggering a host immune response) (53). TepiTool (http://tools.iedb.org/tepitool/) from IEDB was applied to validate HLA class I alleles that bind to CTL epitopes using a consensus algorithm that integrates four methods (54, 55), and it is generally believed that epitopes with IC50 ≤ 500 nm have moderate binding to HLA class I molecules.

2.2.6 Prediction of cytokine induction of HTL epitopes

IFN- γ is a key player in cellular immunity, with the capacity to improve antigen processing and presentation, stimulate T-cell differentiation, increase leukocyte transport, and enhance antibacterial activity (56). IL-2 and IL-4 are also essential players in driving T-cell and B-cell proliferation and differentiation (57, 58). Hence, in this study, we evaluated the capacities of all selected HTL-epitopes to induce IFN-γ, IL-2, and IL-4 secretion by using IFNepitope (https://webs.iiitd.edu.in/raghava/ifnepitope/help.php), IL2Pred (https://webs.iiitd.edu.in/raghava/il2pred/), and IL4Pred (https://webs.iiitd.edu.in/raghava/il4pred/) servers, respectively (59–61). Epitopes that can induce the production of IFN-γ and at least one of IL-2 and IL-4 were finally selected.

2.3 Molecular docking between T-cell epitopes and MHC molecules

The MHC molecules as essential molecules in the human body are involved in the presentation of antigen molecules, the interaction between immune cells, and the differentiation of T cells. It is therefore necessary to investigate the interactive models between T-cell epitopes and MHC molecules. First, the selected T-cell epitopes were submitted to the PEP-FOLD 3 server (https://bioserv.rpbs.univ-paris-diderot.fr/services/PEP-FOLD3/) for generating peptide 3D structures (62). The 3D structures of MHC class I molecules (HLA-A*01:01, HLA-B*58:01, HLA-B*15:02, HLA-B*35:01) and MHC class II molecules (HLA-DRB1*01:01) were directly obtained from the RCSB PDB website (https://www.rcsb.org/) (63), while the structures (HLA-DRB1*03:01, HLA-DRB1*04:05, HLA-DRB1*07:01, HLA-DRB4*01:01) not available on the website were modeled through the SWISS-MODEL server (https://swissmodel.expasy.org/) (64). The quality of the model was validated using PROCHECK, ERRAT, and the ProSA-web servers. Then, the Swiss-PdbViewer software was used for the energy minimization of receptors and ligands (65), and Autodock Vina in the PyRx v0.8 was employed to perform molecular docking between T-cell epitopes and MHC

molecules (66). The docking results were subsequently analyzed with LigPlot+ v.2.2 (67).

2.4 Vaccine construction

Compared to conventional vaccines, multi-epitope peptide vaccines are weakly immunogenic. Human beta-defensins (HBDs) are small molecular cationic antimicrobial peptides produced by epithelial cells that exhibit antibacterial and immunomodulatory activity, which is considered to be part of the innate and adaptive immune response (68). Hence, to enhance the immunogenicity of the vaccine candidate, β-defensin 3 was added to the vaccine's N-terminus as an adjuvant. Further, for avoiding the formation of newly connected epitopes and ensuring the independent immunogenicity of each epitope, appropriate connectors were added between the epitopes. Then, the EAAAK linker was utilized to connect adjuvants with the vaccine (69), and the CTL, HTL, and B cell epitopes were linked by AAY, GPGPG, and KK linkers, respectively. The HEYGAEALERAG linkers, acting as cleavage sites for the proteasomal and lysosomal systems, were chosen as spacer linkers to connect CTL, HTL, and B cell epitopes (70). The PADRE sequence, which can facilitate antibody responses, was linked to the C-terminal of the vaccine using the EAAAK linker (71).

3.5 Features of vaccine construct

The VaxiJen2.0 server was used to predict the antigenicity of the vaccine candidate, which was then confirmed by the ANTIGENpro server. The allergenicity and toxicity were checked by AllerTOP v.2.0 and the ToxinPred2 server, respectively. Thereafter, the ProtParam tool was employed to check the physiochemical properties of the designed vaccine, including molecule weight, instability index, the number of amino acids, theoretical isoelectric point (PI), aliphatic index, and GRAVY and half-life. The potential for soluble expression of the vaccine candidate in *E. coli* was evaluated by the SOLpro server (http://scratch.proteomics.ics.uci.edu/) with an accuracy of about 74% (72). Also, the DeepTMHMM and SignalP6.0 servers were employed to predict possible transmembrane helices and signal peptides in the vaccine, respectively.

2.6 Secondary and 3D structure predictions, 3D structure refinement and validation

The secondary structure of the vaccine was predicted by the PSIPRED 4.0 server (http://bioinf.cs.ucl.ac.uk/psipred/) with an accuracy of 84.2% (73). The putative 3D structure of the vaccine was generated using the Robetta server (http://www.robetta.org/), which executes comparative modeling if a suitable template is in the database and executes *ab initio* structure prediction otherwise. Then, the primary structures were submitted to GalaxyRefine for refinement (74). The GalaxyRefine server (https://galaxy.seoklab.org/cgi-bin/submit.cgi?type=REFINE) can improve the structure quality by rebuilding side chains and relaxing the overall structure, and its main parameter MolProbity was used to evaluate the quality of refined models (the lower the MolProbity score, the better the quality of the model). Furthermore, the quality of refined models was validated by the PROCHECK -generated Ramachandran plot, the ERRAT score, and the Z score generated ProSA-web.

2.7 Disulfide engineering of vaccine

To assist protein folding and improve the stability of the protein structure, the Disulfide by Design (DbD) v2.13 server (http://cptweb.cpt.wayne.edu/DbD2/) was employed to conduct disulfide engineering of the designed vaccine, which could check residue pairs with the ability to form disulfide bonds if the amino acid mutated to cysteine (75). The potential residue pairs were then selected based on the criteria of chi3 value -87° or +97° ± 30 and energy value< 2.2 kcal/mol. Subsequently, the PROCHECK, ERRAT, and ProSA-web servers were used to assess the quality of the model with selected disulfide bonds.

2.8 Vaccine-Toll-like receptors docking

The molecular docking of the designed vaccine with the receptor can help clear the binding mode between two molecules. Toll-like receptor 4 (TLR4), a type I transmembrane protein expressed in a variety of tissues including monocytes and macrophages, plays a key role in activating innate immunity by directly recognizing pathogen-related molecular patterns (PAMP), such as lipopolysaccharide (LPS), lipoteichoic acid (LTA), double-stranded RNA (dsRNA), etc (76). TLR2, another member of the TLR family, can recognize various microbial components from gram-positive bacteria such as lipopeptide, peptidoglycan, and fatty acids, and regulate the phenotype and function of dendritic (DC) cells, T cells, natural killer (NK) cells, macrophages and other immune cells (76, 77). Hence, the molecular docking between the multi-epitope vaccine and TLR2 (PDB ID:2Z7X) or TLR4 (PDB ID:4G8A) was realized by the ClusPro 2.0 server (https://cluspro.org/help.php), which ranks the cluster of docking complexes according to their central and lowest energy scores (78). Then, the best docking model was submitted to the HADDOCK 2.4 server (https://wenmr.science.uu.nl/haddock2.4/) for refinement, with the parameters set to default (79). Besides, the PDBsum server (http://www.ebi.ac.uk/thornton-srv/databases/cgi-bin/pdbsum/GetPage.pl?pdbcode=index.html) was used to analyze the interacting residues between the vaccine and TLRs (80).

2.9 Molecular dynamics simulation and analysis

2.9.1 MD simulation

The MD simulation was run using the Gromacs v2022.1 software to understand the dynamics and stability of vaccine–TLR docking complexes (81), and all MD simulations and corresponding analyses were run in triplicate for ensuring the accuracy of the results. During the initial phase, the AMBER14SB_PARMBSC1 force field was added to generate the coordinate file and topology of the vaccine-receptor complex (82). The complex was then solvated by adding transferable

intermolecular potential 3P (TIP3P) water molecules, followed by the addition of counter ions (Na+ and Cl-) to neutralize the charge of the simulated system. Subsequently, energy minimization was performed until reaching the desired threshold (the maximum force ≤1000.0 kJ/mol/nm). To achieve a stable temperature and pressure environment, NVT and NPT simulations were run for 200ps and 1ns, respectively, and the system's temperature and pressure were equilibrated to 310K and 1atm, respectively. The modified Berendsen thermostat was employed to regulate the temperature of the system (83), while the Parinello-Rahman barostat was used to equilibrate the pressure (84). Subsequently, the MD simulation was run for 100 ns with an isothermal and isobaric system. At last, the LINCS algorithm was used to constrain the hydrogen bonds (85), and the Particle-Mesh Ewald summation scheme was executed to calculate long-range electrostatic interactions (86). Finally, the VMD v1.93 software was used to generate the movie of the MD simulations (87).

2.9.2 MM-PBSA calculation

To calculate the binding free energy estimates between the vaccine and TLRs, the last 10 ns of the trajectory was extracted and further submitted to the gmx_MMPBSA v1.56 tool (88). Besides, the energy contribution of all residues within 4 Å of the receptor and ligand was also analyzed using the gmx_MMPBSA v1.56 tool. In this study, the MM-PBSA method was adopted to predict the binding free energy of the complex, whose mathematical explanation is:

$$\Delta G_{bind,solv} = \Delta G_{bind,vaccum} + \Delta G_{solv,complex} - (\Delta G_{solv,ligand} + \Delta G_{solv,receptor})$$

2.9.3 Principal component analysis and dynamical cross-correlation analysis

The principal components (PCs) are eigenvectors that determine the direction of motion, and the extent of residual motion during the MD is defined by the corresponding eigenvalues. In this study, PCs were mainly projected to two dimensions, the principal component 1 (PC1) and the principal component 2 (PC2). Then, the DCC analysis was performed to understand the correlation between the motions of the residues of the vaccine chain and the motions of the residues of the TLRs chain (89). The last 50 ns of the trajectory was extracted and used for the analyses of PCA and DCC, which were operated using the Bio3D package in R version 4.21 (90).

2.10 Immune simulation

The immune simulation of the designed vaccine was performed using the C-ImmSim server (https://kraken.iac.rm.cnr.it/C-IMMSIM/index.php?page=0), which can simulate the immune response generated by a mammalian thymus (T cells), bone marrow (lymph and bone marrow cells), and a lymphoid organ (91). The simulation results could help us estimate the immunogenicity of the vaccine and the immune response it might induce in the human body. According to previous studies, the administration scheme adopted in this study was 1000 vaccine units at a time, once every four weeks, for a total of three injections. The total number of steps was set to 1050, with 1, 84, and 168 time steps for the first to the third injection, respectively. The host MHC molecule combinations were HLA-A*01:01, HLA-B*07:02, and HLA-DRB1*01:01, and other parameters were kept unchanged.

2.11 Population coverage

The proportion of the population that will respond to the vaccine (population coverage) is another important indicator to consider in the vaccine design process. Distinct epitopes bind to different HLA alleles, and the distribution frequency of distinct alleles varies across different regions and ethnicities. Based on the distribution frequency of different HLA alleles and the HLA alleles bound to the vaccine, the global population coverage of the vaccine was calculated using the Population Coverage tool (http://tools.iedb.org/population/) in IEDB (92).

2.12 Codon optimization and cloning

To improve the efficiency of vaccine expression in the selected expression host, the vaccine constructs were submitted to the online tool VectorBuilder (https://www.vectorbuilder.cn/tool/codon-optimization.html) for codon optimization, and *E. coli* (Strain K12) was selected as the expression host in this study. The codon adaptation index (CAI) and percentage GC content, generated by the VectorBuilder server, were utilized to evaluate protein expression levels. The values of CAI vary from 0 to 1, and a high CAI value indicates a high-level expression of genes. The recommended range of GC content varies from 30% to 70%. Then, the Xhoi and BamHI restriction endonuclease sites were attached to the vaccine's C terminal and N terminal, respectively. At last, the final sequence of the vaccine was inserted into the pET-28a (+) vector using the GenSmart tool (https://www.genscript.com/gensmart-design/).

2.13 Prediction of the vaccine mRNA secondary structure

The Transcription and Translation Tool (http://biomodel.uah.es/en/lab/cybertory/analysis/trans.htm) was applied to obtain the mRNA sequence of the vaccine. Two online servers, Mfold v2.3 (http://www.unafold.org/mfold/applications/rna-folding-form-v2.php) (93) and RNAfold (http://rna.tbi.univie.ac.at/cgi-bin/RNAWebSuite/RNAfold.cgi) (94) were used to predict the secondary structure of the vaccine mRNA. The main output result was the minimum free energy (ΔG Kcal/mol), and the lower the minimum free energy, the more stable the folding structure of mRNA.

3 Results

3.1 Pan-proteomics analysis of primary data

A total of 218 proteomes available for the 6 representative *Nocardia* subspecies were obtained from the NCBI database. The detailed information was shown in Supplementary Data Sheet 1. The results of pangenome analysis predicted by the BPGA tool revealed that 1,336 core proteins were found in the 218 proteomes (Supplementary Data Sheet 2).

The flow chart for the design of a multi-epitope vaccine against 6 *Nocardia* subspecies was presented in Figure 1.

3.2 Selection of essential, virulence, resistance, and non-homologous proteins

The results of BLASTp indicated that there were 711 essential proteins out of the 1,336 core proteins (Supplementary Data Sheet 3), and there were 100 virulent proteins (Supplementary Data Sheet 4), 63 resistant proteins (Supplementary Data Sheet 5), and 28 proteins presenting with virulent and resistant functions among the 711 essential proteins (Supplementary Data Sheet 6). Only 76 non-homologous proteins remained after removing proteins with homology to the human proteome (Supplementary Data Sheet 7), of which 3 ideal proteins were identified after analyses of antigenicity, subcellular localization, transmembrane domains, signal sequence, allergenicity, toxicity, and physicochemical properties. From Table 1, it could be seen that all these 3 proteins were antigenic, non-allergic, non-toxic, non-homologous with human proteins, stable and of a suitable molecular

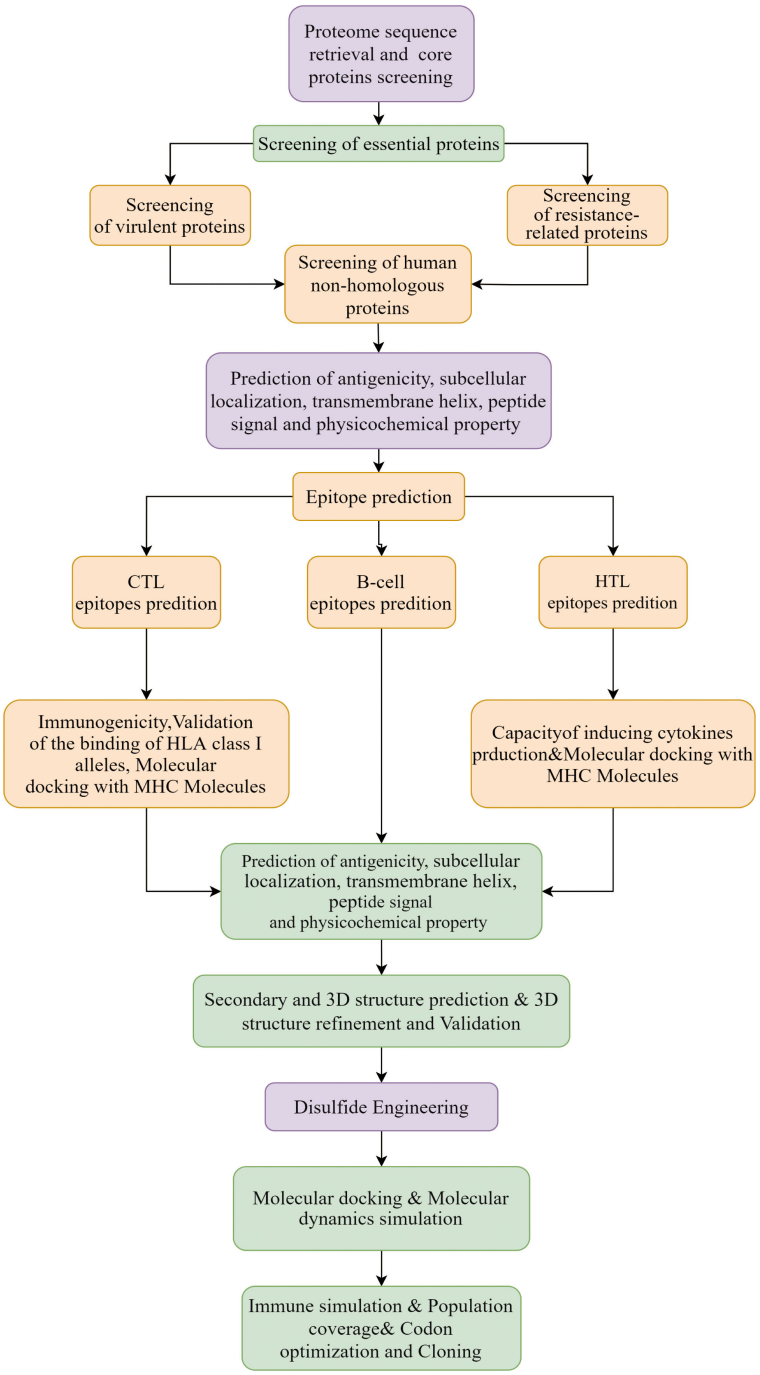

FIGURE 1
Workflow designed for 6 common *Nocardia* subspecies vaccines.

10.3389/fimmu.2023.1100188

weight. Also, all the 3 proteins were essential for bacteria, and two of them were associated with antibiotic resistance, and one with bacterial virulence. After sequence alignment with the NCBI database using BLASTp, it was further found that one of the 3 proteins was a transglycosylase domain-containing protein, one was a penicillin-binding protein, and the other was type VII secretion-associated serine protease myosin-like protein. The structures of the target proteins were shown in Supplementary Data Sheet 8; Figures S1–S3.

3.3 Epitopes screening

After the prediction of antigenicity, immunogenicity, toxicity, allergenicity, and the ability to induce the generation of INF-γ, IL-4 and IL-2. Then, we identified 4 ideal CTL epitopes from 356 epitopes (Table 2), 6 desirable HTL epitopes from 305 epitopes (Table 3), and 8 appropriate B cell epitopes from 61 epitopes for designing a multi-epitope vaccine (Table 4). All selected epitopes were located on the surface of the target protein and visualized by PyMOL v2.4 (Figure 2).

3.4 Molecular docking between T cell epitopes and MHC molecules

The docking results of Autodock Vina revealed that the binding affinity of CTL epitopes to MHC I alleles varied between -9.1 and -8.4 kcal/mol (Figure 3), whereas the binding affinity of HTL epitopes to MHC II alleles varied between -6.6 and -4.4 kcal/mol. According to relevant research, the binding energy is often used to determine the likelihood that a ligand will bind to a protein target, with a larger negative binding affinity value indicating a stronger interaction between the receptor and ligand. From the above, it was suggested that T cell epitopes had a good affinity for MHC allele molecules in this study. Furthermore, the predicted results of Ligplot+ v2.2 also indicated that there were strong interactions between T-cell epitopes and MHC allele molecules, as detailed in Supplemental File 8 Tables S1, S2. The quality verification results of MHC molecules modeled by the SWISS-MODEL server are shown in Supplementary Data Sheet 8; Table S3.

3.5 Vaccine construct and features

The final vaccine sequence is shown in Figure 4A. According to the projected results of VaxiJen2.0 and ANTIGENpro, the antigenicity scores of the vaccine were 1.1966 and 0.9672, respectively. The results from the ToxinPred2 and AllerTOP v.2.0 servers revealed that the vaccine was non-toxic and non-allergic. Analysis of physicochemical characteristics revealed that the vaccine construct was composed of 392 amino acids, with a molecular weight of 40.30 kDa, and its theoretical pI was 9.47. The instability index of the vaccine was 26.07, indicating a stable nature. The aliphatic index of the vaccine was 55.64, suggesting that the vaccine was thermostable. The GRAVY value of the vaccine was -0.677, which demonstrated a hydrophilic nature. The developed vaccine had an estimated half-life of 30 hours in mammalian reticulocytes, over 20 hours in yeasts, and over 10 hours in *E. coli*. According to the prediction results of the SOLpro server, the probability of the

TABLE 1 The target protein from 6 common *Nocardia* species.

Protein	Protein name	Antigenicity		Localization		No of Residues	Mol.Wt.kDa	Instablity Index	Stablity	transmembrane helix	Signal	Allergic	Toxicity
		Vaxijen	ANTIGENpro	PSORTb	Cell-Ploc								
CORE_REP|Org125_Gene1111	transglycosylase domain-containing protein	0.7858	0.963922	Unknown	Cell membrane, Extracell	973	100.1	39.62	stable	1	0	–	–
CORE_REP|Org97_Gene925	penicillin-binding protein	0.52	0.943565	CytoplasmicMembrane	Cell membrane	831	87.01	38.03	stable	1	0	–	–
CORE_REP|Org5_Gene928	type VII secretion-associated serine protease mycosin	0.6548	0.640472	Extracellular	Extracell	503	50.57	35.71	stable	1	1	–	–

10.3389/fimmu.2023.1100188

TABLE 2 The selected CTL epitopes for the vaccine construct.

Protein	Start	Peptide	Antigenicity	immunogenicity	Allergic	Toxicity	Tepitool		
							MHC I alllele	IC50(nM)	Rank%
Gene1111	959	STDGTGDGY	2.8514	0.14952	–	–	HLA-A*01:01	10.79	0.02
							HLA-A*30:02	482.39	0.69
	558	KSGAVRAYY	1.2303	0.17015	–	–	HLA-A*30:02	8.84	0.01
							HLA-B*58:01	65.32	0.25
							HLA-A*30:01	90.7	0.43
							HLA-C*16:01	98.36	0.3
							HLA-B*15:25	163.17	0.85
							HLA-B*57:01	181.13	0.27
							HLA-A*29:02	288	0.44
							HLA-B*15:01	306.85	0.84
							HLA-A*11:01	411.25	1.3
							HLA-C*03:02	489.86	0.91
Gene928	279	ISPAWFSPY	1.2337	0.21557	–	–	HLA-C*03:02	16.69	0.07
							HLA-B*15:25	23.66	0.14
							HLA-C*16:01	27.04	0.09
							HLA-C*12:03	44.51	0.1
							HLA-A*30:02	50.05	0.07
							HLA-C*14:02	58.29	0.22
							HLA-A*29:02	60.57	0.15
							HLA-B*15:01	62.86	0.23
							HLA-C*12:02	109.67	0.09
							HLA-B*15:02	189.88	0.22
							HLA-C*02:02	294.87	0.12
							HLA-C*02:09	294.87	0.12
Gene925	665	SMAGAAYIY	0.5453	0.19637	–	–	HLA-A*29:02	5.26	0.02
							HLA-B*15:25	7.5	0.03
							HLA-A*30:02	11.77	0.02
							HLA-B*15:02	16.58	0.02
							HLA-B*15:01	19.31	0.06
							HLA-B*35:01	72.23	0.13
							HLA-C*03:02	97.12	0.3
							HLA-C*14:02	210.44	0.53
							HLA-C*16:01	272.86	0.63
							HLA-A*11:01	340.63	1.1
							HLA-A*32:01	352.38	0.29
							HLA-A*03:01	436.2	0.86

10.3389/fimmu.2023.1100188

TABLE 3 The screened HTL epitopes for the vaccine construct.

Protein	Start	MHCII alleles	Peptide	Rank_EL %	IC50 (nM)	Antigenicity	Allergic	Toxicity	IFN-γ	IL-4	IL-2
Gene1111	885	DRB1_0101	KPSQVEILPGITIPV	0.35	16.11	0.7823	–	–	+	+	–
	551	DRB1_0301	TAVVSVDPKSGAVRA	0.02	65.27	1.2461	–	–	+	+	–
	552	DRB1_0301	AVVSVDPKSGAVRAY	0.1	71.21	1.1765	–	–	+	+	–
Gene925	294	DRB1_0405	DTLIQNIPSRADEFR	0.33	150.99	0.7800	–	–	+	+	–
	612	DRB1_0701	EPGLANTLANALSQD	0.12	58.97	0.5813	–	–	+	–	+
	359	DRB4_0101	GYLIRTTLDPAVQNS	0.28	33.33	0.5034	–	–	+	+	+

TABLE 4 The selected B cell epitopes for the vaccine construct.

Protein	Start	B cell epitope	Antigenicity	Allergic	Toxicity
Gene1111	956	GVGNSTDGTGDGYTNS	2.4246	–	–
	930	PADGSSPSTSNSGDTS	1.7579	–	–
	346	GSTITQQYVKNAMVGN	0.6965	–	–
	936	PSTSNSGDTSGNSRSQ	2.2641	–	–
	944	TSGNSRSQRPGAGVGN	2.1359	–	–
Gene928	178	LQYEAKNHRDDDTGKVAAGGYGD	1.3327	–	–
Gene925	731	RGSNNAQIPDVNGMSE	1.1028	–	–
	166	SGEVQQG	2.1954	–	–

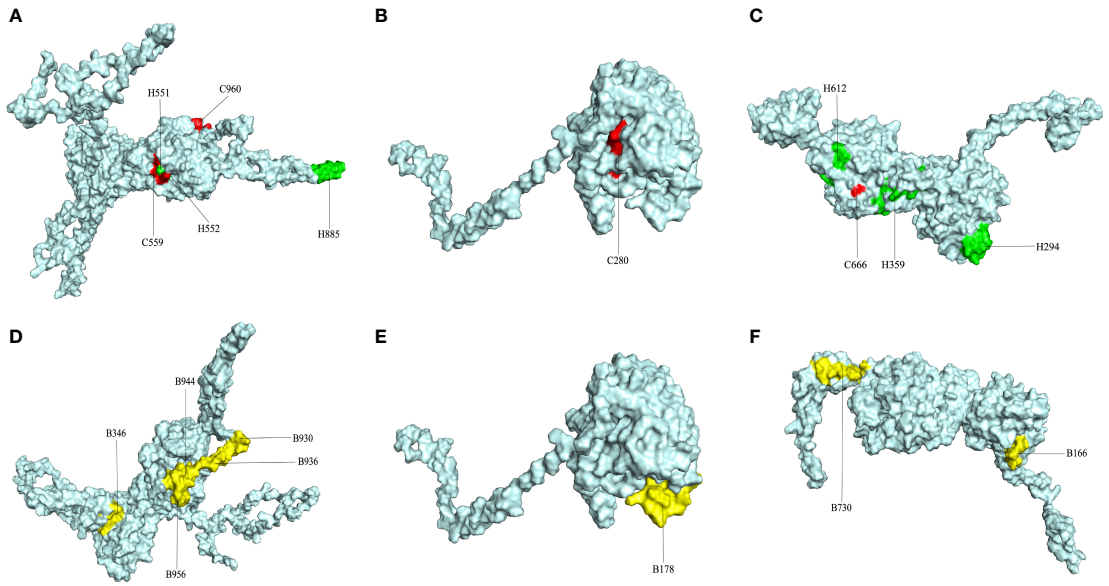

FIGURE 2
The plot of surface positions of all final selected epitopes. **(A)** The Cytotoxicity T Lymphocytes (CTL) and Helper T lymphocyte (HTL) epitopes of CORE_REP|Org125_Gene1111. **(B)** The CTL and HTL epitopes of CORE_REP|Org5_Gene928. **(C)** The CTL and HTL epitopes of CORE_REP|Org97_Gene925; **(D)** The B-cell epitopes of CORE_REP|Org125_Gene1111. **(E)** The B-cell epitopes of CORE_REP|Org5_Gene928. **(F)** The B-cell epitopes of CORE_REP|Org97_Gene925. Each CTL epitope is shown using a combination of C and its starting position. Each HTL epitope is shown using a combination of H and its starting position. Each B-cell epitope is shown using a combination of B and its starting position.

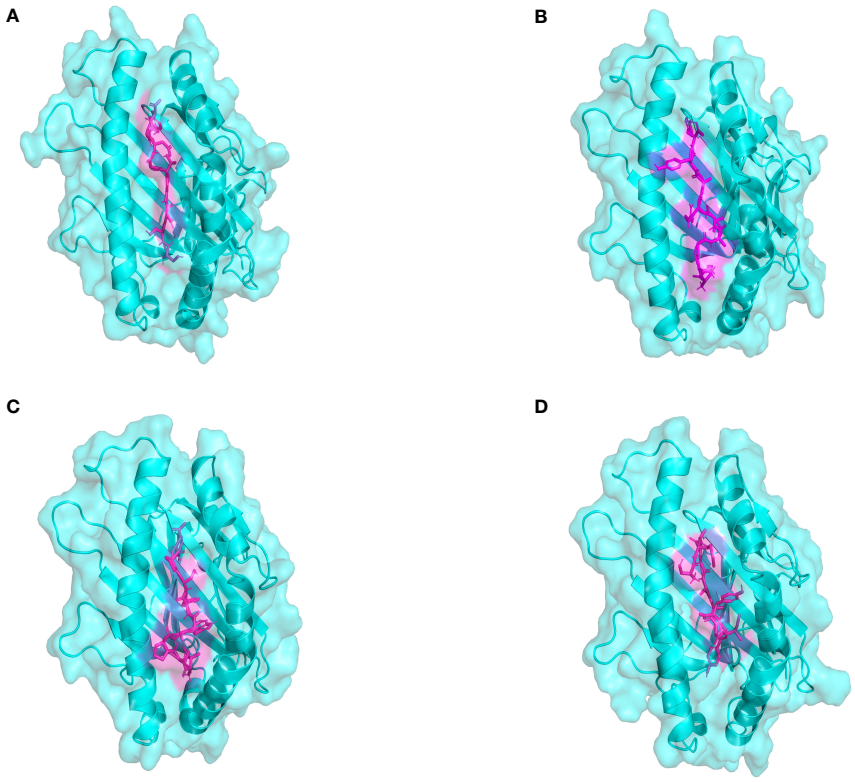

FIGURE 3
The plot of the binding patterns of CTL epitopes with MHC class I molecules. The MHC I allele molecules were presented in blue and the CTL epitope peptides were presented as magenta. **(A)** The STDGTGDGY epitope bind with HLA-A0101 **(B)** The KSGAVRAYY epitope bind with HLA-B5801 **(C)** The ISPAWFSPY epitope bind with HLA-B1502 **(D)** The AETASPERI epitope bind with HLA-B4402.

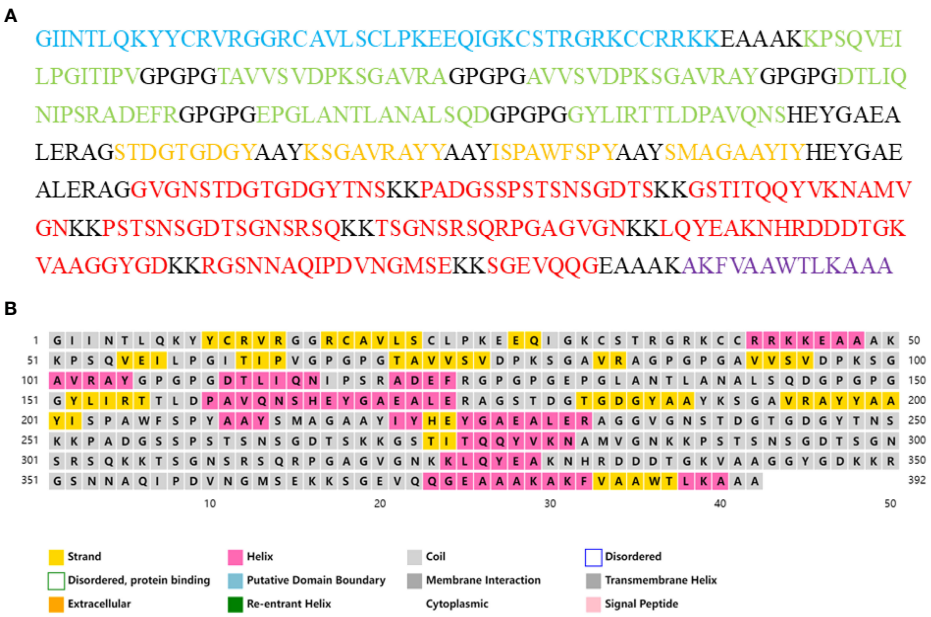

FIGURE 4
(A) The amino acid sequences of the vaccine construct. The adjuvant is colored blue, the HTL epitopes are colored green, and the CTL epitopes are colored yellow, The B-cell epitopes and the Pan HLA DR-binding epitope (PADRE) are colored red, all linkers are colored black. **(B)** The secondary structure of the vaccine construct.

vaccine being soluble when overexpressed in *E. coli* was 0.784691. Neither signal peptide nor transmembrane helix was detected in the vaccine construct, so there was no obvious difficulty in expressing the vaccine *in vivo* (Supplementary Data Sheet 8; Figures S4, S5).

3.6 Secondary and tertiary structure predictions, tertiary structure refinement and validatio

The secondary structure of the vaccine, as analyzed by the PSIPRED 4.0 server, was composed of 65.05% coil, 19.39% α-helix and 15.56% β-strand (Figure 4B). The Robetta server was employed to generate the primary 3D structure of the vaccine, which was further refined by GalaxyRefine(Figure 5A). The best refined vaccine model, with a MolProbity of 1.897, was validated by the PROCHECK, ERRAT, and ProSA-web servers. The Ramachandran plot generated by the PROCHECK server revealed that the vaccine had 90.3% residues in the most favored regions, 8.8% residues in additional allowed regions, and only 0.3% residues in generously allowed regions (Figure 5B). The ERRAT score of the vaccine was 93.017(Figure 5D), and the Z-score generated by the ProSA-web server was -7.3(Figure 5C). The PROCHECK server was employed to examine the stereochemistry of protein structures in detail. Over 90% of residues in the most favored regions suggested a good quality of the vaccine model. The ERRAT server was then utilized to distinguish correct and incorrect regions in the protein structure based on characteristic atomic interactions, and a high ERRAT score indicates a good quality of the structure. The Z score generated by the ProSA-web server was used to indicate the overall model quality, and the lower the Z score, the better the model quality. All of the above analysis results suggested that the developed vaccine had a reliable and stable 3D structure.

3.7 Disulfide engineering of vaccine

The inter- and intra-chain disulfide bonds were evaluated by the DbD2 server, which reported 52 pairs of amino acid residues with the ability to form disulfide bonds. Given that 90% of native disulfide bonds have an energy value< 2.2 kcal/mol, 2.2 kcal/mol was set as the threshold for screening disulfide bonds in this study. According to the energy value and chi3 value, only 3 residue pairs (i.e., LEU6-TYR9, GLU28-ARG43, and GLY234-ALA376) were chosen and they were not falling into any of the epitope regions, which could minimize the effect of disulfide engineering on vaccine immunogenicity (Supplementary Data Sheet 8; Figure S6A). Analyses of the Ramachandran plot, ERRAT score, and Z-score were shown in Supplementary Data Sheet 8 (Figure S6B–S6D), which indicated that the model with disulfide was of good quality.

3.8 The analysis of molecular docking of vaccine-Toll like receptors

To assess the binding affinity between the vaccine construct and TLRs (TLR2 and TLR4), molecular docking was performed using the Cluspro2.0 server. The server generated a total of 30 candidate models of the vaccine-TLR2 complex with different binding energies, from which

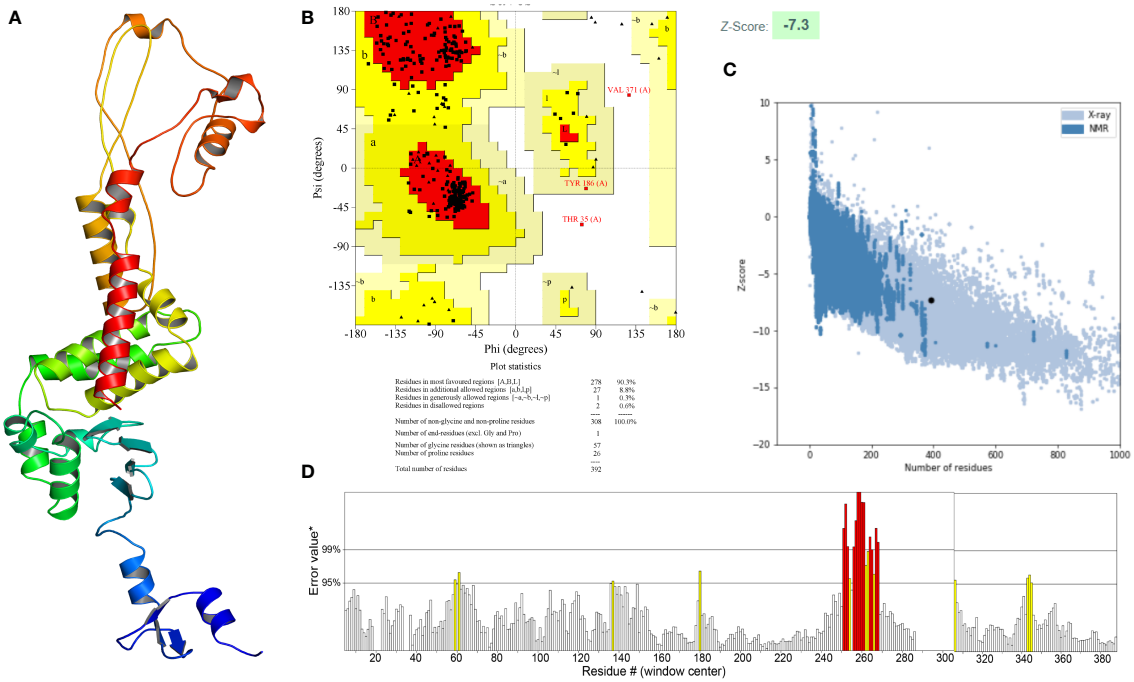

FIGURE 5
(A) Three-dimensional (3D) structure of the vaccine. **(B)** The Ramachandran plot of the refined 3D model generated by the PROCHECK server, the red-colored regions are the most favored regions, the dark yellow and light yellow regions are the additional allowed and generously allowed regions, the white regions are the disallowed regions. **(C)** The Z-score plot of the refined 3D model generated by the ProSA-web server. **(D)** The ERRAT score of the refined 3D model generated by the ERRAT server.

the top-ranked model with the lowest binding energy score of -837.3 was selected for further refinement. Also, a total of 30 model complexes of vaccine-TLR4 were generated, and the top-ranked model with the lowest binding energy score of -835.1 was chosen. The HADDOCK 2.4 server was then used to refine the vaccine-receptor complex, and the HADDOCK scores of the vaccine-TLR2 complex and vaccine-TLR4 complex were -194.9 ± 1.0 and -243.4 ± 1.7, respectively. The low HADDOCK scores revealed the good binding between the vaccine and TLRs. The analysis results of the PDBsum server revealed that there were 14 hydrogen bonds and 2 salt bridges formed between the vaccine and TLR2, and 12 hydrogen bonds and 7 salt bridges formed between the vaccine and TLR4 (Supplementary Data Sheet 8; Table S4). For the vaccine-TLR2 complex, the amino acid residues of the vaccine involved in salt bridge formation were GLU174 and ASP180, and the residues involved in hydrogen bonds formation were ARG12, PRO89, VAL92, SER94, LYS79, TYR213, GLU174, TYR105, TYR225, ARG103, and ASP180 (Figure 6A). For the vaccine-TLR4 complex, the amino acid residues of the vaccine involved in salt bridge formation were LYS98, ASP96, ARG84, LYS79, ASP77, and GLU224, and the residues involved in hydrogen bonds formation were LYS98, ASP96, HIS223, ARG84, LYS79, ASP77, and LYS51 (Figure 6B). The above results suggested that there were strong interactions between the designed vaccine and TLRs (TLR2 and TLR4).

3.9 MD simulation

MD simulation was performed to understand the stability of vaccine-receptor complexes at the atomic level using Gromacs v2022.1. A primary analysis of trajectories was performed, including the calculation of the Backbone root-mean-square deviation (RMSD), the radius of gyration (Rg), root mean square fluctuation (RMSF), total

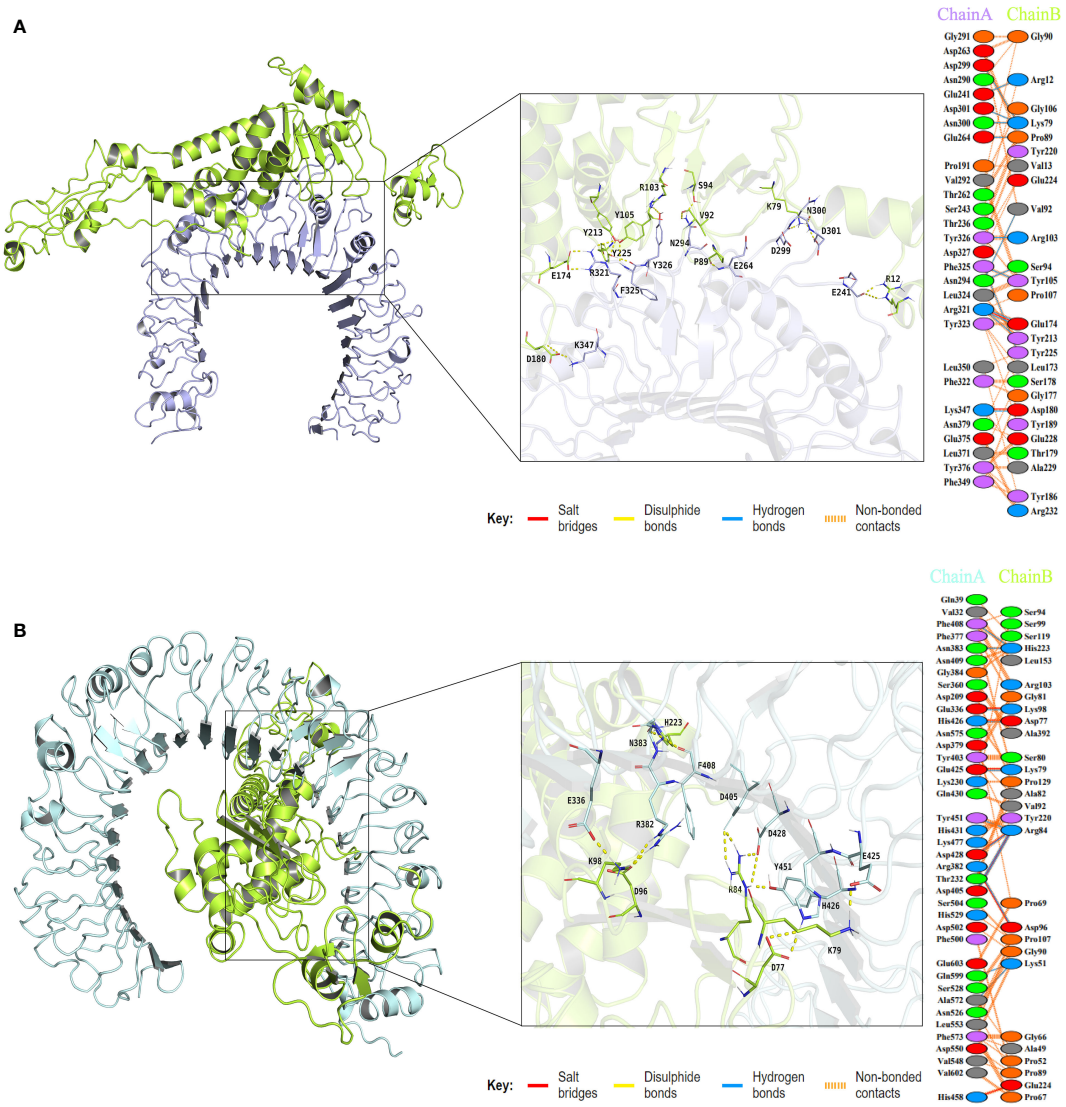

FIGURE 6
The plot of visualized analysis and the interacting amino acid residues of the docking complex. The TLR2 receptor is colored lightblue, the TLR4 receptor is colored palecyan, and the vaccine is colored limon. **(A)** The visualization of the vaccine and TLR2 complex and Interacting residues. The chain A refers to TLR2 receptor and the chain B refers to vaccine. **(B)** The visualization of the vaccine and TLR4 complex and Interacting residues. The chain A refers to TLR4 receptor and the chain B refers to vaccine.

10.3389/fimmu.2023.1100188

solvent accessible surface area (SASA), and the number of hydrogen bonds. RMSD reflects the conformational fluctuations of vaccine-receptor complexes based on the initial structure. For the vaccine-TLR2 complex, the RMSD of the first and third simulations reached relative stability around 10 ns, but the RMSD of the second simulation reached stability around 15 ns (Figure 7A). Overall, the RMSD curves for the three simulations have similar trends. The mean RMSD values of the three simulations were 0.826 ± 0.101nm, 0.821 ± 0.139nm, and 0.850 ± 0.140nm, respectively. For the vaccine-TLR4 complex, the mean RMSD values of the three simulations were 0.791 ± 0.085 nm,1.223 ± 0.190 nm, and 1.182 ± 0.356 nm, respectively. In the first and second simulations, the RMSD reached equilibrium around 10ns and 20ns, respectively. In the third simulation, RMSD reached the first equilibrium around 10ns, fluctuated again at 40 ns, and reached the second equilibrium around 45 ns (Figure 7B). Rg characterizes the compactness of a protein structure. The Rg value of the vaccine-TLR2 complex decreased at first and then remained at a constant level at about 15ns in all three simulations (Figure 7C). For the vaccine-TLR4 complex, the Rg values of the second and third simulations were lower than those of the first simulation, indicating a more compact structure of the complex during the second and third simulations (Figure 7D). The analysis of Rg also showed that the vaccine-TLR4 complex underwent two conformational changes before reaching equilibrium in the third simulation (Figure 7D). Overall, the results of Rg indicated that the structures of both the

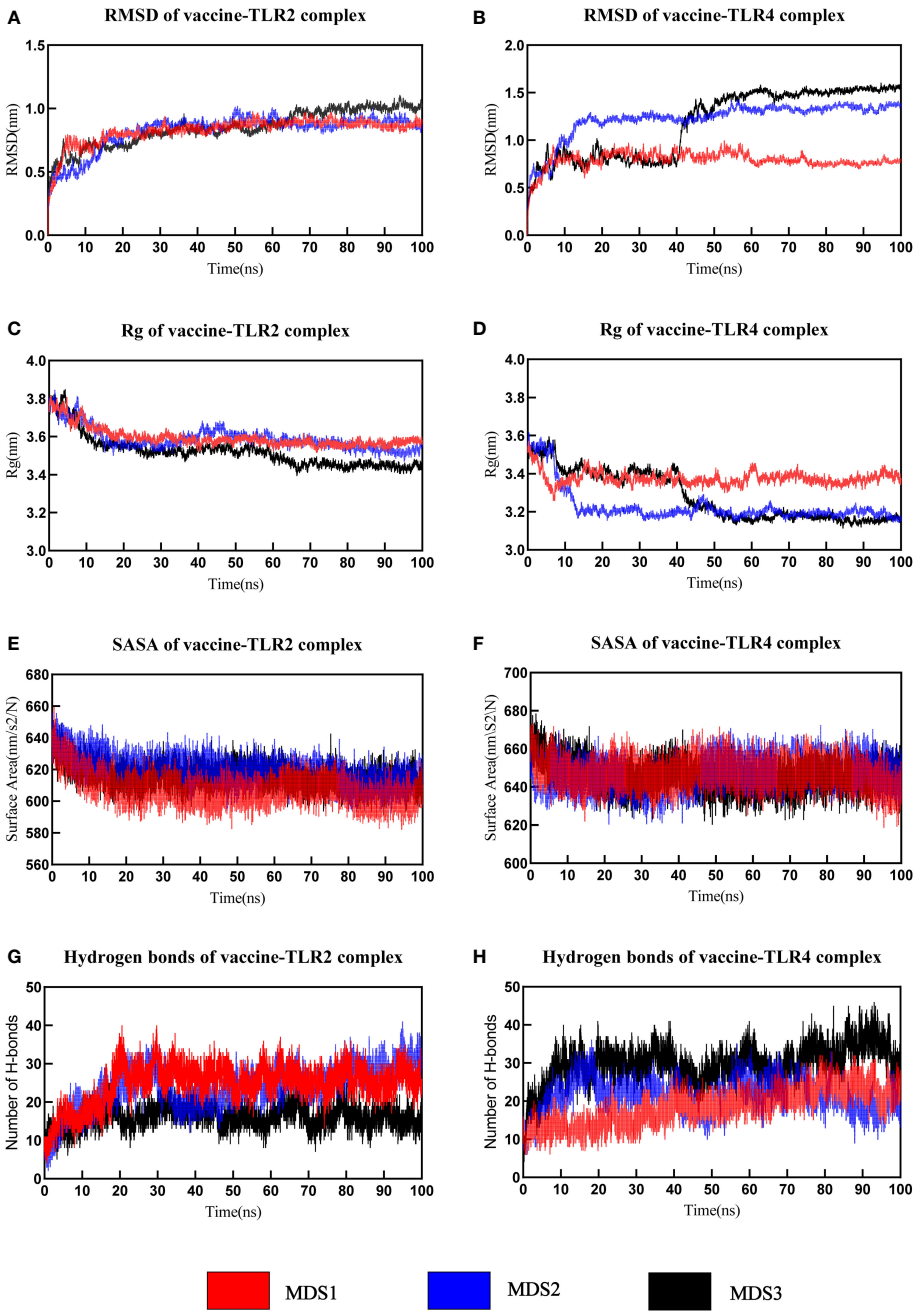

FIGURE 7
The analysis of molecular dynamics simulation of vaccine-TLRs. **(A, B)** RMSD (root mean square deviation) plots **(C, D)** Rg (Radius of gyration) **(E, F)** SASA (solvent accessible surface area) **(G, H)** Hydrogen bonds.

vaccine-TLR2 complex and vaccine-TLR4 complex were compact and stable over time during the three MD simulations. The RMSF value reflects the flexibility of a single amino acid of a protein throughout the MD simulation. RMSF analysis revealed that the residues 380-392 of the vaccine chain and the residues 27-100 of TLR2 in the vaccine-TLR2 complex were highly flexible in all three simulations (Supplementary Data Sheet 8; Figure S7A and S7C). For the vaccine-TLR4 complex, it was found that the residues 250-360 of the vaccine chain were highly flexible in the first simulation, while the RMSF of the vaccine had lower values in the other two simulations. Residues 250-360 did not interact with the receptor and the vaccine structure is not compact enough resulting in high flexibility of the residues during the first simulation (Supplementary Data Sheet 8; Figure S7B). Meanwhile, residues 27-300 of the TLR4 had higher flexibility in the third simulation and the RMSF of TLR4 was relatively lower than that of the vaccine in the other two simulations (Supplementary Data Sheet 8; Figure S7D). The analysis of the total solvent accessible surface area showed the change in the complex surface area with respect to time. The curve trend of the SASA plot was opposite to that of RMSD indicating that the better interaction between receptor and ligand led to a lower surface area of the protein complexes (Figures 7E, F). The results of the analysis of SASA once again revealed the stable binding between the vaccine and TLRs (TLR2 and TLR4). The vaccine-TLR2 complex presented about 10 hydrogen bonds at the beginning of the simulation. After 20 seconds, the number of hydrogen bonds formed in the vaccine-TLR2 complex increased and then maintained relative stability in all three simulations (Figure 7G). During the three simulations, the number of hydrogen bonds of the vaccine-TLR4 complex increased from 10 at the beginning to about 25 hydrogen bonds at the end of the simulation (Figure 7H). The formation of hydrogen bonds suggested that the vaccine had a good affinity for TLRs. Finally, the movies of the MD simulations generated by VMD v1.93 were shown in the Supplementary Data Sheet 9-14.

3.10 MM-PBSA calculation

The tracks of 100ps extracted from each interval during the final 10ns simulation period were processed with the calculation of MM-PBSA and several binding interaction energies, including van der Waals, electrostatic, polar solubility, solvent accessible surface area (SASA), and binding energy ($\Delta G_{binding}$) of vaccine-receptor complexes. The binding energy of the vaccine-TLR2 complex was -161.07 kJ/mol, -208.24 kJ/mol, and -148.16 kJ/mol, respectively. For the vaccine-TLR4 complex, the binding energy were -203.16 kJ/mol, -176.99 kJ/mol, and -240.85 kJ/mol in three simulations, respectively. The detailed energy analysis presented in Table 5 revealed that the vaccine had a good affinity for both TLR2 and TLR4 molecules. For the vaccine-TLR2 complex, residues (LYS79, ALA92, and ARG232) in the vaccine chain contribute significantly to vaccine binding to the TLR2 receptor, particularly residues (ARG232) (Supplementary Data Sheet 8; Figure S8A, S8C and S8E). For the vaccine-TLR4 complex, MM/PBSA decomposition analysis showed that residues (PRO69, LYS77, ARG84, PRO89, SER99, TYR105 and LYS389) in the vaccine chain contributed to the binding of the vaccine to the TLR4, with a greater contribution from the residue (ARG84) (Supplementary Data Sheet 8; Figures S8B, S8D, S8F). However, the residue (GLU224) negatively affected the binding of the vaccine to TLR2 and TLR4 receptors. Overall, the results of all MM-PBSA calculations indicated that the vaccine can stably bind to the TLR2 and TLR4.

3.11 PCA and DCC analysis

To study and evaluate the association between different protein conformations, PCA was conducted for the trajectories of all C atoms in 50-100ns in the simulated system. PCA translates atomic coordinates into a limited number of PCs (commonly 2 or 3 PCs) that signify the directions in which the structure set has the greatest collective variability. The PCA scatter plots revealed that the color of instantaneous conformations changed from blue to red over time. In the direction of PC1, the successive color shifts (from blue to white to red) indicated that the conformation in both systems gradually evolved to another state during the simulation. PC1 and PC2 characterized 40.02%, 45.89%, and 49.24% of the system's motility with respect to the vaccine-TLR2 complex (Figure 8A; Supplementary Data Sheet 8; Figure S9A, S9C) and 64.38%, 50.86% and 47.68% of the system's motility with respect to the vaccine-TLR4 complex (Figure 8D; Supplementary Data Sheet 8; Figures S9E, S9G) in three MD simulations, respectively. Over 80% of the motion of both systems in 20 dimensions could be explained (Figure 8B, E; Supplementary Data Sheet 8; Figures S9B, S9D, S9F, S9H).

The dynamical cross-correlation matrix (DCCM) was utilized to display the information about interchain and intrachain residue-residue contacts and motions. Figures 8C, G and Supplementary Data Sheet 8; Figure S10 depict the DCCM matrices of the vaccine-TLR2 and vaccine-TLR4 complexes. The color gradients from blue to white to red in the

TABLE 5 The results of binding free energy, estimated by MMPBSA for the vaccine-TLRs complex.

Complex	Molecular dynamics simulation	van der Waal energy (kJ/mol)	Electrostatic energy (kJ/mol)	Polar solvation energy (kJ/mol)	Solvent accessible surface area energy (kJ/mol)	Binding energy (ΔGbinding) (kJ/mol)
vaccine-TLR2	MDS1	-271.97 (11.34)	-1871.02 (98.55)	2013.21 (92.74)	-31.29 (1.04)	-161.07 (15.29)
	MDS2	-215.32 (9.69)	-1634.28 (71.58)	1665.53 (65.57)	-24.17 (0.73)	-208.24 (15.68)
	MDS3	-216.43 (10.92)	-1775.62 (72.26)	1868.89 (70.43)	-24.99 (0.96)	-148.16 (12.45)
vaccine-TLR4	MDS1	-244.11 (11.39)	-3138.56 (77.46)	3206.89 (76.91)	-27.38 (0.90)	-203.16 (14.52)
	MDS2	-210.10 (11.81)	-3400.95 (93.34)	3460.52 (93.45)	-26.45 (1.54)	-176.99 (14.30)
	MDS3	-257.86 (12.71)	-3850.23 (182.20)	3899.90 (168.15)	-32.65 (0.94)	-240.85 (22.88)

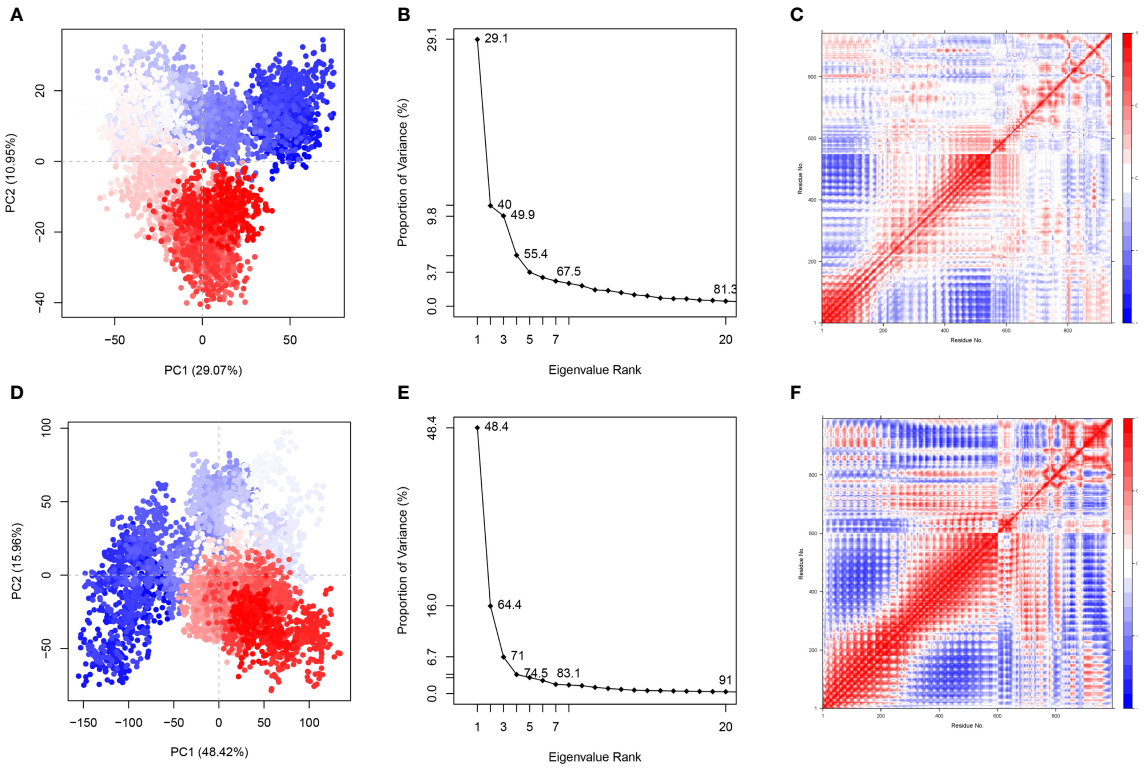

FIGURE 8
Principal component analysis(PCA) and dynamical cross-correlation (DCC) analysis for first MD simulation. **(A)** The plot of PC1 and PC2 about vaccine-TLR2 complex **(B)** The plot of PCA analysis about vaccine-TLR2 complex **(C)** The DCCM plot of vaccine-TLR2 complex **(D)** The plot of PC1 and PC2 about vaccine-TLR4 complex **(E)** The plot of PCA analysis about vaccine-TLR4 complex **(F)** The DCCM plot of vaccine-TLR4 complex.

figures correspond to the correlation coefficients of -1, 0 and 1, respectively, and a deeper shade of the same color represents a stronger correlation. For example, the correlation coefficient of light blue is -0.5 and that of light red is 0.5. DCC analysis of the vaccine-TLR2 complex in three MD simulations showed that the residues surrounding 1 to 51 (550 to 600 in a plot) and 151 to 231 (700 to 780 in the plot) from the vaccine were positively correlated with the residues surrounding 200 to 548 (200 to 548 in a plot) and 300 to 400 (300 to 400 in the plot) from the TLR2 chain, respectively. (Figure 8C; Supplementary Data Sheet 8 and Figure S10A and S10B). For the vaccine-TLR4 complex, the residues surrounding 9 to 79 (610 to 680 in the plot) and 99 to 199 (700 to 800 in the plot) were positively correlated with the residues surrounding 500 to 601(500 to 601 in the plot) and 200 to 400 (200 to 400 in the plot) from the TLR4 chain, respectively (Figure 8F; Supplementary Data Sheet 8 and Figure S10C and S10D).

3.12 Immune simulation and population coverage

The immune stimulation of the vaccine was carried out using the C-ImmSim web server, which predicts whether the vaccine can induce significant adaptive immunity in the human body. Following the first injection, lower lgM antibody titers, a B-cell isotype lgM population, and a slight B-cell isotype lgG population were detected. After the second and third injections, higher levels of IgM antibody with IgG1, IgG1+IgG2 and lgG+lgM as well as a substantial number of memory B cells were found (Figures 9A, B). In addition to the B-cell, the plasma B cells, the total, memory and active TH-cell (helper T cell) populations also increased during the secondary and tertiary immune responses (Figures 9B-E). Besides, TC cells (cytotoxic T lymphocytes) were observed during the immune simulation, with the maximum TC cell count exceeding 1,150 cells per mm^3 (Figure 9F). Further, the NK cells and macrophages were activated after exposure to the vaccine (Figures 9G, H). Figure 9I showed that the vaccine was able to activate a wide range of cytokines, including IFN-γ, IL-2, and IL-4. In summary, the designed vaccine was capable of inducing the generation of a large number of immune cells and a variety of cytokines, indicating that it can successfully induce adaptive immunity and memory immunity in the host body.

Population coverage analysis suggested that 89% of the world's population might respond to the designed vaccine. More specifically, its population coverage in Europe, the United States, and China reached 93.47%, 88.91%, and 86.63% (Supplementary Data Sheet 8; Table S5), respectively. The results of immunization simulation and population coverage demonstrated that the developed vaccine was highly immunogenic and able to protect the vast majority of the global population.

3.13 Codon optimization and cloning

To ensure high-level expression and easy production of the vaccine, codon optimization was performed *via* the VectorBuilder server. The cDNA length of the optimized vaccine was 1,176 bps and

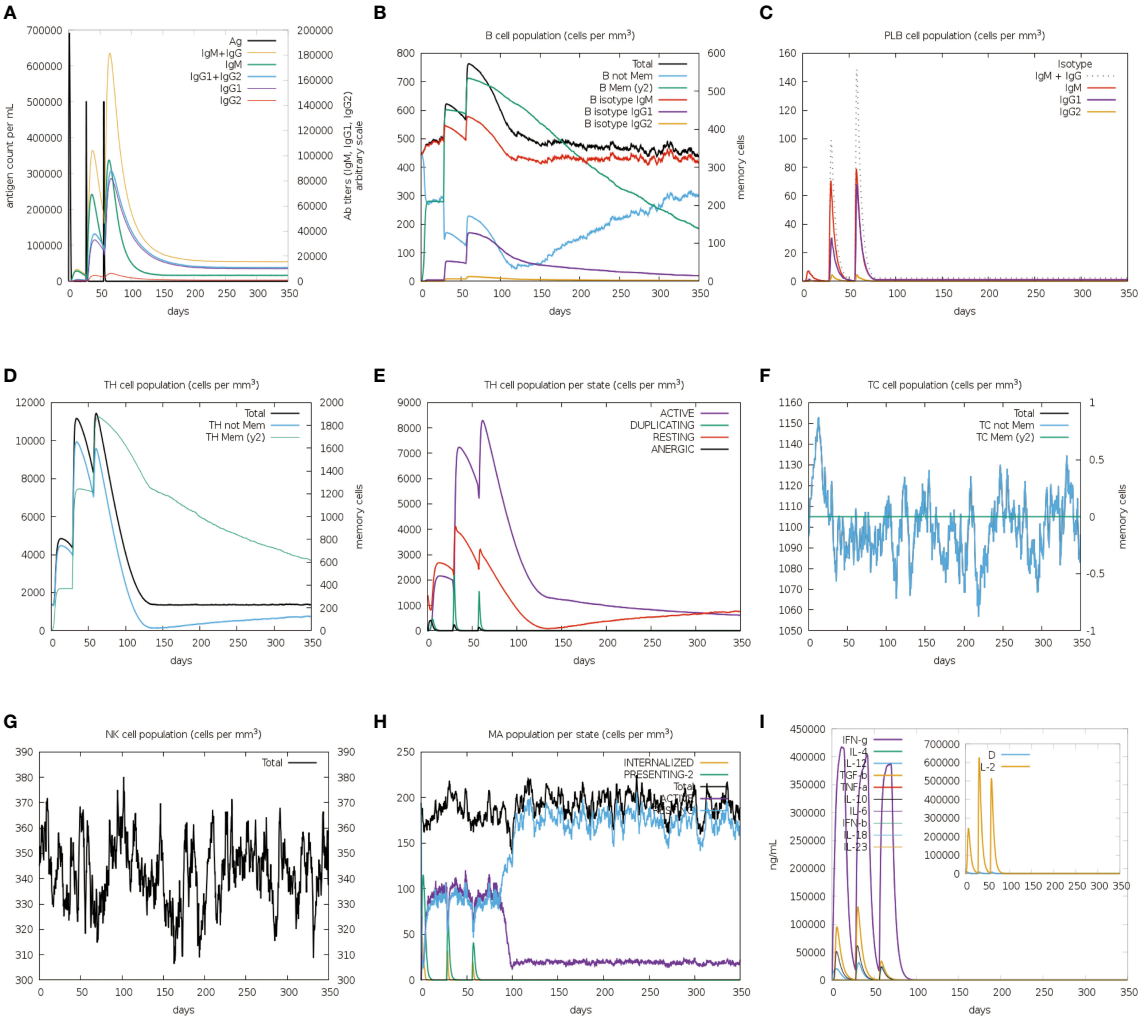

FIGURE 9
In silico immune simulation spectrum. **(A)** Changes in antibody titers after three vaccine injections; **(B)** Changes in B cell population after three vaccine injections; **(C)** Changes in plasma B-cell population after three vaccine injections; **(D)** Changes in helper T cell population after three vaccine injections; **(E)** Changes in helper T cell population per state after three vaccine injections; **(F)** Changes in cytotoxic T cell population per state after three vaccine injections; **(G)** Changes in natural killer (NK) cell population after three vaccine injections; **(H)** Changes in macrophages (MA) population per state after three vaccine injections **(I)**.

a stop codon was added to the Terminal of cDNA (Supplementary File 8). Both the CAI value of the vaccine (i.e., 0.89) and the GC content (i.e., 59.46%) were desirable, indicating a high gene expression potential and excellent expression ability in *E. coli* (K12 strain). Then, the GenSmart tool was used to clone the cDNA sequence of the vaccine into the pET28a(+) vector (Figure 10A).

3.14 Secondary structure of vaccine mRNA

According to the RNAfold server, the best secondary structure of the vaccine mRNA had a minimum free energy of -474.30 kcal/mol (Figure 10B), whereas the centroid secondary structure had a minimum free energy of -407.80 kcal/mol (Figure 10C). The minimum free energy of the optimal secondary structure of the vaccine mRNA was determined to be -413.80 kcal/mol by the mFold v2.3 server (Supplementary Data Sheet 8; Figure S11). Because mRNA is more stable when its minimal free energy is lower, the vaccine was predicted to be stable after expression *in vivo*.

4 Discussion

So far, *Nocardia* is still a significant threat to aquaculture animals and immunocompromised people, such as the elderly, transplant recipients, HIV-infected individuals, malignant tumor patients, and patients treated with glucocorticoids (4, 95–97). Moreover, *Nocardia* infections have also been found in people with normal immune function (98, 99). Due to the elevated incidence and fatality rate of nocardiosis, and increased *Nocardia* resistance to existing antibiotics, the need of developing a vaccine to mitigate *Nocardia* infections has been underscored.

Because there is a large number of *Nocardia* species and many of them are pathogenic to humans, our goal was to develop a broad-

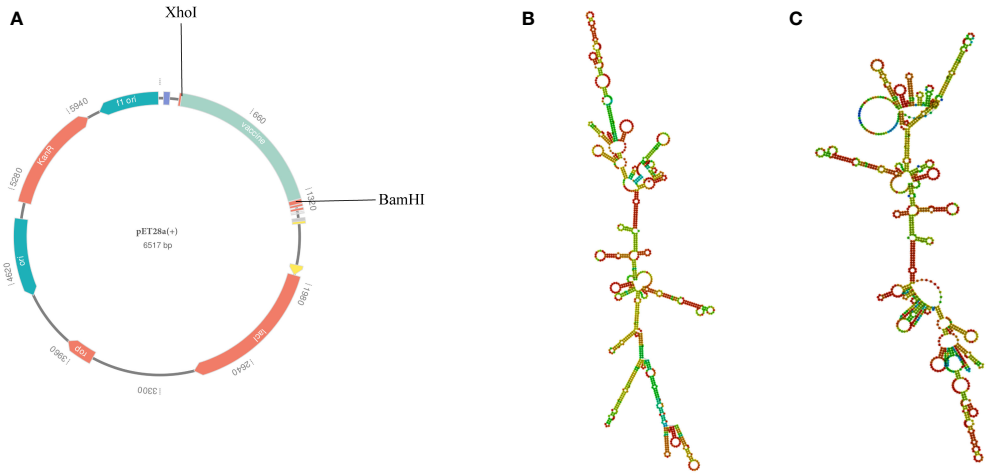

FIGURE 10
(A) In silico cloning of the multi-epitope vaccine into the pET28a (+) expression vector; the light green part presents the vaccine's codon. **(B)** The best secondary structure of the vaccine mRNA. **(C)** The centroid secondary structure of the vaccine mRNA.

spectrum multi-epitope vaccine that can protect against the majority of *Nocardia*, but it is a huge challenge for traditional vaccinology. Compared with traditional techniques, RV is capable of performing batch analysis of thousands of biological parameters within a shorter time while ensuring more reliable results, thereby opening up a novel door to the research and development of vaccines (23, 24). To enable the designed vaccine to take effect on most pathogenic *Nocardia* strains, 218 complete proteome sequences of 6 common *Nocardia* species were downloaded from NCBI, and the proteins containing 50% similar sequences from all strains were included for further analysis. Then, less significant proteins, such as the human proteome, essential genes, virulent factor proteins, antibiotic-resistant proteins, and human interacting proteins, were subtracted from several other databases. Besides recognizing the virulent and antibiotic-resistant factors, the identification of potential vaccine candidates must also focus on checking their antigenicity, allergenicity, subcellular localization, and other physicochemical properties, such as the aliphatic index, GRAVY, and instability index. Finally, 3 outer membrane proteins, including one virulence factor protein and two antibiotic resistance proteins, were selected for the identification of epitopes.

Epitope selection is a critical step in the development of multi-epitope vaccines. In this study, the antigenicity, toxicity, and allergenicity of all predicted epitopes were evaluated, and both the T-cell (CTL and HTL) and B-cell epitopes were included in the multi-epitope construction, which can avoid unsatisfactory immune effects due to insufficient immune response that is induced by T-cell epitopes or B-cell epitopes alone while ensuring safety. It is well known that CTL cells can only recognize the antigens presented by MHC class I molecules, while HTL can only recognize the antigens presented by MHC class II molecules (100). Therefore, the capacity of the epitope to bind to HLA alleles is a crucial predictor of whether it can effectively induce an immune response or not. It is worth mentioning that we performed molecular docking between all ultimately selected T-cell epitopes and HLA alleles, and the docking results suggested that the affinity between them was strong, indicating that the epitopes could be effectively presented *via* MHC molecules. IL-2 is indispensable for the proliferation as well as differentiation of naive T cells into effector T cells (58). Both IL-4 and INF-γ are important activators of T helper cells, and IFN-γ also participates in the activation of macrophages (56, 57). The potential of HTL epitopes to induce the IL-2, IL-4, and INF-γ generation was examined in this study. With all that mentioned, the eventually-selected epitope has the potential to construct an effective multi-epitope vaccine that is characterized by few side effects.

Adjuvants can not only improve the immunogenicity of multi-epitope vaccines but also help induce a more durable immune response (101). In this study, the β-defensin, which can attenuate toxicity and enhance systemic antibody responses when administered together with antigens, was incorporated into the vaccine construct as an adjuvant (102). It is well known that TLRs can recognize different PAMPs and play an indispensable role in the innate and adaptive immune response (77). The binding affinity with TLRs is an important reference factor in evaluating the immune effect of a multi-epitope vaccine candidate. From the docking results, we observed stable interactions and high affinity between the multi-epitope vaccine and TLRs (TLR4 and TLR2), indicating that the vaccine candidate can effectively trigger the body's immune response. Furthermore, the docked complexes were molecularly simulated to assess the stability and agility of the vaccine-TLR complexes in a simulated biological environment. In the three MD simulations of the vaccine-TLR2 complex, the RMSDs all remained stable in the last 80% of the simulation period, showing that the structure of the vaccine-TLR2 complex was relatively stable. For the trend of RMSD of vaccine-TLR4 complex, although there were differences in the three simulations, RMSDs all reached equilibrium at 50ns in the three simulations. The Rg values of two vaccine-TLR complex systems also tended to stabilize after 50 ns, which further confirmed the stability of the complex. In all MD simulations, there were quite negative correlations between RMSD and SASA, which verifies the good binding between vaccine and receptor (TLR2 and TLR4) on the other hand. In all MD simulations, more hydrogen bonds were formed in both the vaccine-TLR2 and vaccine-TLR4 complexes, demonstrating high affinity of the vaccine chain to the TLR2 and TL42 chains.

The MM-PBSA analysis indicated that very little energy was required to keep the two complexes stable. The DCC analysis revealed the existence of positively correlated contacts between vaccine-TLR2 amino acid residues and vaccine-TLR4 amino acid residues, indicating that the associations between the vaccine and TLRs (TLR2 and TLR4) were good. According to the above analysis, the designed vaccine is able to firmly bind to TLRs and successfully transport into the body in the natural environment, thereby inducing effective immunity. In the process of immune simulation, we observed the proliferation of TC, TH and B cells, and the production of lgA, lgG, INF- γ, IL-2 and other cytokines with the injection of the vaccine. In addition, memory B cells were also observed following repeated exposures to the vaccine, which suggested that the vaccine was capable of inducing not only cellular and humoral immunity but also long-term immunity against *Nocardia*. Finally, to evaluate the feasibility of mass production, codon optimization and cloning were implemented for the vaccine construct, and the values of CAI and GC contents suggested that the designed vaccine could be well expressed in the E. coil K12 strain. Besides, the lower minimum free energy scores of the secondary structure of vaccine mRNA suggested that the vaccine was expected to behave stable in the body.

5 Conclusion

Nocardiosis poses a major public health threat due to the expansion of susceptible populations, underdiagnosis and lack of adequate awareness. In this study, we designed an antigenic, non-allergic and non-toxic multi-epitope vaccine against *Nocardia* using RV and immunoinformatics techniques. The results of molecular docking and MD simulation show that the designed multi-epitope vaccine has a strong affinity for different innate immune receptors of the host, and that the vaccine-receptor complex is dynamically stable in the natural environment. In addition, the designed vaccine has the potential to induce humoral immunity and immunity. Finally, the codon optimization and cloned analysis show that the vaccine is feasible for mass production. To sum up, the designed vaccine may have a good protective effect on *Nocardia*, but the proposed candidate vaccine needs to be tested both *in vivo* and *in vitro* to determine its efficacy and safety.

Data availability statement

The datasets presented in this study can be found in online repositories. The names of the repository/repositories and accession number(s) can be found in the article/Supplementary Material.

Author contributions

Conceptualization: FZ. Methodology: FZ. Validation: SM and HY. Formal analysis: PZ, WP, MR and YC. Writing—original draft preparation: FZ and CT. Writing—review and editing: JC and CL. Supervision, PP and JC. Project administration, PP and JC. Funding acquisition, PP. All authors contributed to the article and approved the submitted version.

Funding

1. The National Natural Science Foundation of China (No.81770080). 2. Supported by the Project Program of National Clinical Research Center for Geriatric Disorders (Xiang ya Hospital, Grant No. 2020LNJJ05). 3. The National Natural Science Foundation of China (No.8210012334). 4. National Key R&D Program of China (No. 2016YFC1304204). 5. The national key clinical specialist construction programs of China (Grant Number z047-02). 6. Research Project on Education and Teaching Reform of Central South University (No.2021 jy139-2). 7. China Postdoctoral Science Foundation (2022M713520). 8. Project on the topic of emergency response to combat the COVID-19 epidemic in Hunan Province (2022SK2122)

Acknowledgments

The author thanks his classmates Cheng Zhao and Shuang Chen for their help in bioinformatics. The author thanks his friend Haocheng Yun for his help in MD simulation trajectory analysis.The authors thank Mr. Sean Liu from QS Translation for his English language proofreading service.

Conflict of interest

The authors declare that the research was conducted in the absence of any commercial or financial relationships that could be construed as a potential conflict of interest.

Publisher's note

All claims expressed in this article are solely those of the authors and do not necessarily represent those of their affiliated organizations, or those of the publisher, the editors and the reviewers. Any product that may be evaluated in this article, or claim that may be made by its manufacturer, is not guaranteed or endorsed by the publisher.

Supplementary material

The Supplementary Material for this article can be found online at: https://www.frontiersin.org/articles/10.3389/fimmu.2023.1100188/full#supplementary-material

References

1. Brown-Elliott BA, Brown JM, Conville PS, Wallace RJJr. Clinical and laboratory features of the nocardia spp. based on current molecular taxonomy. *Clin Microbiol Rev* (2006) 19(2):259–82. doi: 10.1128/cmr.19.2.259-282.2006

2. Conville PS, Brown-Elliott BA, Smith T, Zelazny AM. The complexities of nocardia taxonomy and identification. *J Clin Microbiol* (2018) 56(1):20171226. doi: 10.1128/jcm.01419-17

3. Hamdi AM, Fida M, Deml SM, Abu Saleh OM, Wengenack NL. Retrospective analysis of antimicrobial susceptibility profiles of nocardia species from a tertiary hospital and reference laboratory, 2011 to 2017. *Antimicrob Agents Chemother* (2020) 64 (3):20200221. doi: 10.1128/aac.01868-19

4. Wang H, Zhu Y, Cui Q, Wu W, Li G, Chen D, et al. Epidemiology and antimicrobial resistance profiles of the nocardia species in China, 2009 to 2021. *Microbiol Spectr* (2022) 10(2):e0156021. doi: 10.1128/spectrum.01560-21

5. Yu S, Wang J, Fang Q, Zhang J, Yan F. Specific clinical manifestations of nocardia: A case report and literature review. *Exp Ther Med* (2016) 12(4):2021–6. doi: 10.3892/etm.2016.3571

6. Baldawa S, Nayak N, Kukreja S, D'Souza D, Diyora B, Sharma A. Cerebral nocardiosis. *Asian J Neurosurg* (2014) 9(4):245. doi: 10.4103/1793-5482.146661

7. Takamatsu A, Yaguchi T, Tagashira Y, Watanabe A, Honda H. Nocardiosis in Japan: A multicentric retrospective cohort study. *Antimicrob Agents Chemother* (2022) 66 (2):e0189021. doi: 10.1128/aac.01890-21

8. Davis-Scibienski C, Beaman BL. Interaction of nocardia asteroides with rabbit alveolar macrophages: Association of virulence, viability, ultrastructural damage, and phagosome-lysosome fusion. *Infect Immun* (1980) 28(2):610–9. doi: 10.1128/iai.28.2.610-619.1980

9. Beaman BL, Beaman L. Nocardia species: Host-parasite relationships. *Clin Microbiol Rev* (1994) 7(2):213–64. doi: 10.1128/cmr.7.2.213

10. Poonyagariyagorn HK, Gershman A, Avery R, Minai O, Blazey H, Asamoto K, et al. Challenges in the diagnosis and management of nocardia infections in lung transplant recipients. *Transpl Infect Dis* (2008) 10(6):403–8. doi: 10.1111/j.1399-3062.2008.00338.x

11. Lebeaux D, Freund R, van Delden C, Guillot H, Marbus SD, Matignon M, et al. Outcome and treatment of nocardiosis after solid organ transplantation: New insights from a European study. *Clin Infect Dis* (2017) 64(10):1396–405. doi: 10.1093/cid/cix124

12. Baio PV, Ramos JN, dos Santos LS, Soriano MF, Ladeira EM, Souza MC, et al. Molecular identification of nocardia isolates from clinical samples and an overview of human nocardiosis in Brazil. *PloS Negl Trop Dis* (2013) 7(12):e2573. doi: 10.1371/journal.pntd.0002573

13. Yasuike M, Nishiki I, Iwasaki Y, Nakamura Y, Fujiwara A, Shimahara Y, et al. Analysis of the complete genome sequence of nocardia seriolae Utf1, the causative agent of fish nocardiosis: The first reference genome sequence of the fish pathogenic nocardia species. *PloS One* (2017) 12(3):e0173198. doi: 10.1371/journal.pone.0173198

14. Mehta H, Weng J, Prater A, Elworth RAL, Han X, Shamoo Y. Pathogenic nocardia cyriacigeorgica and nocardia Nova evolve to resist trimethoprim-sulfamethoxazole by both expected and unexpected pathways. *Antimicrob Agents Chemother* (2018) 62(7): e00364-18. doi: 10.1128/aac.00364-18

15. Zhao P, Zhang X, Du P, Li G, Li L, Li Z. Susceptibility profiles of nocardia spp. to antimicrobial and antituberculotic agents detected by a microplate alamar blue assay. *Sci Rep* (2017) 7:43660. doi: 10.1038/srep43660

16. Muñoz J, Mirelis B, Aragón LM, Gutiérrez N, Sánchez F, Español M, et al. Clinical and microbiological features of nocardiosis 1997-2003. *J Med Microbiol* (2007) 56(Pt 4):545–50. doi: 10.1099/jmm.0.46774-0

17. Wang HL, Seo YH, LaSala PR, Tarrand JJ, Han XY. Nocardiosis in 132 patients with cancer: Microbiological and clinical analyses. *Am J Clin Pathol* (2014) 142(4):513–23. doi: 10.1309/ajcpw84aftuwmhyu

18. Wilson JW. Nocardiosis: Updates and clinical overview. *Mayo Clin Proc* (2012) 87 (4):403–7. doi: 10.1016/j.mayocp.2011.11.016

19. Uhde KB, Pathak S, McCullum IJr., Jannat-Khah DP, Shadomy SV, Dykewicz CA, et al. Antimicrobial-resistant nocardia isolates, united states, 1995-2004. *Clin Infect Dis* (2010) 51(12):1445–8. doi: 10.1086/657399

20. Tremblay J, Thibert L, Alarie I, Valiquette L, Pépin J. Nocardiosis in Quebec, Canada, 1988-2008. *Clin Microbiol Infect* (2011) 17(5):690–6. doi: 10.1111/j.1469-0691.2010.03306.x

21. Nabel GJ. Hiv vaccine strategies. *Vaccine* (2002) 20(15):1945–7. doi: 10.1016/s0264-410x(02)00074-9

22. Moxon R, Reche PA, Rappuoli R. Editorial: Reverse vaccinology. *Front Immunol* (2019) 10:2776. doi: 10.3389/fimmu.2019.02776

23. Monterrubio-López GP, González YMJA, Ribas-Aparicio RM. Identification of novel potential vaccine candidates against tuberculosis based on reverse vaccinology. *BioMed Res Int* (2015) 2015:483150. doi: 10.1155/2015/483150

24. Naz A, Obaid A, Shahid F, Dar HA, Naz K, Ullah N, et al. Chapter 16 - reverse vaccinology and drug target identification through pan-genomics. In: Barh D, Soares S, Tiwari S, Azevedo V, editors. *Pan-genomics: Applications, challenges, and future prospects*, (Elsevier Science and Technology: Academic Press) (2020). p. 317–33. doi: 10.1016/C2018-0-00570-8

25. Li M, Zhu Y, Niu C, Xie X, Haimiti G, Guo W, et al. Design of a multi-epitope vaccine candidate against brucella melitensis. *Sci Rep* (2022) 12(1):10146. doi: 10.1038/s41598-022-14427-z

26. Chiang MH, Sung WC, Lien SP, Chen YZ, Lo AF, Huang JH, et al. Identification of novel vaccine candidates against acinetobacter baumannii using reverse vaccinology. *Hum Vaccin Immunother* (2015) 11(4):1065–73. doi: 10.1080/21645515.2015.1010910

27. Chaudhari NM, Gupta VK, Dutta C. Bpga- an ultra-fast pan-genome analysis pipeline. *Sci Rep* (2016) 6:24373. doi: 10.1038/srep24373

28. Edgar RC. Search and clustering orders of magnitude faster than blast. *Bioinformatics* (2010) 26(19):2460–1. doi: 10.1093/bioinformatics/btq461

29. Camacho C, Coulouris G, Avagyan V, Ma N, Papadopoulos J, Bealer K, et al. Blast +: Architecture and applications. *BMC Bioinf* (2009) 10:421. doi: 10.1186/1471-2105-10-421

30. Zhang R, Ou HY, Zhang CT. Deg: A database of essential genes. *Nucleic Acids Res* (2004) 32(Database issue):D271–2. doi: 10.1093/nar/gkh024

31. Chen L, Yang J, Yu J, Yao Z, Sun L, Shen Y, et al. Vfdb: A reference database for bacterial virulence factors. *Nucleic Acids Res* (2005) 33(Database issue):D325–8. doi: 10.1093/nar/gki008

32. Alcock BP, Raphenya AR, Lau TTY, Tsang KK, Bouchard M, Edalatmand A, et al. Card 2020: Antibiotic resistome surveillance with the comprehensive antibiotic resistance database. *Nucleic Acids Res* (2020) 48(D1):D517–d25. doi: 10.1093/nar/gkz935

33. Doytchinova IA, Flower DR. Vaxijen: A server for prediction of protective antigens, tumour antigens and subunit vaccines. *BMC Bioinf* (2007) 8:4. doi: 10.1186/1471-2105-8-4

34. Magnan CN, Zeller M, Kayala MA, Vigil A, Randall A, Felgner PL, et al. High-throughput prediction of protein antigenicity using protein microarray data. *Bioinformatics* (2010) 26(23):2936–43. doi: 10.1093/bioinformatics/btq551

35. Yu NY, Wagner JR, Laird MR, Melli G, Rey S, Lo R, et al. Psortb 3.0: Improved protein subcellular localization prediction with refined localization subcategories and predictive capabilities for all prokaryotes. *Bioinformatics* (2010) 26(13):1608–15. doi: 10.1093/bioinformatics/btq249

36. Chou KC, Shen HB. Cell-ploc: A package of web servers for predicting subcellular localization of proteins in various organisms. *Nat Protoc* (2008) 3(2):153–62. doi: 10.1038/nprot.2007.494

37. Hallgren J, Tsirigos KD, Pedersen MD, Almagro Armenteros JJ, Marcatili P, Nielsen H, et al. Deeptmhmm predicts alpha and beta transmembrane proteins using deep neural networks. *bioRxiv* (2022). doi: 10.1101/2022.04.08.487609

38. Teufel F, Almagro Armenteros JJ, Johansen AR, Gíslason MH, Pihl SI, Tsirigos KD, et al. Signalp 6.0 predicts all five types of signal peptides using protein language models. *Nat Biotechnol* (2022) 40(7):1023–5. doi: 10.1038/s41587-021-01156-3

39. Wilkins MR, Gasteiger E, Bairoch A, Sanchez JC, Williams KL, Appel RD, et al. Protein identification and analysis tools in the expasy server. *Methods Mol Biol* (1999) 112:531–52. doi: 10.1385/1-59259-584-7:531

40. Sharma N, Naorem LD, Jain S, Raghava GPS. Toxinpred2: An improved method for predicting toxicity of proteins. *Brief Bioinform* (2022) 23(5):bbac174. doi: 10.1093/bib/bbac174

41. Dimitrov I, Bangov I, Flower DR, Doytchinova I. Allertop V.2–a server for in silico prediction of allergens. *J Mol Model* (2014) 20(6):2278. doi: 10.1007/s00894-014-2278-5

42. Kim DE, Chivian D, Baker D. Protein structure prediction and analysis using the robetta server. *Nucleic Acids Res* (2004) 32(Web Server issue):W526–31. doi: 10.1093/nar/gkh468

43. Morris AL, MacArthur MW, Hutchinson EG, Thornton JM. Stereochemical quality of protein structure coordinates. *Proteins* (1992) 12(4):345–64. doi: 10.1002/prot.340120407

44. Colovos C, Yeates TO. Verification of protein structures: Patterns of nonbonded atomic interactions. *Protein Sci* (1993) 2(9):1511–9. doi: 10.1002/pro.5560020916

45. Wiederstein M, Sippl MJ. Prosa-web: Interactive web service for the recognition of errors in three-dimensional structures of proteins. *Nucleic Acids Res* (2007) 35(Web Server issue):W407–10. doi: 10.1093/nar/gkm290

46. Stranzl T, Larsen MV, Lundegaard C, Nielsen M. Netctlpan: Pan-specific mhc class I pathway epitope predictions. *Immunogenetics* (2010) 62(6):357–68. doi: 10.1007/s00251-010-0441-4

47. Reynisson B, Barra C, Kaabinejadian S, Hildebrand WH, Peters B, Nielsen M. Improved prediction of mhc ii antigen presentation through integration and motif deconvolution of mass spectrometry mhc eluted ligand data. *J Proteome Res* (2020) 19 (6):2304–15. doi: 10.1021/acs.jproteome.9b00874

48. Saha S, Raghava GP. Prediction methods for b-cell epitopes. *Methods Mol Biol* (2007) 409:387–94. doi: 10.1007/978-1-60327-118-9_29

49. Saha S, Raghava GP. Prediction of continuous b-cell epitopes in an antigen using recurrent neural network. *Proteins* (2006) 65(1):40–8. doi: 10.1002/prot.21078

50. Jespersen MC, Peters B, Nielsen M, Marcatili P. Bepipred-2.0: Improving sequence-based b-cell epitope prediction using conformational epitopes. *Nucleic Acids Res* (2017) 45(W1):W24–w9. doi: 10.1093/nar/gkx346

51. Ponomarenko J, Bui HH, Li W, Fusseder N, Bourne PE, Sette A, et al. Ellipro: A new structure-based tool for the prediction of antibody epitopes. *BMC Bioinf* (2008) 9:514. doi: 10.1186/1471-2105-9-514

52. Delano WL. The pymol molecular graphics system. *Proteins* (2002) 30:442–54.

53. Calis JJ, Maybeno M, Greenbaum JA, Weiskopf D, De Silva AD, Sette A, et al. Properties of mhc class I presented peptides that enhance immunogenicity. *PloS Comput Biol* (2013) 9(10):e1003266. doi: 10.1371/journal.pcbi.1003266

54. Paul S, Sidney J, Sette A, Peters B. Tepitool: A pipeline for computational prediction of T cell epitope candidates. *Curr Protoc Immunol* (2016) 114:18.9.1–.9.24. doi: 10.1002/cpim.12

55. Moutaftsi M, Peters B, Pasquetto V, Tscharke DC, Sidney J, Bui HH, et al. A consensus epitope prediction approach identifies the breadth of murine T(Cd8+)-cell responses to vaccinia virus. *Nat Biotechnol* (2006) 24(7):817–9. doi: 10.1038/nbt1215

56. Kak G, Raza M, Tiwari BK. Interferon-gamma (Ifn-Γ): Exploring its implications in infectious diseases. *Biomol Concepts* (2018) 9(1):64–79. doi: 10.1515/bmc-2018-0007

57. Dinarello CA. Historical insights into cytokines. *Eur J Immunol* (2007) 37 Suppl 1 (Suppl 1):S34–45. doi: 10.1002/eji.200737772

58. Malek TR. The main function of il-2 is to promote the development of T regulatory cells. *J Leukoc Biol* (2003) 74(6):961–5. doi: 10.1189/jlb.0603272

59. Dhanda SK, Vir P, Raghava GP. Designing of interferon-gamma inducing mhc class-ii binders. *Biol Direct* (2013) 8:30. doi: 10.1186/1745-6150-8-30

60. Dhanda SK, Gupta S, Vir P, Raghava GP. Prediction of Il4 inducing peptides. *Clin Dev Immunol* (2013) 2013:263952. doi: 10.1155/2013/263952

61. Lathwal A, Kumar R, kaur D, Raghava GPS. In silico model for predicting il-2 inducing peptides in human. *bioRxiv* (2021). doi: 10.1101/2021.06.20.449146

62. Lamiable A, Thévenet P, Rey J, Vavrusa M, Derreumaux P, Tufféry P. Pep-Fold3: Faster de Novo structure prediction for linear peptides in solution and in complex. *Nucleic acids research* (2016) 44(W1):W449–W454. doi: 10.1093/nar/gkw329

63. Sussman JL, Lin D, Jiang J, Manning NO, Prilusky J, Ritter O, et al. Protein Data Bank (PDB): database of three-dimensional structural information of biological macromolecules[J]. *Acta Crystallographica Section D: Biological Crystallography* (1998) 54(6):1078–84. doi: 10.1107/s0907444998009378

64. Waterhouse A, Bertoni M, Bienert S, Studer G, Tauriello G, Gumienny R, et al. Swiss-Model: Homology modelling of protein structures and complexes. *Nucleic Acids Res* (2018) 46(W1):W296-303. doi: 10.1093/nar/gky427

65. Guex N, Peitsch Mc Fau - Schwede T, Schwede T. Automated comparative protein structure modeling with Swiss-model and Swiss-pdbviewer: A historical perspective. *Electrophoresis* (2009) 30(S1):S162-73. doi: 10.1002/elps.200900140

66. Trott O, Olson AJ. Autodock vina: Improving the speed and accuracy of docking with a new scoring function, efficient optimization, and multithreading. *Journal of computational chemistry* (2010) 31(2):455-61. doi: 10.1002/jcc.21334

67. Laskowski RA, Swindells MB. Ligplot+: Multiple ligand-protein interaction diagrams for drug discovery. *J Chem Inf Model* (2011) 51(10):2778-86. doi: 10.1021/ci200227u

68. Dhople V, Krukemeyer A, Ramamoorthy A. The human beta-Defensin-3, an antibacterial peptide with multiple biological functions. *Biochimica et Biophysica Acta* (2006) 1758(9):1499-512. doi: 10.1016/j.bbamem.2006.07.007

69. Chen X, Zaro Jl W-C, Shen WC. Fusion protein linkers: Property, design and functionality. *Adv Drug Deliv Rev* (2013) 65(10):1357-69. doi: 10.1016/j.addr.2012.09.039

70. Athanasiou E, Agallou M, Tastsoglou S, Kammona O, Hatzigeorgiou A, Kiparissides C, et al. A Poly(Lactic-Co-Glycolic) acid nanovaccine based on chimeric peptides from different leishmania infantum proteins induces dendritic cells maturation and promotes peptide-specific ifnγ-producing Cd8(+) T cells essential for the protection against experimental visceral leishmaniasis. *Front Immunol* (2017) 8:684. doi: 10.3389/fimmu.2017.00684

71. Alexander J, del Guercio M-F, Maewal A, Qiao L, Fikes J, Chesnut RW, et al. Linear padre T helper epitope and carbohydrate b cell epitope conjugates induce specific high titer igg antibody responses. *J Immunol* (2000) 164(3):1625. doi: 10.4049/jimmunol.164.3.1625

72. Magnan CN, Randall A, Baldi P. Solpro: Accurate sequence-based prediction of protein solubility. *Bioinformatics* (2009) 25(17):2200–7. doi: 10.1093/bioinformatics/btp386

73. Buchan DWA, Jones DT. The psipred protein analysis workbench: 20 years on. *Nucleic Acids Res* (2019) 47(W1):W402–w7. doi: 10.1093/nar/gkz297

74. Heo L, Park H, Seok C. Galaxyrefine: Protein structure refinement driven by side-chain repacking. *Nucleic Acids Res* (2013) 41(Web Server issue):W384–8. doi: 10.1093/nar/gkt458

75. Craig DB, Dombkowski AA. Disulfide by design 2.0: A web-based tool for disulfide engineering in proteins. *BMC Bioinf* (2013) 14:346. doi: 10.1186/1471-2105-14-346

76. Takeda K, Akira S. Toll-like receptors. *Curr Protoc Immunol* (2015) 109:14.2.1–.2.0. doi: 10.1002/0471142735.im1412s109

77. Vijay K. Toll-like receptors in immunity and inflammatory diseases: Past, present, and future. *Int Immunopharmacol* (2018) 59:391–412. doi: 10.1016/j.intimp.2018.03.002

78. Kozakov D, Hall DR, Xia B, Porter KA, Padhorny D, Yueh C, et al. The cluspro web server for protein-protein docking. *Nat Protoc* (2017) 12(2):255–78. doi: 10.1038/nprot.2016.169

79. van Zundert GCP, Rodrigues J, Trellet M, Schmitz C, Kastritis PL, Karaca E, et al. The Haddock2.2 web server: User-friendly integrative modeling of biomolecular complexes. *J Mol Biol* (2016) 428(4):720–5. doi: 10.1016/j.jmb.2015.09.014

80. Laskowski RA, Jabłońska J, Pravda L, Vařeková RS, Thornton JM. Pdbsum: Structural summaries of pdb entries. *Protein Sci* (2018) 27(1):129–34. doi: 10.1002/pro.3289

81. Kutzner C, Páll S, Fechner M, Esztermann A, de Groot BL, Grubmüller H. Best bang for your buck: Gpu nodes for gromacs biomolecular simulations. *J Comput Chem* (2015) 36(26):1990–2008. doi: 10.1002/jcc.24030

82. Maier JA, Martinez C, Kasavajhala K, Wickstrom L, Hauser KE, Simmerling C. Ff14sb: Improving the accuracy of protein side chain and backbone parameters from Ff99sb. *J Chem Theory Comput* (2015) 11(8):3696–713. doi: 10.1021/acs.jctc.5b00255

83. Berendsen HJC, Postma JPM, WFv G, DiNola A, Haak JR. Molecular dynamics with coupling to an external bath. *J Chem Phys* (1984) 81(8):3684–90. doi: 10.1063/1.448118

84. Parrinello M, Rahman A. Strain fluctuations and elastic constants. *J Chem Phys* (1982) 76:2662–6. doi: 10.1063/1.443248

85. Hess B, Bekker H, Berendsen HJC, Fraaije JGEM. Lincs: A linear constraint solver for molecular simulations. *J Comput Chem* (1997) 18(12):1463–72. doi: 10.1002/(SICI)1096-987X(199709)18:12<1463::AID-JCC4>3.0.CO;2-H

86. Darden T, York D, Pedersen L. Particle mesh ewald: An N·Log(N) method for ewald sums in Large systems. *J Chem Phys* (1993) 98(12):10089–92. doi: 10.1063/1.464397

87. Humphrey W, Dalke A, Schulten K. Vmd: Visual molecular dynamics. *J Mol Graph* (1996) 14(1):33–8. doi: 10.1016/0263-7855(96)00018-5

88. Valdés-Tresanco MS, Valdés-Tresanco ME, Valiente PA-O, Moreno EA-O. Gmx_MMPBSA: A New Tool to Perform End-State Free Energy Calculations with GROMACS[J]. *Journal of Chemical Theory and Computation* (2021) 17(10):6281–6291. doi: 10.1021/acs.jctc.1c00645

89. Arnold GE, Ornstein RL. Molecular dynamics study of time-correlated protein domain motions and molecular flexibility: Cytochrome P450bm-3. *Biophysical Journal* (1997) 73(3):1147-59. doi: 10.1016/S0006-3495(97)78147-5

90. Grant BJ, Rodrigues Ap, ElSawy KM, McCammon JA, Caves LSD. Bio3d: An r package for the comparative analysis of protein structures. *Bioinformatics* (2006) 22 (21):2695–96. doi: 10.1093/bioinformatics/btl461

91. Rapin N, Lund O, Bernaschi M, Castiglione F, Castiglione F. Computational immunology meets bioinformatics: The use of prediction tools for molecular binding in the simulation of the immune system. *PloS one* (2010) 5(4):e9862. doi: 10.1371/journal.pone.0009862

92. Bui HH, Sidney J, Dinh K, Southwood S, Newman MJ, Sette A. Predicting population coverage of T-cell epitope-based diagnostics and vaccines. *BMC bioinformatics* (2006) 7(1):1-5. doi: 10.1186/1471-2105-7-153

93. Zuker M. Mfold web server for nucleic acid folding and hybridization prediction. *Nucleic acids research* (2003) 31(13):3406–15. doi: 10.1093/nar/gkg595

94. Gruber AR, Lorenz R, Bernhart SH, Neuböck R, Hofacker IL. The Vienna rna websuite. *Nucleic Acids Res* (2008) 36(Web Server issue):W70–4. doi: 10.1093/nar/gkn188

95. Maekawa S, Yoshida T, Wang PC, Chen SC. Current knowledge of nocardiosis in teleost fish. *J Fish Dis* (2018) 41(3):413–9. doi: 10.1111/jfd.12782

96. Valdezate S, Garrido N, Carrasco G, Medina-Pascual MJ, Villalón P, Navarro AM, et al. Epidemiology and susceptibility to antimicrobial agents of the main nocardia species in Spain. *J Antimicrob Chemother* (2017) 72(3):754–61. doi: 10.1093/jac/dkw489

97. Steinbrink J, Leavens J, Kauffman CA, Miceli MH. Manifestations and outcomes of nocardia infections: Comparison of immunocompromised and nonimmunocompromised adult patients. *Med (Baltimore)* (2018) 97(40):e12436. doi: 10.1097/md.0000000000012436

98. Wintheiser GA, Venable ER, Temesgen Z. Disseminated nocardia in an immunocompetent host. *Mayo Clin Proc* (2021) 96(4):847–8. doi: 10.1016/j.mayocp.2020.11.019

99. Li J, Cao J, Wu Y, Wan N, Pan L, Chen Y. A case of an immunocompetent young man obtaining community-acquired disseminated nocardia brasiliensis. *Heart Lung* (2014) 43(2):164–7. doi: 10.1016/j.hrtlng.2013.12.002

100. Miller JF, Vadas MA. Antigen activation of T lymphocytes: Influence of major histocompatibility complex. *Cold Spring Harb Symp Quant Biol* (1977) 41 Pt 2:579–88. doi: 10.1101/sqb.1977.041.01.067

101. Kwissa M, Kasturi SP, Pulendran B. The science of adjuvants. *Expert Rev Vaccines* (2007) 6(5):673–84. doi: 10.1586/14760584.6.5.673

102. Dhople V, Krukemeyer A, Ramamoorthy A. The human beta-Defensin-3, an antibacterial peptide with multiple biological functions. *Biochim Biophys Acta* (2006) 1758(9):1499–512. doi: 10.1016/j.bbamem.2006.07.007

frontiers | Frontiers in Immunology

TYPE Original Research
PUBLISHED 10 February 2023
DOI 10.3389/fimmu.2023.1100161

Check for updates

OPEN ACCESS

EDITED BY
Nargis Khan,
University of Calgary, Canada

REVIEWED BY
Pierre Guermonprez,
Centre National de la Recherche Scientifique (CNRS), France
Bas G.J. Surewaard,
University of Calgary, Canada
Ajitha Thanabalasuriar,
McGill University, Canada

*CORRESPONDENCE
Kevin Dhaliwal
Kev.Dhaliwal@ed.ac.uk
Vincent Pavot
Vincent.Pavot@sanofi.com

SPECIALTY SECTION
This article was submitted to Vaccines and Molecular Therapeutics, a section of the journal Frontiers in Immunology

RECEIVED 16 November 2022
ACCEPTED 30 January 2023
PUBLISHED 10 February 2023

CITATION
Humphries DC, O'Connor RA, Stewart HL, Quinn TM, Gaughan EE, Mills B, Williams GOS, Stone JM, Finlayson K, Chabaud-Riou M, Boudet F, Dhaliwal K and Pavot V (2023) Specific *in situ* immuno-imaging of pulmonary-resident memory lymphocytes in human lungs. *Front. Immunol.* 14:1100161. doi: 10.3389/fimmu.2023.1100161

COPYRIGHT
© 2023 Humphries, O'Connor, Stewart, Quinn, Gaughan, Mills, Williams, Stone, Finlayson, Chabaud-Riou, Boudet, Dhaliwal and Pavot. This is an open-access article distributed under the terms of the Creative Commons Attribution License (CC BY). The use, distribution or reproduction in other forums is permitted, provided the original author(s) and the copyright owner(s) are credited and that the original publication in this journal is cited, in accordance with accepted academic practice. No use, distribution or reproduction is permitted which does not comply with these terms.

Specific *in situ* immuno-imaging of pulmonary-resident memory lymphocytes in human lungs

Duncan C. Humphries[1,2], Richard A. O'Connor[1], Hazel L. Stewart[1], Tom M. Quinn[1], Erin E. Gaughan[1], Beth Mills[1], Gareth O.S. Williams[1], James M. Stone[1,3], Keith Finlayson[1], Martine Chabaud-Riou[2], Florence Boudet[2], Kevin Dhaliwal[1]* and Vincent Pavot[2]*

[1]Translational Healthcare Technologies Group, Centre for Inflammation Research, Queen's Medical Research Institute, The University of Edinburgh, Edinburgh, United Kingdom, [2]Research & Development, Sanofi, Marcy L'Etoile, France, [3]Centre for Photonic and Physics, Bath University, Bath, United Kingdom

Introduction: Pulmonary-resident memory T cells (T_{RM}) and B cells (B_{RM}) orchestrate protective immunity to reinfection with respiratory pathogens. Developing methods for the *in situ* detection of these populations would benefit both research and clinical settings.

Methods: To address this need, we developed a novel *in situ* immunolabelling approach combined with clinic-ready fibre-based optical endomicroscopy (OEM) to detect canonical markers of lymphocyte tissue residency *in situ* in human lungs undergoing *ex vivo* lung ventilation (EVLV).

Results: Initially, cells from human lung digests (confirmed to contain T_{RM}/B_{RM} populations using flow cytometry) were stained with CD69 and CD103/CD20 fluorescent antibodies and imaged *in vitro* using KronoScan, demonstrating it's ability to detect antibody labelled cells. We next instilled these pre-labelled cells into human lungs undergoing EVLV and confirmed they could still be visualised using both fluorescence intensity and lifetime imaging against background lung architecture. Finally, we instilled fluorescent CD69 and CD103/CD20 antibodies directly into the lung and were able to detect T_{RM}/B_{RM} following *in situ* labelling within seconds of direct *intra-alveolar* delivery of microdoses of fluorescently labelled antibodies.

Discussion: *In situ*, no wash, immunolabelling with *intra-alveolar* OEM imaging is a novel methodology with the potential to expand the experimental utility of EVLV and pre-clinical models.

KEYWORDS

resident memory T cells, resident memory B cells, lung, optical endomicroscopy, fluorescence lifetime imaging

10.3389/fimmu.2023.1100161

Introduction

Human and non-human primate (NHP) studies have highlighted the protective role of lung-resident memory T cells (T_{RM}) in controlling respiratory pathogens (1–3). Constituting the majority of T cells within the lung (4), T_{RM} have a unique phenotype that differentiates them from other memory T cell subsets and their sequestration within the lung offers an ideal location to respond to respiratory infections (5). Requiring only cognate antigen for their activation (6), T_{RM} are highly proliferative, producing polyfunctional progeny with superior effector function (7, 8). Activated $CD4^+$ and $CD8^+$ T_{RM} in the lungs of patients with *Mycobacterium tuberculosis* (MTB) limit intracellular MTB replication in macrophages (9), whilst increased numbers of $CD8^+$ T_{RM} in BAL is associated with reduced symptoms and viral load following human respiratory syncytial virus (RSV) infection (1). In human influenza infection, $CD4^+$ and $CD8^+$ T_{RM} confer heterosubtypic protection (10), with $CD8^+$ T_{RM} recognising universally conserved peptides expressed by influenza A, B and C viruses (11). Virus-specific pulmonary $CD8^+$ T_{RM} also have shown "innate like properties" that amplify inflammation and enhance neutrophil recruitment following noncognate bacterial infection to aid clearance, as demonstrated in murine models (12). While most actions of T_{RM} benefit the host, following chronic exposure to allergens, T_{RM} can also be detrimental and contribute significantly to pathology in experimental allergic asthma (13, 14), indicating monitoring the frequency and phenotype of T_{RM} has relevance beyond respiratory infections.

Antigen-experienced lungs are also enriched with B cells expressing a resident memory phenotype (15). Murine parabiosis studies have demonstrated that pulmonary-resident memory B cells (B_{RM}) require local antigen encounter and early CD40/CD40 ligand interactions with T cells for their formation and are phenotypically and functionally distinct from their systemic counterparts (5, 16). Murine B_{RM} play a protective role in response to both viral influenza (16–18) and bacterial pneumococcal pneumonia (15) infections, providing rapid antibody secreting cells (ASC) capable of producing a range of class switched, cross-reactive antibodies to confer heterosubtypic protection (15–17).

Vaccination strategies designed to induce pulmonary resident memory lymphocyte populations have been successfully demonstrated in murine models (19). In NHP, pulmonary mucosal delivery of MTB vaccine is associated with enhanced protection over standard intradermal immunization *via* the induction of lung T_{RM} (20). As T_{RM} and B_{RM} formation is dependent on pulmonary cognate antigen encounter (16, 21), it's anticipated that pulmonary mucosal vaccination will also generate B_{RM}. This can induce higher levels of local immunity than that generated by natural MTB infection (20). Strategies that establish antigen-specific T_{RM} and B_{RM} populations or enhance pre-existing populations have the potential to provide local long lasting heterosubtypic protection where it is most needed. Current methods for evaluating respiratory vaccine efficacy, however, rely mostly on peripheral blood sampling to reveal the level of humoral protection and circulating central memory T cell (T_{CM}) and effector memory T cell (T_{EM}) populations. However, as T_{RM} and B_{RM} do not circulate and limited blood biomarker surrogates exist, current methods for assessing local immunity are limited.

These studies highlight the pivotal role of T_{RM} and B_{RM} in orchestrating and directing protective responses to respiratory infections. The spatial and temporal characterisation of such pulmonary resident immune cells is thus of key importance, but most available methods require biopsy, tissue digestion and post-mortem studies (16, 22). In this study, we aimed to develop an *in situ* method for the direct detection of these cells in the human lung by exploiting recent advances in *in situ*-optical endomicroscopy, within the alveoli (23), which may provide a valuable tool for quantifying pulmonary resident memory populations following infection and vaccination.

The objective was to develop a technical platform for direct alveolar imaging of pulmonary T_{RM} and $B_{RM.}$ We aimed to develop an *in situ* immunolabelling approach with a clinic-ready fibre-based optical endomicroscopy (OEM) system that combined both intensity imaging and fluorescence lifetime imaging (FLIM) to ensure contrast and specificity was achieved over endogenous elastin fluorescence of the lung. With NHP providing an ideal model for translational studies, this project also aimed to establish a cross-reactive antibody panel capable of detecting T_{RM} and B_{RM} in both humans and NHP species.

FLIM is a fluorescence imaging technique where the contrast is based on the lifetime of individual fluorophores rather than their emission spectra. The fluorescence lifetime (FLT) is defined as the average time that a molecule remains in an excited state prior to returning to the ground state by emitting a photon. The FLT of the fluorophore, rather than its intensity, is used to create the image in FLIM. FLT depends on the local micro-environment of the fluorophore, thus precluding any erroneous measurements in fluorescence intensity due to change in brightness of the light source, background light intensity or limited photo-bleaching (24).

A clinic-ready fibre-based FLIM system (KronoScan), incorporating a time-resolved spectrometer and an achromatic advanced confocal laser scanning microscope system was used coupled to a fully biocompatible multifunctional endoscopic fibre (Panoptes) with an outer diameter of 1.8 mm, which comprises an imaging fibre bundle packaged alongside two capillary channels for delivery and extraction of fluids

T cells recovered from bronchoalveolar lavage and lung tissue digests from *ex vivo* whole human lungs showed characteristic features of T_{RM} with $CD69^+CD103^+$ $CD8^+$ T_{RM} being the most abundant population in the BAL and higher than in the lung tissue. A cross reactive panel of antibodies detected T cells bearing T_{RM} markers in NHP lung, although at much lower levels than in human lung. Cells isolated from human lung digests co-expressing CD69 and CD103 could be visualised using fibre-based imaging *via* both fluorescence intensity and lifetime imaging when labelled with anti-CD69 and anti-CD103 antibodies, both *in vitro* and after instillation into human lungs. Using KronoScan with Panoptes (25), dual antibody labelled cells (expressing markers of tissue retention) were detected *in situ* within human lungs undergoing EVLV within seconds of direct *in situ* delivery.

Our study extends the methods available for live imaging of leukocytes at the host-environment interface of the lung and demonstrates the potential of specific immunolabelling for distal lung interrogation. The *ex vivo* human lung model, closely resembles the *in vivo* situation, enabling validation of imaging modalities and facilitates transfer to both research and clinical settings.

Methods

Tissue source

Human lungs from deceased subjects deemed non-suitable for transplantation were received from National Health Service Blood and Transplant (NHSBT), United Kingdom. Following explantation and perfusion, lungs were placed on ice and transported to the University of Edinburgh within 48 hours prior to ventilation/lavage. Whole NHP (cynomolgus macaque from Mauritius) lungs were obtained from Charles River Laboratories (Edinburgh, UK) and transported in Roswell Park Memorial Institute (RPMI) 1640 medium (11875-093, Gibco) prior to tissue digest. NHP lungs were non-perfused and obtained from healthy control animals not subjected to experimental manipulation.

Ex vivo lung ventilation

Human lungs undergoing EVLV were placed on a Dräger Savina 300 ventilator following placement of an endotracheal tube and ventilated with a tidal volume of 7 mL/kg (patient body mass) at a respiratory rate of 12 breaths per minute (Supplementary Figure 1A). Ventilation was volume controlled, air driven, and positive end expiratory pressure (PEEP) was set at 5 cm H_2O. The airway pressure limit setting on the ventilator was increased to the maximum setting to prevent under ventilation.

Bronchoalveolar lavage

Bronchoalveolar lavage (BAL) was obtained from human lungs undergoing EVLV by instilling 100 mL phosphate-buffered saline (14190-094, PBS, Gibco) into the right middle lobe or selected lobes *via* a bronchoscope. Aspirated cells were passed through a 40 µm cell strainer (431750, Corning, USA) and counted using a NucleoCounter cell counter (Chemometec, Denmark). Cells were processed fresh or cryopreserved in liquid nitrogen using Recovery™ Cell Culture Freezing Medium (12648010, Thermo Fisher).

Lung tissue digest

Human (EVLV-derived samples from the distal lung) and NHP lung tissues were dissected with a scalpel and finely cut with scissors prior to incubation in 37°C DMEM (21969-035, Gibco) containing 1 mg/mL Collagenase IV (C5138, Sigma-Aldrich) and 0.1 mg/mL DNASE I (DN25 – Sigma Aldrich) for 1 hour with constant agitation. The sample was strained through a 70 µm cell strainer (22-363-549, Thermo Fisher) and spun at 350 x g for 5 minutes at room temperature. Red blood cell (RBC) lysis was performed using RBC lysis buffer (320301, Biolegend) for 10 minutes at room temperature prior to addition of DMEM and spun for another 5 minutes at 350 x g. Cells were counted using a NucleoCounter and processed for direct flow cytometry analysis or cryopreserved.

Peripheral blood mononuclear cells

Human peripheral blood mononuclear cells (PBMCs) were isolated from whole blood using Percoll gradients (26). PBMCs were then cryopreserved. Cryopreserved cynomolgus PBMCs were obtained from BioIVT (BioIVT, United Kingdom).

Flow cytometric analysis of lung tissue and BAL

Fresh lung digest and BAL cells were placed in 5 mL flow cytometry tubes. For cryopreserved cells, cells were gently warmed in 37°C water, placed in DMEM containing 10% foetal calf serum (FCS) and washed at 350 x g for 10 minutes prior to transfer to flow tubes. Cells were stained with live/dead marker Zombie UV (423107, Biolegend) in PBS for 30 minutes in the dark at room temperature. Cells were washed with FACS buffer (PBS + 2% FCS) and incubated with Fc block (564220, BD Biosciences) for 10 minutes prior to cell surface antibody staining containing BD Brilliant Horizon™ Staining Buffer (563794, BD Biosciences) (for details of flow cytometry antibodies used, see Supplementary Table 1). Following a 25-minute incubation in the dark at 4°C, cells were washed at 350 x g for 5 minutes and resuspended in Fixation Buffer (420801, Biolegend) for 20 minutes at room temperature before spinning at 350 x g for 5 minutes and resuspending in FACS buffer. For intracellular Ki-67 staining, cells were washed following cell surface antibody staining and processed using the Foxp3/Transcription Factor Staining Buffer Set (00-5523-00, Thermo Fisher Scientific) according to the manufacturer's instructions. Ki-67 antibodies were used at dilutions recommended by the manufacturer (Supplementary Table 1). Samples were assessed using a 5L LSR Fortessa flow cytometer (BD Biosciences). Compensation was calculated using UltraComp eBeads™ (01-222-42, Thermo Fisher Scientific). Data analysis was performed using FlowJo software, version 10.7.2 (BD).

T_{RM}/B_{RM} immunofluorescence staining

Human and NHP lung tissues were placed in optimal cutting temperature compound (OCT, KMA-0100-00A, CellPath, UK) and snap frozen in liquid nitrogen. 10 µm sections were cut on to Super Frost microscope slides (12312148, Thermo Fisher) using a cryostat. Sections were air dried overnight at room temperature and then fixed in -20°C acetone for 10 minutes. Sections were air dried for <20 minutes prior to x2 washes with PBS. Multiplex immunofluorescence was performed on lung sections using a fully automated Bond-Rx Multiplex IHC Stainer (Leica Biosystems) and OPAL Multiplex IHC Detection Kit and counterstained with DAPI (Akoya Biosciences) according to a previously published protocol (27). T_{RM} were stained with purified, cross-reactive CD4 (OKT4, Biolegend), CD8 (SK1, Biolegend), CD69 (FN50, Biolegend) and CD103 (2G5.1, Bio-Rad, UK) antibodies. B_{RM} were stained with purified, cross-reactive CD20 (2H7, Biolegend), CD27 (M-T271, Biolegend) and CD69 (FN50, Biolegend) antibodies. Human lung (n=5) and NHP lung (n=3) sections were stained simultaneously using the same protocol and antibody concentrations. For full details, see online supplement.

10.3389/fimmu.2023.1100161

Fluorescence intensity and lifetime imaging system (KronoScan) and fibre (Panoptes)

The clinic-ready fibre-based FLIM system (Supplementary Figures 1B–D) (KronoScan), incorporates a time-resolved spectrometer (with 32 lifetime channels) and achromatic advanced confocal laser scanning microscope system, using a supercontinuum laser (SuperK EVO, NKT Photonics, Denmark) filtered to excitation band 490 nm and 590 nm. 50 frame fluorescence intensity and lifetime video sequences were simultaneously recorded using 128 x 128-pixel images (350 x 350 µm) matching fibre bundle characteristics. Spectral emission ranges of 498-565 nm and 620-764 nm were selected for analysis. Lifetime decays were fitted using rapid lifetime determination method (28), which assumes a single exponential decay, enabling high-processing speeds and real-time imaging at 3 frames per second (20 µs exposure time).

Panoptes (25) is a fully biocompatible multi-functional endoscopic device, with an outer diameter of 1.6 mm. It comprises an imaging fibre bundle packaged alongside two capillary channels for delivery and extraction of fluids. The low-index contrast imaging fibre (0.3 numerical aperture (NA)) is derived from multi-mode telecommunications preforms (OM1 PCVD rods). It is fabricated by multi-stacking arrays of different sized cores to optimise pixel density and suppress core-to-core crosstalk (29). This high-resolution OEM & FLIM imaging fibre, which comprises 8100 cores, with 450 µm diagonal field of view, is deliverable *via* existing bronchoscopic and transthoracic platforms.

Fluorescence intensity and lifetime T_{RM}/B_{RM} fibre imaging *in vitro*

$5x10^6$ human lung digest cells or PBMCs were stained with 15 µL FITC-conjugated CD69 (FN50, Biolegend) and PE-Dazzle CD103 (BerACT8, Biolegend) to identify T_{RM}, or 15 µL FITC-conjugated CD69 and PE-Dazzle-labelled CD20 (2H7, Biolegend) to identify B_{RM}, for 20 minutes at 4°C in FACS buffer. Cells were spun at 350 x g for 5 minutes, resuspended in 100 µL PBS and transferred to a black 96-well plate. Fluorescence intensity and lifetime imaging was performed using OEM KronoScan Imaging system and Panoptes Multifunctional fibre. Videos were saved retrospectively when events were detected and analysed using the KronoScan Player (Firefinch Software Development, UK).

In situ detection of T_{RM}/B_{RM}

Using a bronchoscope, the Panoptes multifunctional fibre was navigated to the distal airways *via* autofluorescence intensity imaging to visualise airways and alveoli (Figure 1E). $5x10^6$ pre-labelled human T_{RM} or B_{RM} were prepared as outlined in the previous section. For *in situ* T_{RM}/B_{RM} detection, 20 µL (2 µg) CD69 + 20 µL (0.5 µg) CD103 or 20 µL (0.8 µg) CD20 + CD69 was diluted in 500 µL PBS. Antibodies or pre-labelled cells were instilled into different alveolar segments (to prevent cross contamination) of human lungs undergoing EVLV *via* the delivery channel of Panoptes Multifunctional Fibre. Fluorescence intensity and lifetime imaging was performed after 5 minutes using KronoScan OEM.

Statistics

All data in text are represented as mean ± standard deviation (SD). All data in figures are represented as mean ± standard error of the mean (SEM). All graphs were generated using GraphPad Prism 9 (GraphPad Software, California, USA).

Results

Characterisation of human and NHP pulmonary T_{RM}

To identify and characterise human and NHP pulmonary T_{RM}, cells isolated from lung tissue were stained with cross-reactive antibodies for human and cynomolgus macaque and analysed by flow cytometry. Based on the existing knowledge (5), T_{RM} were phenotyped as $CD3^+$, $CD4^+$/$CD8^+$, CD62-L^-, $CD69^+$, ± CD103 (for T_{RM} gating strategy, see Supplementary Figure 2). Exclusion of CD62-L^+ (L-selectin) cells helped eliminate any contaminating circulating T_{CM} present within the vasculature of the lung tissue.

$CD4^+$ and $CD8^+$ T_{RM} were detected in human lung and BAL but were expectedly absent in peripheral blood (Figure 1A). The highest levels of CD103 expressing cells were seen in $CD8^+$ T_{RM} in the BAL where $CD69^+CD103^+$ T_{RM} were the most abundant population (33.3% ± 22.9, Figures 1A, C). $CD69^+$ $CD4^+$ and $CD8^+$ T_{RM} were also detected in NHP lung, although at much lower levels than that found in human lung (Figures 1B, C). 57% ± 14.3 of $CD4^+$ T cells in human lung were positive for CD69 compared to 28% ± 11 in NHP lung. 32.8% ± 14 of $CD8^+$ T cells in human were positive for CD69 compared to 15.8% ± 11.7 in NHP lung. There were some similarities in the expression of CD69 and CD103 in human and NHP samples: $CD69^+$ T cells were present at higher frequencies in lung versus peripheral blood (Figures 1A, B) and lung $CD8^+$ T cells showed higher levels of CD103 expression than their $CD4^+$ counterparts in both species (Figure 1C). However, the overall frequency of $CD69^+$ T_{RM} (± CD103) was lower in NHP than in human samples and co-expression of CD69 and CD103 was rarely observed in NHP (Figures 1A–C). Human lung contained 66.9% ± 17.6 and 58.7% ± 21.8 $CD4^+$ and $CD8^+$ $T_{RM,}$ respectively, compared to 30.6% ± 11.9 and 17.4% ± 12.3 in NHP lung. In NHP lung, only 1.74% ± 1.9 of $CD4^+$ and 1.52% ± 0.8 of $CD8^+$ cells co-expressed CD69 and CD103, compared to 9.9% ± 10.7 $CD4^+$ and 25.9% ± 17.1 $CD8^+$ cells within human lung. $CD62L^-CD69^-CD103^-$ T_{EM} were the largest population observed in NHP lung, with 67% ± 17.5 of $CD4^+$ T cells and 78% ± 21.6 of $CD8^+$ T cells failing to express tissue-residency markers.

To assess rates of proliferation, intracellular levels of Ki-67 were measured in pulmonary T_{RM}. Low levels of Ki-67 were observed in human $CD4^+$ and $CD8^+$ T cells isolated from lung and BAL (Figure 1D). Ki-67 levels were slightly higher in NHP lung, particularly in $CD69^-$ T cells, in line with their effector memory profile (Figure 1E).

Despite differences in expression of CD69 and CD103 between species, expression patterns of other markers associated with T_{RM} phenotype, CD49a and programmed cell death protein 1 (PD-1), were similar on human and NHP T_{RM}. CD49a was absent on peripheral blood T cells but expressed by human and NHP $CD69^+$ T_{RM}, particularly those co-expressing CD103 (Supplementary Figure 3). Increased levels of PD-1 were also observed on human and NHP T_{RM},

10.3389/fimmu.2023.1100161

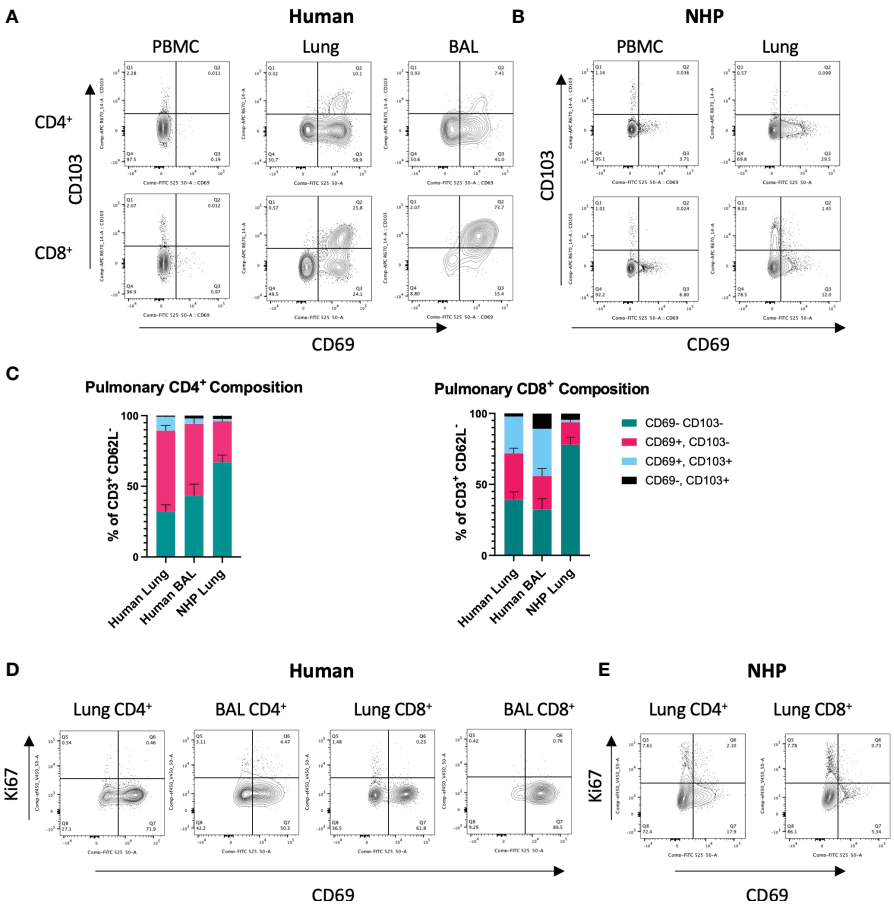

FIGURE 1
Characterisation of Human and NHP Pulmonary T_{RM}. T_{RM} from BAL and/or tissue digests were compared with peripheral T cells. **(A)** Identification of human pulmonary $CD4^+$ and $CD8^+$ T_{RM}. T_{RM} (live, $CD3^+$, $CD4^+/CD8^+$, $CD62\text{-}L^-$) were identified based on their expression of CD69 and CD103. **(B)** Identification of NHP $CD4^+$ and $CD8^+$ T_{RM}. **(C)** Proportion of $CD69^+$ and $CD69^+CD103^+$ T_{RM} in human and NHP lung. **(D)** Ki-67 staining in human $CD4^+$ and $CD8^+$ T_{RM}. **(E)** Ki-67 staining in NHP $CD4^+$ and $CD8^+$ T_{RM}. Human and NHP samples were concatenated for analysis. Data represented as representative flow cytometry plots or compiled frequencies with mean ± SEM **(C)** from human lungs (n=15), BAL (n=9) and NHP lung (n=5).

with expression highest on $CD103^+$ T_{RM} and T_{RM} isolated from BAL (Supplementary Figure 3).

Characterisation of human and NHP pulmonary B_{RM}

Human and NHP lung cells were stained for pulmonary B_{RM} markers. B_{RM} were phenotyped as $CD62\text{-}L^-$, $B220^+$, $CD20^+$, $CD27^+$, $CD69^+$ (5, 15) (for B_{RM} gating strategy, see Supplementary Figure 4). Both human and NHP lungs contained $CD27^+CD69^-$ memory B cells (B_{MEM}) but a distinct population of $CD27^+CD69^+$ B_{RM} was mostly observed in human BAL (Figures 2A, B). $CD27^+$ B_{MEM} were also detected in human and NHP peripheral blood, however these cells did not express CD69. Human lung and BAL contained similar frequencies of B_{MEM} (41.1% and 40.6%, respectively) (Figure 2C). NHP lung contained significantly fewer B_{MEM}, with only 9.5% present. Human BAL contained the highest proportion of B_{RM}, with 25.6% of memory B cells expressing CD69 compared to 8.4% in human lung and only 1.4% in NHP lung (Figure 2C). Although BAL contained the highest proportion of B_{RM}, numbers were far fewer than those found in the lung interstitium.

Despite being fewer in frequency, NHP B cells from lung digests shared a similar surface marker phenotype to their human counterparts, expressing increased CD45RB, CD80 and CXCR3 levels compared to circulating B cells (Figure 2D).

T_{RM}/B_{RM} tissue immunofluorescence

Having identified the most robust markers and cross-reactive antibodies for detecting human and NHP T_{RM} and B_{RM}, frozen lung sections were stained for immunofluorescence imaging. Acetone-fixed frozen sections were used due to the sensitivities of CD69 and CD103 epitopes to formalin fixation. Tyramide signal amplification was also used as all primary antibodies were raised in mouse. Therefore, we investigated the localization of $CD103^+$ and $CD69^+$ $CD4^+$ and $CD8^+$ T_{RM} and $CD20^+CD27^+CD69^+$ B_{RM} in human and NHP lungs.

$CD69^+$ and $CD69^+CD103^+$ $CD4^+$ and $CD8^+$ T_{RM} were identified within both human and NHP distal airway (Figure 3A – for individual fluorescent channels, see Supplementary Figures 5, 6). $CD69^-CD103^-$ $CD4^+$ and $CD8^+$ T cells were also evident. $CD20^+CD27^+CD69^+$ B_{RM} were located within human and NHP distal lung, with less observed in

10.3389/fimmu.2023.1100161

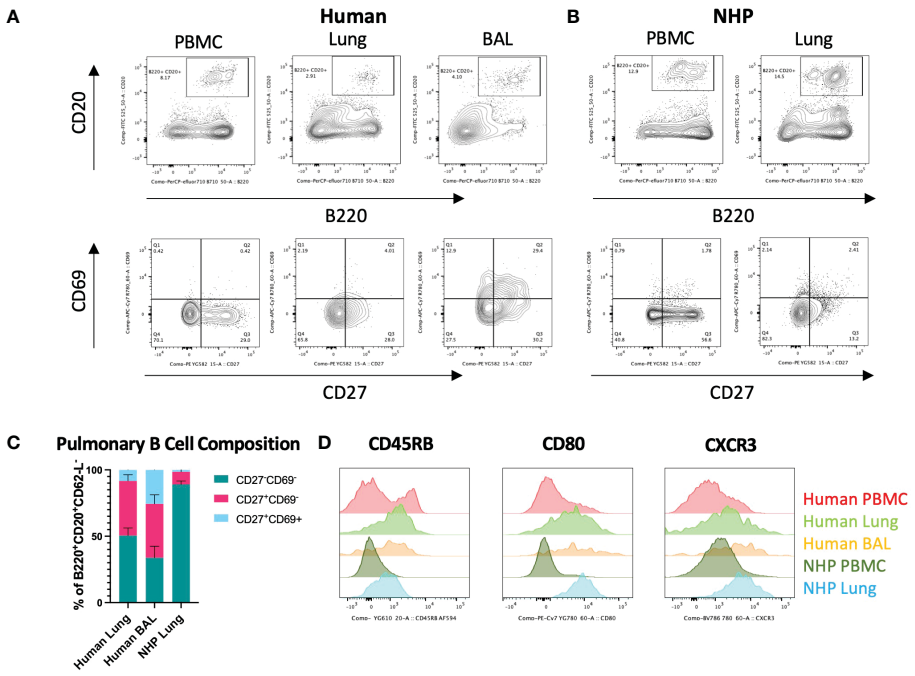

FIGURE 2
Characterisation of Human and NHP Pulmonary B_{RM}. B_{RM} were isolated from BAL and/or tissue digests and compared with peripheral B cells. **(A)** Identification of human pulmonary B_{RM}. B_{RM} (live, $CD62L^-$, $B220^+$, $CD20^+$ (lower panels)) were identified based on their expression of CD27 and CD69. **(B)** Identification of NHP pulmonary B_{RM}. **(C)** Proportion of B_{RM} in human and NHP lung. **(D)** Human and NHP B_{RM} surface marker expression. Human and NHP samples were concatenated for analysis. Surface marker expression was compared to B cells isolated from peripheral blood (PBMC). Data represented as representative flow cytometry plots, compiled frequencies with mean ± SEM or histograms from human lungs (n=9), BAL (n=7) and NHP lung (n=5).

NHP lung, mirroring flow cytometric results (Figure 3B). High frequencies of $CD20^+CD27^-CD69^-$ B cells were also observed in NHP lung, again mirroring flow cytometric results. No evidence of repair-associated memory depots (RAMD) or inducible bronchus-associated lymphoid tissue (iBALT) was apparent as shown by a lack of clusters of $CD4^+/CD8^+$ T_{RM} or $CD20^+$ B cells observed by immunofluorescence. DAPI staining following both staining protocols appeared diffuse, suggesting deterioration of the acetone-fixed, frozen tissue from the numerous wash and heat steps.

Fluorescence intensity and lifetime imaging of human pulmonary T_{RM}/B_{RM}

As the current KronoScan system is optimised for two excitation channels, we were unable to employ the lineage-based gating strategies commonly used in flow cytometry and could not definitively label T_{RM} in initial experiments. However, we assessed the potential of KronoScan to detect expression of CD69 and CD103, or CD69 and CD20, as the phenotypically distinguishing surface markers of T_{RM} and B_{RM}, respectively. Utilising the excitation wavelengths (490 nm and 590 nm) and two spectral windows (498-565 nm, "green", and 620-764 nm, "red") of KronoScan, FITC-conjugated CD69 and PE-Dazzle conjugated CD103 or CD20 were selected for fluorescence intensity and lifetime imaging. As a proof-of-concept experiment, human lung digest cells were stained with fluorescent antibodies for CD69 and CD103 or CD20, and subsequently imaged *in vitro* with KronoScan (Figure 4A). Human pulmonary $CD69^+$ and $CD69^+CD103^+$ cells could be visualised *via* both fluorescence intensity and lifetime imaging (Figure 4B + Supplementary Video 1) as well as $CD69^+CD20^+$ cells (Figure 4C + Supplementary Video 2). No fluorescence intensity or lifetime signal was observed from unstained lung cells in either the green or red channels (Supplementary Figure 7A). As expected, no CD69 or CD103 signal was detected from PBMCs (as negative controls) (Supplementary Figure 7B + Supplementary Video 3), however $CD20^+$ B cells were observed (Supplementary Figure 7C + Supplementary Video 4).

In situ detection of human pulmonary T_{RM}/B_{RM}

To observe whether KronoScan and Panoptes could detect pulmonary $CD69^+/CD103^+$ and $CD69^+/CD20^+$ cells *in situ*, single cell suspensions from human lung digest were pre-stained for CD69 and CD103 or CD69 and CD20 and instilled into the alveolar space of lungs undergoing EVLV (Figure 5A). Fluorescence intensity imaging with 490 nm excitation was used to confirm that the Panoptes multifunctional fibre was within the alveolar space prior to instillation (Figure 5B + Supplementary Video 5). Alveolar lung architecture could be visualised *via* elastin autofluorescence of alveolar septae. No fluorescence intensity or lifetime signal was detected from lung tissue in the red channel. Upon instillation of labelled cells, $CD69^+$ (Figure 5C + Supplementary Video 6), $CD69^+CD103^+$ cells (Figure 5D + Supplementary Video 7) and

10.3389/fimmu.2023.1100161

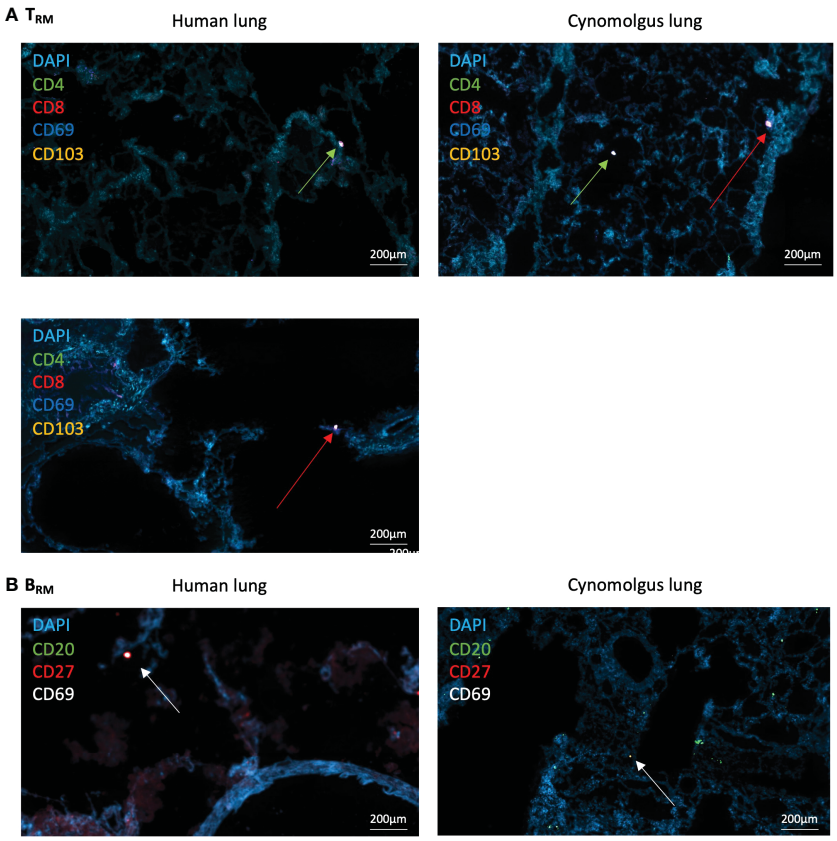

FIGURE 3
Human and NHP Immunofluorescence T_{RM}/B_{RM} Detection. Frozen lung sections or BAL cells were stained using tyramide signal amplification. **(A)** Human and NHP T_{RM} detection in lung. $CD4^+$ and $CD8^+$ T_{RM} were detected based on their expression of CD69 and CD103. **(B)** Human and NHP B_{RM} detection in lung. B_{RM} were detected based on their expression of CD20, CD27 and CD69. Images taken at x400 magnification. Green arrows represent $CD4^+$ T_{RM} and red arrows represent $CD8^+$ T_{RM} **(A)**, and white arrows represent B_{RM} **(B)**.

$CD69^+CD20^+$ cells (Figure 5E + Supplementary Video 8) could be visualised *via* an increase in fluorescence intensity counts as well as a lower lifetime signature of labelled cells that differentiated them from alveolar tissue and intrinsic unlabelled tissue cells.

We next progressed to *in situ* labelling and detection of $CD69^+CD103^+$ and $CD69^+CD20^+$ cells following *intra-alveolar* delivery of microdoses (0.5–2 µg) of fluorescently labelled antibodies (Figure 6A). Baseline lung imaging confirmed that Panoptes was successfully navigated to the distal lung (Figure 6B). An instantaneous and rapid rise in fluorescence intensity counts confirmed successful delivery of the fluorescent antibody solution within the alveolar space (Supplementary Video 9). Within 120 seconds of CD69 and CD103 antibody delivery, $CD69^+$ cells and $CD69^+CD103^+$ cells were visible *via* increased fluorescence intensity counts and a lifetime signature lower than that of lung tissue (Figures 6C, D + Supplementary Videos 10, 11). Pulmonary B_{RM} were also visualised within the airways and alveolar space following instillation of CD69 and CD20 antibodies (Figure 6E + Supplementary Video 12).

Discussion

Using cross-reactive antibodies for CD69 and CD103, we identified pulmonary T_{RM} in the lungs of humans and cynomolgus macaques. Both cell surface markers display key properties in the lung. CD69, although described as a marker of recent T cell activation induced through antigen stimulation and inflammatory cytokine exposure, supports effector T cell retention *via* the downregulation of sphingosine-1-phophsate receptor (S1PR1) and is considered as the main residency marker of pulmonary T_{RM} (30, 31). CD103, preferentially expressed on pulmonary $CD8^+$ T_{RM}, promotes adherence to E-cadherin and contributes towards initial recruitment and persistence to aid surveillance (32). Moreover, human and NHP $CD4^+$ and $CD8^+$ $CD69^+$ T_{RM} expressed CD49a, particularly those co-expressing CD103. This integrin, specific for collagen IV, may contribute to the functionality of T_{RM} in the lung by facilitating locomotion for surveillance and through its critical role in cell survival by limiting apoptosis (32). Increased levels of PD-1 were also detected on human and NHP T_{RM}, particularly on $CD8^+$ T_{RM} and those isolated from human BAL. This marker may serve as a protective mechanism to prevent aberrant activation and excessive inflammation (33).

Although $CD69^+$ T cells were identified in NHP lung with a higher frequency than in PBMC, there were notably fewer T_{RM} than were found in human lung or BAL. High levels of pulmonary $CD69^+$ T_{RM} have been observed by others in Rhesus macaque, however $CD69^+CD103^+$ T_{RM} frequencies were low, similar to our study, even post vaccination (34). We obtained lungs from healthy control

10.3389/fimmu.2023.1100161

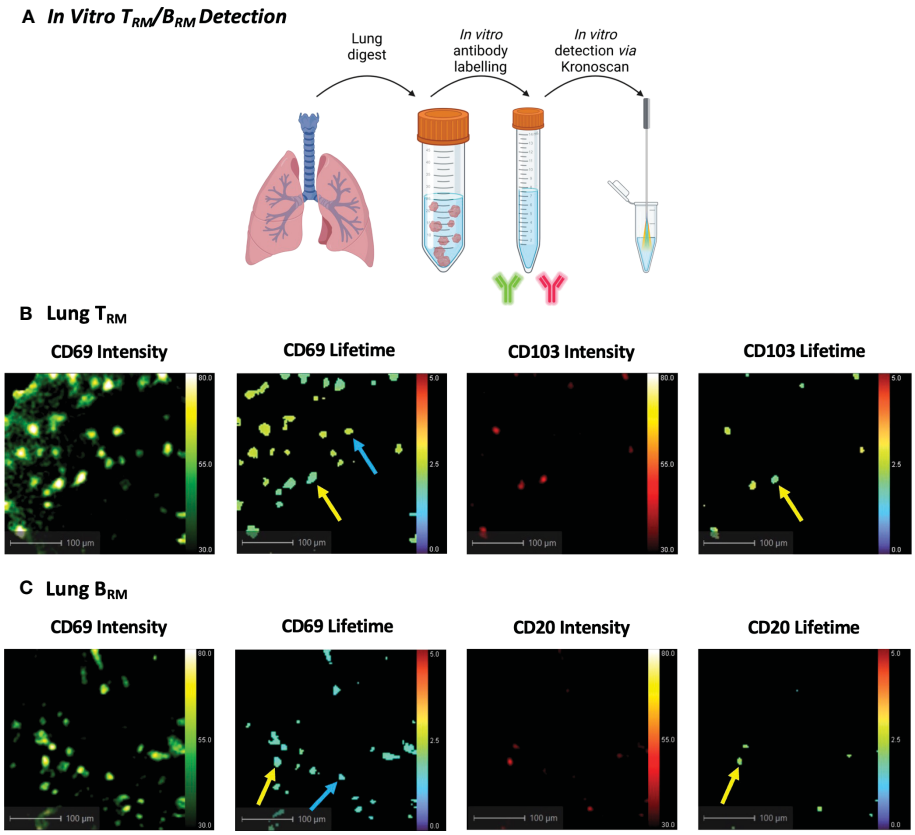

FIGURE 4
In Vitro Human T_{RM} and B_{RM} Detection using KronoScan and Panoptes. **(A)** Cells from human lung tissue digests were stained with T_{RM} or B_{RM} antibodies and imaged *in vitro* using KronoScan imaging system and Panoptes multifunctional fibre. **(B)** Human T_{RM} detection. T_{RM} were detected *via* expression of CD69 and CD103. Blue arrow indicates $CD69^+$ cells and yellow arrow points $CD69^+CD103^+$ T_{RM}. **(C)** Human B_{RM} detection. Blue arrow indicates $CD69^+$ cells and yellow arrow points $CD69^+$ $CD20^+$ B_{RM}. Representative images from n=3 experiments.

animals bred in clean laboratory conditions, which differ greatly to human antigen experienced lungs. Human T_{RM} frequencies are consistently higher than in mice maintained in clean conditions (35). In fact, CD69 expression in "dirty" pet store mice is more like that of humans (36). Limited pathogen exposure may therefore account for the reduced frequencies seen in this study. Moreover, T_{RM} have been described to undergo "retrograde migration" to the mediastinal lymph node where they provide longer-lived regional memory (37).This, combined with limited pathogen exposure, may contribute to a reduction in number of pulmonary T_{RM} in NHP macaques.

CD69 was also used to identify B_{RM} in the lungs of humans and NHP, which has been shown to be a marker of residency rather than recent activation (15, 38). However, expression levels were very low and $CD69^+$ B_{RM} were only readily detectable in human BAL. Human and NHP lung B cells shared a similar phenotype to those reported in mice, with expression of CD80 and the chemokine receptor CXCR3 (17), suggesting their ability to rapidly differentiate into antibody secreting plasma cells (39). CD45RB, expressed by human B_{RM} in the gut and tonsil, was also detected in our study on pulmonary B cells (40).

Human lung T_{RM} weakly expressed Ki-67, indicating low level proliferation. Expression was similar to that found in blood, mirroring previous results (41). Murine studies suggest interstitial $CD8^+$ T_{RM} sustain airway T_{RM} through a process of homeostatic proliferation (42), however we observed increased proliferation in human BAL. Proliferation was higher in NHP lung T_{RM}. Of note, one human sample obtained from an individual who had suffered cardiac arrest out of hospital and aspirated expressed high levels of Ki-67 in lung and BAL T_{RM} which may reflect significant lung injury and infection.

Pulmonary $CD69^+$ $CD103^+$ and $CD69^+$ $CD20^+$ human cells were successfully visualised *in situ via* fluorescence intensity and lifetime imaging using KronoScan and Panoptes OEM. The lung is highly autofluorescent in the green channel due to the presence of collagen and elastin (43) which can interfere with fluorescent signatures and mask positive signals when using fluorescence intensity imaging alone. In contrast to fluorescence intensity imaging, FLIM is insensitive to the concentration of probe bound to target, meaning only microdoses of antibody are required to visualise a target making FLIM particularly advantageous for lung endomicroscopy. Using both in combination allows for the imaging fibre to be successfully navigated to the alveolar space using fluorescence intensity imaging and FLIM used for the detection of labelled cells. This also allows for the use of commonly employed green channel fluorophores which may not be easily detected against background lung autofluorescence using fluorescence intensity imaging alone.

The direct instillation of fluorescently-tagged monoclonal antibodies into the lungs of living humans may raise ethical concerns. It will therefore be necessary to consider the functional properties of the antibodies and whether target engagement would directly affect ongoing local or systemic immune responses. Labelled

10.3389/fimmu.2023.1100161

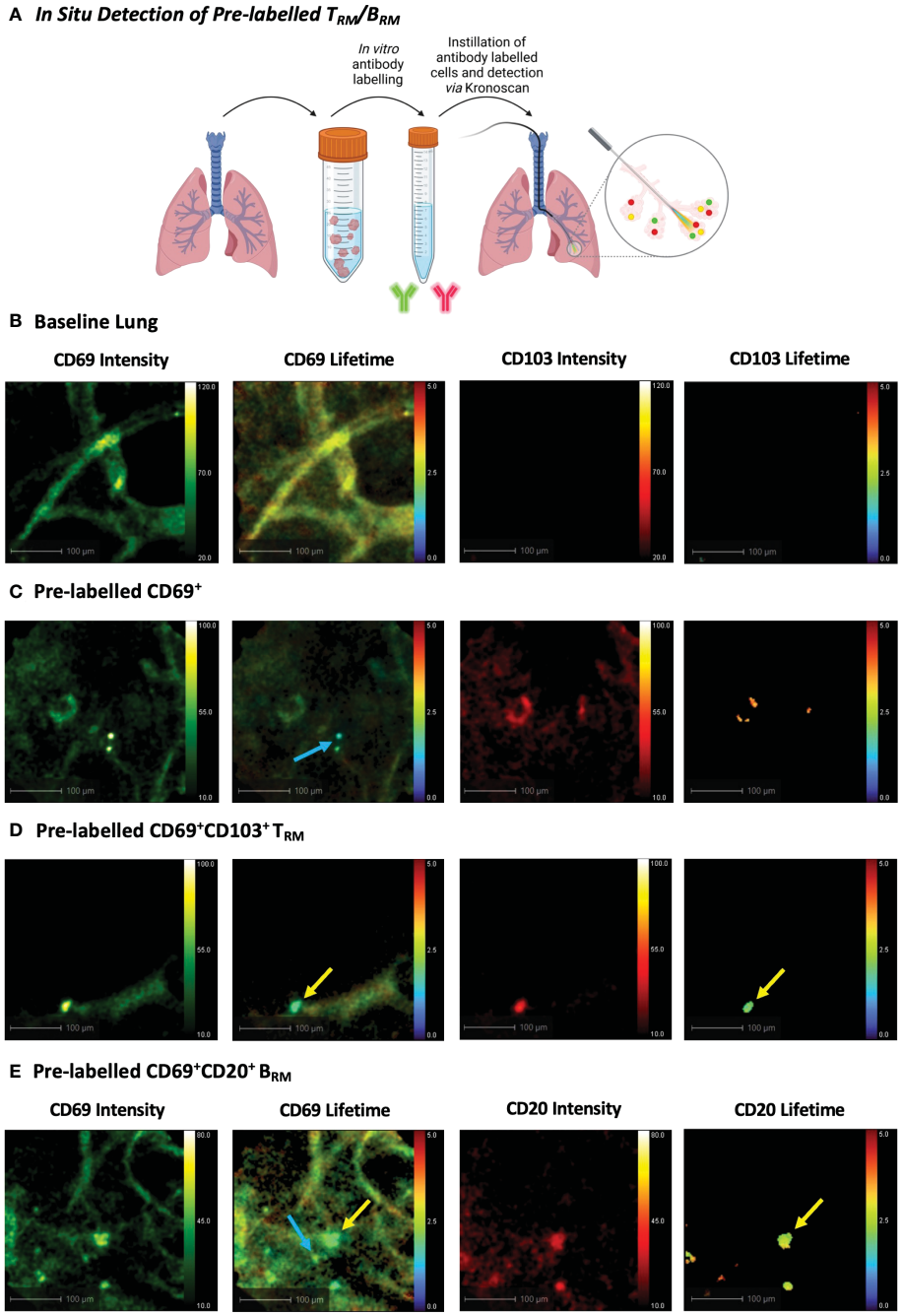

FIGURE 5
In Situ Detection of Pre-labelled T_{RM}/B_{RM} in Human Lung. **(A)** Pre-labelled human pulmonary T_{RM} and B_{RM} in suspension were instilled into the alveolar space and detected using KronoScan and Panoptes during human EVLV. **(B)** Baseline lung imaging prior to pre-labelled cell instillation. **(C)** *In situ* imaging of pre-labelled $CD69^+$ cells. Lung tissue digest cells were stained with fluorescent CD69 and CD103 antibodies prior to instillation into the alveolar space using Panoptes. Cells were imaged with KronoScan. Blue arrow indicates $CD69^+$ cells. **(D)** *In situ* imaging of pre-labelled $CD69^+CD103^+$ T_{RM}. Yellow arrow indicates $CD69^+CD103^+$ T_{RM}. **(E)** *In situ* imaging of pre-labelled B_{RM}. Lung tissue digest cells were stained with fluorescent CD20 and CD69 antibodies prior to instillation to the alveolar space. Blue arrow indicates $CD69^+$ cells and yellow arrow points $CD69^+CD20^+$ B_{RM}. Representative images from n=3 experiments.

humanised antibodies would be advantageous, whilst fluorescently labelled Fab or Fv antibody fragments lacking the Fc portion would prevent issues associated with antibody-dependent cellular cytotoxicity. In addition, as FLIM is largely independent of concentration, only very small amounts of antibody would be required. In this work the amount of antibody used (0.5 – 2 μg per experiment) is likely to fall within the microdose range and lack systemic effects when compared to the repeated mg/kg doses often used in immuno-oncology and is therefore likely to be well tolerated.

The lifetime signature of the fluorophores used in this study were lower than that of the lung tissue. Fluorescence lifetime is environmentally sensitive (43), meaning the temperature, oxygen saturation/hypoxia and pH within the lung will affect lifetime values and thus absolute lifetime values may differ from tissue to tissue. Thus,

10.3389/fimmu.2023.1100161

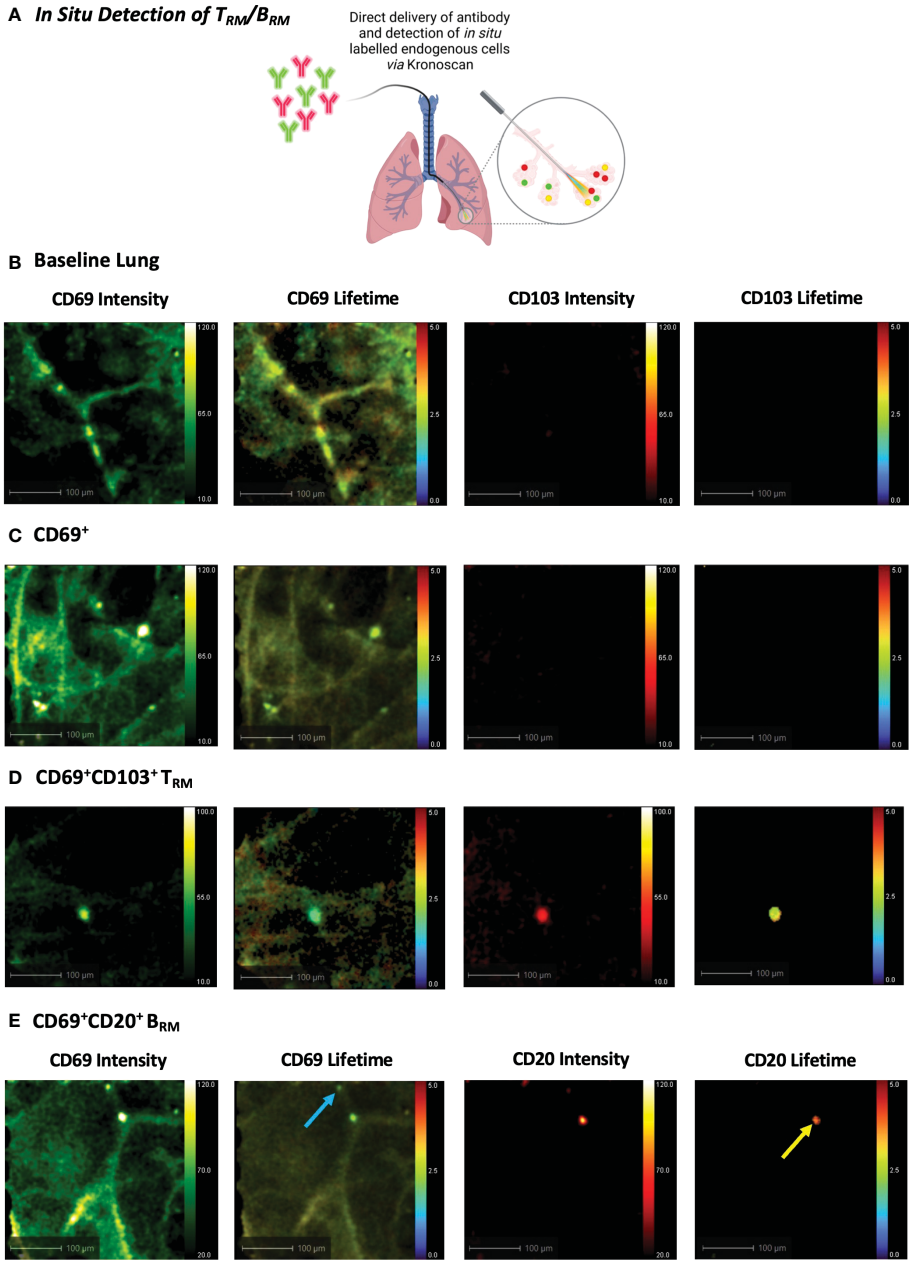

FIGURE 6
In Situ Detection of T_{RM}/B_{RM} in Human Lung following Antibody Delivery. **(A)** T_{RM} or B_{RM} antibodies were instilled into the alveolar space *via* Panoptes fibre and imaged with KronoScan. **(B)** Baseline lung imaging prior to antibody delivery. **(C)** *In situ* detection of $CD69^+$ cells. CD69 and CD103 antibodies were instilled into the alveolar space to detect T_{RM}. **(D)** *In situ* detection of $CD69^+CD103^+$ T_{RM}. **(E)** *In situ* detection of B_{RM}. CD20 and CD69 antibodies were instilled into the alveolar space to detect B_{RM}. Blue arrow indicates $CD69^+$ cells and yellow arrow points $CD69^+CD20^+$ B_{RM}. Representative images from n=3 experiments.

FLIM was used as a contrast tool for visualising fluorophores and labelled cells against the background lung rather than as an absolute measure of specific FLT values. The combination of high fluorescence intensity with a FLT value lower than that of background lung distinctly shows the presence of labelled T_{RM}/B_{RM}. The lifetime values of antibody-labelled cells are consistently lower than that of background lung tissue and are consistent between experiments (i.e., prelabelled or *in situ* labelling of both T_{RM} and B_{RM}).

FITC conjugated antibodies have the most spectral similarity to endogenous elastin and tissue autofluorescence, yet the FITC-CD69 was readily distinguishable with high specificity with KronoScan. The high concentration of local cell-specific labelling has been shown to diminish FLT as a function of antibody labelling concentration on the cell surface and is consistent with self-quenching effects expected at high densities of FITC molecules (44).

Due to limited fluorophore combinations on CD103 (clone 2G5) (and the spectral detection capabilities of KronoScan), we used the Ber-ACT8 CD103 clone. Although the Ber-ACT8 CD103 clone did not work in our cynomolgus model, it has been successfully used in Rhesus macaque models (34) and so has good translational potential. In the future, altering the band pass filters on KronoScan will enable the use of other fluorophore/cross reactive antibody combinations. Increasing the

number of filter sets will also increase the number of fluorophore combinations that can be used simultaneously, allowing for more information to be collected (e.g., identifying and differentiating $CD4^+$ or $CD8^+$ T_{RM}, or differentiating T_{RM} and B_{RM} subpopulations) and unmixed using both intensity and lifetime measurements.

In the wake of the COVID-19 pandemic, the realization that disease-relevant local immune responses in the lung are not reflected in the blood prompted a rallying call to immunologists to recognize that tissues, rather than blood, are where immune cells function (45). Understanding and investigating immune processes *in situ* is therefore essential. Successful *in situ* labelling of immune cells after direct delivery of small amounts (microdoses) of antibody by fluorescence intensity/lifetime imaging extends the methods available for molecular imaging and visualising cells in the distal lung following vaccination and infection. The large number of directly conjugated antibodies available for flow cytometry should make this technique readily adaptable to study the major immune cell types present in alveolar tissues. Direct antibody labelling could also be coupled with the use of activation based smart-probes or *in situ* imaging of pathogens in experimental settings to visualise infection-driven inflammatory interactions. A recent call for the development of intranasal vaccines capable of eliciting greater mucosal immunity may help to overcome the shortcomings of current COVID vaccines and prevent viral transmission (46). This highlights the potential benefits of increasing tissue-based immunity. Assessing local immunity with our *in situ* detection method could enhance the evaluation of such vaccines.

Fluorescent intensity-based OEM has shown proof of concept for real-time alveolar imaging, when combined with imaging agents for neutrophil activation (23), gram-negative (25) and gram-positive (47) bacteria. This is however the first report of alveolar fibre based FLIM imaging in the human lung, demonstrating that combining intensity and FLIM delivers contrast enhancement and multiplexing capability above and beyond existing OEM platforms. The multifunctional Panoptes fibre platform, which is designed as a single use disposable device, enables *in situ* delivery of microdoses of imaging agents and therapies.

We established a cross reactive antibody staining panel for assessing pulmonary T_{RM} and B_{RM} in human and cynomolgus macaque. Many of the antibodies used are cross reactive to other NHP species, including rhesus macaque, and so offer great translational research potential. This work reveals similarities and differences between human and NHP pulmonary resident memory lymphocyte subpopulations and demonstrates the potential of *in situ* pulmonary optical imaging for rapidly detecting immunologically diverse cells.

Data availability statement

The original contributions presented in the study are included in the article/Supplementary Material. Further inquiries can be directed to the corresponding authors.

Ethics statement

The studies involving human participants were reviewed and approved by London - Central Research Ethics Committee 16-LO-1883. Written informed consent was not provided because this study involves the use of human lungs that are unfit for transplant. Specialist Nurses for Organ Donation (SNODs) approach relatives of potential donors and obtain authorisation for the use of the donor's organs and tissues for transplantation using the standard NHS Authorisation form. Using the same authorisation form, the SNODs also obtain authorisation for the use of the donor's organs and tissues removed but subsequently found to be unsuitable for transplantation for other purposes (i.e. research studies, education, training). The use of lungs in this study has been approved by an independent ethics committee and NHSBT, the body responsible for organ donation and transplantation across the UK.

Author contributions

RO'C, KF, MC-R, FB, KD, and VP conceptualised the project. DH, RO'C, and KD provided methods. DH, RO'C, HS, TQ, EG, and BM performed the experiments. GW and JS provided materials and technical expertise. DH and HS performed the data analysis. DH wrote the manuscript. DH, RO'C, MC-R, FB, KD, and VP edited the manuscript. All authors contributed to the article and approved the submitted version.

Acknowledgments

We thank the Queen's Medical Research Institute (QMRI) Flow Cytometry and Histology Facilities at the University of Edinburgh for assistance. We thank Charles River (Edinburgh, UK) for gifting lung tissue from cynomolgus macaque. All figures created with BioRender.com. This work was financially supported by Sanofi, EPSRC Healthcare Impact Partnership award (EP/S025987/1), CARB-X.

Conflict of interest

Authors DH, MC-R, FB and VP were employed by company Sanofi.

The remaining authors declare that the research was conducted in the absence of any commercial or financial relationships that could be construed as a potential conflict of interest.

The authors declare that this study received funding from Sanofi. The funder had the following involvement in the study: study design, data analysis, decision to publish, and preparation of the manuscript.

Publisher's note

All claims expressed in this article are solely those of the authors and do not necessarily represent those of their affiliated organizations, or those of the publisher, the editors and the reviewers. Any product that may be evaluated in this article, or claim that may be made by its manufacturer, is not guaranteed or endorsed by the publisher.

Supplementary material

The Supplementary Material for this article can be found online at: https://www.frontiersin.org/articles/10.3389/fimmu.2023.1100161/full#supplementary-material

SUPPLEMENTARY VIDEO 1
In Vitro Fluorescence Imaging of Pulmonary T_{RM}. Cells from human lung tissue digests were stained with T_{RM} antibodies and imaged using KronoScan imaging system and Panoptes multifunctional fibre.

SUPPLEMENTARY VIDEO 2
In Vitro Fluorescence Imaging of Pulmonary B_{RM}. Cells from human lung tissue digests were stained with B_{RM} antibodies and imaged using KronoScan imaging system and Panoptes multifunctional fibre.

SUPPLEMENTARY VIDEO 3
Human PBMC CD69 CD103 In Vitro Fluorescence Imaging. Human PBMCs were stained with T_{RM} antibodies and imaged using KronoScan imaging system and Panoptes multifunctional fibre.

SUPPLEMENTARY VIDEO 4
Human PBMC CD69 CD20 In Vitro Fluorescence Imaging. Human PBMCs were stained with B_{RM} antibodies and imaged using KronoScan imaging system and Panoptes multifunctional fibre.

SUPPLEMENTARY VIDEO 5
Baseline Lung Fluorescence Imaging Prior to Pre-labelled Cell Instillation. KronoScan and Panoptes imaging fibre was navigated to the alveolar space prior to pre-labelled cell instillation.

SUPPLEMENTARY VIDEO 6
In Situ Fluorescence Imaging of Pre-labelled Human Pulmonary $CD69^+$ cells. Lung tissue digest cells were stained with fluorescent CD69 and CD103 antibodies prior to instillation into the alveolar space using Panoptes. Cells were imaged with KronoScan.

SUPPLEMENTARY VIDEO 7
In Situ Fluorescence Imaging of Pre-labelled Human Pulmonary $CD69^+CD103^+$ T_{RM}. Lung tissue digest cells were stained with fluorescent CD69 and CD103 antibodies prior to instillation into the alveolar space using Panoptes. Cells were imaged with KronoScan.

SUPPLEMENTARY VIDEO 8
In Situ Fluorescence Imaging of Pre-labelled Human Pulmonary $CD69^+CD20^+$ B_{RM}. Lung tissue digest cells were stained with fluorescent CD69 and CD20 antibodies prior to instillation into the alveolar space using Panoptes. Cells were imaged with KronoScan.

SUPPLEMENTARY VIDEO 9
Baseline Lung Fluorescence Imaging Prior to Antibody Delivery. KronoScan and Panoptes imaging fibre was navigated to the alveolar space prior to fluorescent antibody delivery.

SUPPLEMENTARY VIDEO 10
In Situ Imaging of Human $CD69^+$ Cells Following Antibody elivery. CD69 and CD103 antibodies were delivered to the alveolar space and subsequently imaged.

SUPPLEMENTARY VIDEO 11
In Situ Imaging of Human $CD69^+CD103^+$ T_{RM} Following Antibody Delivery. CD69 and CD103 antibodies were delivered to the alveolar space and subsequently imaged.

SUPPLEMENTARY VIDEO 12
In Situ Fluorescence Imaging of Human Pulmonary B_{RM} Following Antibody Delivery. CD69 and CD20 antibodies were delivered to the alveolar space and subsequently imaged.

References

1. Jozwik A, Habibi MS, Paras A, Zhu J, Guvenel A, Dhariwal J, et al. RSV-Specific airway resident memory CD8+ T cells and differential disease severity after experimental human infection. *Nat Commun* (2015) 6:1–15. doi: 10.1038/ncomms10224

2. Darrah PA, Zeppa JJ, Maiello P, Hackney JA, Wadsworth MH, Hughes TK, et al. Prevention of tuberculosis in macaques after intravenous BCG immunization. *Nature* (2020) 577:95–102. doi: 10.1038/s41586-019-1817-8

3. Ogongo P, Tezera LB, Ardain A, Nhamoyebonde S, Ramsuran D, Singh A, et al. Tissue-resident-like CD4+ T cells secreting IL-17 control mycobacterium tuberculosis in the human lung. *J Clin Invest* (2021) 131:e142014. doi: 10.1172/JCI142014

4. Snyder ME, Farber DL. Human lung tissue resident memory T cells in health and disease. *Curr Opin Immunol* (2019) 59:101–8. doi: 10.1016/j.coi.2019.05.011

5. Humphries DC, O'Connor RA, Larocque D, Chabaud-Riou M, Dhaliwal K, Pavot V. Pulmonary-resident memory lymphocytes: Pivotal orchestrators of local immunity against respiratory infections. *Front Immunol* (2021) 12:738955. doi: 10.3389/fimmu.2021.738955

6. de Bree GJ, van Leeuwen EMM, Out TA, Jansen HM, Jonkers RE, van Lier RAW. Selective accumulation of differentiated CD8+ T cells specific for respiratory viruses in the human lung. *J Exp Med* (2005) 202:1433–42. doi: 10.1084/jem.20051365

7. Pizzolla A, Nguyen THO, Sant S, Jaffar J, Loudovaris T, Mannering SI, et al. Influenza-specific lung-resident memory T cells are proliferative and polyfunctional and maintain diverse TCR profiles. *J Clin Invest* (2018) 128:721–33. doi: 10.1172/JCI96957

8. Pichyangkul S, Yongvanitchit K, Limsalakpetch A, Kum-Arb U, Im-Erbsin R, Boonnak K, et al. Tissue distribution of memory T and b cells in rhesus monkeys following influenza a infection. *J Immunol* (2015) 195:4378–86. doi: 10.4049/jimmunol.1501702

9. Yang Q, Zhang M, Chen Q, Chen W, Wei C, Qiao K, et al. Cutting edge: Characterization of human tissue-resident memory T cells at different infection sites in patients with tuberculosis. *J Immunol* (2020) 204:2331–6. doi: 10.4049/jimmunol.1901326

10. Pizzolla A, Wakim LM. Memory T cell dynamics in the lung during influenza virus infection. *J Immunol* (2019) 202:374–81. doi: 10.4049/jimmunol.1800979

11. Koutsakos M, Illing PT, Nguyen THO, Mifsud NA, Crawford JC, Rizzetto S, et al. Human CD8 + T cell cross-reactivity across influenza a, b and c viruses. *Nat Immunol* (2019) 20:613–25. doi: 10.1038/s41590-019-0320-6

12. Ge C, Monk IR, Pizzolla A, Wang N, Bedford JG, Stinear TP, et al. Bystander activation of pulmonary trm cells attenuates the severity of bacterial pneumonia by enhancing neutrophil recruitment. *Cell Rep* (2019) 29:4236–44. doi: 10.1016/j.celrep.2019.11.103

13. Turner DL, Goldklang M, Cvetkovski F, Paik D, Trischler J, Barahona J, et al. Biased generation and *In situ* activation of lung tissue-resident memory CD4 T cells in the pathogenesis of allergic asthma. *J Immunol* (2018) 200:1561–9. doi: 10.4049/jimmunol.1700257

14. Bošnjak B, Kazemi S, Altenburger LM, Mokrović G, Epstein MM. Th2-TRMs maintain life-long allergic memory in experimental asthma in mice. *Front Immunol* (2019) 10:840. doi: 10.3389/fimmu.2019.00840

15. Barker KA, Etesami NS, Shenoy AT, Arafa EI, Lyon de Ana C, Smith NM, et al. Lung-resident memory b cells protect against bacterial pneumonia. *J Clin Invest* (2021) 131:e141810. doi: 10.1172/JCI141810

16. Allie SR, Bradley JE, Mudunuru U, Schultz MD, Graf BA, Lund FE, et al. The establishment of resident memory b cells in the lung requires local antigen encounter. *Nat Immunol* (2019) 20:97–108. doi: 10.1038/s41590-018-0260-6

17. Onodera T, Takahashi Y, Yokoi Y, Ato M, Kodama Y, Hachimura S, et al. Memory b cells in the lung participate in protective humoral immune responses to pulmonary influenza virus reinfection. *Proc Natl Acad Sci U.S.A.* (2012) 109:2485–90. doi: 10.1073/pnas.1115369109

18. Rangel-Moreno J, Carragher DM, Misra RS, Kusser K, Hartson L, Moquin A, et al. B cells promote resistance to heterosubtypic strains of influenza *via* multiple mechanisms. *J Immunol* (2008) 180:454–63. doi: 10.4049/jimmunol.180.1.454

19. Knight FC, Wilson JT. Engineering vaccines for tissue-resident memory T cells. *Adv Ther (Weinh)* (2021) 4. doi: 10.1002/adtp.202000230

20. Dijkman K, Aguilo N, Boot C, Hofman SO, Sombroek CC, Vervenne RAW, et al. Pulmonary MTBVAC vaccination induces immune signatures previously correlated with prevention of tuberculosis infection. *Cell Rep Med* (2021) 2. doi: 10.1016/j.xcrm.2020.100187

21. McMaster SR, Wein AN, Dunbar PR, Hayward SL, Cartwright EK, Denning TL, et al. Pulmonary antigen encounter regulates the establishment of tissue-resident CD8 memory T cells in the lung airways and parenchyma. *Mucosal Immunol* (2018) 11:1071–8. doi: 10.1038/s41385-018-0003-x

22. Snyder ME, Finlayson MO, Connors TJ, Dogra P, Senda T, Bush E, et al. Generation and persistence of human tissue-resident memory T cells in lung transplantation. *Sci Immunol* (2019) 4:eaav5581. doi: 10.1126/sciimmunol.aav5581

23. Craven TH, Walton T, Akram AR, Scholefield E, McDonald N, Marshall ADL, et al. Activated neutrophil fluorescent imaging technique for human lungs. *Sci Rep* (2021) 11:976. doi: 10.1038/s41598-020-80083-w

24. Suhling K, Hirvonen LM, Levitt JA, Chung P-H, Tregidgo C, le Marois A, et al. Fluorescence lifetime imaging (FLIM): Basic concepts and some recent developments. *Med Photonics* (2015) 27:3–40. doi: 10.1016/j.medpho.2014.12.001

25. Parker HE, Stone JM, Marshall ADL, Choudhary TR, Thomson RR, Dhaliwal K, et al. Fibre-based spectral ratio endomicroscopy for contrast enhancement of bacterial imaging and pulmonary autofluorescence. *BioMed Opt Express* (2019) 10:1856–69. doi: 10.1364/BOE.10.001856

26. Dorward DA, Lucas CD, Doherty MK, Chapman GB, Scholefield EJ, Conway Morris A, et al. Novel role for endogenous mitochondrial formylated peptide-driven formyl peptide receptor 1 signalling in acute respiratory distress syndrome. *Thorax* (2017) 72:928–36. doi: 10.1136/thoraxjnl-2017-210030

27. Millar M. Mixed multiplex staining: Automated RNAscopeTM and OPALTM for multiple targets. In: Nielsen BS, Jones J, editors. *Situ hybridization protocols*. New York, NY: Springer US (2020). p. P. 277–298. doi: 10.1007/978-1-0716-0623-0

28. Li D, Arlt J, Tyndall D, Walker R, Richardson J, Henderson R, et al. Video-rate fluorescence lifetime imaging camera with CMOS single-photon avalanche diode arrays and high-speed imaging algorithm. *J BioMed Opt* (2011) 16:096012. doi: 10.1117/1.3625288

29. Stone JM, Wood HAC, Harrington K, Birks TA. Low index contrast imaging fibers. *Opt Lett* (2017) 42:1484–7. doi: 10.1364/OL.42.001484

30. Takamura S. Persistence in temporary lung niches: A survival strategy of lung-resident memory CD8+ T cells. *Viral Immunol* (2017) 30:438–50. doi: 10.1089/vim.2017.0016

31. Mackay LK, Braun A, Macleod BL, Collins N, Tebartz C, Bedoui S, et al. Cutting edge: CD69 interference with sphingosine-1-Phosphate receptor function regulates peripheral T cell retention. *J Immunol* (2015) 194:2059–63. doi: 10.4049/jimmunol.1402256

32. Reilly EC, Emo KL, Buckley PM, Reilly NS, Smith I, Chaves FA, et al. TRM integrins CD103 and CD49a differentially support adherence and motility after resolution of influenza virus infection. *Proc Natl Acad Sci U.S.A.* (2020) 117:12306–14. doi: 10.1073/pnas.1915681117

33. Kumar BV, Ma W, Miron M, Granot T, Guyer RS, Carpenter DJ, et al. Human tissue-resident memory T cells are defined by core transcriptional and functional signatures in lymphoid and mucosal sites. *Cell Rep* (2017) 20:2921–34. doi: 10.1016/j.celrep.2017.08.078

34. Layton ED, Barman S, Wilburn DB, Yu KKQ, Smith MT, Altman JD, et al. T Cells specific for a mycobacterial glycolipid expand after intravenous bacillus calmette-guérin vaccination. *J Immunol* (2021) 206:1240–50. doi: 10.4049/jimmunol.2001065

35. Miron M, v. KB, Meng W, Granot T, Carpenter DJ, Senda T, et al. Human lymph nodes maintain TCF-1 hi memory T cells with high functional potential and clonal diversity throughout life. *J Immunol* (2018), 01(7):2132–40. doi: 10.4049/jimmunol.1800716

36. Beura LK, Hamilton SE, Bi K, Schenkel JM, Odumade OA, Casey KA, et al. Normalizing the environment recapitulates adult human immune traits in laboratory mice. *Nature* (2016) 532. doi: 10.1038/nature17655

37. Stolley JM, Johnston TS, Soerens AG, Beura LK, Rosato PC, Joag V, et al. Retrograde migration supplies resident memory t cells to lung-draining LN after influenza infection. *J Exp Med* (2020) 217:e20192197. doi: 10.1084/jem.20192197

38. Tan H-X, Juno JA, Esterbauer R, Kelly HG, Wragg KM, Konstandopoulos P, et al. Lung-resident memory b cells established after pulmonary influenza infection display distinct transcriptional and phenotypic profiles. *Sci Immunol* (2022) 7:eabf5314. doi: 10.1126/sciimmunol.abf5314

39. Zuccarino-Catania GV, Sadanand S, Weisel FJ, Tomayko MM, Meng H, Kleinstein SH, et al. CD80 and PD-L2 define functionally distinct memory b cell subsets that are independent of antibody isotype. *Nat Immunol* (2014) 15:631-7. doi: 10.1038/ni.2914

40. Weisel NM, Weisel FJ, Farber DL, Borghesi LA, Shen Y, Ma W, et al. Comprehensive analyses of b-cell compartments across the human body reveal novel subsets and a gut-resident memory phenotype. *Blood* (2020), 136(24):2774–85. doi: 10.1182/blood.2019002782

41. Purwar R, Campbell J, Murphy G, Richards WG, Clark RA, Kupper TS. Resident memory T cells (T(RM)) are abundant in human lung: Diversity, function, and antigen specificity. *PloS One* (2011) 6:e16245–5. doi: 10.1371/journal.pone.0016245

42. Takamura S, Kato S, Motozono C, Shimaoka T, Ueha S, Matsuo K, et al. Interstitial-resident memory CD8+ T cells sustain frontline epithelial memory in the lung. *J Exp Med* (2019) 216:2736–47. doi: 10.1084/jem.20190557

43. Berezin MY, Achilefu S. Fluorescence lifetime measurements and biological imaging. *Chem Rev* (2010) 110:2641-84. doi: 10.1021/cr900343z

44. Deka C, Lehnert BE, Lehnert NM, Jones GM, Sklar LA, Steinkamp JA. Analysis of fluorescence lifetime and quenching of FITC-conjugated antibodies on cells by phase-sensitive flow cytometry. *Cytometry* (1996) 25:271–9. doi: 10.1002/(SICI)1097-0320(19961101)25:3<271::AID-CYTO8>3.0.CO;2-I

45. Farber DL. Tissues, not blood, are where immune cells function. *Nature* (2021) 593:506–9. doi: 10.1038/d41586-021-01396-y

46. Topol EJ, Iwasaki A. Operation nasal vaccine-lightning speed to counter COVID-19. *Sci Immunol* (2022) 7:eadd9947. doi: 10.1126/sciimmunol.add9947

47. Mills B, Megia-Fernandez A, Norberg D, Duncan S, Marshall A, Akram AR, et al. Molecular detection of gram-positive bacteria in the human lung through an optical fiber-based endoscope. *Eur J Nucl Med Mol Imaging* (2021) 48:800–7. doi: 10.1007/s00259-020-05021-4

frontiers | Frontiers in Immunology

TYPE Methods
PUBLISHED 16 February 2023
DOI 10.3389/fimmu.2023.1049673

Check for updates

OPEN ACCESS

EDITED BY
P. Bernard Fourie,
University of Pretoria, South Africa

REVIEWED BY
Rajesh Pandey,
CSIR-Institute of Genomics and Integrative Biology (CSIR-IGIB), India
Isabelle Viana,
Fiocruz Pernambuco, Brazil

*CORRESPONDENCE
S. Moses Dennison
moses.sekaran@duke.edu
Georgia D. Tomaras
gdt@duke.edu

†PRESENT ADDRESS
Ulrike Wille-Reece,
BioNTech US, Cambridge, MA, United States
Lindsay C. Dahora,
Department of Microbiology and Immunology, University of North Carolina, Chapel Hill, NC, United States
Richard H. C. Huntwork,
Department of Chemistry, University of Wisconsin, Madison, WI, United States

‡These authors share senior authorship

SPECIALTY SECTION
This article was submitted to Vaccines and Molecular Therapeutics, a section of the journal Frontiers in Immunology

RECEIVED 20 September 2022
ACCEPTED 18 January 2023
PUBLISHED 16 February 2023

CITATION
Li K, Dodds M, Spreng RL, Abraha M, Huntwork RHC, Dahora LC, Nyanhete T, Dutta S, Wille-Reece U, Jongert E, Ewer KJ, Hill AVS, Jin C, Hill J, Pollard AJ, Munir Alam S, Tomaras GD and Dennison SM (2023) A tool for evaluating heterogeneity in avidity of polyclonal antibodies.
Front. Immunol. 14:1049673.
doi: 10.3389/fimmu.2023.1049673

COPYRIGHT
© 2023 Li, Dodds, Spreng, Abraha, Huntwork, Dahora, Nyanhete, Dutta, Wille-Reece, Jongert, Ewer, Hill, Jin, Hill, Pollard, Munir Alam, Tomaras and Dennison. This is an open-access article distributed under the terms of the Creative Commons Attribution License (CC BY). The use, distribution or reproduction in other forums is permitted, provided the original author(s) and the copyright owner(s) are credited and that the original publication in this journal is cited, in accordance with accepted academic practice. No use, distribution or reproduction is permitted which does not comply with these terms.

A tool for evaluating heterogeneity in avidity of polyclonal antibodies

Kan Li[1,2], Michael Dodds[3], Rachel L. Spreng[4], Milite Abraha[1,2], Richard H. C. Huntwork[1,2†], Lindsay C. Dahora[1,5†], Tinashe Nyanhete[1,5], Sheetij Dutta[6], Ulrike Wille-Reece[7†], Erik Jongert[8], Katie J. Ewer[9], Adrian V. S. Hill[9,10], Celina Jin[11], Jennifer Hill[11], Andrew J. Pollard[10,11], S. Munir Alam[4,12], Georgia D. Tomaras[1,2,4,5,13*‡] and S. Moses Dennison[1,2*‡]

[1]Center for Human Systems Immunology, Duke University, Durham, NC, United States, [2]Department of Surgery, Duke University, Durham, NC, United States, [3]Integrated Drug Development, Certara, Seattle, WA, United States, [4]Duke Human Vaccine Institute, Duke University, Durham, NC, United States, [5]Department of Immunology, Duke University, Durham, NC, United States, [6]Structural Vaccinology Lab, Malaria Biologics Branch, Walter Reed Army Institute of Research, Silver Spring, MD, United States, [7]PATH's Center for Vaccine Innovation and Access, Washington, DC, United States, [8]GSK Vaccines, Rixensart, Belgium, [9]The Jenner Institute, University of Oxford, Oxford, United Kingdom, [10]National Institute for Health and Care Research (NIHR) Oxford Biomedical Research Center, Oxford, United Kingdom, [11]Oxford Vaccine Group and Department of Pediatrics, University of Oxford, Oxford, United Kingdom, [12]Department of Pathology, Duke University, Durham, NC, United States, [13]Department of Molecular Genetics and Microbiology, Duke University, Durham, NC, United States

Diversity in specificity of polyclonal antibody (pAb) responses is extensively investigated in vaccine efficacy or immunological evaluations, but the heterogeneity in antibody avidity is rarely probed as convenient tools are lacking. Here we have developed a polyclonal antibodies avidity resolution tool (PAART) for use with label-free techniques, such as surface plasmon resonance and biolayer interferometry, that can monitor pAb-antigen interactions in real time to measure dissociation rate constant (k_d) for defining avidity. PAART utilizes a sum of exponentials model to fit the dissociation time-courses of pAb-antigens interactions and resolve multiple k_d contributing to the overall dissociation. Each k_d value of pAb dissociation resolved by PAART corresponds to a group of antibodies with similar avidity. PAART is designed to identify the minimum number of exponentials required to explain the dissociation course and guards against overfitting of data by parsimony selection of best model using Akaike information criterion. Validation of PAART was performed using binary mixtures of monoclonal antibodies of same specificity but differing in k_d of the interaction with their epitope. We applied PAART to examine the heterogeneity in avidities of pAb from malaria and typhoid vaccinees, and individuals living with HIV-1 that naturally control the viral load. In many cases, two to three k_d were dissected indicating the heterogeneity of pAb avidities. We showcase examples of affinity maturation of vaccine induced pAb responses at component level and enhanced resolution of heterogeneity in avidity when antigen-binding fragments (Fab) are used instead of polyclonal IgG antibodies. The utility of PAART can be manifold in examining circulating pAb characteristics and could inform vaccine strategies aimed to guide the host humoral immune response.

KEYWORDS

dissociation rate, avidity, binning, polyclonal antibodies, Typhim, RTS,S/AS01, biolayer interferometry (BLI), Typbar TCV

Introduction

Avidity of polyclonal antibodies (pAbs) in serum, plasma and mucosal fluids refers to the overall strength of pAbs-antigen binding and depends on the affinities of pAbs for the antigen and the valency of pAbs and the antigen. Avidity of pAbs for a given antigen can be related to their functional efficiency (1–4). Avidity measurement is important to monitor affinity maturation of the humoral response to vaccines and can aid in developing immunization strategies, such as using different engineered immunogens, adjuvants and routes, to guide pAb affinity maturation against desired protective epitopes (5). PAb avidity data is also used to measure the incidence of recent infections as low avidity antibodies are mounted after the onset of infection (6, 7). Moreover, avidity measurements are immensely helpful in immune correlate analysis of vaccines as higher avidity antibodies may associate with protection (3, 8, 9).

While avidity is classically measured by monitoring binding under chaotropic conditions using ELISA and other methods (10), kinetics based methods for measuring avidity of pAbs using surface plasmon resonance (SPR) and biolayer interferometry (BLI) techniques have been widely employed (8, 11–22). Both SPR and BLI are label-free techniques for studying kinetics of biomolecular interactions where one of the binding partners is immobilized (ligand) on an appropriate sensor chip or surface and the other binding partner, termed as analyte, is kept in solution to monitor interaction. Specific binding time-courses are obtained by appropriate reference subtraction to remove binding responses due to non-specific interactions. The association and dissociation rate constants (k_a and k_d respectively) and the apparent dissociation constant (K_D) of the interaction are then obtained by fitting the specific binding time-courses globally to a 1:1 binding model. The K_D values for monoclonal antibodies (mAbs) interacting with immobilized ligands determined using a 1:1 binding model will include the avidity effect due to the bivalency of antibodies resulting in slower k_d unless the ligands are immobilized at surface densities low enough to remove avidity effect. When pAbs are studied, the concentrations of the interacting antibodies at clonal level remain unknown and so the k_a and hence the K_D cannot be determined. However, the k_d, which is concentration independent, can be readily measured. Since the k_d is inversely related to the stability of antigen-antibody complex, the avidity of the pAbs for a given antigen can be inferred by simply measuring the k_d of the interaction. A slower (smaller) k_d value measured would indicate higher avidity of pAbs and a faster (larger) k_d value estimated would indicate lower avidity of the pAbs. The label-free real-time detection of interactions by SPR and BLI techniques enables monitoring the dissociation of antigen-antibody complexes without the use of any chaotrope. This is particularly helpful when studying chaotrope sensitive paratope or epitope (23).

PAbs-antigen binding, unlike that of mAbs, is multifaceted because pAbs are heterogeneous and recognize a range of epitopes (24). It includes antibodies competing for certain epitope(s), parallel binding to different epitopes and the binding or displacement of antibodies of certain specificity allosterically regulated by the binding of antibodies of a different specificity. All the above manifest often in complex time-course profiles. Currently, the standard practice in SPR and BLI analysis of pAbs binding to a given antigen is to measure the antigen specific binding response as a direct readout and estimate the k_d of the interaction using a Langmuir dissociation model assuming a 1:1 interaction (8, 11–22),

$$R(t) = \alpha e^{-k_d t} \quad (1)$$

where $R(t)$ is the dissociation time-course, α is the response at the beginning of dissociation and k_d is the dissociation rate constant (dissociation rate from here on). Fitting of non-monophasic pAbs dissociation curves to a Langmuir dissociation model (equation 1) yields a k_d that is more weighted towards antibodies with slower dissociation rates among the multiple antibodies that simultaneously interact with the antigen potentially targeting different epitopes within the antigen. The inadequacy of the Langmuir model to describe the data will be conspicuous in the residuals plot when the goodness of fit of pAbs dissociation time-courses is judged. Yet the pAbs dissociation time-courses are continued to be analyzed using Langmuir dissociation model (8, 11–22) or dissected into fast and slow phases manually (25) as convenient tools are lacking. Thus, models that account for the contribution of various antibodies differing in k_d to the observed dissociation time-courses of pAbs-antigen interaction would be appropriate for better understanding of the heterogeneity in avidity of pAbs. For this purpose, we developed the **p**olyclonal **a**ntibodies **a**vidity **r**esolution **t**ool (PAART), that uses a sum of exponentials model (described in methods), for fitting the polyclonal antibody dissociation kinetics to determine the minimal number of antibody components with different k_d and the respective fractions required to adequately describe the data. Our aim is to use PAART for dissociation rate (and hence the avidity) binning of the time-courses of pAbs interacting with (a) single-epitope antigens to find different bins of antibodies with varying avidity that compete for the same epitope and (b) multi-epitope antigens for understanding the overall heterogeneity in avidity as epitope specificity of PAART derived antibody components (k_d values) cannot be assigned.

In this report, we first describe the validity of PAART using a simple mimic of pAbs created in a controlled fashion such as binary and ternary mixtures of mAbs targeting the same epitope with comparable k_a but differing in their k_d. The estimates of k_d and their fractions obtained from the dissociation phase data alone of binary mixtures by PAART were comparable to the estimates predicted by a competing reactions model using both the association and dissociation phases. We then demonstrate the utility of PAART in (1) dissecting avidity heterogeneity of phase 2 clinical studies' post-vaccination serum IgG antibodies of (a) malaria vaccinees against a single-epitope peptide antigen and (b) typhoid vaccinees against a multi-epitope polysaccharide antigen, (2) component level affinity maturation of a malaria vaccine induced serum antibody responses against different antigens, (3) comparing the avidity heterogeneity between two typhoid vaccine regimens and between protected and not-protected malaria vaccinees, and (4) enhancing refinement of avidity heterogeneity by using polyclonal antigen-binding fragments (Fab) instead of polyclonal IgG antibodies of Human Immunodeficiency Virus type-1 (HIV-1) controllers sera. Insights on avidity diverseness of vaccine induced pAbs that can be obtained from PAART analysis as illustrated here will be valuable for the characterization of the optimal antibody response of an efficacious vaccine.

Materials and equipment

Antigens

An amino terminal biotin-Aminohexanoic acid (biotin-Ahx) tagged peptides corresponding to the *Plasmodium falciparum* Circumsporozoite protein (PfCSP) repeat region (NPNA3; biotin-Ahx-NPNANPNANPNA with an amidated carboxy terminal, NANP6 (biotin-Ahx-NANPNANPNANPNANPNANPNANP), N-terminal junctional region (N-interface; biotin-Ahx-KQPADGNPDPNANPN with an amidated carboxy terminal) and the negative control peptide C1 (Biotin-KKMQEDVISL WDQSLKPCVK LTPLCV) were custom made by CPC Scientific (Sunnyvale, CA). A recombinant CSP (CSP) containing the N-terminal region, 3 NVDP and 19 NANP repeats followed by the C-terminal region was produced and purified as described previously (26). A World Health Organization (WHO) international standard Vi polysaccharide (Vi-PS) from C. *freundii* was obtained from the National Institute for Biological Standards and Controls, United Kingdom. A recombinant HIV-1 glycoprotein construct BG505gp140 T332N SOSIP.664 was produced as previously described (27).

Monoclonal antibodies

The CSP central repeat region specific mAbs AB334, AB315 and AB395 were derived from individuals that participated in the RTS,S/AS01 malaria vaccine study described in Regules et al. (28). The protocol of RTS,S vaccinees plasmablasts isolation, cloning and antibodies sequencing were described in the earlier report (28). The Fab of AB334 was generated by digesting AB334 IgG1 using Fab preparation kit from Thermo Fisher Scientific (Waltham, MA) following supplied procedure.

Study samples

Samples from participants in phase 2 clinical trials of malaria vaccines (Clinical Trial Registration: NCT01883609 and NCT01366534), typhoid vaccines (Clinicaltrials.gov ID: NCT02324751) and a HIV-1 virus controller cohort enrolled through Infectious Diseases Clinic at Duke University Medical Center were collected following informed consent. Sample analyses were performed with approval from the Duke Medicine Institutional Review Board for Clinical Investigations (Protocol Pro00074497, Pro00104803 and Pro00009701). The efficacy and/or immunological evaluations for these studies were reported earlier (8, 11, 13, 22, 29–31). All study participants had previously provided consent for future use of samples for research, and all samples were de-identified. Polyclonal IgG antibodies were purified from sera or plasma samples using Protein G HP MultiTrap plates (GE Healthcare, USA) using manufacturer provided procedure.

Biolayer Interferometry equipment

All BLI data were collected using Fortebio OctetRed 384 instruments and biosensors (Fortebio- currently Sartorius, Fremont, CA). Both data acquisition and analyses were performed with United States Food and Drug Administration's Title 21 Code of Federal Regulations Part 11 (FDA Title 21 CFR Part 11) compliant software versions (Data Acquisition 9.0 and Data Analysis 9.0 or 10.0 packages).

Method

Biolayer interferometry assay

The kinetics of the biomolecular interactions were examined by immobilizing the ligand on an appropriate sensor surface and keeping the analyte in solution (Figure 1A). Antigens were loaded onto Streptavidin (SA) or Aminopropylsilane (APS) or Amine reactive (AR2G) biosensors as detailed previously for testing the binding antibodies (8, 11–13, 22). For this method, the form of the antibody will influence the kinetics of binding to the immobilized antigen as demonstrated by differences in the kinetics of epitope-matched Fab and IgG1 (Fab form, Figure 1B; IgG1 form, Figure 1C). The estimated K_D corresponds to affinity for Fab binding (Figure 1B) and avidity for IgG1 (Figure 1C) to the antigen. Additionally, the form of the antigen will influence how many Fab-epitope interactions can occur simultaneously (Figure 1D). When sera or plasma that contains a polyclonal mix of antibodies (Figure 1E) is tested, the sensorgram plot visualizes the results from multiple antibodies binding to an antigen.

The binding of AB334 Fab, AB334, AB315, AB395 mAbs and mAbs-mixtures to NPNA3 peptide was carried out using SA sensors. The NPNA3 peptide and negative control peptide C1 (for subtracting out responses due to non-specific interactions) were loaded onto SA sensors with a loading threshold set to not exceed 0.1 nm. Baseline step was monitored by dipping NPNA3 and C1 sensors in 1x kinetics buffer wells (Fortebio- currently Sartorius, Fremont, CA), followed by association step by dipping sensors into wells containing antibodies diluted in 1x kinetics buffer. The dissociation was monitored by dipping sensors back into 1x kinetics buffer wells used in baseline step to facilitate inter-step correction. Specific binding responses were obtained by parallel referencing of C1 sensors and fitted globally to a 1:1 Langmuir binding model. The dissection of component antibody binding time-courses of binary mAbs mixtures binding to NPNA3 was performed using a heterogeneous analyte (competing reactions) model after exporting the reference subtracted time-courses to BiaEval 4.1 software (GE Healthcare Biacore LifeSciences). In the case of polyclonal samples, the standard analyses of dissociation phases were performed as per manufacturer's technical note for dissociation rate ranking of crude samples as described earlier (8, 12, 13).

Polyclonal antibodies avidity resolution tool (PAART)

The PAART method was developed and implemented using R statistical software version 3.6.1 (R Foundation for Statistical Computing, Vienna, Austria). Briefly, for multiple antibodies

10.3389/fimmu.2023.1049673

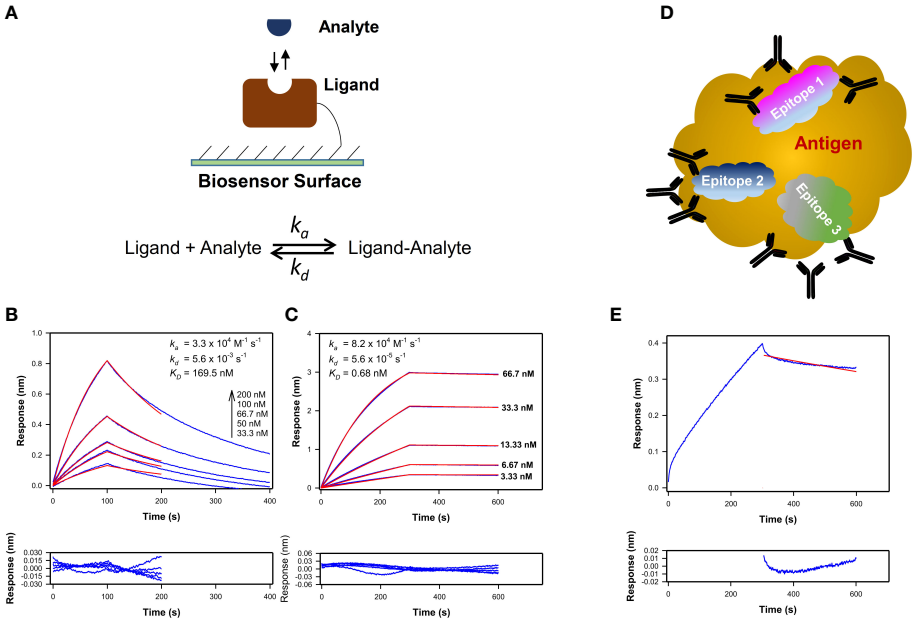

FIGURE 1
Kinetics profiles of monoclonal and polyclonal antibodies interaction with antigens. **(A)** Schematics showing the assay configuration for kinetics measurements of a homogenous analyte binding to a ligand immobilized on SPR or BLI biosensor to estimate the association and dissociation rate constants (k_a and k_d respectively) and K_D value. **(B, C)** Time-courses of Plasmodium falciparum circumsporozoite protein central repeat region specific mAb AB334 in its Fab form **(B)** and IgG1 form **(C)** binding (blue lines) at different indicated concentrations to a NANP repeat peptide NPNA3 with their best fit to a 1:1 binding model overlaid (red lines) on them are shown. The residuals plots of the fit are shown below the binding time-courses. The K_D values estimated correspond to affinity in case of AB334 Fab binding **(B)** and avidity in case of AB334 IgG1 **(C)** respectively. **(D)** Schematic of a macromolecular antigen is shown as a gold colored cloud shape. The antigen presents multiple epitopes on its surface that are targeted by polyclonal antibodies. Three such epitopes are represented as cloud shapes in different colors (Epitopes 1-3). The observed macromolecular antigen binding time-courses arise from antibodies binding to different epitopes in parallel and some antibodies competing against each other for certain epitope(s). For simplicity, only monomeric antibodies are portrayed. **(E)** As an example of polyclonal antibodies binding, 1:50 diluted serum of a malaria vaccinee in a phase 2a trial (NCT01857869) binding to the NPNA3 peptide is shown (blue line) along with the 1:1 model fit of the dissociation phase (red line). The residuals plot of the fit is shown below the sensorgram plot.

interaction with an antigen, the observed response at the beginning of the dissociation time-course should equal to the sum of binding responses from each group of antibodies with similar dissociation features (antibody component) that is bound to the antigen at the end of the association phase. Then the dissociation time course can be modeled to a sum of exponentials as below,

$$R(t) = \sum_{i=1}^{n} \alpha_i e^{-k_{d_i} t} \tag{2}$$

where α_i is the response associated with antibody component i at time t=0 (beginning of dissociation phase), k_{di} is the dissociation rate associated with antibody component i, n is the number of exponentials, and $R(t)$ is the total response at time t. For each polyclonal sample, the dissociation phase is fit sequentially to the sum of exponentials model (Equation 2) for increasing values of n continuing until the model with n +1 components has a larger value of the Akaike information criterion (AIC) than the model with n components. AIC balances goodness of fit with complexity, guarding against overfitting of data by penalizing overly complex models. Thus, PAART analysis yields the minimal number of antibody components with different k_d and the respective fractions (f defined in Equation 3) required to adequately describe the pAbs dissociation phase data.

$$f = \frac{\alpha_i}{\sum_{i=1}^{n} \alpha_i} \tag{3}$$

The standard error of the estimates of k_{d_i}, plots of time-courses calculated from the best fit overlaid on the experimental time-courses and the fitting residuals are used to judge the goodness of fit.

A flow chart detailing the steps used to perform PAART analysis is shown in Figure 2. The code for sequential fitting of dissociation phase of antibody-antigen interaction using R software along with relevant annotations and a working example can be found in GitHub[1].

Results

Verification of PAART

In order to verify whether PAART would resolve dissociation rates of different antibodies present in a polyclonal mixture, as a testing ground, we used binary mixtures of mAbs targeting the central repeat region of *Pf*CSP that consists of major repeats of NANP motif along with interspersed minor repeats of NVDP motif. The repeats region specific mAbs we used in this study differ mostly in the k_d of their interaction with a synthetic peptide NPNA3 (32) that contains 2.5 NANP repeats (Table 1). We selected mAbs that differed in k_d by

1 Li, K., H.C. Huntwork, R., Dodds, M., L. Spreng, R., & Dennison, S. M. Polyclonal Antibodies Avidity Resolution Tool (PAART) [Computer software] https://github.com/DukeCHSI/PAART.

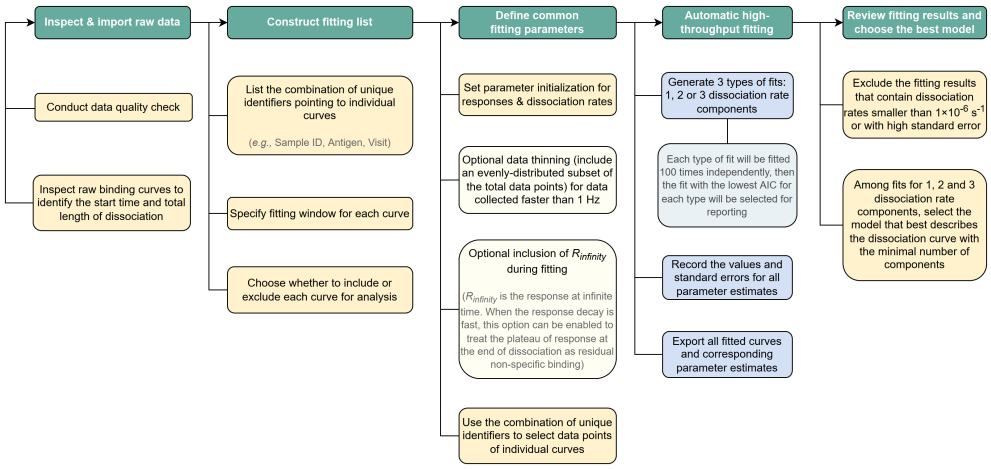

FIGURE 2
Schematic of the steps used to perform PAART analysis. A flow chart showing step-wise procedure for performing PAART analysis.

660.7-fold; a high avidity (slower k_d) mAb (AB334, Figure 1C) and a low avidity (faster k_d) mAb (AB395, Figure S1B) to make binary mixtures. The binding time-courses to NPNA3 of mAbs AB334 and AB395 alone and the binary mixtures of these two mAbs at various compositions are shown in Figure 3A. The biphasic nature of both the association and dissociation phases is evident in all binary mixtures (Figure 3A). We used a heterogeneous analyte (competing reactions) model (Figure 3B), that describes the interaction of two analytes that compete for the same ligand with different kinetics features (k_a and k_d), to simultaneously fit both the association and dissociation phases of the binary mixtures to obtain k_a and k_d pairs corresponding to the two antibodies. This analysis resolved the contribution of each competing antibody to the observed binding time-courses. A representative data is shown in Figure 3C for the binary mixture of AB334 and AB395 at 25:75 molar ratio. The component antibodies binding curves obtained using heterogeneous analyte model fitting of binary mixture binding curve (Figure 3C) reveal the dynamics of antibodies interacting with the epitope NPNA3 as follows. The low avidity mAb AB395 with a faster k_a dominates the very early phase of the binding but gets replaced progressively by the high avidity mAb AB334 such that at the end of the association phase about 36% of AB395 ($\frac{Response\ of\ AB395\ at\ the\ end\ of\ association}{Response\ of\ Binary\ mixture\ at\ the\ end\ of\ association} \times 100$) remained bound to NPNA3 despite being at a higher proportion (75%) in the mixture. The antibody dynamics observed in different compositions of the binary mixtures is summarized in Figure 3D, showing the correlation between the percentage of bound antibodies at the end of a 300 seconds association phase and the percentage of antibodies present in the binary mixtures. At equilibrium, the ratio of occupancy for the interacting epitope between the two binary antibody mixture components is simply the ratio between their K_D values and their concentrations. Before attaining equilibrium, the epitope occupancy of antibodies would vary with time depending upon the kinetics features of the antibodies' interaction with the epitope. This is evident from the component time-courses of competing antibodies in Figure 3C and simulations (Figure S2) that the length of association phase will determine the fraction of antigen occupancy of competing antibodies at the beginning of dissociation. Thus, when the association phase was shortened to 100 seconds, a higher proportion of low avidity antibody AB395 remained bound to the antigen (Figure 3E), whereas prolonging the association phase to 1800 seconds resulted in low proportions of AB395 remaining bound to antigen (Figure 3F).

The analyses above of fitting both the association and dissociation phases can be performed only when the concentrations of the antibodies in the binary mixtures are known. But when examining polyclonal samples, relevant concentrations of antibodies remain unknown, restricting the kinetics analysis to only the dissociation phase. Therefore, it is important to understand whether the sum of exponentials analysis of dissociation phases alone would recapitulate the dissected k_d (from the simultaneous fits of association and dissociation phases) and their fractions appropriately. Thus, we performed PAART analysis of dissociation phases of the mAbs AB334, AB395 and their binary mixtures to obtain k_d and their fractions (Figures 4A, B). Expectedly, two k_d values were resolved in the binary mixtures with fractions similar to those obtained by fitting both the association and dissociation phases simultaneously to a competing reactions model (Figure 3D). We further increased the complexity by adding to the mixture a third mAb AB315 (Figure S1A) which has a ~4.3 fold faster k_d compared to the high avidity mAb AB334 (Table 1). Analysis of the ternary mixtures of mAbs AB334, AB315 and AB395 dissociation phases resolved only two k_d values (Figure 4C); one corresponding to low avidity (1-3 × 10^{-2} s^{-1}) and another to high avidity (1 × 10^{-5} to 1 × 10^{-4} s^{-1}). The faster k_d can be assigned to the low avidity mAb AB395 whereas the slower k_d appears to be an averaged k_d value of the two high avidity mAbs AB334 and AB315. This lack of fine resolution in k_d between the two high avidity antibody components could be due to small difference (4.3 fold) between their k_d. In fact, when

TABLE 1 Characteristics of NPNA3 peptide binding of mAbs chosen for making binary and ternary mixtures.

Antibody	k_a (M^{-1} s^{-1})	k_d (s^{-1})	K_D (nM)
AB334	8.2 × 10^4	5.6 × 10^{-5}	0.68
AB315	1.8 × 10^5	2.4 × 10^{-4}	1.36
AB395	4.7 × 10^5	3.7 × 10^{-2}	79.1

10.3389/fimmu.2023.1049673

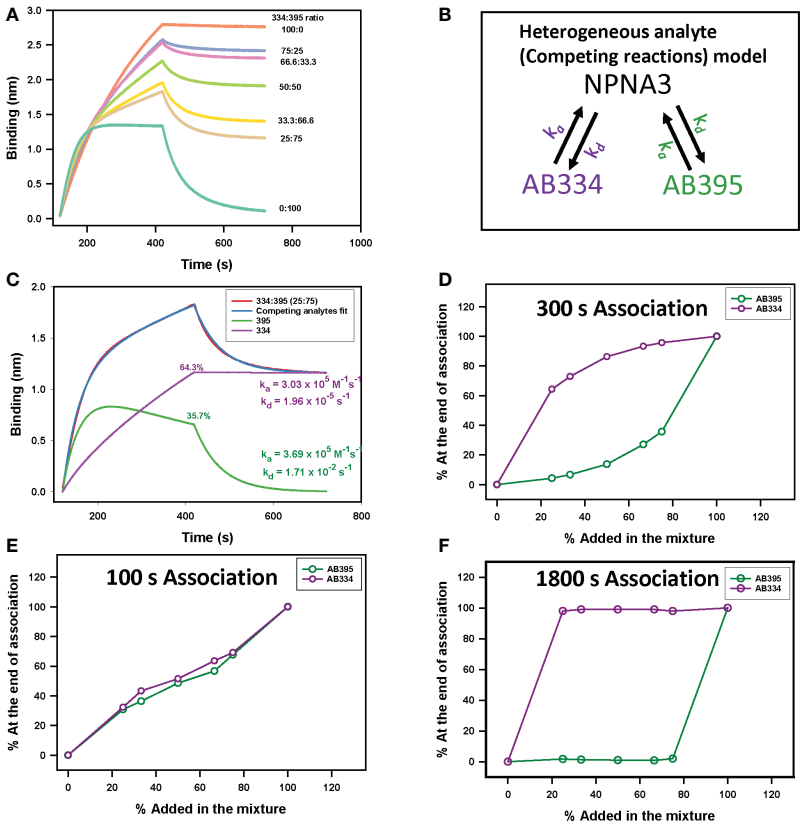

FIGURE 3
Epitope occupancy dynamics in binary antibody mixtures. **(A)** NPNA3 peptide binding time-courses of 5 µg/ml of a high avidity antibody AB334, a low avidity antibody AB395, and these two mAbs mixed at different ratios maintaining a total concentration of 5 µg/ml are shown. **(B)** Schematic of a heterogeneous analyte (competing reactions) model used to dissect total binding into component antibody binding kinetics is shown. The mAbs AB334 (purple) and AB395 (green) compete for binding to the immobilized antigen NPNA3. The k_a and k_d of each mAb are color coded to match the respective mAb. **(C)** Resolution of component antibodies binding time-courses contributing to the total observed binding of AB334 and AB395 mixed at 25:75 ratio predicted by a competing analytes model fit. **(D–F)** Plots of fraction of response of antibodies bound at the end of association phase **(D)** 300 s, **(E)** 100 s and **(F)** 1800 s respectively) for different compositions of the binary mixture are shown.

the binary mixtures of AB334 and AB315 were tested PAART resolved a major contributor (>96%) to the total binding with k_d values ranging from 5.1×10^{-5} to 1.2×10^{-4} s^{-1} and a negligible contributor (≤3.3%) to total binding with k_d of ~1×10^{-2} s^{-1} (Figure S3). It is also interesting to note from Figure 4C that the low avidity mAb AB395 in the ternary mixture exhibited epitope occupancy of only 15% (for AB334:AB315: AB395 at 1:1:6 ratio) to <5% (for all other mixing ratios used) at the end of 300 s association phase. Taken together these results show that the PAART analysis of dissociation phases of binary and ternary mixtures of mAbs of different avidity (i.e differing in k_d values) can successfully dissect low avidity antibodies (k_d values ~ 1×10^{-2} s^{-1}) from high avidity antibodies (k_d values 1×10^{-4} - 1×10^{-5} s^{-1}).

PAART dissects avidity heterogeneity of malaria vaccine-induced polyclonal serum IgG antibodies

Next we used PAART to analyze the dissociation phases of vaccine induced pAbs interacting with antigens to investigate whether PAART would dissect different k_d and thus help quantify the heterogeneity in avidity. For this, we used IgG antibodies purified from the sera of select vaccinees that participated in a phase 2a malaria vaccine clinical trial (Clinical Trial Registration: NCT01883609) and received RTS,S/AS01 vaccine at months 0, 1 and 2 (31). The kinetics of vaccinees' serum IgG antibodies binding to a minimal repeat peptide NPNA3 (32) corresponding to the central repeat region of PfCSP was tested. The post-3rd vaccination serum IgG antibodies drawn on the day before *Pf* sporozoite challenge showed varying binding responses (ranging from 0.2083 to 0.8661 nm) to NPNA3 peptide indicating the differences in quantity of NPNA3 specific IgG antibodies (Figure 5A). The dissociation phases of these serum IgG antibodies interaction with NPNA3 were biphasic (Figure 5A). The standard analysis of dissociation phases yielded a median k_d 1.1×10^{-3} s^{-1} (ranging from 0.7 to 2.2×10^{-3} s^{-1}) as depicted in Figure 5C. In comparison, PAART analysis of the same dissociation courses shown in Figure 5A resulted in better fit of the data (Figure 5B) as judged by the χ^2 values of the fits; PAART analysis median χ^2 2.9×10^{-4} (range 2.3×10^{-4} – 4.1×10^{-4}) compared to the standard analysis median χ^2 2.4×10^{-2} (range 1.9×10^{-3} – 9.0×10^{-2}). As shown in Figure 5D, the PAART analysis yielded two k_d values; a slower k_d (median k_d = 7.3×10^{-4} s^{-1}) similar to the k_d obtained by standard analysis and a faster k_d (median k_d = 1.0×10^{-2} s^{-1}). The fraction of slower k_d was higher (79.2 to 94.8%) than the fraction of faster k_d (5.2 to 20.8%). These percentages do not represent the fractions of the antibodies associated with each of the k_d but rather the

10.3389/fimmu.2023.1049673

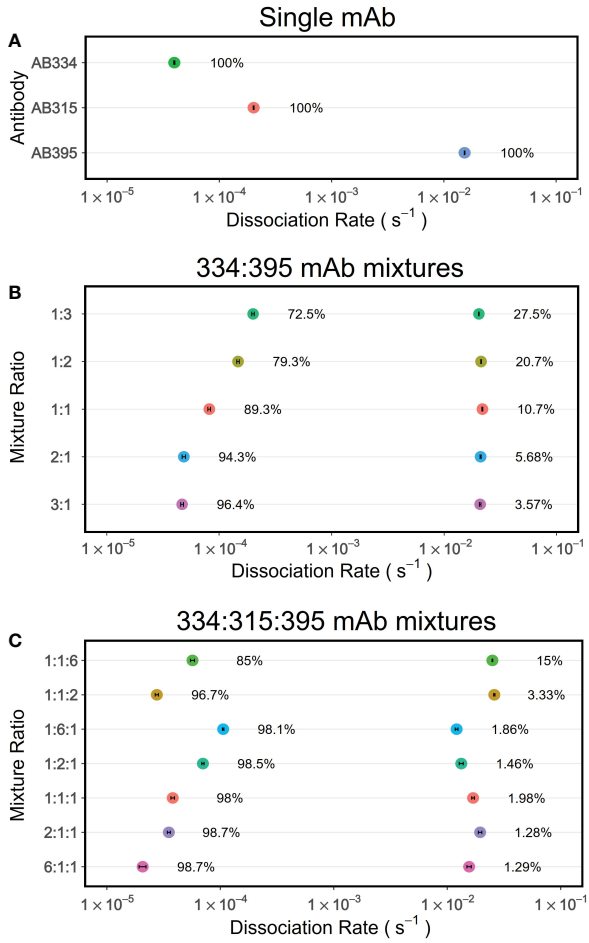

FIGURE 4
PAART analyses of dissociation phases of mAbs mixtures interacting with NPNA3 dissect different dissociation rates. The dissociation rates and their fractions estimated by PAART analysis of dissociation phases of mAbs alone **(A)**, the binary mixtures of AB334 and AB395 at various compositions **(B)** and the ternary mixtures of AB334, AB315 and AB395 **(C)** at different compositions are shown. The dissociation phases used here were recorded after 5 minutes of association phase. In each panel, the error bars associated with symbols indicate the standard error in the estimate of k_d values.

fractions of antigen occupancy at the beginning of dissociation. In short, for malaria vaccinees' IgG antibodies binding to NPNA3 antigen, the PAART analysis of dissociation phases has separated the avidity of antibodies into two bins differing in median k_d by roughly 14-fold, revealing the avidity diverseness of NPNA3 specific antibodies.

PAART resolves up to three antibody avidity components in Typhoid vaccinees serum IgG antibodies binding to Vi polysaccharide antigen

As an additional testing, we applied the PAART analysis to polyclonal IgG antibodies purified from the participants' sera of the Vaccines Against *Salmonella Typhi* (VAST) trial (29). We used purified IgG antibodies from VAST trial vaccinees that received a single dose of either a purified Vi polysaccharide (Vi-PS) or a Vi tetanus toxoid conjugate (Vi-TT) vaccine, and reported k_d values of Vi-PS interaction obtained using standard analysis previously (11). Here we focused on the Day 0 time point (4 weeks after immunization) serum IgG for PAART analysis of dissociation time-courses. Interestingly, 2-3 antibody components were resolved by PAART analysis (Figure 6). Serum IgG antibodies 28 days post vaccination revealed a higher proportion of participants that exhibited two or more k_d resolved in the Vi-TT group than in the Vi-PS group (Figure 6B). The slower k_d (2×10^{-5} to 1×10^{-3} s^{-1}) were associated with higher responses (60 to 95% of the total response) than the $>1\times10^{-2}$ s^{-1} k_d (5 to 50% of the responses) as shown in Figure 6A. The Vi-PS being a polymeric antigen likely presents different epitopes that can be targeted by the vaccine elicited antibodies and hence the heterogeneity in avidity observed here could arise not only due to competition but also due to difference in fine specificities (33). Overall, PAART analysis dissected the avidity of polyclonal IgG antibodies of most of the VAST study vaccinees into at least two bins differing in dissociation rates (k_d ranging from 2×10^{-5} to 1×10^{-3} s^{-1} and $k_d \geq 1\times10^{-2}$ s^{-1}) and further revealed the inter-group difference in proportion of avidity diverseness.

PAART analysis fine-resolves affinity maturation of malaria vaccine-induced serum antibody responses to different CSP antigens

The kinetics method of tracking affinity maturation of polyclonal antibody responses involves monitoring the k_d of the interaction of longitudinal samples with the antigens of interest. A decrease in k_d values, going from the samples drawn at early time points of immunization or pathogen exposure to those drawn at later time points, would indicate affinity maturation as the slower k_d values are associated with higher avidity antibodies. Since it can dissect different avidities, PAART stands in good stead to fine-resolve affinity maturation of polyclonal antibody responses towards antigens. To demonstrate this utility, we perused a longitudinal data set of a phase 2 malaria vaccine trial (NCT01366534) participants' sera binding kinetics that we reported earlier (8, 30). PAART analysis was performed for vaccinees that showed serum binding responses higher than the limit that is optimal for dissociation rate determination for a given antigen at all post-immune time points. Data obtained on sera of a vaccinee protected against *Pf* sporozoite challenge are shown in Figure 7 to showcase the fine resolution of affinity maturation of antibody responses. The time-courses of post-immune 1, 2 and 3 sera (Days 28, 56 and 77 respectively) of a protected vaccinee receiving the standard dose of RTS,S/AS01 interacting with CSP antigens are shown in Figures 7A–C. The CSP antigens tested include a recombinant CSP (Figure 7A), NANP6; a peptide corresponding to the central repeat region of CSP (Figure 7B) and N-interface; a peptide corresponding the junctional region immediately upstream of the central repeat region of CSP (Figure 7C). The RTS,S vaccine does not include the N-terminal junctional region, but the NANP repeat specific antibodies induced by RTS,S vaccination, as reported earlier, cross react with it (Figure 7C). The antigen specific binding responses were low at Day 28 and increased at Days 56 and 77 showing increase in antibody magnitude after second and third immunizations (Figures 7A–C). PAART analysis derived two

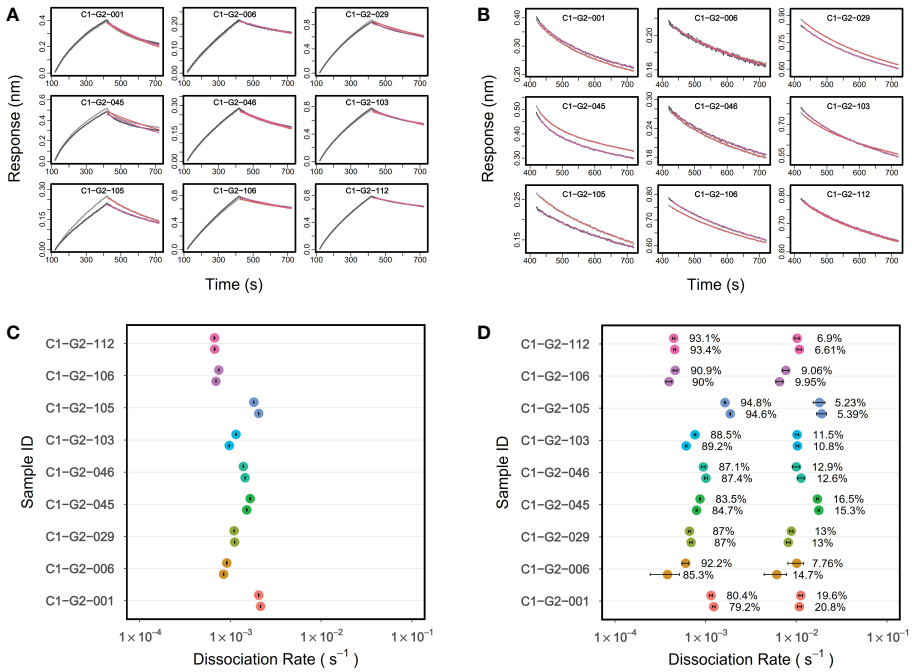

FIGURE 5
PAART analysis dissects two dissociation rates from malaria vaccinees' serum IgG antibodies-NPNA3 interaction. **(A)** Association and dissociation time-courses in duplicate (grey and black lines) of serum IgG antibodies (at 50 µg/ml concentration) of vaccinees from a Phase 2a malaria vaccine trial interacting with NPNA3 peptide are shown along with the overlaid fits (red lines) obtained using Langmuir dissociation. The vaccinees received three doses of RTS,S/AS01 vaccine at months 0,1 and 2. IgG antibodies were purified from the post third immunization sera a day before the Pf sporozoite challenge. **(C)** The dissociation rates (in duplicate) estimated using standard Langmuir dissociation fit are displayed for different vaccinees **(B)** Dissociation time-courses of vaccinees shown in panel A with overlaid best fits from PAART analysis are shown. **(D)** PAART analysis derived dissociation rates (in duplicate) and their fractions of different vaccinees are displayed. In panels **(C, D)**, the error bars associated with symbols indicate the standard error in the estimate of k_d values.

different k_d values for CSP and NANP6 binding at Day 28; one with a k_d in the order of 10^{-4} s^{-1} (average k_d 7.0×10^{-4} s^{-1} and 5.7×10^{-4} s^{-1} for CSP and NANP6 respectively) and another with a k_d in the order of 10^{-2} s^{-1} (average k_d 1.2×10^{-2} s^{-1} and 1×10^{-2} s^{-1} for CSP and NANP6 respectively) corresponding to ~88 and 12% respectively of the total binding responses (Figures 7D, E). Interestingly, at Day 56 the slower k_d values decreased further (to 2.7×10^{-4} and 3.1×10^{-4} s^{-1} for CSP and NANP6 respectively) contributing to ~94% of total binding response whereas the faster k_d values remained essentially unchanged but with a decreased contribution (5%) to the total binding response (Figures 7D, E). At Day 77, a < 2-fold decrease in slower k_d values was noted for CSP and NANP6 binding with an essentially unchanged faster k_d values and percent contribution to total binding of both faster and slower k_d values. These results indicate that in this protected

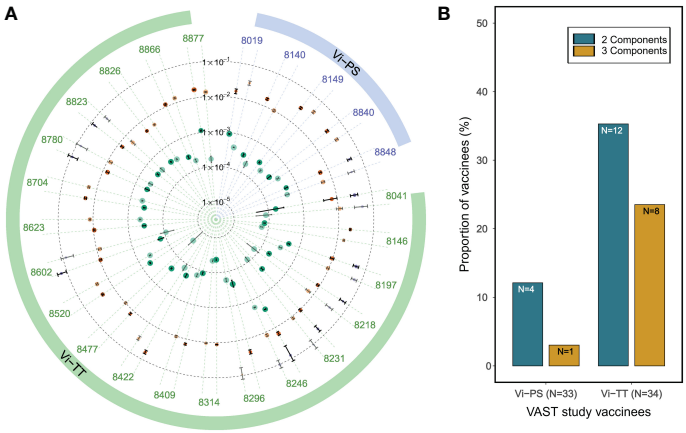

FIGURE 6
PAART analysis differentiates the avidity heterogeneity between Typhoid vaccine arms. **(A)** A radial plot of different k_d values dissected from the dissociation phases (in duplicate) of serum IgG antibodies of VAST clinical trial participants that received either a Vi-PS or a Vi-TT vaccine are shown. Duplicate data shown are the best two replicates of the triplicate time-courses measured. **(B)** The proportion of vaccinees with ≥5% of 2 and 3 antibody avidity components resolved by PAART analysis are shown for Vi-PS and Vi-TT groups of VAST clinical trial participants. In panel A, the error bars associated with symbols indicate the standard error in the estimate of k_d values.

10.3389/fimmu.2023.1049673

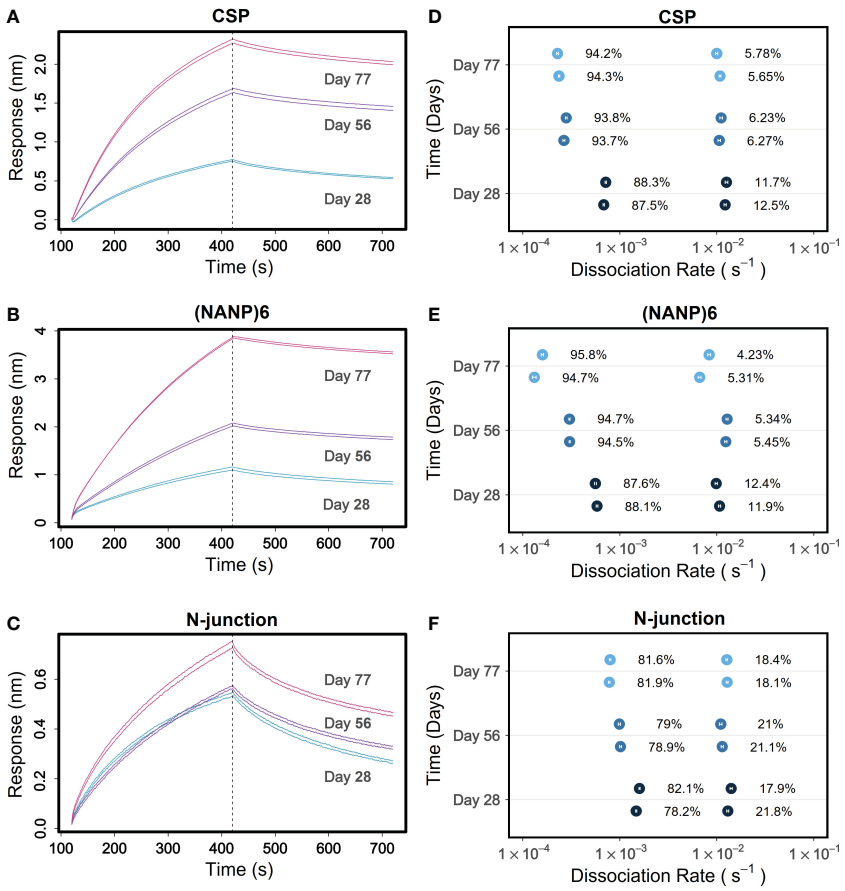

FIGURE 7
Tracking of fine-resolved affinity maturation of antibody responses to different CSP antigens elicited in a protected RTS,S/AS01 malaria vaccinee. **(A–C)** Time-courses of 1:50 diluted sera from days 28, 56 and 77 corresponding to post-immune 1, 2 and 3 time points respectively of a protected RTS,S/AS01 vaccinee are shown for binding to antigens recombinant CSP **(A)**, NANP6 peptide **(B)** and N-interface peptide **(C)** in duplicate. **(D–F)** Different k_d values dissected for each replicate at days 28, 56 and 77 are shown for binding to CSP **(D)**, NANP6 **(E)** and N-interface **(F)**. In panels **(D–F)**, the error bars associated with symbols indicate the standard error in the estimate of k_d values.

vaccinee, there remains a population of NANP6- and CSP specific antibodies heterogeneous in avidity after the first RTS,S/AS01 immunization; a stronger one that matures 4-fold in avidity upon second and third immunization to contribute predominantly to the observed binding plus a weaker one that did not affinity mature yet. PAART analysis resolved two different k_d values (average values 1.5×10^{-3} s^{-1} and 1.4×10^{-2} s^{-1}) from the N-interface binding of protected vaccinee's serum at Day 28 as well (Figure 7F). Unlike the 4-fold decrease in the slower component (k_d values in the order of 10^{-4} s^{-1}) observed for NANP6 and CSP binding, there was only a marginal decrease in k_d (1.9 fold decrease between Day 28 Day 77) of N-interface specific slower component. Overall, these results demonstrate the utility of obtaining a fine-resolution feature of antigen specific affinity maturation of vaccine-induced serum antibody responses.

PAART analysis resolves differences in avidity heterogeneity between protected and not-protected malaria vaccinees in a phase 2 clinical trial

Examining vaccine induced antibody avidity differences between protected and not-protected vaccinees is important in immune correlate analysis of vaccines as it would reveal whether or not the vaccine elicited antibody avidity associates with protection. Here we explored whether PAART could be applied to identify differences in heterogeneity in vaccine induced antibody avidity between protected and not-protected vaccinees. For this purpose, we used the dissociation kinetics data obtained for a phase 2 malaria vaccine trial specimen reported earlier (8, 30). In the dissociation rate measurement analysis we reported earlier (8), on the day of challenge (visit 20, post-dose 3), vaccinees receiving the RTS,S/AS01 standard dose showed no significant difference in CSP-specific serum antibody avidity (k_d) between the protected and not-protected vaccinees from Pf sporozoite infection. Interestingly, PAART analysis showed that all but one vaccinee serum had two antibody components; one contributing dominantly to the total binding response (93-98%) with mean $k_d \sim 1\times10^{-4}$ s^{-1} and another contributing only 2-7% to the total binding response with a $k_d \sim 1\times10^{-2}$ s^{-1} (Figure 8A). When compared, 36.4% (4 out of 11) of the protected vaccinees exhibited >5% of the weak avidity antibody component whereas only 10% (1 out of 10) of the not-protected vaccinees had more >5% of the weak avidity antibody component (Figure 8B). Since CSP contains various epitopes, the epitope specificities of the two antibody components cannot be assigned. It

10.3389/fimmu.2023.1049673

would require further probing to understand why more protected subjects have weak avidity antibodies. In brief, these results demonstrate the capability of PAART to probe the differences in heterogeneity of avidity between protected and not-protected vaccinees in clinical trials.

Polyclonal Fab provide enhanced resolution compared to polyclonal IgG antibodies in identifying antibody components

While immobilization of an antigen on sensor surfaces facilitates developing an antibody-antigen binding assays that are convenient for probing serum and plasma samples, it also improves the bivalent interaction of antibodies due to higher local concentration of antigen. Thus, the binding results obtained in this format includes an avidity effect (34, 35). If the antigen is not monomeric, the avidity effect will be compounding. One way to minimize the avidity effect and measure affinity is to immobilize antigens at low density so that antibody-antigen interactions are monovalent. An alternate strategy would be to use antibody Fab instead of intact antibodies. The former strategy might not be possible when working with serum or plasma samples as low abundance antibodies binding would not be detected. Therefore, using antibody Fab is a preferred way for measuring average affinity of pAbs. Here we demonstrate that the dissociation phase data obtained for polyclonal Fab when analyzed by PAART can provide enhanced resolution in dissecting different antibody components as compared to using data obtained from the corresponding IgG antibodies. Nyanhete et al. (22) recently reported broadly HIV-1 neutralizing polyclonal antibody activity in a subset of virus controllers (VCs). We performed PAART analysis on the polyclonal antibody Fab and the intact IgG antibodies from VCs plasma binding to a native like HIV-1 envelope glycoprotein BG505gp140 T332N SOSIP.664. The k_d values from the PAART analysis of the VCs plasma IgG and Fab dissociation from BG505gp140 T332N SOSIP.664 are shown for Figures 9A, B respectively. Two k_d values were resolved for the dissociation of polyclonal plasma IgG of all six virus controllers; one corresponding to higher avidity (k_d ranging from 2.6 – 3.4×10^{-4} s^{-1}) with a dominant contribution (92.2 – 93.9%) to the binding response and another attributable to lower avidity (k_d ranging from 1.5 to 1.7×10^{-2} s^{-1}) with a minor contribution (6.1 – 7.8%) to the binding. On the other hand, the polyclonal antibody Fab dissociation of VCs were resolved into 2 to 3 antibody components with different k_d values (Figure 9B). Unlike the IgG dissociation data that did not vary between VCs either in the slower or the faster k_d values, the PAART derived k_d values of the Fab dissociation data showed a marked difference between VC (Figure 9B). When compared with the slower k_d values of IgG data (Figure 9A), the slower k_d values resolved for Fab dissociation were similar in two VC (VC AA and VC AQ), 2 fold faster in two VC (VC AL and VA AP) and ~ 10 fold faster in two VC (VC N and VC BA) pointing out the differing levels of the affinity of the pAbs that contributed to the total binding of BG505gp140 T332N SOSIP.664 (Figure 9B). The VCs exhibited higher fractions of faster k_d values for Fab dissociation than the IgG dissociation. Differences in faster k_d values between VCs were also observed and a third k_d was also resolved in VC N and VC AQ Fab dissociation. Overall, these results exemplify the utility of PAART and polyclonal Fab-antigen binding kinetics data to get enhanced resolution of antibody heterogeneity.

Discussion

Characterization of pAbs for the distribution of specificity (22, 36, 37) and avidity (38, 39) by different techniques has been reported recently. Our focus is on utilizing pAbs-antigen binding kinetics data obtained with the commonly employed label-free platforms to dissect distributions of avidities. The pAbs-antigen interaction time-courses comprise important kinetics information that can reveal the

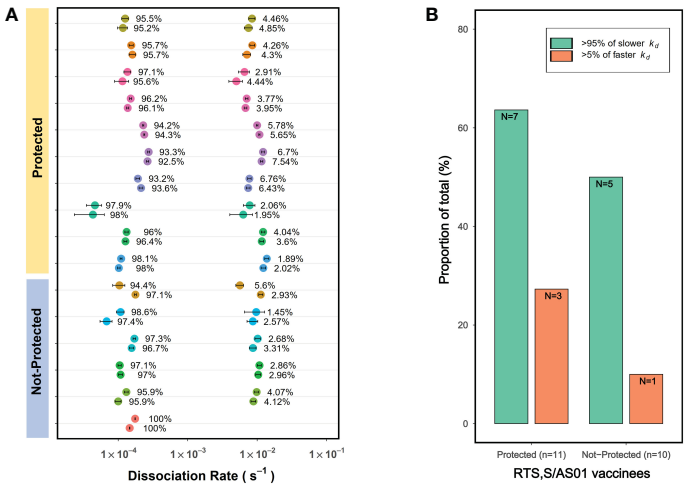

FIGURE 8
PAART analysis resolves differences in avidity heterogeneity between protected and infected malaria vaccinees in a phase 2 clinical trial. **(A)** The k_d values derived from PAART analysis of dissociation time-courses of 1:50 diluted sera from visit 20 corresponding to post-immune 3 (Day of Challenge) time point are shown for standard dose regimen RTS,S/AS01 vaccinees. Two best replicates data from PAART analysis are shown. **(B)** The proportion of total vaccinees from the protected and not-protected groups with >95% of slower k_d and >5% of faster k_d are shown. Binding responses were below the dissociation rate quantifiable limit for 1 and 4 vaccinees from the protected and not-protected groups respectively. In panel A, the error bars associated with symbols indicate the standard error in the estimate of k_d values.

10.3389/fimmu.2023.1049673

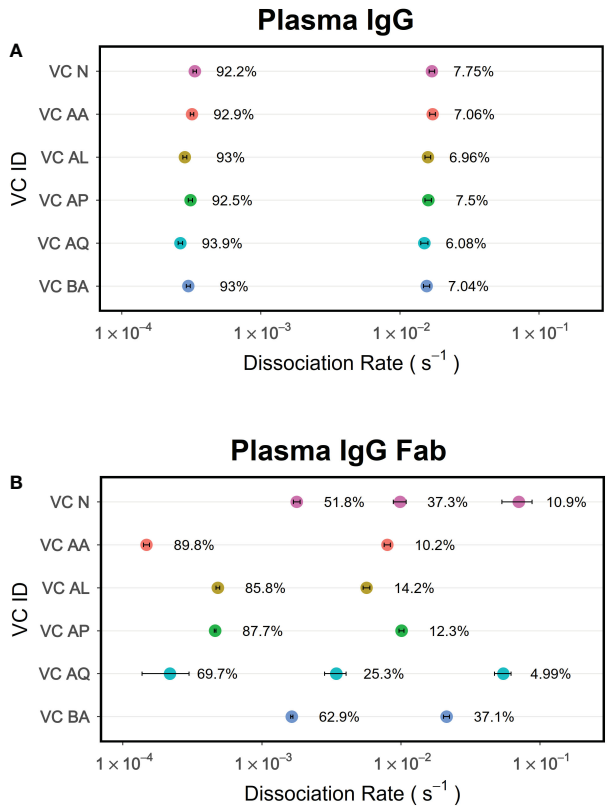

FIGURE 9
PAART analysis of polyclonal antibody Fab dissociation rather than the polyclonal IgG antibodies provides enhanced resolution of antibody heterogeneity. Data of polyclonal IgG antibodies **(A)** and the corresponding Fab **(B)** from the HIV-1 virus controllers interacting with BG505gp140 T332N SOSIP.664 antigen were analyzed using PAART to derive the minimal number of k_d values needed to explain the dissociation phase. The error bars associated with symbols indicate the standard error in the estimate of k_d values.

underlying antibody dynamics. Avidity distributions need to be mined out from the time-courses of pAbs-antigen interaction for better understanding the antibody dynamics that are occurring during this interaction. While delineation of antibody avidity heterogeneity down to clonal level is not feasible, binning the pAbs into various groups differing in avidity is achievable by appropriate modeling of the dissociation phases. To accomplish this, we have reported here the development, validation and application of PAART for analyzing the dissociation phase of pAbs-antigen interaction data. This is a substantial development in enabling avidity binning of pAbs which yields additional insights in the antibody dynamics compared to the weighted avidity obtained using standard analysis fitting of the antibodies dissociation time-courses to a 1:1 Langmuir dissociation model.

The sum of exponentials model utilized in the PAART has been employed previously in fragment-based drug discovery using dissociation phase screening of crude reaction mixtures that contain low affinity starting material and different amounts of desired high affinity product(s) for target ligand (40). In fragment-based discovery, this has been restricted to a system of only two components. In contrast, PAART has been designed to resolve more than two dissociation rate components and is equipped to guard against overfitting of data to select a parsimonious model for a given dissociation course using Akaike information criterion. PAART has been successfully tested using binary mixtures of mAbs differing in dissociation rates to recover appropriate fractions of different dissociation rates accounting for the antibody competition.

Application of PAART to malaria and typhoid vaccinees' IgG antibodies-antigen binding data revealed heterogeneity in the avidity and identified inter-group differences in avidity heterogeneity of typhoid vaccinees' antibodies. The additional information of avidity heterogeneity could provide more insights when correlated with the vaccine efficacy. Additional application of PAART includes tracking of component level affinity maturation of pAbs over time in response to vaccination or exposure to pathogens. As an example, we demonstrated tracking the fine-resolved affinity maturation of antibody response against different CSP antigens in a protected malaria vaccinee (Figure 7); an affinity maturing antibody component and the other that did not mature. The latter could be due to lack of affinity maturation of antibodies elicited after first immunization or due to the emergence of new antibody responses after second and third immunization that are yet to affinity mature. Affinity maturation tracking *via* dissociation rate binning could be used to make comparisons between individuals, groups or vaccine candidates to reveal fine-differences that would help form strategies intended to guide the host immune response in a desired fashion. PAART could also be applied to better understand vaccine breakthrough infections by analyzing the differences in avidity heterogeneity of vaccinees' antibodies to the vaccine antigen and antigens representing the evolving variants.

Successful utility of PAART in the analysis of pAbs will depend on the choice of antigen and assay conditions. The first choice should be the use of antigen constructs that present a minimal epitope of interest such as the ones targeted by protective/neutralizing antibody responses, compared to a full-length antigen. It will be advantageous as the binned avidity of antibodies studied will be specific to the epitope. The epitope-specific dissociation rate binning data can be used to draw a correlation with the functional activity of the polyclonal sample. It may be easier to pursue this strategy for linear epitopes but might require design and production of antigen constructs for presenting conformational epitopes. If full-length antigens or multi-epitope antigens are used, the fine specificity of binned dissociation rates will remain unknown and might render it difficult to draw correlation with functional data. If dissociation rate binning can be done using full-length antigen and as many minimum epitopes/domains as needed, comprehensive dissociation rate binning database could be built for drawing correlation with different functional properties. Regarding assay conditions, as outlined in our testing, the length of association phase will determine the antigen occupancy of antibodies if competition is involved. Therefore, a lengthy association time e.g 10 minutes or more should be avoided so that detection of weak avidity antibodies does not get lost. Similarly, shortening the association phase will decrease antigen occupancy by antibodies with slow association rate. Thus, 2 to 5 minutes monitoring of association phase before following dissociation phase would be appropriate. Another point to note is that choosing an appropriate window of the dissociation phase is important for a meaningful analysis. Distortion in the binding response signal is not uncommon during the initial few seconds of the dissociation time-courses and should be excluded in the analysis

as done in Langmuir dissociation analysis. Similarly, residual non-specific binding, if any, towards the end of the dissociation phase should be excluded from the analysis window to avoid PAART resolving that phase as a slow dissociation rate contributing to the overall dissociation. An alternative option is to include a term corresponding to the response at infinite time (R_∞) in the sum of exponentials model employed by PAART.

Limitations of PAART include the decreased resolving power if the difference in k_d values of antibodies in a sample is small. Another limitation is to assign epitope specificity of the dissociation rate binned antibodies if the interaction followed was with a multi-epitope antigen. However, together with additional investigations using other techniques such as electron microscopy polyclonal epitope mapping (22), PAART would be valuable in understanding the distributions of specificity and avidity of pAbs.

To conclude, we have developed and demonstrated the capability of an analytical tool for dissociation rate binning of pAbs-antigen interaction time-courses. The binned dissociation rates reveal the heterogeneity in the avidity of pAbs and the fractions of binding response associated with these different dissociation rates indicate the respective antigen occupancy levels of the binned antibodies. The dissociation rate binning data obtained using PAART analysis could be applied in immunogenicity analyses, evaluating vaccine constructs, vaccine formulations and also for tracking affinity maturation.

Data availability statement

The raw data supporting the conclusions of this article will be made available by the authors, without undue reservation.

Ethics statement

The studies involving human participants were reviewed and approved by Walter Reed Army Institute of Research (WRAIR) Institutional Review Board and the PATH-Malaria Vaccine Initiative's Western Institutional Review Board for study NCT01366534; United Kingdom National Research Ethics Service, Committee South Central–Oxford A (reference 13/SC/0208), the Western Institution Review Board (reference 20130698), and the United Kingdom Medicines and healthcare Products Regulatory Agency (reference 21584/0317/001-0001) for study NCT01883609; South Central Oxford A Ethics Committee (reference 14/SC/1427) for study NCT02324751; and Duke University Institutional Review Board for HIV-1 virus controller cohort. The patients/participants provided their written informed consent to participate in this study.

Author contributions

MD, SMD, and GDT conceived and designed study. MD developed code, RLS and KL performed code optimization. UW-R, EJ, KJE, AVSH, CJ, JH, and AJP provided study samples. SD made reagent. MA, RHCH, LCD, and TN performed experiments, KL and RLS analyzed data. SMD wrote the manuscript. KL, MD, RLS, LCD, UW-R, EJ, SMA, and GDT edited manuscript. MA, RHCH, TN, SD, KJE, AVSH, CJ, JH, and AJP reviewed manuscript. All authors contributed to the article and approved the submitted version.

Funding

This work was supported by a grant for the Antibody Dynamics platform of the Global Health – Vaccine Accelerator Platforms (GH-VAP) from the Bill and Melinda Gates Foundation (BMGF) to GDT (grant numbers OPP1151372 and INV-008612) and by the funding from the National Institutes of Health (NIH): National Institute of Allergy and Infectious Diseases (NIAID) for Duke Center for AIDS Research (CFAR) (P30 AI064518) to GDT, P01 AI120756 to GDT, and R01 AI052779 to GDT.

Acknowledgments

We acknowledge Dr. James Peacock in the Duke Human Vaccine Institute (DHVI) Protein Production Facility which received funding support from the Collaboration for AIDS Vaccine Research of the BMGF (OPP1066832) for recombinant HIV-1 envelope glycoprotein and monoclonal antibody production work. We thank Dr. Kevin Saunders at DHVI for designing BG505gp140 T332N SOSIP.664 production. We thank Matthew Reichartz for technical help with preliminary experiments, Dr. Sarah Mudrak for expert program management, Wes Rountree and Dr. Janice McCarthy for statistical expertise, Mark Sampson and Dr. Elizabeth Feeney for contributions to code development, David Beaumont for managing GitHub repository of PAART code, R. Glenn Overman for IgG purification work, Judith Lucas for Good Clinical Laboratory Practice (GCLP) management at Duke University, and Dr. Karen Maker, BMGF GH-VAP Senior Program Officer, for expert guidance and advice. We are thankful to PATH's Center for Vaccine Innovation and Access (CVIA), GlaxoSmithKline Biologicals SA (Belgium) and Atreca (Redwood City, CA) for providing CSP IgG mAbs. We thank the NCT01883609, NCT01366534 and NCT02324751 clinical trials participants. We thank the participants and the clinical staff of the HIV-1 virus controller cohort at Duke Adult Infectious Diseases Clinic, Duke University Medical Center and the clinical staff: Dr. Coleen Cunningham, Dr. John Bartlett, Stuart Carr, Sunita Patil, Dr. Gary Cox, Dr. Nathan Thielman, Dr. Cameron Wolfe, Dr. Elizabeth Livingston, Dr. Brianna Norton, Dr. Kristen Dicks, Dr. Mehri McKellar, Dr. Vivian Chu, Dr. Jason Stout, and Ann Mosher.

Conflict of interest

MD is an employee of Certara. EJ is an employee of the GSK group of companies and holds shares or restricted shares in the GSK group of companies. GDT was a recipient of a research subcontract through Duke University from GSK and Macrogenics for work unrelated to this study. UW-R was an employee of GSK group of

companies during the course of data analysis reported here and during the review process of this article.

The remaining authors declare that the research was conducted in the absence of any commercial or financial relationships that could be construed as a potential conflict of interest.

Publisher's note

All claims expressed in this article are solely those of the authors and do not necessarily represent those of their affiliated organizations, or those of the publisher, the editors and the reviewers. Any product that may be evaluated in this article, or claim that may be made by its manufacturer, is not guaranteed or endorsed by the publisher.

Supplementary material

The Supplementary Material for this article can be found online at: https://www.frontiersin.org/articles/10.3389/fimmu.2023.1049673/full#supplementary-material

References

1. Bauer G. The potential significance of high avidity immunoglobulin G (Igg) for protective immunity towards sars-Cov-2. *Int J Infect Dis* (2021) 106:61–4. doi: 10.1016/j.ijid.2021.01.061

2. Ssewanyana I, Arinaitwe E, Nankabirwa JI, Yeka A, Sullivan R, Kamya MR, et al. Avidity of anti-malarial antibodies inversely related to transmission intensity at three sites in Uganda. *Malar J* (2017) 16(1):67. doi: 10.1186/s12936-017-1721-3

3. Usinger WR, Lucas AH. Avidity as a determinant of the protective efficacy of human antibodies to pneumococcal capsular polysaccharides. *Infect Immun* (1999) 67(5):2366–70. doi: 10.1128/iai.67.5.2366-2370.1999

4. Benner SE, Patel EU, Laeyendecker O, Pekosz A, Littlefield K, Eby Y, et al. Sars-Cov-2 antibody avidity responses in covid-19 patients and convalescent plasma donors. *J Infect Dis* (2020) 222(12):1974–84. doi: 10.1093/infdis/jiaa581

5. Doria-Rose NA, Joyce MG. Strategies to guide the antibody affinity maturation process. *Curr Opin Virol* (2015) 11:137–47. doi: 10.1016/j.coviro.2015.04.002

6. Boon D, Bruce V, Patel EU, Quinn J, Srikrishnan AK, Shanmugam S, et al. Antibody avidity-based approach to estimate population-level incidence of hepatitis c. *J Hepatol* (2020) 73(2):294–302. doi: 10.1016/j.jhep.2020.03.028

7. Rikhtegaran Tehrani Z, Azadmanesh K, Mostafavi E, Gharibzadeh S, Soori S, Azizi M, et al. High avidity anti-integrase antibodies discriminate recent and non-recent hiv infection: Implications for hiv incidence assay. *J Virol Methods* (2018) 253:5–10. doi: 10.1016/j.jviromet.2017.12.003

8. Seaton KE, Spreng RL, Abraha M, Reichartz M, Rojas M, Feely F2nd, et al. Subclass and avidity of circumsporozoite protein specific antibodies associate with protection status against malaria infection. *NPJ Vaccines* (2021) 6(1):110. doi: 10.1038/s41541-021-00372-x

9. Thompson HA, Hogan AB, Walker PGT, White MT, Cunnington AJ, Ockenhouse CF, et al. Modelling the roles of antibody titre and avidity in protection from plasmodium falciparum malaria infection following Rts,S/As01 vaccination. *Vaccine* (2020) 38 (47):7498–507. doi: 10.1016/j.vaccine.2020.09.069

10. Klasse PJ. How to assess the binding strength of antibodies elicited by vaccination against hiv and other viruses. *Expert Rev Vaccines* (2016) 15(3):295–311. doi: 10.1586/14760584.2016.1128831

11. Dahora LC, Jin C, Spreng RL, Feely F, Mathura R, Seaton KE, et al. Iga and Igg1 specific to vi polysaccharide of salmonella typhi correlate with protection status in a typhoid fever controlled human infection model. *Front Immunol* (2019) 10:2582. doi: 10.3389/fimmu.2019.02582

12. Dennison SM, Reichartz M, Abraha M, Spreng RL, Wille-Reece U, Dutta S, et al. Magnitude, specificity, and avidity of sporozoite-specific antibodies associate with protection status and distinguish among Rts,S/As01 dose regimens. *Open Forum Infect Dis* (2020) 8(2). doi: 10.1093/ofid/ofaa644

13. Dennison SM, Reichartz M, Seaton KE, Dutta S, Wille-Reece U, Hill AVS, et al. Qualified biolayer interferometry avidity measurements distinguish the heterogeneity of antibody interactions with plasmodium falciparum circumsporozoite protein antigens. *J Immunol* (2018) 201(4):1315–26. doi: 10.4049/jimmunol.1800323

14. Dennison SM, Sutherland LL, Jaeger FH, Anasti KM, Parks R, Stewart S, et al. Induction of antibodies in rhesus macaques that recognize a fusion-intermediate conformation of hiv-1 Gp41. *PloS One* (2011) 6(11):e27824. doi: 10.1371/journal.pone.0027824

15. Fuentes S, Hahn M, Chilcote K, Chemaly RF, Shah DP, Ye X, et al. Antigenic fingerprinting of respiratory syncytial virus (Rsv)-a-Infected hematopoietic cell transplant recipients reveals importance of mucosal anti-rsv G antibodies in control of rsv infection in humans. *J Infect Dis* (2020) 221(4):636–46. doi: 10.1093/infdis/jiz608

16. Haynes BF, Gilbert PB, McElrath MJ, Zolla-Pazner S, Tomaras GD, Alam SM, et al. Immune-correlates analysis of an hiv-1 vaccine efficacy trial. *N Engl J Med* (2012) 366 (14):1275–86. doi: 10.1056/NEJMoa1113425

17. Hessell AJ, Malherbe DC, Pissani F, McBurney S, Krebs SJ, Gomes M, et al. Achieving potent autologous neutralizing antibody responses against tier 2 hiv-1 viruses by strategic selection of envelope immunogens. *J Immunol* (2016) 196(7):3064–78. doi: 10.4049/jimmunol.1500527

18. Hu JK, Crampton JC, Cupo A, Ketas T, van Gils MJ, Sliepen K, et al. Murine antibody responses to cleaved soluble hiv-1 envelope trimers are highly restricted in specificity. *J Virol* (2015) 89(20):10383–98. doi: 10.1128/jvi.01653-15

19. Kasturi SP, Rasheed MAU, Havenar-Daughton C, Pham M, Legere T, Sher ZJ, et al. 3m-052, a synthetic tlr-7/8 agonist, induces durable hiv-1 envelope-specific plasma cells and humoral immunity in nonhuman primates. *Sci Immunol* (2020) 5(48). doi: 10.1126/sciimmunol.abb1025

20. Kimuda SG, Biraro IA, Bagaya BS, Raynes JG, Cose S. Characterising antibody avidity in individuals of varied mycobacterium tuberculosis infection status using surface plasmon resonance. *PloS One* (2018) 13(10):e0205102. doi: 10.1371/journal.pone.0205102

21. Lynch HE, Stewart SM, Kepler TB, Sempowski GD, Alam SM. Surface plasmon resonance measurements of plasma antibody avidity during primary and secondary responses to anthrax protective antigen. *J Immunol Methods* (2014) 404:1–12. doi: 10.1016/j.jim.2013.11.026

22. Nyanhete TE, Edwards RJ, LaBranche CC, Mansouri K, Eaton A, Dennison SM, et al. Polyclonal broadly neutralizing antibody activity characterized by Cd4 binding site and V3-glycan antibodies in a subset of hiv-1 virus controllers. *Front Immunol* (2021) 12:670561. doi: 10.3389/fimmu.2021.670561

23. Alexander MR, Ringe R, Sanders RW, Voss JE, Moore JP, Klasse PJ. What do chaotrope-based avidity assays for antibodies to hiv-1 envelope glycoproteins measure? *J Virol* (2015) 89(11):5981–95. doi: 10.1128/jvi.00320-15

24. Lipman NS, Jackson LR, Trudel LJ, Weis-Garcia F. Monoclonal versus polyclonal antibodies: Distinguishing characteristics, applications, and information resources. *Ilar J* (2005) 46(3):258–68. doi: 10.1093/ilar.46.3.258

25. Alam SM, Cronin K, Parks R, Anasti K, Ding H, Go EP, et al. Antigenicity and immunogenicity of hiv-1 envelope trimers complexed to a small-molecule viral entry inhibitor. *J Virol* (2020) 94(21). doi: 10.1128/jvi.00958-20

26. Schwenk R, DeBot M, Porter M, Nikki J, Rein L, Spaccapelo R, et al. Igg2 antibodies against a clinical grade plasmodium falciparum csp vaccine antigen associate with protection against transgenic sporozoite challenge in mice. *PloS One* (2014) 9(10): e111020. doi: 10.1371/journal.pone.0111020

27. Sanders RW, Derking R, Cupo A, Julien JP, Yasmeen A, de Val N, et al. A next-generation cleaved, soluble hiv-1 env trimer, Bg505 Sosip.664 Gp140, expresses multiple epitopes for broadly neutralizing but not non-neutralizing antibodies. *PloS Pathog* (2013) 9(9):e1003618. doi: 10.1371/journal.ppat.1003618

28. Regules JA, Cicatelli SB, Bennett JW, Paolino KM, Twomey PS, Moon JE, et al. Fractional third and fourth dose of Rts,S/As01 malaria candidate vaccine: A phase 2a controlled human malaria parasite infection and immunogenicity study. *J Infect Dis* (2016) 214(5):762–71. doi: 10.1093/infdis/jiw237

29. Jin C, Gibani MM, Moore M, Juel HB, Jones E, Meiring J, et al. Efficacy and immunogenicity of a vi-tetanus toxoid conjugate vaccine in the prevention of typhoid fever using a controlled human infection model of salmonella typhi: A randomised controlled, phase 2b trial. *Lancet* (2017) 390(10111):2472–80. doi: 10.1016/s0140-6736(17)32149-9

30. Ockenhouse CF, Regules J, Tosh D, Cowden J, Kathcart A, Cummings J, et al. Ad35.Cs.01-Rts,S/As01 heterologous prime boost vaccine efficacy against sporozoite challenge in healthy malaria-naïve adults. *PloS One* (2015) 10(7):e0131571. doi: 10.1371/journal.pone.0131571

31. Rampling T, Ewer KJ, Bowyer G, Bliss CM, Edwards NJ, Wright D, et al. Safety and high level efficacy of the combination malaria vaccine regimen of Rts,S/As01b with chimpanzee adenovirus 63 and modified vaccinia Ankara vectored vaccines expressing me-trap. *J Infect Dis* (2016) 214(5):772–81. doi: 10.1093/infdis/jiw244

32. Oyen D, Torres JL, Wille-Reece U, Ockenhouse CF, Emerling D, Glanville J, et al. Structural basis for antibody recognition of the nanp repeats in plasmodium falciparum circumsporozoite protein. *Proc Natl Acad Sci U.S.A.* (2017) 114(48):E10438–e45. doi: 10.1073/pnas.1715812114

33. Dahora LC, Verheul MK, Williams KL, Jin C, Stockdale L, Cavet G, et al. Salmonella typhi vi capsule prime-boost vaccination induces convergent and functional antibody responses. *Sci Immunol* (2021) 6(64):eabj1181. doi: 10.1126/sciimmunol.abj1181

34. Oda M, Azuma T. Reevaluation of stoichiometry and Affinity/Avidity in interactions between anti-hapten antibodies and mono- or multi-valent antigens. *Mol Immunol* (2000) 37(18):1111–22. doi: 10.1016/s0161-5890(01)00028-1

35. Rheinnecker M, Hardt C, Ilag LL, Kufer P, Gruber R, Hoess A, et al. Multivalent antibody fragments with high functional affinity for a tumor-associated carbohydrate antigen. *J Immunol* (1996) 157(7):2989–97. doi: 10.4049/jimmunol.157.7.2989

36. Antanasijevic A, Sewall LM, Cottrell CA, Carnathan DG, Jimenez LE, Ngo JT, et al. Polyclonal antibody responses to hiv env immunogens resolved using cryoem. *Nat Commun* (2021) 12(1):4817. doi: 10.1038/s41467-021-25087-4

37. Nogal B, Bianchi M, Cottrell CA, Kirchdoerfer RN, Sewall LM, Turner HL, et al. Mapping polyclonal antibody responses in non-human primates vaccinated with hiv env trimer subunit vaccines. *Cell Rep* (2020) 30(11):3755–65.e7. doi: 10.1016/j.celrep.2020.02.061

38. Budroni S, Buricchi F, Cavallone A, Bourguignon P, Caubet M, Dewar V, et al. Antibody avidity, persistence, and response to antigen recall: Comparison of vaccine adjuvants. *NPJ Vaccines* (2021) 6(1):78. doi: 10.1038/s41541-021-00337-0

39. Fiedler S, Piziorska MA, Denninger V, Morgunov AS, Ilsley A, Malik AY, et al. Antibody affinity governs the inhibition of sars-Cov-2 Spike/Ace2 binding in patient serum. *ACS Infect Dis* (2021) 7(8):2362–9. doi: 10.1021/acsinfecdis.1c00047

40. Murray JB, Roughley SD, Matassova N, Brough PA. Off-rate screening (Ors) by surface plasmon resonance. an efficient method to kinetically sample hit to lead chemical space from unpurified reaction products. *J Med Chem* (2014) 57(7):2845–50. doi: 10.1021/jm401848a

frontiers | Frontiers in Immunology

TYPE Original Research
PUBLISHED 13 March 2023
DOI 10.3389/fimmu.2023.1112816

Check for updates

OPEN ACCESS

EDITED BY
P Bernard Fourie,
University of Pretoria, South Africa

REVIEWED BY
Xiancai Rao,
Army Medical University, China
Hardik Patel,
Seattle Children's Research Institute, United States

*CORRESPONDENCE
Chunhui Li
lichunhui@csu.edu.cn
Anhua Wu
xywuanhua@csu.edu.cn
Pinhua Pan
pinhuapan668@csu.edu.cn

†These authors have contributed equally to this work

SPECIALTY SECTION
This article was submitted to Vaccines and Molecular Therapeutics, a section of the journal Frontiers in Immunology

RECEIVED 30 November 2022
ACCEPTED 21 February 2023
PUBLISHED 13 March 2023

CITATION
Tan C, Zhu F, Pan P, Wu A and Li C (2023) Development of multi-epitope vaccines against the monkeypox virus based on envelope proteins using immunoinformatics approaches. *Front. Immunol.* 14:1112816. doi: 10.3389/fimmu.2023.1112816

COPYRIGHT
© 2023 Tan, Zhu, Pan, Wu and Li. This is an open-access article distributed under the terms of the Creative Commons Attribution License (CC BY). The use, distribution or reproduction in other forums is permitted, provided the original author(s) and the copyright owner(s) are credited and that the original publication in this journal is cited, in accordance with accepted academic practice. No use, distribution or reproduction is permitted which does not comply with these terms.

Development of multi-epitope vaccines against the monkeypox virus based on envelope proteins using immunoinformatics approaches

Caixia Tan[1,2†], Fei Zhu[2,3,4,5,6†], Pinhua Pan[2,3,4,5,6*], Anhua Wu[1,2*] and Chunhui Li[1,2*]

[1]Department of Infection Control Center of Xiangya Hospital, Central South University, Changsha, Hunan, China, [2]National Clinical Research Center for Geriatric Disorder, Xiangya Hospital, Changsha, Hunan, China, [3]Department of Respiratory Medicine, National Key Clinical Specialty, Branch of National Clinical Research Center for Respiratory Disease, Xiangya Hospital, Central South University, Changsha, Hunan, China, [4]Center of Respiratory Medicine, Xiangya Hospital, Central South University, Changsha, Hunan, China, [5]Hunan Engineering Research Center for Intelligent Diagnosis and Treatment of Respiratory Disease, Changsha, Hunan, China, [6]Clinical Research Center for Respiratory Diseases in Hunan Province, Changsha, Hunan, China

Background: Since May 2022, cases of monkeypox, a zoonotic disease caused by the monkeypox virus (MPXV), have been increasingly reported worldwide. There are, however, no proven therapies or vaccines available for monkeypox. In this study, several multi-epitope vaccines were designed against the MPXV using immunoinformatics approaches.

Methods: Three target proteins, A35R and B6R, enveloped virion (EV) form-derived antigens, and H3L, expressed on the mature virion (MV) form, were selected for epitope identification. The shortlisted epitopes were fused with appropriate adjuvants and linkers to vaccine candidates. The biophysical andbiochemical features of vaccine candidates were evaluated. The Molecular docking and molecular dynamics(MD) simulation were run to understand the binding mode and binding stability between the vaccines and Toll-like receptors (TLRs) and major histocompatibility complexes (MHCs). The immunogenicity of the designed vaccines was evaluated via immune simulation.

Results: Five vaccine constructs (MPXV-1-5) were formed. After the evaluation of various immunological and physicochemical parameters, MPXV-2 and MPXV-5 were selected for further analysis. The results of molecular docking showed that the MPXV-2 and MPXV-5 had a stronger affinity to TLRs (TLR2 and TLR4) and MHC (HLA-A*02:01 and HLA-DRB1*02:01) molecules, and the analyses of molecular dynamics (MD) simulation have further confirmed the strong binding stability of MPXV-2 and MPXV-5 with TLRs and MHC molecules. The results of the immune simulation indicated that both MPXV-2 and MPXV-5 could effectively induce robust protective immune responses in the human body.

Conclusion: The MPXV-2 and MPXV-5 have good efficacy against the MPXV in theory, but further studies are required to validate their safety and efficacy.

KEYWORDS

monkeypox virus (MPXV), multi-epitope vaccine, molecular docking, molecular dynamics (MD) simulation, immunoinformatics

1 Introduction

Monkeypox is a zoonotic disease caused by an enveloped double-stranded DNA (dsDNA) virus known as monkeypox virus (MPXV), which belongs to the Orthopoxvirus genus of the Poxviridae family (1). Most cases of monkeypox present with mild disease symptoms, such as fever, rash, lymphadenopathy and intense asthenia, but certain population groups (children, pregnant women, and immunocompromised individuals) may suffer from severe disease or complications, including secondary bacterial infections, pneumonitis, respiratory distress, sepsis, encephalitis and even loss of vision following cornea infection (2). The MPXV was first identified in humans in 1970 (3). Since then, sporadic cases have been detected from time to time, but most of them were confined to West and Central African nations, or have a history of travel to African countries or exposure to imported animals (3). However, since May 2022, there has been a sharp increase in the number of MPXV infections worldwide, with the majority of confirmed cases occurring in countries that have not historically reported human monkeypox, and there are no obvious links between the documented cases in different countries (4). As of 13 November 2022, a total of 79,411 laboratory-confirmed monkeypox cases and 50 deaths have been reported in 109 countries, according to WHO (5). However, aside from several antiviral drugs for smallpox (Tecovirimat, cidofovir, and brincidofovir) that can be used to treat monkeypox under certain conditions, there is no proven post-exposure treatment (6). Hence, an effective vaccination against MPXV is warranted.

To date, there is no specialized vaccine against MPXV, but a small study based on previous African data estimated that the smallpox vaccine may provide approximately 85% cross-protection against MPXV (7). There are several available smallpox vaccines, including ACAM20, MVA-BN and LC16. ACAM2000, a live vaccinia virus-based preparation, and MVA-BN, a non-replicating smallpox vaccine, were both licensed by the US Food and Drug Administration (FDA) for active immunization against smallpox (8). However, the former may lead to secondary vaccinia infection in vaccine recipients and those in close contact with them, and some vaccine recipients may develop myocarditis or pericarditis (8). Although data from human immunogenicity trials and pre-clinical studies suggested that the later might offer some protection against MPXV in humans, no large-scale clinical study has been conducted to determine its actual level of protection against monkeypox infection in humans (8). Similar to MVA-BN, LC16 is a live, non-replicating attenuated vaccine, that was approved for the prevention of monkeypox in August 2022 in Japan (8). Also, its efficacy against monkeypox is extrapolated from data from animal studies rather than direct human trials. So, in short, there are research gaps in the monkeypox vaccine research that needs to be filled.

The multi-epitope vaccine, a novel type of vaccine developed in recent decades, has shown good immune effects against microbial infections and has fewer side effects than traditional vaccines in animals and early clinical trials (9). The application of immunoinformatics in vaccine development offers a more effective, cost-effective, and time-saving approach to developing vaccines for infectious diseases (10). The selection of targets is crucial for developing effective multi-epitope vaccines. Since no specific receptor for MPXV on the host cell membrane has been found so far, several envelope proteins, playing a key role in the invasion of host cells by MPXV, may be attractive targets for MPXV vaccine development (11, 12). A35R, homologous to vaccinia virus A33R, is an envelope glycoprotein of EV and is required for the formation of actin-containing microvilli and virion transmission between cells (13). B6R, located both on the membranes of infected cells and on the enveloped virion (EV) envelope, is similar to the complement control protein-like B5R of the vaccinia virus. Mice immunized with a subunit vaccine containing B5 could produce anti-B5 antibodies capable of neutralizing extracellular viruses, and destroying infected cells, according to Paran et al (14). Of note, existing neutralization tests demonstrate only the antibody reaction to B5 is available for neutralizing EV (14). Studies have shown that mice immunized with H3L can produce anti-H3L antibodies that protect them from a lethal dose of vaccinia virus (15). In addition, H3L can be recognized as an antigen by CD8+ T cells (16). Given the above, A35R, B6R, and H3L are attractive targets for MPXV vaccine development.

A recent study found that MPXV has an high mutation rate, which was 6 to 12 times higher than previously believed, and some of these mutations led to stronger MPXV infectivity (17).To provide broader protection against different strains of MPXV, three reference strains from three different epidemic phases of monkeypox were selected as the research objects, and the A35R, B6R and H3L of virus strains were selected as the protein targets to develop a promising multi-epitope vaccine using the immunoinformatics approaches.

2 Methodology

2.1 Data retrieval and sequence alignment

The amino acid sequences of A35R, B6R and H3L of three strains (Zaire-96-I-16, 2001, GenBank: GCA_000857045.1; MPXV-UK_P2, 2018, GenBank: MT903344.1; 2022 reference strain, GenBank: GCA_014621545.1) were obtained in FASTA format from National Center for Biotechnology Information (NCBI) (https://www.ncbi.nlm.nih.gov/) database. To identify the common and specific sites of the single protein from different strains, we performed alignment of the target protein sequences from three objective MPXV strains using the Clustal Omega program (https://www.ebi.ac.uk/Tools/msa/clustalo/) available on the EMBL-EBI server. The visualization of the results of sequence alignment performed by Jalview v 2.11 software (18).

2.2 Prediction and selection of epitope

2.2.1 Prediction and selection of cytotoxic T lymphocyte epitope

The NetCTL 1.2 server (https://services.healthtech.dtu.dk/service.php?NetCTL-1.2) (19) was utilized to predict the Cytotoxic T Lymphocyte (CTL) epitopes restricted to 12 major histocompatibility complex (MHC) class I supertypes (A1, A2, A3, A24, A26, B7, B8, B27, B39, B44, B58, and B62). This method combines the prediction of peptide MHC class I binding, proteasomal C terminal cleavage and Transporter associated with Antigen processing (TAP) transport efficiency (19), and only epitopes with a combined score ≥0.75 were chosen for antigenicity testing using the VaxiJen v2.0 server (http://www.ddg-pharmfac.net/vaxijen/VaxiJen/VaxiJen.html) (20). VaxiJen allows antigen classification entirely based on protein physicochemical properties, overcoming the limitations of alignment-dependent methods. The accuracy of the VaxiJen in predicting the protective antigen of the virus is 70% (20). To minimize the toxicity and allergenicity of the vaccine and improve the safety of the vaccine, ToxinPred2 (https://webs.iiitd.edu.in/raghava/toxinpred2/algo.html), with an accuracy of 95.54% (21), and AllerTOP v. 2.0 (https://www.ddg-pharmfac.net/AllerTOP/index.html) (22), with an accuracy of 85.3%, were used to predict the toxicity and allergenicity of the epitopes, respectively.

The strength of immunogenicity reflects the ability of the antigen to induce an immune response. Class-I Immunogenicity tool hosted in IEDB (http://tools.iedb.org/immunogenicity/) (23) is considered to be able to predict the immunogenicity of peptides to some extent. So, the antigenic epitopes were further submitted to the Class-I Immunogenicity tool to check their immunogenicity. T cells require the detection of epitopes on MHC molecules to be activated and to exert their effector activity. The Tepitool tool (http://tools.iedb.org/tepitool/) (24) provided on Immune Epitope Database (IEDB) helps to predict the affinity between the peptide and class I human leukocyte antigen (HLA) alleles, and the IC50 is an indicator to evaluate the binding affinity of the HLA molecule to a peptide. Hence, The CTL epitopes with antigenicity, immunogenicity, non-allergenicity and non-toxicity were submitted to the Tepitool tool, and the default threshold IC50 (affinity) ≤ 500nM was used as the screening criteria.

2.2.2 Prediction and selection of helper T lymphocyte epitope

The NetMHCIIpan-4.1 server (https://services.healthtech.dtu.dk/service.php?NetMHCpan-4.1) (25), appearing stronger predictive power for the prediction of HTL epitopes and class II MHC molecules compared to other servers, was employed to predict the (Helper T Lymphocyte) HTL epitopes that possess a good affinity to 14 HLA class II alleles (HLA-DRB1*01:01, HLA-DRB1*03:01, HLA-DRB1*04:01, HLA-DRB1*04:04, HLA-DRB1*04:05, HLA-DRB1*07:01, HLA-DRB3*02:02, HLA-DRB1*09:01, HLA-DRB1*11:01, HLA-DRB1*13:02, HLA-DRB1*15:01, HLA-DRB3*01:01, HLA-DRB4*01:01, HLA-DRB5*01:01) covering 95% of the world's the population. For each HTL epitope, the IC50 and percentile rank were determined, and the epitopes with an IC50 ≤500 and a percentile rank ≤ 5% were selected for antigenicity, toxicity and allergenicity prediction *via* VaxiJen v2.0, ToxinPred2 and AllerTOP v. 2.0 servers, respectively. Interferon-gamma (IFN-γ) plays an essential role in viral clearance and the activation of the host immune response (26). In addition to regulating B cell growth and immunoglobulin secretion, interleukin 4(IL-4) also influences T cell differentiation (27). Interleukin 2(IL-2) is also a multifunctional cytokine that helps T cells grow, proliferate, and differentiate and potently enhances the function of B-cells (28). Hence, the selected HTL epitopes were further submitted to IFNepitope (http://crdd.osdd.net/raghava/ifnepitope/) (29), IL4Pred (http://crdd.osdd.net/raghava/il4pred/) (30) and IL2Pred (https://webs.iiitd.edu.in/raghava/il2pred/) (31) servers to assess their potential to induce IFN-γ, IL-4, and IL-2 secretion, and only epitopes that induce IFN-γ production and at least IL-2 or IL-4 production would be ultimately considered for vaccine construction.

2.2.3 Prediction and selection of B-cell epitope

The ABCpred (https://webs.iiitd.edu.in/raghava/abcpred/) was applied to predict linear B-cell epitopes based on recurrent neural network (RNN). The 16 amino acids were selected as the window length (32). As with T-cell epitopes, the antigenicity was checked by VaxiJen v2.0, and only epitopes with an antigenicity over 0.8 were further submitted to AllerTOP v. 2.0 and ToxinPred2 servers to check their allergenicity and toxicity, respectively.

2.2.4 Population coverage prediction of T cell epitopes

Population coverage in different regions is one of the important indicators in measuring the effectiveness of the vaccine. And its level

size is mainly affected by the distribution and expression frequency of the HLA alleles that bind to the multi-epitope vaccine. To increase the population coverage of limited length multi-epitope vaccine, we calculated the world population coverage for each selected CTL and HTL epitope using the IEDB's population coverage tool (http://tools.iedb.org/population/) (33), and only epitopes with a world population coverage greater than 5% were subjected to further analysis.

2.2.5 Homology analysis of selected epitopes with human proteomes

The Peptide match server can quickly and accurately match the submitted peptides with the UniProtKB Human complete proteome (34). To avoid inducing host autoimmune diseases and cross-reactions, each selected epitope was further submitted to the Peptide match server (https://research.bioinformatics.udel.edu/peptidematch/index.jsp) (34) to check their homology to the human proteome, and only the epitopes are non-homologous to the human proteome were selected for vaccine construction.

2.3 Molecular docking of T-cell epitopes with major histocompatibility complex molecules

MHC molecules are essential for presenting the pathogen-derived peptides to the respective T cells. Thus, it is necessary to perform molecular docking between T-cell epitopes and MHC molecules to understand the possible binding mode between them. First, the PEP-FOLD 3.5 server (https://bioserv.rpbs.univ-paris-diderot.fr/services/PEP-FOLD3/) (35)was used to model the three-dimensional (3D) structure of T-cell epitopes as the ligand, and RCSB Protein Data Bank (RCSB PDB) website (https://www2.rcsb.org/search/advanced/sequence) (36) was employed to acquire the 3D structure of MHC molecules as for the receptor. For some class I and class II MHC molecules for which the 3D structures are unavailable on the RCSB PDB website, we use the 3D structures of HLA-A*02:01 and HLA-DRB1*01:01 as the substitutes, respectively. Then, the energy minimization of receptors and ligands was carried out by Swiss-PdbViewer PDB viewer software (37), and following that, the molecular docking was run by Autodock Vina software hosted in PyRx v0.8 (38). AutoDock Vina, a classic molecular docking tool, has better performance for the prediction of docking between small molecules and proteins (39). The docking results were further analyzed using LigPlot+ v.2.2 software (40). Furthermore, to comparatively evaluate of binding affinity between the selected epitopes and MHC molecules, the molecular dockings between seven experimental verified antigen epitopes of poxvirus and HLA-A*02:01 molecules were selected as the positive controls.

2.4 Design of multi-epitope vaccine constructs

All T-cell and B-cell epitopes that satisfied the filtration criteria were incorporated into the construction of the multi-epitope vaccine. The linker is an essential part of recombinant fusion proteins, which is capable of forming effective epitope conjugation between epitopes and allowing the independent immunological activities of the epitopes (41). Low immunogenicity is a major deficiency of multi-epitope vaccines. According to the previous study, a suitable adjuvant molecule can significantly boost the peptide vaccine's immunogenicity and longevity (42). 50s ribosomal protein L7/L12 from Mycobacterium tuberculosis is capable of promoting DC maturation and diverse pro-inflammatory cytokine production *via* interacting with TLR4, which helps enhance cellular immunity (43). In addition to direct antiviral activity, β-defensins can regulate adaptive immunity to viral infection by recruiting naive T cells and immature dendritic cells (DCs) to the infected site (44). LT-IIC, a type II heat-intolerant enterotoxin (HLT) produced by Escherichia coli (*E.coli*), is an attractive adjuvant with the unique property of enhancing the body's humoral and cellular immune responses to co-administered antigens (45). The Cholera Toxin B subunit (CTB) is also considered an attractive adjuvant due to its ability to efficiently bind to antigen-presenting cells and enhance the stability and half-life of the entire vaccine molecule (46). RS09, an LPS peptide mimic, is an agonist of TLR4. When used as an adjuvant in certain vaccines, it is capable of resulting in stronger immune activation and higher antibody production (47). All five adjuvants have been widely used in the design of multi-epitope vaccines in silico (48–51) and have been shown to stimulate the host's immune response in animal experiments (43, 45, 52–54). So, in this study, each of the five adjuvants was added to the N-terminus of the vaccine using EAAAK liners, resulting in the formation of five vaccine constructs. Afterward, the PADRE sequence was linked to the adjuvant with the help of the EAAAK linker. When added to the vaccine construct, the PADRE, which can bind to most common HLA-DR molecules with high affinity, has been shown to optimize antibody responses and deliver significant helper T-cell activity *in vivo* (55). The CTL epitopes were connected by AAY linkers, the HTL epitopes were linked using GPGPG linkers, and the B-cell epitopes were spaced with the help of KK linkers. The last CTL epitope was linked to the first HTL epitope and the first HTL epitope was connected to the first B-cell-epitopes using the HEYGAEALERAG linker. Finally, the "6xHis tag" was appended to the C-terminal of the vaccine construct *via* the RVRR linker to facilitate protein purification but not affect the functionality of the fusion protein.

2.5 Prediction of biophysical and biochemical features of the multi-epitope vaccine constructs

2.5.1 Prediction of antigenicity, allergenicity, toxicity and physicochemical properties of the vaccine

To determine the ability of the vaccine constructs to bind to immune cell receptors (antigenicity), both the VaxiJen and the ANTIGENpro (http://scratch.proteomics.ics.uci.edu/) servers were employed. The allergenicity of the vaccine was assessed using

AllerTOP v. 2.0 server. The vaccine's toxicity was predicted by the ToxinPred2 server. The physicochemical properties of vaccine constructs, including molecular weight, the number of amino acids, theoretical isoelectric point (pI), estimated half-life, instability index, aliphatic index, and grand average of hydropathicity (GRAVY) index, were predicted using ProtParam tool (https://web.expasy.org/protparam/) (56).

2.5.2 The prediction of transmembrane domains, probability of solubility, and signal peptide sequence of the vaccine

Since most amino acids constituting transmembrane region proteins are hydrophobic amino acids and membrane proteins cannot be expressed in prokaryotic expression systems, it is necessary to predict the transmembrane sequence of vaccines. The DeepTMHMM (https://dtu.biolib.com/DeepTMHMM) server, which is the most complete and best-performing method for the prediction of the topology of both alpha-helical and beta-barrel transmembrane proteins (57), was employed to predict the transmembrane domains of the vaccine. Many experimental studies are hampered by protein insolubility. The SOLpro server (http://scratch.proteomics.ics.uci.edu/) (58) can accurately predict the probability of solubility in *E. coli* of the protein upon overexpression. So, all designed vaccines were submitted to the SOLpro server to predict their solubility. To avoid the amino acid sequence of the vaccine from being cut off by signal peptidase as a signal peptide, the signalP-6.0 online server(https://services.healthtech.dtu.dk/service.php?SignalP-6.0) (59) was utilized to predict whether a vaccine has signal peptides, as well as the location of their cleavage sites.

2.6 Secondary structure prediction, tertiary structure modeling, refinement, and validation

Out of all vaccine constructs, only antigenic, non-allergenic, non-toxic, stable, hydrophilic, thermostable, without transmembrane domains and signal peptide sequence, and highly soluble constructs were further submitted to the PSIPRED 4.0 server (http://bioinf.cs.ucl.ac.uk/psipred/) to obtain its secondary structure. The PSIPRED 4.0 server performed protein secondary structure prediction based on position-specific scoring matrices with a prediction accuracy of over 84% (60). The tertiary structures of the vaccine constructs were modeled using the Robetta server (http://robetta.bakerlab.org). Based on the fact that a confident template for the putative domains of a submitted sequence is available or unavailable, this server performs comparative modeling or *de novo* modeling, respectively (61). And this server will generate five models of each submitted sequence. Then, the optimal crude 3D models of each vaccine sequence were submitted to the GalaxyRefine module placed in the GalaxyWEB server(https://galaxy.seoklab.org/), which can rebuild unreliable loops or termini of the initial model structures using an optimization-based refinement method and further generate five refined models of each crude model (62). Referring to the criterion that the better model with a lower MolProbity score, we picked the best 3D refined model for each vaccine construct and submitted it to the ERRAT tool, PROCHECK tool of structure validation service SAVES v6.0 (https://saves.mbi.ucla.edu/) and ProSA-Web server (https://prosa.services.came.sbg.ac.at/prosa.php) for quality verification. The overall quality factor generated by the ERRAT program is the number of non-bonded interactions (side chains) formed between pairs of different atomic types within 0.35nm, and models with an overall quality factor value greater than 85 are generally considered to have good quality (63). The Ramachandran plot generated by the PROCHECK tool checks the stereochemical quality of the protein structure, and a better model has more residues in the Ramachandran-favored region and fewer residues in the Ramachandran-disallowed region. The Z-score predicted by the ProSA-Web server reflects the overall quality of the model, and a positive Z-score indicates the input structure has problematic or erroneous parts (64).

2.7 Molecular docking

Stable interaction between the vaccine candidate and immune receptor is an important precondition to generating successful immune reactions. The TLRs not only hold a vital position in the first line of defense against pathogens but also play a vital role in linking innate immunity with adaptive immunity (65). Previous studies revealed that TLR2 and TLR4 can induce antiviral immune responses by detecting the virus coat proteins (66, 67). Class I and class II MHC molecules help the CD4+ T and CD8+ T cells recognize foreign antigens(vaccine). Therefore, the molecular docking of the vaccine candidates with TLRs (TLR2, TLR4) and MHCs (HLA-A*02:01, HLA-DRB1*01:01) was performed using the ClusPro 2.0 server (https://cluspro.bu.edu/login.php) (68). Since 2004, ClusPro has consistently been one of the best docking servers as demonstrated in Critical Assessment of Predicted Interactions (CAPRI), providing high predictive performance for the docking of protein-protein complexes (68). In each docking case, a total of thirty models were generated, and ten models with highly populated clusters were presented. Then, the best model in each docking case was further submitted to the HADDOCK 2.4 server (https://wenmr.science.uu.nl/haddock2.4/) (69), which is capable of refining the complex structures by rearranging the side-chain in the restricted interface and optimizing soft rigid-body, for refinement. After refinement, the docked models were submitted to the PRODIGY server (https://bianca.science.uu.nl/prodigy/) (70) for predicting binding energy. Furthermore, the PDBsum server (http://www.ebi.ac.uk/thornton-srv/databases/cgi-bin/pdbsum/GetPage.pl?pdbcode=index.html) (71) was utilized to investigate interacting residues between docked chains (i.e., the vaccines, the TLRs and MHCs). The PyMOL v2.5 was used to visualize the vaccine-receptor complex (72), and the Blender v3.3 software was employed to render the final image (73).

2.8 Molecular dynamics simulation and MM-PBSA analysis

2.8.1 Molecular dynamics simulation

The Molecular dynamics (MD) simulations of several complexes with better docking results were conducted using the Gromacs v2022.1 software (74), which is helpful in better understanding the dynamics and structural stability of the docking complexes. In the preprocessing stage, the Amber14SB _parmbsc1 force field parameters were added to the complex system to obtain the coordinate file and topology file of the vaccine-receptor complexes (75). Subsequently, each system was solvated using the transferable intermolecular potential 3P (TIP3P) water model, following being neutralized with Cl- ions, leaving the topological and structural coordinates in a steady state. Following this preprocessing, energy minimization was performed for the entire protein complex system; Then, under the NVT ensemble, each system was gradually heated from 0K to 310 K, and the modified Berendsen thermostat was used to equilibrium temperature (76). Then, in the NPT ensemble, the pressure of the system was adjusted to 1atm with regulating of Parinello-Rahman barostat (77). Finally, a 50ns MD simulation was run for all docking complex systems, adopting constant temperature and pressure. The LINCS algorithm (78) and the PME (Particle mesh Ewald) method (79) were used to constrain the hydrogen bond and calculate the long-range electrostatic energy, respectively. After 50ns MD simulation, the post-MD simulation analyses of the MD trajectories were performed, including the root mean square deviation (RMSD) of each system, each system chain's root mean square fluctuation (RMSF), the radius of gyration (Rg) and hydrogen bonds of each system.

Then, the trajectories of the last 20ns were extracted for further analysis. In addition to classic MD analysis, the conformational free energy of each complex was studied at the transient stages *via* studying free energy landscapes (FELs) (80). The PCA was run using gmx covar and gmx anaeig programs, and the PC1 and PC2 were further used to calculate and analyze Gibb's free energy landscape (Gibb's FEL) with the gmx sham program (80). Gibb's FEL plots were generated using the DuIvyTools (DOI:10.5281/zenodo.6340263). In Gibb's FEL plots, the stable energy states were shown blue. In addition, the correlations between the position fluctuations of each residue in the vaccine chain and the position fluctuations of each residue in the receptor chain were analyzed with the dynamical cross-correlation (DCC) analysis by the Bio3D package in the R v4.22 software.

2.8.2 MM-PBSA calculations

The Gmx_MMPBSA v1.52 tool was applied to calculate the binding free energy between the vaccine and the receptors using Poisson–Boltzmann and surface area continuum solvation (MM-PBSA) method (81), and the calculation formula is as follows:

$$\Delta G_{bind,slov} = \Delta G_{bind,vaccum} + \Delta G_{slov,complex} - (\Delta G_{solv,\,ligand} + \Delta G_{solv,receptor})$$

2.9 Population coverage

More than a thousand distinct HLA alleles have been identified in humans, and the frequency of distribution of each HLA allele varies across regions and ethnicities. Given that T lymphocytes can only recognize molecular complexes composed of epitopes bound to MHC molecules, a particular epitope triggers immune responses only in individuals expressing HLA alleles with an affinity for this epitope. The IEDB population coverage tool (http://tools.iedb.org/population/) was employed to calculate the population coverage of the designed vaccine in this work based on the data of TCR specificity, HLA restriction, and HLA allele frequencies.

2.10 Immune simulation

For assessing the potential immune efficacy of the designed vaccine, we submitted it to the C-IMMSIM v10.1 tool (https://kraken.iac.rm.cnr.it/C-IMMSIM/) (82). The C-IMMSIM server recognizes epitopes by Position Specific Scoring Matrix (PSSM) methods, and can simultaneously stimulate the immune response of three compartments that represent three separate anatomical regions found in mammals (the bone marrow, the thymus and lymph nodes) to antigen epitopes. During the immune simulation, all parameters except for time steps were left at their default settings. In this study, the simulation time steps were set to 1050 (1-time step equals 8 h), and each injection point was set at time steps 1, 84, and 168, respectively. The default dose of each antigen injection was 1,000, and the time interval between each dose was four weeks, which is the recommended interval between injections for most commercial vaccines. To comparatively evaluate the candidate vaccine's immunogenicity, a novel multi-epitope vaccine against Echinococcus granulosus, whose antigenicity and immunogenicity had been verified *in vitro* and *in vivo* experiments (83), was chosen as a positive control.

2.11 Codon optimization and *in silico* cloning

Due to the degeneracy of codons, each amino acid may correspond to multiple codons. However, there are great differences in codon preference among different species and organisms. To acquire the codon that is capable of efficiently encoding the targeted amino acid in the selected expression host, the codon optimization of the vaccine was conducted using the JCat server (http://www.jcat.de/CAICalculation.jsp) (84). The JCat server is an easy-to-use program, which can perform real-time calculations, eliminate the need for the definition of highly expressed genes, and avoid cleavage sites for specific restriction enzymes (84). The Escherichia coli (*E. coli*) K12 strain was selected as the expression host. Two parameters, codon adaptation index (CAI), and the percentage of GC content, were used to evaluate the expression efficiency of the vaccine in E. coli. The CAI, with a value range of 0 to

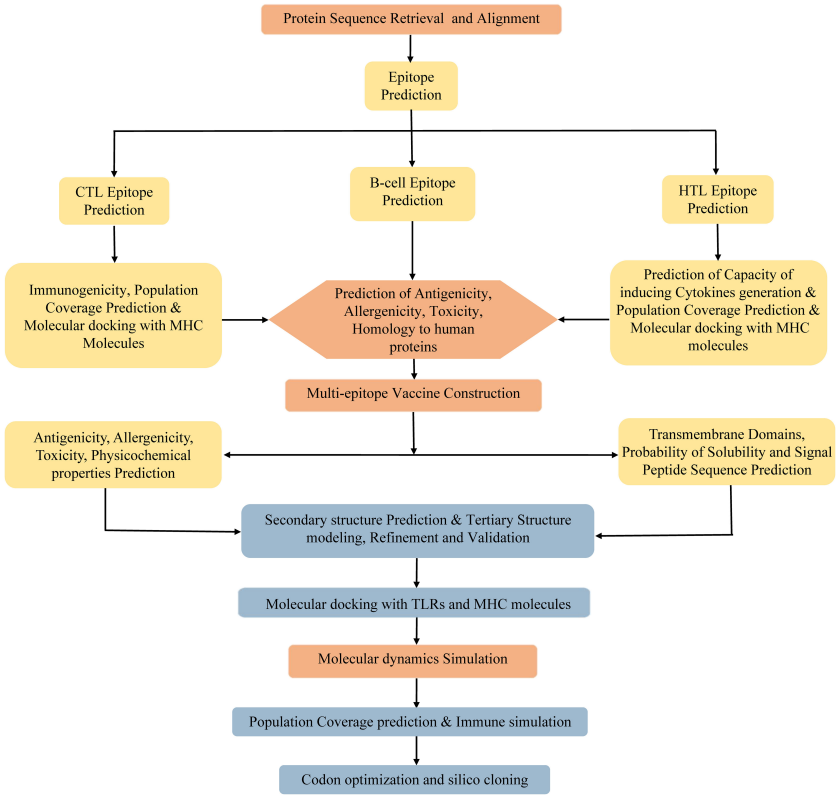

FIGURE 1
Flowchart of the multi-epitope vaccine design.

1, refers to the coincidence degree between synonymous codons and optimal codons, and a higher CAI indicates a higher expression level of the foreign gene in the host. The percentage of GC content represents the guanine (G)+cytosine (C) ratio in the DNA sequence, and its optimal range is 30%–70%. Otherwise, undesirable gene expression levels and transcriptional efficiency will result. Afterward, the BamHI and XhoI restriction endonuclease sites were integrated into the N- and C-terminal sites of optimized codon sequences, respectively. The entire sequence was cloned into the pET28a (+) vector using SnapGene software. Finally, the MPXV-5 vaccine protein was synthesized by Sangon Biotech co ltd (Shanghai, China). The flowchart of vaccine design is illustrated in Figure 1.

3 Result

3.1 Protein sequences retrieval and alignment

The NCBI accession numbers and amino acid sequences of A35R, B6R and H3L derived from three objective MPXV strains were presented in Supplementary Table 1. Protein sequence alignment results (Figure 2) demonstrated that there was no difference in three target protein sequences (A35R, B6R and H3L) between MPXV-UK_P2 and 2022 reference strain. Compared with the Zaire-96-I-16 MPXV strain, there were 3 mutation sites in A35R and 2 mutation sites in H3L, but no mutation sites in B6R. As shown in Figure 2, there were two mutation sites falling into the epitope regions.

3.2 Epitopes selection

The immune system is comprised of many specialized cell types, all of which work together to keep people healthy. CTLs, the main force of cellular immunity, are immune cells that can directly mediate the death of target cells and eliminate circulating antigens in the host body (85). Stimulated B cells can differentiate into antibody-producing plasma cells that play a vital role in the generation of humoral immune responses (86). HTLs, another group of immune cells, can assist both humoral and cellular immunity by secreting different cytokines (87). Hence, to construct an effective multi-epitope vaccine, both T-cell epitopes (CTL and HTL epitopes) and B-cell epitopes should be incorporated. After the layer-by-layer screening (Figure 3), a total of 7 CTL epitopes (Table 1), 6 HTL epitopes (Table 2), and 7 liner B-cell epitopes (Table 3) were finally included in the vaccine constructs. The binding affinity (IC50) of the experimentally determined poxvirus-specific T cell epitopes to HLA molecules was shown in Supplementary Table 2.

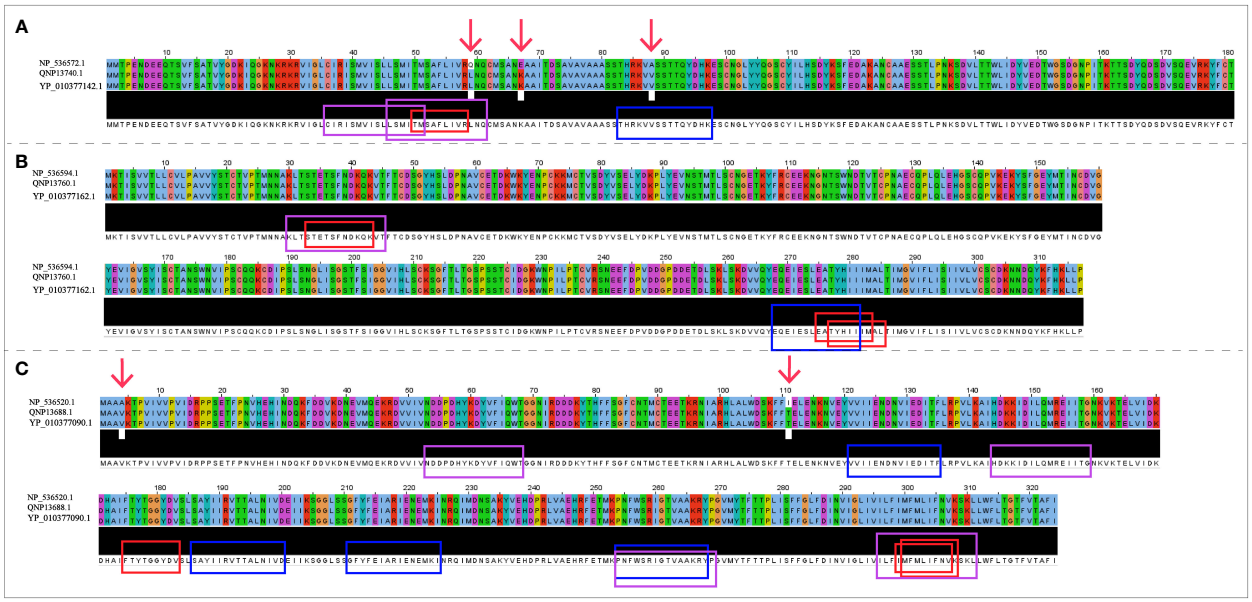

FIGURE 2
The sequence alignment of three target proteins in three selected reference strains. **(A)** The sequences of A35R; **(B)** The sequences of B6R; **(C)** The sequences of H3L; The Zaire-96-I-16 strain is selected as the reference sequence in the sequence alignment, i.e., the first-row sequences were the sequences of Zaire-96-I-16 strain, the second-row sequences were the sequences of MPXV-UK_P2 strain, and the third-row sequences were the sequences of 2022 reference strain. The red arrows refer to mutation sites; The CTL, HTL, and B cell epitopes were highlighted with red, blue and purple box lines in the sequence, respectively.

3.3 Molecular docking of the T-cell epitopes with MHC molecules

Except for only one epitope (STETSFNDK), all other epitopes had multiple binding alleles. Some had even as high as 8 (TMSAFLIVR) or 13 (FTYTGGYDV) alleles (Table 1). In this study, we performed molecular docking between each T-cell epitope and one of their corresponding alleles for a representative docking analysis (Supplementary Table 3). As shown in Supplementary Table 3, Autodock Vina docking data indicated that the binding energy between CTL epitopes and MHC class I alleles ranged from -10.2 to -5.9 Kcal/mol, and the binding energy range between HTL epitopes and MHC class II alleles was -7 to -5.8 Kcal/mol, the binding energy range between seven experimental verified antigen epitopes of poxvirus and HLA-A*02:01 molecules was -9 to -5.8 Kcal/mol, indicating the T-cell epitopes had a good affinity for MHC molecules. The predicted results of Ligplus v2.25 demonstrated that many hydrogen bonds were formed between T-cell epitopes and MHC molecules, and salt bridges were also detected in certain docking cases (Supplementary Table 3), which once again proved that T-cell epitopes had a strong affinity to MHC molecules.

3.4 Multi-epitope vaccine features

3.4.1 Prediction of antigenicity, allergenicity, and toxicity of the vaccine construct

The final multi-epitope vaccine construct was built with the following six parts: CTL epitopes, HTL epitopes, B-cell epitopes, PADRE, adjuvant and His-tag sequence. Five different adjuvants (50S ribosomal protein L7/L12, β-defensin, LT-IIC, CTB, RS09) resulted in five different vaccine constructs (Supplementary Table 4) named MPXV-1, MPXV-2, MPXV-3, MPXV-4 and MPXV-5, respectively. Except for the adjuvant, all other components of these constructs are identical. The antigenicity ranges of five vaccine constructs predicted by VaxiJen and ANTIGENpro servers were 0.62~0.69 and 0.56~0.84, respectively, which demonstrated that the five vaccine constructs can bind or interact with the immune effector cells or soluble antibodies (Table 4). Moreover, none of the five vaccine constructs were allergenic. However, the ToxinPred2 predicted results showed that MPXV-3 and MPXV-4 were toxic. So, the vaccine bodies of MPXV-3-4 and their corresponding adjuvants were separately submitted to the ToxinPred2 server, and its results revealed that the vaccine bodies were not toxic, while both adjuvants were toxic.

3.4.2 Physicochemical properties analysis of the vaccine construct

The physicochemical properties of the vaccine constructs are presented in Table 4. The molecular weight of five vaccine constructs (MPXV-1–5) was below 110 kDa, which was considered favorable for vaccine development. The theoretical pI for all vaccine constructs ranged from 8.61 to 9.56. The range of instability index (II) values for all constructs was between 34.19 and 36.62, suggesting that the constructs were stable in a test tube. In general, proteins with an instability index of less than 40 were considered to be stable. The aliphatic index is regarded as a positive factor for the increase in thermostability of globular proteins. In all developed constructs, the aliphatic index ranged from 82.25 to

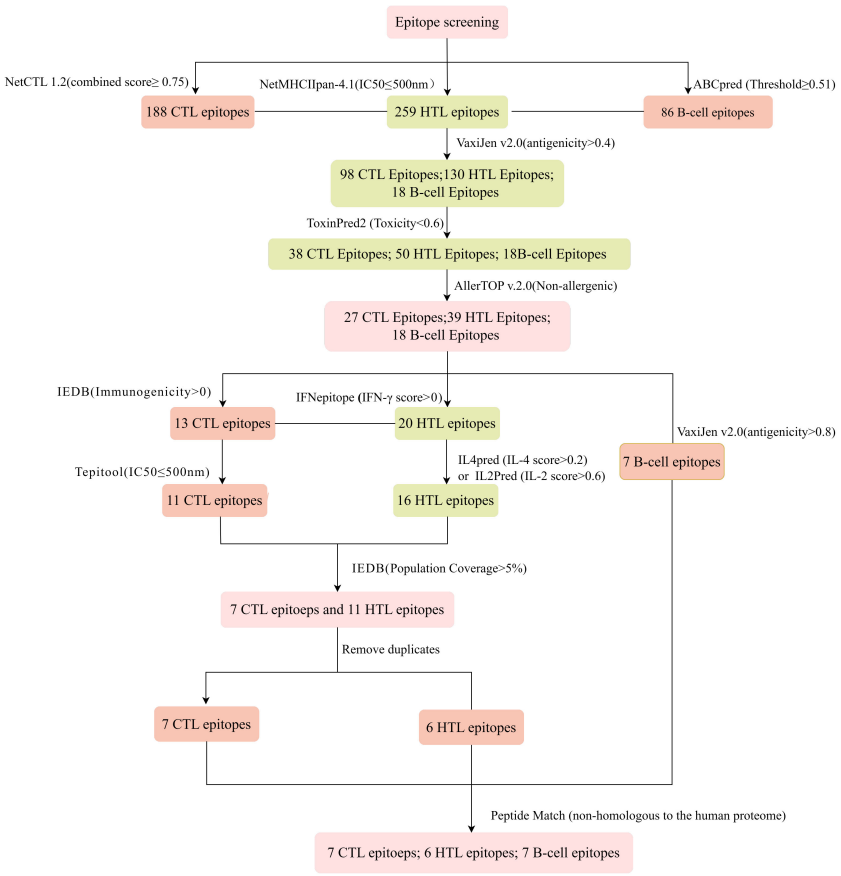

FIGURE 3
Flowchart of the epitope screening.

89.06, indicating that these constructs were thermostable. All designed vaccines have an estimated half-life of 30 hours in mammalian reticulocytes, >20 hours in yeast, and >10 hours in E. coli. The range of the GRAVY index of MPXV-1-5 was -0.19 to -0.051. The GRAVY index is correlated with protein solubility, with negative GRAVY indicating a hydrophilic molecule.

Predictions from the DeepTMHMM server showed that none of the constructed vaccines, except MPXV-1, has a transmembrane helix (Supplementary Figure 1). This may be due to the adjuvant of MPXV-1 is located inside the membrane while the vaccine body is located outside the membrane, resulting in the formation of transmembrane sequences at the bridging site between the two parts. The probabilities of being soluble upon overexpression in E. coli of five constructs were 0.975118 (MPXV-1), 0.835770 (MPXV-2), 0.610239 (MPXV-3), and 0.867569 (MPXV-4), 0.869869 (MPXV-5), respectively, which demonstrated that all vaccine constructs had good solubility when heterologous expression in E. coli. Moreover, the predicted results of the signalP-6.0 server revealed that none of the vaccines had signal peptide sequences (Supplementary Figure 2).

Based on all the above predictions about the properties of all vaccine constructs, MPXV-2 and MPXV-5 were regarded as the most ideal vaccine constructs for immunological applications. Therefore, MPXV-2 and MPXV-5 were selected for further analysis.

3.5 Secondary structure prediction of the vaccine construct

The secondary structures of the final selected vaccine constructs were predicted by the PSIPRED server and predicted results (Supplementary Figure 3) showed that the MPXV-2 contained 58.22% α-helix, 31.22% coils and 10.56% β-strands. Compared to MPXV-2, the MPXV-5 secondary structure comprised a greater proportion of α-helix (61.10%), a smaller proportion of β-strands (6.79%), with the similar proportion of coils (32.11%) (Supplementary Figure 3).

3.6 Three-dimensional structure prediction, refinement, and validation of the vaccine construct

The 3D structure of the selected vaccine constructs was predicted by the Robetta server and then refined by the GalaxyWEB server. Based on the model quality of the refined models (Supplementary Table 5), the refined model 5 (Figure 4A) for MPXV-2 and the refined model 4 (Figure 4A) for MPXV-5 were chosen for further quality validation. The corresponding Overall Quality Factors generated by the ERRAT program were 91.8465

TABLE 1 List of the CTL epitopes selected for vaccine construction.

Protein	Start position	Epitope	Antigenicity	Immunogenicity	Allergenicity	Toxicity	HLA-I alleles	IC50	Population coverage	Homology to human proteins
A35	50	TMSAFLIVR	0.5770	0.22567	NA	NT	HLA-A*31:01	20.01	52.29%	NH
							HLA-A*68:01	22.41		
							HLA-A*33:03	32.24		
							HLA-A*33:01	54.26		
							HLA-B*08:01	81.41		
							HLA-A*11:01	105.3		
							HLA-A*74:01	192.2		
							HLA-A*03:01	371.7		
B6R	275	EATYHIIIM	0.4046	0.35574	NA	NT	HLA-C*16:01	174.96	24.49%	NH
							HLA-C*12:03	239.53		
							HLA-C*03:02	370.67		
							HLA-B*35:01	410.23		
	277	TYHIIIMAL	0.4999	0.27396	NA	NT	HLA-C*14:02	14.31	44.02%	NH
							HLA-A*23:01	148.36		
							HLA-A*24:02	329.44		
							HLA-C*07:02	484.42		
	33	STETSFNDK	1.4414	0.02816	NA	NT	HLA-A*11:01	125.15	15.53%	NH
H3L	175	FTYTGGYDV	0.5030	0.1126	NA	NT	HLA-A*68:02	15.26	73.10%	NH
							HLA-A*02:06	20.57		
							HLA-C*12:03	28.93		
							HLA-C*15:02	68.73		
							HLA-C*03:02	70.97		
							HLA-C*03:03	76.09		
							HLA-C*03:04	76.09		
							HLA-C*16:01	76.1		
							HLA-A*02:01	143.89		

(Continued)

10.3389/fimmu.2023.1112816

TABLE 1 Continued

Protein	Start position	Epitope	Antigenicity	Immunogenicity	Allergenicity	Toxicity	HLA-I alleles	IC50	Population coverage	Homology to human proteins
							HLA-C*17:01	159.26		
							HLA-C*12:02	217.08		
							HLA-C*02:02	328.68		
							HLA-C*02:09	328.68		
	299	IMFMLIFNV	0.4464	0.0708	NA	NT	HLA-A*02:01	6.73	44.14%	NH
							HLA-A*02:06	15.39		
							HLA-A*32:01	322.73		
	300	MFMLIFNVK	1.1933	0.1903	NA	NT	HLA-A*33:01	105.2	20.7%	NH
							HLA-A*31:01	145.5		
							HLA-A*68:01	157.1		
							HLA-A*33:03	180.6		
							HLA-A*30:01	261.4		

NT, Non-toxic; NA, Non-allergenic; NH, Non-homologous to human proteins.

10.3389/fimmu.2023.1112816

TABLE 2 List of the HTL epitopes selected for vaccine construction.

Protein	Start position	Epitope	HLA-II alleles	IC50	Rank %	Antigenicity	Allergenicity	Toxicity	IFN-γ score	IL-4 score	IL-2 score	Population coverage	Homology to human proteins
A35	83	THRKVVSSTTQYDHK	HLA-DRB1_0405	141.45	0.29	0.7	NA	NT	0.29103344	0.34	0.591	24.24%	NH
			HLA-DRB1_0404	323.42	1.77								
			HLA-DRB1_0401	367.21	2.61								
			HLA-DRB1_0901	393.12	1.08								
B6R	268	EQEIESLEATYHIII	HLA-DRB1_0101	46.96	1.82	0.7	NA	NT	0.95981859	1.41	0.662	11.53%	NH
H3L	254	PNFWSRIGTVAAKRY	HLA-DRB1_0101	11.51	2.5	1.1	NA	NT	0.092049799	- 0.11	0.542	37.70%	NH
			HLA-DRB1_0401	26.99	0.34								
			HLA-DRB1_1101	60.33	3.18								
			HLA-DRB1_0405	68.39	1.99								
			HLA-DRB1_0404	77.11	3.37								
			HLA-DRB3_0202	428.23	4.72								
	186	SAYIIRVTTALNIVD	HLA-DRB1_0701	19.1	0.53	0.8	NA	NT	0.14153398	0.67	0.536	40.98%	NH
			HLA-DRB1_0404	29.89	1.61								
			HLA-DRB1_1501	68.69	4.39								
			HLA-DRB1_0405	69.85	4.88								
	121	VVIIENDNVIEDITF	HLA-DRB3_0101	185.04	2.68	0.6	NA	NT	0.70710024	0.31	0.602	30.81%	NH
				278.97	2.42								

(Continued)

10.3389/fimmu.2023.1112816

10.3389/fimmu.2023.1112816

TABLE 2 Continued

Protein	Start position	Epitope	HLA-II alleles	I-C5-0	Rank %	Antigenicity	Allergenicity	Toxicity	IFN-γ score	IL-4 score	IL-2 score	Population coverage	Homology to human proteins
			HLA-DRB1_0301										
			HLA-DRB3_0202	406.75	4.41								
			HLA-DRB1_0405	410.33	3.45								
	211	GFYFEIARIENEMKI	HLA-DRB1_0405	49.22	2.17	0.6	NA	NT	0.0688676505	1.36	0.478	19.34%	NH
			HLA-DRB1_1101	67.46	2.36								
			HLA-DRB1_0901	111.2	3.62								

NT, Non-toxic; NA, Non-allergenic; Epitopes with positive IFN-γ scores, predicted using SVM model, are graded as IFN-γ inducers; Epitopes with an IL-4 score >0.2 are graded as IL-4 inducers; Epitopes with an IL-2 score >0.6 are graded as IL-2 inducers; NH, Non-homologous to human proteins.

(MPXV-2-5) and 89.2105 (MPXV-5-4) (Supplementary Figure 4), and the corresponding Z-scores predicted by the ProSA-Web server were -6.94 (MPXV-2-5) and -6.36 (MPXV-5-4) (Figure 4B). The Ramachandran plot analysis of the refined model MPXV-2-5 revealed that 92.3% of residues located in the most favorable region, 6.4% in the allowed region, and only 1.3% in the disallowed region (Figure 4C). For the refined model MPXV-5-4, 92.4% of residues suited in the most favored region, 6.4% in the allowed region, and only 1.2% of residues in the disallowed regions (Figure 4C). The above analysis confirmed the excellent quality of the refined 3D models of the MPXV-2 and MPXV-5 vaccine constructs.

3.7 Molecular docking

The ClusPro generated thirty clusters in each docking case, and the best one with the largest cluster size in each docking case was selected to present (Table 5). Table 5 displayed the detailed docking results for all refined docking complexes. Compared with the MPXV-2-immune receptor complexes, all corresponding MPXV-5-immune receptor complexes had lower docking scores and binding energy, indicating that MPXV-5 had stronger affinity for all immune receptors (TLR2, TLR4, HLA-A*02:01 and HLA-DRB1*01:01). The predicted results of the PDBsum server (Figure 5; Supplementary Figure 5 and Table 5) showed that 6 hydrogen bonds, 11 hydrogen bonds and 2 salt bridges, 12 hydrogen bonds and 1 salt bridges, 16 hydrogen bonds and 6 salt bridges were formed in MPXV-2-TLR2, MPXV-2-TLR4, MPXV-2-HLA-A*02:01 and MPXV-2-HLA-DRB1*02:01 complexes, respectively. There are 12 hydrogen bonds with 3 salt bridges, 18 hydrogen bonds with 3 salt bridges, 12 hydrogen bonds with 3 salt bridges, and 12 hydrogen bonds with 5 salt bridges in MPXV-5-TLR2, MPXV-5-TLR4 and MPXV-5-HLA-A*02:01 and MPXV-HLA-DRB1*02:01 complexes, respectively (Figure 5; Supplementary Figure 5 and Table 5). Docking studies showed that there were significant interactions between the designed vaccines (MPXV-2 and MPXV-5) and the immune receptors.

3.8 Molecular dynamics simulation

3.8.1 Root mean square deviation, root mean square fluctuation radius of gyration and hydrogen bonds analyses

RMSD can be used to measure changes in protein structure during MD simulations compared to the starting point. A leveling off of the RMSD curve can also indicate that the protein structure has equilibrated. The RMSD value of all MPXV-2-receptors complexes (MPXV-2-TLR2, MPXV-2-TLR4, MPXV-2-HLA-A*01:01) increased gradually in the range of 1-20ns and then maintained the level of about 1.3nm, 0.9nm, 1.0nm, respectively (Figure 6A). The average RMSD value of the MPXV-5-TLR2 was 0.82nm (Figure 6B), and several small fluctuations in RMSD value were observed. The average RMSD value of MPXV-5-TLR4 complex was the highest among all complexes, which was 1.51nm

TABLE 3 List of the B-cell epitopes selected for vaccine construction.

Protein	Start position	Epitope	Antigenicity	Toxicity	Allergenicity	Homology to human proteins
A35	36	CIRISMVISLLSMITM	1.1317	NT	NA	NH
	46	LSMITMSAFLIVRQNQ[a]	0.8507	NT	NA	NH
B6R	30	KLTSTETSFNDKQKVT	1.1997	NT	NA	NH
H3L	53	NDDPDHYKDYVFIQWT	0.9084	NT	NA	NH
	144	HDKKIDILQMREIITG	0.8853	NT	NA	NH
	254	PNFWSRIGTVAAKRYP	1.0417	NT	NA	NH
	296	ILFIMFMLIFNVKSKL	1.2217	NT	NA	NH

Epitope[a]: The epitope only appears in the Zaire-96-I-16 strain. NT, Non-toxic; NA, Non-allergenic; NH, Non-homologous to human proteins.

(Figure 6B). The RMSD value of the MPXV-5-HLA-A*01:01 complex stabilized at about 20 ns of the MD simulation with an average value of 1.05 nm (Figure 6B).

The radius of gyration (Rg) is defined as the distribution of atoms of a protein around its axis and can be used to characterize the compactness of molecules. To some extent, it can characterize the overall changes in the ligand structure upon binding to the receptor protein. In this study, the RG values of MPXV-2-TLR4 and MPXV-2-HLA-A*02:01 complex systems were all kept at a relatively constant level (Figure 6C), indicating that the protein complex system was relatively stable with no obvious conformational change. The RG value of the MPXV-2-TLR2 complex initially maintained a stable level, began to decline at about 9 ns and reached a stable level again at about 22 ns (Figure 6C). The RG values of all MPXV-5-receptors complexes (MPXV-5-TLR2, MPXV-5-TLR4, MPXV-5-HLA-A*01:01) fluctuated slightly in the initial phase, and keep stable at about 20ns of the MD simulation (Figure 6D).

RMSF is a measurement of individual residue flexibility and the higher the RMSF value indicates better flexibility. The RMSF value of MPXV-2 chain in complex with TLR2 and TLR4 had less magnitude of fluctuation with an average value of 0.40 ± 0.11nm and 0.35 ± 0.12 nm, respectively (Figure 6E). In the case of MPXV-2 chain complexed with HLA-A*02:01, the RMSF value of residues 228 to 317 showed significant fluctuations, reaching a peak value of 1.51nm (Figure 6E). The RMSF value of MPXV-5 chain in complex with TLR2 had little magnitude of fluctuation with an average value of 0.33 ± 0.09 nm (Figure 6F). In the case of MPXV-5 chain in the

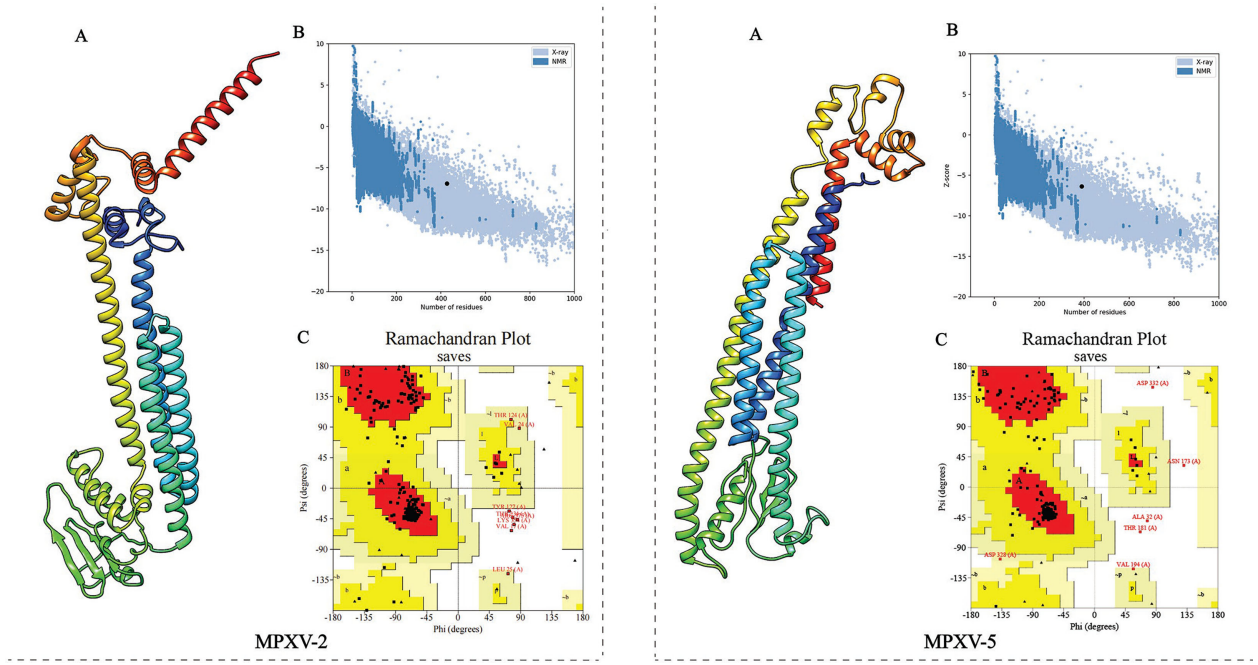

FIGURE 4
Refinement and quality validation of the three dimensional (3D) structure. **(A)** The refined 3D structure. **(C)** Ramachandran plots of the refined 3D structure generated by PROCHECK server; Red regions represent the most favored regions, dark yellow regions represent the additional allowed region, light yellow regions represent the generally allowed regions, and white regions denote the disallowed regions. **(B)** Z-Score plot of the refined 3D structure predicted by ProSA-Web server.

TABLE 4 Properties of the vaccine constructs.

Properties	V1	V2	V3	V4	V5
adjuvant	50S ribosomal L7/L12	Beta-defensin	LT-IIC	Cholera Toxin B subunit (CTB)	RS09
Antigenicity (Vaxijen/ANTIGENpro)	0.62/0.56	0.68/0.60	0.64/0.59	0.66/0.84	0.69/0.59
Allergenicity (AllerTOP v2.0+AlgPred)	NA	NA	NA	NA	NA
Toxicity	NT	NT	toxic	toxic	NT
Number of amino acids	511	426	479	484	388
Molecular weight (Da)	56700.70	48421.41	53920.37	54905.58	43952.00
Theoretical isoelectric point (pI)	8.61	9.56	9.35	9.27	9.39
The estimated half-life[(a)]	30 hours	30 hours	30 hours	30 hours	30 hours
The estimated half-life[(b)]	>20 hours	>20 hours	>20 hours	>20 hours	>20 hours
The estimated half-life[(c)]	>10 hours	>10 hours	>10 hours	>10 hours	>10 hours
The instability index (II)	30.91	36.62	34.19	35.65	35.68
Aliphatic index	89.06	82.25	84.15	84.52	84.05
Grand average of hydropathicity (GRAVY)	-0.051	-0.19	-0.13	-0.171	-0.127
Solubility	0.975118	0.835770	0.610239	0.867569	0.869869

The estimated half-life[(a)]: Estimated half-life of the vaccine in mammalian reticulocytes (*in vitro*); The estimated half-life[(b)]: Estimated half-life of the vaccine in yeast (*in vitro*); The estimated half-life[(c)]: Estimated half-life of the vaccine in *Escherichia coli (in vivo)*.
NA, Non-allergenic; NT, Non-toxic.

MPXV-5-TLR4 and MPXV-5-HLA-A-02:01 complexes, residues 386-389 and residues 235-241 showed the largest magnitude of fluctuations, respectively, and the average RMSF value of them was 0.33 ± 0.13nm and 0.29 ± 0.09 nm, respectively (Figure 6F). For MPXV-2-receptors complexes, the RMSF values of almost all residues of the TLR2 chain were less than 0.5 nm, except for a few residues, such as residues 34-36 and 377-381(Supplementary Figure 6); for the TLR4 chain, the maximum and minimum RMSF values were 0.5838 nm and 0.1759 nm, respectively, and the RMSF values of bulk amino acids were less than 0.5nm (Supplementary Figure 6); for both A chain and B chain of HLA-A-02:01, the RMSF values showed major fluctuations in almost all residues. For MPXV-5-receptor complexes, the RMSF values of the TLR2 chain and HLA-A*02:01 chain had less magnitude of fluctuation, with an average value of 0.24nm ± 0.06 and 0.24 ± 0.05/0.30 ± 0.07(A chain/B chain), respectively (Supplementary Figure 6). In the MPXV-5-TLR4 complex, the maximum and minimum RMSF values in the TLR4 chain were 0.66 and 0,16, with a higher average value of 0.32 ± 0.09 nm (Supplementary Figure 6).

Hydrogen bonds is a nonbonded interaction, which is essential in maintaining the overall stability of the vaccine-receptor complex. In general, the number of hydrogen bonds in all complexes except the MPXV-5-TLR4 complex increased with time. The number of hydrogen bonds in MPXV-2-TLR2, MPXV-2-HLA-A02:01, MPXV-2-TLR4, MPXV-5-TLR2, MPXV-5-HLA-A02:01, MPXV-5-TLR4 complexes finally stabilized at approximately 7, 12, 8, 11,15 and 8, respectively (Figures 6G, H). The calculations of RMSD, RG, RMSF and hydrogen bonds demonstrated the stability and stiffness of the vaccine-TLRs and vaccine-HLA-A-02:01 complexes.

3.8.2 Gibb's free energy analysis

The low Gibb's free energy value corresponds to the stable conformation and system. In this study, the calculation of Gibb's free energy value was based on the two principal components: the two-dimensional projections of PC1 *vs* PC2 were analyzed. As shown in Figure 7 and Supplementary Figure 7, among the six complexes, MPXV-5-TLR4, MPXV-2-HLA-A*02:01 and MPXV-2-TLR4 complexes have more lowest energy basins, followed by MPXV-5-TLR3 and MPXV-5-HLA-A*02:01, MPXV-5-TLR2 complexes, while MPXV-5-TLR2 complex has the fewer lowest energy basins. The lowest energy conformations of the MPXV-2-TLR2 complex were limited to the narrow range of energy basins -8.7 to 10.8 kJ/mol on PC1 and -5.6 to 7.5 kJ/mol on PC2 (Figure 7A). For the MPXV-5-TLR2 complex, the energy range for PC1 was -11.9 to 10.7 kJ/mol and -8.6 to 10.8 kJ/mol for PC2 (Figure 7B). For the MPXV-2-TLR4 complex, the energy range for PC1 was -16.1 to 14.1 kJ/mol and -11.6 to 12.7 kJ/mol for PC2 (Figure 7C). For the MPXV-5-TLR4 complex, the energy range was -8.8 to 6.6 kJ/mol for PC1 and -5.8 to 7.4 kJ/mol for PC2 (Figure 7D). For the MPXV-2- HLA-A*02:01 complex, the energy range was wider, with PC1 having an energy range of -16.1 to 15.2 kJ/mol and PC2 having an energy range of -11.4 to 12.7 kJ/mol (Supplementary Figure 7A). For the MPXV-5-HLA-A*02:01 complex, the energy range for PC1 was -8.9 to 16.0 kJ/mol and -6.2 to 8.2 kJ/mol for PC2 (Supplementary Figure 7B).

3.8.3 MM-PBSA calculation

The trajectories extracted at 100 ps during the 40-50-ns simulation periods were submitted to MM-PBSA calculation. As

10.3389/fimmu.2023.1112816

TABLE 5 Docking analysis of vaccine-receptors complexes.

Server	Parameter	MPXV-2-TLR2	MPXV-2-TLR4	MPXV-2-HLA-A*02:01	MPXV-2-HLA-DRB1*01:01	MPXV-5-TLR2	MPXV-5-TLR4	MPXV-5-HLA-A*02:01	MPXV-5-HLA-DRB1*01:01
ClusPro 2.0	Center	-953.1	-1088	-998.6	-1092.7	-1203.8	-1166.8	-875.8	-1224.5
	Lowest Energy	-1110.3	-1473.3	-1033.6	-1330.8	-1203.8	-1261.8	-1037.5	-1224.5
HADDOCK 2.4	HADDOCK score	-171.0 +/- 0.9	-242.1 +/- 3.7	-378.0 +/- 3.4	-676.9 +/- 2.4	-275.6 +/- 3.2	-306.2 +/- 1.6	-423.8 +/- 7.2	-675.7 +/- 1.7
	Cluster size	20	20	20	20	20	20	20	20
	RMSD from the overall lowest-energy structure	0.6 +/- 0.4	0.6 +/- 0.3	0.6 +/- 0.3	0.6 +/- 0.3	0.6 +/- 0.4	0.6 +/- 0.3	0.6 +/- 0.3	0.6 +/- 0.3
	Van der Waals energy	-84.8 +/- 2.3	-115.0 +/- 2.6	-176.2 +/- 2.2	-304.9 +/- 6.4	-122.2 +/- 1.4	-138.5 +/- 1.8	-186.7 +/- 3.0	-316.1 +/- 2.4
	Electrostatic energy	-108.1 +/- 6.0	-297.5 +/- 22.0	-589.8 +/- 25.1	-1254.2 +/- 23.7	-364.6 +/- 11.1	-323.4 +/- 35.9	-703.2 +/- 17.4	-1154.4 +/- 21.3
	Desolvation energy	-64.6 +/- 3.3	-67.6 +/- 2.2	-83.7 +/- 2.0	-121.1 +/- 1.4	-80.4 +/- 1.4	-103.0 +/- 5.7	-96.5 +/- 6.8	-128.8 +/- 4.2
	Restraints violation energy	0.0 +/- 0.0	0.0 +/- 0.0	0.0 +/- 0.0	0.0 +/- 0.0	0.0 +/- 0.0	0.0 +/- 0.0	0.0 +/- 0.0	0.0 +/- 0.0
	Buried Surface Area	2557.1 +/- 16.1	3619.9 +/- 65.0	5011.4 +/- 65.8	7923.8 +/- 34.6	3871.2 +/- 70.5	4361.5 +/- 75.1	5447.7 +/- 98.5	8418.8 +/- 83.3
	Z-Score	0	0	0	0	0	0	0	0
PRODIG	ΔG (kcal/mol)	-9.4	-19.1	-11.9	-11.6	-16.1	-16.5	-12.9	-12.3
	Kd (M) at 25.0 °C	1.30E-07	1.00E-14	1.80E-09	2.90E-09	1.70E-12	7.70E-13	3.50E-10	8.80E-10
PDBsum	Number of hydrogen bonds	6	11	12	16	12	18	12	12
	Number of salt Bridges	0	2	1	6	3	3	3	5

ΔG, binding energy; Kd, dissociation constant.

shown in Table 6, the total binding free energies (ΔTOTAL) of MPXV-2-TLR2, MPXV-2-TLR4, MPXV-2-HLA-A*02:01, MPXV-5-TLR2, MPXV-5-TLR4, MPXV-5-HLA- A*02:01 complexes were -143.12 kcal/mol, -129.11 kcal/mol, -126.44 kcal/mol, -103.64 kcal/mol, -184.82kcal/mol, and -100.55 kcal/mol, respectively, indicating that both MPXV-2 and MPXV-5 have good affinity to TLR2, TLR4 and HLA-A*02:01. The analysis of detailed interaction energies was shown in Table 6.

3.8.4 Dynamic cross-correlation analysis

The correlations between the movements of different residues of the two chains in the vaccine-receptor complex systems were shown with the DCCM generated by DDC analysis. In the figure of DCCM, the direction and strength of the correlation between different residues were shown in different colors, and the red, white and blue corresponded to the correlation coefficients of 1 0, and -1, respectively. As shown in Supplementary Figure 8, both positively and negatively correlated residue contacts were detected between all vaccine chains and all receptor chains. In the MPXV-2-TLR2 complex, the residues around 51-151 (residues 600-700 in the figure) in the vaccine chain showed a slightly positive correlation with the residues 240-500 (residues 240-500 in the figure) from the TLR2 chain (Supplementary Figure 8A). In the MPXV-2-TLR4 complex, the relatively strong positive correlations between the residues 49-149 and 299-339 (residues 650-750, 900-940 in the figure) from the vaccine chain and the TLR4 chain were observed (Supplementary Figure 8B). In the MPXV-2-HLA-A*02:01 complex, the residues 28-128 (residues 400-500 in the figure) from the vaccine chain showed a positive correlation with the residues 1-200 (residues 1-200 in the figure) from the A chain of HLA-A*02:01 (Supplementary Figure 8C). In the MPXV-5-TLR2 complex, the residues around 26-46, 61-111 and 251-331(residues 575-595, 610-650 and 800-880 in the figure) from the vaccine chain showed positive correlations with the residues 1-300 (residues 1-300 in the figure) from the TLR2 chain (Supplementary Figure 8D). In the MPXV-5-TLR4 complex, the residues around 9-109 and 249-299 (residues 610-710 and 850-900 in the figure) from the vaccine chain showed positive correlations with the residues 1-250 (residues 1-250 in the figure) from the TLR4 chain (Supplementary Figure 8E). In the MPXV-5-HLA-A*02:01 complex, the residues around 28-118 (residues 400-490 in the figure) from the vaccine

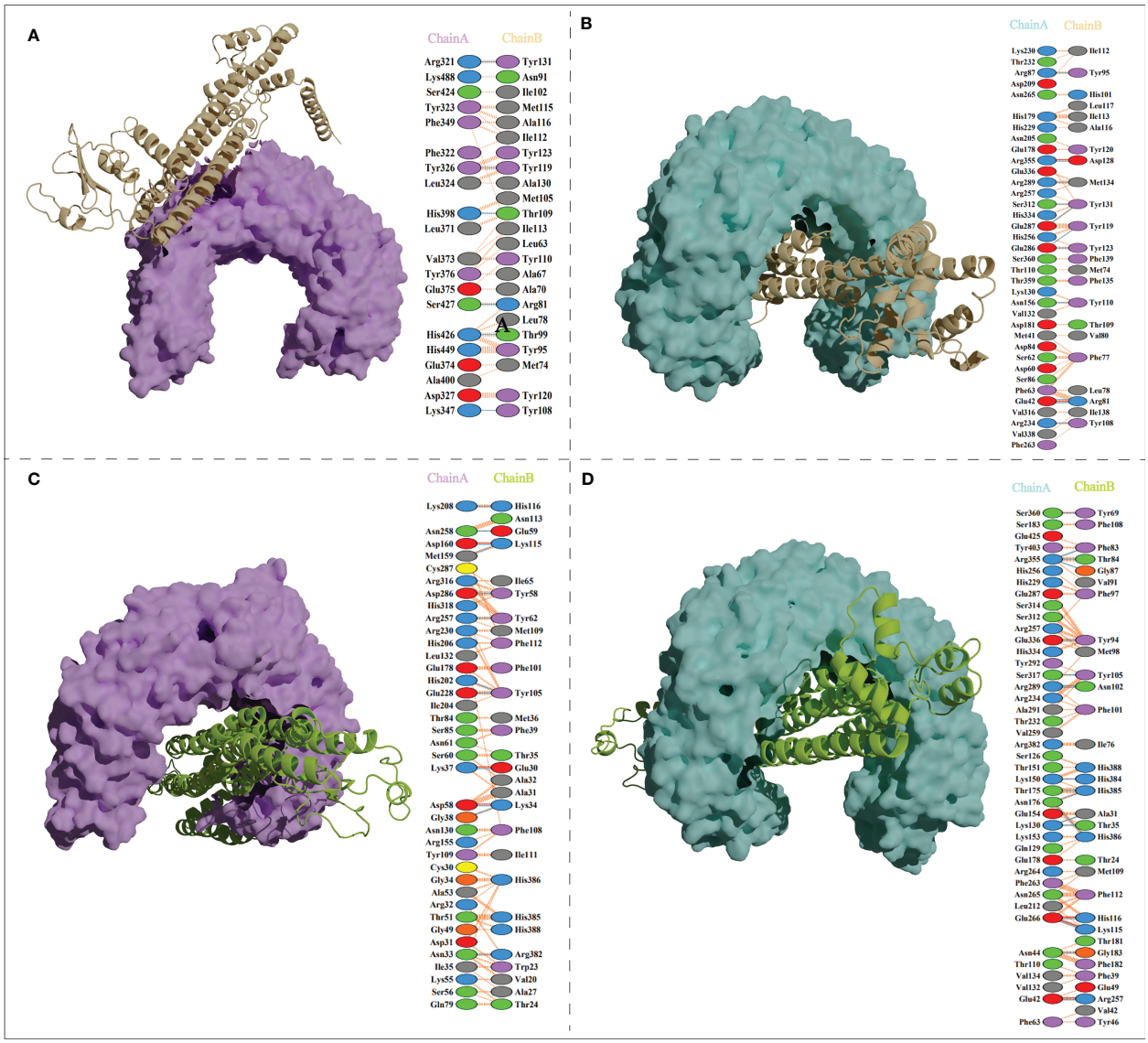

FIGURE 5
Vaccine candidates (MPXV-2 and MPXV-5) docked with TLR2 and TLR4. **(A)** The binding mode between the MPXV-2 and TLR2 and the interacting residues of the MPXV-2 with TLR2; **(B)**The binding mode between the MPXV-2 and TLR4 and the interacting residues of the MPXV-2 with TLR4; **(C)** The binding mode between the MPXV-5 and TLR2 and the interacting residues of the MPXV-5 with TLR2; **(D)** The binding mode between the MPXV-5 and TLR4 and the interacting residues of the MPXV-5 with TLR4.

chain showed positive correlations with the residues 1-190 (residues 1-190 in the figure) from the HLA-A*02:01 chain (Supplementary Figure 8F).

3.9 Population coverage

Based on the HLA alleles binding to T-cell epitopes in the multi-epitope vaccine, the population coverage predictions were performed to determine the proportion of the population in different parts of the world that would respond to the designed vaccines. As shown in Figure 8, the population coverage of the multi-epitope vaccine was high in countries suffering relatively severe MPXV attacks in this outbreak, such as Europe (Spain, France, Germany, the United Kingdom, the Netherlands, Portugal), North America (Mexico, Canada, the United States), and South America (Brazil, Peru). The analyses of population coverage were suggestive of the fact that the designed vaccine candidates (MPXV-2 and MPXV-5) have the potential to combat the MPXV infection globally.

3.10 Immune simulation

The immune simulation results of MPXV-2, MPXV-5 and control group (C1) were shown in Figure 9; Supplementary Figure 9. Similar immune response patterns were observed between the simulations of candidate vaccines (MPXV-2 and

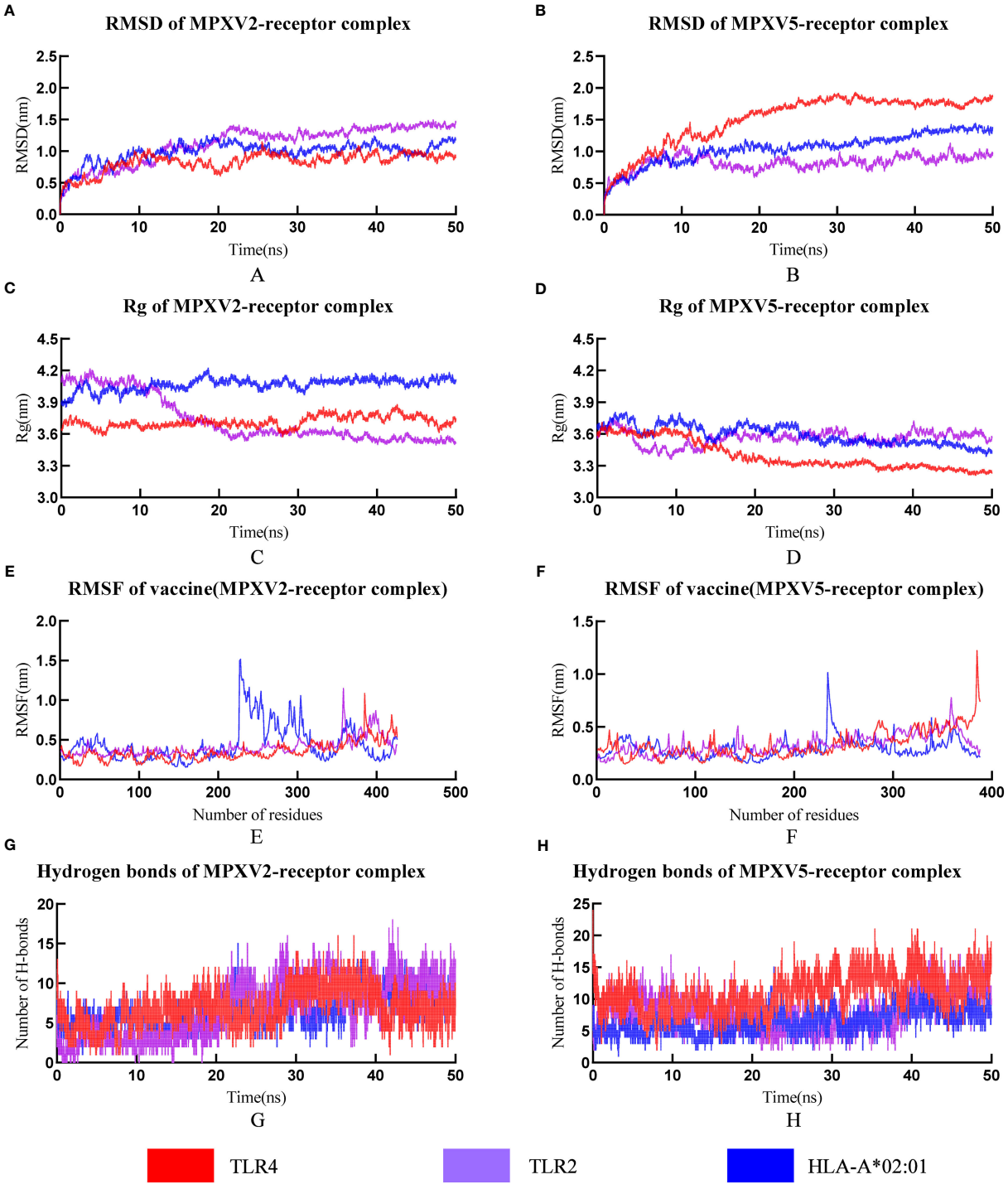

FIGURE 6
The plot of Root means square deviation (RMSD), Root means square fluctuation (RMSF), Radius of Gyration (Rg) and hydrogen bonds of vaccine-receptor complexes during the Molecular dynamics (MD) simulation. **(A)** RMSD of MPXV-2-TLR2, MPXV-2-TLR4 and MPXV-2-HLA-A*02:01 complexes; **(B)** RMSD of MPXV-5-TLR2, MPXV-5-TLR4 and MPXV-5-HLA-A*02:01 complexes; **(C)** Rg of MPXV-2-TLR2, MPXV-2-TLR4 and MPXV-2-HLA-A*02:01 complexes; **(D)** Rg of MPXV-5-TLR2, MPXV-5-TLR4 and MPXV-5-HLA-A*02:01 complexes; **(E)** RMSF of MPXV-2 chain in MPXV-5-TLR2, MPXV-5-TLR4 and MPXV-5-HLA-A*02:01 complexes; **(F)** RMSF of MPXV-5 chain in MPXV-5-TLR2, MPXV-5-TLR4 and MPXV-5-HLA-A*02:01; **(G)** Hydrogen bonds in MPXV-2-TLR2, MPXV-2-TLR4 and MPXV-2-HLA-A*02:01 complexes; **(H)** Hydrogen bonds in MPXV-5-TLR2, MPXV-5-TLR4 and MPXV-5-HLA-A*02:01 complexes.

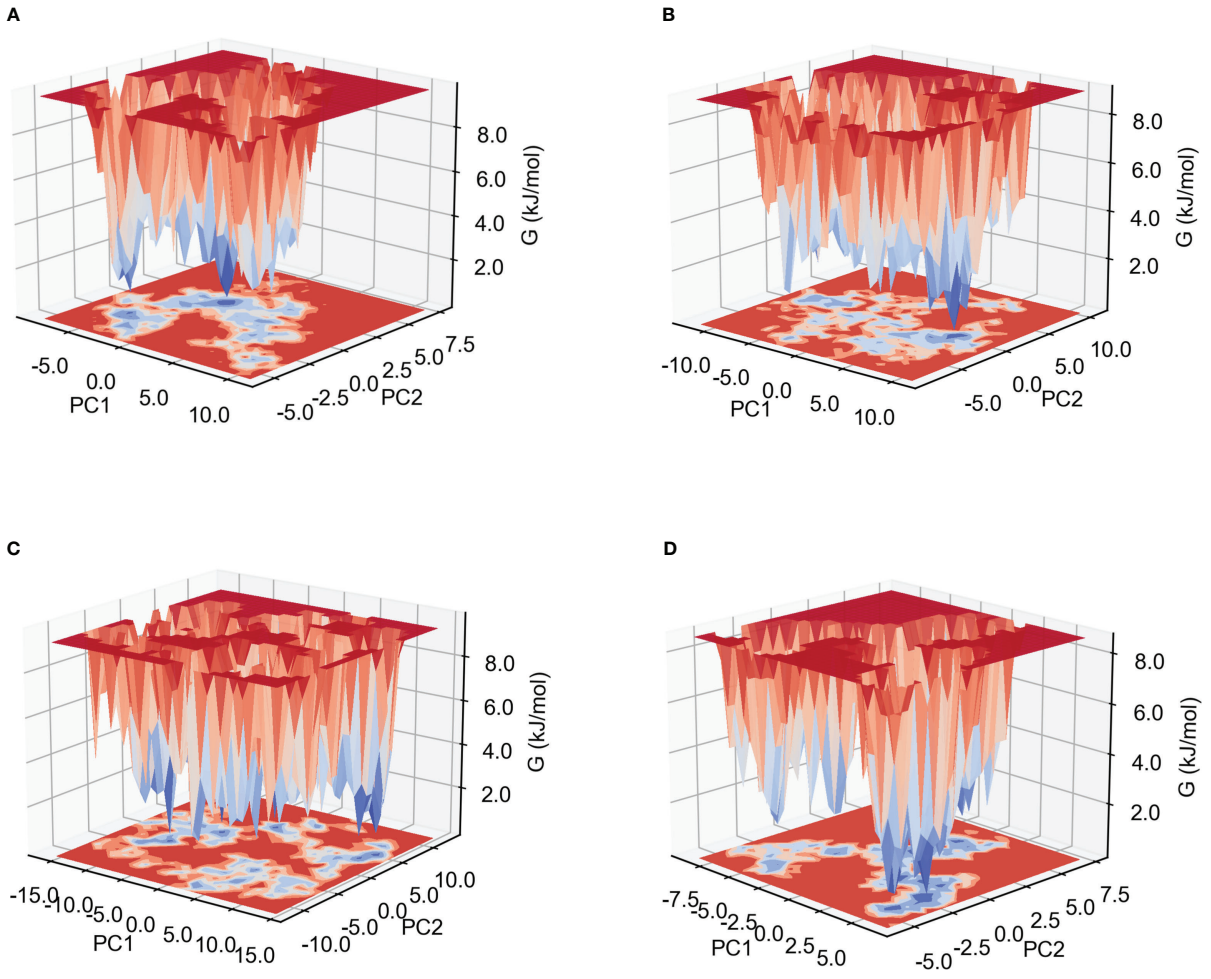

FIGURE 7
Gibb's free energy landscape. **(A)** MPXV-2-TLR2 complex. **(B)** MPXV-5-TLR2 complex. **(C)** MPXV-2-TLR4 complex. **(D)** MPXV-5-TLR4 complex.

MPXV-5) and C1. The primary response in the three simulations were both characterized by elevated immunoglobulin IgM (Figure 9A; Supplementary Figure 9A), B cells (isotype: lgM) (Figure 9B; Supplementary Figure 9B) and plasma cells (isotype: lgM) (Supplementary Figure 9C). In secondary and tertiary reactions, these elevations were elevated to a greater degree, and the elevation of different immunoglobulins and the immunocomplexes (IgM+IgG, IgG1+IgG2, IgG1, memory B cells and plasma cells (isotype: lgG1, lgG2) were also observed (Figures 9B, C; Supplementary Figure 9B, C). As shown in

TABLE 6 MM-PBSA calculations of vaccines-receptors complexes.

Energy component	Average (MPXV-2)			Average (MPXV-5)		
	TLR2	TLR4	HLA-A*02:01	TLR2	TLR4	HLA-A*02:01
ΔVDWAALS(KJ/mol)	-164.52	-139.06	-143.93	-147.37	-223.37	-166.71
ΔEEL(KJ/mol)	-3030.72	-3750.02	-1574.48	-792.96	-2822.84	-116.11
ΔEPB(KJ/mol)	3072.22	3777.71	1609.49	853.81	2890.32	201.12
ΔENPOLAR(KJ/mol)	-20.10	-17.73	-17.51	-17.12	-28.93	-18.85
ΔGGAS(KJ/mol)	-3195.24	-3889.09	-1718.41	-940.33	-3046.21	-282.82
ΔGSOLV(KJ/mol)	3052.13	3759.98	1591.97	836.69	2861.38	182.27
ΔTOTAL(KJ/mol)	-143.12	-129.11	-126.44	-103.64	-184.82	-100.55

ΔVDWAALS, van der Waals energy; ΔEEL, Electrostatic energies; ΔEPB, Polar solvation energy; ΔENPOLAR, Nonpolar solvation energy; ΔGGAS = ΔVDWAALS+ΔEEL; ΔGSOLV = ΔEPB +ΔENPOLAR; ΔTOTAL = ΔGSOLV +ΔGGAS.

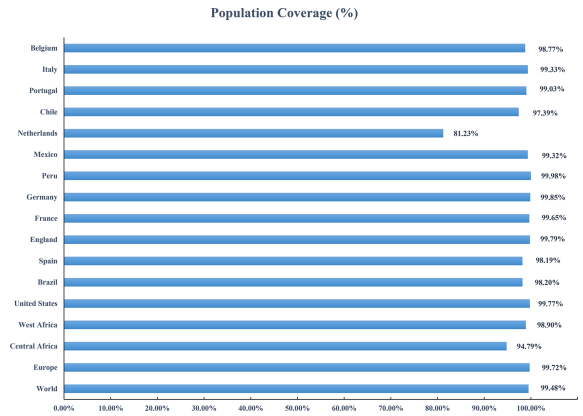

FIGURE 8
Population coverage of the designed vaccine in different regions suffering relatively severe MPXV attacks is calculated by the IEDB population coverage tool.

Figures 9A–C; Supplementary Figure 9A–C the titers of antibody (IgM + IgG, IgG1 + IgG2) and the level of plasma B cell (isotype: IgG1) in MPXV-2 group were higher than those in C1, while the titer of antibody (IgM + IgG, IgG1 + IgG2) and the level of plasma B cell (isotype: IgG1) in MPXV-5 group were lower than those in C1. Additionally, the helper T-cells along with corresponding memory cells were observed for two vaccine candidates and C1 (Figure 9D; Supplementary Figure 9D). The levels of active cytotoxic T cells and resting cytotoxic T cells in MPXV-2 and MPXV-5 groups changed significantly with time, while the resting cytotoxic T cell level in C1 changed little, and no inactive cytotoxic t cells were observed in the C1 group (Figures 9E; Supplementary Figure 9E). High levels of IFN-γ and IL-2 were observed in vaccine candidate groups and C1 group in the cytokines' simulation plot (Figure 9F; Supplementary Figure 9F), while the concentration level of IL-2 was slightly higher for MPXV-2. During the immune simulation, the increased level of NK cells, macrophage (MA) and DC cells were also detected in three groups (Figure 9G–I; Supplementary Figure 9G–I). Together, the simulation results suggest that the MPXV-2 and MPXV-5 both can induce stronger immunity in the host body, thereby effectively combating the MPXV. Moreover, we can know that the humoral

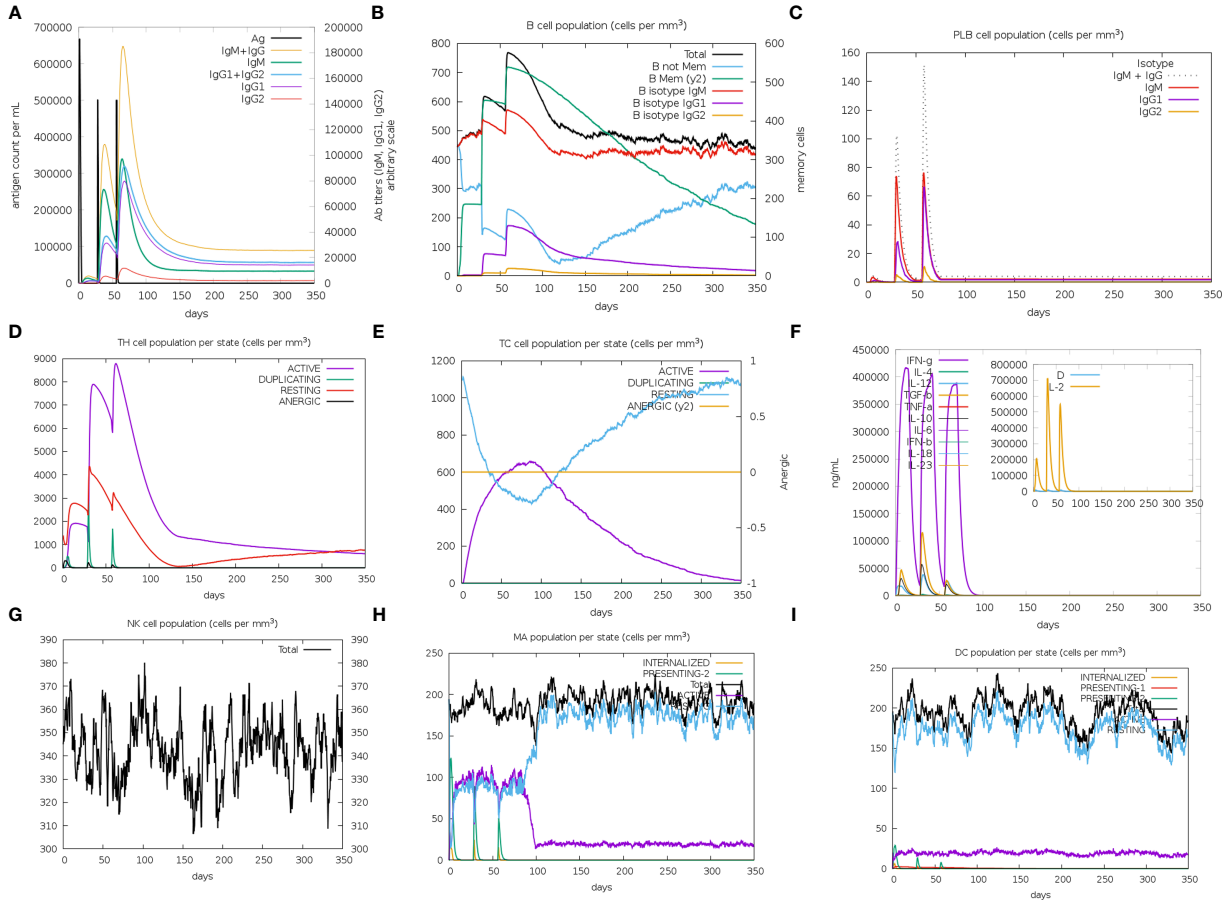

FIGURE 9
The plots relative to the immune stimulation of MPXV-5. **(A)** Titers of immunoglobulins and the immunocomplexes after vaccination. **(B)** Levels of B-cell population after vaccination. **(C)** Levels of plasma B-cell after vaccination. **(D)** Levels of helper T-cell cell population after vaccination. **(E)** Levels of cytotoxic T cells population after vaccination. **(F)** Concentration of cytokines and interleukins after vaccination. **(G)** Levels of NK cell population after vaccination. **(H)** Levels of MA population after vaccination. **(I)** Levels of DC population after vaccination.

immune response provoked by MPXV-2 was much stronger than that of MPXV-5.

3.11 Codon optimization and *in silico* cloning

For the optimized codon sequences of MPXV-2 and MPXV-5 (Supplementary Data), the CAI were 0.97 and 0.94 respectively, and the GC content was 48.79% and 48.18%, respectively, showing that both the MPXV-2 and MPXV-5 might well express in *E. coli* K12 strain and have the potential for mass production. The optimized codon sequences of MPXV-2 and MPXV-5 were inserted into the pET28a (+) vector (Supplementary Figure 10). Electrophoretogram of enzyme digestion of pET28a (+)-MPXV-5 was shown in (Supplementary Figure 11).

4 Discussion

Since May 2022, monkeypox has broken the traditional prevalent situation, beginning to spread across several countries at the same time (4). However, no available therapeutics and preventions are available for MPXV infections highlighting the need for the development of a novel vaccine against MPXV. The multi-epitope vaccine can elicit specific and strong immune responses based on multiple conserved epitopes in several antigenic proteins, avoiding adverse reactions against undesirable epitopes (88). The application of immunoinformatics methods to design multi-epitope vaccines is becoming increasingly popular, which can significantly save time and expense in vaccine development. The selection of the target protein will deeply affect the vaccine's efficacy. A35R, B6R and H3L, which were needed for viral attachment and entry and targeted by neutralizing antibodies (nAbs), were potential targets for diagnostic tests and vaccine/drug development (89). It is well known that mutations in the strain will weaken the effectiveness of the vaccine. Hence, to design a vaccine as effective as possible against the current epidemic MPXV strains and most MPXV strains, we contrived a multi-epitope vaccine from three reference strains of monkeypox at different epidemic stages as objects and A35R, B6R and H3L as targets.

Polypeptide-combined T-cell and B-cell epitopes often equip much stronger immunogenicity than T-cell or B-cell epitopes alone. So, to maximize the immunogenicity of the designed vaccine, every vaccine construct involved both T-cell epitopes (CTL and HTL epitopes) and B-cell epitopes of each target protein. Moreover, all selected epitopes were antigenic, non-allergenic, non-toxic and non-homologous with the human proteome, indicating that the multi-epitope vaccine can induce safe antigenic response but no cross-reaction with proteins in humans. Cytokines are a category of signaling molecules that play an important role in mediating and regulating immunity and inflammation. IFN-γ, IL-4 and IL-2 are several important cytokines produced by the immune system, which contribute to the differentiation of T cells and mediate cytotoxicity and antibody production (26–28). Hence, all antigenic HTL epitopes were assessed for the potential to induce the IFN-γ, IL-2 and IL-4 secretion, and only HTL epitopes that were capable of mediating the release of IFN-γ and IL-4 or IL-2 were considered for vaccine construction. Notably, the molecular docking between the T-cell epitopes and MHC molecules was performed, and the docking results revealed that the T-cell epitopes could successfully bind to MHC molecules, thereby being recognized by the antigen-presenting cell.

To acquire the optional vaccine candidates, five adjuvants were applied in this study. Although five selected adjuvants have been widely used in the design of multi-epitope vaccines in silico (48–51) and have been shown to stimulate the host's immune response in animal experiments (43, 45, 52–54), any of these adjuvants have not been used for human vaccination. In the future, we can perform experiments to compare the immune enhancement effects of the adjuvants used in human vaccination, such as aluminum hydroxide and MF59 (90), and these adjuvants on multi-epitope vaccines. After the analysis of predicted biophysical and biochemical features of each vaccine construct (MPXV-1–5), two antigenic, safe, stable, thermostable and hydrophilic and soluble upon expression vaccine constructs (MPXV-2 and MPXV-5) were regarded as excellent vaccine candidates and subjected to further analysis.

Molecular docking analysis revealed strong binding affinities between MPXV-2 and MPXV-5 with TLRs (TLR2 and TLR4) and MHC molecules, which confirmed the capacity of the multi-epitope vaccine to be recognized by the human immune system, inducing stable and strong immune responses. MD simulation analysis indicated the MPXV-2-receptors and MPXV-5-receptors complexes' stability through varying environmental conditions, including changing pressure, temperature, and motion. The initial trajectory evaluations, including the calculation of RMSD, RG, RMSF and hydrogen bonds, all correspond to the high stability of the vaccine-TLR and vaccine-MHC complexes in a biological environment. Gibb's free energy analysis indicated that the MPXV-5-TLR4 had more stable conformations than other complexes. As shown in MM-PBSA calculations, the values of binding free energy of all complexes were negative, showing that all vaccine-receptor complexes could remain stable under natural conditions, especially the MPXV-5-TLR4 complex. Also, compared with other complexes, the binding mode of MPXV-5-TLR4 might be the most stable under natural conditions.

Notably, comparative immune stimulation was conducted between vaccine candidates and positive control. Similar immune response patterns were observed between the simulations of vaccine candidates (MPXV-2 and MPXV-5) and control group (C1), and the results of immune stimulation revealed that the MPXV-2 and MPXV-5 both can induce protective immune responses in the host. However, immune simulation performed by the C-IMMSIM server has simplified the process of antigen presentation. In general, the CTL and HTL epitopes are processed and presented by two distinct, proteasomal degradation (endogenous) and endo-lysosomal degradation (exogenous) pathways, respectively (91–93). The multi-epitope vaccine is considered an extracellular antigen. After being injected into the host body, the vaccine mainly activates CD4+T cells through the exogenous pathway to induce adaptive immunity and then activates B cells to generate humoral immunity. In the field of synthetic peptide vaccines, because the clinical

benefits of early direct injection of synthetic peptides or the synthetic peptides loaded on DC cells are relatively inefficient, the use of complete proteins or long peptides to activate cellular immunity by cross-presentation had attracted more attention (94). The designed multi-epitope vaccines (MPXV-2 and MPXV-5) belong to long peptides. Therefore, the CTL epitopes from MPXV-2 and MPXV-5 can be cross-presented by DCs, thus activating CD8+T cells and generating cellular immunity. However, the cellular immunity induced by multi-epitope vaccines cross-presented by DC cells may not be strong enough. The high salt for mulation of Al(OH)3 can be selected as an adjuvant, which can significantly enhance the cross-presentation of extracellular antigens by DC cells (95). However, in the future, *in vitro* and *in vivo* experiments still need to verify that the multi-epitope vaccine with a suitable adjuvant can trigger an effective cellular immune response

5 Conclusion

Since May 2022, the United Kingdom, the United States, France, Spain, Brazil and other countries have successively reported their "first" cases of monkeypox, followed by a continuous increase in the number of cases. However, no specific treatment or vaccine for MPXV is currently available on the market. In this study, five multi-epitope vaccine constructs were developed against MPXV using immunoinformatics approaches, and the MPXV-2 and MPXV-5 were identified as the most promising vaccine constructs after the immunological and physiochemical analyses. The molecular docking and MD simulation confirmed that the MPXV-2 and MPXV-5 can form stable bindings to immune receptors and thereby trigger effective immune responses against MPXV. Additionally, the results obtained from immune simulation suggested that the MPXV-2 and MPXV-5 equip the capacity to elicit immune responses in the human body, but the antibody response induced by the MPXV-2 was stronger. Having said all this, the MPXV-2 and MPXV-5 could, in theory, effectively combat the MPXV.

6 Limitation

First, the immunogenicity of multi-epitope vaccines is weaker than that of inactivated or attenuated vaccines. The application of other available adjuvants, such as aluminum hydroxide, may address this issue (95, 96). Second, the immunogenicity of multi-epitope vaccines can be affected by the expression system, necessitating careful selection of the expression system during vaccine preparation. Although animal experiments using immunoinformatics to construct multi-epitope vaccines have shown promising results, and several vaccines designed using this approach are currently in clinical studies, as an emerging technology, more in-depth studies are still needed to verify its effectiveness. Finally, its protective effect needed to be confirmed by *in vitro* and *in vivo* experiments.

Data availability statement

The original contributions presented in the study are included in the article/Supplementary Material, further inquiries can be directed to the corresponding author/s.

Author contributions

CT, FZ, PP, AW and CL designed the research and analyzed the data; CT and FZ charged the drawing; CT, FZ, PP, AW and CL wrote the paper. PP, AW and CL reviewed and edited the paper. CL, AW and PP acquired the funding. All authors contributed to the article and approved the submitted version.

Funding

This research was supported by the National Key Research and Development Program of China (No. 2022YFC2009801), the Natural Science Foundation of Hunan Province (No. 2021JJ31071), the National Clinical Research Center for Geriatric Disorders (Xiangya Hospital, No. 2021KFJJ05) and the Research Project on Education and Teaching Reform of Central South University (No. 2021 jy139-2). Health Development Research Center of the National Health Commission, "Evidence-based Evaluation and Demonstration Base Construction Project of Infection Control Measures in Healthcare Institutions"(CNHDRC-KJ-L-2020-53-04375).

Conflict of interest

The authors declare that the research was conducted in the absence of any commercial or financial relationships that could be construed as a potential conflict of interest.

Publisher's note

All claims expressed in this article are solely those of the authors and do not necessarily represent those of their affiliated organizations, or those of the publisher, the editors and the reviewers. Any product that may be evaluated in this article, or claim that may be made by its manufacturer, is not guaranteed or endorsed by the publisher.

Supplementary material

The Supplementary Material for this article can be found online at: https://www.frontiersin.org/articles/10.3389/fimmu.2023.1112816/full#supplementary-material

References

1. Weaver JR, Isaacs SN. Monkeypox virus and insights into its immunomodulatory proteins. *Immunol Rev* (2008) 225:96–113. doi: 10.1111/j.1600-065X.2008.00691.x

2. Pourriyahi H, Aryanian Z, Afshar ZM, Goodarzi A. A systematic review and clinical atlas on mucocutaneous presentations of monkeypox: With a comprehensive approach to all aspects of the new and previous monkeypox outbreaks. *J Med Virol* (2022) 95(2):e28230. doi: 10.1002/jmv.28230

3. Petersen E, Kantele A, Koopmans M, Asogun D, Yinka-Ogunleye A, Ihekweazu C, et al. Human monkeypox: Epidemiologic and clinical characteristics, diagnosis, and prevention. *Infect Dis Clin North Am* (2019) 33(4):1027–43. doi: 10.1016/j.idc.2019.03.001

4. Thornhill JP, Barkati S, Walmsley S, Rockstroh J, Antinori A, Harrison LB, et al. Monkeypox virus infection in humans across 16 countries - April-June 2022. *N Engl J Med* (2022) 387(8):679–91. doi: 10.1056/NEJMoa2207323

5. World Health Organization. *Multi-country outbreak of monkeypox, external situation report 10* (Accessed 27 November 2022).

6. McCarthy MW. Therapeutic strategies to address monkeypox. *Expert Rev Anti Infect Ther* (2022) 20(10):1249–52. doi: 10.1080/14787210.2022.2113058

7. Fine PE, Jezek Z, Grab B, Dixon H. The transmission potential of monkeypox virus in human populations. *Int J Epidemiol* (1988) 17(3):643–50. doi: 10.1093/ije/17.3.643

8. Gruber MF. Current status of monkeypox vaccines. *NPJ Vaccines* (2022) 7(1):94. doi: 10.1038/s41541-022-00527-4

9. Lennerz V, Gross S, Gallerani E, Sessa C, Mach N, Boehm S, et al. Immunologic response to the survivin-derived multi-epitope vaccine Emd640744 in patients with advanced solid tumors. *Cancer Immunol Immunother* (2014) 63(4):381–94. doi: 10.1007/s00262-013-1516-5

10. Oli AN, Obialor WO, Ifeanyichukwu MO, Odimegwu DC, Okoyeh JN, Emechebe GO, et al. Immunoinformatics and vaccine development: An overview. *Immunotargets Ther* (2020) 9:13–30. doi: 10.2147/itt.S241064

11. Hatmal MM, Al-Hatamleh MAI, Olaimat AN, Ahmad S, Hasan H, Ahmad Suhaimi NA, et al. Comprehensive literature review of monkeypox. *Emerg Microbes Infect* (2022) 11(1):2600–31. doi: 10.1080/22221751.2022.2132882

12. Hooper JW, Custer Dm, Thompson E. Four-Gene-Combination DNA vaccine protects mice against a lethal vaccinia virus challenge and elicits appropriate antibody responses in nonhuman primates. *Virology* (2003) 306(1):181–95. doi: 10.1016/s0042-6822(02)00038-7

13. Roper RL, Wolffe Ej, Weisberg A, Moss B. The envelope protein encoded by the A33r gene is required for formation of actin-containing microvilli and efficient cell-to-Cell spread of vaccinia virus. *J Virol* (1998) 72(5):4192–204. doi: 10.1128/jvi.72.5.4192-4204.1998

14. Paran N, Lustig S. Complement-bound human antibodies to vaccinia virus B5 antigen protect mice from virus challenge. *Expert Rev Vaccines* (2010) 9(3):255–9. doi: 10.1586/erv.10.5

15. Davies DH, McCausland Mm, Valdez C, Huynh D, Hernandez JE, Mu Y, et al. Vaccinia virus H3l envelope protein is a major target of neutralizing antibodies in humans and elicits protection against lethal challenge in mice. *J Virol* (2005) 79 (18):11724–33. doi: 10.1128/jvi.79.18.11724-11733.2005

16. Drexler I, Staib C, Kastenmuller W, Stevanović S, Schmidt B, Lemonnier FA, et al. Identification of vaccinia virus epitope-specific hla-a*0201-Restricted T cells and comparative analysis of smallpox vaccines. *Proc Natl Acad Sci USA* (2003) 100(1):217–22. doi: 10.1073/pnas.262668999

17. Isidro J, Borges V, Pinto M, Sobral D, Santos JD, Nunes A, et al. Phylogenomic characterization and signs of microevolution in the 2022 multi-country outbreak of monkeypox virus. *Nat Med* (2022) 28(8):1569–72. doi: 10.1038/s41591-022-01907-y

18. Waterhouse AM, Procter JB, Martin DM, Clamp M, Barton GJ. Jalview version 2–a multiple sequence alignment Editor and analysis workbench. *Bioinformatics* (2009) 25(9):1189–91. doi: 10.1093/bioinformatics/btp033

19. Larsen MV, Lundegaard C, Lamberth K, Buus S, Lund O, Nielsen M. Large-Scale validation of methods for cytotoxic T-lymphocyte epitope prediction. *BMC Bioinf* (2007) 8:424. doi: 10.1186/1471-2105-8-424

20. Doytchinova IA, Flower DR. Vaxijen: A server for prediction of protective antigens, tumour antigens and subunit vaccines. *BMC Bioinf* (2007) 8:4. doi: 10.1186/1471-2105-8-4

21. Sharma NA-O, Naorem LA-O, Jain SA-O, Raghava GA-O. Toxinpred2: An improved method for predicting toxicity of proteins. *Brief Bioinform* (2022) 23(5):1–12. doi: 10.1093/bib/bbac174

22. Magnan CN, Zeller M, Kayala MA, Vigil A, Randall A, Felgner PL, et al. High-throughput prediction of protein antigenicity using protein microarray data. *Bioinformatics* (2010) 26(23):2936–43. doi: 10.1093/bioinformatics/btq551

23. Calis JJ, Maybeno M, Greenbaum JA, Weiskopf D, De Silva AD, Sette A, et al. Properties of mhc class I presented peptides that enhance immunogenicity. *PloS Comput Biol* (2013) 9(10):e1003266. doi: 10.1371/journal.pcbi.1003266

24. Paul S, Sidney J, Sette A, Peters B. Tepitool: A pipeline for computational prediction of T cell epitope candidates. *Curr Protoc Immunol* (2016) 114:18.9.1-.9.24. doi: 10.1002/cpim.12

25. Reynisson B, Barra C, Peters B, Nielsen M. Improved prediction of mhc ii antigen presentation through integration and motif deconvolution of mass spectrometry mhc eluted ligand data. *J Proteome Res* (2020) 19(6):2304–15. doi: 10.1021/acs.jproteome.9b00874

26. Kak G, Raza M, Tiwari BK. Interferon-gamma (Ifn-Γ): Exploring its implications in infectious diseases. *Biomol Concepts* (2018) 9(1):64–79. doi: 10.1515/bmc-2018-0007

27. Smiley ST, Grusby MJ. Interleukin 4. In: Delves PJ, editor. *Encyclopedia of immunology, 2nd ed.*, vol. . p . Oxford: Elsevier (1998). p. 1451–3.

28. Olejniczak K, Kasprzak A. Biological properties of interleukin 2 and its role in pathogenesis of selected diseases–a review. *Med Sci Monit* (2008) 14(10):Ra179–89.

29. Dhanda SK, Vir P, Raghava GPS. Designing of interferon-gamma inducing mhc class-ii binders. *Biol Direct* (2013) 8(1):30. doi: 10.1186/1745-6150-8-30

30. Dhanda SK, Gupta S, Vir P, Raghava GPS. Prediction of Il4 inducing peptides. *Clin Dev Immunol* (2013) 2013:263952. doi: 10.1155/2013/263952

31. Lathwal A, Kumar R, Kaur D, Raghava GPS. In silico model for predicting il-2 inducing peptides in human. *bioRxiv* (2021). doi: 10.1101/2021.06.20.449146

32. Saha S, Raghava GP. Prediction of continuous b-cell epitopes in an antigen using recurrent neural network. *Proteins* (2006) 65(1):40–8. doi: 10.1002/prot.21078

33. Bui H-H, Sidney J, Dinh K, Southwood S, Newman MJ, Sette A. Predicting population coverage of T-cell epitope-based diagnostics and vaccines. *BMC Bioinf* (2006) 7(1):153. doi: 10.1186/1471-2105-7-153

34. Chen C, Li Z, Huang H, Suzek BE, Wu CH. A fast peptide match service for uniprot knowledgebase. *Bioinformatics* (2013) 29(21):2808–9. doi: 10.1093/bioinformatics/btt484

35. Lamiable A, Thévenet P, Rey J, Vavrusa M, Derreumaux P, Tufféry P. Pep-Fold3: Faster de Novo structure prediction for linear peptides in solution and in complex. *Nucleic Acids Res* (2016) 44(W1):W449–54. doi: 10.1093/nar/gkw329

36. Sussman JL, Lin D, Jiang J, Jiang J, Manning NO, Prilusky J, et al. Protein data bank (Pdb): Database of three-dimensional structural information of biological macromolecules. *Acta Crystallogr D Biol Crystallogr* (1998) 54(Pt 6 Pt 1):1078–84. doi: 10.1107/s0907444998009378

37. Kaplan W, Littlejohn TG. Swiss-Pdb viewer (Deep view). *Brief Bioinform* (2001) 2(2):195–7. doi: 10.1093/bib/2.2.195

38. Eberhardt J, Santos-Martins DA-O, Tillack AA-O, Forli SA-O. Autodock vina 1.2.0: New docking methods, expanded force field, and Python bindings. *J Chem Inf Model* (2021) 61(8):3891–8. doi: 10.1021/acs.jcim.1c00203

39. Trott O, Olson AJ. Autodock vina: Improving the speed and accuracy of docking with a new scoring function, efficient optimization, and multithreading. *J Comput Chem* (2010) 31(2):455–61. doi: 10.1002/jcc.21334

40. Laskowski RA, Swindells MB. Ligplot+: Multiple ligand-protein interaction diagrams for drug discovery. *J Chem Inf Model* (2011) 51(10):2778–86. doi: 10.1021/ci200227u

41. Chen X, Zaro Jl Fau - Shen W-C, Shen WC. Fusion protein linkers: Property, design and functionality. *Adv Drug Deliv Rev* (2013) 65(10):1357–69. doi: 10.1016/j.addr.2012.09.039

42. Marciani DJ. Vaccine adjuvants: Role and mechanisms of action in vaccine immunogenicity. *Drug Discov Today* (2003) 8(20):934–43. doi: 10.1016/S1359-6446(03)02864-2

43. Lee SJ, Shin SJ, Lee MH, Lee MG, Kang TH, Park WS, et al. A potential protein adjuvant derived from mycobacterium tuberculosis Rv0652 enhances dendritic cells-based tumor immunotherapy. *PloS One* (2014) 9(8):e104351. doi: 10.1371/journal.pone.0104351

44. Yang D, Chertov O, Bykovskaia Sn, Chen Q, Buffo MJ, Shogan J, et al. Beta-defensins: Linking innate and adaptive immunity through dendritic and T cell Ccr6. *Science* (1999) 286(5439):525–8. doi: 10.1126/science.286.5439.525

45. Hu JC, Mathias-Santos C, Greene CJ, King-Lyons ND, Rodrigues JF, Hajishengallis G, et al. Intradermal administration of the type ii heat-labile enterotoxins Lt-iib and Lt-iic of enterotoxigenic escherichia coli enhances humoral and Cd8+ T cell immunity to a Co-administered antigen. *PloS One* (2014) 9(12):e113978. doi: 10.1371/journal.pone.0113978

46. Antonio-Herrera L, Badillo-Godinez O, Medina-Contreras O, Tepale-Segura A, García-Lozano A, Gutierrez-Xicotencatl L, et al. The nontoxic cholera b subunit is a potent adjuvant for intradermal dc-targeted vaccination. *Front Immunol* (2018) 9:2212. doi: 10.3389/fimmu.2018.02212

47. Shanmugam A, Rajoria S, George AL, Mittelman A, Suriano R, Tiwari RK. Synthetic toll like receptor-4 (Tlr-4) agonist peptides as a novel class of adjuvants. *PLoS One* (2012) 7(2):e30839. doi: 10.1371/journal.pone.0030839

48. Aziz S, Waqas M, Halim SA, Ali A, Iqbal A, Iqbal M, et al. Exploring whole proteome to contrive multi-Epitope-Based vaccine for neocov: An immunoinformtics

and in-silico approach. *Front Immunol* (2022) 13:956776. doi: 10.3389/fimmu.2022.956776

49. Tan C, Zhu F, Xiao Y, Wu Y, Meng X, Liu S, et al. Immunoinformatics approach toward the introduction of a novel multi-epitope vaccine against clostridium difficile. *Front Immunol* (2022) 13:887061. doi: 10.3389/fimmu.2022.887061

50. Guo L, Yin R, Liu K, Lv X, Li Y, Duan X, et al. Immunological features and efficacy of a multi-epitope vaccine ctb-ue against h. pylori in Balb/C mice model. *Appl Microbiol Biotechnol* (2014) 98(8):3495–507. doi: 10.1007/s00253-013-5408-6

51. Ojha R, Pandey RK, Prajapati VK. Vaccinomics strategy to concoct a promising subunit vaccine for visceral leishmaniasis targeting sandfly and leishmania antigens. *Int J Biol Macromol* (2020) 156:548–57. doi: 10.1016/j.ijbiomac.2020.04.097

52. Li M, Jiang Y, Gong T, Zhang Z, Sun X. Intranasal vaccination against hiv-1 with adenoviral vector-based nanocomplex using synthetic tlr-4 agonist peptide as adjuvant. *Mol Pharm* (2016) 13(3):885–94. doi: 10.1021/acs.molpharmaceut.5b00802

53. Hou J, Liu Y, Hsi J, Wang H, Tao R, Shao Y. Cholera toxin b subunit acts as a potent systemic adjuvant for hiv-1 DNA vaccination intramuscularly in mice. *Hum Vaccin Immunother* (2014) 10(5):1274–83. doi: 10.4161/hv.28371

54. Kalenik BM, Góra-Sochacka A, Sirko A. β-defensins - underestimated peptides in influenza combat. *Virus Res* (2018) 247:10–4. doi: 10.1016/j.virusres.2018.01.008

55. Alexander J, del Guercio M-F, Maewal A, Qiao L, Fikes J, Chesnut RW, et al. Linear padre T helper epitope and carbohydrate b cell epitope conjugates induce specific high titer igg antibody responses. *J Immunol* (2000) 164(3):1625. doi: 10.4049/jimmunol.164.3.1625

56. Gasteiger E, Gattiker A, Hoogland C, Ivanyi I, Appel RD, Bairoch A. Expasy: The proteomics server for in-depth protein knowledge and analysis. *Nucleic Acids Res* (2003) 31(13):3784–8. doi: 10.1093/nar/gkg563

57. Hallgren J, Tsirigos KD, Pedersen MD, Almagro Armenteros JJ, Marcatili P, Nielsen H, et al. Deeptmhmm predicts alpha and beta transmembrane proteins using deep neural networks. *bioRxiv* (2022). doi: 10.1101/2022.04.08.487609

58. Magnan CN, Randall A, Baldi P. Solpro: Accurate sequence-based prediction of protein solubility. *Bioinformatics* (2009) 25(17):2200–7. doi: 10.1093/bioinformatics/btp386

59. Nielsen H, Tsirigos KD, Brunak S, von Heijne G. A brief history of protein sorting prediction. *Protein J* (2019) 38(3):200–16. doi: 10.1007/s10930-019-09838-3

60. Buchan DWA, Jones DT. The psipred protein analysis workbench: 20 years on. *Nucleic Acids Res* (2019) 47(W1):W402–w7. doi: 10.1093/nar/gkz297

61. Kim DE, Chivian D Fau - Baker D, Baker D. Protein structure prediction and analysis using the robetta server. *Nucleic Acids Res* (2004) 32(Web Server issue):W526-31. doi: 10.1093/nar/gkh468

62. Ko J, Park H Fau - Heo L, Heo L Fau - Seok C, Seok C. Galaxyweb server for protein structure prediction and refinement. *Nucleic Acids Res* (2012) 40(Web Server issue):W294–7. doi: 10.1093/nar/gks493

63. Colovos C, Yeates TO. Verification of protein structures: Patterns of nonbonded atomic interactions. *Protein Sci* (1993) 2(9):1511–9. doi: 10.1002/pro.5560020916

64. Wiederstein M, Sippl MJ. Prosa-web: Interactive web service for the recognition of errors in three-dimensional structures of proteins. *Nucleic Acids Res* (2007) 35(Web Server issue):W407–10. doi: 10.1093/nar/gkm290.

65. Vijay K. Toll-like receptors in immunity and inflammatory diseases: Past, present, and future. *Int Immunopharmacol* (2018) 59:391–412. doi: 10.1016/j.intimp.2018.03.002

66. Zhou R, Liu L, Wang Y. Viral proteins recognized by different tlrs. *J Med Virol* (2021) 93(11):6116–23. doi: 10.1002/jmv.27265

67. Sartorius R, Trovato M, Manco R, D'Apice L, De Berardinis P. Exploiting viral sensing mediated by toll-like receptors to design innovative vaccines. *NPJ Vaccines* (2021) 6(1):127. doi: 10.1038/s41541-021-00391-8

68. Kozakov D, Hall DR, Xia B, Porter KA, Padhorny D, Yueh C, et al. The cluspro web server for protein-protein docking. *Nat Protoc* (2017) 12(2):255–78. doi: 10.1038/nprot.2016.169

69. van Zundert GCP, Rodrigues JPGLM, Trellet M, Schmitz C, Kastritis PL, Karaca E, et al. The Haddock2.2 web server: User-friendly integrative modeling of biomolecular complexes. *J Mol Biol* (2016) 428(4):720–5. doi: 10.1016/j.jmb.2015.09.014

70. Vangone A, Bonvin AMJJ. Contacts-based prediction of binding affinity in protein–protein complexes. *eLife* (2015) 4:e07454. doi: 10.7554/eLife.07454

71. Laskowski RA-O, Jabłońska J, Pravda L, Vařeková RS, Thornton JM. Pdbsum: Structural summaries of pdb entries. *Protein Sci* (2018) 27(1):129–34. doi: 10.1002/pro.3289

72. Delano WL. The pymol molecular graphics system. *Proteins* (2002) 30:442–54.

73. Wickes RD ed. Blender overview. In: *Foundation blender compositing*. Berkeley, CA: Apress. p. 1–23.

74. Kutzner C, Páll S, Fechner M, Esztermann A, de Groot BL, Grubmüller H. Best bang for your buck: Gpu nodes for gromacs biomolecular simulations. *J Comput Chem* (2015) 36(26):1990–2008. doi: 10.1002/jcc.24030

75. Maier JA, Martinez C, Kasavajhala K, Wickstrom L, Hauser KE, Simmerling C. Ff14sb: Improving the accuracy of protein side chain and backbone parameters from Ff99sb. *J Chem Theory Comput* (2015) 11(8):3696–713. doi: 10.1021/acs.jctc.5b00255

76. Berendsen HJ, Postma Jv, Van Gunsteren WF, DiNola A, Haak JR. Molecular dynamics with coupling to an external bath. *J Chem Phys* (1984) 81(8):3684–90. doi: 10.1063/1.448118

77. Parrinello M, Rahman A. Strain fluctuations and elastic constants. *J Chem Phys* (1982) 76(5):2662–6. doi: 10.1063/1.443248

78. Hess B, Bekker H, Berendsen HJC, Fraaije JGEM. Lincs: A linear constraint solver for molecular simulations. *J Comput Chem* (1997) 18(12):1463–72. doi: 10.1002/(SICI)1096-987X(199709)18:12<1463::AID-JCC4>3.0.CO;2-H

79. Darden T, York D, Pedersen L. Particle mesh ewald: An N·Log(N) method for ewald sums in Large systems. *J Chem Phys* (1993) 98(12):10089–92. doi: 10.1063/1.464397

80. Maisuradze GG, Liwo A, Scheraga HA. Relation between free energy landscapes of proteins and dynamics. *J Chem Theory Comput* (2010) 6(2):583–95. doi: 10.1021/ct9005745

81. Valdés-Tresanco MS, Valdés-Tresanco ME, Valiente PA, Moreno E. Gmx_Mmpbsa: A new tool to perform end-state free energy calculations with gromacs. *J Chem Theory Comput* (2021) 17(10):6281–91. doi: 10.1021/acs.jctc.1c00645

82. Rapin N, Lund O, Bernaschi M, Castiglione F. Computational immunology meets bioinformatics: The use of prediction tools for molecular binding in the simulation of the immune system. *PloS One* (2010) 5(4):e9862. doi: 10.1371/journal.pone.0009862

83. Yu M, Zhu Y, Li Y, Chen Z, Sha T, Li Z, et al. Design of a novel multi-epitope vaccine against echinococcus granulosus in immunoinformatics. *Front Immunol* (2021) 12:668492. doi: 10.3389/fimmu.2021.668492

84. Grote A, Hiller K, Scheer M, Münch R, Nörtemann B, Hempel DC, et al. Jcat: A novel tool to adapt codon usage of a target gene to its potential expression host. *Nucleic Acids Res* (2005) 33(Web Server issue):W526–31. doi: 10.1093/nar/gki376

85. Chaudhri G, Quah BJ, Wang Y, Tan AH, Zhou J, Karupiah G, et al. T Cell receptor sharing by cytotoxic T lymphocytes facilitates efficient virus control. *Proc Natl Acad Sci USA* (2009) 106(35):14984–9. doi: 10.1073/pnas.0906554106

86. Cancro MP, Tomayko MM. Memory b cells and plasma cells: The differentiative continuum of humoral immunity. *Immunol Rev* (2021) 303(1):72–82. doi: 10.1111/imr.13016

87. Bacchetta R, Gregori S, Roncarolo MG. Cd4+ regulatory T cells: Mechanisms of induction and effector function. *Autoimmun Rev* (2005) 4(8):491–6. doi: 10.1016/j.autrev.2005.04.005

88. Vartak A, Sucheck SJ. Recent advances in subunit vaccine carriers. *Vaccines (Basel)* (2016) 4(2):12–19. doi: 10.3390/vaccines4020012

89. Pacchioni SM, Bissa M, Zanotto C, Morghen CDG, Illiano E, Radaelli A. L1r, A27l, A33r and B5r vaccinia virus genes expressed by fowlpox recombinants as putative novel orthopoxvirus vaccines. *J Transl Med* (2013) 11:95. doi: 10.1186/1479-5876-11-95

90. Pulendran B, Arunachalam PS, O'Hagan DT. Emerging concepts in the science of vaccine adjuvants. *Nat Rev Drug Discov* (2021) 20(6):454–75. doi: 10.1038/s41573-021-00163-y

91. Tellam J, Connolly G, Green KJ, Miles JJ, Moss DJ, Burrows SR, et al. Endogenous presentation of Cd8+ T cell epitopes from Epstein-Barr virus-encoded nuclear antigen 1. *J Exp Med* (2004) 199(10):1421–31. doi: 10.1084/jem.20040191

92. Vyas JM, van der Veen AG, Ploegh HL. The known unknowns of antigen processing and presentation. *Nat Rev Immunol* (2008) 8(8):607–18. doi: 10.1038/nri2368

93. Pishesha N, Harmand TJ, Ploegh HL. A guide to antigen processing and presentation. *Nat Rev Immunol* (2022) 22(12):751–64. doi: 10.1038/s41577-022-00707-2

94. Joffre OP, Segura E, Savina A, Amigorena S. Cross-presentation by dendritic cells. *Nat Rev Immunol* (2012) 12(8):557–69. doi: 10.1038/nri3254

95. Luo M, Shao B, Yu JY, Liu T, Liang X, Lu L, et al. Simultaneous enhancement of cellular and humoral immunity by the high salt formulation of Al(Oh)(3) adjuvant. *Cell Res* (2017) 27(4):586–9. doi: 10.1038/cr.2017.14

96. Güven E, Duus K, Laursen I, Højrup P, Houen G. Aluminum hydroxide adjuvant differentially activates the three complement pathways with major involvement of the alternative pathway. *PloS One* (2013) 8(9):e74445. doi: 10.1371/journal.pone.0074445

frontiers | Frontiers in Immunology

TYPE Perspective
PUBLISHED 29 March 2023
DOI 10.3389/fimmu.2023.1107266

Check for updates

OPEN ACCESS

EDITED BY
P Bernard Fourie,
University of Pretoria, South Africa

REVIEWED BY
Jinghua Lu,
National Institute of Allergy and Infectious Diseases (NIH), United States

*CORRESPONDENCE
Andre Franke
a.franke@ikmb.uni-kiel.de

SPECIALTY SECTION
This article was submitted to Vaccines and Molecular Therapeutics, a section of the journal Frontiers in Immunology

RECEIVED 24 November 2022
ACCEPTED 13 March 2023
PUBLISHED 29 March 2023

CITATION
ElAbd H, Bacher P, Tholey A, Lenz TL and Franke A (2023) Challenges and opportunities in analyzing and modeling peptide presentation by HLA-II proteins. *Front. Immunol.* 14:1107266. doi: 10.3389/fimmu.2023.1107266

COPYRIGHT
© 2023 ElAbd, Bacher, Tholey, Lenz and Franke. This is an open-access article distributed under the terms of the Creative Commons Attribution License (CC BY). The use, distribution or reproduction in other forums is permitted, provided the original author(s) and the copyright owner(s) are credited and that the original publication in this journal is cited, in accordance with accepted academic practice. No use, distribution or reproduction is permitted which does not comply with these terms.

Challenges and opportunities in analyzing and modeling peptide presentation by HLA-II proteins

Hesham ElAbd[1], Petra Bacher[1,2], Andreas Tholey[3], Tobias L. Lenz[4] and Andre Franke[1]*

[1]Institute of Clinical Molecular Biology, University of Kiel, Kiel, Germany, [2]Institute of Immunology, University of Kiel, Kiel, Germany, [3]Proteomics & Bioanalytics, Institute for Experimental Medicine, University of Kiel, Kiel, Germany, [4]Research Unit for Evolutionary Immunogenomics, Department of Biology, University of Hamburg, Hamburg, Germany

The human leukocyte antigen (HLA) proteins are an indispensable component of adaptive immunity because of their role in presenting self and foreign peptides to T cells. Further, many complex diseases are associated with genetic variation in the HLA region, implying an important role for specific HLA-presented peptides in the etiology of these diseases. Identifying the specific set of peptides presented by an individual's HLA proteins *in vivo*, as a whole being referred to as the immunopeptidome, has therefore gathered increasing attention for different reasons. For example, identifying neoepitopes for cancer immunotherapy, vaccine development against infectious pathogens, or elucidating the role of HLA in autoimmunity. Despite the tremendous progress made during the last decade in these areas, several questions remain unanswered. In this perspective, we highlight five remaining key challenges in the analysis of peptide presentation and T cell immunogenicity and discuss potential solutions to these problems. We believe that addressing these questions would not only improve our understanding of disease etiology but will also have a direct translational impact in terms of engineering better vaccines and in developing more potent immunotherapies.

KEYWORDS

HLA-II & autoimmunity, immunogenicitiy, TCR - T cell receptor, mass-spectrometry (MS) based immunopeptidomics, neoantigen, immunotherapy

Introduction

The human leukocyte antigen class II (HLA-II) proteins are a class of glycoproteins that are mainly expressed on the surface of antigen presenting cells (APCs) where they present peptides to $CD4^+$ T cells. These peptides are derived from within the APCs itself, *e.g.* through autophagy (1), or from the cellular microenvironment, *e.g.* through receptor-mediated endocytosis (2) and macropinocytosis (3). As a result, APCs are able to present self-peptides together with foreign peptides, *e.g.* pathogens-driven peptides, to T cells. Thus, by identifying and analyzing the set of peptides presented on the surface of APCs, the

set of potential T cell epitopes can be narrowed down considerably into a manageable set of peptides and proteins. Nonetheless, HLA-II genes are extremely polymorphic, with most of the observed genetic variants located inside the peptide binding pocket, indicating that different HLA-II alleles encode for proteins that present different peptides, *i.e.* different alleles result in different immunopeptidomes. Moreover, HLA-II proteins present a diverse set of peptides, hence, the combination of these two factors results in an astronomically large number of peptide HLA-II complexes. Consequently, a lot of effort has been directed toward identifying and characterizing the set of HLA-II presented peptides for a plethora of aims, ranging from investigating autoimmune diseases (4) to neoepitope identification and cancer immunotherapy (5–7).

The rise of MS-based immunopeptidomics during the last decade has revolutionized our ability to identify peptides presented by HLA proteins *in vivo*. This has led to a "*Cambrian explosion*" in the field of neoepitope identification where continuous efforts are being directed at improving the experimental (8) and the computational aspects (9–11) of the technology to enable an accurate identification of neoepitopes. For example, Feola et al. (12) have recently described an immunopeptidomics-based pipeline for neoantigen identification and cancer vaccine development. Meanwhile, Chong and colleagues have recently developed *NewAnce* for identifying non-canonical peptides presented by HLA proteins on tumors (13). Beside identifying presented peptides and neoepitopes, a lot of efforts has been directed at improving the quantification of peptides presented by HLA proteins (14, 15).

MS-immunopeptidomics has been also utilized for vaccine candidate prioritization. Recently, Bettencourt et al. (16) utilized this technology for identifying *Mycobacterium tuberculosis* (Mtb) presented peptides, subsequently, a proof-of-concept vaccine against Mtb was developed using a subset of the presented peptides. Further, an mRNA-based vaccine against *Listeria monocytogenes* was recently developed by Mayer and colleagues (17) using an MS-immunopeptidomics guided approach. MS-immunopeptidomics was also utilized for mapping the presentation of SARS-CoV-2 spike glycoprotein proteins by common HLA-DR proteins (18).

Despite the recent progress, deciphering the principles governing peptide generation from potential protein candidates has proven to be an extremely challenging task. A reliable prediction of immunogenicity and immunodominance is therefore still lacking. In addition, the impact of the cellular microenvironment, genetic alterations in the non-HLA components of the peptide presentation machinery, the ageing of the host cells and other environmental factors on peptide presentation by HLA-II proteins is still far from being completely understood. In this perspective, we thus highlight five open questions that are likely to improve our understanding of the biology of HLA-II peptide presentation and its influence on T cell immunogenicity.

What is the role of digestive enzymes in shaping HLA-II immunopeptidomes?

Arguably, one of the crucial and, nonetheless, not-completely understood steps in peptide presentation by HLA-II proteins is the loading of HLA-II molecules. Conceptually, loading can be divided into two processes that operate asynchronously. Firstly, peptide generation, and secondly, the actual molecular loading. The former happens through the sequential cleavage of proteins inside the lysosome (19–21) which can be derived from, for example, self-proteins (22, 23), from microbes (16) or from environmental sources such as pollen allergens (24). Proteins in the lysosomes are mainly cleaved using a group of proteases referred to as cathepsins (Cat) (25). Although some cathepsins are ubiquitously expressed in all tissues, *e.g.* Cat B (26), Cat D (27), and Cat L (28), some show a tissue-restricted expression, for example, Cat S (28) in APCs.

Recent findings have suggested an important role for cathepsins in shaping peptide presentation and immunogenicity. For example, Riese et al. (29) identified a critical role for Cat S in antigen presentation in B cells and dendritic cells. Meanwhile, Dheilly et al. (30) have shown that the same enzyme also regulates antigen presentation by non-Hodgkin Lymphoma. Besides Cat S, Cat L has been shown to be a major regulator of presentation by epithelium cells (31) and in the production of an IgA antibodies against *M. pneumonia* (32). Cat L has also been shown to impact the specialization of the generated T cell response where treating *Leishmania major* infected mice with Cat L inhibitors worsen the disease by changing the T cell response from a Th1 to a Th2 response (33). Moreover, inhibiting Cat L in Non-obese diabetic (NOD) mice protected these mice form developing type I diabetes supposedly by increasing the fraction of T regulatory cells in these mice relative to untreated mice (34). These findings illustrate the need to study the influence of cathepsins on HLA-II peptide presentation in depth using recent technological advances in MS-immunopeptidomics and other omics fields. The provided insights would help in establishing a link between the digestive capacity of the cell (*i.e.* which digestive enzyme is expressed and at what level) and presentation by HLA-II proteins.

Different methods can be used to delineate the role of cathepsins in shaping HLA-II immunopeptidomes such as the combination of mass spectrometry (MS)-based immunopeptidomics and gene-editing methods. This can be accomplished either by knocking down one of the cathepsins in a cell culture and measure its impact on the immunopeptidome and/or by using a mixture of knock-ins and knockouts of different combinations of digestive enzymes and subsequently investigate the impact on the immunopeptidome. Machine-learning methods could then be set up to extract generalizable patterns from these experiments.

What is the impact of cell type and cellular micro-environment on HLA-II presentation?

Although the experiments proposed above would provide much-needed insights into the role of proteases in shaping HLA-II immunopeptidomes, it is only one piece of the larger puzzle as it only delineates the determinants of the digestive process. Nonetheless, the actual pool of proteins available to these proteases, *i.e.* the pool of substrate proteins, is also still poorly understood. Recently, Wang et al. (4) have described differences in peptides presented by B cells and monocytes, and argued that differences in the preprocessing machinery and the available proteins to each cell-type might explain this difference. Along these lines, Marcu et al. (35) have revealed qualitative and quantitative differences in the immunopeptidome of different tissues. Further, presentation of viral and tumors proteins has been shown to increase after tagging these proteins for autophagy (36–39), pointing to an important rule for autophagy and the non-HLA components of the presentation machinery in modeling the set of presented peptides. These components can also be influenced by external and internal signals such as inflammation, stress, and calorie restriction (40–42). Therefore, future efforts should focus on deciphering the link among the cellular status, the cellular micro-environment and HLA-II immunopeptidomes, for example, using simultaneous deep multi-omics profiling, *e.g.* proteomics and transcriptomics, coupled with MS-based immunopeptidomics across different cellular states and across different tissues and organs.

What are the temporal aspects of HLA-II presentation?

An additional challenge is the extent of variation in the duration of presentation, *i.e.* the duration a given peptide is presented on the cell surface by an HLA-II protein. Differences in the lifespan, *i.e.* duration of presentation, of different peptide HLA-I complexes have been proposed to be a major factor shaping the immunogenicity of different peptides (43, 44). For example, Micheletti et al. (45) have identified an important rule for the lifespan of HLA-I peptide complexes and the efficiency of the generated T cell response. Despite the prominent role of presentation dynamics in shaping immunogenicity, it is a poorly understood and characterized process.

Different experimental approaches can be utilized to investigate this problem, for example, by recording the presentation dynamic of a knocked-in gene-of-interest, *e.g.*, specific antigenic proteins or tumor-associated neoantigen with a controllable level of expression. In such systems the link between expression levels and temporal presentation behavior can be delineated by varying either the strength and/or the duration of expression and quantifying the effect on presentation dynamics using immunopeptidomics.

How do post-translational modifications shape HLA-II immunopeptidome formation and how is this linked to the cellular state?

As illustrated above, the immunopeptidome is an extremely complex, dynamic, and only partially understood entity. One of the factors that require further investigation are post-translational modifications (PTMs), for example phosphorylation, acylation or deamination. Such PTM can change the physicochemical interaction between peptides and HLA-proteins (46) as well as the interaction between a peptide-HLA complex and TCRs and, as a result, affect the generated T cell response (47). Indeed, in different autoimmune diseases such as type I diabetes some of the target antigens were found to harbor PTMs, for example, insulin/proinsulin (48) and GRP7 (49).

Multiple challenges render the identification of PTMs in the immunopeptidome troublesome. For example, peptides with PTMs have a low abundance or at least a lower abundance relative to the un-modified peptides (50) (at least this holds true in proteomics). Moreover, some PTMs might interfere with peptide ionization and hence decrease the detectability by MS (50). Besides these experimental challenges, there are computational challenges associated with identifying PTMs. Mainly, the database search which becomes computationally impractical when a large number of PTMs is included (51). Nonetheless, through the development of PTM-aware search engines such as *MSFragger* (52), *and MODa* (53), or through the developed of tailored pipelines such as PROMISE (54) progress is being made in addressing this challenging task.

What are the factors that shape the T cell response to a particular peptide-HLA complex?

Conceptually, factors shaping the interaction between an APC and a T cell can be broken-down into five interwoven layers (Figure 1): starting with (A) the molecular layer, then (B) the supramolecular layer, followed by (C) the cellular layer, then (D) the micro-environmental layer, and finally (E) the temporal layer (see below).

Molecular layer

The molecular layer refers to the interaction between an HLA-peptide complex and a TCR. At this level, the sequence-based physicochemical properties of the three molecular components would determine which set of TCRs will recognize a particular peptide-HLA complex. The strength of this interaction also governs different aspects of the generated T cell response, for example, Tubo et al. (58) have recently shown that the strength of TCR-peptide-

10.3389/fimmu.2023.1107266

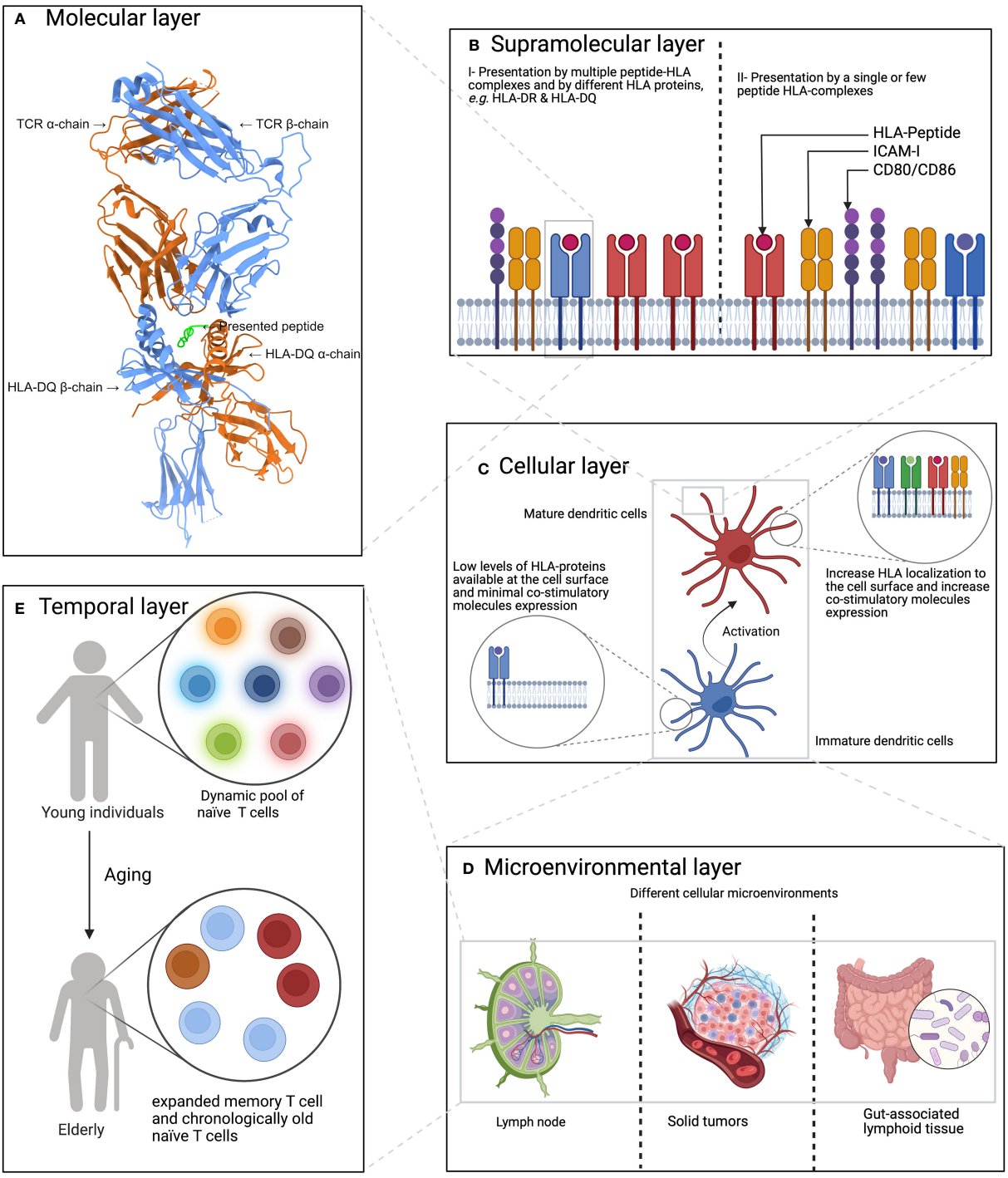

FIGURE 1
A hierarchal model of factors influencing or shaping the T cell response. **(A)** The molecular layer which focuses on HLA-peptide-TCR interaction. Here, the interaction between HLA- DQ 2.2 loaded with a gluten-derived peptide and a TCR is shown. The panel was created using ChimeraX (55), the protein 3D structure was obtained from Protein Data Bank (56) under the identifier 6PX6 (57). **(B)** The supramolecular layer which describes the impact of co-stimulatory molecules and the count of HLA-P complexes, among others. **(C)** Describes the impact of the cell types on both sides of the immunological synapse, *i.e.* the type of APCs and T cells, on shaping the generated T cell response. **(D)** The CME layer which describes the impact of the cellular micro-environment on shaping T cell response where extra cellular signaling can influence both antigen presentation, T cell priming and subsequently the generated T cell response. **(E)** The impact of aging on shaping T cell response where the T cell pool becomes dominated by expanded memory T cells and chronological old naïve T cells.

MHCII interaction have an important role in shaping the differentiation of naïve $CD4^+$ T cells.

Supramolecular layer

The supramolecular layer involves the formation of an immunological synapse (59) between an APC and a T cell where a collection of co-stimulatory molecules and their receptors, along with the TCR and its intracellular signaling components, assemble to form an efficient signaling and communication channel between the two cells. One of the open questions here is the impact of presentation density on T cell activation, *i.e.* the absolute number of HLA-II proteins presenting the same peptide, and which HLA-II proteins present the peptide to the T cell. Previous work by Irvine et al. (60) illustrated the exceptional sensitivity of $CD4^+$ T cells towards MHC-II molecules where a single MHC-peptide complex is sufficient for driving the T cell response. Hence, a potential future direction is to disentangle the impact of affinity, *i.e.* the affinity of a particular TCR toward a particular HLA-peptide complex, from the impact of the count, *i.e.* the number of HLA-peptide complexes.

Cellular layer

The cellular level refers to the type of APCs and T cells: although HLA-II molecules are mainly expressed on professional APCs, their expression can be induced on a variety of other cell types by inflammatory cytokines, *e.g.* INF-γ (61, 62). Additionally, different cell types can act as professional APCs such as dendritic cells and macrophages (63) each of which is also subclassified further into different cell types. For example, dendritic cells are classified into conventional dendritic cells (cDCs) and plasmacytoid dendritic cells, inflammatory dendritic cells and Langerhans cells (64). cDCs are further subclassified into cDC1 and cDC2 (65), each with a different phenotype and function. For example, cDC1 are efficient cross-presenters (65, 66) while cDC2 cells can efficiently prime naïve $CD4^+$ T cells (65, 67, 68). On the other side of the immunological synapse, T cells can exist in different states, for example, naïve, effector, memory, and anergic T cells, each of which have a different antigenic sensitivity (69, 70), and even utilize different metabolic pathways (71). Hence, characterizing the cellular impact on presentation and T cell activation is of paramount importance for a deeper understanding of immunogenicity.

Microenvironmental layer

The cellular micro-environment (CME) can play a vital role in shaping either antigen presentation and/or the resulting T cell response. In the former, the CME plays a pivotal role in determining which proteins are available to the presentation machinery along with finetuning the cellular state, *e.g.* which digestive enzymes are expressed and/or which co-stimulatory molecules are expressed through cellular signaling (72–74). For the T cell response, CME signaling can have a crucial role in shaping the behavior of T cells, *e.g.* TGF-β and the induction of regulatory T cells (75).

Temporal layer

Finally, the temporal level which refers to the (immune system) age of the host along with previous exposure to the same antigen or to a similar antigen. These two factors will likely shape the resulting response greatly by changing the pool of available T cells, *e.g.* in young individuals the T cell pool is shaped by more dynamic naïve T cells, while in older individuals it is mainly characterized by expanded memory T cells and chronologically older naïve T cells (76). Hence, a deeper characterization of the impact of aging on antigen-presentation and T cell expansion is vital because it might provide strategies to design vaccines that would work on the elderly, which has proven to be a challenging task, too (77, 78).

Concluding remarks

Recent advances in computational (9, 10) and experimental approaches, *e.g.* improved sensitivity of MS analysis, are enabling much deeper and more accurate characterization of the immunopeptidome. Nonetheless, we are still far from a complete understanding of all the factors shaping the formation of the immunopeptidome and its dynamics. Furthermore, despite the recent improvement in predicting peptide-presentation *in vivo*, this improvement has not translated into a reliable *in silico* prediction of immunogenicity. Indeed, factors governing immunogenicity and immunodominance are still poorly understood. In this perspective we aimed at highlighting gaps in our understanding of peptide presentation and T cell activation, and discussed approaches for further investigation. Coordinated, systematic and large-scale efforts are urgently needed to provide deeper insights into antigen presentation and T cell activation. These insights would help developing more efficient vaccines, better immunotherapies, and also improve our understanding of immunity and host-pathogen interactions more generally.

Data availability statement

The original contributions presented in the study are included in the article/supplementary material. Further inquiries can be directed to the corresponding author.

Author contributions

HE and AF conceived the manuscript. HE wrote the manuscript with input from TL, AT, PB and AF. All authors read and approved the final manuscript.

Funding

The manuscript was funded by the German Research Foundation DFG Research Unit 5042: miTarget—miTarget—The Microbiome as a Therapeutic Target in Inflammatory Bowel Diseases along with funding from the Cluster of Excellence 2167 "Precision Medicine in Chronic Inflammation (PMI)". TL was funded by the Deutsche Forschungsgemeinschaft (DFG, German Research Foundation) – 437857095. The funding agencies had no role in the design, collection, analysis, and interpretation of data and neither in writing the manuscript.

Acknowledgments

Figure 1 was created with BioRender.com.

Conflict of interest

The authors declare that the research was conducted in the absence of any commercial or financial relationships that could be construed as a potential conflict of interest.

Publisher's note

All claims expressed in this article are solely those of the authors and do not necessarily represent those of their affiliated organizations, or those of the publisher, the editors and the reviewers. Any product that may be evaluated in this article, or claim that may be made by its manufacturer, is not guaranteed or endorsed by the publisher.

References

1. Schuck S. Microautophagy – distinct molecular mechanisms handle cargoes of many sizes. *J Cell Sci* (2020) 133, jcs246322. doi: 10.1242/jcs.246322

2. Kaksonen M, Roux A. Mechanisms of clathrin-mediated endocytosis. *Nat Rev Mol Cell Biol* (2018) 19:313–326. doi: 10.1038/nrm.2017.132

3. Liu Z, Roche PA. Macropinocytosis in phagocytes: regulation of MHC class-II-restricted antigen presentation in dendritic cells. *Front Physiol* (2015) 6. doi: 10.3389/fphys.2015.00001

4. Wang J, Jelcic I, Mühlenbruch L, Haunerdinger V, Toussaint NC, Zhao Y, et al. HLA-DR15 molecules jointly shape an autoreactive T cell repertoire in multiple sclerosis. *Cell* (2020) 183:1264–81. doi: 10.1016/j.cell.2020.09.054

5. Bassani-Sternberg M, Bräunlein E, Klar R, Engleitner T, Sinitcyn P, Audehm S, et al. Direct identification of clinically relevant neoepitopes presented on native human melanoma tissue by mass spectrometry. *Nat Commun* (2016) 7, 13404. doi: 10.1038/ncomms13404

6. Chong C, Coukos G, Bassani-Sternberg M. Identification of tumor antigens with immunopeptidomics. *Nat Biotechnol* (2022) 40:175–188. doi: 10.1038/s41587-021-01038-8

7. Rivero-Hinojosa S, Grant M, Panigrahi A, Zhang H, Caisova V, Bollard CM, et al. Proteogenomic discovery of neoantigens facilitates personalized multi-antigen targeted T cell immunotherapy for brain tumors. *Nat Commun* (2021) 12, 6689. doi: 10.1038/s41467-021-26936-y

8. Abelin JG, Harjanto D, Malloy M, Suri P, Colson T, Goulding SP, et al. Defining HLA-II ligand processing and binding rules with mass spectrometry enhances cancer epitope prediction. *Immunity* (2019) 51:766–779.e17. doi: 10.1016/j.immuni.2019.08.012. Elsevier.

9. Bichmann L, Nelde A, Ghosh M, Heumos L, Mohr C, Peltzer A, et al. MHCquant: Automated and reproducible data analysis for immunopeptidomics. *J Proteome Res Am Chem Soc* (2019) 18:3876–84. doi: 10.1021/acs.jproteome.9b00313

10. ElAbd H, Degenhardt F, Koudelka T, Kamps A-K, Tholey A, Bacher P, et al. Immunopeptidomics toolkit library (IPTK): A python-based modular toolbox for analyzing immunopeptidomics data. *BMC Bioinf* (2021) 22, 405. doi: 10.1186/s12859-021-04315-0

11. ElAbd H, Degenhardt F, Lenz TL, Franke A, Wendorff M. VCF2Prot: An efficient and parallel tool for generating personalized proteomes from VCF files. *bioRxiv* (2022). doi: 10.1101/2022.01.21.477084

12. Feola S, Chiaro J, Martins B, Russo S, Fusciello M, Ylösmäki E, et al. A novel immunopeptidomic-based pipeline for the generation of personalized oncolytic cancer vaccines. *Elife* (2022) 11:e71156. doi: 10.7554/eLife.71156

13. Chong C, Müller M, Pak HS, Harnett D, Huber F, Grun D, et al. Integrated proteogenomic deep sequencing and analytics accurately identify non-canonical peptides in tumor immunopeptidomes. *Nat Commun* (2020) 11. doi: 10.1038/s41467-020-14968-9

14. Stopfer LE, Mesfin JM, Joughin BA, Lauffenburger DA, White FM. Multiplexed relative and absolute quantitative immunopeptidomics reveals MHC I repertoire alterations induced by CDK4/6 inhibition. *Nat Commun* (2020) 11, 2760. doi: 10.1038/s41467-020-16588-9

15. Pollock SB, Rose CM, Darwish M, Bouziat R, Delamarre L, Blanchette C, et al. Sensitive and quantitative detection of MHC-I displayed neoepitopes using a semiautomated workflow and TOMAHAQ mass spectrometry. *Mol Cell Proteomics* (2021) 20, 100108. doi: 10.1016/j.mcpro.2021.100108

16. Bettencourt P, Müller J, Nicastri A, Cantillon D, Madhavan M, Charles PD, et al. Identification of antigens presented by MHC for vaccines against tuberculosis. *NPJ Vaccines* (2020) 5:2. doi: 10.1038/s41541-019-0148-y.

17. Mayer RL, Verbeke R, Asselman C, Aernout I, Gul A, Eggermont D, et al. Immunopeptidomics-based design of mRNA vaccine formulations against listeria monocytogenes. *Nat Commun* (2022) 13:6075. doi: 10.1038/s41467-022-33721-y

18. Knierman MD, Lannan MB, Spindler LJ, McMillian CL, Konrad RJ, Siegel RW. The human leukocyte antigen class II immunopeptidome of the SARS-CoV-2 spike glycoprotein. *Cell Rep* (2020) 33. doi: 10.1016/j.celrep.2020.108454. Elsevier.

19. Neefjes J. CIIV, MIIC and other compartments for MHC class II loading. *Eur J Immunol* (1999) 29:1421–1425. doi: 10.1002/(SICI)1521-4141(199905)29:05<1421::AID-IMMU1421>3.0.CO;2-C

20. Michelet X, Garg S, Wolf BJ, Tuli A, Ricciardi-Castagnoli P, Brenner MB. MHC class II presentation is controlled by the lysosomal small GTPase, Arl8b. *J Immunol* (2015) 194:2079–88. doi: 10.4049/jimmunol.1401072

21. Lützner N, Kalbacher H. Quantifying cathepsin s activity in antigen presenting cells using a novel specific substrate*. *J Biol Chem* (2008) 283:36185–94. doi: 10.1074/jbc.M806500200

22. Nimmerjahn F, Milosevic S, Behrends U, Jaffee EM, Pardoll DM, Bornkamm GW, et al. Major histocompatibility complex class II-restricted presentation of a cytosolic antigen by autophagy. *Eur J Immunol* (2003) 33:1250–92003. doi: 10.1002/eji.200323730

23. Dengjel J, Schoor O, Fischer R, Reich M, Kraus M, Müller M, et al. Autophagy promotes MHC class II presentation of peptides from intracellular source proteins. *Proc Natl Acad Sci Proc Natl Acad Sci* (2005) 102:7922–7. doi: 10.1073/pnas.0501190102

24. Blume C, Foerster S, Gilles S, Becker W-M, Ring J, Behrendt H, et al. Human epithelial cells of the respiratory tract and the skin differentially internalize grass pollen allergens. *J Invest Dermatol* (2009) 129:1935–44. doi: 10.1038/jid.2008.459

25. Yadati T, Houben T, Bitorina A, Shiri-Sverdlov R. The ins and outs of cathepsins: Physiological function and role in disease management. *Cells* (2020) 9. doi: 10.3390/cells9071679

26. Ni J, Lan F, Xu Y, Nakanishi H, Li X. Extralysosomal cathepsin b in central nervous system: Mechanisms and therapeutic implications. *Brain Pathol* (2022) 32:e13071. doi: 10.1111/bpa.13071. John Wiley & Sons, Ltd.

27. Hoes M, Tromp J, Ouwerkerk W, Bomer N, Oberdorf-Maass S, Samani N, et al. The role of cathepsin d in the pathophysiology of heart failure and its potentially beneficial properties: A translational approach. *Eur J Heart Fail* (2019) 22:2102–11. doi: 10.1002/ejhf.1674

28. Mohamed MM, Sloane BF. Multifunctional enzymes in cancer. *Nat Rev Cancer* (2006) 6:764–75. doi: 10.1038/nrc1949

29. Riese RJ, Mitchell RN, Villadangos JA, Shi GP, Palmer JT, Karp ER, et al. Cathepsin s activity regulates antigen presentation and immunity. *J Clin Invest* (1998) 101:2351–63. doi: 10.1172/JCI1158. The American Society for Clinical Investigation.

30. Dheilly E, Battistello E, Katanayeva N, Sungalee S, Michaux J, Duns G, et al. Cathepsin s regulates antigen processing and T cell activity in non-Hodgkin lymphoma. *Cancer Cell* (2020) 37:674–89. doi: 10.1016/j.ccell.2020.03.016

31. Beck H, Schwarz G, Schröter CJ, Deeg M, Baier D, Stevanovic S, et al. Cathepsin s and an asparagine-specific endoprotease dominate the proteolytic processing of human

myelin basic protein *in vitro*. *Eur J Immunol* (2001) 31:3726–36. doi: 10.1002/1521-4141(200112)31:12<3726::AID-IMMU3726>3.0.CO;2-O. John Wiley & Sons, Ltd.

32. Zhang N, Gao P, Yin B, Li J, Wu T, Kuang Y, et al. Cathepsin l promotes secretory IgA response by participating in antigen presentation pathways during mycoplasma hyopneumoniae infection. *PLoS One* (2019) 14:e0215408. doi: 10.1371/journal.pone.0215408

33. Onishi K, Li Y, Ishii K, Hisaeda H, Tang L, Duan X, et al. Cathepsin l is crucial for a Th1-type immune response during leishmania major infection. *Microbes Infect* (2004) 6:468–74. doi: 10.1016/j.micinf.2004.01.008

34. Maehr R, Mintern JD, Herman AE, Lennon-Duménil A-M, Mathis D, Benoist C, et al. Cathepsin l is essential for onset of autoimmune diabetes in NOD mice. *J Clin Invest* (2005) 115:2934–43. doi: 10.1172/JCI25485. The American Society for Clinical Investigation.

35. Marcu A, Bichmann L, Kuchenbecker L, Kowalewski DJ, Freudenmann LK, Backert L, et al. HLA ligand atlas: A benign reference of HLA-presented peptides to improve T-cell-based cancer immunotherapy. *J Immunother Cancer* (2021) 9:e002071. doi: 10.1136/jitc-2020-002071

36. Schmid D, Pypaert M, Münz C. MHC class II antigen loading compartments continuously receive input from autophagosomes. *Immunity* (2007) 26:792007. doi: 10.1016/j.immuni.2006.10.018

37. Jin Y, Sun C, Feng L, Li P, Xiao L, Ren Y, et al. Regulation of SIV antigen-specific CD4 + T cellular immunity *via* autophagosome-mediated MHC II molecule-targeting antigen presentation in mice. *PLoS One* (2014) 9:e931432014. doi: 10.1371/journal.pone.0093143

38. Fonteneau JF, Brilot F, Münz C, Gannagé M. The tumor antigen NY-ESO-1 mediates direct recognition of melanoma cells by CD4+ T cells after intercellular antigen transfer. *J Immunol* (2016) 196:64–71. doi: 10.4049/jimmunol.1402664

39. Münz C. The macroautophagy machinery in MHC restricted antigen presentation. *Front Immunol* (2021) 12:628429. doi: 10.3389/fimmu.2021.628429

40. Dikic I, Elazar Z. Mechanism and medical implications of mammalian autophagy. *Nat Rev Mol Cell Biol* (2018) 19:349–64. doi: 10.1038/s41580-018-0003-4

41. He L, Zhang J, Zhao J, Ma N, Kim SW, Qiao S, et al. Autophagy: The last defense against cellular nutritional stress. *Adv Nutr* (2018) 9:493–504. doi: 10.1093/advances/nmy011

42. Chung KW, Chung HY. The effects of calorie restriction on autophagy: Role on aging intervention. *Nutr* (2019) 11. doi: 10.3390/nu11122923

43. Levitsky V, Zhang QJ, Levitskaya J, Masucci MG. The life span of major histocompatibility complex-peptide complexes influences the efficiency of presentation and immunogenicity of two class I-restricted cytotoxic T lymphocyte epitopes in the Epstein-Barr virus nuclear antigen 4. *J Exp Med* (1996) 183:915–26. doi: 10.1084/jem.183.3.915

44. Nelson CA, Petzold SJ, Unanue ER. Peptides determine the lifespan of MHC class II molecules in the antigen-presenting cell. *Nature* (1994) 371:250–2. doi: 10.1038/371250a0

45. Micheletti B, Canella M, Traniello G. The lifespan of major histocompatibility complex class i/peptide complexes determines the efficiency of cytotoxic T-lymphocyte responses. *Immunology* (1999) 96:411–5. doi: 10.1046/j.1365-2567.1999.00707.x.

46. Mei S, Ayala R, Ramarathinam SH, Illing PT, Faridi P, Song J, et al. Immunopeptidomic analysis reveals that deamidated HLA-bound peptides arise predominantly from deglycosylated precursors. *Mol Cell Proteomics* (2020) 19:1236–47. doi: 10.1074/mcp.RA119.001846

47. McGinty JW, Marré ML, Bajzik V, Piganelli JD, James EA. T Cell epitopes and post-translationally modified epitopes in type 1 diabetes. *Curr Diabetes Rep* (2015) 15:90. doi: 10.1007/s11892-015-0657-7

48. Mannering SI, Harrison LC, Williamson NA, Morris JS, Thearle DJ, Jensen KP, et al. The insulin a-chain epitope recognized by human T cells is posttranslationally modified. *J Exp Med* (2005) 202:1191–7. doi: 10.1084/jem.20051251. 2005/10/31The Rockefeller University Press.

49. Wicker LS, Chen SL, Nepom GT, Elliott JF, Freed DC, Bansal A, et al. Naturally processed T cell epitopes from human glutamic acid decarboxylase identified using mice transgenic for the type 1 diabetes-associated human MHC class II allele, DRB1*0401. *J Clin Invest* (1996) 98:2597–603. doi: 10.1172/JCI119079

50. Larsen M, Trelle M, Thingholm T, Jensen O. Analysis of posttranslational modifications of proteins by tandem mass spectrometry. *Biotechniques* (2006) 40:790–8. doi: 10.2144/000112201

51. Yuan Z-F, Lin S, Molden RC, Garcia BA. Evaluation of proteomic search engines for the analysis of histone modifications. *J Proteome Res* (2014) 13:4470–8. doi: 10.1021/pr5008015

52. Yu F, Teo GC, Kong AT, Haynes SE, Avtonomov DM, Geiszler DJ, et al. Identification of modified peptides using localization-aware open search. *Nat Commun* (2020) 11:4065. doi: 10.1038/s41467-020-17921-y

53. Na S, Bandeira N, Paek E. Fast multi-blind modification search through tandem mass spectrometry. *Mol Cell Proteomics* (2012) 11:M111.010199. doi: 10.1074/mcp.M111.010199

54. Kacen A, Javitt A, Kramer MP, Morgenstern D, Tsaban T, Solomon A, et al. Uncovering the modified immunopeptidome reveals insights into principles of PTM-driven antigenicity. *bioRxiv* (2021). doi: 10.1101/2021.04.10.438991

55. Pettersen EF, Goddard TD, Huang CC, Meng EC, Couch GS, Croll TI, et al. UCSF ChimeraX: Structure visualization for researchers, educators, and developers. *Protein Sci* (2021) 30:70–82. doi: 10.1002/pro.3943

56. Berman HM, Westbrook J, Feng Z, Gilliland G, Bhat TN, Weissig H, et al. The protein data bank. *Nucleic Acids Res* (2000) 28:235–42. doi: 10.1093/nar/28.1.235

57. Tian TY, Shiva D-K, Keshia KHS, Shuo-Wang Q, Neumann RS, Lundin KEA, et al. A molecular basis for the T cell response in HLA-DQ2.2 mediated celiac disease. *Proc Natl Acad Sci* (2020) 117:3063–73. doi: 10.1073/pnas.1914308117. Proceedings of the National Academy of Sciences.

58. Tubo NJ, Pagán AJ, Taylor JJ, Nelson RW, Linehan JL, Ertelt JM, et al. Single naive CD4+ T cells from a diverse repertoire produce different effector cell types during infection. *Cell* (2013) 53:758–96. doi: 10.1016/j.cell.2013.04.007

59. Dustin ML. The immunological synapse. *Cancer Immunol Res* (2014) 2:1023–33. doi: 10.1158/2326-6066.CIR-14-0161

60. Irvine DJ, Purbhoo MA, Krogsgaard M, Davis MM. Direct observation of ligand recognition by T cells. *Nature* (2002) 419:845–9. doi: 10.1038/nature01076

61. Thelemann C, Eren RO, Coutaz M, Brasseit J, Bouzourene H, Rosa M, et al. Interferon-γ induces expression of MHC class II on intestinal epithelial cells and protects mice from colitis. *PLoS One* (2014) 9:e86844–e86844. doi: 10.1371/journal.pone.0086844

62. Helbig H, Kittredge KL, Palestine AG, Coca-Prados M, Nussenblatt RB. Gamma-interferon induces differential expression of HLA-DR, -DP and -DQ in human ciliary epithelial cells. *Graefe's Arch Clin Exp Ophthalmol* (1991) 229:191–4. doi: 10.1007/BF00170556

63. Gaudino SJ, Kumar P. Cross-talk between antigen presenting cells and T cells impacts intestinal homeostasis, bacterial infections, and tumorigenesis. *Front Immunol* (2019) 10. doi: 10.3389/fimmu.2019.00360

64. Balan S, Saxena M, Bhardwaj N. Chapter one - dendritic cell subsets and locations. In: Lhuillier C, Galluzzi L, editors. *Immunobiol dendritic cells part a*. (2019) Amsterdam: Academic Press.

65. Sasaki I, Kato T, Hemmi H, Fukuda-Ohta Y, Wakaki-Nishiyama N, Yamamoto A, et al. Conventional type 1 dendritic cells in intestinal immune homeostasis. *Front Immunol* (2022) 13. doi: 10.3389/fimmu.2022.857954

66. Heath WR, Carbone FR. Cross-presentation, dendritic cells, tolerance and immunity. *Annu Rev Immunol* (2001) 19:472001. doi: 10.1146/annurev.immunol.19.1.47

67. Kumamoto Y, Linehan M, Weinstein JS, Laidlaw BJ, Craft JE, Iwasaki A. CD301b+ dermal dendritic cells drive T helper 2 cell-mediated immunity. *Immunity* (2013) 39:733–432013. doi: 10.1016/j.immuni.2013.08.029

68. Plantinga M, Guilliams M, Vanheerswynghels M, Deswarte K, Branco-Madeira F, Toussaint W, et al. Conventional and monocyte-derived CD11b+ dendritic cells initiate and maintain T helper 2 cell-mediated immunity to house dust mite allergen. *Immunity* (2013) 38:322–352013. Elsevier. doi: 10.1016/j.immuni.2012.10.016

69. Grayson JM, Harrington LE, Lanier JG, Wherry EJ, Ahmed R. Differential sensitivity of naive and memory CD8+ T cells to apoptosis *in vivo*. *J Immunol* (2002) 169:3760–70. doi: 10.4049/jimmunol.169.7.3760

70. Kumar R, Ferez M, Swamy M, Arechaga I, Rejas MT, Valpuesta JM, et al. Increased sensitivity of antigen-experienced T cells through the enrichment of oligomeric T cell receptor complexes. *Immunity* (2011) 35:375–87. doi: 10.1016/j.immuni.2011.08.010

71. Gerriets VA, Rathmell JC. Metabolic pathways in T cell fate and function. *Trends Immunol* (2012) 33:168–73. doi: 10.1016/j.it.2012.01.010

72. Kobie JJ, Wu RS, Kurt RA, Lou S, Adelman MK, Whitesell LJ, et al. Transforming growth factor β inhibits the antigen-presenting functions and antitumor activity of dendritic cell vaccines. *Cancer Res* (2011) 63:1860–42003.

73. Strobl H, Knapp W. TGF-β1 regulation of dendritic cells. *Microbes Infect* (1999) 1:1283–90. doi: 10.1016/S1286-4579(99)00256-7

74. Oh J, Shin J-S. Molecular mechanism and cellular function of MHCII ubiquitination. *Immunol Rev* (2015) 266:134–44. doi: 10.1111/imr.12303

75. Wan YY, Flavell RA. 'Yin–yang' functions of transforming growth factor-β and T regulatory cells in immune regulation. *Immunol Rev* (2007) 220:199–213. doi: 10.1111/j.1600-065X.2007.00565.x.

76. Salam N, Rane S, Das R, Faulkner M, Gund R, Bughani U, et al. T Cell ageing: Effects of age on development, survival & function. *Indian J Med Res* (2013) 138:595–6082013.

77. Ciabattini A, Nardini C, Santoro F, Garagnani P, Franceschi C, Medaglini D. Vaccination in the elderly: The challenge of immune changes with aging. *Semin Immunol* (2018) 40:83–94. doi: 10.1016/j.smim.2018.10.010

78. Aspinall R, Del Giudice G, Effros RB, Grubeck-Loebenstein B, Sambhara S. Challenges for vaccination in the elderly. *Immun Ageing* (2007) 4:9. doi: 10.1186/1742-4933-4-9

frontiers | Frontiers in Immunology

TYPE Original Research
PUBLISHED 30 March 2023
DOI 10.3389/fimmu.2023.1129245

Check for updates

OPEN ACCESS

EDITED BY
Mrinmoy Sanyal,
Stanford University, United States

REVIEWED BY
Kaissar Tabynov,
Kazakh National Agrarian University, Kazakhstan
Bert Schepens,
VIB-UGent Center for Inflammation Research (IRC), Belgium

*CORRESPONDENCE
Ilias B. Esmagambetov
esmagambetovib@gmail.com

†These authors have contributed equally to this work

SPECIALTY SECTION
This article was submitted to Vaccines and Molecular Therapeutics, a section of the journal Frontiers in Immunology

RECEIVED 21 December 2022
ACCEPTED 15 March 2023
PUBLISHED 30 March 2023

CITATION
Esmagambetov IB, Ryabova EI, Derkaev AA, Shcheblyakov DV, Dolzhikova IV, Favorskaya IA, Grousova DM, Dovgiy MA, Prokofiev VV, Gosudarev AI, Byrikhina DV, Zorkov ID, Iliukhina AA, Kovyrshina AV, Shelkov AY, Naroditsky BS, Logunov DY and Gintsburg AL (2023) rAAV expressing recombinant antibody for emergency prevention and long-term prophylaxis of COVID-19. *Front. Immunol.* 14:1129245. doi: 10.3389/fimmu.2023.1129245

COPYRIGHT
© 2023 Esmagambetov, Ryabova, Derkaev, Shcheblyakov, Dolzhikova, Favorskaya, Grousova, Dovgiy, Prokofiev, Gosudarev, Byrikhina, Zorkov, Iliukhina, Kovyrshina, Shelkov, Naroditsky, Logunov and Gintsburg. This is an open-access article distributed under the terms of the Creative Commons Attribution License (CC BY). The use, distribution or reproduction in other forums is permitted, provided the original author(s) and the copyright owner(s) are credited and that the original publication in this journal is cited, in accordance with accepted academic practice. No use, distribution or reproduction is permitted which does not comply with these terms.

rAAV expressing recombinant antibody for emergency prevention and long-term prophylaxis of COVID-19

Ilias B. Esmagambetov*†, Ekaterina I. Ryabova†, Artem A. Derkaev†, Dmitry V. Shcheblyakov, Inna V. Dolzhikova, Irina A. Favorskaya, Daria M. Grousova, Mikhail A. Dovgiy, Vladimir V. Prokofiev, Andrey I. Gosudarev, Daria V. Byrikhina, Ilia D. Zorkov, Anna A. Iliukhina, Anna V. Kovyrshina, Artem Y. Shelkov, Boris S. Naroditsky, Denis Y. Logunov and Alexander L. Gintsburg

Federal State Budget Institution, National Research Center for Epidemiology and Microbiology Named after Honorary Academician N.F. Gamaleya of the Ministry of Health of the Russian Federation, Moscow, Russia

Introduction: Numerous agents for prophylaxis of SARS-CoV-2-induced diseases are currently registered for the clinical use. Formation of the immunity happens within several weeks following vaccine administration which is their key disadvantage. In contrast, drugs based on monoclonal antibodies, enable rapid passive immunization and therefore can be used for emergency pre- and post-exposure prophylaxis of COVID-19. However rapid elimination of antibody-based drugs from the circulation limits their usage for prolonged pre-exposure prophylaxis.

Methods: In current work we developed a recombinant adeno-associated viral vector (rAAV), expressing a SARS-CoV-2 spike receptor-binding domain (RBD)-specific antibody P2C5 fused with a human IgG1 Fc fragment (P2C5-Fc) using methods of molecular biotechnology and bioprocessing.

Results and discussions: A P2C5-Fc antibody expressed by a proposed rAAV (rAAV-P2C5-Fc) was shown to circulate within more than 300 days in blood of transduced mice and protect animals from lethal SARS-CoV-2 virus (B.1.1.1 and Omicron BA.5 variants) lethal dose of 10^5 TCID50. In addition, rAAV-P2C5-Fc demonstrated 100% protective activity as emergency prevention and long-term prophylaxis, respectively. It was also demonstrated that high titers of neutralizing antibodies to the SARS-CoV-2 virus were detected in the blood serum of animals that received rAAV-P2C5-Fc for more than 10 months from the moment of administration.Our data therefore indicate applicability of an rAAV for passive immunization and induction of a rapid long-term protection against various SARS-CoV-2 variants.

KEYWORDS

recombinant adeno-associated viral vector (rAAV), single-domain antibodies, VHH, COVID-19, SARS-CoV-2, passive immunization, prophylaxis

1 Introduction

Coronavirus disease (COVID-19) is a severe acute respiratory illness, recorded for the first time in Wuhan, China at the end of 2019 (1). COVID-19 pandemic was declared March 11, 2020 (2). A severe acute respiratory syndrome coronavirus 2 (SARS-CoV-2) (Betacoronavirus: Coronaviridae) is the causative agent of the disease. More than 579 million confirmed COVID-19 cases and 6.4 million deaths, associated with COVID-19 are registered worldwide at the moment (3).

Vaccination, associated with formation of collective immunity represents an important factor, limiting spread of the disease. At least 198 vaccines are being investigated in the preclinical settings and 170 agents are being tested in clinical trials nowadays (4). Most of vaccines however induce the formation of immunity within several weeks following administration (5–8) and therefore are not applicable for emergency prevention of COVID-19. Monoclonal antibodies represent a more appropriate strategy for emergency prevention and therapy of COVID-19 and are successfully used in the clinic (9). Tixagevimab/cilgavimab (Evusheld™), regdanvimab (Regkirona™), sotrovimab (Xevudy™), bamlanivimab/etesevimab and casirivimab/imdevimab (REGEN-COV™) are currently approved for the clinical usage. Prolonged prophylaxis with these drugs however is not optimal due to their limited circulation time in the human body (10). Given aforementioned limitations of existing treatment approaches, development of a drug suitable for pre- and post-exposure as well as prolonged COVID-19 prophylaxis is still relevant and passive immunization with recombinant adenoviral vectors (rAAV) enabling delivery and prolonged expression of specific antibodies within the organism can serve as a valuable therapeutic strategy. There is evidence demonstrating the efficacy of this approach for induction of prolonged protection against Ebola, Marburg and influenza viral diseases as well as botulinum neurotoxin intoxication (11–15). The choice of rAAV was dictated by their ability to transduce a wide spectrum of cellular targets, low immunogenicity, safety and prolonged persistence in the body as episome (16).

In our previous study we had generated a panel of antibodies specific to the SARS-CoV-2 spike receptor-binding domain (RBD) (17). The most perspective antibodies with the highest neutralizing capacity against the most alarming SARS-CoV-2 variants (Alpha, Beta, Gamma and Omicron) had been selected. In current study we developed an rAAV, expressing a previously generated antibody (clone P2C5) fused to the human IgG1-fragment (P2C5-Fc). The obtained rAAV-P2C5-Fc demonstrated prolonged expression and circulation of P2C5-Fc in serum of transduced mice (more than 300 days). Given as emergency prevention and long-term prophylaxis rAAV-P2C5-Fc enabled full protection of ACE-2 transgenic mice from a lethal dose of SARS-CoV-2 virus. In addition, to study the biodistribution of rAAV upon intramuscular administration, we obtained rAAV-Luc expressing the luciferase gene. It was found that injection of rAAV into the hind limb is followed local tissue transduction and expression of the transgene at the administration site within at least 60 days.

2 Material and methods

2.1 Cell lines and viruses

Vero E6 (ATCC CRL-1586) cells were maintained in Dulbecco's modified Eagle's medium (DMEM, HyClone, Cytiva, USA), supplemented with 10% or 2% of heat-inactivated fetal bovine serum (FBS, Capricorn Scientific, Germany), L-glutamine (4 mM) and penicillin/streptomycin solution (100 IU/mL; 100 µg/mL) (PanEco, Moscow, Russia).

The SARS-CoV-2 variants B.1.1.1 or PMVL-1 (GISAID EPI_ISL_421275) and Omicron BA.5 (hCoV-19/Russia/SPE-RII-25357S/2022) initially isolated from a nasopharyngeal swab were obtained from the State Collection of Viruses of the Gamaleya Center in Moscow and used in both challenge and Microneutralization Assay. Isolation and further propagation were performed in Vero E6 cells in DMEM (HyClone Cytiva, Austria) with 2% heat-inactivated FBS (Capricorn Scientific GmbH, Germany): the cells were infected at multiplicity of infection (MOI) = 0.01 and incubated at 37°C in 5% CO2. The culture medium was collected at 72 h and clarified by centrifugation at 9000 g for 10 min at +4°C. The culture medium containing the virus was aliquoted, frozen and stored at −80°C.

2.2 Animal housing conditions

Female BALB/c mice (6 weeks old, weighing 18–20 g) were purchased from "Pushchino breeding facility" (Pushchino, Moscow, Russia) accredited by the Association for Assessment and Accreditation of Laboratory Animal Care (AAALAC International) and maintained at the central animal facility of the Gamaleya Research Center for Epidemiology and Microbiology. Mice were kept at constant temperature (22 ± 2°C) and relative humidity (50%) with 12 h of artificial light per day, housed in individual T2-type cages (eight animals per cage), and fed with dried food and water *ad libitum*.

Transgenic hemizygous female and male K18-hACE2 mice (B6.Cg-Tg(K18-ACE2)2Prlmn/J; 4–5 weeks old) congenic on a C57BL/6 genetic background were initially purchased from the Jackson Laboratory (USA) and subsequently bred according to the official breeding considerations and following the General Terms and Conditions policy. Mice were housed in ventilated ISOCage P and N systems (Techniplast, Italy) for immunological and infection (BSL3 conforming) studies, respectively, with free access to autoclaved drinking water and standard chow diet. All of the experimental procedures were conducted in N.F. Gamaleya National Research Center for Epidemiology and Microbiology in compliance with the Guide for the Care and Use of Laboratory Animals (NIH Publication #85–23, revised 1996), and approved by the local animal ethics committee (protocol #25, 22 Apr 2022) and conducted.

2.3 Production and characterization of rAAV

Recombinant viral vectors rAAV-P2C5-Fc, rAAV-B11-Fc and rAAV-Luc were obtained as described previously (15, 18). Briefly,

the AAV-DJ plasmid system was used to produce rAAV-P2C5-Fc, rAAV-B11-Fc and rAAV-Luc. (Cell Biolabs, CIIIA). Single domain P2C5 antibody was obtained as described (17). The nucleotide sequence encoding P2C5-Fc antibody was synthesized at Evrogen Company (Moscow, Russia). The optimized sequence of the firefly luciferase gene Fluc was obtained from the vector pGL4.51[luc2/CMV/Neo] (Promega). Both sequences were cloned into the rAAV–EGFP Control Vector plasmid instead of the EGFP gene at the EcoRI and XbaI restriction sites, thus obtaining the rAAV-P2C5-Fc and rAAV-Luc plasmids, respectively. rAAV-P2C5-Fc and rAAV-Luc were produced by transient transfections of HEK293 cells (obtained from the cell cultures collection of the Gamaleya National Research Center for Epidemiology and Microbiology) and cultured in a BioFlo 320 bioreactor (Eppendorf, Germany) with a BioBLU 5c disposable vessel (Eppendorf, Germany) filled with Fibra-Cel matrix (Eppendorf, Germany). rAAV-P2C5-Fc and rAAV-Luc purification was performed using an AKTA flux S tangential flow filtration system (Cytiva Life Sciences, USA) and a Hollow Fiber Cartridge, 100 kDa (Cytiva Life Sciences, USA) following affinity chromatography using AVB Sepharose resin (Cytiva Life Sciences, USA) according to the manufacturer's protocol.

The purity of the obtained rAAV-P2C5-Fc and rAAV-Luc was assessed by SDS-PAGE with 4%–20% Mini-PROTEAN TG Precast Protein Gel (Bio-Rad, USA) under reducing conditions. The number of rAAV-P2C5-Fc and rAAV-Luc genomic copies was determined by the AAVpro Titration Kit (for Real Time PCR) Ver.2 according to the manufacturer's protocol.

An *in vitro* transduction efficiency of the purified rAAV-P2C5-Fc preparation was evaluated using HEK293 cell culture. Cells were seeded in 96-well microtiter plates containing 100 µL of DMEM media (4 mM glutamine, 10% FBS, 3.8 g/L sodium bicarbonate) at a concentration of $0.5*10^6$ cells/ml and incubation continued for 4 hours. The cells were then infected with rAAV-P2C5-Fc, the cultural medium was collected 48 hours after and used for measurement of P2C5-Fc recombinant antibody levels. An ELISA kit developed at the Gamaleya National Research Center for Epidemiology and Microbiology and registered for clinical use in Russia (P3H 2020/10393 2020-05-18) was used for SARS-CoV-2 RBD-specific IgG analysis. Concentration of the antibody was estimated using optical density of the culture medium samples and standards, represented by purified P2C5-Fc solutions with prespecified antibody concentrations.

2.4 Investigation of rAAV distribution in mice

A single intramuscular injection of rAAV-Luc at a dose of 10^{10} gc/animal was used to investigate rAAV distribution in mouse. Intraperitoneal injections of D-luciferin at a dose of 2.5 µg were performed on day 7 and 60 after the rAAV-Luc administration. Then after 5 min exposition bioluminescence in mice was visualized in IVIS Lumina II under isoflurane anesthesia.

2.5 Evaluation of *in vivo* protective capacity of rAAV-P2C5-Fc

In vivo studies were performed using a mice transgenic for human angiotensin-converting enzyme 2 (ACE-2) receptors (K18-hACE2 mice). A single injection of rAAV-P2C5-Fc into the thigh muscles of the hind limb was performed and the mouse were infected intranasally with SARS-COV2 at a dose of 10^5 TCID50 per animal. Intact mice were used as controls. Each group consisted of 5 animals. Clinical signs of the disease, such as weight loss were monitored twice daily throughout the experiment. Intact mice or mice treated with rAAV-B11-Fc were used as a negative control.

2.6 Determination of viral load in the lungs of infected animals

Determination of viral load in the lungs of mice transduced with rAAV-P2C5-Fc and infected with SARS-CoV-2 B.1.1.1 was performed as described previously (19). Primers for the mouse and hamster beta-actin gene were used to control RNA isolation (mice: F: CTATTGGCAACGAGCGGTTC, R: CGGATGTC AACGTCACACTTC, P: ROX-GCTCTTTTCCAGCCTTCCTT CTTG-BHQ2; hamsters: F: ACTGCCGCATCCTCTTCCT, R: TCGTTGCCAATGGTGATGAC, P: FAM-CCTGGAGAAG AGCTATGAGCTGCCTGATG-BHQ1 (20).

2.7 Evaluation of the pharmacokinetic profile of P2C5-Fc antibody expressed after *in vivo* rAAV–P2C5-Fc transduction

A number of BALB/c female mice weighing 18–20 g were treated with a single intramuscular injection of rAAV-P2C5-Fc at a dose of $2*10^{11}$ gc/mouse. The blood samples were collected from the facial vein before rAAV-P2C5-Fc transduction (point 0) and 1, 2, 3, 7, 14, 21, 45, 60, 90, 120, 150, 180, 210, 240, 270, and 300 days after rAAV-P2C5-Fc transduction. Serum was collected and stored at–20°C until further analysis. Serum samples were taken from three animals per time point. The concentration of P2C5-Fc antibody in collected serum samples was measured as described in section "2.3 Production and characterization of rAAV."

2.8 Evaluation of immunogenicity of rAAV-P2C5-Fc and P2C5-Fc antibody, expressed *via* rAAV-P2C5-Fc transduction

Evaluation of immunogenicity of rAAV-P2C5-Fc and P2C5-Fc antibody, expressed *via* rAAV-P2C5-Fc transduction, was performed as described previously (15). Immunogenicity of rAAV-P2C5-Fc vector was evaluated by the detection of anti-rAAV capsid protein antibodies in the serum of rAAV-P2C5-Fc-

treated mice. Immunogenicity of P2C5-Fc antibody, expressed *via* rAAV-P2C5-Fc transduction, was evaluated by the detection of anti- P2C5-Fc antibodies in the serum of rAAV-P2C5-Fc-treated mice. Samples obtained in the section "Evaluation of pharmacokinetic of P2C5-Fc antibody expressed *via in vivo* rAAV-P2C5-Fc transduction" were used for analysis.

2.9 Microneutralization assay with Live SARS-CoV-2

Serum samples from rAAV-P2C5-Fc-transduced mice were two-fold serially diluted starting from 1/10 in complete Dulbecco`s modified Eagle medium (DMEM) supplemented with 2% heat-inactivated fetal bovine serum (HI-FBS). All of following manipulations were performed as described previously (17). The minimal neutralizing dilutions of serum were defined as the highest serum titers that completely inhibited CPE of the virus in two or three of the three replicable wells. All experiments were performed in a Biosafety Level 3 facility (BSL-3). Samples obtained in the section "Evaluation of the pharmacokinetic profile of P2C5-Fc antibody expressed after *in vivo* rAAV-P2C5-Fc transduction" were used for analysis. In order to immediately obtain the average value of the virus-neutralizing titer for each point, sera samples from different animals from the same time point were mixed with each other in equal proportions.

2.10 Statistical analysis

Data were analyzed using EXCEL 2010, Graphpad Prism 9.0, and ELISA Master (AlkorBio, Russia) software. The Mann–Whitney U-test and the Gehan–Wilcoxon test with a significance level of 0.05 were used to assess intergroup differences in antibody titers and animal survival. Median survival was determined using Kaplan–Meier analysis. The p-value was determined using the t-test and log-rank test.

3 Results

3.1 Production and characterization of rAAV expressing P2C5-Fc antibody

P2C5 single-domain antibody specific to RBD of the viral S protein and demonstrating virus neutralization potency was developed as described earlier (17). On the next step an N terminus of the amino acid sequence of the antibody was modified with a signal peptide of a heavy chain of the human IgG1 and a C terminus was modified with an Fc fragment of human IgG1. A P2C5-Fc coding nucleotide sequence was synthesized by Evrogene company and further cloned into pAAV-DJ-vector. rAAV-P2C5-Fc was obtained as described earlier (15, 18). Transducing activity of obtained rAAV-P2C5-Fc as well as expression and specific activity of P2C5-Fc antibody were analyzed using ELISA. An adherent HEK293 cell culture was transduced with 10^2 gc/cell of rAAV-P2C5-Fc. Level of RBD specific antibodies in cultural medium was analyzed 0, 24, 48 and 72 hours after the transduction using an 'ELISA SARS Gamaleya' kit. A range of purified P2C5-Fc concentrations was used as a standard. As a result, an average level of P2C5-Fc antibody in a culture medium of transduced cells reached 8 ng/mL and further increased to 22 and 56 ng/ml 24, 48 and 72 hours after the procedure, respectively. Key steps of rAAV-P2C5-Fc preparation as well as analysis of its purity, authenticity and transducing capacity are shown in (Figures 1A–D).

Summarizing all mentioned above, we can say that the generated rAAV expressing P2C5-Fc antibody specific to RBD of the viral S protein, demonstrated high transducing capacity of the vector and showed functional activity of the expressed antibody.

3.2 Selection of an optimal rAAV-P2C5-Fc protective dose

Evaluation of rAAV-P2C5-Fc protective activity was performed using a lethal ACE-2 humanized murine infection model. At the first step selection of an optimal protective rAAV-P2C5-Fc dose was done *via* infection of the experimental animals with a lethal SARS-CoV-2 virus B.1.1.1 variant at a dose of 10^5 TCID50. Based on the results of the previous studies evaluating protective activity of an rAAV-B11-Fc agent, expressing a recombinant antibody specific to botulotoxin type A (15), as well as observed *in vitro* activity of P2C5-Fc antibody (minimal *in vitro* neutralizing concentration of P2C5-Fc against SARS-CoV-2 virus B.1.1.1 is about 6 ng/ml) rAAV-P2C5-Fc doses of $2*10^{10}$, 10^{11} and $2*10^{11}$ gc/mouse were selected. Three days after the rAAV-P2C5-Fc injection animals were challenged with the native SARS-CoV-2 virus. Intact mice (received normal saline solution) were used as a negative control. The scheme of the experiment is shown in Figure 2A. As a result, animal survival was 60%, 60% and 100% in groups treated with $2*10^{10}$, 10^{11} and $2*10^{11}$ gc/mouse doses, respectively. A significant body weight decrease of more than 10% was observed in animals, treated with $2*10^{10}$ gc/mouse dose whereas no symptoms of the disease were observed in the group received $2*10^{11}$ gc/mouse dose. Animal death in the control group was observed 7-11 days after the challenge. Experimental results are shown in (Figures 2B, C). Based on the aforementioned observations an rAAV-P2C5-Fc dose of $2*10^{11}$ gc/mouse or 10^{13}gc/kg was considered to be the optimal one and used for further studies.

3.3 Evaluation of efficacy of early and emergency pre- and post-exposure prophylaxis with rAAV-P2C5-Fc against SARS-CoV-2 induced disease

To assess the applicability of rAAV-P2C5-Fc for early and emergency pre- and post-exposure prophylaxis of SARS-CoV2 induced disease a humanized ACE-2 mouse model was used analogously to the previous experiment. The animals were

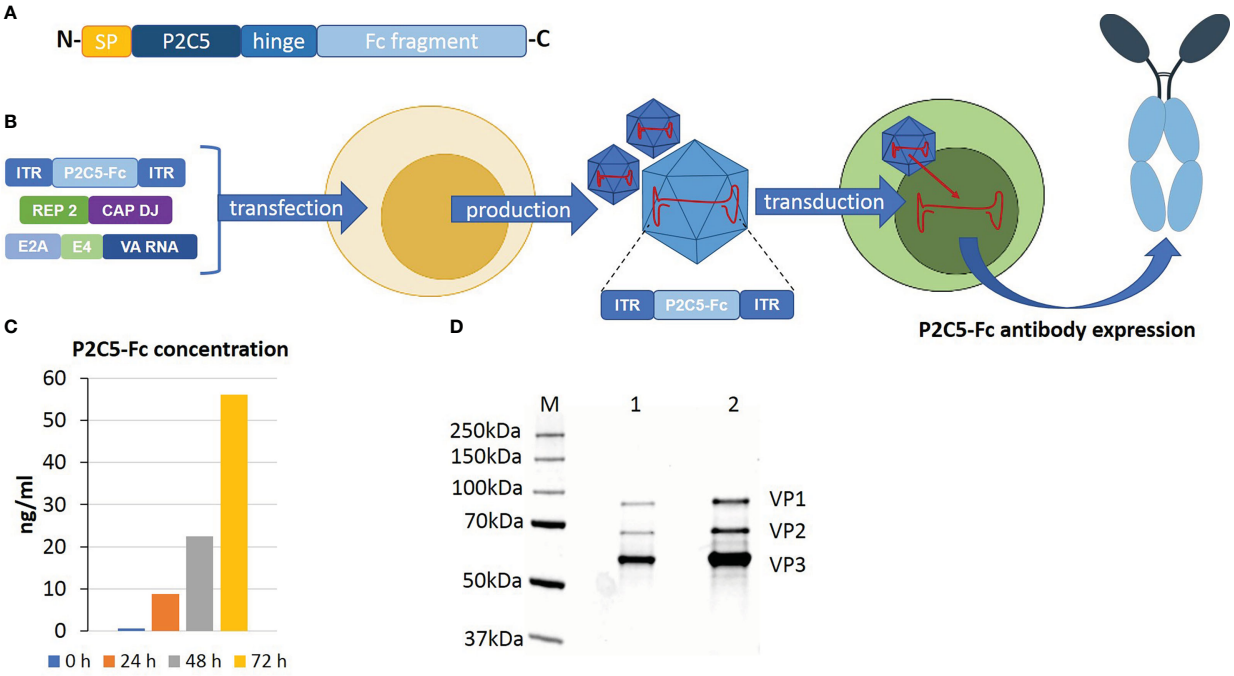

FIGURE 1
An overview of rAAV-P2C5-Fc preparation and analysis. **(A)** Structure of recombinant P2C5-Fc antibody: SP – amino acid sequence of signal peptide of IgG1 heavy chain; P2C5 – amino acid sequence of P2C5 single domain antibody; hinge – amino acid sequence of hinge region of IgG1; Fc fragment amino acid sequence Fc fragment of IgG1. **(B)** Schematics of rAAV-P2C5-Fc production and mechanism of action. **(C)** Evaluation of rAAV-P2C5-Fc transducing activity using HEK293 cells: bars indicate concentration of P2C5-Fc antibody in cultural media, cultivation time is shown by color. **(D)** SDS-PAGE of an rAAV-P2C5-Fc purity and authenticity analysis: M – protein molecular weight marker; 1, 2 fractions of purified rAAV-P2C5-Fc; VP1, VP2, VP3 rAAV capsid proteins.

transduced with rAAV-P2C5-Fc dose of $2*10^{11}$ gc/mouce and challenged with 10^5 TCID50 of SARS-CoV-2 at different time points before or after the treatment. A 16-hour delay between the challenge and rAAV-P2C5-Fc administration was considered as a post-exposure prophylaxis scenario. Pre-exposure emergency prophylaxis regimen implied simultaneous rAAV-P2C5-Fc administration and animal infection; in early pre-exposure prophylaxis groups rAAV-P2C5-Fc was given 24 hours, 3,7 or 14 days before the challenge. Animals that did not receive the rAAV-P2C5-Fc treatment and administrated with normal saline solution were used as a control. The scheme of the experiment is shown in Figure 3A. Experimental results indicate a 40% survival and more than 10% body weight decrease in post-exposure prophylaxis group whereas a 100% survival and no weight loss were observed in other groups, treated with rAAV-P2C5-Fc (Figures 3B–E). As in the previous study all animals from the control group died within 11 days after the SARS-CoV-2 infection.

To control the possibility of induction of non-specific protection mediated by rAAV, a group of mice was transduced rAAV-B11-Fc obtained in a previous study (15) and simultaneous infected with 10^5 TCID50 of SARS-CoV-2. The scheme of the experiment is shown in Figure 4A. Animals treated with rAAV-B11-Fc lost weight and fell at approximately the same time as intact mice (Figures 4B, C). Thus, the absence of non-specific protection of animals following rAAV administration was demonstrated.

Generated experimental data therefore demonstrate applicability of rAAV-P2C5-Fc for early and emergent pre-exposure prophylaxis of the SARS-CoV-2 induced infection; post-exposure prophylaxis with rAAV-P2C5-Fc showed limited efficacy of 40%.

3.4 Evaluation of duration of SARS-CoV-2 induced infection protection with rAAV-P2C5-Fc

Duration of protective rAAV-P2C5-Fc action was evaluated using humanized ACE-2 mice. Animals were transduced with a drug dose of $2*10^{11}$ gc/mouse and challenged with a SARS-CoV-2 infective dose of 10^5 TCID50 on 60, 90 and 140 days after the transduction. Selection of the time points was done based on our previous studies, where duration of the protective action of a similar preparation against botulotoxin A was shown to be more than 120 days (15). Control mice did not receive an rAAV-P2C5-Fc injection. Scheme of the experiment is shown in Figure 5A.

In the current study we evaluated not only animal survival and body weight decrease but also examined sterilizing immunity induced by rAAV-P2C5-Fc. To do so persistence of live virus in lungs, upper respiratory tract and brain of challenged animals was evaluated *via* an *in vitro* titration (Figure 5B).

Experimental observations demonstrated full animal protection against SARS-CoV-2 induced infection within at least 4.5 months after the transduction (Figures 5C, D). It is very important to note that no signs of the disease as well as no live virus was detected in

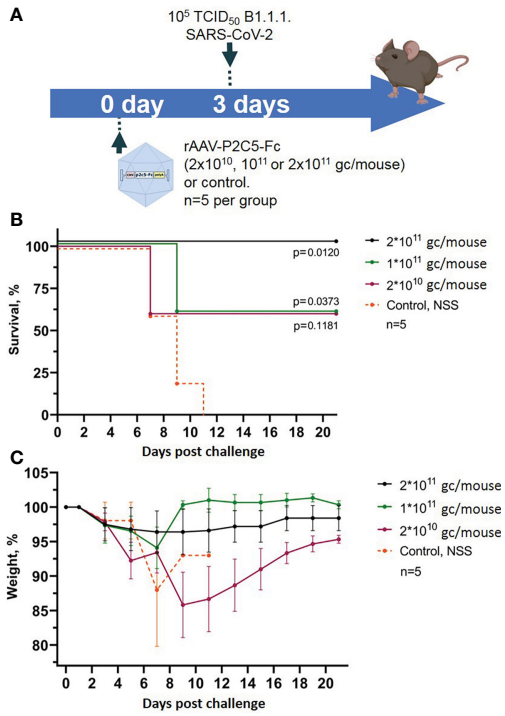

FIGURE 2
Evaluation of rAAV-P2C5-Fc optimal dose. **(A)** Scheme of the experiment: mice were treated with different doses of rAAV-P2C5-Fc and challenged with 10^5 TCID50 SARS-CoV-2 B.1.1.1 variant on day 3 after the transduction. **(B)** Animal survival. **(C)** Body weight loss. Lines – mean values, error bars – SD, numbers indicate statistical significance evaluated compared with the vehicle group using a logrank test. Data from different rAAV-P2C5-Fc treatment groups are shown by color. Control, NSS – mice received normal saline solution. n – number of animals per group.

tissues and organs of the transduced mice, challenged with SARS-CoV-2 at the day 140 after transduction. At the same time high virus concentration was detected in lungs, brain and upper respiratory tract epithelium of the control animals, infected with SARS-CoV-2 virus (Figure 5B).

Generated evidence indicated that rAAV-P2C5-Fc induces an immediate animal protection which lasts for at least 4.5 months following the drug injection. In addition, in our study we demonstrated formation of sterilizing immunity preventing virus replication within the body in response to rAAV-P2C5-Fc administration.

3.5 Evaluation of protective activity of rAAV-P2C5-Fc against SARS-CoV-2 variant Omicron BA.5

To evaluate effectiveness of our agent against various SARS-CoV-2 variants a humanized ACE-2 mouse model was used. Animals received rAAV-P2C5-Fc at a dose of $2*10^{11}$ gc/mouse and were challenged with SARS-CoV-2 variant Omicron BA.5 at a dose of 10^5 TCID50. Control animals, challenged with the virus variants Omicron BA.5 and B.1.1.1 did not receive the treatment. Scheme of the experiment is shown in Figure 6A.

As a result, 100% survival was shown in the group of animals challenged with variants Omicron BA.5 and B.1.1.1. and treated with rAAV-P2C5-Fc. In control group of animals, infected with SARS-CoV-2 variant Omicron BA.5, 50% survival and a significant weight loss was observed, whereas all control animals, infected with B.1.1.1 died within 8 days following the challenge. Experimental results are shown in Figures 6B, C.

Accumulated data confirms protective activity of rAAV-P2C5-Fc against various SARS-CoV-2 variants including Omicron BA.5.

3.6 Evaluation of rAAV biodistribution within the body of transduced mice

To evaluate localization of the target gene expression following an rAAV intramuscular injection an rAAV expressing firefly luciferase (rAAV-Luc) was used. BALB/c mice received a single intramuscular injection of rAAV-Luc at a dose of 10^{10} gc/animal into thigh muscles of the hind limb. Intact mice and mice received rAAV-P2C5-Fc, were used as a control group. A luciferase activity was detected solely at the site of rAAV-Luc injection on the day 7 and 60 after the transduction. No luciferase activity was observed in control animals. Experimental results, shown in Figures 7A, B, indicate that intramuscular administration of rAAV provides prolonged local expression of the transgene, lasting more than 60 days. In addition, the expression level of luciferase on day 60 was at least 10 fold higher than on day 7.

3.7 Evaluation of virus neutralization activity of blood serum obtained from animals, transduced with rAAV-P2C5-Fc

Final stage of rAAV-P2C5-Fc protective activity investigation was dedicated to evaluation of virus neutralization activity of mouse blood serum against SARS-CoV-2 variant B.1.1.1. Serum samples were collected at 0, 1, 2, 3, 7, 14, 21, 45, 60, 90, 120, 150, 180, 210, 240, 270 and 300 days after the transduction. Blood serum of the untreated intact mice was used as a negative control.

Scheme of the experiments as well as experimental results are presented in Figures 8A, B. A significant virus neutralization activity was detected already at the day 7 after the transduction (antibody titer of 1/320) and further increased to values of 1/5120, 1/20480 and 1/40960 on days 14, 21 and 120, respectively. It was also noted that high titer of virus neutralizing antibodies (1/40960) remained until day 150 after the transduction. Starting from the day 180 of the experiment level of the virus neutralizing antibodies decreased to 1/20480, reached value of 1/5120 on day 210 and remained unchanged within 300 days.

Generated data therefore indicate rapid achievement of extended virus neutralization activity of blood serum after a single rAAV-P2C5-Fc administration.

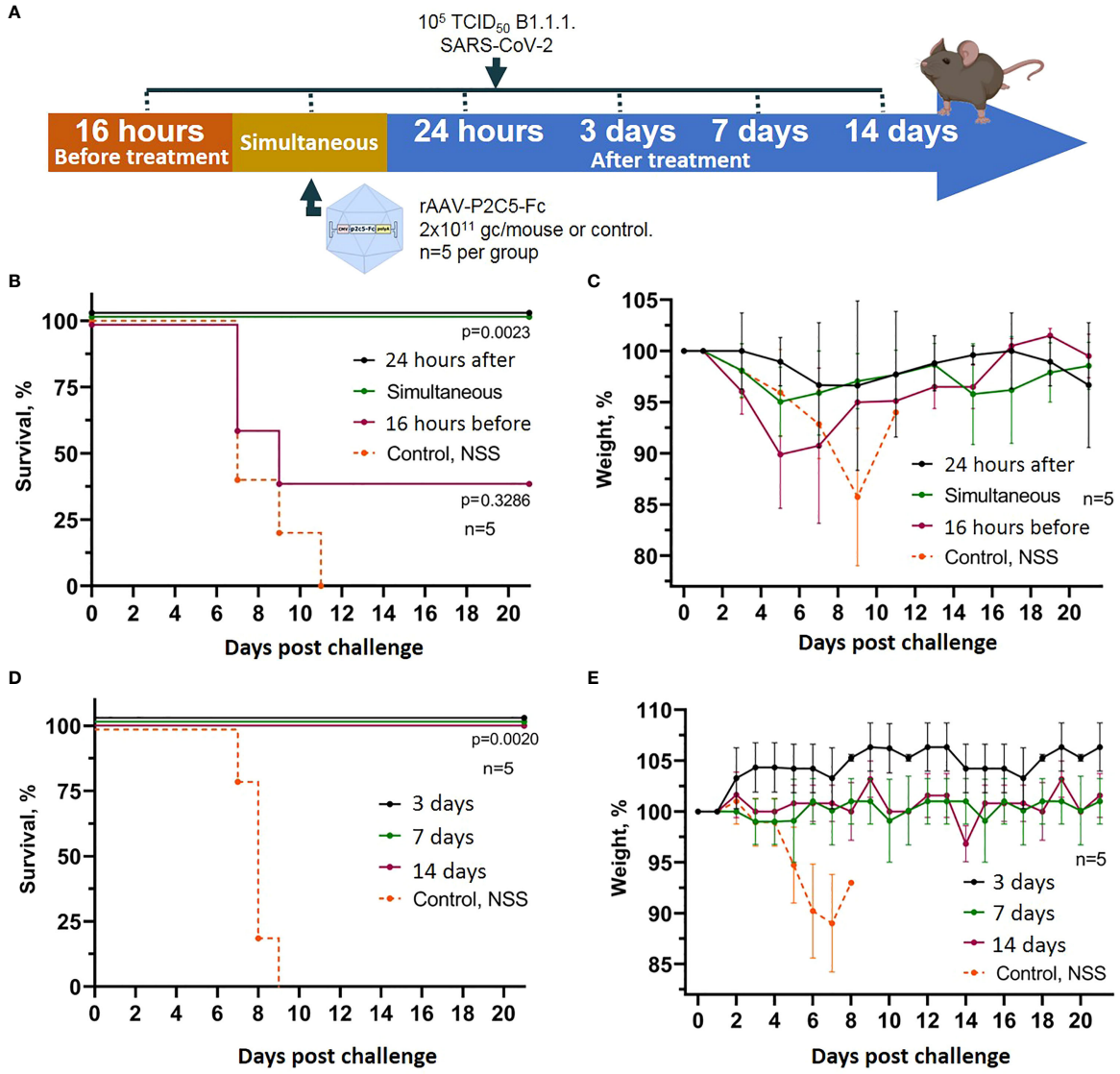

FIGURE 3
Evaluation of rAAV-P2C5-Fc efficacy for early and emergency prophylaxis and prevention of SARS-CoV-2 infection. **(A)** Scheme of the experiment: briefly, mice were challenged with 10^5 TCID50 SARS-CoV-2 B.1.1.1 and treated with $2*10^{11}$ gc/mouse of rAAV-P2C5-Fc at different time intervals. **(B, C)** Survival and body weight loss in emergency prophylaxis animal groups (challenge at 16 hours before, simultaneous with and 24 hours after rAAV-P2C5-Fc transduction). **(D, E)** Survival and body weight loss in early prophylaxis animal groups (transduction at 3,7 and 14 before the challenge). Lines – mean values, error bars – SD, numbers indicate statistical significance evaluated compared with the vehicle group using a logrank test. Data from different rAAV-P2C5-Fc treatment groups are shown by color. Control, NSS – mice received normal saline solution. n – number of animals per group.

3.8 Evaluation of pharmacokinetics of P2C5-Fc antibody expressed by rAAV-P2C5-Fc

To evaluate pharmacokinetic properties of P2C5-Fc antibody female BALB/c mice were transduced with an rAAV-P2C5-Fc dose of $2*10^{11}$ gc/animal. In total 10 animals were used. Blood serum was collected at 0, 1, 2, 3, 7, 14, 21, 45, 60, 90, 120, 150, 180, 210, 240, 270 and 300 days after the transduction. Sampling scheme is summarized in Figure 8A.

As a result, P2C5-Fc was detected in serum already 48 hours following mice transduction with rAAV-P2C5-Fc and its level further significantly increased during the next 5 days. At the day 28 the antibody concentrations exceed 100 μg/mL and remained above this level until day 150. On days 180, 210, 240, 270 and 300 after transduction, the serum P2C5-Fc concentrations were 86, 75, 73, 63 and 49 μg/mL, respectively. Experimental results are shown in Figure 8C.

Summarizing all mentioned above it can be said that usage of rAAV-P2C5-Fc enables rapid accumulation and prolonged circulation of P2C5-Fc antibody within the living organism.

3.9 Evaluation of rAAV-P2C5-Fc immunogenicity

To evaluate immunogenicity of rAAV-P2C5-Fc blood serum samples from Figure 8A were used. Concentration of anti-idiotypic

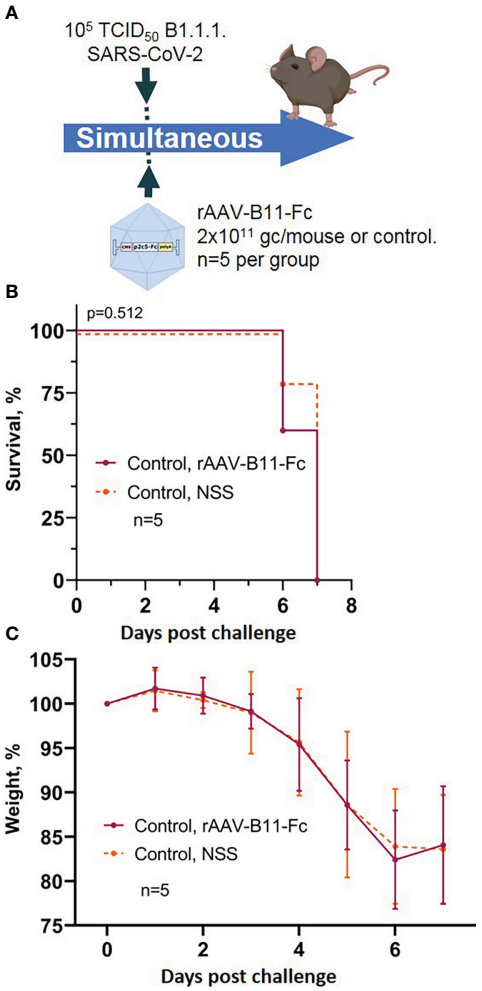

FIGURE 4
Evaluation of non-specific protective activity of rAAV against SARS-CoV-2 infection. **(A)** Scheme of the experiment: briefly, mice were infected with 10^5 TCID50 SARS-CoV-2 B.1.1.1 and simultaneous treated with $2*10^{11}$ gc/mouse of rAAV-B11-Fc. **(B)** Animal survival. **(C)** Body weight loss. Lines – mean values, error bars – SD, numbers indicate statistical significance evaluated compared with the vehicle group using a logrank test. Data from different treatment groups are shown by color. Control, NSS – mice received normal saline solution. n – number of animals per group.

antibodies to P2C5-Fc antibody was below quantification limit whereas a significant level of antibodies specific to rAAV capsid proteins was detected on day 14, reached maximum on day 90 and remained detectable within at least 300 days after the transduction (Figure 8D).

Summarizing these observations, it can be said that no significant production of P2C5-Fc specific antibodies was observed but substantial level of the antibodies specific to rAAV capsid proteins was detected.

4 Discussion

Development of COVID-19 prophylaxis and treatment strategies remains relevant. Antigenic evolution and emergence of new variants of the virus with selective advantage and increased transmissivity driven by high antigen variability combined with natural selection leads to their rapid spread. This antigenic shift can lead to a decrease in efficacy of recently approved vaccines and therapeutic agents which emphasizes the relevance of new agents for prophylaxis and therapy of diseases caused by SARS-CoV-2 virus.

In a previous study we had used a bactrial camel immunization followed by selection of monoclonal antibodies with the highest phagocytic activity to generate a panel of specific monoclonal antibodies with the highest neutralizing capacity against concerning variants of SARS-CoV-2 virus (17). As a result, P2C5 antibody had been chosen for further studies based on virus-neutralizing concentration, equilibrium dissociation constants and specific activity to RBD of S glycoprotein, measured by immunofluorescence assay.

In current work we proposed an alternative immunization strategy implying the use of rAAV expressing a P2C5-Fc recombinant antibody to induce rapid long-term protection against SARS-CoV-2 viruses. A P2C5-Fc recombinant antibody represents a P2C5 antibody fused with an Fc-fragment of human IgG1 enabling its dimerization. This modification can increase avidity and specific activity as well as circulation time of the molecule due to an increase in molecular weight and interaction with neonatal Fc receptor for IgG (FcRn) (21). The proposed recombinant Fc-fusion single-domain antibody variant may be more effective than a monoclonal antibody due to the presence of long CDR3 loops enabling their binding to conservative hard-to-reach epitopes of viral antigens. Thus, such recombinant antibodies can have a wide range of neutralizing activity against various variants of the influenza virus, Ebola virus and SARS-CoV-2 (16, 17, 21). Thus, the emergence of antibody-resistant virus strains is less likely.

Application of rAAV as a vector for delivery, expression of genes encoding neutralizing antibodies and induction of passive immunity has been tested in prophylaxis of various infection diseases (11–15, 22). Selection of rAAV for delivery and expression of antibodies is dictated by their safety, low immunogenicity, ability to transduce a wide spectrum of different cells, prolonged persistence in a body in a form of episomes and inability of their integration into the host genome (23). A similar study demonstrating a prolonged expression of a recombinant antibody specific to botulotoxin type A following rAAV administration had been conducted previously by our group (15). This study also implied use of an antibody modified by an Fc fragment of human IgG1. We had demonstrated that the generated recombinant vector enables expression of the antibody in transduced mice for 4 months and therefore protect the animals from lethal doses of botulotoxin type A.

As in the previous aforementioned study in current work we used an rAAV-DJ system enabling derivation of a recombinant AAV with a hybrid serotype, which was produced and purified as described previously (15, 18). By analogy with the previous work an *in vitro* transduced activity of rAAV-P2C5-Fc and specific activity of P2C5-Fc expressed by rAAV were studied.

On the next step an effective dose of $2*10^{11}$ gc/mouse (10^{13} gc/kg) of rAAV-P2C5-Fc was selected based on the data from

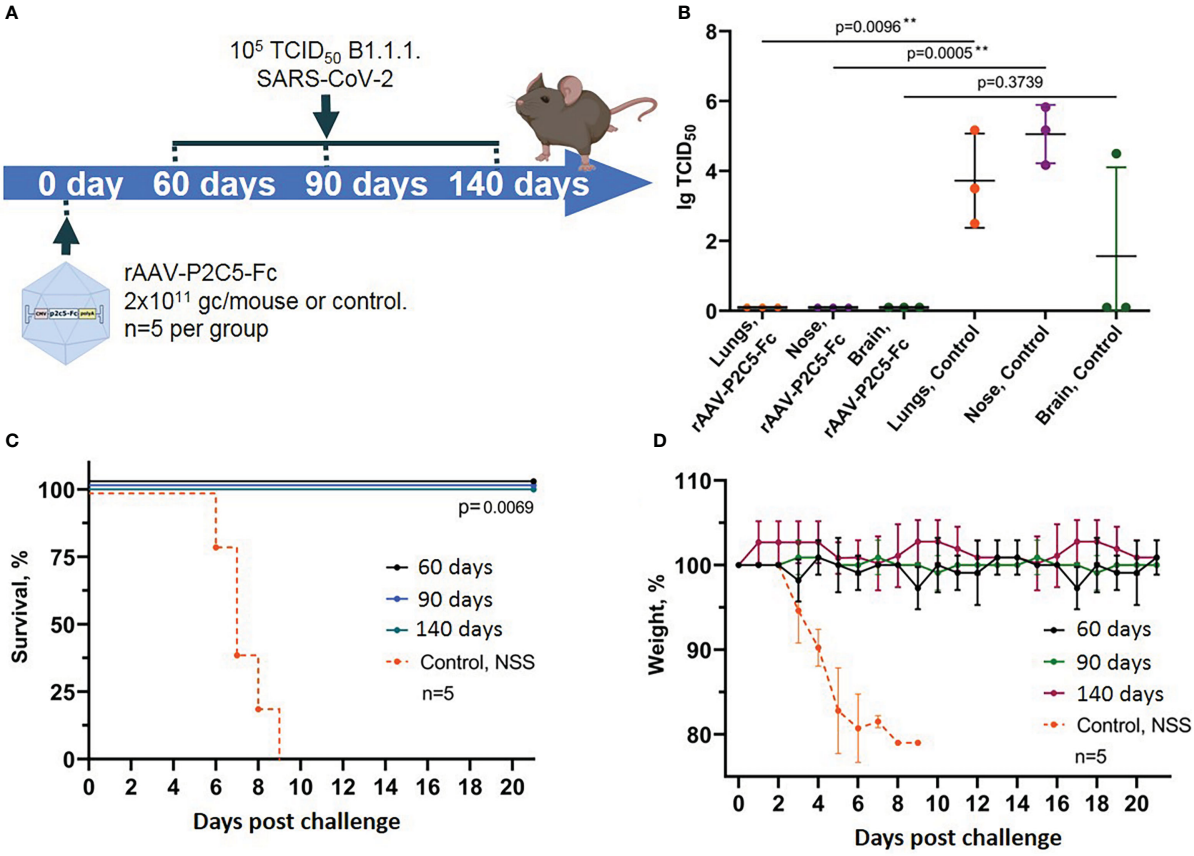

FIGURE 5
Evaluation of long-term protective activity of rAAV-P2C5-Fc against SARS-CoV-2. **(A)** Scheme of the experiment: mice were treated with rAAV-P2C5-Fc at a dose of $2*10^{11}$ gc/animal on days 60, 90, 140 before the challenge with SARS-CoV-2 B.1.1.1 variant at a dose of 10^5 TCID50. **(B)** Viral load in the organs of animals infected with SARS-CoV-2 on day 140 after the treatment. **(C)** Animal survival. **(D)** Body weight loss. Lines – mean values, error bars – SD, numbers indicate statistical significance evaluated compared with the vehicle group using a logrank test (survival) or Mann–Whitney U test (viral load). Data from different treatment groups are shown by color. Control, NSS – mice received normal saline solution. n – number of animals per group. ** means statistically significant.

humanized mouse ACE-2 model of lethal infection. This finding is in line with previous studies where protective doses of rAAV preparations expressing antibodies ranged from 10^{10} to 10^{12} gc/animal (24–27). In a previous study we had investigated protective activity of a similar agent rAAV-B11-Fc which was 10^{11} gc/mouse. Lower protective dose of rAAV-B11-Fc vs rAAV-P2C5-Fc was attributable to lower neutralizing B11-Fc concentration against botulotoxin A vs neutralizing P2C5-Fc concentration against SARS-CoV-2 virus.

We further investigated protective capacity of rAAV-P2C5-Fc as an early and emergency pre-exposure as well as post-exposure prophylaxis. A humanized ACE-2 mice were transduced simultaneously (emergency prophylaxis) or 1, 3, 7 and 14 days before (early prophylaxis) or 16 hours after (post-exposure prophylaxis) SARS-CoV-2 B.1.1.1 variant injection for this purpose. Early and emergency COVID-19 prophylaxis with rAAV-P2C5-Fc was associated with full animal protection and lack of any disease symptoms in mice. At the same time a 40% survival rate and a significant body weight decrease was detected in an animal group received post-exposure prophylaxis. Development of the infection process followed by animal death takes about 7-8 days after the virus exposure and a significant P2C5-Fc accumulation in blood serum happens by that time in case of simultaneous administration of rAAV-P2C5-Fc and the virus. An accumulated P2C5-Fc enables virus neutralization and stopping the pathological process which can explain high efficacy of the rAAV-P2C5-Fc for emergency pre-exposure prophylaxis. This hypothesis can be confirmed indirectly by evaluation of P2C5-Fc pharmacokinetics in rAAV-P2C5-Fc-transdused mice. It was demonstrated that the levels of virus neutralizing antibodies in blood serum of mice on day 7 after rAAV-P2C5-Fc-transduction significantly exceeds those in blood of people recovered from a single COVID-19 episode (1/320 *vs* an about 1/200 neutralizing antibodies titer in convalescent plasma) (7). In addition, it was experimentally confirmed that protection against SARS-CoV-2 infection following mice transduction with rAAV-P2C5-Fc is mediated *via* the expression of a specific P2C5-Fc antibody, since mice transduced with rAAV-B11-Fc expressing B11-Fc antibody specific to botulinum toxin died as well as control mice after SARS-CoV-2 infection.

Evaluation of duration of rAAV-P2C5-Fc protective activity against SARS-CoV-2 B.1.1.1 variant was performed using the

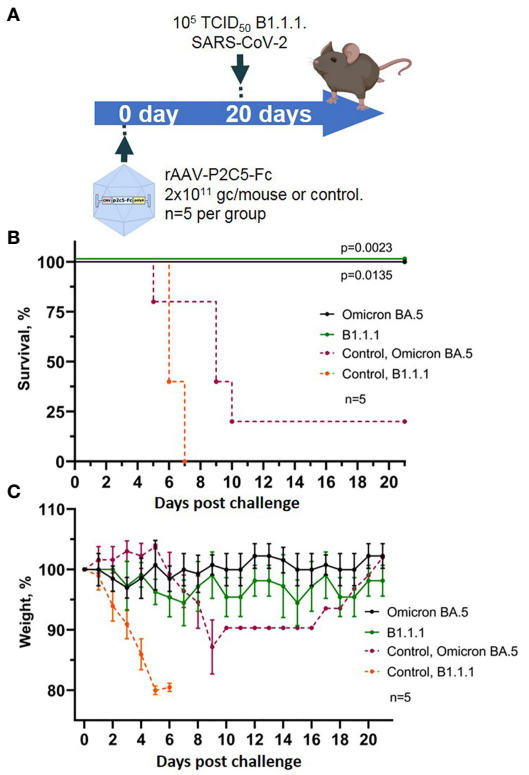

FIGURE 6
Evaluation of rAAV-P2C5-Fc protective capacities against SARS-CoV-2 variants Omicron BA.5. **(A)** Scheme of the experiment: mice were challenged with 10^5 TCID50 SARS-CoV-2 variants Omicron BA.5 and B.1.1.1 on day 14 after administration of rAAV-P2C5-Fc at a dose of $2*10^{11}$ gc/animal. **(B)** Animal survival. **(C)** Body weight loss. Lines – mean values, error bars – SD, numbers indicate statistical significance evaluated compared with the vehicle group using a logrank test. Data from different treatment groups are shown by color. Control, NSS – mice received normal saline solution. n – number of animals per group.

humanized ACE-2 mouse model. The study results were also in line with measured P2C5-Fc pharmacokinetic profile and a virus neutralizing activity of mouse blood serum collected from rAAV-P2C5-Fc transduced animals. The data generated in our study demonstrated that protection of the rAAV-P2C5-Fc-transduced mice against SARS-CoV-2 variant B.1.1.1 lasts at least 140 days following rAAV administration. Concentrations of both P2C5-Fc antibody and virus neutralizing antibodies in the blood serum were shown to rise sharply starting from day 7, reached plateau approximately on day 28 and remained stable till day 150 after the transduction. It is also important to note that the level of virus neutralizing antibodies to SARS-CoV-2 B.1.1.1 variant in mouse blood serum, measured starting from 28 days post transduction exceeded that from the blood serum of the COVID-19 convalescents and persons vaccinated with Sputnik V (6, 7). The possible influence of rAAV on the induction of non-specific protection in the long-term prophylaxis regimen cannot be completely ruled out. However, we believe this is unlikely, since Liao G. et al. (28) showed that the administration of a control rAAV expressing EGFP does not induce immunogenicity and protection against SARS-CoV-2 virus in a long-term prophylaxis regimen.

According to our study minimal neutralizing concentration of P2C5-Fc antibody against SARS-CoV-2 virus B.1.1.1 *in vitro* is about 6 ng/ml. Considering maximal neutralizing dilutions of the serum derived from rAAV-P2C5-Fc treated mice and *in vivo* concentrations of P2C5-Fc antibody the minimum neutralizing activity of P2C5-Fc antibody in the serum of rAAV-P2C5-Fc treated mice should be about 3-12 ng/ml, which is in line with *in vitro* data. In a previous study, we had shown that protective rAAV activity directly correlates with level of neutralizing antibodies in blood serum (15). Accumulated evidence therefore suggests that rAAV-P2C5-Fc provides protection against SARS-CoV-2 induced infection during the P2C5-Fc circulation, that is, at least 300 days, and, most likely, even more.

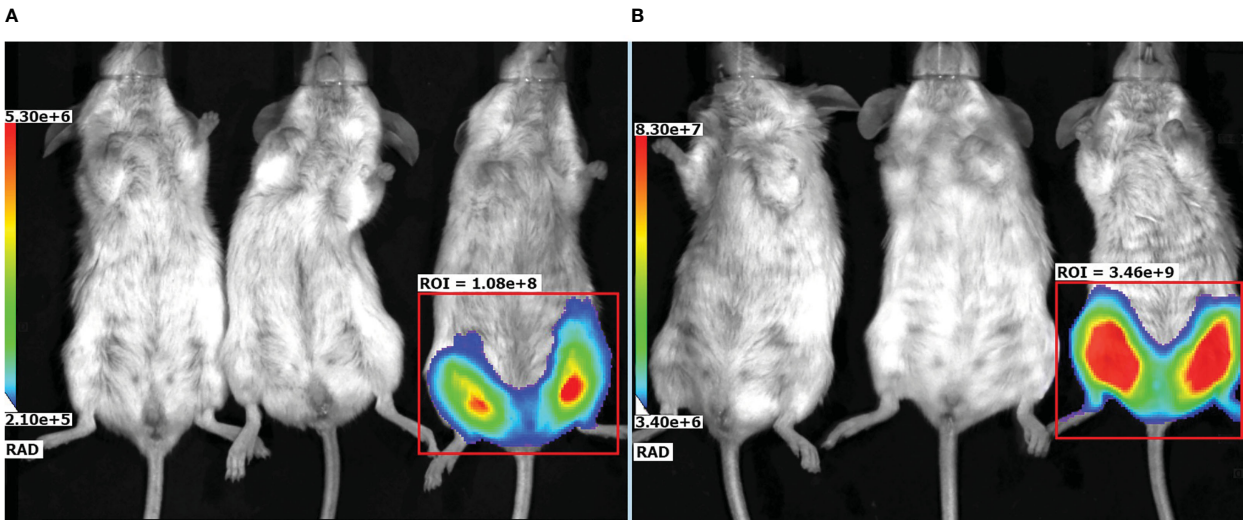

FIGURE 7
Representative bioluminescent pseudocolored images of luciferase activity in live mice, measured on **(A)** day 7 and **(B)** day 60 after an intramuscular injection of PBS (placebo), rAAV-P2C5-Fc or rAAV-Luc at a dose of 10^{10} gc/mouse into the hind limb. Mice received an i.p. injection of luciferin and was anaesthetized prior to imaging. The intensity of bioluminescence (i.e., luciferase activity) is shown by color.

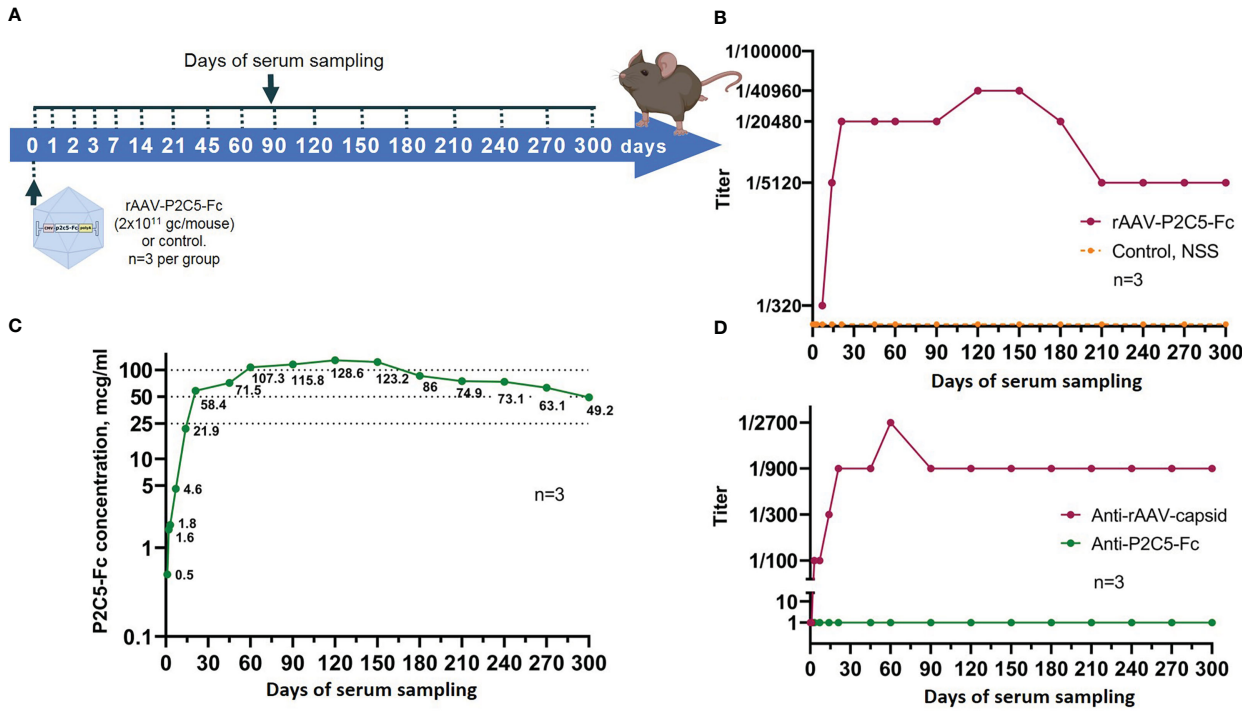

FIGURE 8
Evaluation of blood serum samples collected from mice treated with rAAV-P2C5-Fc. **(A)** Scheme of the experiment: a single intramuscular injection of rAAV-P2C5-Fc at a dose of $2*10^{11}$ gc/mouse was performed. Serum samples were taken at days 0, 1, 2, 3, 7, 14, 21, 45, 60, 90, 120, 150, 180, 210, 240, 270, and 300 after the injection; **(B)** Titers of virus-neutralizing antibodies to SARS-CoV-2 B.1.1.1 variant, **(C)** Levels of P2C5-Fc antibody and **(D)** Titers of rAAV- and P2C5-Fc-specific antibodies in blood serum of the animals. Lines – mean values, n – number of animals per group.

In our study the maximum concentration of P2C5-Fc antibody in the mouse blood serum on days 60-150 after administration of $2*10^{11}$ gc of rAAV-P2C5-Fc was about 100-130 μg/ml. In the work of Del Rosario et al. (22), several rAAVs expressing recombinant molecules consisting of single-domain antibodies fused with Fc-fragments of various mouse IgG isotypes were obtained. The antibodies demonstrated specific activity against various variants of influenza A virus *in vitro* and were used for *in vivo* immunization with rAAV at the doses of 10^{10}, $3.3*10^{10}$ and 10^{11} gc per animal. As a result, Del Rosario and colleagues showed significantly higher expression of recombinant antibodies (500-1000 μg/ml) compared our results. This is most likely related to the fact that the authors used mouse IgG Fc-fragments, and the efficiency of their expression in mice can be greater compared to the human ones used in our study. In addition higher affinity of mouse IgG2A for murine Fc-receptors (29) can explain a sharper rise and a stronger accumulation of antibodies in the organism of mice observed in the Del Rosario et al. study. The authors also demonstrated that antibodies expressed after rAAV transduction circulate in the blood serum of mice for six months without a significant decrease. In our study, the antibody concentration in the blood serum of transduced mice began to noticeably decline only after day 150-180, which does not contradict the data of Del Rosario and colleagues.

To evaluate rAAV biodistribution following intramuscular drug administration we generated an rAAV expressing a luciferase gene (rAAV-Luc). Specific luciferase activity was detected solely at the site of the drug administration (the thigh muscles of the hind limb) which indicates local transduction of the muscle cells and lack of the systemic transduction under the treatment. Luciferase activity was detected for at least 60 days after the transduction, which indicates persistence of the rAAV expressing the target transgene for a long time. Prolonged persistence of rAAV in muscle cells as an episome for many months after a single intramuscular injection was shown in a non-human primate model by Penaud-Budloo M. et al. (30).

Investigation of rAAV-P2C5-Fc immunogenicity showed presence of antibodies to rAAV capsid proteins in a blood serum of transduced mice however no antibodies to P2C5-Fc were detected, which can explain much longer circulation of P2C5-Fc expressed by rAAV in the current study compared to rAAV-B11-Fc, expressing B11-Fc antibody, used in a previous study (15).

In our previous study we had also demonstrated protective capacity of P2C5 antibody against various SARS-CoV-2 variants including Omicron B.1.1.529. In current work we showed efficacy of SARS-CoV-2 Omicron BA.5 variant prophylaxis with rAAV-P2C5-Fc. As P2C5-Fc activity against Omicron BA.5 is lower compared to that against B.1.1.1, virus inoculation was performed at the day 20 after transduction to ensure sufficient antibody level at the time of exposure to the virus. We had demonstrated that minimal neutralizing concentration of P2C5-Fc antibody against SARS-CoV-2 B.1.1.1 and SARS-CoV-2 BA.5 was about 6 ng/ml and 1.2 μg/ml, respectively.

In conclusion it can be said that the efficacy of passive immunization with a recombinant adeno-associated viral vector rAAV-P2C5-Fc expressing a recombinant neutralizing antibody P2C5-Fc for protection against SARS-CoV-2 infection was first shown in our study. In addition, we demonstrated high protective

capacity of rAAV-P2C5-Fc against various SARS-CoV-2 variants, including Omicron BA5. And finally, we showed 100% efficacy of the developed rAAV for an emergency prevention and long-term prophylaxis, respectively.

Data availability statement

The original contributions presented in the study are included in the article/supplementary material. Further inquiries can be directed to the corresponding author.

Ethics statement

The study was conducted according to the guidelines of the Guide for the Care and Use of Laboratory Animals published by the National Institutes of Health (NIH Publication #85–23, revised 1996) and National Standard of the Russian Federation GOST R 53434–2009, approved by the Institutional Animal Care and Use Committee (IACUC) of the Federal Research Centre of Epidemiology and Microbiology named after Honorary Academician N.F. Gamaleya and were performed under Protocol №25 dated Apr 22, 2022.

Author contributions

Conceptualization: IE, DS, DL, BN. Methodology: IE, ER, AD, ID, IF, DG, AGo. Validation: IE, ER, AD, ID, DG. Formal analysis: ER, IE, AD. Investigation: ER, AD, IE, VP, MD, ID, DG, IZ, AI, AK, AS, AGo, D.V.B., IF. Resources, DL, AG, DS, BN, Data curation: IE. Writing – original draft preparation: IE, AD, ER. Writing – review & editing: IE, DS, ID. Visualization: AD, IE, ER, ID, DG. Supervision: IE. Project administration: DL, DS, BN, AGi. All authors contributed to the article and approved the submitted version.

Funding

Ministry of Health of the Russian Federation, grant #123030200047-8.

Conflict of interest

The authors declare that the research was conducted in the absence of any commercial or financial relationships that could be construed as a potential conflict of interest.

Publisher's note

All claims expressed in this article are solely those of the authors and do not necessarily represent those of their affiliated organizations, or those of the publisher, the editors and the reviewers. Any product that may be evaluated in this article, or claim that may be made by its manufacturer, is not guaranteed or endorsed by the publisher.

References

1. World Health Organization. *Coronavirus disease (COVID-19) pandemic*. Available at: https://www.who.int/health-topics/coronavirus#tab=tab_1 (Accessed November 12, 2022).

2. World Health Organization. *WHO director-general's opening remarks at the media briefing on COVID-19* . Available at: https://www.who.int/dg/speeches/detail/who-director-general-s-opening-remarks-at-the-media-briefing-on-covid-19—11-march-2020 (Accessed November 12, 2022).

3. World Health Organization. *Coronavirus (COVID-19) dashboard*. Available at: https://covid19.who.int (Accessed November 12, 2022).

4. World Health Organization. *COVID-19 vaccine tracker and landscape*. Available at: https://www.who.int/publications/m/item/draft-landscape-of-covid-19-candidate-vaccines (Accessed November 12, 2022).

5. Tukhvatulin AI, Dolzhikova IV, Shcheblyakov DV, Zubkova OV, Dzharullaeva AS, Kovyrshina AV, et al. An open, non-randomised, phase 1/2 trial on the safety, tolerability, and immunogenicity of single-dose vaccine "Sputnik light" for prevention of coronavirus infection in healthy adults. *Lancet Reg Health Eur* (2021) 11: 100241. doi: 10.1016/j.lanepe.2021.100241

6. Logunov DY, Dolzhikova IV, Shcheblyakov DV, Tukhvatulin AI, Zubkova OV, Dzharullaeva AS, et al. Safety and efficacy of an rAd26 and rAd5 vector-based heterologous prime-boost COVID-19 vaccine: an interim analysis of a randomised controlled phase 3 trial in Russia. *Lancet* (2021) 397(10275):671–81. doi: 10.1016/S0140-6736(21)00234-8

7. Logunov DY, Dolzhikova IV, Zubkova OV, Tukhvatullin AI, Shcheblyakov DV, Dzharullaeva AS, et al. Safety and immunogenicity of an rAd26 and rAd5 vector-based heterologous prime-boost COVID-19 vaccine in two formulations: two open, non-randomised phase 1/2 studies from Russia. *Lancet* (2020) 396(10255):887–97. doi: 10.1016/S0140-6736(20)31866-3

8. Tregoning JS, Flight KE, Higham SL, Wang Z, Pierce BF. Progress of the COVID-19 vaccine effort: viruses, vaccines and variants versus efficacy, effectiveness and escape. *Nat Rev Immunol* (2021) 21(10):626–36. doi: 10.1038/s41577-021-00592-1

9. Centers for Medicare & Medicaid Services. *Centers for Medicare & Medicaid services*. Available at: https://www.cms.gov/monoclonal (Accessed December 10, 2022).

10. Godakova SA, Noskov AN, Vinogradova ID, Ugriumova GA, Solovyev AI, Esmagambetov IB, et al. Camelid VHHs fused to human fc fragments provide long term protection against botulinum neurotoxin a in mice. *Toxins* (2019) 11(8):464. doi: 10.3390/toxins11080464

11. Casazza JP, Cale EM, Narpala S, Yamshchikov GV, Coates EE, Hendel CS, et al. Safety and tolerability of AAV8 delivery of a broadly neutralizing antibody in adults living with HIV: a phase 1, dose-escalation trial. *Nat Med* (2022) 28(5):1022–30. doi: 10.1038/s41591-022-01762-x

12. Laura PL, Amira DR, Wenguang C, Shihua H, Geoff S, Wenjun Z, et al. AAV-monoclonal antibody expression protects mice from Ebola virus without impeding the endogenous antibody response to heterologous challenge. *Mol Ther* (2022) 26:505–18. doi: 10.1016/j.omtm.2022.08.003

13. Rghei AD, Lieshout LP, Cao W, He S, Tierney K, Lopes JA, et al. Adeno-associated virus mediated expression of monoclonal antibody MR191 protects mice against marburg virus and provides long-term expression in sheep. *Gene Ther* (2022). doi: 10.1038/s41434-022-00361-2

14. Adam VS, Crosariol M, Kumar S, Ge MQ, Czack SE, Roy S, et al. Adeno-associated virus 9-mediated airway expression of antibody protects old and immunodeficient mice against influenza virus. *Clin Vaccine Immunol* (2014) 21 (11):1528–33. doi: 10.1128/CVI.00572-14

15. Derkaev AA, Ryabova EI, Esmagambetov IB, Shcheblyakov DV, Godakova SA, Vinogradova ID, et al. rAAV expressing recombinant neutralizing antibody for the botulinum neurotoxin type a prophylaxis. *Front Microbiol* (2022) 13:960937. doi: 10.3389/fmicb.2022.960937

16. Voronina DV, Shcheblyakov DV, Favorskaya IA, Esmagambetov IB, Dzharullaeva AS, Tukhvatulin AI, et al. Cross-reactive fc-fused single-domain antibodies to hemagglutinin stem region protect mice from group 1 influenza a virus infection. *Viruses*. (2022) 14(11):2485. doi: 10.3390/v14112485

17. Favorskaya IA, Shcheblyakov DV, Esmagambetov IB, Dolzhikova IV, Alekseeva IA, Korobkova AI, et al. Single-domain antibodies efficiently neutralize SARS-CoV-2 variants of concern. *Front Immunol* (2022) 13:822159. doi: 10.3389/fimmu.2022.822159

18. Ryabova EI, Derkaev AA, Esmagambetov IB, Shcheblyakov DV, Dovgiy MA, Byrikhina DV, et al. Comparison of different technologies for producing recombinant adeno-associated virus on a laboratory scale. *BIOpreparations* (2021) 21(4):266–78. doi: 10.30895/2221-996X-2021-21-4-266-278

19. Tukhvatulin AI, Gordeychuk IV, Dolzhikova IV, Dzharullaeva AS, Krasina ME, Bayurova EO, et al. Immunogenicity and protectivity of intranasally delivered vector-based heterologous prime-boost COVID-19 vaccine Sputnik V in mice and non-human primates. *Emerg Microbes Infect* (2022) 11(1):2229–47. doi: 10.1080/22221751.2022.2119169

20. Zivcec M, Safronetz D, Haddock E, Feldmann H, Ebihara H. Validation of assays to monitor immune responses in the Syrian golden hamster (Mesocricetus auratus). *J Immunol Methods* (2011) 368(1-2):24–35. doi: 10.1016/j.jim.2011.02.004

21. Esmagambetov IB, Shcheblyakov DV, Egorova DA, Voronina OL, Derkaev AA, Voronina DV, et al. Nanobodies are potential therapeutic agents for the Ebola virus infection. *Acta Naturae* (2021) 13(4):53–63. doi: 10.32607/actanaturae.11487

22. Del Rosario JMM, Smith M, Zaki K, Risley P, Temperton N, Engelhardt OG, et al. Protection from influenza by intramuscular gene vector delivery of a broadly neutralizing nanobody does not depend on antibody dependent cellular cytotoxicity. *Front Immunol* (2020) 11:627. doi: 10.3389/fimmu.2020.00627

23. Nieto K, Salvetti A. AAV vectors vaccines against infectious diseases. *Front Immunol* (2014) 5:5. doi: 10.3389/fimmu.2014.00005

24. Pien GC, Basner-Tschakarjan E, Hui DJ, Mentlik AN, Finn JD, Hasbrouck NC, et al. Capsid antigen presentation flags human hepatocytes for destruction after transduction by adeno-associated viral vectors. *J Clin Invest* (2009) 119(6):1688–95. doi: 10.1172/JCI36891

25. Balazs AB, Bloom JD, Hong CM, Rao DS, Baltimore D. Broad protection against influenza infection by vectored immunoprophylaxis in mice. *Nat Biotechnol* (2013) 31:647–52. doi: 10.1038/nbt.2618

26. Greig JA, Peng H, Ohlstein J, Medina-Jaszek CA, Ahonkhai O, Mentzinger A, et al. Intramuscular injection of AAV8 in mice and macaques is associated with substantial hepatic targeting and transgene expression. *PLoS One* (2014) 9(11):e112268. doi: 10.1371/journal.pone.0112268

27. Hanlon KS, Meltzer JC, Buzhdygan T, Cheng MJ, Sena-Esteves M, Bennett RE, et al. Selection of an efficient AAV vector for robust CNS transgene expression. *Mol Ther Methods Clin Dev* (2019) 15:320–32. doi: 10.1016/j.omtm.2019.10.007

28. Liao G, Lau H, Liu Z, Li C, Xu Z, Qi X, et al. Single-dose rAAV5-based vaccine provides long-term protective immunity against SARS-CoV-2 and its variants. *Virol J* (2022) 19(1):212. doi: 10.1186/s12985-022-01940-w

29. Shcheblyakov D, Esmagambetov I, Simakin P, Kostina L, Kozlov A, Tsibezov V, et al. Development and characterization of two GP-specific monoclonal antibodies, which synergistically protect non-human primates against Ebola lethal infection. *Antiviral Res* (2019) 172:104617. doi: 10.1016/j.antiviral.2019.104617

30. Penaud-Budloo M, Le Guiner C, Nowrouzi A, Toromanoff A, Chérel Y, Chenuaud P, et al. Adeno-associated virus vector genomes persist as episomal chromatin in primate muscle. *J Virol* (2008) 82(16):7875–85. doi: 10.1128/JVI.00649-08

frontiers | Frontiers in Immunology

TYPE Original Research
PUBLISHED 31 March 2023
DOI 10.3389/fimmu.2023.1113175

Check for updates

OPEN ACCESS

EDITED BY
Nargis Khan,
University of Calgary, Canada

REVIEWED BY
Lei Li,
Oracle, Australia
Thuy-Tien Nguyen,
Stanford University, United States

*CORRESPONDENCE
Hyun Goo Woo
hg@ajou.ac.kr

SPECIALTY SECTION
This article was submitted to Vaccines and Molecular Therapeutics, a section of the journal Frontiers in Immunology

RECEIVED 01 December 2022
ACCEPTED 22 March 2023
PUBLISHED 31 March 2023

CITATION
Shah M, Shin J-Y and Woo HG (2023) Rational strategies for enhancing mAb binding to SARS-CoV-2 variants through CDR diversification and antibody-escape prediction. *Front. Immunol.* 14:1113175. doi: 10.3389/fimmu.2023.1113175

COPYRIGHT
© 2023 Shah, Shin and Woo. This is an open-access article distributed under the terms of the Creative Commons Attribution License (CC BY). The use, distribution or reproduction in other forums is permitted, provided the original author(s) and the copyright owner(s) are credited and that the original publication in this journal is cited, in accordance with accepted academic practice. No use, distribution or reproduction is permitted which does not comply with these terms.

Rational strategies for enhancing mAb binding to SARS-CoV-2 variants through CDR diversification and antibody-escape prediction

Masaud Shah[1], Ji-Yon Shin[1,2] and Hyun Goo Woo[1,3]*

[1]Department of Physiology, Ajou University School of Medicine, Suwon, Republic of Korea, [2]Korea Initiative for Fostering University of Research and Innovation (KIURI) Program, Ajou University School of Medicine, Suwon, Republic of Korea, [3]Department of Biomedical Science, Graduate School, Ajou University, Suwon, Republic of Korea

Since the emergence of SARS-CoV-2, dozens of variants of interest and half a dozen variants of concern (VOCs) have been documented by the World Health Organization. The emergence of these VOCs due to the continuous evolution of the virus is a major concern for COVID-19 therapeutic antibodies and vaccines because they are designed to target prototype/previous strains and lose effectiveness against new VOCs. Therefore, there is a need for time- and cost-effective strategies to estimate the immune escape and redirect therapeutic antibodies against newly emerging variants. Here, we computationally predicted the neutralization escape of the SARS-CoV-2 Delta and Omicron variants against the mutational space of RBD-mAbs interfaces. Leveraging knowledge of the existing RBD-mAb interfaces and mutational space, we fine-tuned and redirected CT-p59 (Regdanvimab) and Etesevimab against the escaped variants through complementarity-determining regions (CDRs) diversification. We identified antibodies against the Omicron lineage BA.1 and BA.2 and Delta variants with comparable or better binding affinities to that of prototype Spike. This suggests that CDRs diversification by hotspot grafting, given an existing insight into the Ag-Abs interface, is an exquisite strategy to redirect antibodies against preselected epitopes and combat the neutralization escape of emerging SARS-CoV-2 variants.

KEYWORDS

SARS-CoV-2, omicron, Omicron (B.1.1.529), immune escape, antibody, CDR diversification

1 Introduction

After the emergence of SARS-CoV-2, the virus has been in a relative evolutionary stasis, but as the virus began to evolve by the end of 2020, and new variants continue to emerge. This has been characterized by the identification of variants of concerns (VOCs) and variants of interest (VOIs). These VOCs are characterized as rapidly transmissible, immune evading, and more

pathogenic in some cases, likely due to the variable immune profile of the host population as the virus spread across the globe (1). Among the first four VOCs, namely Alpha, Beta, Gamma, and Delta, the Delta variant was expected to pose a challenge to the neutralization of FDA-approved monoclonal antibodies (mAbs) (2) and the effectiveness of FDA-approved vaccines, as the neutralization efficacy of the BNT162b2 vaccinees sera dropped by 5.8-fold and that of Pfizer vaccine dropped by 3-fold (3). More worrisome is that the neutralizability of the single dose AstraZeneca vaccine is completely lost and infection can occur even after two doses of the vaccine (4). Among the four FDA-approved mAbs of Regeneron and AbCellera & Eli Lilly under Emergency Use Authorization (EUA) at that time, Bamlanivimab completely lost its neutralization against the delta variant. A single mutation L452R in the RBD^{delta} located at the RBD-mAb interface was responsible for the loss in neutralizing activity (4), suggesting that one hotspot mutation in the emerging SARS-CoV-2 variants can allow for escape from highly effective mAbs that have undergone through extensive biosafety evaluation and clinical trials. Similarly, the neutralization of the sera from the convalescent donors after vaccination with BNT162b2 fell 7.6-fold for the Mu variant, which was substantially worse than other VOCs (3).

The new VOC, Omicron, and its subvariants contain at least 15 mutations in the RBD region alone (5). Due to the triple mutations H655Y, N679K, and P681H in the furin cleavage site (6), this variant is thus far known to be the fastest spreading variant (7). Moreover, several single mutations in potential epitopes that overlap with the ACE2-binding interface have been reported to escape neutralizing antibodies (nAbs) (8, 9). Particularly, Lys417Asn, Gly446Ser, Leu452Arg, Glu484Ala, and Gln493Arg mutations play a major role in this escape. Based on sufficient data gathered on the neutralization efficacy of mAbs against Omicron, the FDA has amended its approval for the use of two mAbs-based cocktail therapies in COVID-19. Patients can benefit from the use of casirivimab and imdevimab (used as cocktail therapy) and Etesevimab and bamlanivimab (administered together) only if they are exposed to a variant susceptible to these treatments. As Omicron and its sub-variants are fully resistant to individual or cocktail treatment of these mAbs (10).

A recent cohort study involving 936 SARS-CoV-2 convalescent patients found ultra-potent broad-spectrum antibodies as “elite neutralizers” from a subset of the convalescent individuals (11). Where some of these mAbs broadly neutralize SARS-CoV-2 VOCs and Omicron sub-variants, others could be resisted due to single point mutations within Omicron sub-variants (12). While mapping the epitopes of these mAbs in our ongoing study, we found that R40-1C8 (mAb) neutralize Wuhan strain and four sub-variants of Omicron, failed to neutralize BA.4/5 variant due to Phe486Val mutation (unpublished). Supporting this notion, Bebtelovimab that broadly neutralizes all SARS-CoV-2 variants was recently reported to be less effective against BQ.1.1 sub-variant of the Omicron that was recently emerged (13). We found that this loss in neutralization was due to the breakage of crucial salt bridges between Lys444 and electrostatic amino acids in CDRH2 of the antibody due to Lys444Thr mutation in RBD (unpublished). However, antibodies that recognize conserved epitopes on RBD and hold pan-sarbecovirus neutralization capacity retains their Omicron neutralization (5, 10) and could be used as cocktail therapy to contain the escape within conserved epitopes.

Here, to complement the lost interaction between SARS-CoV-2 VOCs Spike RBD (Delta and Omicron) and mAbs (CT-p59 and Etesevimab), we analyzed mutational space, van der Waal (vdW), and electrostatic surfaces complementarity, and structural stability parameters. Multiple derivatives of the antibodies were computationally generated and screened against Delta and Omicron variants to restore their binding affinities. The results in this study highlight the utility of our customized structure-based antibody design pipeline for the immediate selection of epitope-specific antibodies against emerging SARS-CoV-2 variants that could be validated *in vitro*. Additionally, the robustness of this protocol ensures broader application in response to future viral threats posed by rapidly emerging mutations.

2 Results

2.1 Single hotspot substitution in Spike can modulate the neutralization of nAbs

2.1.1 CDRs composition and interface insights of CT-p59 and Etesevimab with RBD^{WT}

The α1 helix in the peptidase domain of ACE2 is vital for viral binding and the optimal electrostatic potential and amino acid constitution in this helix are abused by the emerging SARS-CoV-2 variants to strengthen binding and enhance their transmissibility by mutating sub-optimal amino acids in the RBD. We have recently reported that Omicron (BA.1) enhances its ACE2 binding by substituting amino acids in the receptor binding motif (RBM) of RBD (5). The two mAbs selected for CDR diversification, *i.e.*, CT-p59 and Etesevimab, neutralize SARS-CoV-2 by fully overlapping with ACE2 at the RBM. Both mAbs share at least five amino acids Lys417, Leu452, Thr478, Glu484, and Asn501 with ACE2 in their epitopes on RBD (Figure 1A). CT-p59 utilizes CDRH2 and CDRH3 for RBD binding, whereas CDRH1 does not participate in the binding (Figure 1B). Beside hydrogen bonds by multiple residues, three salt bridges established by Arg403, Ly417, and Glu484 favor the CT-p59-RBD interactions (Table S1). Unlike CT-p59 where CDRH1 did not participate in antigen binding, Etesevimab binds RBD through CDRH1 and CDRH3. However, most of these contacts are hydrogen bonds, except Lys417 which established a salt bridges (bond energy=-29.03 kcal/mol) with CDRH3 Asp104 (Figure 1C; Table S2). Interface contacts along with their bonds-length, bonds-energies and bonds-type of both CT-p59 and Etesevimab are listed in Tables S1 and S2 and corresponds to Figure 1. Overall, these findings suggest that CT-p59 and Etesevimab have different compositions of CDRs and therefore respond differently in terms of their therapeutic efficacy against emerging SARS-CoV-2 variants.

2.1.2 The escape mechanism of SARS-CoV-2 VOCs from CT-p59

Antibodies recognize distinct conformational epitopes on antigens that determine their specificity and binding affinity.

10.3389/fimmu.2023.1113175

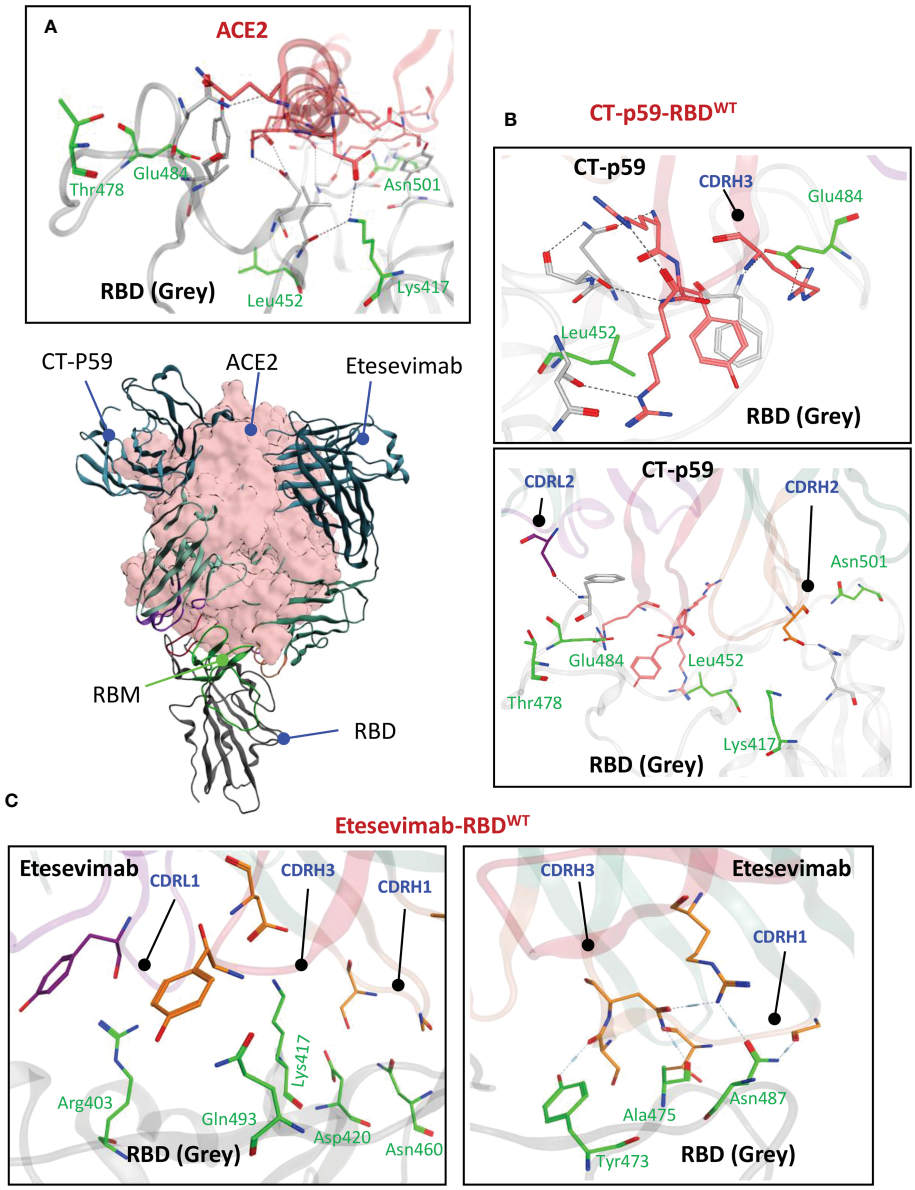

FIGURE 1
Monoclonal antibodies (mAbs) Etesevimab and CT-p59 neutralize SARS-CoV-2 and compete with ACE2 on RBD. **(A)** Both mAbs fully overlap with ACE2 and interact with receptor binding motif (RBM) in RBD. **(B)** CT-p59 utilizes its CDRs H2, H3 and L2 to engage with RBD. **(C)** Etesevimab binds RBD through its CDRs H1, H3, and L1. Amino acids in RBM that are shared by ACE, CT-p59 and Etesevimab are represented by green sticks and labeled green. Interface contacts along with their bonds-length, bonds-energies and bonds-type of both CT-p59 and Etesevimab are listed in Tables S1 and S2.

Substituting a single hotspot residue in the epitope can abrogate mAb-antigen contact (4). To predict what future mutations in RBD would escape/increase CT-p59 neutralization (14), we constructed 176 single-mutation RBD muteins bound to CT-p59, and their relative binding energies were calculated to estimate mAb-resistance and mAb-RBD complex stability. Surprisingly, only 8 out of 176 substitutions, including Asn450Ile, Gly496Cys, Gln493Arg, Gln493Lys, Gln493Leu, Gly485Arg, Gly446Arg, and Gly446Ala in RBD were able to retain or enhance the binding strength of RBD^{Mut}-CT-p59, whereas the rest of mutations weakened the stability of the mAb-RBD as well as increased resistance to CT-p59 (Figure 2A). Affinity change for each of 176 residues corresponding to Figure 2A are listed in Table S3. However, it is not possible to predict whether or not these mutations will occur following the same predicted order in the newly emerging strains of SARS-CoV-2. For example, Gln493Lys/Arg may enhance the CT-p59-RBD^{Mut} binding, while Leu452Arg in RBD is predicted to resist the CT-p59 neutralization. In line with these predictions, we could see that leu452Arg in the CT-p59-RBD^{Delta} model caused a clash with the CDRH3-Arg107 (Figure 2B), whereas Gln493Lys in the CT-p59-RBD^{Omic} established a strong salt bridge with CDRH2-Asp56, contributing 15% of the total binding energy at the interface (Figure 2C). However, Glu484Ala in CT-p59-RBD^{Omic} abolished the salt

10.3389/fimmu.2023.1113175

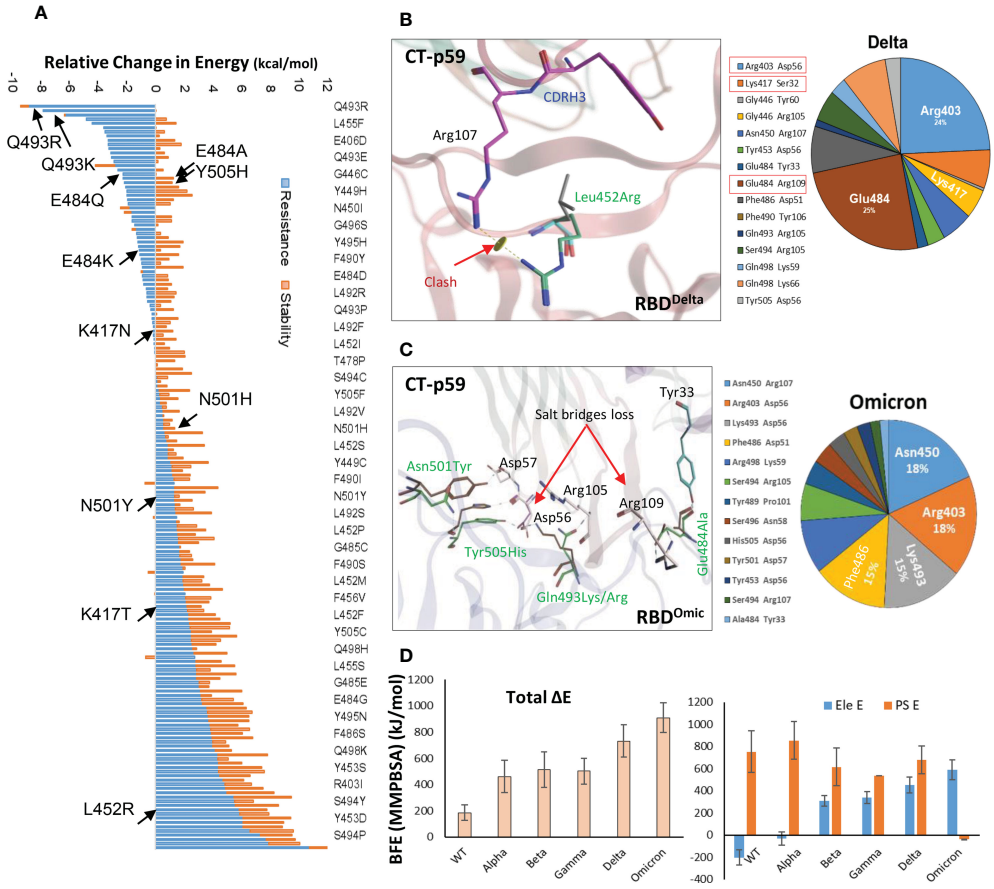

FIGURE 2
Immune escape and escape prediction of the SARS-CoV-2 VOCs. **(A)** SARS-CoV-2 immune escape prediction concerning CT-p59. The amino acid list on the right is shortened for clarity; affinity and stability changes for each of 176 residues corresponding to figure 2A are listed in Table S3. Amino acids and their respective substitutions involved in ACE2 and CT-p59 binding are labeled and indicated with black arrows. Blue bars indicate resistance to CT-p59, where negative values indicate increase in mAb-binding affinity and positive value indicate increase in mAb-escape or loss in affinity. Orange bars indicate stability in Ag-Ag complex. **(B)** Leu452Arg mutation in Delta VOC abolishes the electrostatic contacts between CDRH3 and RBD^{Delta}. The pie chart represents the energy contribution (in percentage, unit is kcal/mol) at the RBD^{Delta}-CT-p59 interface. **(C)** Glu484Ala mutation in $RBD^{Omicron}$ abolishes the salt bridge between CDRH3 and RBD. The pie chart represents the energy contribution at the $RBD^{Omicron}$-Etesevimab interface. Changes in the Interface contacts along with their bonds-length, bonds-energies and bonds-type of CT-p59 bound to WT, Delta ad Omicron variants, corresponding to figure 2A and C are listed in Table S1. **(D)** Free energy perturbation of the CT-p59-RBD complexes of all SARS-CoV-2 VOCs. Wild type and Alpha strains retain their electrostatic energy while other VOCs completely lost this potential.

bridge with CDRH3-Arg109, which was contributing 22% and 25% of binding energy at the RBD^{WT}-CT-p59 and RBD^{Delta}-CT-p59 interfaces, respectively (Figure 2B and Figure S1A). Changes in the interface contacts along with their bonds-length, bonds-energies and bonds-type of CT-p59 bound to WT, Delta ad Omicron variants, corresponding to Figures 2A, C are listed in Table S1. These loss in electrostatic contacts, redistribution of the binding energies, and strong repulsion between the amino acids in CDRs and RBM are the possible causes that disrupt the neutralization of the Delta and Omicron variants. These results suggest that the fate of COVID-19 therapeutic mAbs relies on the serendipity of mutations in their epitopes on SARS-CoV-2 Spike, whereas mAbs that bind relatively conserved epitopes may retain their therapeutic ability, as we previously described (5). In addition, individual mutations in the RBD that retain or enhance the mAbs binding can be used in CDRs' hotspots grafting for the designing of variant-escaped mAbs that share overlapping epitopes. To support the notion that the fate of COVID-19 therapeutic mAbs relies on the serendipity of mutations in their epitopes on SARS-CoV-2 Spike, whereas mAbs that bind relatively conserved epitopes may retain their therapeutic ability, further experimental and computational procedures could be performed.

2.1.3 Free energies perturbations of the SARS-CoV-2 VOCs and CT-p59 complexes

To further support the above findings and expand the CT-p59 escape by other variants, we constructed 3D protein models of CT-p59 with all SARS-CoV-2 VOCs, including Alpha, Beta, Gamma, Delta, and Omicron and investigated their susceptibility and escape through free energy perturbations (FEP). Estimation of the End-point Molecular Mechanics/Generalized Born Surface Area (MMGBSA) energies revealed that CT-p59 may retain its neutralization against the Alpha variant while other variants had reduced the binding affinity, suggesting their potential

neutralization escape (Figure S1B). We could validate this result by calculating MMGBSAs from the eight RBD^{Mut}-CT-p59 and one RBD^{WT}-CT-p59 complex with those of K_D values determined by Surface Plasmon Resonance (SPR) (Figure S1C). We further confirmed these energy terms by simulating the RBD^{Mut}-CT-p59 complexes in a neutralized solvent condition and subjected to MMPBSA-based FEP. The binding free energies of all the VOCs increased by at least 2-fold (Alpha) and up to 5-fold (Omicron), losing their binding affinities (Figure 2D, *left*). The electrostatic potential energy (Ele E) was slightly retained (increased from -202 to -31 kcal/mol) by the Alpha variant but completely lost by other VOCs. Similarly, polar solvation energy (PSE) was retained by the Alpha variant, whereas the mutations in Beta, Gamma, and Delta strains dropped this energy term by 27-30% (Figure 2D, *right*). Due to multiple electrostatic residues substitution at the RBD^{Omic}-CT-p59 interface, we could observe a peculiar shift between the Ele and PSE terms. The Ele E increased by 4-fold while the PSE shifted from positive (RBD^{WT}-CT-p59 = 751 kcal/mol) to negative (RBD^{Omic}-CT-p59=-39 kcal/mol), pointing towards the highly unstable energy state of the complex. These results are consistent with the recently reported experimental data demonstrating that CT-p59 retains its Alpha strain neutralization at reduced efficacy (14). However, in the case of Omicron this effect completely disappeared (15). Taken together, we suggest that at least one hotspot mutation within the epitope of CT-p59 is sufficient to drop, if not fully abolish, the neutralization capacity (*e.g.*, Delta), and that additional mutations can further help the escape (*e.g.* Omicron). However, this notion require further experimental support. The sharp decline in the efficacy of mAbs and nAbs due to emerging variants stresses the development of a robust and effective strategy to redirect these antibodies against emerging VOCs.

2.2 Affinity maturation of the VOCs-escaped mAbs

2.2.1 CDR diversification and affinity maturation strategy

Single hotspot mutation within the epitope can substantially drops the mAbs' neutralization whereas additional mutations can further help in escape (discussed above). Considering this scenario, CDR diversification can be exploited at its best to restore the binding affinity of the escaped mAbs by prudently substituting the lost hotspots within CDRs. We employed a computational method to re-engineer the escaped antibodies guided by the predefined hotspots-mediated epitope-paratope (Epi-Para) interactions. In particular, we considered common and crucial features of the dissociable protein partners in the Ab-Ag complex. After constructing the mAb-RBD^{Mut} complexes and optimization through MDS, we calculated the buried solvent-exposed surface and monitored interfaces including optimized vdW, electrostatic, and hydrogen-bond contacts at the Epi-Para junctions (discussed above). Second, the energy loss leading to the immune escape due to miss-paired hot spots was scrutinized by the previously described protein design methods (16). Third, we restored the lost contacts by reshaping the shape-complementarity of the disoriented CDRs by substituting the miss-paired hot spots at the Epi-Para interface. Hence, this strategy reshapes the dismantled Epi-Para interfaces by highly optimized original hot-spots-like interactions and optimally oriented CDRs with the best shape complementarity. The antibody-designing computational workflow is shown in Figure 3, where steps 1-9 are mostly implemented in this study.

2.2.2 Delta-specific CT-p59 CDR diversification and affinity maturation

We extracted multiple low-energy conformers of the CT-p59-RBD^{Delta} complex from the MDS trajectory and investigated the interface changes as discussed above (Figure 2A). Considering all CDRs but CDRL1 for diversification, we monitored the relative changes in energies for each mutations and their effects on change in binding affinities of CT-p59-derivatives and RBD^{Delta} (Table S4). Single substitutions in the CDRs that restored or compensated the lost Epi-Para contacts and enhanced the binding affinities were combined in CT-p59-derivatives and their combined effect on binding was investigated. All three CDRs in the heavy chain variable domain had a significant impact on CT-p59-RBD^{Delta} complex stability. We selected nine CT-p59 derivatives (e.g. CoVAb1-9) and calculated their end-point binding free energies through MMGBSA against RBD^{Delta}. Mutations carried in the CDRs of CoVAb1-9 are listed in Table S5. CoVAb3, 4, and 5 had reduced total binding energies while the other six derivatives had better binding strength compared to that of CT-p59-RBD^{Delta} (Figure 4A). Only CoVAb6 restored its total and vdW energies (-131 kcal/mol) similar to that of CT-p59-RBD^{WT} (-129 kcal/mol). However, the electrostatic potentials of all CoVAbs, except CoVAb6 and CoVAb7, remained similar to that CT-p59-RBD^{Delta}. CoVAb6 had a dramatic shift in its Ele potential (dropped from 154 kcal/mol to -260 kcal/mol) and acquired overall energy terms similar to that of CT-p59-RBD^{WT} (Figure 4B).

To demonstrate whether mutations in CT-p59 CDRs enhance the binding affinity against RBD^{WT}, we generated mutations in all three heavy chain CDRs and CDRL2 and calculated their per residues change in binding energies against RBD^{WT} (Table S6). CT-p59 derivatives against RBD^{WT} were generated by combining high-affinity mutations for CT-p59 derivatives. According to the MMGBSA-based end-point energy calculation, CT2 derivative showed slightly better total binding energy (-126.08 kcal/mol) whereas the rest of the derivatives CT1, CT3, and CT4 showed similar or lower binding energies as compared to parent CT-p59 (-109.45 kcal/mol) (Figure S2A). This suggests that residues within the CDRs that have already matured for the cognate epitopes may lose their binding potential if substituted.

As MMGBSA calculates the binding energy on a single frame (in this case) and MMPBSA takes the entire trajectory into account containing hundreds of structural frames that evolve during time, we used MMPBSA to validate the binding affinities of CoVAb6 and CoVAb7 against RBD^{Delta}. Due to loss in electrostatic contacts and the establishment of the steric clash between Arg107 of CT-p59 and Arg452 of RBD^{Delta} the Ele E had a vivid shift from –ve (RBD^{WT}=-202 kJ/mol) to +ve (RBD^{Omic}=451 kJ/mol) (Figure 4C, *left*).

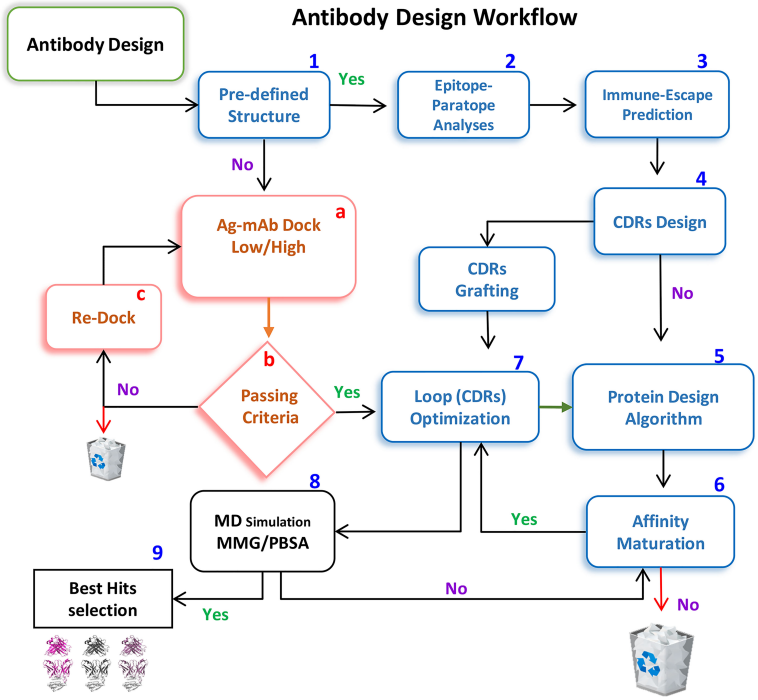

FIGURE 3
A workflow for repositioning SARS-CoV-2-escaped mAbs against emerging strains. Steps 1-9 are implemented to redesign CT-p59 against Delta and Etesevimab against the Omicron variant.

Although the MMGBSA-based energy calculation showed that this loss in Ele potential was fully restored in CoVAb6 and partly in CoVAb7, MMPBSA energy perturbation confirmed that both CoVAb6 and CoVAb7 had substantially restored Ele E potential. The total binding energy was dropped from 732 kJ/mol in CT-p59-RBD^{Delta} to 196 kJ/mol in CoVAb6 and 316 kJ/mol in CoVAb7, where that of CT-p59-RBD^{WT} was 184 kJ/mol (Figure 4C, *right*). Interestingly, we found that CoVAb6-RBD^{Delta} had similar total energies as that of CT-p59-RBD^{WT} in both MMGBSA- and MMPBSA-based calculations. The total number of hydrogen bonds was the lowest in CT-p59-RBD^{Delta}, which were restored or increased in both CoVAb6-RBD^{Delta} and CoVAb7-RBD^{Delta} as compared to CT-p59-RBD^{WT} (Figure 4D). Together, these data suggest that CDR diversification can restore the lost electrostatic potential and further enhance the binding strength of modified mAbs against the escaped antigens.

2.2.3 CoVAb6 and CoVAb7-RBD^{Delta} interface assessment

Five potential hotspots substitution restore the affinity of CT-p59 against escaped the Delta variant (Figure 5A). Among them, Arg107Asp in the CDRH3 was the most crucial substitution, changing the steric clash between Arg107 and Arg452 in RBD^{Delta} into a stable salt bridge and restored the lost electrostatic potential in CoVAb6 and CoVAb7 (Figure 5B). Interface contacts along with their bonds-length, bonds-energies and bonds-type of CoVAb6-RBD^{Delta} and CoVAb7-RBD^{Delta}, corresponding to Figure 5B are listed in Table S7. To validate the stability of salt bridge between Asp107 and Arg452 of RBD, the distances of Arg452 concerning CT-p59^{Arg107}, CoVAb6^{Asp107}, and CoVAb7^{Asp107} were tracked as a function of time. We observed a clear shift from unstable (CT-p59^{Arg107}) to stable salt bridge (CoVAb6^{Asp107}, and CoVAb7^{Asp107}) over 20 ns trajectory (Figure 5C). In addition, the distance between CT-p59^{Ser32} and Lys417 of RBD^{Delta} was 3 Å with some rigor, which was lost during the last quarter of simulation. Ser32Asp substitution in the CDRH1 of CoVAb6 and CoVAb7 established a stable salt bridge with Lys417 in RBD^{Delta}, which remained intact at ~2 Å. We found that aliphatic and aromatic amino acids were the best fits to enhance the complementarity and CDRs fitting onto the epitope (Figure 5B). Single Asn58Trp substitution in the CDRH2 of CoVAb6 was sufficient to restore its binding; however, triple Trp substitution (Gly33Trp, Asn58Trp, and Tyr106Trp) in all three CDRs enhanced the vdW potentials in CoVAb7 (Figure 4C). However, this additional Trp supplementation increased the total binding energy from 196 kJ/mol in CoVAb6 (Asn58Trp substitution only) to 315 kJ/mol in CoVAb7 (Gly33Trp, Asn58Trp, and Tyr106Trp substitutions), suggesting that overabundance of bulky hydrophobic amino acids may compromise the CDR-fitting onto epitopes. Taken together, electrostatic and aliphatic amino acids substitutions in CoVAb6 and CoVAb7 restored their binding strength against RBD^{Delta} and possibly their neutralization as well, which may require further validation through pseudovirus neutralization or biophysical assays such as SPR.

10.3389/fimmu.2023.1113175

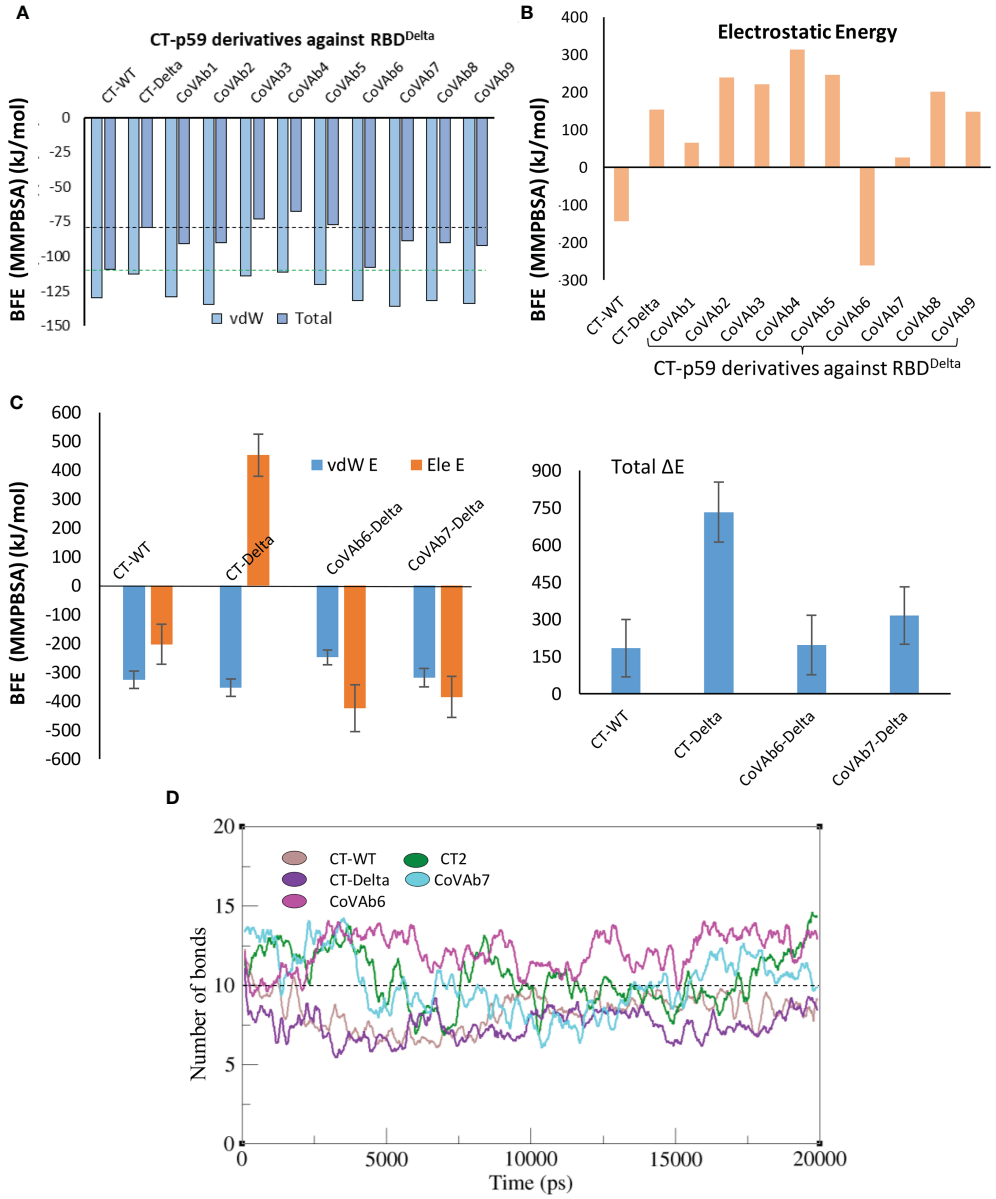

FIGURE 4
Binding free energy perturbation of the CDRs-diversified mAb (CT-p59) against Delta variant. **(A)** Relative changes in the total binding free energy of the CT-p59 derivatives (CoVAb1-9) are calculated through the MMGBSA method. **(B)** Relative change in the electrostatic energy (Ele) of the CT-p59 derivatives (CoVAb1-9). CoVAb6 fully and CoVAb7 partially restore their Ele potential that was lost by CT-p59 against the Delta variant (CT-Delta). **(C)** Binding free energy perturbation (MMPBSA method) of the top hits from CDR-diversified mAbs. **(D)** Change in the number of hydrogen bonds at the RBD-mAbs interface. The lowest number of bonds was recorded in CT-Delta. (CT-Delta=CT-p59-RBD^{Delta}). CoVAbs are CDR-diversified CT-p59 derived mAbs against the Delta variant.

2.2.4 Omicron-specific Etesevimab CDRs diversification and affinity maturation

As discussed above, Etesevimab largely utilizes its CDRH1 and CDRH3, and partly CDRL1 to bind RBD (see Figure 1C). We sought to deduce the effect of RBD mutations reported in the Omicron variant on the Etesevimab escape by constructing a 3D Etesevimab-RBD^{Omic} structural model. Unlike CT-p59-RBD^{Omic} which has no significant steric clashes due to miss-paired Epi-Para contacts, CDRL1 and CHRH3 in Etesevimab clashed with all the three mutated amino acids (i.e. Gln498Arg, Tyr505His, and Gln493Lys) in RBD^{Omic}. Of note, Gln498Arg created a steric clash as well as a repulsive electrostatic environment around Arg31 in CDRL1, which was aided by the π-cation clash between Gln493Lys of RBD^{Omic} and Tyr102 in CDRH3 (Figure 6A).

As with CoVAbs, we designed several Etesevimab derivatives and selected Etsimic1 and Etsimic2 as the best candidates to restore RBD^{Omic} binding and possibly SARS-CoV-2 neutralization. Four amino acids substitutions in CDRL1, CDRH1, and CDRH3 not only restored the binding affinity in Etsimic1 and Etsimic2 but also surpassed that of Etesevimab-RBD^{WT} (E total=173 kJ/mol). Both Etsimics differ at single residue where Tyr102 in Etesevimab was substituted by Glu102 in Etsimic1 and Met102 in Etsimic2

10.3389/fimmu.2023.1113175

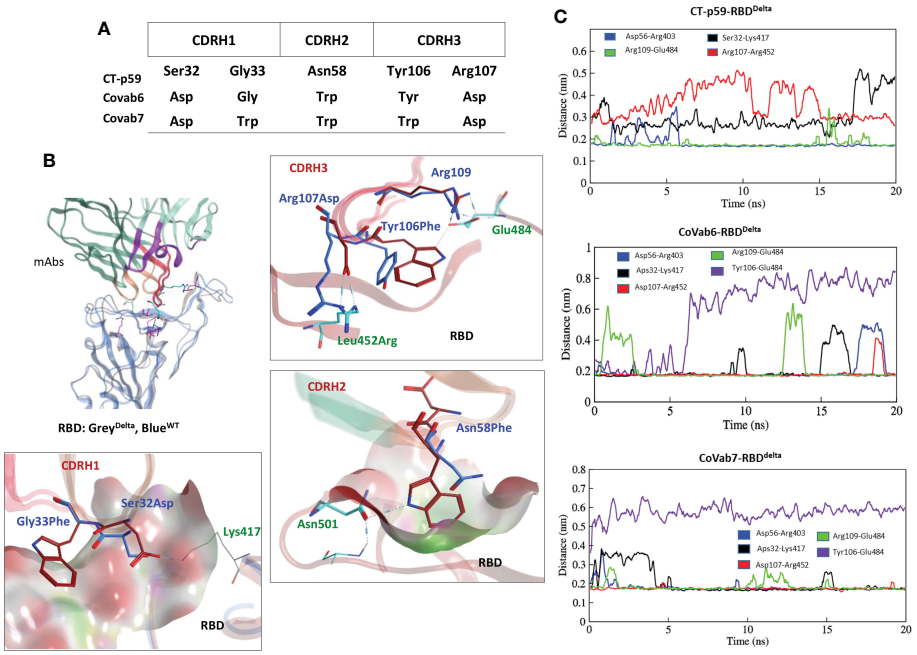

FIGURE 5
CDR diversification and interface analysis of the CoVAb-RBD complexes. **(A)** Contact favorable mutations created in CT-p59 CDRs to restore their efficacy against the Delta variant. **(B)** Interface analysis of the CoVAb6-RBD and CoVAb7-RBD complexes. Salt bridges between Arg452 and Asp107 are restored after Arg107Asp substitution in CDRH3 of CT-p59. Interface contacts along with their bonds-length, bonds-energies and bonds-type of CoVAb6-RBD^{Delta} and CoVAb7-RBD^{Delta}, corresponding to figure 5B are listed in Table S7. **(C)** Changes in the hydrogen bonds and salt bridges during simulation.

(Figure 6B). Asp26 in CDRH1 of Etsimic1 was optimally oriented and established a salt bridge with Thr478Lys and a hydrogen bond with surrounding Asn87 in RBD^{Omic} (Figure 6C). The EEE substitutions (i.e. Arg31Glu, Tyr32Glu) in CDRL1 and Tyr102Glu mutations in CDRH3 created a network of salt bridges around the Glu498Arg, Tyr505His, Glu493Lys, and Arg403 in RBD^{Omic}. We could observe a similar network in Etsimic2-RBD^{Omic} (Figure 6D). Interface contacts along with their bonds-length, bonds-energies and bonds-type of Etsimic1-RBD^{Omic} and Etsimic2-RBD^{Omic}, corresponding to Figures 6B, D are listed in Table S8.

Next, we monitored the stability of these bonds as a function of time, revealing a rigorous fluctuation between Arg31-Gln498Arg, Tyr102-Tyr505His, and Gly26-Lys478 pairs caused by the steric clashes in Etesevimab-RBD^{Omic} complex (Figure S3A). Upon residue substitution, we found a substantial reduction in the minimum bond lengths (dropped from ~8Å in Etesevimab to ~4Å in Etsimics). The clash between Arg31Glu-Arg498 pairs disappeared, establishing a steady salt bridge (bond length ~2Å) in both Etsimics with RBD^{Omic} (Figures S3A, B). In addition, Gly26Asp in CDRL1 established a steady salt bridge with Lys478, which was otherwise absent in Etesevimab-RBD^{WT}. The total number of hydrogen bonds elevated to ~15 in Etsmic2-RBD^{Omic} from ~12 in Etesevimab-RBD^{WT}, which was dropped to ~6 in Etesevimab-RBD^{Omic} (Figure 6E).

The BA.1 lineage of the Omicron variant was found to have either Gln493Lys (non-dominant) or Gln493Arg (dominant variant) (17) and, during this study new sublineages of Omicron BA.2, BA.3, and BA.4/5 appeared, where BA.2 became the dominant variants very quickly (18). The differences and similarities in the RBD of these lineages are depicted in Figure 7A. We sought whether Gln493Lys to Gln493Arg mutation in BA.1 and differences in the BA.1 and BA.2 affect the binding affinity of Esimic1 and Esimic2. The total number of hydrogen bonds was first investigated as a function of time, which slightly dropped in Etsimic1-RBD^{Q493R}; however, Etsimic2-RBD^{Q493R}, Etsimic1-RBD$^{BA.2}$, and Etsimic2-RBD$^{BA.2}$ retained this number (Figure 7B). Interestingly, relative binding FEP analysis revealed that both Etsimic1 and Etsimic2 retained their binding strength against BA.2 and BA.1 (RBD^{Q493R}) variants, where Etsimic1 had relatively better affinity compared to Etsimic2 (Figures 7C-E). This suggests that Etsimics can withstand slight variations in their epitopes and have the potential to neutralize the sublineages of Omicron, although requiring further experimental validation.

3 Discussion

The abrogation of Spike-ACE2 is considered one of the promising COVID-19 therapeutic strategies to block the virus at an early stage of infection. Various nAbs have been approved by FDA for this purpose and many small molecules and peptides are under clinical and pre-clinical evaluation (19–22). Studies have been conducted to probe the antigenicity of the SARS-CoV-2 Spike protein by mapping several overlapping epitopes using structural (23–25) and deep mutational scanning techniques (26). Strikingly,

10.3389/fimmu.2023.1113175

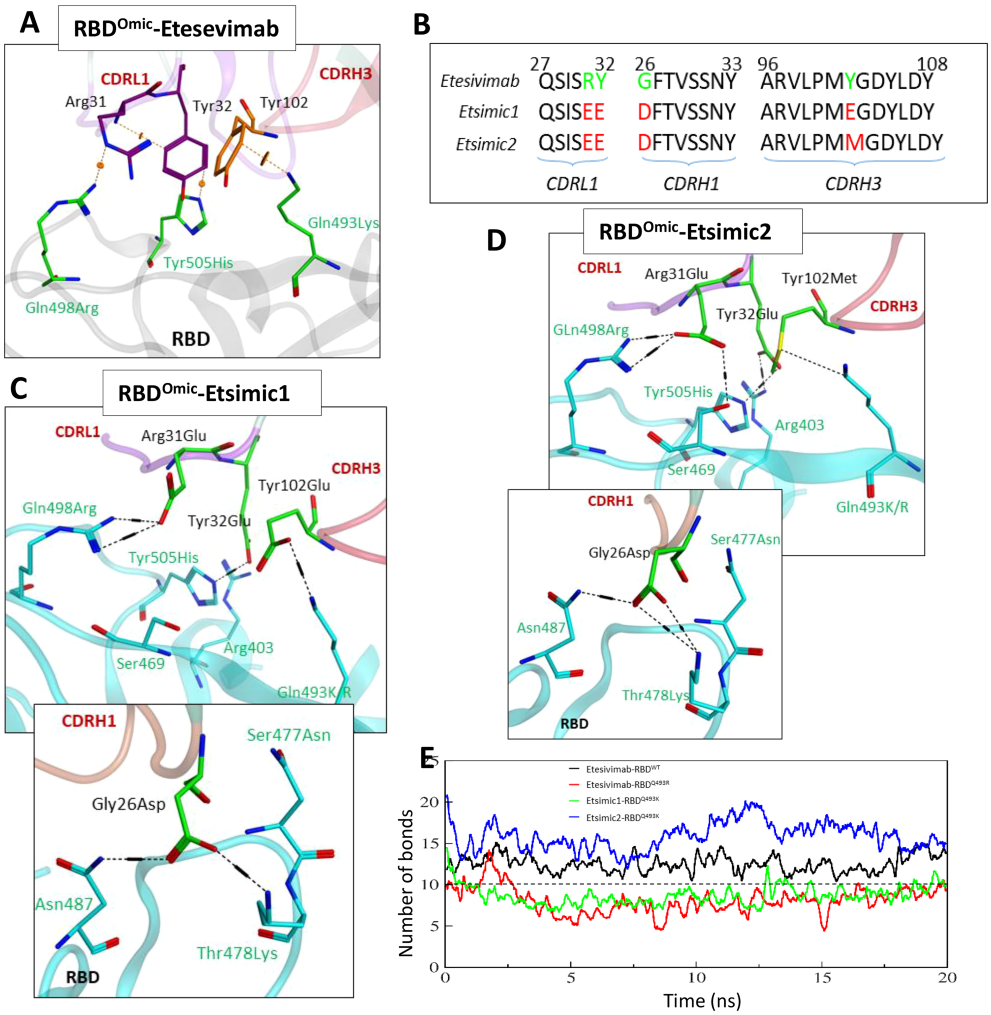

FIGURE 6
Interface analyses and CDR diversification of the Etesevimab against the Omicron variant. **(A)** Three mutations in the RBD^{Omic} i.e. Gln493Lys, Gln498Arg, and Tyr505His, abolish vdW contacts at the Etesevimab-RBD^{Omic} interface. **(B)** Contact favorable mutations created in Etesevimab CDRs (L1, H1, and H3) to restore their efficacy against the Omicron variant. **(C, D)** Interface analyses of the Etesevimab derivatives (Etsimic1 and Etsimic2) and RBD complexes. Hydrogen bonds are restored and salt bridges are established after CDRL1-Arg31Glu, CDRL1-Tyr32Glu, CDRH1-Gly26Asp, and CDRH3-Tyr102Glu/Met substitutions. Interface contacts along with their bonds-length, bonds-energies and bonds-type of Etsimic1-RBD^{Omic} and Etsimic2-RBD^{Omic}, corresponding to figure 6B and 6D are listed in Table S8. **(E)** Change in the number of hydrogen bonds at the RBD-mAbs interface. The lowest number of bonds was recorded in Etesevimab-RBD$^{Omic(BA.1)}$.

over 90% of the convalescent plasma and serum-derived SARS-CoV-2 nAbs target the Spike RBD (27), and most of the FDA-approved RBD-binding nAbs are evaded by the emerging VOCs (5).

Antibodies screening and selecting high-affinity molecules during this process is a hectic task that requires expensive and often time-consuming procedures like affinity maturation, epitope mapping, and binding kinetics of the Ab-Ag complexes (6). The swift failure of the drugs due to viral mutations has put the fate of COVID-19 therapeutics, particularly nAbs, and vaccines in jeopardy. As discussed above, a single mutation in the antigenic epitope can render effective antibodies incapable of neutralization. With the advent of structural and computational biology, the knowledge of pre-defined hotspots-mediated epitope-paratope interfaces could be utilized to redirect/design escaped antibodies against the emerging SARS-CoV-2 variants. Substituting the concerned hotspots in CDRs into structurally favorable and contact-restoring amino acids can help in redirecting the escaped antibodies against new variants. High-resolution structural models of both antigen and antibodies are therefore vital in this regard, as lack of exact interface knowledge may hinder the CDRs diversification rationale.

Computational approaches such as OptMAVEn (28) and AbDesign, utilizing a dock-and-design strategy, generate ensembles of docked conformers followed by tightly bound top-ranked Ab-Ag poses and allow for CDR optimization (see Figure 3). However, the success of precise antigen positioning is constrained by the accuracy of scoring methods and sampling algorithms of the computational tools, which often prioritize the desired binding patches on a static antigen to the antibody scaffold. This biased antigen positioning could be overcome by an induced-fit docking algorithm that allows, to some extent, the mobility of epitope residues during docking. Conformational changes at the Epi-Para

10.3389/fimmu.2023.1113175

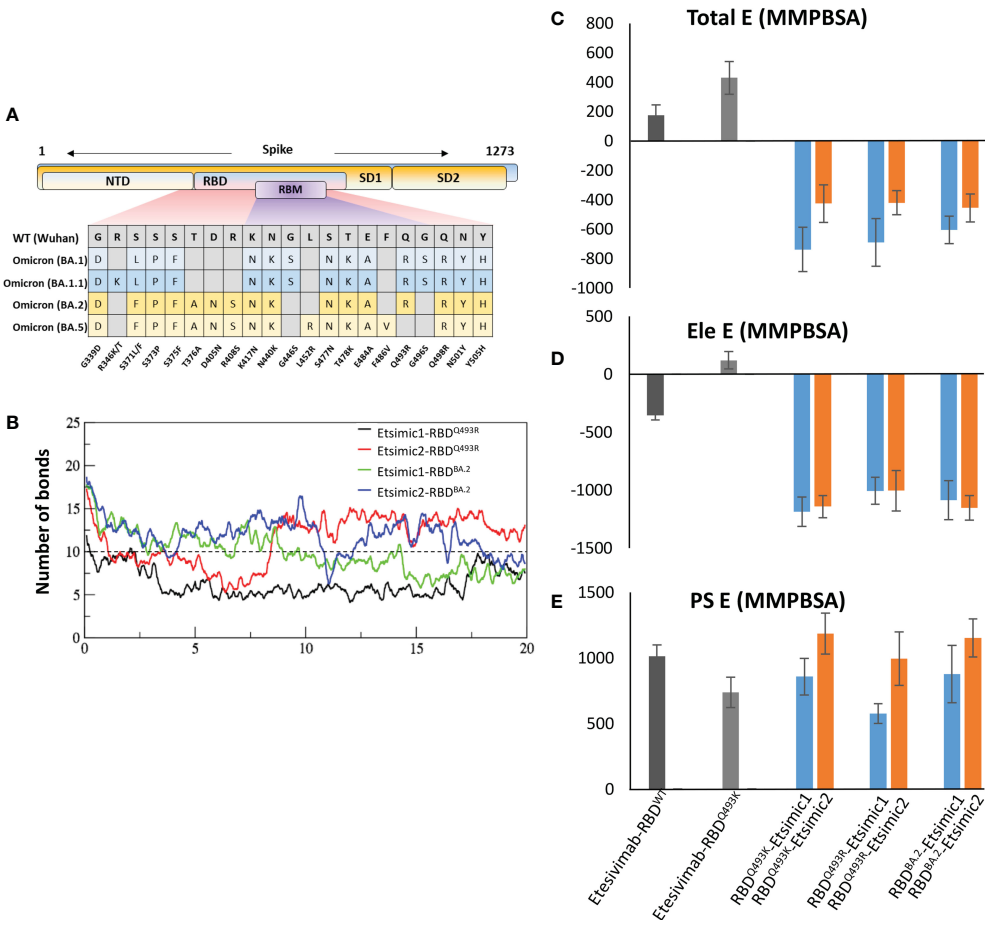

FIGURE 7
Binding free energy perturbation of the CDRs-diversified mAb (Etsimics) against Omicron BA.1 and BA.2 variants. **(A)** Mutations within the RBD domain of Omicron sub-variants concerning the Wuhan strain. **(B)** Change in the number of hydrogen bonds at the $RBD^{BA.2}$-Etsimic interface. **(C-E)** Relative change in the total binding free energy of the Etesevimab derivatives as calculated through the MMGBSA method.

interface of the rigid-body docking procedure may lead to a reorientation of Ab-Ag poses, abominating complexes such as the Prb-Pdar protein complex (29). Therefore, it is important to consider the pre-defined interaction patterns of the cognate binders for CDRs restoration to ensure the favorability of desired binding mode and stability in the solution state.

In this study, we computationally redesign the mAbs targeting disoriented pre-defined epitopes for the immune-escaped Delta and Omicron variants. We established a new approach that entails the heuristic design strategy to some extent and emulates the biased pose-prioritization binding of the docking algorithms. This method involves the reshaping of miss-paired Epi-Para hotspots by substituting amino acids in the corresponding CDRs to accommodate mutations in RBD and regain the lost binding affinity. In addition, in-solvent simulations confirm the stability and resistance of the Ab-Ag poses to conformational changes and reorientation.

Similar techniques, overlapping with the one propose in our study, have been recently put into practice by AstraZeneca, one of the lead COVID-19 fighting companies (30). Here they used a mere computational model of the hybridoma-derived antibody AB1 and its antigen muCCL20 to fine-tune their Epi-Para interface through Ab-Ag docking and in silico alanine mutagenesis, which allowed them identifying two single-point mutations that increased the physical binding affinity (estimated by SPR) of the AB1 derivatives C1 and C1-16 against muCCL20 by four fold (KD=2.3 nM and KD=2.8 nM, respectively) as compared to AB1-muCCL20 affinity (KD=9.1 nM). Reinforcing the in silico antibody designing strategy, a SARS-CoV-1 neutralizing nAbs were redirected against SARS-CoV-2 very recently, by computationally engineering their CDRs and confirming their neutralization *in vitro* and binding affinity through bilayer interferometry (31). Here the crystal structures of SARS-CoV-bound mAbs were investigated for conserved epitopes compared to SARS-CoV-2, and their CDRs were redesigned through computational affinity maturation using the criteria of shape-complementarity, buried solvent-accessible surface area, and number of unsatisfied polar atoms, which is considerably overlapping with the acquired in our study. Out of several hits, D27 (mAb) was found to bind SARS-CoV-2 RBD at KD=177 nM whereas none of its parent mAbs including S230, 80R, m396, and F26G19 showed any cross reactivity with SARS-CoV-2 RBD (31).

Conclusively, the examples of CoVAbs and Etsimics identified here put forth the idea of utilizing computational tools in mAbs

design as a viable strategy to regain the specificities and binding affinities of existing antibody scaffolds, although further experimental validation is required. The structure-based design of antibodies with improved computational accuracy and parallel optimization *via* MDS and FEP provides a complementary and time-efficient method for the fast development of SARS-CoV-2 therapeutic antibodies to meet the demand to combat emerging immune-escaping VOCs.

4 Methods

4.1 Protein structures modeling

The structural coordinates of the proteins used in this study were obtained from the PBD databank, including the following: ACE2- RBD^{WT} (PDB ID: 6MOJ), ACE2-$RBD^{Omic\ (BA.1)}$ (PDB ID: 7WBP), CT-p59-RBD^{WT} (PDB ID: 7CM4), Etesevimab-RBD^{WT} (PDB ID: 7C01), RBD^{Alpha} (PDB ID: 7R15), RBD^{Beta} (PDB ID: 7NXA), RBD^{Delta} (PDB ID: 7WBQ). The structural coordinates constructed by the replacement process are as follows. RBD^{Gamma} was constructed by mutating respective amino acids in RBD^{Beta} (PDB ID: 7NXA). $RBD^{Omic\ (BA.2)}$ was constructed by mutating respective amino acids in $RBD^{Omic\ (BA.1)}$ (PDB ID: 7WBP). The heterotrimeric structure of RBD^{WT} with CT-p59 and Etesevimab was constructed by superimposing RBD in Etesevimab-RBD^{WT} and CT-p59-RBD^{WT} complexes. CT-p59-RBD^{Delta} was built by replacing RBD^{WT} in CT-p59-RBD^{WT} with RBD^{Delta}. Similarly, CT-p59-RBD^{Omic} was built by replacing RBD^{WT} in CT-p59-RBD^{WT} with RBD^{Omic}. Etesevimab-RBD^{Omic} was built by replacing RBD^{WT} in Etesevimab-RBD^{WT} with $RBD^{Omic\ (BA.1)}$ and $RBD^{Omic\ (BA.2)}$. Free BIOVIA Discovery Studio Visualizer was used for constructing mutant RBD, (http://www.accelrys.com). The structural coordinates of manually built models were relaxed by solvating in a cubic box filled with TIP3P water model and energy minimizing in GROMACS 2020 (32) under CHARMM37 force field (33) following a steep descent algorithm.

4.2 Escape prediction and CDR diversification

Antibodies in CT-p59-RBD^{WT} and Etesevimab-RBD^{WT} complexes were annotated as described previously (34, 35). The resistance of RBD^{Mut} towards CT-p59 or Etesevimab was determined through a resistance scan package in MOE 2022 (Chemical Computing Group, Montreal CANADA). One limitation of this approach is that the predicted resistance is limited to the antibody under study and predicted mutation in the RBD will confirm the immune escape of a new variant concerning the same antibody. As the composition of CDRs differs in antibodies, neutralizing antibodies binding to the non-overlapping epitopes on RBD may respond differently to the escape prediction model here. We mutated all residues within 10Å of the CDRs using Unary Quadratic Optimization (UQO) model under the molecular dynamics ensemble that estimates the stability of the output conformers after 1 ps run of simulation at constant temperature (36). The output conformers were saved in a database and ranked according to the resistance and instability criteria. Mutants were considered resistant if the relative change in binding energy was equal to or more than 1.0 kcal/mol. Similarly, all mutants were placed as unstable when the relative change in Ab-RBD^{Mut} was equal to or more than 1.0 kcal/mol. Mutants with more unstable energy but lower resistance were also placed in escape mutants.

For CDRs diversifications we used overlapping criteria; nonetheless, to get better insights about the disoriented Epi-Para interface and miss-paired hotspots in RBD^{Mut}-mAbs, we created electrostatic and vdW (interaction) surfaces at the Epi-Para interfaces using APBS and APBSrun plugins in VMD. Suboptimal residues and those with prominent steric clashes were identified. The hotspots and suboptimal amino acids and their solvent surface exposure were examined through PDBePISA (37) and validated through DrugscorePPI (38). Considering the surface complementarity, miss-paired amino acids, hotspots, and suboptimal residues, CDRs were diversified using a protein design package in MOE 2022. Initially, the CDRs in RBD^{Mut}-mAbs were subjected to single residues substitution and the mutants were sorted and ranked based on high binding energies, as described previously (39). Second, the top-ranked single CDR-mutants were selected and combined in multiple-CDR mutants, producing mAbs with enhanced RBD^{Mut} binding and Epi-Para complementarity. An overall protocol is outlined in Figure 3.

4.3 Molecular dynamics simulations

All protein models were simulated in a separated cubic box saturated with the TIP3P solvent model. The boundaries of the box were 10Å apart from the centralized protein models that were neutralized with Na^+ and Cl^- ions and extra 0.1M NaCl concentrations. All systems were first energy minimized as discussed above and then equilibrated under constant temperature (NVT) and constant pressure (NPT) conditions for 0.5 ns. To keep the systems from breaking, proteins and solvents were separated and constraints were applied to protein atoms. During the NVT step, the temperature was coupled with the v-rescale (modified Berendsen thermostat) method while the unmodified Berendsen algorithm was used in the NPT step (40). All systems were simulated for at least 20 ns with no structural constraints. The long-range electrostatic interactions were computed by utilizing the Particle Mesh Ewald algorithm (41). After completion of the simulation, the artifacts were removed from the MD trajectories using –PBC and –fit flags implemented in the

trjconv tool with different functions including whole, nojump, and rot+trans. For trajectories analyses, built-in options in GROMACS including rmsf, rms, mindist, and hbond were used.

4.4 Free energy perturbation and binding free energies calculation

For binding energy calculations, we used endpoint binding free energy MMGBSA method using HawkDock server (42) and free energy perturbation methods using MMPBSA implemented in GROMACS (v 5.0 and earlier) (43), which is best suited for energy calculation of the different ligands bound to the same target. The newer version of GROMCS is not compatible with MMPBSA, thus, the topology files for each Ab-Ag complex were generated through v 5.0. The optimized simulation trajectory containing 100 frames was analyzed for binding free energies calculation as described previously (44).

Data availability statement

The original contributions presented in the study are included in the article/Supplementary Material. Further inquiries can be directed to the corresponding authors.

Author contributions

MS and HW contributed to the conceptualization of the project. MS designed the methodology. MS, J-YS, and HW wrote the original manuscript draft. HW supervised the study and provided funding acquisition. All authors contributed to the article and approved the submitted version.

Funding

This research was supported by grants from the National Research Foundation of Korea (NRF) funded by the Ministry of Science and ICT (MSIT) (NRF-2019R1A5A2026045) and the grant from the Korea Health Industry Development Institute (KHIDI) funded by the Ministry of Health & Welfare, Republic of Korea (HI21C1003 and HV22C0164). This study was also supported by KREONET (Korea Research Environment Open NETwork), which is managed and operated by KISTI (Korea Institute of Science and Technology Information).

Conflict of interest

The authors declare that the research was conducted in the absence of any commercial or financial relationships that could be construed as a potential conflict of interest.

Publisher's note

All claims expressed in this article are solely those of the authors and do not necessarily represent those of their affiliated organizations, or those of the publisher, the editors and the reviewers. Any product that may be evaluated in this article, or claim that may be made by its manufacturer, is not guaranteed or endorsed by the publisher.

Supplementary material

The Supplementary Material for this article can be found online at: https://www.frontiersin.org/articles/10.3389/fimmu.2023.1113175/full#supplementary-material

References

1. Harvey WT, Carabelli AM, Jackson B, Gupta RK, Thomson EC, Harrison EM, et al. SARS-CoV-2 variants, spike mutations and immune escape. *Nat Rev Microbiol* (2021) 19(7):409–24. doi: 10.1038/s41579-021-00573-0

2. Li M, Lou F, Fan H. SARS-CoV-2 variants of concern delta: a great challenge to prevention and control of COVID-19. *Signal Transduct Target Ther* (2021) 6(1):349. doi: 10.1038/s41392-021-00767-1

3. Wall EC, Wu M, Harvey R, Kelly G, Warchal S, Sawyer C, et al. Neutralising antibody activity against SARS-CoV-2 VOCs B.1.617.2 and B.1.351 by BNT162b2 vaccination. *Lancet* (2021) 397(10292):2331–3. doi: 10.1016/S0140-6736(21)01290-3

4. Planas D, Veyer D, Baidaliuk A, Staropoli I, Guivel-Benhassine F, Rajah MM, et al. Reduced sensitivity of SARS-CoV-2 variant delta to antibody neutralization. *Nature* (2021) 596(7871):276–80. doi: 10.1038/s41586-021-03777-9

5. Shah M, Woo HG. Omicron: A heavily mutated SARS-CoV-2 variant exhibits stronger binding to ACE2 and potently escapes approved COVID-19 therapeutic antibodies. *Front Immunol* (2021) 12:830527. doi: 10.3389/fimmu.2021.830527

6. Shah M, Woo HG. The paradigm of immune escape by SARS-CoV-2 variants and strategies for repositioning subverted mAbs against escaped VOCs. *Mol Ther* (2022) 30 (10):3101–5. doi: 10.1016/j.ymthe.2022.08.020

7. Meng B, Abdullahi A, Ferreira I, Goonawardane N, Saito A, Kimura I, et al. Altered TMPRSS2 usage by SARS-CoV-2 omicron impacts infectivity and fusogenicity. *Nature* (2022) 603(7902):706–14. doi: 10.1038/s41586-022-04474-x

8. Cox M, Peacock TP, Harvey WT, Hughes J, Wright DW, Consortium C-GU, et al. SARS-CoV-2 variant evasion of monoclonal antibodies based on in vitro studies. *Nat Rev Microbiol* (2022). 112–124 doi: 10.1038/s41579-022-00809-7

9. Lapidoth GD, Baran D, Pszolla GM, Norn C, Alon A, Tyka MD, et al. AbDesign: An algorithm for combinatorial backbone design guided by natural conformations and sequences. *Proteins* (2015) 83(8):1385–406. doi: 10.1002/prot.24779

10. Cao Y, Wang J, Jian F, Xiao T, Song W, Yisimayi A, et al. Omicron escapes the majority of existing SARS-CoV-2 neutralizing antibodies. *Nature* (2022) 602 (7898):657–63. doi: 10.1038/s41586-021-04385-3

11. Vanshylla K, Fan C, Wunsch M, Poopalasingam N, Meijers M, Kreer C, et al. Discovery of ultrapotent broadly neutralizing antibodies from SARS-CoV-2 elite neutralizers. *Cell Host Microbe* (2022) 30(1):69–82 e10. doi: 10.1016/j.chom.2021.12.010

12. Gruell H, Vanshylla K, Korenkov M, Tober-Lau P, Zehner M, Munn F, et al. SARS-CoV-2 omicron sublineages exhibit distinct antibody escape patterns. *Cell Host Microbe* (2022) 30(9):1231–41 e6. doi: 10.1016/j.chom.2022.07.002

13. Planas D, Bruel T, Staropoli I, Guivel-Benhassine F, Porrot F, Maes P, et al. Resistance of omicron subvariants BA.2.75.2, BA.4.6 and BQ.1.1 to neutralizing antibodies. *bioRxiv* (2022). doi: 10.1101/2022.11.17.516888

14. Ryu DK, Song R, Kim M, Kim YI, Kim C, Kim JI, et al. Therapeutic effect of CT-P59 against SARS-CoV-2 south African variant. *Biochem Biophys Res Commun* (2021) 566:135–40. doi: 10.1016/j.bbrc.2021.06.016

15. VanBlargan LA, Errico JM, Halfmann PJ, Zost SJ, Crowe JEJr., Purcell LA, et al. An infectious SARS-CoV-2 B.1.1.529 omicron virus escapes neutralization by therapeutic monoclonal antibodies. *Nat Med* (2022) 28(3):490–5. doi: 10.1038/s41591-021-01678-y

16. Shah M, Ung Moon S, Hyun Kim J, Thanh Thao T, Goo Woo H. SARS-CoV-2 pan-variant inhibitory peptides deter S1-ACE2 interaction and neutralize delta and omicron pseudoviruses. *Comput Struct Biotechnol J* (2022) 20:2042–56. doi: 10.1016/j.csbj.2022.04.030

17. Starr TN, Greaney AJ, Dingens AS, Bloom JD. Complete map of SARS-CoV-2 RBD mutations that escape the monoclonal antibody LY-CoV555 and its cocktail with LY-CoV016. *Cell Rep Med* (2021) 2(4):100255. doi: 10.1016/j.xcrm.2021.100255

18. Kurhade C, Zou J, Xia H, Cai H, Yang Q, Cutler M, et al. Neutralization of omicron BA.1, BA.2, and BA.3 SARS-CoV-2 by 3 doses of BNT162b2 vaccine. *bioRxiv* (2022) 2022:485633. doi: 10.1038/s41467-022-30681-1

19. Yuan M, Wu NC, Zhu X, Lee CD, So RTY, Lv H, et al. A highly conserved cryptic epitope in the receptor binding domains of SARS-CoV-2 and SARS-CoV. *Science* (2020) 368(6491):630–3. doi: 10.1126/science.abb7269

20. Wu Y, Wang F, Shen C, Peng W, Li D, Zhao C, et al. A noncompeting pair of human neutralizing antibodies block COVID-19 virus binding to its receptor ACE2. *Science* (2020) 368(6496):1274–8. doi: 10.1126/science.abc2241

21. Cao L, Goreshnik I, Coventry B, Case JB, Miller L, Kozodoy L, et al. *De novo* design of picomolar SARS-CoV-2 miniprotein inhibitors. *Science* (2020) 370 (6515):426–31. doi: 10.1126/science.abd9909

22. Monteil V, Kwon H, Prado P, Hagelkruys A, Wimmer RA, Stahl M, et al. Inhibition of SARS-CoV-2 infections in engineered human tissues using clinical-grade soluble human ACE2. *Cell* (2020) 181(4):905–13.e7. doi: 10.1016/j.cell.2020.04.004

23. Liu L, Wang P, Nair MS, Yu J, Rapp M, Wang Q, et al. Potent neutralizing antibodies against multiple epitopes on SARS-CoV-2 spike. *Nature* (2020) 584 (7821):450–6. doi: 10.1038/s41586-020-2571-7

24. Barnes CO, Jette CA, Abernathy ME, Dam KA, Esswein SR, Gristick HB, et al. SARS-CoV-2 neutralizing antibody structures inform therapeutic strategies. *Nature* (2020) 588(7839):682–7. doi: 10.1038/s41586-020-2852-1

25. Chi X, Yan R, Zhang J, Zhang G, Zhang Y, Hao M, et al. A neutralizing human antibody binds to the n-terminal domain of the spike protein of SARS-CoV-2. *Science* (2020) 369(6504):650–5. doi: 10.1126/science.abc6952

26. Greaney AJ, Starr TN, Gilchuk P, Zost SJ, Binshtein E, Loes AN, et al. Complete mapping of mutations to the SARS-CoV-2 spike receptor-binding domain that escape antibody recognition. *Cell Host Microbe* (2021) 29(1):44–57.e9. doi: 10.1016/j.chom.2020.11.007

27. Piccoli L, Park YJ, Tortorici MA, Czudnochowski N, Walls AC, Beltramello M, et al. Mapping neutralizing and immunodominant sites on the SARS-CoV-2 spike receptor-binding domain by structure-guided high-resolution serology. *Cell* (2020) 183 (4):1024–42.e21. doi: 10.1016/j.cell.2020.09.037

28. Li T, Pantazes RJ, Maranas CD. OptMAVEn–a new framework for the *de novo* design of antibody variable region models targeting specific antigen epitopes. *PloS One* (2014) 9(8):e105954. doi: 10.1371/journal.pone.0105954

29. Karanicolas J, Corn JE, Chen I, Joachimiak LA, Dym O, Peck SH, et al. A *de novo* protein binding pair by computational design and directed evolution. *Mol Cell* (2011) 42(2):250–60. doi: 10.1016/j.molcel.2011.03.010

30. Cannon DA, Shan L, Du Q, Shirinian L, Rickert KW, Rosenthal KL, et al. Experimentally guided computational antibody affinity maturation with *de novo* docking, modelling and rational design. *PloS Comput Biol* (2019) 15(5):e1006980. doi: 10.1371/journal.pcbi.1006980

31. Jeong BS, Cha JS, Hwang I, Kim U, Adolf-Bryfogle J, Coventry B, et al. Computational design of a neutralizing antibody with picomolar binding affinity for all concerning SARS-CoV-2 variants. *MAbs* (2022) 14(1):2021601. doi: 10.1080/19420862.2021.2021601

32. Abraham MJ, Murtola T, Schulz R, Páll Szilárd, Smith JC, Hess B, et al. GROMACS: High performance molecular simulations through multi-level parallelism from laptops to supercomputers. *SoftwareX* (2015) 1(2):19–25. doi: 10.1016/j.softx.2015.06.001

33. Huang J, Rauscher S, Nawrocki G, Ran T, Feig M, de Groot BL, et al. CHARMM36m: an improved force field for folded and intrinsically disordered proteins. *Nat Methods* (2017) 14(1):71–3. doi: 10.1038/nmeth.4067

34. Chothia C, Lesk AM. Canonical structures for the hypervariable regions of immunoglobulins. *J Mol Biol* (1987) 196(4):901–17. doi: 10.1016/0022-2836(87)90412-8

35. Murzin AG, Brenner SE, Hubbard T, Chothia C. SCOP: a structural classification of proteins database for the investigation of sequences and structures. *J Mol Biol* (1995) 247(4):536–40. doi: 10.1016/S0022-2836(05)80134-2

36. Allen MP, Frenkel D. Observation of dynamical precursors of the isotropic-nematic transition by computer simulation. *Phys Rev Lett* (1987) 58(17):1748–50. doi: 10.1103/PhysRevLett.58.1748

37. Krissinel E, Henrick K. Inference of macromolecular assemblies from crystalline state. *J Mol Biol* (2007) 372(3):774–97. doi: 10.1016/j.jmb.2007.05.022

38. Kruger DM, Gohlke H. DrugScorePPI webserver: fast and accurate in silico alanine scanning for scoring protein-protein interactions. *Nucleic Acids Res* (2010) 38 (Web Server issue):W480–6. doi: 10.1093/nar/gkq471

39. Shah M, Anwar MA, Park S, Jafri SS, Choi S. In silico mechanistic analysis of IRF3 inactivation and high-risk HPV E6 species-dependent drug response. *Sci Rep* (2015) 5:13446. doi: 10.1038/srep13446

40. Bussi G, Donadio D, Parrinello M. Canonical sampling through velocity rescaling. *J Chem Phys* (2007) 126(1):014101. doi: 10.1063/1.2408420

41. Wang H, Dommert F, Holm C. Optimizing working parameters of the smooth particle mesh ewald algorithm in terms of accuracy and efficiency. *J Chem Phys* (2010) 133(3):034117. doi: 10.1063/1.3446812

42. Feng T, Chen F, Kang Y, Sun H, Liu H, Li D, et al. HawkRank: a new scoring function for protein-protein docking based on weighted energy terms. *J Cheminform* (2017) 9(1):66. doi: 10.1186/s13321-017-0254-7

43. Kumari R, Kumar ROpen Source Drug Discovery C, , Lynn A. G_mmpbsa–a GROMACS tool for high-throughput MM-PBSA calculations. *J Chem Inf Model* (2014) 54(7):1951–62. doi: 10.1021/ci500020m

44. Shah M, Ahmad B, Choi S, Woo HG. Mutations in the SARS-CoV-2 spike RBD are responsible for stronger ACE2 binding and poor anti-SARS-CoV mAbs cross-neutralization. *Comput Struct Biotechnol J* (2020) 18:3402–14. doi: 10.1016/j.csbj.2020.11.002

frontiers | Frontiers in Immunology

TYPE Methods
PUBLISHED 06 April 2023
DOI 10.3389/fimmu.2023.1127896

Check for updates

OPEN ACCESS

EDITED BY
Nargis Khan,
University of Calgary, Canada

REVIEWED BY
Seong-Eun Kim,
Pohang University of Science and Technology, Republic of Korea
Kim Klonowski,
University of Georgia, United States

*CORRESPONDENCE
Riccardo Dolcetti
Riccardo.Dolcetti@petermac.org

†These authors have contributed equally to this work and share first authorship

‡These authors have contributed equally to this work and share senior authorship

SPECIALTY SECTION
This article was submitted to Vaccines and Molecular Therapeutics, a section of the journal Frontiers in Immunology

RECEIVED 20 December 2022
ACCEPTED 23 March 2023
PUBLISHED 06 April 2023

CITATION
Moi D, Zeng B, Minnie SA, Bhatt R, Wood J, Sester DP, Mazzieri R and Dolcetti R (2023) Multiparametric flow cytometry to characterize vaccine-induced polyfunctional T cell responses and T cell/NK cell exhaustion and memory phenotypes in mouse immuno-oncology models. *Front. Immunol.* 14:1127896. doi: 10.3389/fimmu.2023.1127896

COPYRIGHT
© 2023 Moi, Zeng, Minnie, Bhatt, Wood, Sester, Mazzieri and Dolcetti. This is an open-access article distributed under the terms of the Creative Commons Attribution License (CC BY). The use, distribution or reproduction in other forums is permitted, provided the original author(s) and the copyright owner(s) are credited and that the original publication in this journal is cited, in accordance with accepted academic practice. No use, distribution or reproduction is permitted which does not comply with these terms.

Multiparametric flow cytometry to characterize vaccine-induced polyfunctional T cell responses and T cell/NK cell exhaustion and memory phenotypes in mouse immuno-oncology models

Davide Moi[1,2†], Bijun Zeng[1,2†], Simone A. Minnie[1,3†], Rituparna Bhatt[1], Jack Wood[1], David P. Sester[4], Roberta Mazzieri[1,2,5‡] and Riccardo Dolcetti[1,2,5,6*‡]

[1]The University of Queensland Frazer Institute, Woolloongabba, QLD, Australia, [2]Peter MacCallum Cancer Centre, Melbourne, VIC, Australia, [3]Clinical Research Division, Fred Hutchinson Cancer Research Center, Seattle, WA, United States, [4]TRI Flow Cytometry Suite, Translational Research Institute, Woolloongabba, QLD, Australia, [5]Sir Peter MacCallum Department of Oncology, The University of Melbourne, Melbourne, VIC, Australia, [6]Department of Microbiology and Immunology, The University of Melbourne, Melbourne, VIC, Australia

Suitable methods to assess *in vivo* immunogenicity and therapeutic efficacy of cancer vaccines in preclinical cancer models are critical to overcome current limitations of cancer vaccines and enhance the clinical applicability of this promising immunotherapeutic strategy. In particular, availability of methods allowing the characterization of T cell responses to endogenous tumor antigens is required to assess vaccine potency and improve the antigen formulation. Moreover, multiparametric assays to deeply characterize tumor-induced and therapy-induced immune modulation are relevant to design mechanism-based combination immunotherapies. Here we describe a versatile multiparametric flow cytometry method to assess the polyfunctionality of tumor antigen-specific $CD4^+$ and $CD8^+$ T cell responses based on their production of multiple cytokines after short-term *ex vivo* restimulation with relevant tumor epitopes of the most common mouse strains. We also report the development and application of two 21-color flow cytometry panels allowing a comprehensive characterization of T cell and natural killer cell exhaustion and memory phenotypes in mice with a particular focus on preclinical cancer models.

KEYWORDS

immunomonitoring, polyfunctional T cell assay, multiparametric flow cytometry, cancer vaccines, mouse cancer models, cancer immunotherapy, immune checkpoints

1 Introduction

Despite significant technological advances obtained in the last decade, only a very limited number of cancer vaccines progressed to phase III clinical trials (1). A thorough and in-depth characterization of feasibility, immunogenicity and therapeutic efficacy of cancer vaccines in suitable preclinical models remains critical to overcome current limitations and enhance the clinical applicability of this promising immunotherapeutic strategy. In particular, assays allowing a reliable characterization of T cell responses to endogenous tumor antigens in mouse models is required to assess vaccine potency and improve the antigen formulation. Moreover, multiparametric assays are required to comprehensively characterize the immune modulation and regulatory/immunosuppressive effects generated by the tumor itself or induced by the therapy to design mechanism-based combination immunotherapies.

Therapeutically effective cancer vaccines should generate strong tumor-specific immune responses that need to be evaluated by measuring adequate parameters to assess vaccine potency. In this respect, the mere enumeration of T cells recognizing the antigens targeted by the vaccine is not sufficient and should be implemented by a more appropriate qualitative characterization of the functional properties of vaccine-induced $CD4^+$ and $CD8^+$ T lymphocytes (2, 3). Therefore, assays able to assess the polyfunctionality of antigen-specific T cells are particularly relevant to optimize the antigen formulation of cancer vaccines and assess the strength and quality of the T cell responses induced *in vivo* in naïve or tumor bearing mice. Here we describe a versatile multiparametric flow cytometry method to assess the polyfunctionality of tumor antigen-specific $CD4^+$ and $CD8^+$ T cell responses based on their production of multiple cytokines after short-term *ex vivo* restimulation with relevant mouse tumor epitopes. The method can be useful to characterize the quality of T cell responses induced not only by the antigens targeted by the vaccine, but also by "universal" tumor associated antigens as a measure of therapy-induced epitope spreading.

The generation of strong tumor-specific T cell responses by cancer vaccines is often not sufficient to achieve satisfactory therapeutic responses. Indeed, the efficacy of cancer vaccines and other immunotherapies is hampered by systemic and local immune suppression, which subvert anti-tumor immune responses leading to dysfunctional and exhausted immune cells. T and NK cell function is dependent on the balance between activation/co-stimulation and the consequent upregulation of inhibitory signals triggered by numerous inhibitory immune checkpoint pathways (4). This complex landscape of regulatory molecules evolves dynamically over time and may be also heavily modulated by treatment, particularly immunotherapies. As such, profiling the expression of these regulatory molecules has become a major focus to inform therapeutic choices and identify novel therapeutic targets. Moreover, the assessment of preclinical tumor microenvironments and associated lymphoid organs (spleens and lymph nodes) for changes in expression of regulatory molecules is also required to identify possible evasion mechanisms and facilitate the rationale design of more effective combination therapies (5). Finally, the strength and duration of therapeutic responses induced by immunotherapy are closely dependent on the induction of strong and long-lasting memory immune responses (6). To be able to evaluate local and systemic immune modulation, we have developed two 21-color flow cytometry panels to comprehensively characterize T cell and natural killer (NK) cell exhaustion and memory phenotypes in mice with a particular focus on preclinical cancer models.

Abbreviations: CTRL, Control; NK, Natural killer; NKT, natural killer T; FSC, Forward scatter; MPECs, Memory precursor cells; SLECs, Short lived effector cells; SSC, Side scatter; TAAs, Tumor associated antigens; T_{CM}, Central memory T cells; T_{conv}, Conventional $CD4^+$ T cells; $T_{EFF/EM}$, Effector/effector memory T cells; TILs, Tumor infiltrating lymphocytes; T_N, Naïve T cells; TNEs, Tailored NanoEmusions; T_{PEX}, Precursors of exhausted T cells; T_{regs}, regulatory T cells.

2 Methods

2.1 Cell lines and tissue cultures

Murine triple negative breast cancer 4T1.2 cells were kindly provided by Prof. B. Parker (Peter MacCallum Cancer Centre, Melbourne, Australia). Murine melanoma B16F10 cells were kindly provided by Prof. N. Haas, University of Queensland). Murine melanoma YUMM UV 1.7 UV cells (7) (generated by UV irradiating YUMM 1.7 cells) were kindly provided by Prof. B. Gabrielli (Mater Research, University of Queensland). Cells were grown at 37°C and 5% CO_2 and passed using TrypLE Express when reaching 80% confluence. 4T1.2 and B16F10 cells were cultured in DMEM (Gibco) containing 10% FBS (Gibco), 2mM L-Glutamine (Gibco), 100IU/ml Penicillin (Gibco), 100µg/ml Streptomycin (Gibco) and 1mM Sodium Pyruvate (Gibco). YUMM UV 1.7 UV cells were cultured in DMEM/F12 (Gibco) containing 10% FBS (Gibco), 2mM L-Glutamine (Gibco), 100IU/ml Penicillin (Gibco), 100µg/ml Streptomycin (Gibco) and 1mM Sodium Pyruvate (Gibco).

2.2 Vaccine preparation

Tumor cell lysate preparation. Eighty percent confluent tumor cells from six T75 culture flasks were harvested, washed 3 times with PBS and resuspended in 0.5 mL sterile water and then subjected to 5 cycles of freeze and thaw in liquid nitrogen. Lysates were centrifuged at 10,000 rpm for 20 min at 4°C and the recovered supernatant quantified for protein concentration using a NanoDropTM 2000 spectrophotometer and diluted to 5 mg/mL in water. Aliquots of 200 µL of lysates were converted to powder by snap-freezing in liquid nitrogen followed by overnight lyophilization (0.05 mbar, -80°C) and stored at -80°C. Lysate powder was dissolved in 1 mL ultrapure water to a final protein concentration of 1mg/mL. The tumor cell lysate solution (0.4 mL)

was added to 0.8 mL of CithrolTM GMO HP solution into a 1.5 mL vial and mixed with a sonicator (Branson Sonifier® S-450A, Danbury, United State) for 1 min at 20 W to form stable water in oil (w/o) emulsion. CithrolTM GMO HP solution (1%, w/v) was prepared by dissolving CithrolTM GMO HP (gift from Croda Europe Ltd) in Hexane (Sigma). The resulting emulsion was frozen in dry ice for 2 h before being lyophilized for 24 h. The lyophilized lysate-Cithrol GMO HP pellet was dissolved in Miglyol 812 (10 µL; (gift from Cremer Oleo GmbH & Co. KG) to 5mg/ml and used as oil phase for preparing Clec9A-targeting Tailored NanoEmusions (TNE) loaded with tumor cell lysate as antigen formulation (Lysate-Clec9A-TNE) as described in Zeng et al. (8) and below.

Preparation of Clec9A-targeting Tailored NanoEmusions (TNE) loaded with tumor cell lysate. 490 µL of AM1 (400 µM; GL Biochem, China) was added to 10 µL of lysate loaded Miglyol 812 to give an oil volume fraction of 2% (v/v). The mixture was homogenized using a Branson Sonifier 450A ultrasonicator for four 45 s bursts at 60 W. The resulting oil-in-water (O/W) emulsion was coated with PEG (200 µM; Nanocs, US) and the mouse Clec9A targeting WH peptide fused to anchor peptide DAMP4 (3 µM) by gentle mixing for 60 min at room temperature. Clec9A-TNEs loaded with B16F10 immunogenic neoepitopes were prepared as described (8).

2.3 Mouse studies

All animal experiments were approved by the University of Queensland Animal Ethics Committee (approval number UQDI/252/16). Mice were obtained from the Animal Resources Centre (Perth, WA, Australia).

Murine triple negative breast cancer model. Eight to ten-week-old female Balb/c mice were injected with 0.5×10^6 4T1.2 cells (50 µl) orthotopically in the 3rd shaved mammary fat pad. Three days after tumor injection, mice were injected i.v. with 100 µL Clec9a-TNE loaded with the 4T1.2 lysate (Clec9A-TNE-lysate). At the indicated times tumors and/or draining lymph nodes were collected and processed as described below.

Murine B16F10 melanoma model. Eight to ten-week-old female C57BL/6 mice were injected with 0.25×10^6 B16F10 cells (50 µl) subcutaneously in the shaved right back flank. Ten days after tumor injection, mice were injected i.v. with 100µL Clec9a-TNE loaded with a pool of functionally validated, immunogenic B16F10 neo-epitopes (25 µg) (8). Mice without treatment were included as controls (NT CTRL). Tumor growth was measured two to three times per week using calliper. Tumor volume was measured using an electronic caliper and calculated using the following formula: $(m1)^2$ X m2 X 0.5236 – where m1 stand for the small tumor diameter, and m2 for the long one. Spleens were collected at the indicated times for processing as described below.

Murine YUMM UV 1.7 melanoma model. Tumor-bearing mice were generated by injecting 2×10^6 melanoma cells (50µl) subcutaneously into C57BL/6 mice. Tumors, spleens and draining lymph nodes were collected at the indicated times for processing as described below.

The YUMM UV 1.7 and 4T1.2 mouse models were used to set up and optimize the two multiparametric flow cytometry panels. The 4T1.2 and B16F10 models were used for the polyfunctional assay on blood.

2.4 Polyfunctional T cell assay

Ex vivo restimulation with tumor specific peptides. Blood from tumour-bearing mice was collected into EDTA treated tubes and red blood cells were lysed by adding ACK (Ammonium-Chloride-Potassium) buffer after centrifugation and removal of supernatant and incubating for 5 min on ice. ACK buffer was prepared according to the Cold Spring Harbor Protocol: 150 mM NH4Cl, 10 mM KHCO3, 0.1 mM Na2EDTA. After washing with complete RPMI medium (Gibco), white blood cells were plated in complete RPMI medium (10% FBS, 2mM L-Glutamine, 100IU/ml Penicillin, 100µg/ml Streptomycin and 1mM Sodium Pyruvate) in round bottom 96-well plates at a density of 1×10^6 cells/well and ex vivo re-stimulated for 6 hours at 37°C with the antigens/epitopes listed in Table 1 (20 µg/mL in a total volume of 200 µL). Brefeldin A (Biolegend) was added after 1 hour to block cytokine release at a final concentration of 5 µg/ml.

Antibody staining for the detection of cytokine production. At the end of the re-stimulation the cells were washed with 200 µL PBS by discarding the supernatant after centrifugation for 5 minutes at 500 rcf at 4°C. Pellets were resuspended in 100 µL of FVS440UV (BD Biosciences) working solution (1:1000 in PBS) and incubated for 15 minutes at room temperature in the dark. Cells were washed twice with 200 µL of MACS buffer (2mM EDTA pH8.0, 0.5% BSA in PBS). After the last wash, the supernatant was tipped off and the pellets were resuspended in the 50 µL of residual supernatant that remained. Non-specific antibody binding was limited by adding 0.5 µL of anti-mouse CD16/32 (BioLegend) to samples for 10 minutes on ice. An antibody master mix (Table 2) was then added for 30 minutes on ice, in the dark and the cells were then washed twice with 100 µL of MACS buffer. Samples were fixed using the eBiosciences FoxP3 kit according to manufacturer's instructions. Samples were then left in 50 µL of the permeabilization buffer containing 0.5 µL of anti-mouse CD16/32 overnight at 4°C, protected from light. Incubation with intracellular antibodies was performed in a final volume of 100 µL of permeabilization buffer at room temperature, protected from light, for 1 hour. Samples were then washed with 100 µL of permeabilization buffer. After centrifugation for 5 minutes at 500 rcf at 4°C, samples were resuspended in 200 µL of MACS buffer for same-day acquisition on a BD FACSymphony A5 Cell Analyzer. Cytokine co-expression profiles were quantified using the Boolean function of Flowjo™ software. Figure S1 describes the manual gating strategy carried out on blood cells (related to Figure 1).

2.5 Staining Protocol for Multiparametric Flow Cytometry Panels 1 & 2

Tissue processing. Tissues were harvested immediately prior to processing. Spleens were manually dissociated and contaminating

TABLE 1 Tumor-specific epitope peptides for *ex vivo* restimulation of T cells.

Mouse model	Pool of peptides	Epitope	Sequence	Presenting MHC molecule	Reference
C57Bl/6 mice bearing B16F10 melanoma	neo-epitopes[a]	MUT20	FRRKAFLHWYTGEAMDEMEFTEAESNM	I-A^b, H-2D^b, H-2K^b	Zeng, (8)
		MUT25	STANYNTSHLNNDVWQIFENPVDWKEK		
		MUT30	PSKPSFQEFVDWENVSPELNSTDQPFL		
		MUT33	DSGSPFPAAVILRDALHMARGLKYLHQ		
		MUT36	CGTAFFINFIAIYHHASRAIPFGTMVA		
		MUT44	EFKHIKAFDRTFANNPGPMVVFATPGM		
	universal TAAs	mSurvivin$_{20-28}$	ATFKNWPFL	H-2D^b	Lladser, (9)
		mSurvivin$_{53-67}$	DLAQCFFCFKELEGW	I-A^b	Ciesielski, (10)
		mTERT$_{198-205}$	VGRNFTNL	H-2K^b	Mennuni, (11)
Balb/c mice bearing 4T1.2	autologous tumour cell lysate[a]	Cell lysate-derived epitopes	N/A	N/A	Dolcetti[b]
	universal TAAs	mSurvivin$_{85-93}$	AFLTVKKQM	H-2D^d	Siegel, (12)
		mSurvivin$_{53-67}$	DLAQCFFCFKELEGW	I-A^d, I-E^d	Results presented herein (Figure S2)
		mTERT1$_{67-175}$	AYQVCGSPL	H-2K^d	Mennuni, (11)

a Included in the vaccine formulation.
b Unpublished data.
TAAs: tumor associated antigens.

red blood cells were lysed with ACK buffer (150 mM NH4Cl, 10 mM KHCO3, 0.1 mM Na2EDTA). Peripheral lymph nodes and YUMM UV 1.7 tumors were manually dissociated. All samples were filtered with a 70 µM filter prior to processing for antibody staining. A viable cell count was performed, and 2 x 10^6 cells were aliquoted into 1.5 mL polystyrene FACS tubes. Cells were washed with 600 µL PBS by discarding the supernatant after centrifugation for 5 minutes at 500 rcf at 4°C.

Cell staining. Cell pellets were resuspended in 100 µL of FVS440UV working solution (1:100 in PBS) and incubated for 15 minutes at room temperature in the dark. Cells were washed twice with 600 µL of MACS buffer (2mM EDTA pH8.0, 0.5% BSA in PBS). After the last wash, the supernatant was tipped off and the pellets were resuspended in the 50 µL of residual supernatant that remained. Non-specific antibody binding was limited by adding 0.5 µL of anti-mouse CD16/32 (BioLegend) to samples for 10 minutes on ice. An antibody master mix (Table 3) containing 10 µL of Brilliant Stain Buffer Plus (BD Biosciences) in a volume 50 µL, was then added to samples in 50 µL of MACS buffer; to make a final staining volume of 100 µL. Samples were

TABLE 2 Flow cytometry antibodies used in the polyfunctional T cell assay.

	Specificity	Fluorochrome	Clone	Vendor	Dilution
Surface staining	CD3e	AF488	145-2C11	Biolegend	1/100
	CD8	APC/Cy7	53-6.7	Biolegend	1/100
	CD4	PE/Cy7	RM4-4	Biolegend	1/100
Intracellular staining	TNFα	AF647	MP6-XT22	Biolegend	1/100
	IFNγ	AF700	XMG1.2	Biolegend	1/100
	IL-2	PE	JES6-5H4	Biolegend	1/100

10.3389/fimmu.2023.1127896

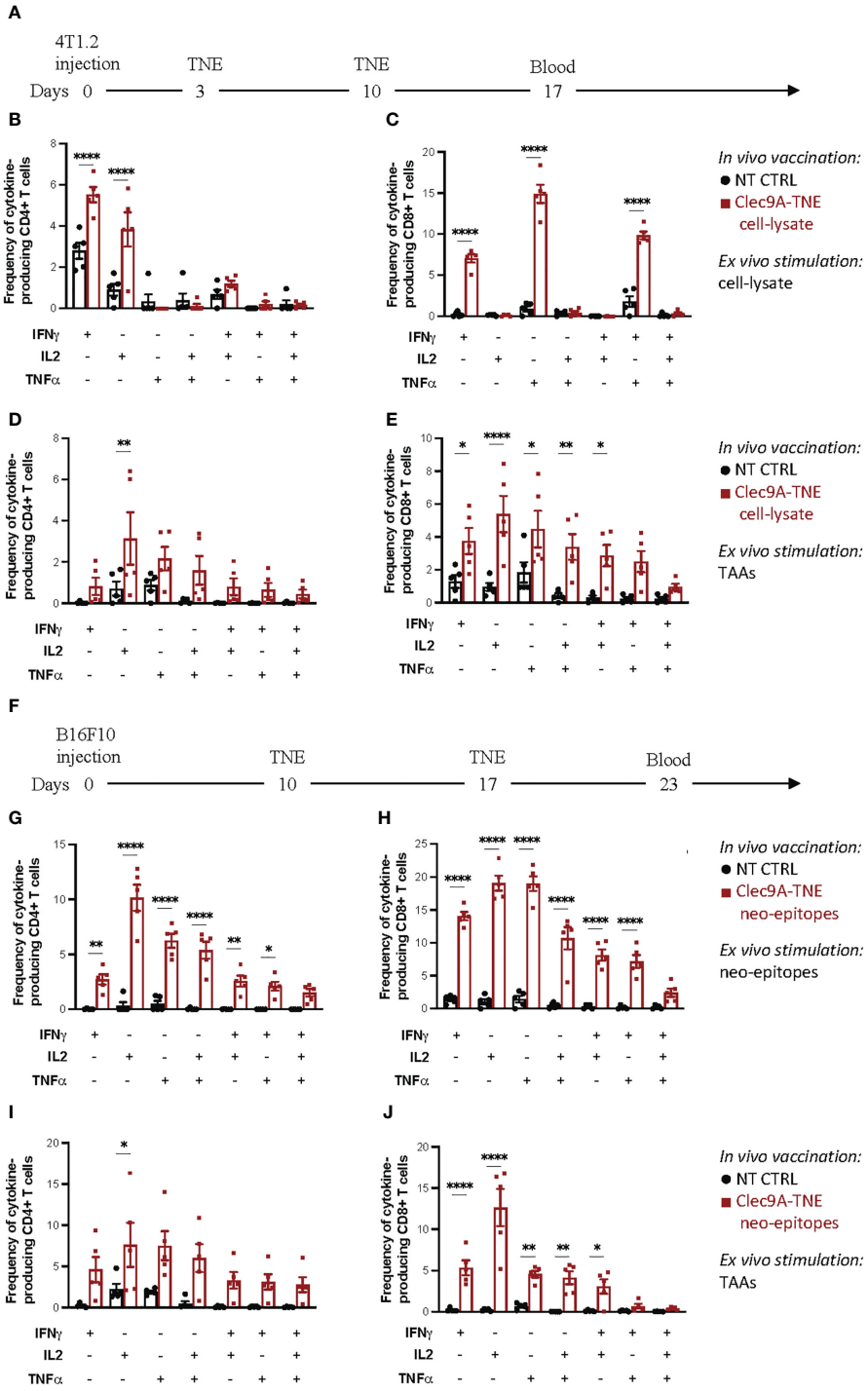

FIGURE 1
Polyfunctional assay on blood T cells. **(A)** Experimental scheme: Balb/c mice were orthotopically injected with $0.5x10^6$ 4T1.2 cells. Three and 10 days after tumor injection, mice were injected i.v. with Clec9a-TNE loaded with the 4T1.2 cell-lysate. On day 17 blood was collected and process as described in Methods. Cytokine production in $CD4^+$ and $CD8^+$ T cells was measured by flow cytometry and intracellular cytokine staining after *ex vivo* stimulation of blood samples with tumor lysate **(B, C)** or a pool of tumor associated antigen (TAA) for 6 h **(D, E)**. **(F)** Experimental scheme: C57BL/6 mice were subcutaneously injected with $0.25x10^6$ B16F10 cells. Ten and 17 days after tumor injection, mice were injected i.v. with Clec9a-TNE loaded with a pool of functionally validated, immunogenic B16F10 neo-epitopes. On day 23 blood was collected and process as described in Methods. Cytokine production in $CD4^+$ and $CD8^+$ T cells was measured by flow cytometry and intracellular cytokine staining after *ex vivo* stimulation of blood samples with B16F10 neo-epitopes **(G, H)** or a pool of tumor associated antigen (TAA) for 6 h **(I, J)**. Data are presented as mean values ± SEM. 0.1234 (ns), 0.0332 (*), (**) 0.0021, <0.0001 (****) (Two-Way ANOVA).

stained for 30 minutes, on ice, in the dark and then washed with 1 mL of MACS buffer. Samples were fixed using the eBiosciences FoxP3 kit according to manufacturer's instructions. Samples were then left in 100 µL of the permeabilization buffer overnight at 4°C, protected from light. Incubation with intracellular antibodies (Table 3) was performed at room temperature, protected from light, for 1 hour. Samples were then washed with 1 mL of permeabilization buffer. After centrifugation for 5 minutes at 500 rcf at 4°C, samples were resuspended in 200 µL of MACS for same-day acquisition on a BD FACSymphony A5 Cell Analyzer (Tables 4, 5).

3 Results and discussion

3.1 Assay to characterize polyfunctional T cell responses to mouse tumor antigens

Cancer vaccine-induced antigen-specific T cell responses can be functionally characterized by *ex vivo* restimulation of peripheral blood cells, splenocytes or isolated tumor infiltrating lymphocytes with the antigens targeted by the vaccine in the form of peptide epitopes or, less frequently, tumor cell lysates. The expression of IFNγ, TNFα and IL-2 by intracellular staining and flow cytometry

TABLE 3 List of antibodies and relative fluorochromes used in Panels 1 & 2 .

Panel	Specificity	Clone	Fluorochrome	Vendor	Titration	Purpose
Shared Back bone	CD45	30-F11	BUV563	BD – 565710	1/800	Lineage
	CD3	145-2C11	BUV737	BD – 564618	1/200	Lineage
	CD4	GK1.5	BUV496	BD – 564667	1/400	Lineage
	CD8	5.3-6.7	BUV805	BD – 564920	1/400	Lineage
	FoxP3*	FJK-16s	PE-Cy5	eBio – 15-5773-82	1/200	Lineage
	CD49b	HMα2	BV786	BD – OptiBuild	1/400	Lineage
	Amine-reactive	N/A	FVS440UV	BD – 566332	1/1000	Viability
	CD44	IM7	APC-Cy7	BD – 560568	1/400	Effector/memory
	CD279 (PD-1)	J43	BUV395	BD - OptiBuild	1/100	Inhibition
	Granzyme B*	QA16A02	PE-Dazzle594	BL – 372216	1/400	Activation
	CD69	H1.2F3	BV480	BD – OptiBuild	1/100	Activation
Markers specific for Panel 1	CD226 (DNAM-1)	TX42.1	BV650	BL – 133621	1/200	Activation
	CD314 (NKG2D)	CX5	BV711	BD – 563694	1/200	Activation
	CD152 (CTLA-4)	UC10-4F10-11	APC-R700	BD – 565778	1/200	Inhibition
	CD366 (TIM-3)	RMT3-23	FITC	eBio – 11-5870-82	1/400	Inhibition
	TIGIT	1G9	BV421	BD – 565270	1/200	Inhibition
	CD223 (LAG-3)	C9B7W	BV750	BD – OptiBuild	1/200	Inhibition
	VISTA	MIH64	PE	BD – 566270	1/200	Inhibition
	NKG2A/C/E	20d5	BV605	BD – 564382	1/200	Inhibition
	Eomes*	Dan11mag	PE-Cy7	eBio – 25-4875-82	1/200	Differentiation
	T-bet*	4B10	AF647	BL – 644804	1/400	Differentiation
Markers specific for Panel 2	CD62L	MEL-14	BB515	BD – 565261	1/400	Effector/memory
	CD103	2-E7	BV605	BL – 121433	1/100	Differentiation
	CD122	TM-β1	BB700	BD – *OptiBuild*	1/100	Differentiation
	CD127	SB/199	BV711	BD – 565490	1/100	Differentiation
	CD197 (CCR7)	4B12	BV650	BD – 564356	1/200	Differentiation
	CD25	PC61	APC-R700	BD – 565134	1/800	Differentiation
	Ki-67*	B56	PE	BD – 556027	1/400	Proliferation
	KLRG1	2F1	BV421	BD – 562897	1/200	Differentiation

(Continued)

TABLE 3 Continued

Panel	Specificity	Clone	Fluorochrome	Vendor	Titration	Purpose
	NKp46	29A1.4	PE-Cy7	BL – 137618	1/200	Differentiation
	TCF-1*	C63D9	AF647	CST – 6709S	1/200	Stemness

*Intracellular staining.
APC, Allophycocyanin; AF, Alexa Fluor; BUV, Brilliant Ultraviolet; BV, Brilliant Violet; PE, Phycoerythrin.

analysis can be used as read out where polyfunctionality of antigen-specific $CD4^+$ and $CD8^+$ T cell responses is given by the extent of stimulated T cells expressing more than one cytokine. Additional functional markers can be also investigated such as CD137, CD107, as well as cytolytic molecules (perforin and granzyme B). Tumor cell lysates can be used for restimulation when no suitable tumor antigen is available. Figure 1A-E shows the results of a polyfunctional T cell assay carried out on blood cells isolated from Balb/c mice carrying a 4T1.2 triple negative breast cancer and vaccinated with Clec9a-TNE loaded with the 4T1.2 cell-lysate.

TABLE 4 Instrument Configuration for Panel 1.

Laser			Optics		Channels		Markers
Wavelength	Power	Type	LP Filter	BP Filter	Name	Flourochrome	Panel 1
355 nm	60 mW	DPSS	None	379/28	UV_379/28	BUV395	CD279 (PD-1)
			410	450/50	UV_450/50	FVS440UV	FVS440UV
			450	515/30	UV_515/30	BUV496	CD4
			550	586/15	UV_586/15	BUV563	CD45
			600	610/20	UV_610/20	–	
			635	670/30	UV_670/30	–	
			690	740/35	UV_740/35	BUV737	CD3
			770	820/60	UV_820/60	BUV805	CD8
406 nm	250 mW	DPSS	410	450/50	V_450/50	BV421	TIGIT
			505	525/50	V_525/50	BV480	CD69
			550	586/15	V_586/15	–	
			600	610/20	V_610/20	BV605	NKG2A/C/E
			635	670/30	V_670/30	BV650	CD226 (DNAM-1)
			690	710/50	V_710/50	BV711	CD314 (NKG2D)
			710	740/35	V_740/35	BV750	CD223 (LAG-3)
			750	780/60	V_780/60	BV786	CD49b
488 nm	150 mW	DPSS	505	515/20	B_515/20	FITC	CD366 (TIM-3)
			600	610/20	B_610/20	–	
			635	670/30	B_670/30	–	
			690	710/50	B_710/50	–	
			750	780/60	B_780/60	–	
			None	488/10	SSC	SSC	
			None	488/10	FSC	FSC	
561 nm	150 mW	DPSS	None	586/15	YG_586/15	PE	VISTA

(Continued)

TABLE 4 Continued

Laser			Optics		Channels		Markers
Wavelength	Power	Type	LP Filter	BP Filter	Name	Flourochrome	Panel 1
			600	610/20	YG_610/20	PE-Dazzle594	Granzyme B
			635	670/30	YG_670/30	PE-Cy5	FoxP3
			690	710/50	YG_710/50	–	
			750	780/60	YG_780/60	PE-Cy7	omes
637 nm	140 mW	DPSS	None	670/30	R_670/30	AF647	T-bet
			690	710/50	R_710/50	APC-R700	CD152 (CTLA-4)
			750	780/60	R_780/60	APC-Cy7	CD44

APC, Allophycocyanin; AF, Alexa Fluor; BUV, Brilliant Ultraviolet; BV, Brilliant Violet; PE, Phycoerythrin.

TABLE 5 Instrument Configuration for Panel 2.

Laser			Optics		Channels		Markers
Wavelength	Power	Type	LP Filter	BP Filter	Name	Fluorchrome	Panel 2
355 nm	60 mW	DPSS	None	379/28	*UV_379/28*	BUV395	CD279 (PD-1)
			410	450/50	*UV_450/50*	FVS440UV	FVS440UV
			450	515/30	*UV_515/30*	BUV496	CD4
			550	586/15	*UV_586/15*	BUV563	CD45
			600	610/20	*UV_610/20*	–	
			635	670/30	*UV_670/30*	–	
			690	740/35	*UV_740/35*	BUV737	CD3
			770	820/60	*UV_820/60*	BUV805	CD8
406 nm	250 mW	DPSS	410	450/50	*V_450/50*	BV421	KLRG1
			505	525/50	*V_525/50*	BV480	CD69
			550	586/15	*V_586/15*	–	
			600	610/20	*V_610/20*	BV605	CD103
			635	670/30	*V_670/30*	BV650	CD197
			690	710/50	*V_710/50*	BV711	CD197 (CCR7)
			710	740/35	*V_740/35*	–	
			750	780/60	*V_780/60*	BV786	CD49b
488 nm	150 mW	DPSS	505	515/20	*B_515/20*	BB515	CD62L
			600	610/20	*B_610/20*	–	
			635	670/30	*B_670/30*	–	
			690	710/50	*B_710/50*	BB700	CD122
			750	780/60	*B_780/60*	–	
			None	488/10	*SSC*	SSC	
			None	488/10	*FSC*	FSC	
561 nm	150 mW	DPSS	None	586/15	*YG_586/15*	PE	Ki67
			600	610/20	*YG_610/20*	PE-Dazzle594	Granzyme B

(Continued)

TABLE 5 Continued

Laser			Optics		Channels		Markers
			635	670/30	*YG_670/30*	PE-Cy5	FoxP3
			690	710/50	*YG_710/50*	–	
			750	780/60	*YG_780/60*	PE-Cy7	NKp46
637 nm	140 mW	DPSS	None	670/30	*R_670/30*	AF647	TCF-1
			690	710/50	*R_710/50*	APC-R700	CD25
			750	780/60	*R_780/60*	APC-Cy7	CD44

Blood cells from controls and vaccinated mice were *ex vivo* restimulated with the tumor cell lysate used for the vaccination (Table 1). As presented in Figure 1C, vaccinated mice showed significantly higher percentages of $CD8^+$ T cells expressing IFNγ, TNFα or both cytokines as evidence of polyfunctionality when compared with control mice. In vaccinated mice, the assay also revealed higher percentages of $CD4^+$ T cells expressing IFNγ or IL-2 as single cytokines, whereas only a slight increase in $CD4^+$ T cells expressing both cytokines was observed (Figure 1B). This data indicate that the lysate included in the vaccine generated only partial tumor-specific polyfunctional T cell responses, mainly involving $CD8^+$ T cells. These results are consistent with the limited immunogenicity of tumor cell lysates, which need to be *ex vivo* manipulated to enhance their therapeutic efficacy (1).

The recent advances in genomics, trancriptomics and tumor epitope prediction allowed the use of neo-antigen epitopes identified in individual tumors to track and characterize neo-antigen specific T cell responses in cancer patients treated with personalized vaccines (1, 13, 14). Tumor neo-epitopes may be also available for some preclinical cancer models (14), allowing thus a more precise assessment of the quality of tumour-specific T cell responses induced in these models by a variety of experimental immunotherapeutic strategies. Figures 1G, H shows the results of polyfunctional responses of $CD4^+$ and $CD8^+$ T cells restimulated with the highly immunogenic B16F10 neo-epitopes (8) used to vaccinate tumor-bearing C57BL/6 mice (Figure 1F).

Although feasible (Figures 1B, C), the characterization of tumor-specific polyfunctional T cell responses in mice vaccinated with tumor cell lysates is hampered by the lack of knowledge of the immunogenic (neo-)antigens targeted by the vaccine. Although re-stimulation of T cells with the whole tumor cell lysate can be an option, this approach suffers from variability among cell lysate batches that may lead to inconsistent results. To obviate these limitations, we exploited epitopes of the "universal" TAAs telomerase and survivin, for which CD4 and CD8 immunogenic epitopes are available for both Balb/c and C57BL/6 mouse strains (Table 1). To complete the panel of suitable "universal" TAAs applicable in the most common preclinical models, we have validated the immunogenicity of the $mSurvivin_{53-67}$ epitope so far applied in C57BL/6 cancer models also in the Balb/c mouse strain (Figure S2). Figures 1D, E reports the results of a polyfunctional T cell assay carried out on blood cells isolated from 4T1.2-bearing Balb/c mice vaccinated with an autologous tumour cell lysate, and *ex vivo* re-stimulated with telomerase and survivin epitopes. Higher percentages of $CD4^+$ T cells expressing IL-2 and $CD8^+$ T cells expressing IFNγ, IL-2, TNFα or the IFNγ/IL-2, and TNFα/IL-2 combinations (polyfunctionality) were observed in immunized mice. These epitopes can be also useful to identify and characterize epitope spreading in both C57BL/6 and Balb/c mice vaccinated with different antigenic formulations or treated with other immunotherapeutic strategies. As representative example of this application, Figures 1I, J reports the $CD4^+$ and $CD8^+$ T cell responses specific for telomerase and survivin detected in C57BL/6 mice bearing B16F10 melanoma and vaccinated with autologous tumor neo-epitopes.

3.2 Integrated multiparametric flow cytometry assays to immune profile mouse T and NK cells.

Two flow cytometry panels were designed to simultaneously allow the comprehensive characterization of NK and T cell exhaustion, activation, functionality, transcription factor profile, memory and differentiation states. When used in combination, these panels can provide a comprehensive overview of the functional status of T and NK cells in the tumor microenvironment and peripheral lymphoid organs in mice. Moreover, the two panels can also be used separately for focused investigation of activation/exhaustion (Panel 1) or memory phenotypes (Panel 2) in a variety of disease settings. The panels share a set of common hematopoietic and lineage markers as backbone (Table 3). In both panels, CD45 was included to identify hematopoietic cells in complex tissues, and this can be adapted to track transferred T cells based on their allotype (CD45.1/CD45.2) in adoptive cell transfer studies. Briefly, in both panels, CD45 and a live/dead marker are used to first gate live hematopoietic cells. FSC and SSC are then used to gate lymphocytes followed by doublet discrimination. Major T cell subsets are identified using CD3, CD4, CD8 and FoxP3, whereas NK cells are identified with CD49b (Figure 2 & Figure S3). The results presented were obtained in the YUMM 1.7

UV mouse melanoma model, which closely recapitulates the main genetic and immunologic features of human cutaneous melanoma (7).

3.3 Panel 1: Activation and exhaustion phenotypes

In addition to the backbone lineage markers, to address activation vs. exhaustion in T and NK cells, the evaluation of the transcription factors Eomesodermin (Eomes) and T-bet was incorporated in Panel 1 given their role in T and NK cell differentiation, activation and exhaustion (15–17) (Figure 2A). To specifically assess activation, antigen experience, and cytolytic activity, CD44, CD69, NKG2D, DNAM-1 and Granzyme-B were included in Panel 1 (Figures 3A, B & Figure S4). Finally, a suite of inhibitory immune checkpoints (TIGIT, VISTA, TIM-3, CTLA-4, NKG2A, PD-1, LAG-3) were added to evaluate the exhaustion state of the different subpopulations during tumor progression and following treatments (Figures 3C, E & Figure S4)

3.3.1 NK cells

Within NK cells (Figure 2A, blue frame), the inhibitory receptors NKG2A, TIM-3, PD-1, LAG-3 and TIGIT together with the activating receptor NKG2D and DNAM-1 can be used to evaluate the effector function of $CD3^{-}CD49b^{+}$ NK cells. The balance between activating and inhibitory receptors determines whether NK cells will have cytolytic functions or contribute to a tolerogenic microenvironment (18). To investigate whether impaired effector functions are associated with reduced activation or cytolytic activity, the early activation and immune modulator CD69, as well as the cytolytic molecule Granzyme-B, can be assessed. The dysfunctional and exhausted phenotype of tumor-associated NK cells can additionally be investigated by analyzing the expression of Eomes and T-bet, T-box transcription factors that drive the differentiation and function of cytotoxic lymphocytes and NK cells (15). In the context of tumor progression, upon adoptive transfer to tumor-bearing mice, NK cells were shown to display a progressive decrease in the expression of both transcription factors and this correlated with a rapid loss of effector function including the ability to control metastasis development (19).

3.3.2 $CD4^{+}$ T cells

Within $CD4^{+}$ T cells, the two main regulatory T cell subsets, Tregs (Figure 2A, green frame) and type 1 regulatory T cells (TR1), can be identified based on FoxP3 and Eomes expression, respectively (19, 20) and distinguished from conventional $CD4^{+}$ T cells (Figure 2A, red frame). CD44, a marker commonly used to assess activation in T cells, can also be employed to identify antigen-experienced T cells. CD44 expression is rapidly up-regulated after antigen encounter and is maintained in memory T cells. T-bet and Eomes were included to report on their expression profile in various $CD4^{+}$ T-helper subsets. Eomes plays an important role in cytotoxic T lymphocytes where it promotes their development and survival *via* upregulation of CD122 (the β-chain of the IL-15 receptor) and represses Th17-type cytokine expression (15). Expression of T-bet and Eomes is induced upon activation and differentiation. Moreover, T-bet promotes Th1 cell differentiation and prevents the development of Th2 and Th17 helper cells. Recent studies have reported that both circulating and tumour-infiltrating Th1-like $CD4^{+}$ T cells expressing T-bet display strong anti-tumour cytotoxic activities (21) (Figure 2A, red frame). However, TGFß-mediated conversion of anti-tumor $T\text{-}bet^{+}$Th1 $CD4^{+}$ T cells into immunosuppressive $T\text{-}bet^{+}Foxp3^{+}$ Tregs was recently described in mice bearing lung carcinoma (22). TIGIT, a co-inhibitory receptor, is highly expressed on Tregs that specifically inhibits Th1 and Th17 responses (23–25), also known as induced T_{regs} (iT_{regs}: $Tbet^{+}TIGIT^{+}$, Figure 2A, green frame).

3.3.3 $CD8^{+}$ T cells

CD44, CD69 and Granzyme-B were included as classical markers to evaluate activation and cytolytic activity of CD8+ T cells (Figure 2A, frame orange), with DNAM-1 and NKG2D included to provide further information on the activation status of the $CD8^{+}$ T cell compartment. Additionally, NKG2D can work as a co-stimulatory molecule in antigen-experienced T cells (26). DNAM-1 acts as a co-stimulatory factor in $CD8^{+}$ cytotoxic T lymphocytes and is down-regulated in dysfunctional tumor-infiltrating $CD8^{+}$ T cells (27, 28). The two transcription factors T-bet and Eomes were used to further evaluate the differentiation status of $CD8^{+}$ T cells. Indeed, high T-bet expression has been associated with an effector phenotype, and high expression of Eomes with a memory phenotype (29, 30). Finally, various immune checkpoints (TIGIT, VISTA, TIM-3, CTLA-4, NKG2A, PD-1, LAG-3) were included to delineate activation vs. exhaustion, and to aid in the identification of dysfunctional $CD8^{+}$ T cells in the tumor microenvironment. Of note, the co-expression of immune checkpoints with DNAM-1 on $CD8^{+}$ T cells, particularly in hematological malignancies, is indicative of activation rather than exhaustion (28, 30). DNAM-1 and TIGIT share the same ligands (CD155 and CD112), however, they have opposing functions (activation vs. suppression, respectively) in tumor infiltrating $CD8^{+}$ T cells (27).

3.3.4 T cell exhaustion signatures

T cell exhaustion signatures may vary between different tumor types. However, they are almost invariably associated with co-expression of several classical immune checkpoint molecules such as PD-1, CTLA-4, TIM-3, LAG-3 and TIGIT. Indeed, high PD-1 expression levels on effector memory T cells can signal either activation or exhaustion depending on the level and repertoire of additional checkpoint molecules expressed (31). It is the progressive upregulation of these additional inhibitors, and loss of co-stimulatory molecules, that determines the hierarchical loss of

10.3389/fimmu.2023.1127896

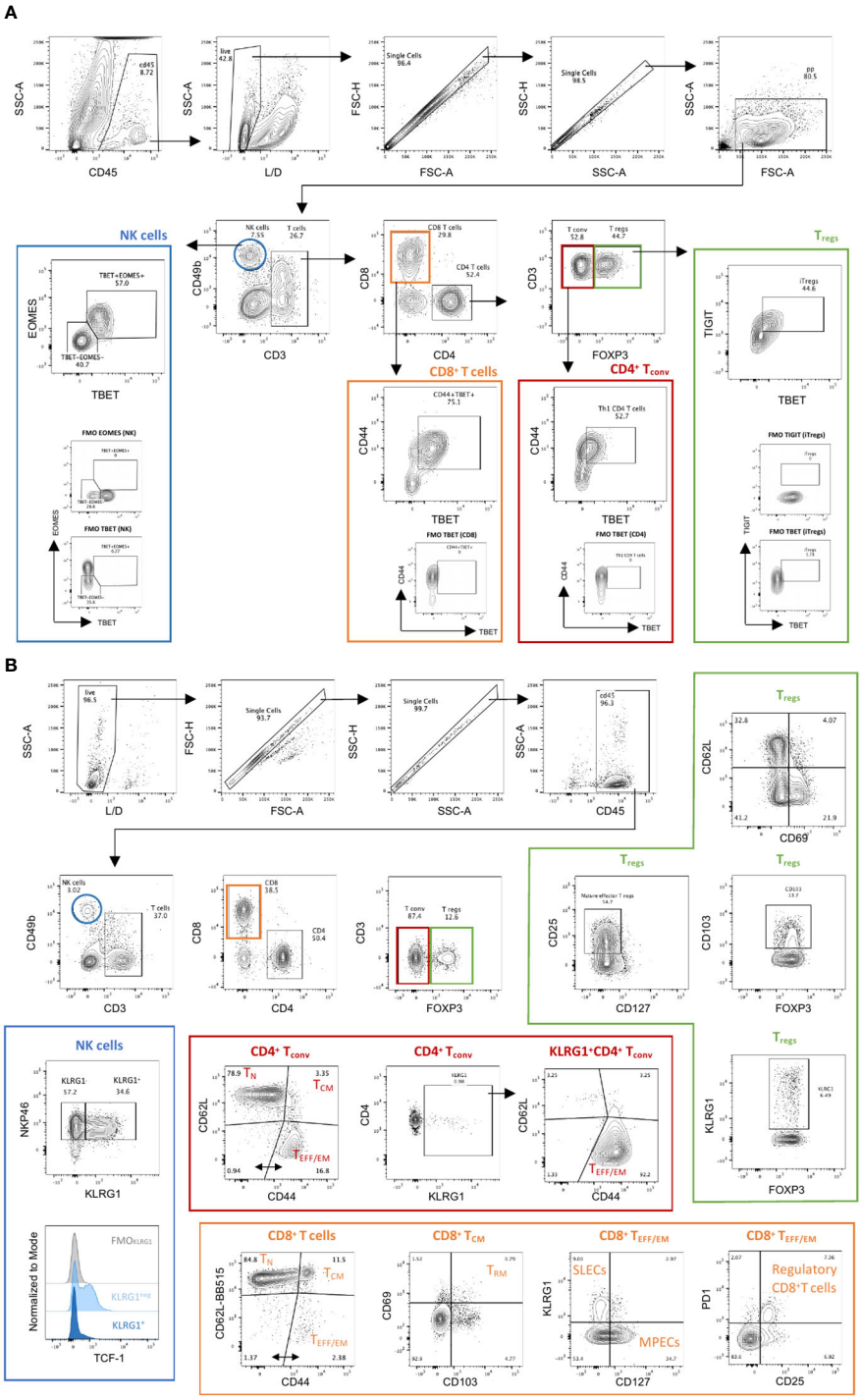

FIGURE 2
Manual gating strategy in Panels 1 & 2. **(A)** Panel 1. Tumor infiltrating immune cells from YUMM UV 1.7 tumors were identified through exclusion of non-viable and CD45$^-$ cells, followed by use of physical parameters to distinguish lymphocytes and exclude doublets. Main immune cell subsets were defined as follows: natural killer cells (blue; NK; CD3$^-$CD49b$^+$); conventional CD4$^+$ T cells (red; CD4$^+$ Tconv; CD3$^+$CD4$^+$FoxP3$^-$); regulatory CD4$^+$ T cells (green; Treg; CD3$^+$CD4$^+$FoxP3$^+$) and CD8$^+$ T cells (orange, CD3$^+$CD8$^+$). Examples of additional subpopulations are also indicated as follow: differentiated and cytotoxic NK cells (T-bet$^+$Eomes$^+$); Th1 CD4$^+$ T cells (CD4$^+$CD44$^+$T-bet$^+$); induced Tregs (iTregs: CD4$^+$FoxP3$^+$T-bet$^+$TIGIT$^+$); Effector CD8$^+$ T cells (CD8$^+$CD44$^+$T-bet$^+$). Fluorescent minus one (FMOs) for Eomes, T-bet and TIGIT are also shown. **(B)** Panel 2. Spleens isolated from C57Bl/6 mice bearing YUMM UV 1.7 melanomas were processed as described in methods. Immune cells were identified through exclusion of non-viable and CD45$^-$ cells; followed by use of physical parameters to distinguish lymphocytes and exclude doublets. Main immune cell subsets were defined as in (**A**). Examples of additional subpopulations are also indicated as follow: mature and differentiated NK cells (NKp46$^+$KLRG1$^+$); Naïve (T_N: CD62L$^+$CD44$^-$), central memory (T_{CM}: D62L$^+$CD44$^+$) or effector/effector memory ($T_{EFF/EM}$: CD62L$^-$CD44$^+$) CD4$^+$ and CD8$^+$ T cells; Cytotoxic CD4$^+$ T cells (CD4$^+$FOXP3$^-$KLRG1$^+$); Tissue resident memory CD8$^+$ T cells (T_{RM}: CD69$^+$CD103$^+$CD8$^+$ T_{CM}); short lived effector cells (SLECs: KLRG1$^+$CD127$^-$ CD8$^+$ $T_{EEF/EM}$) and memory precursor cells (MPECs: KLRG1$^-$CD127$^+$ CD8$^+$ $T_{EEF/EM}$); regulatory CD8 T cells (PD1$^+$CD25$^+$CD8$^+$ $T_{EEF/EM}$).

10.3389/fimmu.2023.1127896

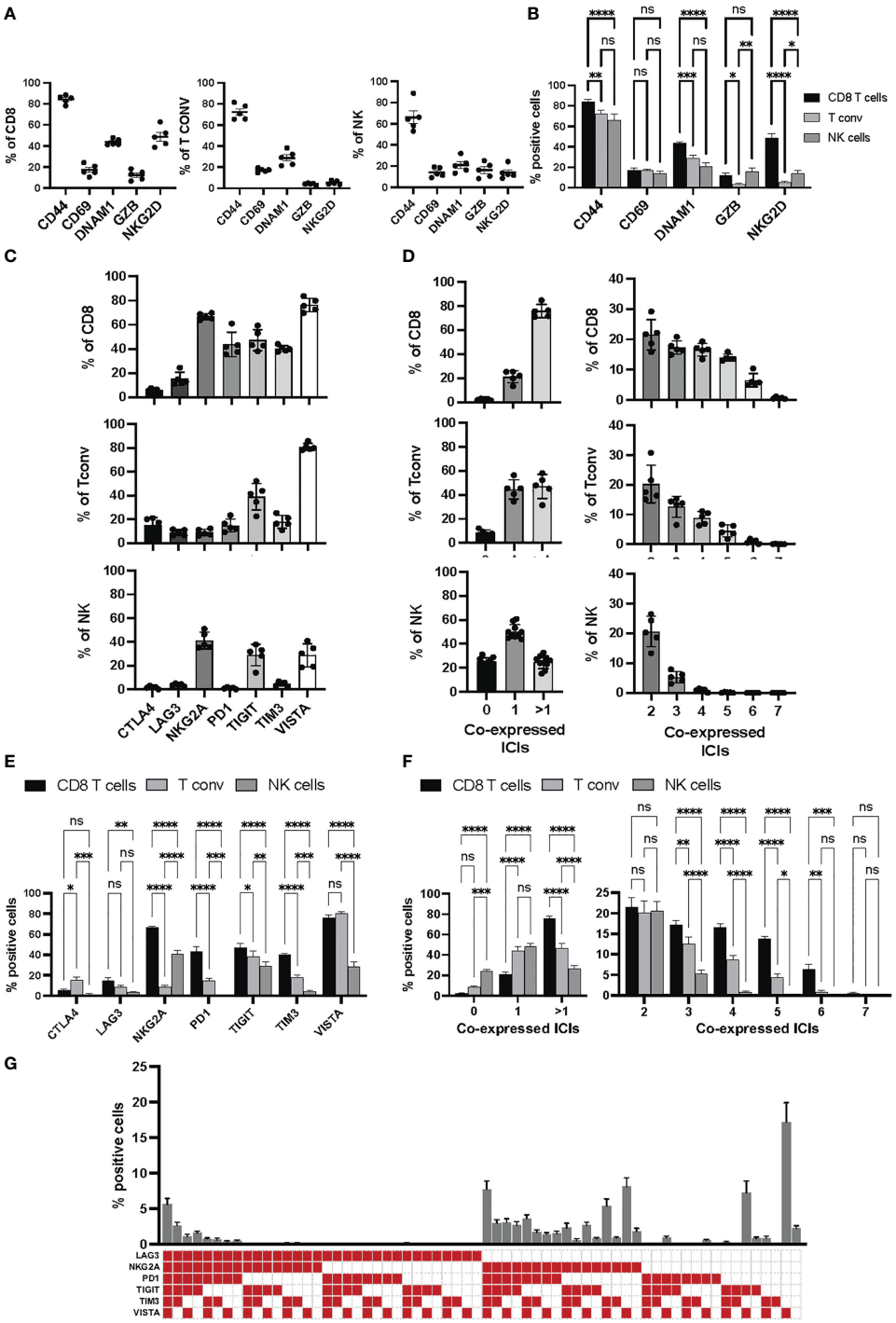

FIGURE 3
Activation and immune checkpoint marker expression in Panel 1. Tumor infiltrating immune cells from YUMM UV 1.7 tumors were analyzed as described in Figure 2A. **(A)** Percentages of cells expressing the indicated activation markers within the $CD8^+$ (left), T_{conv} (middle) or NK (right) cell populations. **(B)** Percentages in **(A)** were grouped to directly compare differences in the percentages of each activation markers across $CD8^+$ T cells, T conv, and NK cells. Data are presented as mean values ± SEM. 0.1234 (ns), 0.0332 (*), 0.0021 (**), 0.0002 (***), <0.0001 (****) (Two-Way ANOVA, Fisher's LSD test). **(C)** Percentages of cells expressing the indicated immune checkpoint molecules within the $CD8^+$ (top), T_{conv} (middle) or NK (bottom cell populations. **(D)** Boolean gating for the identification of the percentage of cells expressing 0, 1 or >1 immune checkpoint inhibitors (ICIs, left column) and 2 to 7 immune checkpoint inhibitors (ICIs, right column) within the $CD8^+$ (top), T_{conv} (middle) or NK (bottom) cell populations. **(E)** Percentages in **(C)** were grouped to directly compare differences in the percentages of each immune checkpoint inhibitor across $CD8^+$ T cells, T conv, and NK cells. Data are presented as mean values ± SEM. 0.1234 (ns), 0.0332 (*), 0.0021 (**), 0.0002 (***), <0.0001 (****) (Two-Way ANOVA, Fisher's LSD test). **(F)** Percentages in **(D)** were grouped to directly compare differences in the percentages of cells co-expressing the indicated numbers of immune checkpoint inhibitors (ICIs) across $CD8^+$ T cells, T_{conv}, and NK cells. Data are presented as mean values ± SEM. 0.1234 (ns), 0.0332 (*), 0.0021 (**), 0.0002 (***), <0.0001 (****) (Two-Way ANOVA, Fisher's LSD test). **(G)** Boolean gating (FLowJo) for 6 different immune checkpoint inhibitors on tumor infiltrating $CD8^+$ T cells. The graph represents the percentage of tumor infiltrating $CD8^+$ T cell positive for any of the immune checkpoint combinations indicated by the red square below the x axes. Data are presented as mean values ± SEMs, n=5.

effector functions and acquisition of dysfunctional/exhausted phenotypes (Figure 3C-G).

3.3.5 LAG-3

LAG-3 is upregulated on activated $CD4^+$ and $CD8^+$ T cells, as well as on a subset of NK cells. Importantly, LAG-3 and PD-1 are frequently co-expressed on both $CD4^+$ and $CD8^+$ tumor infiltrating lymphocytes (TILs) and their co-blockade has been shown to synergize to improve anti-tumor responses in several pre-clinical murine cancer models (32). LAG-3 is highly expressed in Treg cells and its blockade abrogates Treg cell suppressor functions (33). LAG-3 is also expressed on type 1 regulatory (Tr1) T cells, identified in both humans and mice as $FoxP3^{neg}LAG\text{-}3^+CD49b^+$ $CD4^+$ T cells (32).

3.3.6 TIM-3

TIM-3 is a negative regulator of type 1 immunity expressed on IFN-γ-producing $CD4^+$ Th1 helper cells, $CD8^+$ cytotoxic T cells, T_{regs} cells as well as on innate immune cells (dendritic cells, NK cells, monocytes). In these cell types, TIM-3 inhibits immune responses and promotes tolerance (34). Tumor infiltrating $CD8^+$ T cells co-expressing TIM-3 and PD-1 can exhibit a severely dysfunctional or exhausted phenotype and TIM-3 and PD-1 co-blockade is more effective than PD-1 blockade alone in improving anti-tumor immune effector functions in preclinical models of both solid and hematologic cancer (32). TIM-3 also regulates the function of $FoxP3^+$ T_{reg} cells and $TIM\text{-}3^+$ T_{regs} display higher expression of known T_{reg} effector molecules such as IL-10, Granzymes, and perforin. In the context of cancer, high level of TIM-3 on NK cells is associated with a dysfunctional and exhausted phenotype and TIM-3 blockade restores NK cell functions (32).

3.3.7 TIGIT

TIGIT is highly expressed on human and murine TILs in several tumor types. It is often co-expressed with PD-1, TIM-3, and LAG-3 whose co-expression in the absence of co-stimulatory molecules can identify the most dysfunctional $CD8^+$ TILs (24, 27). TIGIT ligands CD155 and CD112 are widely expressed on tumor cells. DNAM-1 (CD226), the agonistic signal of this co-stimulatory pathway, promotes cytotoxicity and enhances anti-tumor responses. In contrast, TIGIT negatively regulates anti-tumor responses, but with a specialized role in the tumor tissue as it is not expressed in peripheral lymphoid organs (34). Of note, TIGIT also promotes the immunosuppressive activity of tumor tissue Treg cells (34, 35). Therefore, targeting TIGIT with monoclonal antibodies may not only enhance effector T cell function, but also suppresses TIGIT cell-mediated immunosuppression (27, 36).

3.3.8 VISTA

VISTA is predominantly expressed in hematopoietic cells with the highest level of expression observed in myeloid cells, particularly microglia and neutrophils, followed by monocytes, macrophages, and dendritic cells. VISTA is also highly expressed on naïve $CD4^+$ and $CD8^+$ T cells, as well as $Foxp3^+$ Treg cells. While most immune checkpoint modulators fine-tune T cell response and fate after activation, VISTA was recently shown to regulate naïve T cell quiescence and peripheral T cell tolerance (37). VISTA is also emerging as a novel targetable immune checkpoint in oncology and its altered expression has been prognostically implicated in different types of cancer (38).

3.3.9 NKG2A

NKG2A is an inhibitory member of the NKG2 family, it dimerizes with CD94 on the cell surface and its major ligand is the non-classical MHC class I molecule HLA-E. NKG2A is expressed on NK cells, natural killer T (NKT) cells and a subset of $CD8^+$ T cells. Importantly, exhausted TILs can display high NKG2A expression, and this correlates with reduced survival in patients with ovarian or colorectal cancer (39).

3.4 Panel 2: Memory phenotypes

The ability to preclinically evaluate the capacity of a new treatment, or a novel combination therapy, to enhance anti-tumor immune responses and subsequent formation of memory populations is vital to formulating new treatment strategies to translate into the clinic. To this end, we have designed and optimized a multiparametric flow cytometry panel (Panel 2) to specifically assess changes in memory cell differentiation, proliferation and effector functions in mouse immune cells (Table 3). The same backbone designed for Panel 1 to identify major T and NK cell subset was used for this panel thus allowing a broad applicability and the simultaneous investigation of activation/exhaustion and memory phenotypes (Figure 2B & S3).

3.4.1 NK cells

To identify mature, effector NK cells, $CD49b^+$ cells were further characterized for the co-expression of NKp46, which is used in mice to specifically and accurately identify NK cells (40), and KLRG1 (Figure 2B and Figure S3, blue frame). Consistently, $NKp46^+KLRG1^+$ cells lack TCF-1 expression (41). However, because KLRG1 may have inhibitory functions upon binding to cadherins abundantly expressed in some tumor microenvironments, its monitoring may inform on the immune modulatory activity of a given therapy on NK cells in a context-dependent manner (42). Of note, the addition of CD25 in this panel also allows the monitoring of "memory-like" NK cells, a subpopulation with enhanced recall function to multiple stimuli (43–45).

3.4.2 T cells

For T cells, CD44 and CD62L gating was used to identify naïve (T_N), central memory (T_{CM}) and effector/effector memory ($T_{EFF/EM}$) subsets (Figure 2B; Figure S3). A marker for 'stemness', TCF-1, was included as it has recently been described as an important indicator of T cell self-renewal capability and, when co-expressed with PD-1, as marker of responsiveness to immune checkpoint inhibition (46, 47). The expression of Ki67 allows the identification of proliferating T cells providing a potential means to identify T cell populations that are responding to any immunotherapy or

vaccination (48). CCR7 was included in this panel to assess T cell trafficking, particularly in lymph node samples, and to monitor T cell differentiation (49).

3.4.3 CD8$^+$ T cells

Within the CD8+ TCM subset (Figure 2B and Figure S3, orange frame), CD122 expression has been identified as a marker denoting antigen experience (50), whereas the expression of CD69 and/or CD103 may identify tissue-resident memory T cells (51, 52). Within the $T_{EFF/EM}$ subset, KLRG1 and CD127 are utilized to delineate short lived effector cells (SLECs) and memory precursor cells (MPECs) (53). Moreover, within the same subset, assessment of PD-1 and CD25 expression allows the identification of suppressive and/or regulatory CD8$^+$ T cells (54, 55). In tumor draining lymph nodes, co-expression of PD-1 and TCF1 can identify precursors of exhausted T cells (T_{PEX}), which are known for their abilities to self-renew and for their properties of functionally restrained effector cells that are emerging as important mediators of cancer immunotherapy (21, 47).

3.4.4 CD4$^+$ conventional T cells

Conventional CD4+ T cells (Figure 2B and Figure S3, red frame) with direct cytotoxic activity are emerging as important players in anti-tumor immunity (56). In this panel, focusing on CD4$^+$FoxP3$^-$ T cells, KLRG1 can be used to identify cytotoxic CD4$^+$ T cells, which display an effector phenotype (57, 58).

3.4.5 Tregs

Within CD4+FOXP3+ T_{regs} (Figure 2B and Figure S3, green frame), CD25 is a useful marker for assessing maturation of these cells (59). CD69 can additionally be used to identify a Treg cell subset known to express high levels of IL-10 in a STAT3-dependent manner (60). CD103 can be used to identify another T_{regs} cell subset present in both lymphoid tissues and tumors, whose expression levels correlate with the level of TGFß secreted by tumor cells (61, 62). KLRG1 was applied to identify a small proportion of T_{regs} in the periphery that exhibit a gene expression profile of "activated and terminally differentiated effector T_{regs} (63).

3.5 Panel 1 & 2: data analysis

The main purpose of these two integrated flow cytometry panels is to allow the simultaneous analysis of the co-expression of multiple checkpoint inhibitors and the characterization of the memory/effector status of distinct T cell and NK cell subpopulations. With regard to Panel 1, this can be achieved by combining manual gating of known sub-populations (Figures 2A, 3A, B, C, E) with Boolean gating (Figures 3D, F, G). This approach allows the assessment of the proportions of cells expressing none, one or different combinations of multiple immune checkpoint molecules within a specific (known) subpopulation of interest. Back-gating on the parental population against specific activation/differentiation markers of interest provides additional information on the functional status of the immune checkpoint expressing cells (Figure S4). For Panel 2, manual gating of known sub-populations can be used followed by downstream analysis within a specific subset (naïve versus effector/memory) for the characterization of additional subpopulations of functional relevance (Figure 2B; Figure S3). Alternatively, the differentiation status (naïve versus effector/memory) of immune cell subsets, such as CD8$^+$ T cells (Figure 4), expressing specific combinations of markers can be elucidated using this panel. Moreover, for an unbiased interrogation of the data, dimension reduction techniques such as tSNE or UMAP combined with clustering algorithms (FlowSOM and PhenoGraph) can be used to identify known and novel subpopulations characterized by the co-expression of specific differentiation, activation, and/or checkpoint molecules in both Panels (Figures 5, 6; S5).

During the development of these integrated panels, antigen classification, resolution ranking, and an instrument specific spillover spread matrix (Figure S6 and Tables S1, S2) were used to predict the best fluorochrome combination and fluorochrome/antigen association listed in Table 3. Please refer to online supplemental material for the optimization of the panel, antibody titration and detailed technical information (Figures S6–S11).

4 Conclusive remarks

One limitation of the results presented herein is the application of the polyfunctional T cell assays to blood immune cells. Although this approach can allow a reliable monitoring of systemic tumor-specific T cell responses over time during immunotherapeutic treatments, it may not accurately reflect the real situation in the tumour microenvironment. However, the same protocol can easily applied to *ex vivo* cultured tumour infiltrating lymphocytes provided that adequate numbers of these cells can be obtained from tumor tissues. Similar approaches assessing the extent of polyfunctional T cell responses to tumor antigens have been successfully applied to the peripheral blood immune cells of tumor patients, providing useful indication of changes in adaptive immunity responses induced by treatment and allowing the identification of potential immune biomarkers predictive of the response to therapy (64, 65). Moreover, the multicolor flow cytometry panels we developed for mouse cells can be easily adapted to characterize T cell/NK cell exhaustion and memory phenotypes of human immune cells. These panels may be particularly useful to identify changes in the expression of targetable immune checkpoint molecules thus allowing a rational tailoring of combination immunotherapy for cancer patients. These panels, however, should take into account the differences between mouse and humans with regard to the level of expression and biological meaning of distinct immune markers.

In summary, the integrated exploitation of the multiparametric flow cytometry-based methods we developed can allow a reliable preclinical assessment of vaccine-induced polyfunctional T cell responses, also including the epitope spreading, and the concomitant characterization and T cell/NK cell exhaustion and memory phenotypes in mouse immuno-oncology models.

10.3389/fimmu.2023.1127896

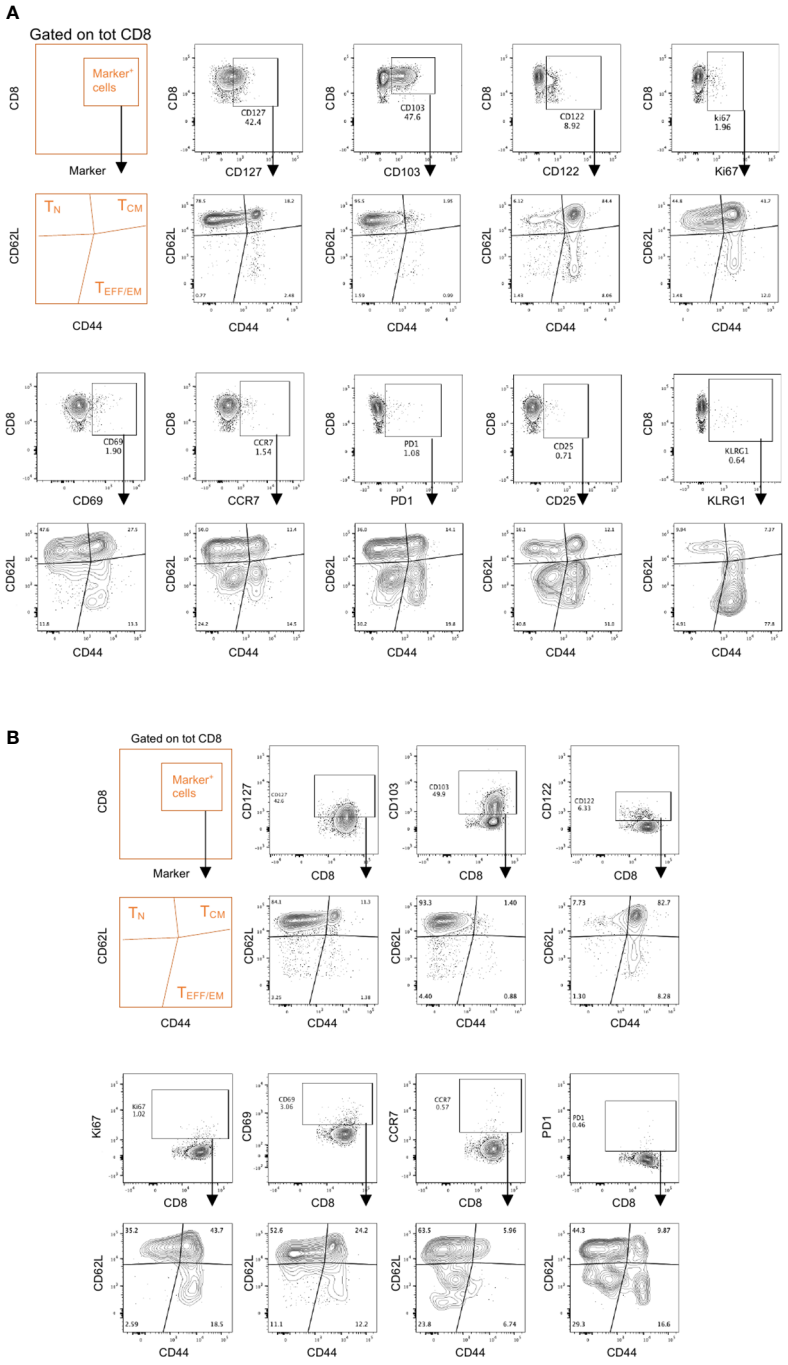

FIGURE 4
Memory effector phenotypes in Panel 2. Spleens and draining lymph nodes isolated from C57Bl/6 mice bearing YUMM UV 1.7 melanomas were processed and stained with Panel 2 as described in methods. **(A, B)** Representative analysis on $CD8^+$ T cells from spleens **(A)** or tumor draining lymph nodes **(B)** where marker positive cells (top contour plots) are interrogated for their memory/effector phenotype (bottom contour plots) using the CD62L and CD44 markers.

10.3389/fimmu.2023.1127896

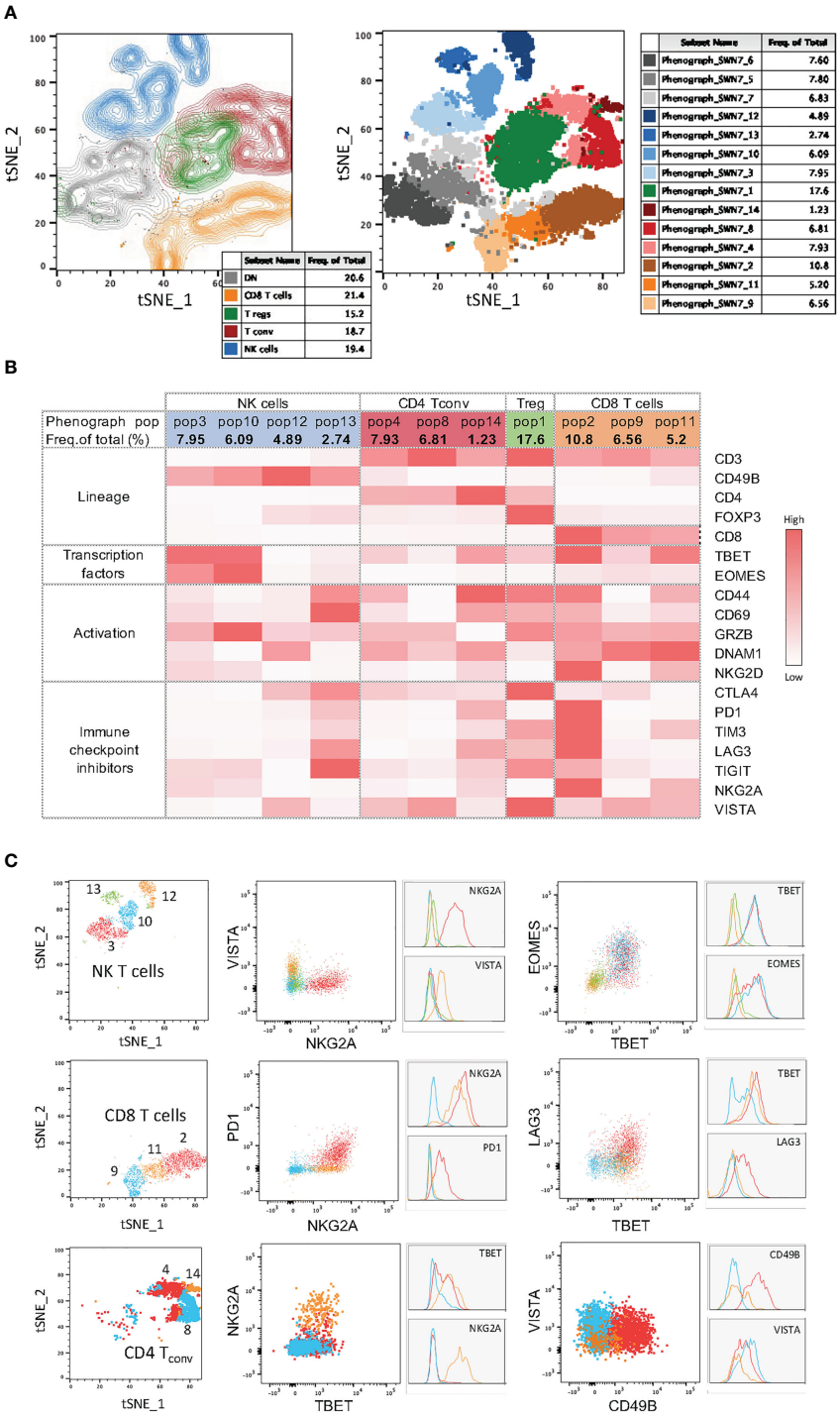

FIGURE 5
High-dimensional data analysis on tumor infiltrating immune cells from YUMM UV 1.7 tumors stained with Panel 1. **(A)** Left: tSNE plots on concatenated T and NK cells from 4 YUMM UV 1.7 tumors with overlayed colored manual gates for $CD8^+$ (orange), $CD4^+$ T_{conv} (red), T_{regs} (green), NK (blue), and double negative ($CD4^-CD8^-$) T cells (grey). Contour plots reveal cell density and main subpopulations. Right: Same tSNE as on the left where cells are color-coded according to the 14 clusters identified with PhenoGraph. **(B)** Mean fluorescence intensity (MFI) heatmap for the indicated markers across the 4 main immune cell population and within each cluster obtained with PhenoGraph. Marker expression intensity is indicated by the scale bar at the right of the table where white is low and red is high. **(C)** Left column: tSNE plots showing cluster overlays in 3 main immune cell population: NK cells, $CD8^+$ T cells, and $CD4^+$ T_{conv}. Middle and right colums: same cluster overlays analysed for differentiation and exhaustion markers. Both dot plots and corresponding histograms are presented.

10.3389/fimmu.2023.1127896

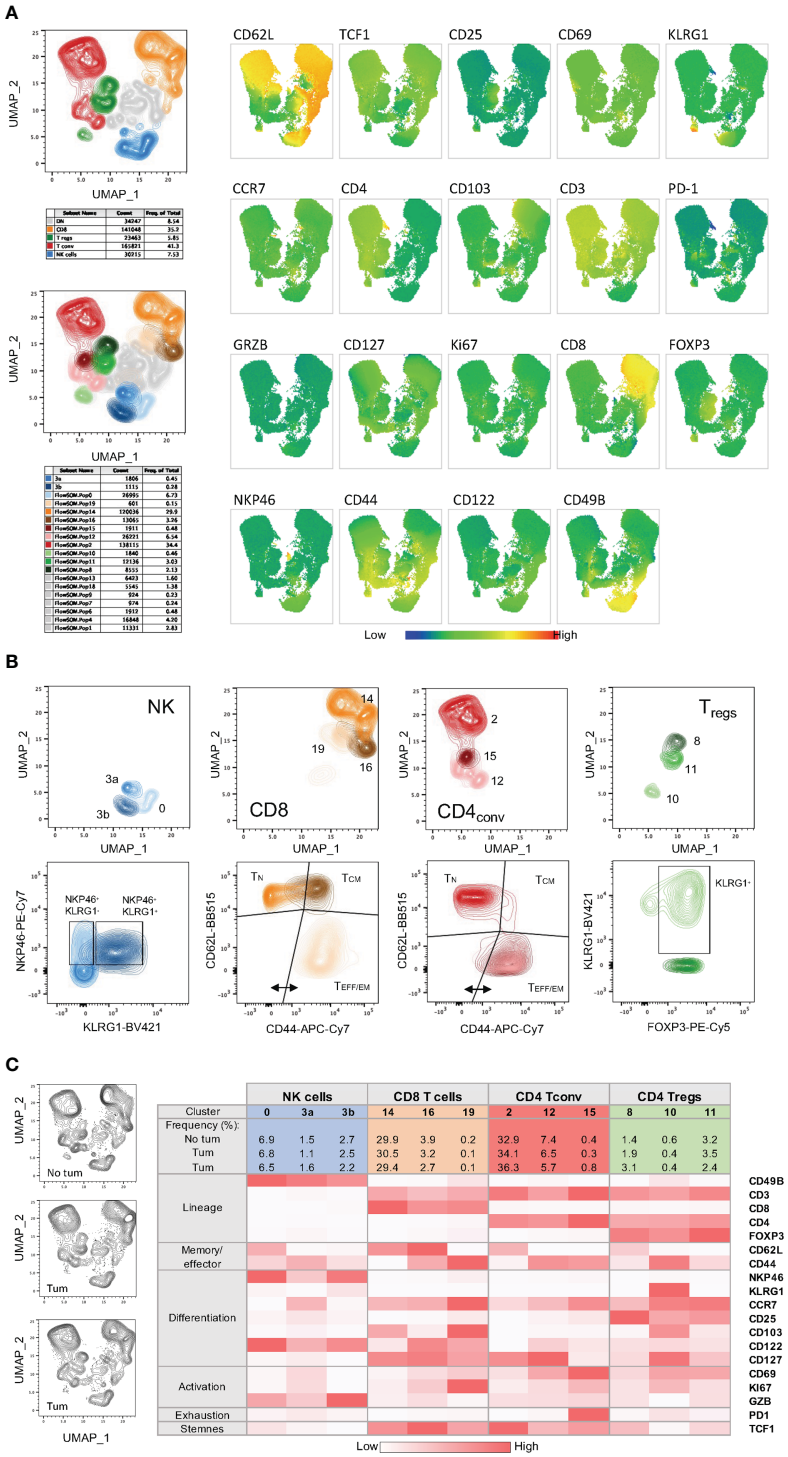

FIGURE 6
High-dimensional data analysis on splenocytes from mice bearing YUMM UV 1.7 tumors and stained with Panel 2. **(A)** Top left: UMAP plot on concatenated T and NK cells from 3 spleens isolated from C57Bl/6 mice bearing YUMM UV 1.7 tumours. The plot shows overlayed coloured manual gates for $CD8^+$ T cells (orange), $CD4^+$ T_{conv} cells (red), $CD4^+$ T_{reg} cells (green), NK cells (blue), and double negative ($CD4^-CD8^-$) T cells (grey). Contour plots reveal cell density and main subpopulations. Bottom left: Same UMAP as in the top plot where cells are color-coded according to the 17 main clusters identified with FlowSOM and additional sub-clusters (3a and 3b) manually defined. Right: visualization of the expression phenotype across all T and NK cell clusters in UMAP. Marker expression intensity is indicated by the scale bar at the bottom of the plots where blue is low and red is high. Each marker is indicated above each plot. **(B)** Top plots: UMAP plots showing clusters and sub-clusters in the 4 main immune cell population: $CD8^+$, $CD4^+$ T_{conv}, $CD4^+$ T_{regs} and NK cells. Bottom plots: same clusters and sub-clusters analysed for maturation and differentiation markers. **(C)** Left: UMAP plots from individual spleens. Right: MFI heatmap for the indicated markers across the 4 main immune cell population and within each cluster and sub-cluster obtained with FlowSOM or manually defined. Marker expression intensity is indicated by the scale bar at the bottom of the table where white is low and red is high.

Application of these protocols may improve the definition of the most effective antigen formulations for next generation cancer vaccines and allow the identification of novel mechanism-based combination immunotherapies.

Data availability statement

The raw data supporting the conclusions of this article will be made available by the authors, without undue reservation.

Ethics statement

The animal study was reviewed and approved by University of Queensland Animal Ethics Committee (approval number UQDI/252/16).

Author contributions

RD, SM, DS and RM designed the research. DM, BZ, SM, RB and JW performed the experiments. DM, BZ, SM, RM and RD analyzed the data. SM and RM drafted the manuscript. RM and RD revised the manuscript. All authors contributed to the article and approved the submitted version.

Funding

The work was supported in part by funding provided by National Breast Cancer Foundation (IIRS-18-047, IIRS-20-124) and by the Peter MacCallum Cancer Centre Foundation (ID #2114). IIRS-23-033 to the National Breast cancer foundation grants.

Acknowledgments

We would like to thank the Flow Cytometry and Animal Core Facilities of the TRI and Peter MacCallum Cancer Centre for technical support during the optimization of these multiparametric panels and the *in vivo* vaccination experiments. We acknowledge financial support provided by TRI *via* access to the Symphony Reagent Support Fund. We also thank Andrew Lim (BD Biosciences) for assistance with panel design, technical support and troubleshooting, Vanessa Seelis (BD Biosciences) for providing advice and reagents, Nick Haas and Brian Gabrielli for the kind gift of cell lines.

Conflict of interest

The authors declare that the research was conducted in the absence of any commercial or financial relationships that could be construed as a potential conflict of interest.

Publisher's note

All claims expressed in this article are solely those of the authors and do not necessarily represent those of their affiliated organizations, or those of the publisher, the editors and the reviewers. Any product that may be evaluated in this article, or claim that may be made by its manufacturer, is not guaranteed or endorsed by the publisher.

Supplementary material

The Supplementary Material for this article can be found online at: https://www.frontiersin.org/articles/10.3389/fimmu.2023.1127896/full#supplementary-material

References

1. Hernandez R, Malek TR. Fueling cancer vaccines to improve T cell-mediated antitumor immunity. *Front Oncol* (2022) 12:878377. doi: 10.3389/fonc.2022.878377

2. Tanyi JL, Chiang CL, Chiffelle J, Thierry AC, Baumgartener P, Huber F, et al. Personalized cancer vaccine strategy elicits polyfunctional T cells and demonstrates clinical benefits in ovarian cancer. *NPJ Vaccines* (2021) 6(1):36. doi: 10.1038/s41541-021-00297-5

3. Keskin DB, Anandappa AJ, Sun J, Tirosh I, Mathewson ND, Li S, et al. Neoantigen vaccine generates intratumoral T cell responses in phase ib glioblastoma trial. *Nature* (2019) 565(7738):234–9. doi: 10.1038/s41586-018-0792-9

4. Pisibon C, Ouertani A, Bertolotto C, Ballotti R, Cheli Y. Immune checkpoints in cancers: From signaling to the clinic. *Cancers (Basel)* (2021) 13(18):4573. doi: 10.3390/cancers13184573

5. Kirchhammer N, Trefny MP, Auf der Maur P, Läubli H, Zippelius A. Combination cancer immunotherapies: Emerging treatment strategies adapted to the tumor microenvironment. *Sci Transl Med* (2022) 14(670):eabo3605. doi: 10.1126/scitranslmed.abo3605

6. Barnaba VT. Cell memory in infection, cancer, and autoimmunity. *Front Immunol* (2022) 12:811968. doi: 10.3389/fimmu.2021.811968

7. Wang J, Perry CJ, Meeth K, Thakral D, Damsky W, Micevic G, et al. UV-Induced somatic mutations elicit a functional T cell response in the YUMMER1. *7 Mouse melanoma Model Pigment Cell Melanoma Res* (2017) 30(4):428–35. doi: 10.1111/pcmr.12591

8. Zeng B, Middelberg AP, Gemiarto A, MacDonald K, Baxter AG, Talekar M, et al. Self-adjuvanting nanoemulsion targeting dendritic cell receptor Clec9A enables antigen-specific immunotherapy. *J Clin Invest* (2018) 128(5):1971–84. doi: 10.1172/JCI96791

9. Liadser A, Ljungberg K, Tufvesson H, Tazzari M, Roos AK, Quest AF, et al. Intradermal DNA electroporation induces survivin-specific CTLs, suppresses angiogenesis and confers protection against mouse melanoma. *Cancer Immunol Immunother* (2010) 59(1):81–92.

10. Ciesielski MJ, Kozbor D, Castanaro CA, Barone TA, Fenstermaker RA. Therapeutic effect of a T helper cell supported CTL response induced by a survivin peptide vaccine against murine cerebral glioma. *Cancer Immunol Immunother* (2008) 57(12):1827–35.

11. Mennuni C, Ugel S, Mori F, Cipriani B, Iezzi M, Pannellini T, et al. Preventive vaccination with telomerase controls tumor growth in genetically engineered and carcinogen-induced mouse models of cancer. *Cancer Res* (2008) 68(23):9865–74.

12. Siegel S, Wagner A, Schmitz N, Zeis M. Induction of antitumour immunity using survivin peptide-pulsed dendritic cells in a murine lymphoma model. *Br J Haematol* (2003) 122(6):911–4.

13. Yu G, He X, Li X, Wu Y. Driving neoantigen-based cancer vaccines for personalized immunotherapy into clinic: A burdensome journey to promising land. *BioMed Pharmacother* (2022) 153:113464. doi: 10.1016/j.biopha.2022.113464

14. Kreiter S, Vormehr M, van de Roemer N, Diken M, Löwer M, Diekmann J, et al. Mutant MHC class II epitopes drive therapeutic immune responses to cancer. *Nature* (2015) 520(7549):692–6. doi: 10.1038/nature14426

15. Zhang J, Marotel M, Fauteux-Daniel S, Mathieu AL, Viel S, Marçais A, et al. T-Bet and eomes govern differentiation and function of mouse and human NK cells and ILC1. *Eur J Immunol* (2018) 48(5):738–50. doi: 10.1002/eji.201747299

16. Li J, He Y, Hao J, Ni L, Dong C. High levels of eomes promote exhaustion of anti-tumor CD8+ T cells. *Front Immunol* (2018) 9:2981. doi: 10.3389/fimmu.2018.02981

17. Gacerez AT, Sentman CL. T-Bet promotes potent antitumor activity of CD4+ CAR T cells. *Cancer Gene Ther* (2018) 25(5-6):117–28. doi: 10.1038/s41417-018-0012-7

18. Long EO, Kim HS, Liu D, Peterson ME, Rajagopalan S. Controlling natural killer cell responses: integration of signals for activation and inhibition. *Annu Rev Immunol* (2013) 31:227–58. doi: 10.1146/annurev-immunol-020711-075005

19. Gill S, Vasey AE, De Souza A, Baker J, Smith AT, Kohrt HE, et al. Rapid development of exhaustion and down-regulation of eomesodermin limit the antitumor activity of adoptively transferred murine natural killer cells. *Blood* (2012) 119 (24):5758–68. doi: 10.1182/blood-2012-03-415364

20. Zhang P, Lee JS, Gartlan KH, Schuster IS, Comerford I, Varelias A, et al. Eomesodermin promotes the development of type 1 regulatory T (TR1) cells. *Sci Immunol* (2017) 2(10):eaah7152. doi: 10.1126/sciimmunol.aah7152

21. Tay RE, Richardson EK, Toh HC. Revisiting the role of CD4+ T cells in cancer immunotherapy-new insights into old paradigms. *Cancer Gene Ther* (2021) 28(1-2):5–17. doi: 10.1038/s41417-020-0183-x

22. Kachler K, Holzinger C, Trufa DI, Sirbu H, Finotto S. The role of Foxp3 and tbet co-expressing treg cells in lung carcinoma. *Oncoimmunology* (2018) 7(8):e1456612. doi: 10.1080/2162402X.2018.1456612

23. Lucca LE, Axisa PP, Singer ER, Nolan NM, Dominguez-Villar M, Hafler DA. TIGIT signaling restores suppressor function of Th1 tregs. *JCI Insight* (2019) 4(3): e124427. doi: 10.1172/jci.insight.124427

24. Chen F, Xu Y, Chen Y, Shan S. TIGIT enhances CD4+ regulatory T-cell response and mediates immune suppression in a murine ovarian cancer model. *Cancer Med* (2020) 9(10):3584–91. doi: 10.1002/cam4.2976

25. Shevyrev D, Tereshchenko V. Treg heterogeneity, function, and homeostasis. *Front Immunol* (2020) 10:3100. doi: 10.3389/fimmu.2019.03100

26. Prajapati K, Perez C, Rojas LBP, Burke B, Guevara-Patino JA. Functions of NKG2D in CD8+ T cells: an opportunity for immunotherapy. *Cell Mol Immunol* (2018) 15(5):470–9. doi: 10.1038/cmi.2017.161

27. Akira Shibuya, Kazuko S. DNAM-1 versus TIGIT: competitive roles in tumor immunity and inflammatory responses. *Int Immunol* (2021) 33(12):687–92. doi: 10.1093/intimm/dxab085

28. Minnie SA, Kuns RD, Gartlan KH, Zhang P, Wilkinson AN, Samson L, et al. Myeloma escape after stem cell transplantation is a consequence of T-cell exhaustion and is prevented by TIGIT blockade. *Blood* (2018) 132(16):1675–88. doi: 10.1182/blood-2018-01-825240

29. Fixemer J, Hummel JF, Arnold F, Klose CSN, Hofherr A, Weissert K, et al. Eomes cannot replace its paralog T-bet during expansion and differentiation of CD8 effector T cells. *PloS Pathog* (2020) 16(9):e1008870. doi: 10.1371/journal.ppat.1008870

30. Liu Q, Sun Z, Chen L. Memory T cells: strategies for optimizing tumor immunotherapy. *Protein Cell* (2020) 11(8):549–64. doi: 10.1007/s13238-020-00707-9

31. Im SJ, Hashimoto M, Gerner MY, Lee J, Kissick HT, Burger MC, et al. Defining CD8+ T cells that provide the proliferative burst after PD-1 therapy. *Nature* (2016) 537 (7620):417–21. doi: 10.1038/nature19330

32. Anderson AC, Joller N, Kuchroo VK. Lag-3, Tim-3, and TIGIT: Co-inhibitory receptors with specialized functions in immune regulation. *Immunity* (2016) 44 (5):989–1004. doi: 10.1016/j.immuni.2016.05.001

33. Huang CT, Workman CJ, Flies D, Pan X, Marson AL, Zhou G, et al. Role of LAG-3 in regulatory T cells. *Immunity* (2004) 21(4):503–13. doi: 10.1016/j.immuni.2004.08.010

34. Kurtulus S, Sakuishi K, Ngiow SF, Joller N, Tan DJ, Teng MW, et al. TIGIT predominantly regulates the immune response *via* regulatory T cells. *J Clin Invest* (2015) 125(11):4053–62. doi: 10.1172/JCI81187

35. Das M, Zhu C, Kuchroo VK. Tim-3 and its role in regulating anti-tumor immunity. *Immunol Rev* (2017) 276(1):97–111. doi: 10.1111/imr.12520

36. Preillon J, Cuende J, Rabolli V, Garnero L, Mercier M, Wald N, et al. Restoration of T-cell effector function, depletion of tregs, and direct killing of tumor cells: The multiple mechanisms of action of a-TIGIT antagonist antibodies. *Mol Cancer Ther* (2021) 20(1):121–31. doi: 10.1158/1535-7163.MCT-20-0464

37. ElTanbouly MA, Zhao Y, Nowak E, Li J, Schaafsma E, Le Mercier I, et al. VISTA is a checkpoint regulator for naïve T cell quiescence and peripheral tolerance. *Science* (2020) 367(6475):eaay0524. doi: 10.1126/science.aay0524

38. Yuan L, Tatineni J, Mahoney KM, Freeman GJ. VISTA: A mediator of quiescence and a promising target in cancer immunotherapy. *Trends Immunol* (2021) 42(3):209–27. doi: 10.1016/j.it.2020.12.008

39. Creelan BC, Antonia SJ. The NKG2A immune checkpoint - a new direction in cancer immunotherapy. *Nat Rev Clin Oncol* (2019) 16(5):277–8. doi: 10.1038/s41571-019-0182-8

40. Walzer T, Bléry M, Chaix J, Fuseri N, Chasson L, Robbins SH, et al. Identification, activation, and selective *in vivo* ablation of mouse NK cells *via* NKp46. *Proc Natl Acad Sci USA.* (2007) 104(9):3384–9. doi: 10.1073/pnas.0609692104

41. Li ZY, Morman RE, Hegermiller E, Sun M, Bartom ET, Maienschein-Cline M, et al. The transcriptional repressor ID2 supports natural killer cell maturation by controlling TCF1 amplitude. *J Exp Med* (2021) 218(6):e20202032. doi: 10.1084/jem.20202032

42. Miller JS, Lanier LL. Natural killer cells in cancer immunotherapy. *Annu Rev Cancer Biol* (2019) 3(1):77–103. doi: 10.1146/annurev-cancerbio-030518-055653

43. Lee SH, Fragoso MF, Biron CA. Cutting edge: a novel mechanism bridging innate and adaptive immunity: IL-12 induction of CD25 to form high-affinity IL-2 receptors on NK cells. *J Immunol* (2012) 189(6):2712–6. doi: 10.4049/jimmunol.1201528

44. Leong JW, Chase JM, Romee R, Schneider SE, Sullivan RP, Cooper MA, et al. Preactivation with IL-12, IL-15, and IL-18 induces CD25 and a functional high-affinity IL-2 receptor on human cytokine-induced memory-like natural killer cells. *Biol Blood Marrow Transplant* (2014) 20(4):463–73. doi: 10.1016/j.bbmt.2014.01.006

45. Gang M, Wong P, Berrien-Elliott MM, Fehniger TA. Memory-like natural killer cells for cancer immunotherapy. *Semin Hematol* (2020) 57(4):185–93. doi: 10.1053/j.seminhematol.2020.11.003

46. Blank CU, Haining WN, Held W, Hogan PG, Kallies A, Lugli E, et al. Defining 'T cell exhaustion'. *Nat Rev Immunol* (2019) 19(11):665–74. doi: 10.1038/s41577-019-0221-9

47. Siddiqui I, Schaeuble K, Chennupati V, Fuertes Marraco SA, Calderon-Copete S. Intratumoral Tcf1+PD-1+CD8+ T cells with stem-like properties promote tumor control in response to vaccination and checkpoint blockade immunotherapy. *Immunity* (2019) 50(1):195–211.e110. doi: 10.1016/j.immuni.2018.12.021

48. Motamedi M, Xu L, Elahi S. Correlation of transferrin receptor (CD71) with Ki67 expression on stimulated human and mouse T cells: The kinetics of expression of T cell activation markers. *J Immunol Methods* (2016) 437:43–52. doi: 10.1016/j.jim.2016.08.002

49. Ren H, Cao K, Wang M. A correlation between differentiation phenotypes of infused T cells and anti-cancer immunotherapy. *Front Immunol* (2021) 12:745109. doi: 10.3389/fimmu.2021.745109

50. Mathews DV, Dong Y, Higginbotham LB, Kim SC, Breeden CP, Stobert EA, et al. CD122 signaling in CD8+ memory T cells drives costimulation-independent rejection. *J Clin Invest* (2018) 128(10):4557–72. doi: 10.1172/JCI95914

51. Park SL, Buzzai A, Rautela J, Hor JL, Hochheiser K, Effern M, et al. Tissue-resident memory CD8(+) T cells promote melanoma-immune equilibrium in skin. *Nature* (2019) 565(7739):366–71. doi: 10.1038/s41586-018-0812-9

52. Mackay LK, Rahimpour A, Ma JZ, Collins N, Stock AT, Hafon ML, et al. The developmental pathway for CD103(+)CD8+ tissue-resident memory T cells of skin. *Nat Immunol* (2013) 14(12):1294–301. doi: 10.1038/ni.2744

53. Joshi NS, Cui W, Chandele A, Lee HK, Urso DR, Hagman J, et al. Inflammation directs memory precursor and short-lived effector CD8(+) T cell fates *via* the graded expression of T-bet transcription factor. *Immunity* (2007) 27(2):281–95. doi: 10.1016/j.immuni.2007.07.010

54. Bienvenu B, Martin B, Auffray C, Cordier C, Becourt C, Lucas B. Peripheral CD8+CD25+ T lymphocytes from MHC class II-deficient mice exhibit regulatory activity. *J Immunol* (2005) 175(1):246–53. doi: 10.4049/jimmunol.175.1.246

55. Chakraborty S, Bhattacharjee P, Panda AK, Kajal K, Bose S, Sa G. Providence of the CD25(+) KIR(+) CD127(-) FOXP3(-) CD8(+) T-cell subset determines the dynamics of tumor immune surveillance. *Immunol Cell Biol* (2018) 96(10):1035–48. doi: 10.1111/imcb.12166

56. Kallies A, Zehn D, Utzschneider DT. Precursor exhausted T cells: key to successful immunotherapy? nat. *Rev Immunol* (2020) 20:128–36. doi: 10.1038/s41577-019-0223-7

57. Oh DY, Fong L. Cytotoxic CD4+ T cells in cancer: Expanding the immune effector toolbox. *Immunity* (2021) 54(12):2701–11. doi: 10.1016/j.immuni.2021.11.015

58. Cachot A, Bilous M, Liu YC, Li X, Saillard M, Cenerenti M, et al. Tumor-specific cytolytic CD4 T cells mediate immunity against human cancer. *Sci Adv* (2021) 7(9): eabe3348. doi: 10.1126/sciadv.abe3348

59. Curiel TJ. Tregs and rethinking cancer immunotherapy. *J Clin Invest* (2007) 117 (5):1167–74. doi: 10.1172/JCI31202

60. Yu L, Yang F, Zhang F, Guo D, Li L, Wang X, et al. CD69 enhances immunosuppressive function of regulatory T-cells and attenuates colitis by prompting IL-10 production. *Cell Death Dis* (2018) 9(9):905. doi: 10.1038/s41419-018-0927-9

61. Anz D, Mueller W, Golic M, Kunz WG, Rapp M, Koelzer VH, et al. CD103 is a hallmark of tumor-infiltrating regulatory T cells. *Int J Cancer* (2011) 129(10):2417–26. doi: 10.1002/ijc.25902

62. Chang LY, Lin YC, Kang CW, Hsu CY, Chu YY, Huang CT, et al. The indispensable role of CCR5 for *in vivo* suppressor function of tumor-derived CD103 + effector/memory regulatory T cells. *J Immunol* (2012) 189(2):567–74. doi: 10.4049/jimmunol.1200266

63. Cheng G, Yuan X, Tsai MS, Podack ER, Yu A, Malek TR, et al. IL-2 receptor signaling is essential for the development of Klrg1+ terminally differentiated T regulatory cells. *J Immunol* (2012) 189(4):1780–91. doi: 10.4049/jimmunol.1103768

64. Muraro E, Comaro E, Talamini R, Turchet E, Miolo G, Scalone S, et al. Improved natural killer cell activity and retained anti-tumor CD8(+) T cell responses contribute to the induction of a pathological complete response in HER2-positive breast cancer patients undergoing neoadjuvant chemotherapy. *J Transl Med* (2015) 13:204. doi: 10.1186/s12967-015-0567-0

65. Muraro E, Furlan C, Avanzo M, Martorelli D, Comaro E, Rizzo A, et al. Local high-dose radiotherapy induces systemic immunomodulating effects of potential therapeutic relevance in oligometastatic breast cancer. *Front Immunol* (2017) 8:1476.61. doi: 10.3389/fimmu.2017.01476

frontiers | Frontiers in Immunology

TYPE Methods
PUBLISHED 05 June 2023
DOI 10.3389/fimmu.2023.1190404

Check for updates

OPEN ACCESS

EDITED BY
Mrinmoy Sanyal,
Stanford University, United States

REVIEWED BY
Wagner Quintilio,
Butantan Institute, Brazil
Hyeonseob Lim,
Stanford University, United States

*CORRESPONDENCE
Sunil Gairola
sunil.gairola@seruminstitute.com

RECEIVED 20 March 2023
ACCEPTED 02 May 2023
PUBLISHED 05 June 2023

CITATION
Rathod V, Kadam L, Gautam M, Gumma PD, Marke K, Asokanathan C, Douglas-Bardsley A, Hassell L, Bhandare S, Gupta S, Parekh S, Pujari P, Rao H, Sharma H, Shaligram U and Gairola S (2023) Multiplexed bead-based assay for the simultaneous quantification of human serum IgG antibodies to tetanus, diphtheria, pertussis toxin, filamentous hemagglutinin, and pertactin. *Front. Immunol.* 14:1190404. doi: 10.3389/fimmu.2023.1190404

COPYRIGHT
© 2023 Rathod, Kadam, Gautam, Gumma, Marke, Asokanathan, Douglas-Bardsley, Hassell, Bhandare, Gupta, Parekh, Pujari, Rao, Sharma, Shaligram and Gairola. This is an open-access article distributed under the terms of the Creative Commons Attribution License (CC BY). The use, distribution or reproduction in other forums is permitted, provided the original author(s) and the copyright owner(s) are credited and that the original publication in this journal is cited, in accordance with accepted academic practice. No use, distribution or reproduction is permitted which does not comply with these terms.

Multiplexed bead-based assay for the simultaneous quantification of human serum IgG antibodies to tetanus, diphtheria, pertussis toxin, filamentous hemagglutinin, and pertactin

Vishal Rathod[1], Laxmikant Kadam[1], Manish Gautam[1], Prabhu Dasu Gumma[1], Kevin Marke[2], Cathy Asokanathan[2], Alex Douglas-Bardsley[2], Laura Hassell[2], Sachin Bhandare[1], Sumit Gupta[1], Sameer Parekh[1], Pramod Pujari[1], Harish Rao[1], Hitt Sharma[1], Umesh Shaligram[1] and Sunil Gairola[1]*

[1]Clinical Bioanalytical Laboratory, Serum Institute of India Pvt. Ltd., Pune, Maharashtra, India, [2]Science, Research and Innovation, Medicines, and Healthcare Products Regulatory Agency, South Mimms, United Kingdom

Background: Luminex bead-based assays offer multiplexing to test antibodies against multiple antigens simultaneously; however, this requires validation using internationally certified reference standards. Therefore, there is an urgent need to characterize existing reference standards for the standardization of multiplex immunoassays (MIAs). Here, we report the development and validation of an MIA for the simultaneous estimation of levels of human serum immunoglobulin G (IgG) antibodies for pertussis toxin (PT), filamentous hemagglutinin (FHA), pertactin (PRN), diphtheria toxoid (DT), and tetanus toxoid (TT).

Methods: The MIA was assessed using a panel of human serum samples and WHO reference standards. The WHO reference standards were also studied for suitability in the MIA. Purified antigens (PT, FHA, PRN, DT, and TT) were coupled to the spectrally unique magnetic carboxylated microspheres. The method was validated in accordance with the United States Food and Drug Administration (US FDA), European Medicines Agency (EMA), and the International Committee of Harmonization Multidisciplinary (ICH M10) guidelines, and parameters such as precision, accuracy, dilutional linearity, assay range, robustness, and stability were assessed. Method agreements with commercially available IgG enzyme-linked immunosorbent assay (ELISA) assays were also evaluated. In addition, the study assessed the level of correlation between the IgG levels estimated by the MIA and the cell-based neutralizing antibody assays for PT and DT.

Results: We identified that an equimix of WHO international standards (i.e., 06/142, 10/262, and TE-3) afforded the best dynamic range for all the antigens in the

MIA. For all five antigens, we observed that the back-fitted recoveries using the four-parameter logistic (4-PL) regression fits ranged between 80% and 120% for all calibration levels, and the percentage coefficient of variation (% CV) was < 20%. In addition, the difference in mean fluorescence intensity (MFI) between the monoplex and multiplex format was < 10% for each antigen, indicating no crosstalk among the beads. The MIA also showed good agreement with conventional and commercially available assays, and a positive correlation (> 0.75) with toxin neutralization assays for PT and DT was observed.

Conclusion: The MIA that was calibrated in accordance with WHO reference standards demonstrated increased sensitivity, reproducibility, and high throughput capabilities, allowing for the design of robust studies that evaluate both natural and vaccine-induced immunity.

KEYWORDS

diphtheria, enzyme-linked immunosorbent assay (ELISA), Luminex (xMAP) method, multiplex immunoassay (MIA), pertussis, tetanus

1 Introduction

Despite good immunization coverage, sporadic cases of vaccine-preventable diseases such as whooping cough/pertussis (1), diphtheria (2), and tetanus (3) are reported globally. Novel combination vaccines for children and adult populations targeting pertussis (subunit/acellular or whole-cell based), diphtheria, and tetanus antigens continue to be developed and tested. Serology continues to provide valuable immunogenicity and diagnostic data on pertussis-based combination vaccines. Levels of antigen-specific immunoglobulin G (IgG), as quantified by validated enzyme-linked immunosorbent assay (ELISA) methods, serve as a correlate of protection for acellular pertussis (aP)-based combination vaccines (4). Immunogenicity testing of aP-based vaccines has been historically carried out using commercially available diagnostic kits. Although validated using international standards (5), the commercial kits have concerns about lot-to-lot variability due to sourcing of required materials and the quality of coating antigens used. In addition, running single-antigen ELISA kits are time and labor-intensive and require large quantities of sera, which are often challenging to procure (6–10).

Multiplex immunoassays (MIA) represent an alternative approach for quantifying IgGs in a highly sensitive, specific, and reproducible manner. Several studies have reported the usefulness of multiplex platforms for immunogenicity assessment of aP-based combination vaccines (11–15). A study evaluating a tetraplex microsphere assay for pertussis antigens showed high concordance with an in-house ELISA (16). The assay demonstrated that the MIA could measure pertussis antigens quickly and accurately (16). However, few studies are available wherein aP antigens are multiplexed with diphtheria and tetanus antigens. A previous study has reported on a pentaplex Luminex assay covering aP, diphtheria, and tetanus antigens to evaluate the immunogenicity of combination vaccines in mouse models (13). The multiplex assay offers the advantage of lesser turnaround time in simultaneously detecting several antigens utilizing lesser sample volumes. The assay is also accurate, has a high-throughput, and reduces material costs and labor compared with conventional ELISA (17).

Microsphere-based Luminex immunoassays use spectrally distinct fluorescent microspheres as the solid support matrix (18). The target antigens are coupled onto the support matrix to simultaneously measure antibodies against multiple analytes from a single reaction well, thus reducing the analysis time, cost, and sample volume (18). The MIAs for human vaccines must be developed and validated to report results in units traceable to an appropriate international reference standard (19). Notably, for aP combination vaccines, three different WHO international reference standards from the National Institute for Biological Standards and Control (NIBSC), namely, 06/142 [pertussis toxin (PT), filamentous hemagglutinin (FHA), and pertactin (PRN)], 10/262 (diphtheria), and TE-3 (tetanus) are recommended for the calibration of immune assays for the determination of levels of antibodies against pertussis, diphtheria, and tetanus antigens, respectively. Although these international standards are suited for monoplex assays (20, 21), MIAs require a single standard to provide unitage to all the targeted antigens. Therefore, we have characterized the existing international standards, namely 06/142, 10/262, and TE-3, according to their suitability in the MIA. Such characterization will provide opportunities for using these reference standards in MIAs and support standardizing and pooling clinical results across multiple studies with greater confidence and reproducibility.

Our study reports on the development and validation of a pentaplex magnetic bead-based Luminex assay for evaluating antibody IgG concentrations against PT, FHA, PRN, diphtheria toxoid (DT), and tetanus toxoid (TT) in human serum samples using international reference standards. Method validation was designed as per the United States Food and Drug Administration (US FDA) (22), European Medicines Agency (EMA) (23), and International Council of Harmonization Multidisciplinary (ICH M10) (24) guidelines. Method agreement with commercially

available assays was also evaluated. In addition, the study analyzed the correlation of the MIA with toxin-neutralization functional antibody assays for diphtheria and pertussis toxin. Ours is the first study to report the characterization of existing international standards (ISs) for MIAs. The unitages established for ISs will also be helpful for the development of MIAs on other platforms.

2 Materials and equipment

2.1 Antigens and reagents

Purified PT, FHA, PRN antigens, DT, and TT were sourced from the Serum Institute of India Pvt. Ltd. (SIIPL, India). All antigens were tested for content and purity. The protein content of the antigens was estimated using a validated bicinchoninic acid (BCA) assay (25). Purity was tested using a validated sodium dodecyl-sulfate polyacrylamide gel electrophoresis (SDS-PAGE) assay. In accordance with the manufacturer's recommendation, antigens were stored in aliquots at temperatures of –20°C or lower. R-phycoerythrin (R-PE) conjugated to anti-human antibody was obtained from Southern Biotech, United States of America (USA). Beads (carboxylated microspheres) were procured from Luminex Corporation, USA, and 1-ethyl-3-(3-dimethyl aminopropyl) carbodiimide (EDAC) was obtained from Bio-Rad Laboratories, India. Sulfo-N Hydroxysulfosuccinimide (sulfo-NHS) was procured from ThermoFisher Scientific, USA, and bovine serum albumin (BSA) was obtained from Sigma Aldrich, India. Tween-20 was purchased from SD Fine Chem Limited, India.

2.2 International standards and reference reagents

WHO ISs and reference reagents were purchased from the NIBSC, UK. Four WHO reference standards were used in the study: 06/142, 10/262, TE-3, and 13/240. The unitages of the reference standards are reported in the international unit (IU)/mL, traceable to the international reference standard. The WHO reference reagent for pertussis antiserum human (06/142) is a freeze-dried preparation of pooled human serum with an assigned anti-PT IgG content of 106 IU/ampoule, an anti-FHA IgG content of 122 IU/ampoule, and an anti-69 K IgG content of 39 IU/ampoule. The WHO IS for diphtheria antitoxin human (10/262) is a freeze-dried preparation of normal human IgG with a diphtheria antitoxin potency of two IU/ampoule. For tetanus, the first WHO International Standard for Anti-Tetanus Immunoglobulin Human (TE-3) is a freeze-dried preparation of human tetanus immunoglobulin with an assigned unitage of 120 IU/ampoule (26). TE-3 has been replaced by a second WHO international standard, 13/240: a freeze-dried preparation with an assigned unitage of 45 IU/mL. These reference standards were supplied in ampoules and were reconstituted as per manufacturer recommendations. The unitages in IU/mL for these standards as per the certificate of analysis are summarized in Table 1.

2.3 Reference standard development for the pentaplex assay

The details of the ISs (WHO reference standards) used in the study are provided in Table 1. These reference standards are human serum preparations (high titers) from vaccinated healthy volunteers, and they are assigned IUs based on multiple global inter-laboratory studies. These standards are developed to calibrate immunoassays focused on determining antibodies against the target antigens. The MIA requires a reference standard that could provide unitage against all five antigens. Therefore, all the reference standards were evaluated to assess their suitability for use in the pentaplex assay. We used the three WHO international reference reagents, that is 06/142, 10/262, and TE-3, to prepare the multiplex reference standard (MRS) by mixing equal proportions of them (1:1:1). Reference standard development for MIA followed WHO recommendations on developing secondary reference standards (27). Briefly, 06/142, 10/262, and TE-3 were screened for antibodies against all five antigens. The antibody levels against PT, FHA, and PRN in each of these standards were quantified using 06/142 as a reference standard. The antibodies against TT and DT in these standards were quantified using the TE-3 and 10/262 reference standards, respectively. Six runs were carried out to quantify IgG levels against TT, DT, PT, FHA, and PRN in these reference standards. The final content (average of six runs) of each reference standard was used to calculate the final stock concentration of MRS. Figure 1 provides the schematic presentation of the approach used to develop MRS using international reference standards.

TABLE 1 WHO reference standards with respective unitages.

Standards	Batch No.	Antibodies (IgG)	IU/ml
Pertussis Antiserum	**06/142**	PT	106
		FHA	122
		Anti-69K (Pertactin)	39
Diphtheria Antitoxin	**10/262**	DT	2
First IS - tetanus immunoglobin	**TE-3**	TT	120
Second IS - tetanus immunoglobulin	**13/240**	TT	45

Anti-69kDa, pertactin; DT, diphtheria toxoid; FHA, filamentous hemagglutinin; IgG, immunoglobulin G; IS, international standard; IU/mL, international units per milliliter; NIBSC, National Institute for Biological Standards and Control; PT, pertussis toxin; TT, tetanus toxoid; WHO, World Health Organization.
The values in bold are used to indicate the codes for the WHO NIBSC reference standards.

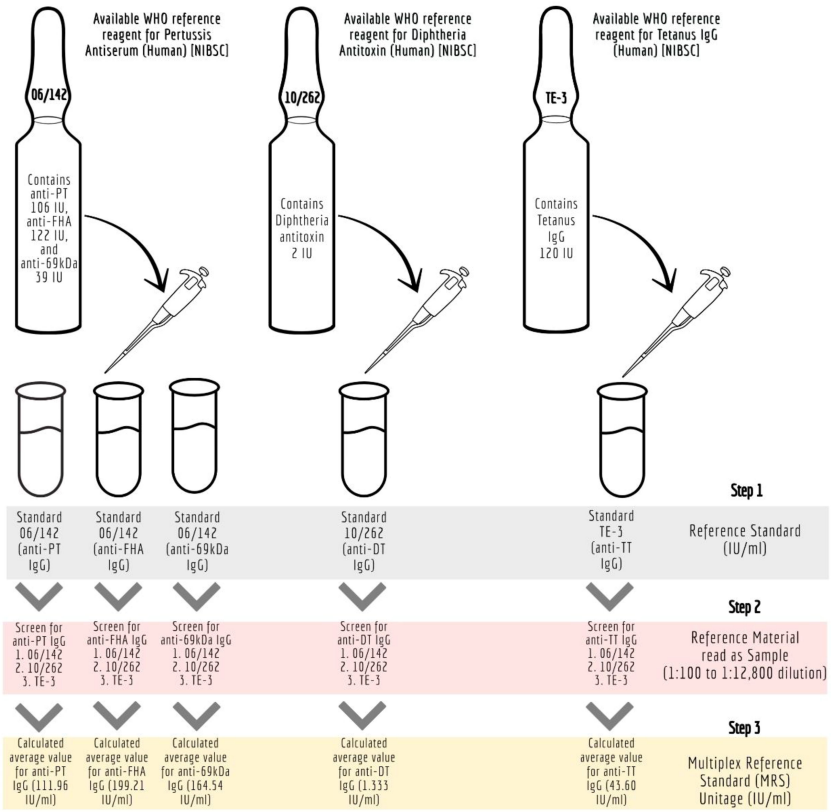

FIGURE 1
Development of Multiplex Immunoassay (MIA) reference standard (MRS) using international reference standards. anti-69kDa, pertactin, DT, diphtheria toxoid; FHA, filamentous hemagglutinin; IU/ml, international units per millilitre; mIU/ ml; milli-international units per millilitre; MRS, Multiplex Reference Standard; NIBSC, National Institute for Biological Standards and Control; Anti-69K, Pertactin; PT, pertussis toxin; TT, tetanus toxoid.

2.4 Internal quality controls

Internal quality controls (IQCs) stock standards were prepared by mixing equal volumes (1:1) of 10/262 and TE-3. The stock standard unitages were determined against the MRS as PT (110.43 IU/mL), FHA (228.70 IU/mL), PRN (212.06 IU/mL), DT (1.737 IU/mL), and TT (61.08 IU/mL). Using the stock standard, five different IQC levels (IQC-1 to IQC-5) were prepared using Luminex assay buffer. Acceptance limits were established by repeated testing of the IQCs (n = 15). Acceptable ranges for the estimates were set as the mean ± 2 standard deviations (SD) of the IgG concentrations of each antigen.

2.5 Human serum samples for method validation

Serum samples (unvaccinated and vaccinated) used for method validation were collected from healthy volunteers aged > 18 years working at SIIPL, India, after obtaining informed consent. The selected sera (n = 15) samples for the study are presented in Table 2. The selected sera samples were of various concentrations, that is negative, low, medium, and high concentrations. All serum samples were used in accordance with local regulations and guidelines and approved by the Independent Research Ethics Committee, Pune (IEC No. IRECP/015/2020). The sera samples were tested using an MIA to quantify the levels of antibodies against all five antigens. Based on concentrations, eight different panels were designed for method validation. Panel 1: Samples for precision and accuracy containing high, medium, and low levels of IgG; Panels 2–4: Samples for selectivity containing negative or low levels of IgG; Panel 5: Samples for dilution linearity containing high levels of IgG; Panel 6: Samples for stability at 2–8°C and room temperature from precision and accuracy panel; Panel 7: Samples for freeze-thaw stability (S1-S8: Reference standard) from precision and accuracy panel; Panel 8: Samples for solution stability, *samples from the precision and accuracy panel.

3 Methods

3.1 Assay development

3.1.1 Coupling of antigens to carboxylated microspheres

The antigens (PT, FHA, PRN, DT, and TT) were coupled to the spectrally unique magnetic carboxylated microspheres using established and commercially available coupling procedures. Two commercially available procedures were evaluated: the first was based on the Luminex cookbook published previously by Kadam L et al. (13, 28) and the second was based on the commercially available kit from AnteoTech (Australia) (29). For the coupling of

TABLE 2 Sera panel used for assay validation.

Sample no.	Panel 1 (Vaccinated Sera)	Panel 2 (Non-vaccinated Sera)	Panel 3 (Hemolytic and Lipemic Sera)	Panel 4 (Antibody Depleted Human sera)	Panel 5 (High Titre Sera)	Panel 6 (Vaccinated sera for Stability)	Panel 7 (Vaccinated sera and MRS)	Panel 8 (MRS and IQC)
1.	DU0001/B/2020/IA	AM0015/NB/2020/IA	Hemolytic sera	Blank Human Sera	DU0001/B/2020/IA*	DU0001/B/2020/IA*	S1	S1
2.	RS0002/B/2020/IA	DG0016/NB/2020/IA	Lipemic sera		RS0002/B/2020/IA*	RS0002/B/2020/IA*	S2	S2
3.	AS0004/B/2020/IA	ST0017/NB/2020/IA			AS0004/B/2020/IA*	SS0007/B/2020/IA*	S3	S3
4.	AN0005/B/2020/IA	SS0018/NB/2020/IA			AN0005/B/2020/IA*	AS0009/B/2020/IA*	S4	S4
5.	SP0006/B/2020/IA	PO0019/NB/2020/IA			MRS	RK0010/B/2020/IA*	S5	S5
6.	SS0007/B/2020/IA	SH0020/NB/2020/IA				IQC 1	S6	S6
7.	AZ0008/B/2020/IA					IQC 2	S7	S7
8.	AS0009/B/2020/IA					IQC 3	S8	S8
9.	RK0010/B/2020/IA						DU0001/B/2020/IA*	IQC 1
10.	IQC 1						RS0002/B/2020/IA*	IQC 1
11.	IQC 2						SS0007/B/2020/IA*	IQC 1
12.	IQC 3							IQC 2
13.	IQC 4							IQC 2
14.	IQC 5							IQC 3
15.								IQC 3

Panel 1 contains samples for precision and accuracy containing high, mid, and low levels of IgG. Panels 2–4 contain samples for selectivity containing negative or low levels of IgG. Panel 5 contains samples for dilution linearity containing a high level of IgG. Panel 6 contains samples for stability at 2–8°C and RT from precision and accuracy. Panel 7 contains samples for freeze—thaw stability (S1–S8: Reference standard) from precision and accuracy. Panel 8 contains samples for solution stability, *samples from the precision and accuracy panel. IQC, internal quality control; MRS, multiplex reference standard.

antigens, microspheres were activated with a carbodiimide derivative, EDAC hydrochloride-containing buffered solution. The intermediate carboxyl groups that formed on the beads as a result of this reaction with EDAC were stabilized using a sulfo-NHS solution. This was followed by three washing steps using a magnetic separator. The respective antigens were added to the activated beads and kept in the dark for 2 h under constant mixing (15–30 rpm). The resulting mixture was washed, and the supernatant was discarded during every washing step. After three stages of pelleting and washing, coupled beads were blocked using 1% BSA in 1x phosphate-buffered saline (PBS) buffer for 30 min and kept in a storage buffer (0.1% w/v BSA in PBS containing 0.05% sodium azide and 0.02% Tween 20).

The coupling, activation, and storage buffers used were procured from AnteoTech, Australia. The beads were activated using the activation buffer for 60 min. The antigens to be coupled were prepared using a conjugation buffer. The antigens were mixed with the activated beads and incubated at room temperature for 60 min. The unbound antigens were removed by washing them thrice with the wash buffer. Beads were then incubated in a blocking buffer (0.1% BSA in conjugation buffer) for 60 min, then stored in a storage buffer. Figure 2 presents the schematic details of MIA.

3.1.2 Characterization of WHO reference standards for the development of MRS

Monoplex bead-based assays were carried out for unitage assessment of 06/142, 10/262, and TE-3, as detailed in Figure 1. Monoplex assay here refers to a setup wherein only one target antigen is added instead of five different beads. The design of the monoplex assay is identical to MIA, with the difference that the

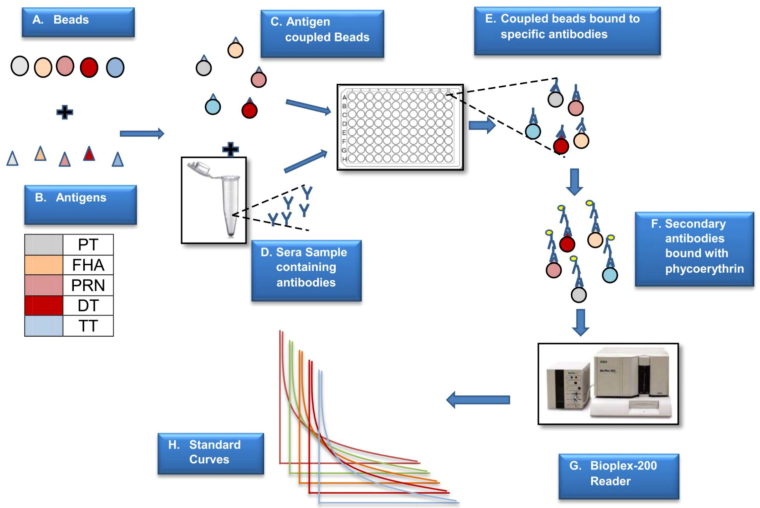

FIGURE 2
Schematic presentation of MIA. The above figure is a step-by-step representation of MIA (5-plex) wherein different beads are used to couple the antigens **(A)**. Antigen coupled beads are incubated with the sera sample to capture specific antibodies **(B–E)**. This binding is monitored by positive reaction with PE labelled secondaryantibody **(F)**. The reaction on beads is analysed using a specific reader **(G)** wherein the reported fluorescence is directly proportional to the amount of antigen specific antibody in the sera sample **(H)**. The assay is based on external reference standard and quantification is performed using standard curve fitted using logistic curve **(H)**. Different colors are used to depict five different antigens.

assay uses monovalent beads (~ 4,000 beads per well were used). Briefly, two-fold serial dilutions (from 1:1,000 to 1:1,28,000) of the respective human reference standards (WHO reference standards 06/142, 10/262, and TE-3) were performed eight times and were added to the monovalent beads. Test serum samples (WHO reference standards) were also assessed at multiple serial dilutions starting from 1:1,000 to 1:1,28,000. Assay blanks were included in the plate as a control. All incubation conditions, numbers of washes, buffers, and instrument settings used were the same as those used for the pentaplex assay (**Section 3.1.5**).

3.1.3 Verification of assigned unitages using commercially available assays

Commercially available Conformité Européenne (CE)-certified ELISA assay kits (IBL, USA, and Euroimmun, Germany) were used to confirm the unitages assigned to all the antigens in MRS. ELISA assays were performed for the PT, FHA, PRN, DT, and TT antigens. The IBL ELISA kits (PRN, DT, and TT) contained the calibrators and positive and negative controls. The WHO standards 06/142, 10/262, and TE-3 were used as test serum samples. The assays were performed as per the manufacturer's instructions. The samples were diluted from 1:100 to 1:12,800, added to the pre-coated plate, and incubated for 1 h at 37°C. Following this, 100 µL of enzyme conjugate (peroxidase-labeled anti-human IgG) was added to each microplate well. This mixture was incubated for 30 min at room temperature and washed thereafter. A volume of 100 µL of chromogen/substrate solution was added to each of the microplate wells. This was incubated for 15 min at room temperature, following which 100 µL of stop solution was added. The optical density (OD) was read at 450 nm using the Biotek ELISA reader (USA). The OD values within the linear part of the curve were converted to IU/mL by interpolation from a four-parameter logistic (4-PL) standard curve.

The Euroimmun (PT, FHA) ELISA test kit was used for the *in vitro* quantification of human antibodies of the IgG class in serum. In the first reaction step, diluted samples were incubated in the wells, and positive samples contained specific IgG antibodies bound to the antigens. A second incubation was carried out using an enzyme-labeled anti-human IgG (enzyme conjugate), catalyzing a color reaction to detect the bound antibodies. Photometric measurement of the color intensity was conducted at a wavelength of 450 nm and a reference wavelength between 620 nm and 650 nm and read within 30 min of the stop solution being added. The results of this assay were compared with those of the bead-based assay.

3.1.4 Unitage confirmation at the National Institute for Biological Standards and Control laboratory

For characterization, MRS was also tested at the National Institute for Biological Standards and Control (NIBSC) laboratory using conventional ELISA assays for PT, FHA, PRN, DT, and TT. For PT, FHA, and PRN, after each step, plates were washed with PBS (pH 7.4) containing 0.05% v/v Tween 20 (phosphate-buffered saline solution with Tween 20, PBST), and all incubations, unless otherwise specified, were carried out at room temperature. Briefly, 96-well ELISA plates (Nunc MaxiSorp, Thermo Fisher Scientific, USA) were coated with 100 µL of two µg/mL solution of either PT (NIBSC in-house), FHA (NIBSC JNIH-4) or PRN (NIBSC 18/154) in carbonate buffer (pH 9.5 containing 0.035 M sodium hydrogen carbonate, 0.015 M sodium bicarbonate, and 7.4 mM sodium azide) per well overnight. Plates were blocked with 100 µL of PBST containing 10% fetal bovine serum (FBS) for 1 h, followed by incubation with samples and reference (WHO reference reagent 06/142) at a starting dilution of 1:100 in blocking buffer for 1.5 h. Two-fold serial dilutions were performed using a blocking buffer as the

diluent. Following this, antigen-specific IgG antibodies were detected with 100 µL of rabbit anti-human IgG labeled with horseradish peroxidase (Sigma, A-8792), diluted at 1:2,000 in a blocking buffer for 1.5 h. Finally, 100 µL of 1% 3,3′,5,5′-tetramethylbenzidine (TMB) substrate (Sigma, T-2885) in dimethyl sulfoxide (DMSO) and 0.03% hydrogen peroxide (Sigma, H1009) in acetate buffer (pH 6.0) was added and color was developed for 15 min, after which 50 µL 1M sulfuric acid was added to stop the reaction. The OD was measured at 450 nm using a Multiskan ELISA plate reader (Molecular Devices, UK). Antibody responses for the MRS were calculated relative to the WHO reference material by parallel line analysis (log OD vs. log dose), using a minimum of three sequential points from the linear section of the dose–response curves and expressed in IU/mL.

For DT and TT, ELISA plates were coated overnight at 4°C with either 100 µL per well of DT (NIBSC 13/212, 3.7 flocculation units/mL) or 100 µL per well of TT (NIBSC 02/126, 0.5 flocculation units/mL) diluted in carbonate buffer (0.05 M, pH 9.6). The ELISA plates were washed three times with PBST and blocked with 150 µL of PBST containing 5% (w/v) dried skimmed milk powder (PBSTM-5%) for 1 h at 37°C. Following a second wash in PBST, serial two-fold dilutions of the WHO reference material (10/262 for diphtheria ELISA and TE-3 for tetanus ELISA) and MRS in PBSTM-1% were prepared in the plate (final volume 100 µL), and the plates were incubated at 37°C for 2 h. Plates were washed as described previously, and antigen-specific IgG antibodies were detected using a horseradish peroxidase-conjugated rabbit anti-human IgG antibody (Sigma, A-8792) diluted 1:2,000 in PBSTM-1%. After incubation for a further 1 h at 37°C and a final wash, 100 µL per well of substrate solution containing 0.5 mg/mL 2,2′-azino-bis (3-ethylbenzthiazoline-6-sulfonic acid) diammonium salt (ABTS, Sigma A9941) and 0.008% hydrogen peroxide (Merck, 107209) in 0.05 M citric acid buffer (pH 4.0) was added, and this mixture was allowed to develop for up to 30 min. The OD was measured at 405 nm using a Multiskan ELISA plate reader (Molecular Devices, UK). Antibody responses for the MRS were calculated relative to the WHO reference material. Analysis of variance was used to determine if there was any significant deviation from the linearity or parallelism of the dose–response relationship ($p < 0.01$).

The unitages were compared against the acceptance criteria of assigned unitages of MRS within a 30% variability margin that was attributed to the use of different assay platforms, antigens, and inter-laboratory variations.

3.1.5 Pentaplex immunoassay

The MRS (mix of 06/142, 10/262, and TE-3) was prepared as detailed in Section 2.3 and was used as an assay calibrator. The MRS was serially diluted two-fold from 1:333 to 1:42,624. The test sera samples were diluted serially two-fold from 1:100 to 1:12,800 using Luminex assay buffer and tested at multiple dilutions. The filter plate was used for the assay. The multivalent beads were added in each well at 50 µL/well (~ 4,000 beads per well) and aspirated. From the dilution plate, 50 µL of reference standard and samples were transferred in duplicate to the filter plate, incubated in the dark for 60 min at 37°C, and shaken at 150 rpm. The plate was aspirated and washed thrice with 100 µL assay buffer. To each well, 50 µL of a 1:100 diluted R-PE goat anti-human antibody was added, incubated in the dark for 30 min at 37°C, and shaken at 150 rpm. The plate was aspirated and washed thrice with 100 µL Luminex assay buffer, and the microspheres were resuspended in 100 µL assay buffer. The assay blank and IQCs were run in each plate. The plate was read in the Protein Suspension Array System (Bioplex-200). The reference standard's backfit of 70%–130%, percentage coefficient of variation (% CV) of ≤ 20%, and IQCs acceptance criteria were used as system suitability criteria.

3.1.6 Toxin neutralization assays

A toxin neutralization assay ($n = 3$) was performed to verify the ability of antibodies in the serum samples to neutralize active pertussis and diphtheria toxins. The Chinese hamster ovary (CHO) cell-clustering assay based on the induction of clusters in non-confluent CHO cell cultures by aP toxin was performed to assess toxin neutralization. Serially diluted sera samples were incubated with a known concentration of toxins at 37°C for 60 min. After incubation, CHO cells with a concentration of 3×10^4 cells/mL were added to all wells of the antigen–antibody mixture, and the plates were incubated at 37 ± 1°C for approximately 48 h. Following this, CHO cells were observed for clustering under an inverted microscope. The highest dilution of sera, which showed cluster neutralization, was recorded as the sample titer. A positive score was assigned when 10 or more CHO cell clusters were evident within a single well (30).

The Vero cell assay has been used to determine the protective level of diphtheria antitoxin in human sera (31). The metabolic activity and survival of Vero cells in cultures are inhibited by diphtheria toxin, and diphtheria antitoxins may neutralize this effect of the toxin in serum samples. Titration of serum samples on Vero cells in the presence of fixed amounts of diphtheria toxin was carried out in three independent assays ($n = 3$). Reading of the Vero assay was based on a microscopic examination of cells to determine the color change in the wells of microtiter plates from red to yellow due to the metabolic formation of acid. To prepare diphtheria toxin, serum dilutions were prepared in a microtiter plate in minimum essential medium (MEM) supplemented with 10% FBS. Diphtheria toxin at a lethal tissue culture (LTC) dose of 100 was added and incubated for 45 min to 1 h at room temperature (20–25°C) for toxin neutralization. We prepared a Vero cell suspension containing 3.5–4.5 × 10^5 cells/mL, added 100 µL to the 96-well microtiter plates, incubated for 5 days at 36 ± 1°C under 5% CO_2 atmosphere, and then observed the cells to determine if metabolic inhibition caused by a non-neutralized toxin had occurred. A Vero cell assay was performed to determine the neutralization of diphtheria toxin. Fixed sera dilutions of diphtheria toxin were prepared and the titer of the serum sample was calculated by comparing the test results with standard diphtheria antiserum. A factor of the highest dilution, showing metabolic inhibition, was multiplied by 0.2 (limit of detection of this method) to report the results in IU/mL.

3.2 Assay validation

The assay was validated based on the FDA, EMA, and ICH M10 guidelines for bioanalytical methods.

3.2.1 Assay specificity

Assay specificity was evaluated in three different runs by (a) inhibition experiments and (b) comparing the MFI difference between the multiplex assay (five antigens simultaneously) and monoplex assay (each antigen individually). For inhibition experiments, MRS was incubated independently with each purified antigen (PT, FHA, PRN, DT, and TT) and with a mixture of all five antigens (PT + FHA + PRN + DT + TT) for 1 h before analysis. The percentage reductions in MFIs due to purified antigens (specific antigens) and a mix of antigens were compared to determine assay specificity.

3.2.2 Assay selectivity

The method's selectivity was evaluated in three independent runs using three human serum matrices: (i) matrix 1—non-vaccinated sera (panel 2; samples 1–6), (ii) matrix 2—hemolytic and lipemic matrix (panel 3; samples 1–2), and (iii) matrix 3—antibody-depleted human sera (panel 4; sample 1) as mentioned in Table 2. These matrices are representative of negative or low-concentration sera. Matrices 1 and 2 were spiked with different concentrations of reference standard and tested at concentrations of 1:400 (high), 1:6,400 (medium), and 1:12,800 (low). Matrix 3 was spiked with the MRS and IQC. Recovery of spiked samples from the different matrices was calculated with the acceptance criteria within the range of 70%–130% of expected concentrations.

3.2.3 Precision

The assay precision was evaluated over 3 days and six runs for different analysts, days, and lots of coupled beads and phycoerythrin (PE) (Table 2, Panel 1). Intra-assay precision refers to the variability observed for the same day. Inter-assay precision refers to the variability in experiments performed on different days by different analysts using different lots of beads and PE lots. The assay precision was reported in terms of the % CV.

3.2.4 Accuracy

Accuracy was assessed over 3 days and six runs using a panel of sera samples (Table 2, Panel 1). These samples were tested at different concentrations in six assays spread over 3 days using three different bead lots and read by two analysts. The estimates were compared with the assigned unitages to determine the accuracy. The resulting IgG concentration of each serum sample was calculated and compared with the assigned values, with an acceptance criterion of recovery of between 70% and 130%.

3.2.5 Dilution linearity

Dilution linearity was evaluated in three different runs using panel 5 (Table 2). Assay dilutability was assessed in three independent runs, using two-fold dilutions starting from 1:100 until the serum sample was quantifiable. Recovery was calculated as a percentage difference between the observed and assigned concentrations. Linearity was considered acceptable if said dilution complied with an acceptable % CV of duplicates (i.e., < 20%) and if the dilution-corrected concentrations were within 70%–130% of the assigned values.

3.2.6 Assay range

The reference standard for the determination of the assay range was evaluated in six runs by two-fold serial dilutions of the MRS from 1:333 to 1:42,624. The assay range for each antigen was determined using estimates from precision, accuracy, and dilution linearity, after which the most stringent lower and upper concentration limits complying with acceptable accuracy (70%–130%) and precision (< 20% CV) and dilutional accuracies of between 70% and 130% were selected. The assay range was also supported by back-calculated concentrations of calibration standards. The back-calculated concentrations were to be within 70%–130%.

3.2.7 Limit of detection and limit of quantification

The limit of detection (LOD) and limit of quantification (LOQ) for each of the five antigens were determined in three runs using curve-fitted MFI at the minimum detectable response (i.e., a three-fold increase in the minimum baseline response) and minimum quantifiable response (i.e., a five-fold increase in the minimum baseline response).

3.2.8 Robustness

Robustness data on IQCs concerning incubation time, temperature, bead lot, and PE lots were assessed. Five IQCs were used to analyze robustness and results were used to estimate the % CV for each parameter tested. The % CV of observed vs. estimated concentrations concerning deliberate parameter variations was assessed. The following parameters were studied during the robustness assessment: assay step 1 and step 2 incubation times, temperature, different lots of secondary antibodies (PE lots), and beads. Both step 1 (incubation with beads; 50–70 min) and step 2 (incubation with PE; 20 to 40 min) incubation time assays and primary and secondary incubation temperatures (32–42°C) were evaluated. Two different PE lots and bead lots were also evaluated for robustness.

3.2.9 Stability study

The stability of the serum samples, MRS, and IQCs from Panel 6 was monitored at 25°C and 2–8°C. Serum samples were assessed for stability at 25°C for up to 72 h and at 2–8°C for up to 168 h. Freeze–thaw stability was evaluated at –20°C for serum samples and MRS (Table 2, panel 7). The samples were aliquoted and exposed to freeze–thaw cycles wherein the sera samples were thawed for 2 h by placing the samples at room temperature (i.e., no higher than 25°C). Later, sera samples were frozen for 24 h at –20°C before thawing. The percentage differences between assigned and observed concentrations were determined for the stability study. The impact of freeze–thaw cycles was evaluated with an acceptance criterion of ± 30% difference relative to the assigned concentrations.

3.2.10 Solution stability

The reference standards and the IQCs from panel 8 (Table 2) were used to evaluate the solution stability. The solution stability of the assay was determined by analyzing the assay plates at pre-determined intervals of 0, 6, 8, 12, and 24 h. The results obtained

atdifferent intervals were compared with the precision study set to determine the hold time of the plate with the acceptance criteria of ≤ 20%.

3.2.11 Edge effect

The edge effect was evaluated in three runs using the assay control. IQC 3 was placed in each well of the 96-well filter plate. The % CV of MFIs was calculated for the 96-well plate, with an acceptance criterion of % CV ≤ 20 for all antigens.

3.2.12 Statistical analysis

A log/log-linear regression model was used to fit the reference standard curve. Calibration curves were generated using the 4-PL logistic fit; the values for back-fitted recoveries were set between 70% and 30%, and the % CV values were set at ≤ 20%. At least 75% of the calibration standards, or a minimum of six standards, had to meet these criteria. Statistical analyses were performed using Microsoft Office Excel 2019 and statistical software GraphPad Prism 7.05. The results generated by MIA were compared with sera neutralization assays using linear regression analysis in Microsoft Office Excel 2019.

The following formula was used for method validation parameters:

The percentage recovery for selectivity assessment was calculated as follows:

$$(observed\ \ concentration\ \ of\ \ spike\ \ sample - observed\ \ concentration\ \ of\ \ unspiked\ \ sample) \div expected\ \ concentration \times 100$$

The following equations were used to calculate MFI for the determination of LOD and LOQ:

$$Minimum\ \ detectable\ \ response = average\ blank\ \ human\ \ serum\ \ MFI + (3 \times SD\ \ of\ \ blank\ \ serum\ \ MFI)$$

$$Minimum\ \ quantifiable\ \ response = 5 \times (MFI\ \ at\ \ minimum\ \ detectable\ \ response)$$

The lowest quantifiable response was multiplied by 200 (minimum two sera dilutions, i.e., 100 and 200) to obtain the LOQ in IU/mL.

4 Results

4.1 Assay development

4.1.1 Optimization of bead coupling procedures

Luminex-based MIA involves using beads (microspheres) with different fluorochromes detected in unique wavelength regions using a particular instrument known as Luminex-200. Targeted proteins are coupled onto these beads following a specific conjugation procedure. We previously reported the optimized conditions for connecting these antigens, wherein two coupling methods were optimized, namely, EDAC/Sulfo-NHS using the Luminex cookbook, and the AMG kit from AnteoTech. A similar procedure was used in this study (13). A coating concentration of 10 µg/mL for PT, FHA, PRN, DT, and TT antigens was used in the study. In this study, coupling procedures were further evaluated concerning performance in the human serum matrix. Suitability was assessed, wherein for each bead set, MRS (positive for all five antigens) was used to generate a standard curve (eight serial dilutions; two-fold) and at each point, the MFI was assessed to demonstrate the linearity across titrations. The coating concentration of 10 µg/mL was found to be suitable, as a good dynamic range of 1:100 to 1:42,624 of MRS was observed for all five antigens. We also evaluated the incubation time (beads with sera) for all five antigens. It was noted that an incubation time of 1 h was suitable, ensuring that a good signal-to-noise ratio was achieved for all five antigens. Luminex assay buffer was optimized to work with a minimum sera dilution of 1:100. The use of Luminex assay buffer with a composition of 1% BSA, 0.2% sodium azide, 0.1% Tween 20, and PBS was conducive to optimal assay performance. The optimized coating concentrations were further evaluated for possible interference by comparing the MFIs of mono and multiplex conditions using human sera. MFIs were comparable: a ≤ 20% difference in % CV was observed, supporting their suitability for use in MIA. Bead cross-reactivity was also assessed using inhibition experiments, wherein the percentage reductions in MFIs were noted against individual antigens as compared with positive uninhibited control. All beads achieved a homologous inhibition of over 85%, which further indicates the suitability of the coupling procedures used in the assay (Figure 3).

4.1.2 Characterization of WHO reference standards for the development of MRS

MRS represents an equimolar mixture of three WHO reference standards. WHO reference standards are serum preparations (high titers) that are sourced from vaccinated healthy volunteers. The unitages of these reference standards are assigned based on multiple global inter-laboratory studies and are more suited to calibrating single antigen immunoassays. An MIA being carried out in a single well requires a reference standard that could provide unitages against all five antigens. Previous studies have used in-house reference standards using sera samples from clinical studies. This study reports on the development of MRS using international standards, as the sourcing of clinical samples in sufficient quantities may not be feasible for all laboratories. The development of MRS was carried out using the approach outlined in Figure 1. The approach comprises three major steps. The first step is the screening study. The objective of the screening study is to evaluate proposed reference standards for the presence of antibodies against other antigens. This is important as these reference standards are sourced from vaccinated volunteers and most vaccines are combination vaccines. Therefore, even though the reference standard provides unitages for a specific antigen, the sera may also be positive for other antigens in the panel.

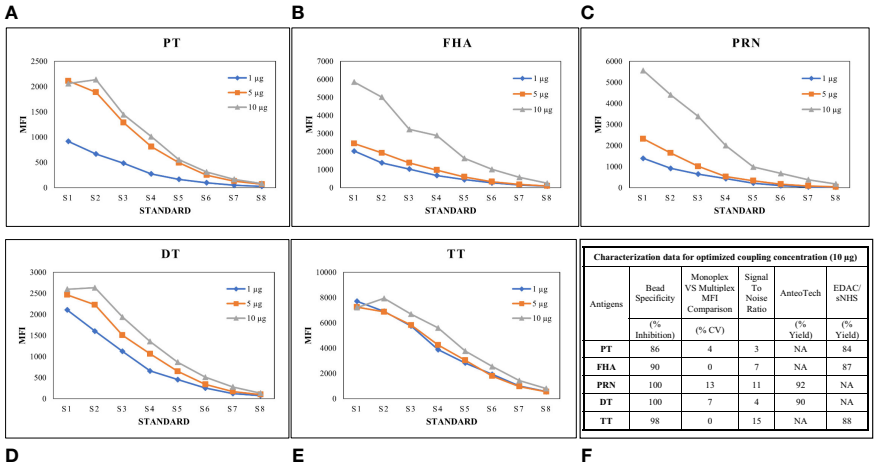

Characterization data for optimized coupling concentration (10 µg)					
Antigens	Bead Specificity	Monoplex VS Multiplex MFI Comparison	Signal To Noise Ratio	AnteoTech	EDAC/ sNHS
	(% Inhibition)	(% CV)		(% Yield)	(% Yield)
PT	86	4	3	NA	84
FHA	90	0	7	NA	87
PRN	100	13	11	92	NA
DT	100	7	4	90	NA
TT	98	0	15	NA	88

FIGURE 3
Optimization of Bead coupling procedures. **(A–E)** represents dilution vs MFI graphs at three different beads coupling concentrations for PT, FHA, PRN, DT and TT antigens. 10ug/ml concentration was found optimum for all the antigens. **(F)** represents the characterization data of bead coupling at 10ug/ml with respect to suitability parameters of bead specificity, signal to noise ratios, yields and MFI comparisons. DT, Diphtheria Toxoid; FHA, Filamentous haemagglutinin; MFI, Mean fluorescence intensity; PRN, Pertactin; PT, Pertussis Toxin; TT, Tetanus Toxoid; S17ndash;S8, Standards.

For example, TE-3 provides unitages for tetanus antibodies; however, the sera were also positive for antibodies against PT, FHA, PRN, and diphtheria. This is expected as vaccines containing tetanus antigens are combination vaccines that also include pertussis and diphtheria antigens. Table 3 provides the results of the screening study for all the WHO reference standards. These results will be important for all the laboratories working on multiplex immunoassays. In the second step, based on the results of the screening study, MRS was established and unitages were assigned. The unitages assigned to the MRS using data from six independent runs are provided in Table 4. In the third step, the assigned unitages to international reference standards and the MRS for all five antigens were also verified using commercially available ELISA assays. These commercially available assays report the unitages traceable to the specific international reference standard. Table 5 provides the comparative assessment of unitages assigned by bead-based assay and commercially available methods. The unitages by bead-based assay were in good agreement with the commercial ELISA assays, as the variabilities of all unitages were ≤ 20%. In addition, the MRS was also sent to NIBSC for characterization studies, and the results of these indicated that there was excellent agreement (Table 6) between the NIBSC estimates and the multiplex assay estimates, as all the estimates were within the acceptable % CV range of ≤ 20%. NIBSC laboratories used the conventional monoplex plate-based ELISA method to confirm the unitages provided by MIA, which further supports the concordance of the MIA with conventional monoplex ELISA assays.

4.1.3 Reference standard curve for MIA

MRS serum with assigned IgG antibody concentrations for all five antigens, as indicated in Table 4, was used for the optimization of the reference standard curve. In any MIA, the reference standard curve should be optimized to cover a broad concentration range for all the antigens included in the MIA. Overall, eight separate two-fold dilutions of the MRS were performed and were fitted using a 4-PL fit. Figure 4 shows the reference standard serum dilution profiles for each of the five antigens. Linearity of response was demonstrated using back-fitted recoveries, and all five antigens showed 80%–120% recoveries for all calibration levels. MRS covered a maximum possible concentration range of 2.63–336 mIU/mL for PT, 4.67–598 mIU/mL for FHA, 3.86–494 mIU/mL for PRN, 0.03–4 mIU/mL for DT, and

TABLE 3 Characterization of WHO reference standards for development of multiplex reference standard.

WHO reference Standard	IU/ml				
	PT	FHA	PRN	DT	TT
06/142	**100.70 (95%)**	**116.99 (96%)**	**36.75 (94%)**	0.18	2.16
10/262	70.57	117.22	155.02	**1.94 (97%)**	11.47
TE-3	164.61	363.42	301.85	1.88	**117.18 (98%)**
13/240	153.25	262.64	202.13	6.55	**40.55 (90%)**

WHO reference standards were screened for IgG antibodies against PT, FHA, PRN DT, and TT using a bead-based assay. Values in bold indicate the observed concentrations, and values in parenthesis indicate their percentage agreement with the official unitages.
DT, diphtheria toxoid, FHA, filamentous hemagglutinin; IU/mL, international units per milliliter; PRN, pertactin, PT, pertussis toxin; TT, tetanus toxoid; WHO, World Health Organization.

10.3389/fimmu.2023.1190404

TABLE 4 Assigned unitages of multiplex reference standard.

Antigen	Assigned unitage (IU/ml)	%CV
PT	111.96	**14**
FHA	199.21	**15**
PRN	164.54	**18**
DT	1.333	**9**
TT	43.60	**3**

Multiplex reference standard is an equimolar mixture of TE-3, 10/262, and 06/142. Based on the screening study, unitages were assigned to MRS. Values are a representation of mean IU/mL (N = 6 assays). Values in bold indicate the % CV of six assays.
% CV, percentage coefficient of variation; DT, diphtheria toxoid, FHA, filamentous hemagglutinin; IU/mL, international units per milliliter; MRS, multiplex reference standard; PRN, pertactin, PT, pertussis toxin; TT, tetanus toxoid.

1.02–131mIU/mL for TT (Table 7). The lower limit (LL) and upper limit (UL) of the assay range were determined using estimates from accuracy, precision, and dilution linearity analysis (Table 7).

4.2 Assay validation

The MIA was validated for specificity, selectivity, precision, accuracy, dilutability, LOQ, and stability using sera samples from vaccinated volunteers. The validation study design was based on the FDA, EMA, and ICH M10 guidelines for bioanalytical methods.

4.2.1 Assay specificity

Specificity was demonstrated by (a) inhibition experiments and (b) comparing the MFI difference between the monoplex and multiplex assays. The MFI response (percentage difference) in monoplex and multiplex format was observed at < 10% for all five antigens (Table 8), which showed that there was no cross-reactivity between the beads. For inhibition experiments, the percentage inhibition of MFI of a positive serum sample following the addition of either an individual antigen or a mixture of antigens was assessed for all five antigens. The concentration of antigens used for the inhibition experiments was 2.62 µg for all five antigens. The addition of homologous antigens, either individually or in a mixture, resulted in an > 85% inhibition of signal for PT, PRN, FHA, DT, and TT antibodies (Table 8), indicating the high specificity of the assay in capturing the respective antibodies in the serum sample.

4.2.2 Assay selectivity

The selectivity of the method was evaluated with respect to the use of different serum matrices for hemolytic, lipemic, non-vaccinated, and antibody-depleted sera. The assay high selectivity, as excellent spike recoveries (80%–120%) were observed in all the matrices (Table 9). No interference was observed in the assay for hemolytic and lipemic matrices covering up to 2.02 g/dL of hemoglobin and 275 mg/dL of total cholesterol, respectively.

4.2.3 Precision

Precision analysis suggested that the assay was precise for different analysts on different days using different lots of beads

TABLE 5 Characterization of WHO reference standards using commercially available ELISA kits and percent agreement with MIA.

Samples	PT			FHA			PRN			DT			TT		
	Bead Based Assay	ELISA	% Agreement	Bead Based Assay	ELISA	% Agreement	Bead Based Assay	ELISA	% Agreement	Bead Based Assay	ELISA	% Agreement	Bead Based Assay	ELISA	% Agreement
06/142	101	115	**88**	117	108	**108**	37	43	**85**	0.2	0.2	**89**	2	2	**108**
10/262	71	61	**116**	117	106	**111**	155	146	**106**	1.9	1.7	**114**	11	14	**82**
TE-3	165	151	**109**	363	317	**115**	302	260	**116**	1.7	1.4	**135**	117	147	**80**
13/240	153	145	**106**	263	272	**97**	202	191	**106**	6.6	5.9	**112**	41	44	**93**

The bead-based assay showed excellent agreement with the commercially available assay. Values in bold indicate the percentage agreement between bead-based monoplex assays and commercially available ELISA assays.
DT, diphtheria toxoid; ELISA, enzyme-linked immunosorbent assay; FHA, filamentous hemagglutinin; MIA, multiplex immunoassay; MRS, multiplex reference standard; PRN, pertactin; PT, pertussis toxin; TT, tetanus toxoid.

TABLE 6 Verification of assigned unitages of MRS using commercial, NIBSC, and multiplex assays.

Antigen	SIIPL Bead-Based Assay (IU/ml)	NIBSC ELISA Assay (IU/ml)	Commercial ELISA kit (IU/ml)	%CV
PT	112	122	134	**9**
FHA	199	169	201	**9**
PRN	165	119	174	**19**
DT	1.33	1.30	1.19	**6**
TT	44	43	47	**5**

%CV, percentage coefficient of variation; DT, diphtheria toxoid; ELISA, enzyme-linked immunosorbent assay; FHA, filamentous hemagglutinin; IU/ml, international units per millilitre; NIBSC, National Institute for Biological Standards and Control; PRN, pertactin; PT, pertussis toxin; SIIPL, Serum Institute of India, Pvt, Ltd; TT, tetanus toxoid; Values in bold indicates the %CV of three assays (Bead-based, commercial and NIBSC).

and PE. The % CV for the combined precision of the two analysts was below 20% for all five antigens (Table 10). Based on the data, the precision-based LLs and ULs ranged from 6.9 to 221 mIU/mL for PT, 14.3 to 457 mIU/mL for FHA, 13.3 to 424 mIU/mL for PRN, 0.11 to 3.4 mIU/mL for DT, and 3.8 to 121.7 mIU/mL for TT (Table 7).

4.2.4 Accuracy

Acceptable recoveries were observed within the range of 80%–120% for PT, FHA, PRN, DT, and TT antigens (Table 10). The accuracy-based LLs and ULs ranged from 6.9–221 mIU/mL for PT, 14.3–457 mIU/mL for FHA, 13.3–424 mIU/mL for PRN, 0.11–3.4 mIU/mL for DT, and 3.8–121.7 mIU/mL for TT (Table 7).

4.2.5 Dilution linearity

The panel samples were tested in three independent runs across a series of sera samples ranging from a dilution of 1:100 to 1:681,984. No loss in dilution integrity was observed, with a two-fold increase in the dilution range recorded for all antigens (Figure 5).

4.2.6 Assay range

The assay range was selected based on the estimates from precision, accuracy, and dilutional linearity study sets. The LL and UL of the assay range were established as ranging from 2.63 to 336 mIU/mL for PT, 4.67 to 598 mIU/mL for FHA, 3.86 to 494 mIU/mL for PRN, 0.03 to 4 mIU/mL for DT, and 1.02 to 131 mIU/mL for TT. The LL of an assay range was the lowest concentration that showed acceptable precision, accuracy, and dilution linearity in the experiments (Table 7).

4.2.7 Robustness

The robustness of the assay was studied using IQCs covering the entire assay range. The critical assay parameters studied included incubation time with beads, incubation time with PE, incubation temperature of beads and PE, different lots of PE, and different bead lots. The % CV of observed versus expected concentrations was calculated for each IQC. The results demonstrated that concentrations of IQCs generated from the assays with deliberate variations were within the acceptable range of < 20% variability for all the antigens (Table 11).

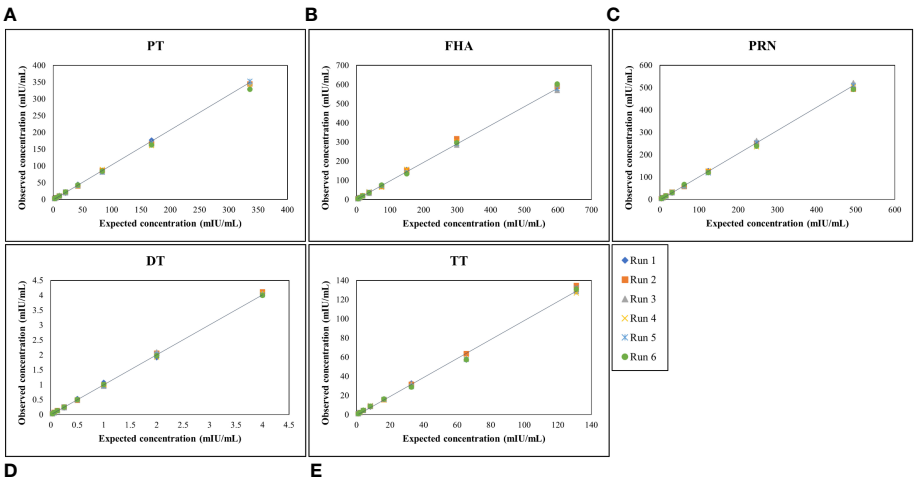

FIGURE 4
Dynamic range of MRS for each antigen. **(A–E)** represents the assay range of MRS for five antigens. The X-axis represents expected concentration (mIU/mL) whereas Y-axis represents obtained concentration (mIU/mL.). Data is representative of 6 runs. DT, Diphtheria Toxoid; FHA, Filamentous haemagglutinin; PRN, Pertactin; PT, Pertussis Toxin; TT, Tetanus Toxoid.

TABLE 7 Final assay range with a lower and upper limit of quantification.

Antigen	Precision (mIU/ml)		Accuracy (mIU/ml)		Dilutional linearity of sample (mIU/ml)		Dilutional linearity of standard (mIU/ml)		Calibration Curve range (mIU/ml)	
	Lower limit	Upper limit	Lower limit	Upper Limit	Lower limit	Upper limit	Lower limit	Upper limit	Lower Limit	Upper limit
PT	6.9	221	6.9	221	**2.63**	336	0.16	336	2.63	336
FHA	14.3	457	14.3	457	**4.67**	598	0.29	598	4.67	598
PRN	13.3	424	13.3	424	**3.86**	494	0.24	494	3.86	494
DT	0.11	3.4	0.11	3.4	**0.03**	4	0.003	4	0.03	4
TT	3.8	121.7	3.8	121.7	**1.02**	131	0.06	131	1.02	131

DT, diphtheria toxoid; FHA, filamentous hemagglutinin; PRN, pertactin; PT, pertussis toxin; TT, tetanus toxoid; mIU/ml, Milli-international unit per milliliter.
Data is representative of estimates in precision, accuracy, and dilution linearity validation parameters. Precision, accuracy, and dilution linearity estimates to support calibration curve range. Values highlighted in bold were used to estimate the lower limit.

4.2.8 Stability studies

Stability studies included assessment at different conditions including room temperature, 2–8°C and freeze–thaw (–20°C). The IQC and sera samples were found to be stable for up to 72 h and 168 h at room temperature and 2–8°C, respectively. In the freeze–thaw study, sera samples were found to be stable for up to 20 freeze–thaw cycles (Supplementary material, Figure S1, Figure S2).

4.2.9 Solution stability

The results of analyzing assay plates at predetermined intervals of 0, 6, 8, 12, and 24 h suggest that a plate hold time of under 12 h would be suitable, as we observed an impact on PRN antigens after 12 h of plate hold time (Supplementary material, Figure S3).

4.2.10 Edge effect

No variability was noted in the wells and all the MFIs were within the acceptable variability of 10% CV (Table 11).

4.2.11 Correlation with sera neutralization assays

PT and DT are major virulence factors of *Bordetella pertussis and Corynebacterium diphtheriae*, respectively. Toxin neutralization assays using CHO and Vero cells for PT and DT were used to measure neutralization antibodies. These *in vitro* cell-based assays measured the functional antibodies. Ten serum samples were analyzed for correlations of results obtained with the MIA. Estimates exhibited positive correlations among the assays with correlation coefficients above 0.75 for both antigens (Figure 6).

5 Discussion and conclusion

The assessment of serum IgG responses to the antigens present in the aP-based combination vaccines has been reported mainly using conventional ELISA tests or commercial kits (7, 32). Such ELISA methods are expensive, time-consuming, and, most importantly, require considerable volumes of sera (33). Our study demonstrates an MIA for multiple applications, including serosurveillance and monitoring of vaccine immune responses. MIAs such as Luminex x-MAP® and Meso Scale Diagnostics offer opportunities by providing rapid procedures for the simultaneous quantification of antibodies to multiple antigens with high sensitivity and selectivity using minimal amounts of sera samples. Luminex technology is based on the use of beads that facilitate the measurement of various analytes from a single sample (34). The beads are color-coded microspheres that contain different proportions of red and infrared fluorophores. These beads, when activated at a specific light spectrum, aid in the quantification of the analyte. Luminex technology allows for the use of both non-magnetic and magnetic beads. The use of magnetic beads in the assay was shown to have a high coupling efficiency and higher reproducibility due to lower inter-assay variation (35). In our study, we used magnetic beads for coupling the antigens and observed

TABLE 8 Specificity of assay.

Antigen	MFI difference monoplex vs. multiplex	Inhibition	
	Difference (%)	Monoplex Inhibition (%)	Multiplex Inhibition (%)
PT	1	88	87
FHA	1	91	90
PRN	8	99	100
DT	8	99	100
TT	-1	99	99

DT, diphtheria toxoid; FHA, filamentous hemagglutinin; MFI, mean fluorescence intensity; PRN, pertactin; PT, pertussis toxin; TT, tetanus toxoid.

10.3389/fimmu.2023.1190404

TABLE 9 Selectivity assessment in different matrices (Panel 2-4).

Panel No.	Samples	Reference Standard Spike Level	Spike % Recovery				
			PT	FHA	PRN	DT	TT
Panel 2	Sample 1	High	97	101	98	97	101
		Middle	95	103	95	95	91
		Low	95	122	98	103	96
	Sample 2	High	92	93	91	91	95
		Middle	89	88	104	92	82
		Low	93	92	113	100	91
	Sample 3	High	98	102	97	97	104
		Middle	97	97	96	108	101
		Low	94	97	93	120	108
	Sample 4	High	92	95	91	91	95
		Middle	100	89	98	95	94
		Low	108	92	107	112	102
	Sample 5	High	105	107	99	101	105
		Middle	85	95	90	100	94
		Low	91	112	97	113	97
	Sample 6	High	100	106	103	100	110
		Middle	96	92	105	108	73
		Low	105	106	118	127	92
Panel 3	Sample 1	High	97	96	93	95	103
		Middle	94	95	92	97	108
		Low	97	100	95	108	125
	Sample 2	High	99	101	94	96	102
		Middle	102	104	98	107	113
		Low	100	114	104	125	131
Panel 4	Sample 1	IQC 1	111	107	104	104	92
		IQC 2	107	99	87	96	83
		IQC 3	100	105	97	97	83

DT, diphtheria toxoid, FHA, filamentous hemagglutinin; IQC, internal quality control; Panel 1, Panel for precision and accuracy; Panel 2, Panel for selectivity parameters; Panel 3, Hemolytic lipemic sera; Panel 4, Blank human sera; PRN, pertactin; PT, pertussis toxin; TT, tetanus toxoid.
Selectivity was assessed using spike recovery experiments in different serum matrices.

high coupling yields and minimum interferences from the matrices. The reproducibility of the coupling method is an essential factor for ensuring the consistency of test results, especially those from larger clinical trials. Ruling out the impact of the conjugation method on antigen epitopes is one of the prerequisites for developing bead-based immunoassays. A study by van Gageldonk PG et al. (11) described using commonly used conjugation protocols for PT, FHA, PRN, DT, and TT antigens. The two commercially available conjugation procedures evaluated in our study (Luminex cookbook and AnteoTech kit) for coupling the antigens to the beads demonstrated assay specificity and linearity for all antigens. The specificity experiments involving inhibition assays using homologous antigen confirmed that antigenic epitopes were unaffected by the coupling process, as the addition of 2.62 µg/mL of antigen inhibited signaling by > 85%. The robustness of the conjugation process was further demonstrated using three different lots of coupled bead assays, which demonstrated good reproducibility. It has previously been reported that MIAs' improved performance and sensitivity are attributed to the control over the purity of antigens in the assays and the correlation of Luminex technology to single antigen ELISA using purified antigens (20). It was also noted that the purity of PT, FHA, and PRN antigens was critical to the assay. The in-house manufactured antigens with a purity of > 95% showed excellent

10.3389/fimmu.2023.1190404

TABLE 10 Precision and accuracy estimates.

Precision	*Analyst (% CV)					**Days (% CV)					***Bead Lot (% CV)				
	PT	FHA	PRN	DT	TT	PT	FHA	PRN	DT	TT	PT	FHA	PRN	DT	TT
Sample 1	12	10	11	12	10	10	10	13	12	11	9	10	13	16	8
Sample 2	8	8	9	5	7	8	7	11	11	11	5	5	8	11	8
Sample 3	11	10	11	11	8	16	14	17	15	18	14	12	7	13	18
Sample 4	7	9	8	5	13	15	10	12	13	18	9	8	15	13	15
Sample 5	12	11	9	7	3	11	8	16	11	12	6	3	6	14	8
Sample 6	7	10	9	6	1	12	9	17	13	13	7	11	11	12	8
Sample 7	5	8	9	8	8	12	13	11	10	11	10	10	10	9	9
Sample 8	7	9	10	6	14	12	15	12	11	14	7	15	4	5	6
Sample 9	4	5	5	7	13	11	10	10	10	11	8	7	7	6	6
Sample 10	7	6	7	7	10	11	6	8	7	14	9	4	6	7	19
Sample 11	6	10	6	7	6	10	11	8	8	9	9	12	7	7	7
Sample 12	7	8	7	7	8	10	10	9	8	8	8	8	7	6	6
Sample 13	10	10	8	10	8	11	11	10	10	9	10	8	8	8	7
Sample 14	11	13	11	15	13	11	14	12	14	12	8	11	9	15	9
Accuracy	*Analyst (% Recovery)					**Days (% Recovery)					***Bead Lot (% Recovery)				
Sample 1	96	102	106	98	104	91	98	99	96	100	92	96	97	99	102
Sample 2	94	97	111	91	102	91	91	102	90	95	91	88	96	94	95
Sample 3	107	100	101	103	118	105	97	89	98	110	99	89	84	92	100
Sample 4	86	92	91	90	112	89	90	87	96	101	90	90	85	95	95
Sample 5	99	94	106	96	108	96	94	100	104	106	95	93	92	109	107
Sample 6	104	109	106	110	112	100	106	97	106	104	99	103	88	96	99
Sample 7	93	99	101	101	106	92	94	96	99	102	92	93	90	96	103
Sample 8	100	106	104	111	110	90	95	95	102	99	83	90	90	96	95
Sample 9	99	104	92	92	97	90	94	87	86	93	85	92	86	84	92
Sample 10	92	106	93	98	93	101	110	96	95	96	100	111	93	94	93
Sample 11	90	106	93	100	83	96	109	96	96	88	97	108	95	97	87
Sample 12	91	95	95	101	86	98	96	97	98	92	98	99	98	101	90
Sample 13	89	91	94	104	94	96	94	96	98	93	93	93	96	100	88
Sample 14	90	94	94	102	97	95	98	100	98	94	100	100	100	100	100

Precision and Accuracy results are determined concerning different analysts, days, and bead lots. DT, diphtheria toxoid; FHA, filamentous hemagglutinin; PRN, pertactin; PT, pertussis toxin; TT, tetanus toxoid. Precision is determined in terms of % CV. Accuracy is reported in terms of % recovery. *Combined precision (% CV) and accuracy (% recovery) of analysts' 1 and 2, **Combined precision and accuracy of 6 runs over 3 days, ***Combined precision and accuracy of multiple bead lots.

results in the MIA. With tight control on the purity of target antigens and the use of magnetic beads, both coupling methods showed good agreement and were found to be suitable for the assay.

With the advent of MIA technologies and increasing regulatory expectations for validating clinical immunogenicity assays, multiplex assays must be validated against a recognized standard to provide uniformity and reproducibility. The NIBSC provided three reference standards, 06/142, 10/262, and TE-3, which had the unitages for aP, DT, and TT antigens. MIAs being carried out in a single well will require a reference standard that provides the unitages of all five antigens. As part of assay development, an equimolar mix of WHO reference standards was assessed as a possible reference standard for the multiplex assay. The characterization of the three reference standards demonstrated that all have a considerable number of antibodies that must be accounted for in an equimolar mix standard for the multiplex assay. The observed unitages of the MRS and other WHO standards were also verified at NIBSC, and an excellent agreement was observed. These unitages will provide opportunities

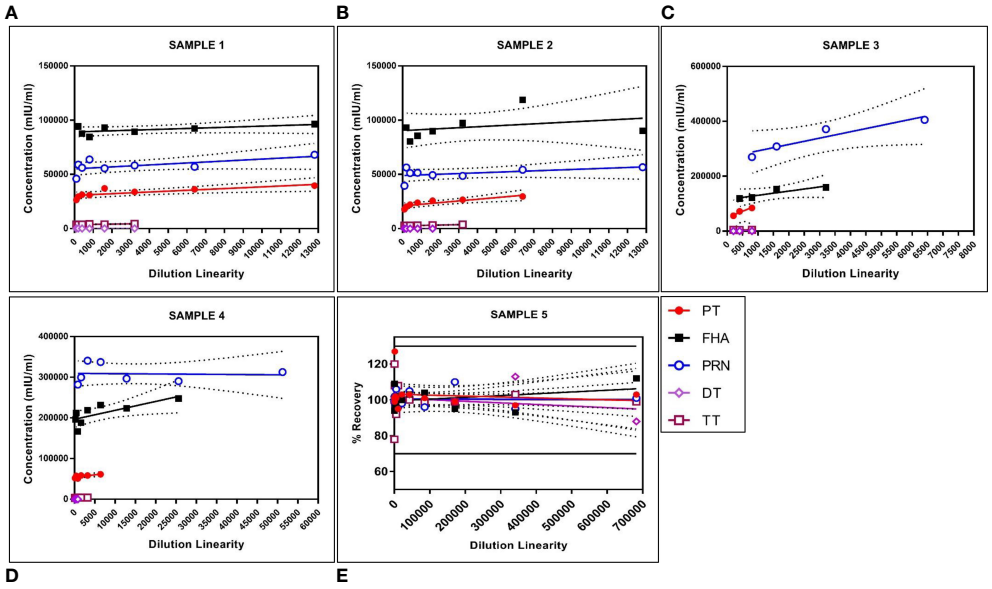

FIGURE 5
Dilution linearity of assay in high tire sera samples and MRS for PT, FHA, PRN, DT, and TT antigens. The X-axis represents the sample's dilutions, and the Y-axis represents the concentration observed in (mIU/ml). **(A–D)** represent dilution linearity graphs for high titer samples. **(E)** represents dilution linearity data for MRS. Sera samples and MRS shows no loss of dilution integrity over the dilution range. The dotted line in the figure represents the 95% confidence interval. DT, Diphtheria Toxoid; FHA, Filamentous Hemaagglutinin; MRS, Multiplex Reference Standard; PRN, Pertactin; PT, Pertussis Toxin; TT, Tetanus Toxoid.

TABLE 11 Assay robustness.

% CV											
Antigen	IQC	Step 1 Incubation Time		Step 2 Incubation Time		Incubation Temperature		Different PE Lots		Different Bead Lots	Edge Effect
		50 min	70 min	20 min	40 min	32°C	42°C	PE Lot 1	PE Lot 2	Bead Lot	
PT	IQC 1	6	10	4	3	2	5	3	1	9	NA
	IQC 2	9	7	2	6	3	9	7	4	9	NA
	IQC 3	6	8	5	6	1	1	4	0	8	5
	IQC 4	7	5	5	9	2	8	3	3	10	NA
	IQC 5	7	11	3	0	3	9	3	0	8	NA
FHA	IQC 1	6	2	4	7	13	8	9	10	4	NA
	IQC 2	0	12	3	5	4	1	8	3	12	NA
	IQC 3	1	16	2	4	4	1	1	8	8	5
	IQC 4	1	6	5	2	11	8	2	2	8	NA
	IQC 5	3	5	5	3	0	2	2	5	11	NA

(Continued)

10.3389/fimmu.2023.1190404

TABLE 11 Continued

% CV											
Antigen	IQC	Step 1 Incubation Time		Step 2 Incubation Time		Incubation Temperature		Different PE Lots		Different Bead Lots	Edge Effect
		50 min	70 min	20 min	40 min	32°C	42°C	PE Lot 1	PE Lot 2	Bead Lot	
PRN	IQC 1	6	9	4	5	0	3	3	4	6	NA
	IQC 2	8	6	6	6	2	9	8	8	7	NA
	IQC 3	7	8	6	5	2	1	9	5	7	4
	IQC 4	14	10	4	1	1	6	4	3	8	NA
	IQC 5	10	8	5	2	5	9	7	4	9	NA
DT	IQC 1	4	8	2	7	6	0	2	9	7	NA
	IQC 2	4	5	6	6	5	3	7	10	7	NA
	IQC 3	5	5	4	8	7	2	7	10	6	5
	IQC 4	7	4	3	0	2	3	5	12	8	NA
	IQC 5	9	12	2	0	4	4	6	10	15	NA
TT	IQC 1	13	25	15	19	17	9	19	16	19	NA
	IQC 2	6	6	11	16	13	17	15	11	7	NA
	IQC 3	10	14	4	12	1	12	3	3	6	2
	IQC 4	16	13	9	0	6	6	6	9	7	NA
	IQC 5	13	20	6	6	0	11	0	13	9	NA

Table reports % CV observed for deliberate variations in critical assay parameters for all the five antigens. % CV represents the percent difference between assigned and values observed post deliberate variation in parameter. Edge effect was studied with the IQC-3, being representative of concentration in mid region of the assay range.
DT, diphtheria toxoid; FHA, filamentous hemagglutinin; IQC, internal quality control; NA, not applicable; PE, phycoerythrin; PRN, pertactin; PT, pertussis toxin; TT, tetanus toxoid.

to use these reference standards in multiplex assays. A second international standard has replaced the TE-3 reference standard, 13/240, which was characterized using a similar approach. The second international reference standard was also positive for antibodies against the other antigens. Nevertheless, the study provides a process and framework to establish a reference standard for MIAs.

Commercially available diagnostic kits for PT, FHA, PRN, DT, and TT are used widely to assess the antibody responses to aP-based combination vaccines. We also compared the multiplex assay results to commercially available ELISA kits, which are calibrated against ISs and provide unitages in IU/mL (5). A good concordance was observed among the multiplex and monoplex assay methods. However, the multiplex assay was more sensitive (2,000 times for PT, 1,000 times for FHA, 250 times for PRN, 330 times for DT, and 100 times for TT) for all the antigens than the commercially available ELISA kit.

Immunogenicity testing of aP-based combination vaccines is mainly based on detecting IgG antibody concentrations. Cell-based *in vitro* methods used for determining levels of toxin-neutralization antibodies for diphtheria and pertussis toxins have been reported in previous studies (30, 36, 37). These neutralization assays are based on determining the number of antibodies to PT and diphtheria antigens that inhibit the toxin-induced clustering of CHO and Vero cells, respectively (30). The CHO cell assay for pertussis toxin and Vero cell assay for diphtheria toxin is laborious, semi-quantitative, and less sensitive than ELISA-based readouts. Various studies have reported a positive correlation between the concentration of IgG

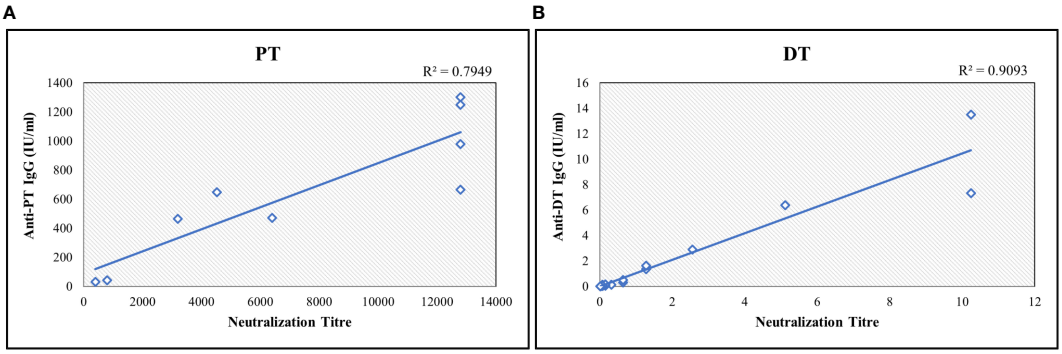

FIGURE 6
Correlation study between bead-based multiplex assay and toxin-neutralization assay for **(A)** PT and **(B)** DT. The neutralization titre is defined as highest serum dilution which shows the inhibition activity. Neutralization assay readout is end-point dilution wherein the highest dilution of sera sample showing the inhibition is reported. Each sample was tested 3 times. Correlation coefficient was determined using regression analysis. R^2 values were determined for agreement between assays. DT, Diphtheria Toxoid; PT, Pertussis Toxin.

antibodies and neutralization antibody titers (30, 36–38). We also studied the agreement between the IgG concentrations estimated by bead-based assay and toxin-neutralization antibodies for pertussis and diphtheria toxin antigens. The assay showed a positive correlation of > 0.75 with PT and DT neutralization assays. The correlation coefficient of 0.75 suggests that there was good agreement considering that both assays operate with different mechanisms and have different sensitivities and readouts, and this was consistent with findings in other studies (30). Immunogenicity testing of vaccines in clinics requires robust method development and validation. Existing regulatory guidance on bioanalytical method validation addresses vaccine immunogenicity assays in only a limited manner. The method was validated in accordance with FDA, EMA, and ICH M10 guidance (22–24). The pentaplex magnetic bead-based assay exhibited a wide, dynamic range and high sensitivity compared with commercially available assays. The assay showed excellent dilutional accuracy for all antigens, which is essential to understanding the full range of antibody responses to all five antigens in pre- and post-vaccinated samples. The validation also established the LOQs for all the antigens using international reference standards. In addition, the sample stability, robustness, and bead-to-bead lot consistency were also established during the validation. Among all the antigens, the PRN antigen was the most sensitive to assay conditions of plate hold time. However, the impact of plate hold time was minimal, as PRN was found to be stable for up to 12 h, which is considered sufficient to address any instrumental breakdowns during routine assay use. The assay was robust over different incubation temperatures and PE lots. This ensures that the assay is unaffected by minor variations, thereby ensuring that the performance of the assay is maintained on repeated use.

Overall, our study reports on a pentaplex assay validated for the simultaneous estimation of IgG antibody levels against PT, FHA, PRN, DT, and TT antigens in IU/mL using WHO reference standards. The assay exhibits a broader dynamic range (to allow quantification across all age groups) than commercially available diagnostic kits. The assay is quantitative with well-defined LOQ compared with the arbitrarily defined cut-offs in commercially available diagnostic kits. Our study also provides a characterization of WHO reference standards that can be used to determine the levels of antibodies present against all five antigens, allowing for their efficient use in multiplex assays. The increased sensitivity, reproducibility, and high throughput of this assay will enable the design of large and robust clinical studies for evaluating both natural and vaccine-induced immunity. Furthermore, since this assay was developed using Luminex technology, it provides opportunities for further expansion to include new antigens.

Data availability statement

The original contributions presented in the study are included in the article/Supplementary Material. Further inquiries can be directed to the corresponding author.

Ethics statement

The studies involving human participants were reviewed and approved by Independent Research Ethics Committee, Pune (IEC No. IRECP/015/2020. Written informed consent for participation was secured for this study in accordance with national legislation and institutional requirements.

Author contributions

VR, LK, MG, PD, SB, SGu, SP, PP, HR, HS, US, SGa, KM, CA, AD-B, and LH participated in the conception, design, development, and validation of the assay, analysis, and interpretation of the data and drafting the article and revising it critically for important intellectual content. All authors contributed to the article and approved the submitted version.

Funding

The authors thank the Serum Institute of India Pvt. Ltd. for all the funding support. This research received no specific grant from funding agencies in the public, commercial, or not-for-profit sectors.

Acknowledgments

The authors acknowledge the support of Dr. Rajesh Gupta (Biologics Quality and Regulatory Consultants, LLC) for providing critical inputs during the method validation. The authors would also like to thank Lakshmi Hariharan and Md. Najeeb Ashraf of SciVoc Consulting Inc. Toronto, for providing medical editing and submission support for the manuscript.

Conflict of interest

Authors VR, LK, MG, PD, SB, SGu, SP, PP, HR, HS, US, and SGa are employees of the company Serum Institute of India Pvt. Ltd.

The remaining authors declare that the research was conducted in the absence of any commercial or financial relationships that could be construed as a potential conflict of interest.

The authors declare that this study received funding from Serum Institute of India Pvt. Ltd. The funder was involved in the study design, data collection and analysis, decision to publish, or preparation of the manuscript.

Publisher's note

All claims expressed in this article are solely those of the authors and do not necessarily represent those of their affiliated organizations, or those of the publisher, the editors and the reviewers. Any product that may be evaluated in this article, or claim that may be made by its manufacturer, is not guaranteed or endorsed by the publisher.

Supplementary material

The Supplementary Material for this article can be found online at: https://www.frontiersin.org/articles/10.3389/fimmu.2023.1190404/full#supplementary-material

References

1. Sala-Farré M, Arias-Varela C, Recasens-Recasens A, Simó-Sanahuja M, Muñoz-Almagro C, Pérez-Jové J. Pertussis epidemic despite high levels of vaccination coverage with acellular pertussis vaccine. *Enferm Infecc Microbiol Clin* (2015) 33(1):27–31. doi: 10.1016/j.eimc.2013.09.013

2. Muscat M, Gebrie B, Efstratiou A, Datta SS, Daniels D. Diphtheria in the WHO European region, 2010 to 2019. *Euro Surveill* (2022) 27(8):2100058. doi: 10.2807/1560-7917.ES.2022.27.8.2100058

3. Kyu HH, Mumford JE, Stanway JD, Barber RM, Hancock JR, Vos T, et al. Mortality from tetanus between 1990 and 2015: findings from the global burden of disease study 2015. *BMC Public Health* (2017) 17(1):179. doi: 10.1186/s12889-017-4111-4

4. Hanvatananukul P, Chanidapa P, Sarachai S, Aurpibul L, Sintupat K, Khampan R, et al. Seroprevalence of antibodies against diphtheria, tetanus, and pertussis among healthy Thai adolescents. *Int J Infect Dis* (2020) 96:422–30. doi: 10.1016/j.ijid.2020.04.088

5. Markey K, Douglas-Bardsley A, Asokanathan C, Fry NK, Barkoff A, Bacci S, et al. Improvement in serological diagnosis of pertussis by external quality assessment. *J Med Microbiol* (2019) 68(5):741–7. doi: 10.1099/jmm.0.000926

6. Park C, Huh DH, Han SB, Choi GS, Kang KR, Kim JA, et al. Development and implementation of standardized method for detecting immunogenicity of acellular pertussis vaccines in Korea. *Clin Exp Vaccine Res* (2019) 8(1):35–42. doi: 10.7774/cevr.2019.8.1.35

7. Reder S, Riffelmann M, Becker C, von König CHW. Measuring immunoglobulin G antibodies to tetanus toxin, diphtheria toxin, and pertussis toxin with single-antigen enzyme-linked immunosorbent assays and a bead-based multiplex assay. *Clin Vaccine Immunol* (2008) 15(5):744–9. doi: 10.1128/CVI.00225-07

8. Coombes L, Stickings P, Tierney R, Rigsby P, Sesardic D. Development and use of a novel *in vitro* assay for testing of diphtheria toxoid in combination vaccines. *J Immunol Methods* (2009) 350(1-2):142–9. doi: 10.1016/j.jim.2009.09.002

9. Coombes L, Tierney R, Rigsby P, Sesardic D, Stickings P. *In vitro* antigen ELISA for quality control of tetanus vaccines. *Biologicals* (2012) 40(6):466–72. doi: 10.1016/j.biologicals.2012.07.011

10. Edwards KM, Decker MD. Combination vaccines consisting of acellular pertussis vaccines. *Pediatr Infect Dis J* (1997) 16(4 Suppl):S97–102. doi: 10.1097/00006454-199704001-00005

11. van Gageldonk PGM, van Schaijk FG, ven der Klis FR, Berbers GAM. Development and validation of a multiplex immunoassay for the simultaneous determination of serum antibodies to bordetella pertussis, diphtheria and tetanus. *J Immunol Methods* (2008) 35(1-2):79–89. doi: 10.1016/j.jim.2008.02.018

12. Rajam G, Carlone G, Kim E, Choi J, Paulos S, Park S, et al. Development and validation of a robust multiplex serological assay to quantify antibodies specific to pertussis antigens. *Biologicals* (2019) 57:9–20. doi: 10.1016/j.biologicals.2018.11.001

13. Kadam L, Patel K, Gautam M, Thorat S, Kale P, Ghule AK, et al. Development and validation of magnetic bead pentaplex immunoassay for simultaneous quantification of murine serum IgG antibodies to acellular pertussis, diphtheria, and tetanus antigens used in combination vaccines. *Methods* (2019) 158:33–43. doi: 10.1016/j.ymeth.2019.01.015

14. Varghese K, Bertlett W, Zheng L, Bookhout S, Vincent D, Huleatt J, et al. A new electrochemiluminescence-based multiplex assay for the assessment of human antibody responses to bordetella pertussis vaccines. *Infect Dis Ther* (2021) 10(4):2539–61. doi: 10.1007/s40121-021-00530-7

15. Brindle E, Stevens D, Crudder C, Levin CE, Garrett D, Lyman C, et al. A multiplex immunoassay method for simultaneous quantification of iron, vitamin a and inflammation status markers. *PloS One* (2014) 9(12):e115164. doi: 10.1371/journal.pone.0115164

16. Prince HE, Lape-Nixon M, Matud J. Evaluation of a tetraplex microsphere assay for bordetella pertussis antibodies. *Clin Vaccine Immunol* (2006) 13(2):266–70. doi: 10.1128/CVI.13.2.266-270.2006

17. Ahsan H. Monoplex and multiplex immunoassays: approval, advancements, and alternatives. *Comp Clin Path* (2022) 31(2):333–45. doi: 10.1007/s00580-021-03302-4

18. Stenger RM, Smilts M, Kuipers B, Kessen SFM, Boog CJP, van Els CACM. Fast, antigen-saving multiplex immunoassay to determine levels and avidity of mouse serum antibodies to pertussis, diphtheria, and tetanus antigens. *Clin Vaccine Immunol* (2011) 18(4):595–603. doi: 10.1128/CVI.00061-10

19. *Working and other standards*. NIBSC. Available at: https://www.nibsc.org/products/brm_product_catalogue/working:standards.aspx (Accessed September 2022).

20. Pickering JW, Martins TB, Schroder MC, Hill HR. Comparison of a multiplex flow cytometric assay with enzyme-linked immunosorbent assay for quantitation of antibodies to tetanus, diphtheria, and haemophilus influenzae type b. *Clin Diagn Lab Immunol* (2002) 9(4):872–6. doi: 10.1128/CDLI.9.4.872-876.2002

21. *MagPlex® microspheres*. Luminex. Available at: https://www.luminexcorp.com/magplex-microspheres/#overview (Accessed September 2022).

22. *Bioanalytical method validation- guidance for industry*. Food and Drug Administration. Available at: https://www.fda.gov/files/drugs/published/Bioanalytical-Method-Validation-Guidance-for-Industry.pdf (Accessed September 2022).

23. *Guideline on bioanalytical method validation*. European Medicines Agency. Available at: https://www.ema.europa.eu/en/documents/scientific-guideline/guideline-bioanalytical-method-validation_en.pdf (Accessed September 2022).

24. *ICH M10 on bioanalytical method validation*. European Medicines Agency. Available at: https://www.ema.europa.eu/en/ich-m10-bioanalytical-method-validation (Accessed September 2022).

25. Bainor A. Bicinchoninic acid (BCA) assay in low volume. *Anal Biochem* (2011) 410(2):310–2. doi: 10.1016/j.ab.2010.11.015

26. Sesardic D, Wong MY, Gaines Das RE, Corbel MJ. The first international standard for anti-tetanus immunoglobulin, human; pharmaceutical evaluation and

international collaborative study. *Biologicals* (1993) 21:67–75. doi: 10.1006/biol.1993.1048

27. *WHO manual for the establishment of national and other secondary standards for vaccines*. World Health Organization. Available at: http://whqlibdoc.who.int/hq/2011/WHO_IVB_11.03_eng.pdf (Accessed September 2022).

28. Pavliakova D, Giardina PC, Moghazeh S, Sebastien S, Koster M, Pavliak V, et al. Development and validation of 13-plex luminex-based assay for measuring human serum antibodies to streptococcus pneumoniae capsular polysaccharides. *mSphere* (2018) 3(4):e00128–18. doi: 10.1128/mSphere.00128-18

29. *AMG™ universal coupling kit (AI-VMPAKMP-01.00)*. Anteo Technologies. Available at: https://www.veritastk.co.jp/products/pdf/AI-VMPAKMP-01.00_AMG_Universal_Coupling_Kit.pdf (Accessed September 2022).

30. Barkoff A, Knuutila A, Mertsola J, He Q. Evaluation of anti-PT antibody response after pertussis vaccination and infection: the importance of both quantity and quality. *Toxins (Basel)* (2021) 13(8):508. doi: 10.3390/toxins13080508

31. Gupta RK, Siber GR. Use of in vitro vero cell assay and ELISA in the united states potency test of vaccines containing adsorbed diphtheria and tetanus toxoids. *Dev Biol Stand* (1996) 86:207–15.

32. Dalby T, Sørensen C, Petersen JW, Krogfelt KA. Pertussis serology: assessment of IgG anti-PT ELISA for replacement of the CHO cell assay. *APMIS* (2010) 118 (12):968–72. doi: 10.1111/j.1600-0463.2010.02664.x

33. Sakamoto S, Putalun W, Vimolmangkang S, Phoolcharoen W, Shoyama Y, Tanaka H, et al. Enzyme-linked immunosorbent assay for the quantitative/qualitative analysis of plant secondary metabolites. *J Nat Med* (2018) 72(1):32–42. doi: 10.1007/s11418-017-1144-z

34. Caboré RN, Piérard D, Huygen K. A Belgian Serosurveillance/Seroprevalence study of diphtheria, tetanus and pertussis using a luminex xMAP technology-based pentaplex. *Vaccines (Basel)* (2016) 4(2):16. doi: 10.3390/vaccines4020016

35. Maňásková SH, van Belkum A, Endtz HP, Bikker FJ, Veerman ECI, van Wamel WJB. Comparison of non-magnetic and magnetic beads in bead-based assays. *J Immunol Methods* (2016) 436:29–33. doi: 10.1016/j.jim.2016.06.003

36. Hewlett EL, Sauer KT, Myers GA, Cowell JL, Guerrant RL. Induction of a novel morphological response in Chinese hamster ovary cells by pertussis toxin. *Infect Immun* (1983) 40(3):1198–203. doi: 10.1128/iai.40.3.1198-1203.1983

37. Winsnes R, Sesardic D, Daas A, Behr-Gross M-E. Collaborative study for the validation of serological methods for potency testing of diphtheria toxoid vaccines-part 1. *Pharmeuropa Bio* (2004) 2003(2):35–68.

38. Millen SH, Bernstein DI, Connelly B, Ward JI, Chang SJ, Weiss AA. Antibodymediated neutralization of pertussis toxin-induced mitogenicity of human peripheral blood mononuclear cells. *Infect Immun* (2004) 72(1):615–20. doi: 10.1128/IAI.72.1.615-620.2004

frontiers | Frontiers in Immunology

TYPE Original Research
PUBLISHED 16 June 2023
DOI 10.3389/fimmu.2023.1178688

Check for updates

OPEN ACCESS

EDITED BY
Nargis Khan,
University of Calgary, Canada

REVIEWED BY
Ying Xu,
Fudan University, China
Won-Jong Jang,
Konkuk University, Republic of Korea
Jae-Min Song,
Sungshin Women's University,
Republic of Korea
Sajid Nadeem,
University of Alabama at Birmingham,
United States

*CORRESPONDENCE
Do Hyeon Jeong
tony@raphas.com
Bum-Joon Kim
kbumjoon@snu.ac.kr

†These authors have contributed equally to this work and share first authorship

RECEIVED 03 March 2023
ACCEPTED 05 June 2023
PUBLISHED 16 June 2023

CITATION
Lee M-H, Seo H, Lee M-S, Kim BJ, Kim HL, Lee DH, Oh J, Shin JY, Jin JY, Jeong DH and Kim B-J (2023) Protection against tuberculosis achieved by dissolving microneedle patches loaded with live *Mycobacterium paragordonae* in a BCG prime-boost strategy. *Front. Immunol.* 14:1178688. doi: 10.3389/fimmu.2023.1178688

COPYRIGHT
© 2023 Lee, Seo, Lee, Kim, Kim, Lee, Oh, Shin, Jin, Jeong and Kim. This is an open-access article distributed under the terms of the Creative Commons Attribution License (CC BY). The use, distribution or reproduction in other forums is permitted, provided the original author(s) and the copyright owner(s) are credited and that the original publication in this journal is cited, in accordance with accepted academic practice. No use, distribution or reproduction is permitted which does not comply with these terms.

Protection against tuberculosis achieved by dissolving microneedle patches loaded with live *Mycobacterium paragordonae* in a BCG prime-boost strategy

Mi-Hyun Lee[1,2,3†], Hyejun Seo[1,4,5†], Moon-Su Lee[6], Byoung Jun Kim[1], Hye Lin Kim[1,4], Du Hyung Lee[1,4], Jaehun Oh[1,2,3], Ju Yeop Shin[6], Ju Young Jin[6], Do Hyeon Jeong[6*] and Bum-Joon Kim[1,2,3,4,5,7*]

[1]Department of Microbiology and Immunology, College of Medicine, Seoul National University, Seoul, Republic of Korea, [2]Department of Biomedical Sciences, College of Medicine, Seoul National University, Seoul, Republic of Korea, [3]BK21 FOUR Biomedical Science Project, Seoul National University College of Medicine, Seoul, Republic of Korea, [4]Cancer Research Institute, College of Medicine, Seoul National University, Seoul, Republic of Korea, [5]Institute of Endemic Diseases, Seoul National University Medical Research Center (SNUMRC), Seoul, Republic of Korea, [6]Medical Business Division, Raphas Co., Ltd., Seoul, Republic of Korea, [7]Liver Research Institute, College of Medicine, Seoul National University, Seoul, Republic of Korea

Introduction: Skin vaccination using dissolving microneedle patch (MNP) technology for transdermal delivery is a promising vaccine delivery strategy to overcome the limitations of the existing vaccine administration strategies using syringes. To improve the traditional microneedle mold fabrication technique, we introduced droplet extension (DEN) to reduce drug loss. Tuberculosis remains a major public health problem worldwide, and BCG revaccination had failed to increase the protective efficacy against tuberculosis. We developed an MNP with live *Mycobacterium paragordonae* (Mpg) (Mpg-MNP) as a candidate of tuberculosis booster vaccine in a heterologous prime-boost strategy to increase the BCG vaccine efficacy.

Materials and methods: The MNPs were fabricated by the DEN method on a polyvinyl alcohol mask film and hydrocolloid-adhesive sheet with microneedles composed of a mixture of mycobacteria and hyaluronic acid. We assessed the transdermal delivery efficiency by comparing the activation of the dermal immune system with that of subcutaneous injection. A BCG prime Mpg-MNP boost regimen was administered to a mouse model to evaluate the protective efficacy against *M. tuberculosis*.

Results: We demonstrated the successful transdermal delivery achieved by Mpg-MNP compared with that observed with BCG-MNP or subcutaneous vaccination *via* an increased abundance of MHCII-expressing Langerin+ cells within the dermis that could migrate into draining lymph nodes to induce T-cell activation. In a BCG prime-boost regimen, Mpg-MNP was more protective than BCG-only immunization or BCG-MNP boost, resulting in a lower bacterial burden in the lungs of mice infected with virulent *M. tuberculosis*. Mpg-MNP-boosted mice

showed higher serum levels of IgG than BCG-MNP-boosted mice. Furthermore, Ag85B-specific T-cells were activated after BCG priming and Mpg-MNP boost, indicating increased production of Th1-related cytokines in response to *M. tuberculosis* challenge, which is correlated with enhanced protective efficacy.

Discussion: The MNP fabricated by the DEN method maintained the viability of Mpg and achieved effective release in the dermis. Our data demonstrate a potential application of Mpg-MNP as a booster vaccine to enhance the efficacy of BCG vaccination against *M. tuberculosis*. This study produced the first MNP loaded with nontuberculous mycobacteria (NTM) to be used as a heterologous booster vaccine with verified protective efficacy against *M. tuberculosis*.

KEYWORDS

Mycobacterium tuberculosis, *Mycobacterium paragordonae*, microneedle patch, BCG booster vaccine, droplet extension method

Introduction

Tuberculosis has been a persistent global challenge since it emerged as an epidemic in Europe in the 18th century (1). Indeed, since the introduction of the Bacillus Calmette-Guérin (BCG) vaccine based on an attenuated BCG strain in 1921, a BCG vaccination campaign has been implemented around the world, and the actual tuberculosis incidence rate is decreasing (2). However, 10 million people fell ill with TB and 1.5 million people died due to TB in 2020; TB is still ranked as one of the top 10 causes of death and is considered the deadliest infectious disease worldwide (3, 4). Although BCG is the only licensed vaccine for TB and has 70-80% efficacy against childhood TB, it has shown limited effectiveness against adult TB (5).

Since worldwide BCG vaccine coverage reached over 90% in 2018, a prime-boost vaccination strategy has been considered an efficient vaccine-enhancing strategy to enhance the effectiveness of BCG (6, 7). However, there is a lack of evidence concerning the efficacy of BCG revaccination *via* repeated BCG doses in protecting against TB (8). To overcome the limitations of BCG vaccination, exposure to nontuberculous mycobacteria (NTM) could be a solution to enhance the protective effect of BCG vaccination. A recent study demonstrated that exposure to *M. avium*, an environmental NTM strain, increases T-cell activation in branchial lymph nodes and improves the protective effects of BCG vaccination by inducing Th1 and Th17 immune responses (9, 10). In addition, the SRL172 strain of *M. vaccae*, an inactivated environmental NTM, is the only new tuberculosis booster vaccine candidate considered to show efficacy in a phase 3 trial (11). These findings highlight the potential of developing a BCG booster vaccine using NTM strains.

Previously, we reported that a temperature-sensitive NTM, *Mycobacterium paragordonae* (Mpg), is a potent tuberculosis vaccine candidate. Mpg induced enhanced protective immune responses against *M. tuberculosis* and *M. abscessus* infection by eliciting a Th1 immune response (12). Moreover, the development of recombinant Mpg expressing human immunodeficiency virus (HIV)-1 p24 or the severe acute respiratory syndrome coronavirus 2 (SARS-CoV-2) RBD has shown the potential of Mpg as a delivery vector for vaccines (13, 14). Based on the high immunogenicity of Mpg, we suggest Mpg as a potent booster vaccine after BCG priming against tuberculosis.

A transdermal delivery strategy can be effective in managing infectious diseases (15). The epidermis and dermis contain professional antigen-presenting cells (APCs) that can initiate adaptive immunity effectively by migrating to draining lymph nodes (16). The microneedle drug delivery system has been considered a promising platform to complement hypodermic injection (17). In particular, hyaluronic acid (HA), which has been approved by the US FDA, has been widely used to dissolve microneedle components due to its biodegradability, biocompatibility, and skin permeability (18, 19). In this study, Mpg-MNP was manufactured with HA using Raphas' proprietary droplet extension method (DEN) (20, 21). The DEN method provides a gentle manufacturing environment without heat or UV irradiation because blowing air is applied directly to the polymer droplet to solidify a microneedle shape.

In this study, we developed a safe and painless BCG booster vaccine by fabricating Mpg-MNP and demonstrated the enhanced protective efficacy of Mpg-MNP in a virulent *M. tuberculosis* infection model. We also evaluated the protective effects of strengthened cellular immune responses, including induction of Th1-biased immunity *via* successful transdermal delivery of live Mpg.

Materials and methods

Mycobacterial strains and culture

The mycobacterial strains used were as follows: *Mycobacterium paragordonae* (Mpg) JCM 18565^T, *Mycobacterium bovis* BCG Tokyo

strain, *Mycobacterium tuberculosis* strain H37Ra ATCC 25177, and *M. tuberculosis* K-strain NCCP 15986. The pathogen resources (NCCP 15986) for this study were provided by the National Culture Collection for Pathogens. The strains were cultured from frozen stocks (−80°C) and subcultured in 7H9 broth with 2.5% glycerol, 0.2% Tween-80, and 10% ADC or on 7H10 agar plates with 0.5% glycerol and 10% OADC at 37°C or 30°C (in the case of Mpg).

Fabrication of Mpg-loaded MNPs *via* the DEN method

Mpg cultured in 7H9-ADC was provided by the Institute of Medicine of Seoul University (Seoul, Korea) and was harvested and washed two times with phosphate-buffered saline (PBS) (pH 7.4). After washing, Mpg was reconstructed in PBS and mixed with sodium hyaluronate. (HA, EP-1, Bloomage Freda Biopharm Co Ltd, China) (25%, wt). This mixture was homogenized with a planetary centrifugal mixer (ARV-310, THINKY Corp., Japan) at room temperature. The temperature during MNP production can rise up to 45 to 50°C which does not affect the activation of used mycobacterial strains. The DEN method was used to prepare Mpg-loaded MNPs. The mixture was dropped onto polyvinyl alcohol (PVA) mask film and hydrocolloid-based adhesive, which was dispensed onto an adhesive patch by a solution dispenser (Super Sigma CMII, Musashi, Japan). Then, solid-state microneedles were fabricated from the liquid-phase mixture through elongation and air-blowing processes. Each patch was designed as 24 microneedle arrays (needle pitch, 1.4 mm; needle length, 0.6 mm).

Physical strength of Mpg-loaded MNPs

The mechanical fracture force was measured with a universal testing machine (Z0.5TN, Zwick/Roell, Germany). After a single microneedle was attached to the rigid stainless-steel station, microneedles were pressed by the sensor probe at a speed of 1.1 mm/s for axial force application. The axial force required to move the probe was tracked by the universal testing machine as a function of distance. The maximum force before the force drop was measured as the axial fracture force for Mpg-MNPs 0.6mm in length.

Analysis of mycobacterial encapsulation and viability in MNPs

A single MNP was immersed in 1 ml of PBS at room temperature for two hours to elute mycobacteria loaded on the patch. The eluted samples were centrifuged, and the pellets were used to confirm the number and viability of MNP-loaded mycobacteria through real-time quantitative PCR (RT−qPCR) and ATP bioluminescence assays.

To quantify the number of MNP-loaded mycobacteria through RT−qPCR, 0.1, 0.5, 1, 5, and 10 x 10^6 CFU of mycobacteria (standard) and the eluted pellets from MNPs were disrupted by a mini-bead beater with TRIzol™ (Invitrogen, Massachusetts, USA) and glass beads (0.1~0.3 mm). Then, the lysates were centrifuged into three aqueous layers, and DNA was extracted *via* the manufacture's protocol for TRIzol™. Briefly, the DNA samples were isolated from the intermediate layer using an ethanol precipitation method and used as templates. RT−qPCR was performed with a SensiFAST™ SYBR Lo-ROX One-Step kit (Bioline, London, UK) and *hsp65* primers (Forward primer: 5'- GTCGAGGAGTCCAACACCTT- 3'; Reverse primer: 5'-GAGCTGACCAGCAGGATGTA-3') to quantify the number of MNP-loaded mycobacteria. The standardization of RT−qPCR was carried out with DNA from mycobacterial samples (standard). The number of the MNP-loaded bacteria was determined based on a standard curve of Cq value of the *hsp65* versus the log CFU (Supplementary Figure 1A). The eluted pellets of MNPs were reacted with a 3M™ Clean-Trace™ Water Plus – Total ATP kit (3 M, Minnesota, USA) to check the viability of MNP-loaded mycobacteria. The reaction mixture was transferred to a Nunclon™ 96-well white flat-bottom plate (Invitrogen, Massachusetts, USA) to measure the luminescence, which reveals the amount of ATP in the sample, indicating viability.

In vivo experimental models

Seven-week-old female BALB/c mice were purchased from Orientbio (Seoul, South Korea) and used for experiments at the age of 8 weeks. In the prime-boost vaccination protocol, all mice were anesthetized prior to subcutaneous injection of BCG (1×10^6 CFUs in 100 µl of PBS). The hair on the back was completely removed with an electric shaver and hair removal cream. MNPs were applied on the back and wrapped around the torsos of the mice, and MNPs were removed after 24 hr. In a virulent *M. tuberculosis* (MTB) K-strain challenge model, MTB (1×10^6 CFUs in 100 µl of PBS) was injected through the tail vein of mice after anesthetization. All mice were sacrificed by CO_2 asphyxiation.

Isolation of primary cells

After isolation, the skin-draining lymph nodes, which were axillary, lateral axillary, and inguinal lymph nodes, were incubated in 750 µL of a 1 mg/mL collagenase IV (Sigma−Aldrich, Massachusetts, USA) and 0.2 mg/mL DNase I (Sigma−Aldrich, Massachusetts, USA) mixture at 37°C for 30 minutes with shaking to digest connective tissue, and the reaction was terminated by adding 100X EDTA (7.5 µL). Spleens and digested lymph nodes were homogenized using a 70 µm cell strainer (SPL, Pocheon, Republic of Korea) and the plunger from a 5 cc syringe and centrifuged. To prevent contamination of red blood cells, the pellets of each organ were treated with red blood cell lysis buffer (Sigma−Aldrich, Massachusetts, USA), and the reaction was terminated by adding complete RPMI [supplemented with 10% fetal bovine serum (FBS)] twice. After centrifugation, the isolated primary cells were used for further experiments.

Cytokine assay

The isolated primary cells of lymph nodes or spleens were cultured ($1x10^6$ cells/well) in 96-well round-bottom plates. Then, the cells were restimulated with 5 μg/mL of H37Ra lysate, which was a sonicated sample of *M. tuberculosis* strain H37Ra, or 5 μg/mL of the Ag85B protein, which was produced by *Escherichia coli*, for 3 days, and IL-10, IL-12p40, TNF-α, and IFN-γ levels in the supernatant were measured using an Invitrogen cytokine ELISA kit. For IFN-γ ELISPOT, PVDF membrane-based ELISPOT plates were activated with 75% ethanol and coated with 3 μg/mL anti-mouse IFN-γ capture antibody (100 μL per well; clone: AN-18; Invitrogen, Massachusetts, USA) at 4°C overnight. Then, $1x10^6$ splenocytes per well were loaded onto an ELISPOT plate, which was washed with PBS-T and PBS, and restimulated with 5 μg/mL of H37Ra lysate or Ag85B peptide pool (144-152, IYAGSLSAL; 151-165, ALLDPSQGMGPSLIG; and 262-279, HSWEYWGA QLNAMKGDLQ; each peptide was added at a concentration of 2 μg/mL), which was synthesized by Peptron (Daejeon, Republic of Korea), at 37°C for 20 h. After the washed plate was incubated with anti-mouse-IFN-γ-biotin (3 μg/mL; 100 μL per well; clone: XMG 1.2; Invitrogen, Massachusetts, USA) and then with streptavidin-HRP (BD, New Jersey, USA), spots were developed using an AEC substrate kit (BD, New Jersey, USA). IFN-γ ELISPOT has been described in more detail previously (14).

Flow cytometry

Primary cells from lymph nodes or spleens were isolated and cultured ($1x10^6$ cells/well) in 96-well round-bottom plates. Cells were blocked with anti-CD16/32 (BioLegend, #101301) in buffer (PBS containing 10% FBS and 10 mM EDTA) for Fc receptor blocking for 10 min at RT and stained with surface marker-specific antibodies (1:500) for 30 min on ice. For intracellular cytokine staining, the cells were fixed and permeabilized with cytofix/cytoperm solution (BD biosciences, #BDB554714) for 20 min. After permeabilization, intracellular cytokine-specific antibodies (1:200) were added to the permeabilization buffer and incubated for 40 min on ice. Flow cytometry was performed using BD LSRFortess™ X-20 and the full gating strategy is presented in (Supplementary Figure 2). The data were analyzed by FlowJo 10 software and FMO controls were used for gating.

Histological staining and confocal imaging

The collected skin was stored in 4% paraformaldehyde (PFA) and frozen with optimal cutting temperature compound for cryosectioning. The cryosections were fixed with 4% PFA for 20 min at room temperature and stained with Alexa Fluor® 488 MHCII (Biolegend, #107615), langerin Alexa Fluor® 594 (Santa Cruz, #SC-271272 AF594) or Alexa Fluor® 488 Ki-67 (Biolegend, #151204) antibodies (1:100) overnight at 4°C. The cryosections were mounted with mounting medium containing DAPI (Vectashield, #H-1200), and images were obtained by confocal microscopy (Olympus, FV3000).

For hematoxylin and eosin (H&E) staining, 4% PFA-fixed the lung was embedded in paraffin, and sectioned and made to 5 μm thickness slide. The cryosectioned skin and sectioned lung were stained with hematoxylin and eosin (H&E). The scanned images were analyzed through Aperio ImageScope (CA, USA).

CFU enumeration assay

The organ lysate was serially diluted in PBS, and the optimally diluted sample was dropped onto a 7H10 agar plate (supplemented with glycerol and OADC). After confirming that the droplet had been dried, the plates were incubated at 37°C with 5% CO_2 for 3 or 4 weeks to wait for colony formation. The number of CFUs per organ was calculated by considering the number of colonies and the dilution factor.

Statistical analysis

All experimental data were analyzed by using GraphPad Prism 5 (GraphPad, CA, USA), and every experiment was performed as two or more independent replicates. All results were analyzed by one- or two-way ANOVA with Tukey's multiple comparison tests to compare multiple experimental groups, and Student's t-test was applied to compare two experimental groups. The data represent the mean ± standard deviation (SD), and statistical significance is indicated with asterisks as follows: $*P < 0.05$, $**P < 0.01$, and $***P < 0.001$ (ns, not significant).

Results

Fabrication of the dissolved Mpg-MNP and viability of the loaded Mpg

Mycobacterium-loaded MNPs were constructed with a mixture of mycobacteria and dissolvable HA *via* the DEN method (Figure 1A). The circular hydrocolloid adhesive patches measured 10x10 mm and contained 24 circular cone-shaped microneedles up to ~600 μm in height and ~78μm in tip diameter that could penetrate into the mouse dermis (Figure 1B). To examine the transdermal penetration capacity, the mechanical fracture force of a single Mpg-loaded microneedle was measured with a universal testing machine. The axial fracture force was 0.111 N, two times the margin of the minimum average insertion force (0.058 N) of microneedles of this geometry (Figure 1C and Table S1). We intentionally designed the HA-based Mpg-MNP to quickly achieve transdermal delivery with self-administration.

In addition, we determined the amount of Mpg or BCG on the MNPs *via* a dissolution test using real-time PCR with *hsp65*-specific nested PCR primers. The amount of DNA, which is based on the standard curve between the number of mycobacteria and its Cq value ($R^2 > 0.99$, Supplementary Figure 1A), extracted from a dissolved Mpg-MNP in PBS showed a 5.68 ± 0.03 $\log_{10}$ CFU bacterial load, and that

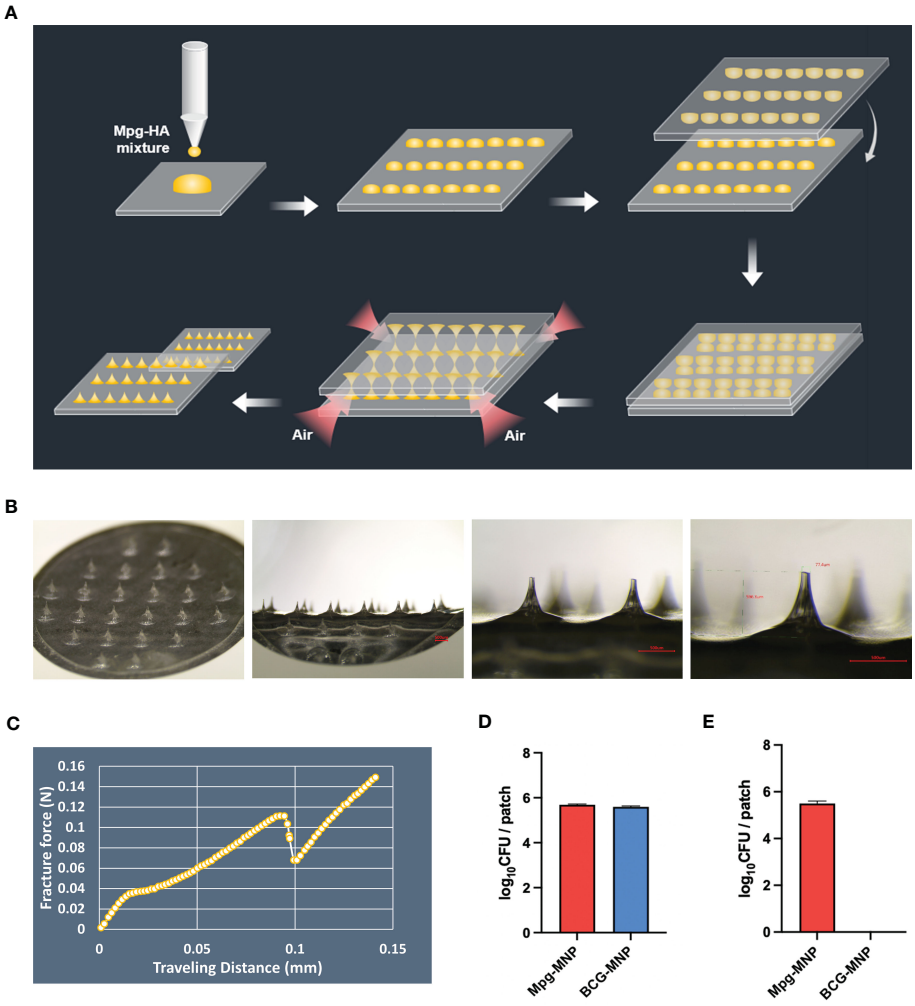

FIGURE 1
Description of *mycobacterium*-loaded MNPs. **(A)** Schematic illustration of the MNP manufacturing process *via* the DEN method. **(B)** Microscopic images of the microneedle patch at 13.4X, 40X, and 60X magnifications (bar: 500 μm). **(C)** The graph shows the mechanical fracture force of the microneedle patch fabricated by the DEN method. **(D)** The amount of loaded Mpg or BCG on the MNPs was assessed *via* qPCR, and **(E)** the viable Mpg or BCG on the MNPs was measured *via* a CFU assay.

extracted from a BCG-MNP showed a 5.59 ± 0.04 $\log_{10}$ CFU bacterial load per patch (Figure 1D). However, the opposite trend was observed for the viability of Mpg and BCG on the MNPs. Recovery of live mycobacteria in Mpg or BCG-MNPs was evaluated by confirming CFU and ATP levels after 90 days of storage at 4°C. The CFU log value of the Mpg-MNP was 5.49 ± 0.23 $\log_{10}$ CFU, which implies approximately 96.6% viability of Mpg after loading. However, in the case of the BCG-MNP, we did not detect any viable cells after dissolution (Figure 1E). Furthermore, we evaluated intracellular ATP in the dissolved solution, and the results of the ATP assay also demonstrated very low levels of bioluminescence in the dissolved BCG-MNP solution, suggesting its poor preservation ability (Supplementary Figure 1B). Since we fabricated *mycobacterium*-loaded MNPs without any supplements intended to preserve the viability of the mycobacteria, loss of BCG viability was observed (22). In contrast to BCG, the environmental NTM can survive during starvation and can persist during low-nutrient stress, suggesting that Mpg maintains its high viability after the fabrication of MNPs (23, 24). These results suggest that compared with BCG, Mpg is a suitable strain for HA-based MNP manufacturing *via* the DEN method and for long-term storage.

Transdermal delivery of Mpg-MNP and activation of the dermal immune system

The transdermal delivery efficacy of Mpg-MNP was compared with that of BCG-MNP or subcutaneous vaccination *via* a hypodermic syringe (Figure 2A). MNPs were applied for 24 h on the backs of female BALB/c mice after removing the hair (Figure 2B). Seven days post-vaccination, we harvested the back skin tissues to evaluate alterations in the frequency of immune cells. We found that the Mpg-MNP-treated group showed an increased number of infiltrating cells in the dermis compared to that of all other groups (Figures 2C, D). Interestingly, we detected a large subset of activated antigen-presenting cells in the dermis of the Mpg-MNP group; MHCII+ langerin+ cells represented 18.5% of cells in the dermis of the Mpg-MNP-immunized group but only

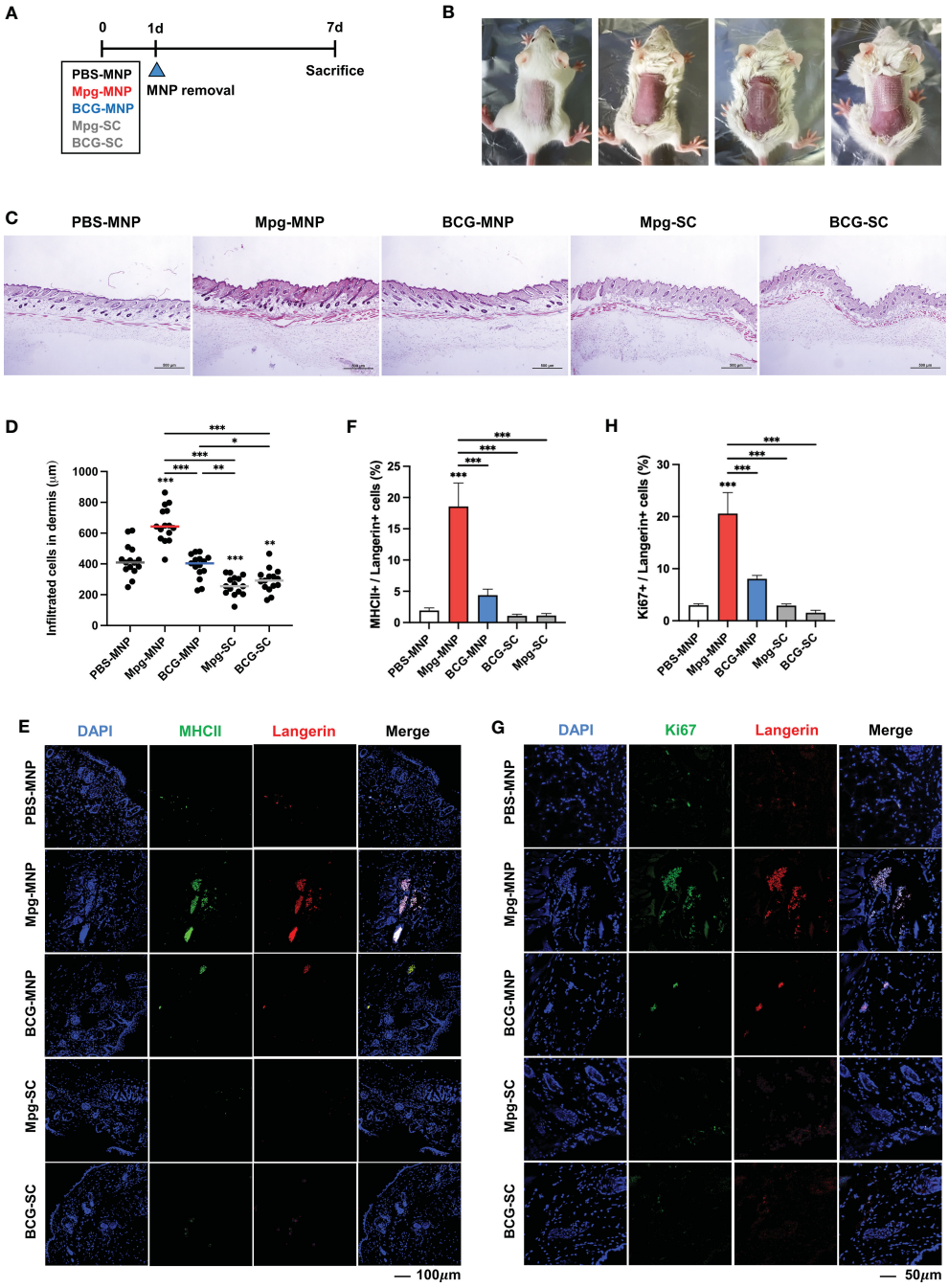

FIGURE 2
Altered frequencies of immune cells in the dermis after Mpg-MNP application. **(A)** Schematic of the mouse (BALB/c, female, n=5 per group) immunization schedule used to compare the immune responses after MNP application and S.C. injection. **(B)** The process of attaching the microneedle patch to the back of the mouse. **(C)** Representative images of H&E-stained skin after fixing the dorsal skin of mice. **(D)** The counts of infiltrated cells in the dermis are shown as a graph. **(E, G)** Representative confocal microscopy images of mouse dorsal skin. **(E)** Tissue sections were stained for MHCII (green) and Langerin (red) or **(G)** Ki67 (green) and Langerin (red). **(F)** The bar graph shows the frequency of MHC+/Langerin+ cells, which was obtained from **(E)**, and **(H)** the frequency of Ki67+/Langerin+ cells is also shown as a bar graph from **(G)**. Statistical analysis: One-way ANOVA with Tukey's multiple comparison test, *P < 0.05, **P < 0.01 and ***P < 0.001.

4.3% of cells in the BCG-MNP group, 1.9% of cells in the PBS-MNP group, 1.1% of cells in the Mpg-SC group and 1.07% of cells in the BCG-SC-immunized group (Figures 2E, F). In particular, high levels of Ki-67 expression were found in langerin+ subsets in the dermis, with 20.6% Ki-67+ langerin+ cells after Mpg-MNP application, whereas at most, 8.05% Ki-67+ langerin+ cells were observed in the BCG-MNP group, 2.99% Ki-67+ langerin+ cells were observed in the PBS-MNP group, 2.92% Ki-67+ langerin+ cells were observed in the Mpg-SC group and 1.54% Ki-67+ langerin+ cells were observed in the BCG-SC immunized group (Figures 2G, H). Dermal MHCII+ langerin+ cells exhibit migratory capacity, and they proliferate before and after migration (25). Migratory MHCII+

langerin+ cells play an initiating role in the induction of T- or B-lymphocyte-mediated immune responses in the draining lymph nodes (26). Indeed, we found that dermal langerin+ cells in the Mpg-MNP group formed large clusters during proliferation due to the adjacent proliferative Ki-67+ langerin+ cells, which promoted migration (Figure 2G) (27, 28). Overall, compared with BCG-MNP or subcutaneous immunization, Mpg-MNP immunization strongly induces migratory MHCII+ langerin+ cells in the dermis that can skew the adaptive immune response.

Mpg-MNPs induce cellular immune responses in the skin-draining lymph nodes

As live Mpg was successfully delivered into the dermis by MNPs, we further analyzed cellular immune responses in the skin-draining lymph nodes. To investigate the induction of adaptive immune responses by migratory antigen-presenting cells from the dermis, we compared the surface profiles of DCs in the draining lymph nodes. Higher expression of CD40, CD80 and CD86 in DCs was observed in response to Mpg-MNP immunization than in response to BCG-MNP, Mpg-SC or BCG-SC immunization, implying the potential to activate T-cell-mediated immune responses (Figure 3A). Additionally, upregulated MHCII expression levels in DCs were also identified, suggesting an enhanced ability to present antigens to naïve T cells in response to Mpg-MNP immunization. These data demonstrate the superiority of Mpg-MNP in promoting the maturation of DCs, which is related to the activation of antigen-presenting cells in the dermis.

Next, we assessed CD4+ and CD8+ T-cell priming by mature DCs after restimulation with Ag85B protein for 3 days. FACS analysis of the activation markers, IFN-γ and TNF-α showed that Mpg-MNP immunization increased the frequencies of both active CD4+ and CD8+ T cells in the draining lymph nodes compared with those in the BCG-MNP-immunized group (Figures 3B, C). In particular, consistent with our previous study, enhanced antigen-specific IFN-γ secretion potentiated the induction of a Th1-skewed immune response by Mpg-MNP immunization (12). In addition, we performed ELISA to analyze the cytokine profiles on day 3 after restimulation with the Ag85B protein to identify the cytokines secreted into the supernatant. Significantly higher levels of IFN-γ, TNF-α and IL-12p40 were detected in the Mpg-MNP-immunized group than in the BCG-MNP-immunized group, and these levels were correlated with the level of Th1 cell activation. In addition, no noticeable alteration in IL-10 secretion levels was observed in response to Mpg-MNP immunization (Figure 3D) (12). Collectively, these data showed that the Mpg-MNP induces both CD4+ and CD8+ T-cell activation by highly mature DCs in the draining lymph nodes, leading to enhanced secretion of Th1 cytokines compared with that observed after BCG-MNP immunization.

The BCG-prime/Mpg-MNP boost regimen improves protective efficacy against *M. tuberculosis*

To verify the protective efficacy of Mpg-MNP against *M. tuberculosis* in a BCG prime-boost regimen, female BALB/c mice were boosted with Mpg- or BCG-MNP at week 2 post-BCG vaccination. Another 2 weeks after Mpg- or BCG-MNP boost, the mice were challenged with the virulent *M. tuberculosis* K-strain intravenously, which is a Beijing family member showing hypervirulent features (Figure 4A). At week 4 post-challenge, the BCG prime/Mpg-MNP (BCG/MP) group showed a significantly reduced bacterial burden, with low CFUs in the lungs, compared with the BCG prime only or BCG prime/BCG-MNP (BCG/BP) group (Figure 4B).

The amelioration of inflammatory cellular accumulation caused by *M. tuberculosis* infection was investigated by histopathological observation. Consistent with the counts of bacteria in the lungs, inflamed pulmonary lesions were decreased in the BCG/MP group compared with all other groups, with alleviation of inflammation and moderate fibrosis (Figure 4C). These observations demonstrate that an enhanced protective effect against *M. tuberculosis* infection is conferred by boosting with Mpg-MNP compared to BCG-MNP.

Induction of Th1-biased immune responses by an Mpg-MNP boost in a virulent *M. tuberculosis* infection model

To explain the protective effect of an Mpg-MNP boost after BCG priming against *M. tuberculosis*, the induction of a systemic immune response was analyzed. We evaluated Ag85B-specific IgG subtypes, IgG1 and IgG2a, which are markers of Th2 and Th1 immune responses, respectively, in the sera. Although the BCG/MP group showed levels of Ag85B-specific total IgG similar to those of the other groups, increased levels of both IgG1 and IgG2a were identified in Mpg-MNP-boosted mice, which implies that Mpg-MNP can elicit both Th1 and Th2 immune responses (Figure 5A). In particular, the observation that the highest Ag85B-specific IgG2a/IgG1 level was in the BCG/MP group demonstrates that a Th1-biased immune response plays a key role in protection against tuberculosis after BCG vaccination.

Following the induction of the systemic immune response by the Mpg-MNP boost, we further analyzed the altered immune milieu in splenocytes. Increased expression levels of CD40, CD80, CD86 and MHCII were found in the Mpg-MNP boost group compared with the BCG prime only group, suggesting DC maturation (Figure 5B). Next, we identified the frequency of IFN-γ-secreting cells among splenocytes; IFN-γ is mainly produced by Th1 cells. Increased IFN-γ spot-forming cells (SFCs) were detected in the BCG/MP group after restimulation with Ag85B protein versus either BCG prime only or BCG/BP group (Figure 5C). In addition, as shown by FACS analysis, compared with the BCG prime or BCG/BP group, the BCG/MP group noticeably induced the generation of Ag85B-specific CD4+ and CD8+ T cells expressing IFN-γ, consistent with ELISPOT analysis. Additionally, the frequency of TNF-α-expressing CD4+ or CD8+ T cells was also greatly increased in response to the Mpg-MNP boost (Figure 5D and Supplementary Figure 4). Therefore, highly activated T lymphocytes expressing both IFN-γ and TNF-α correlated with the strengthening of Th1 immune responses by the Mpg-MNP boost (29). The levels of Th1 immune response-related cytokines,

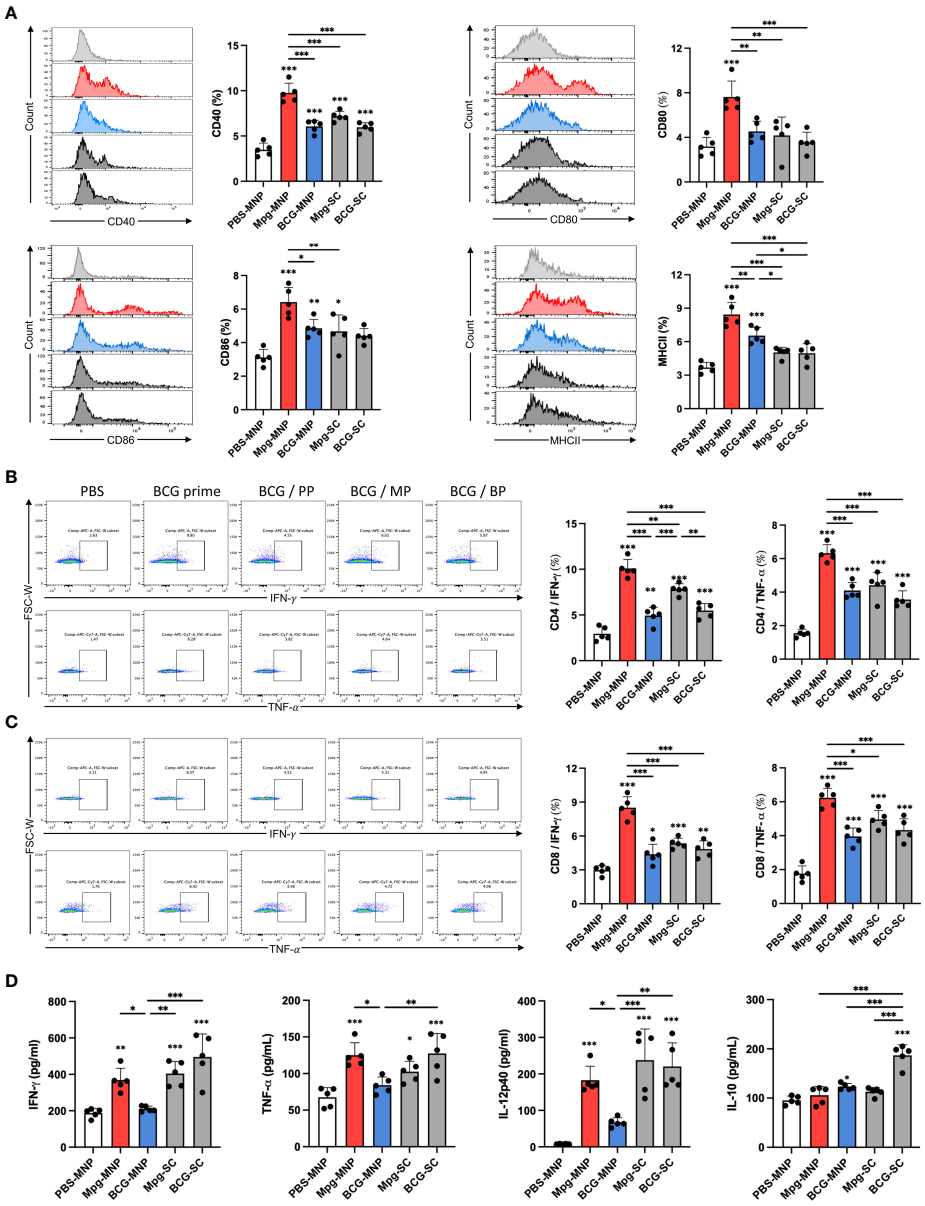

FIGURE 3
Induction of immune responses in the skin-draining lymph nodes by Mpg-MNP. **(A)** The costimulatory factors CD40$^+$ (upper left), CD80$^+$ (upper right), CD86$^+$ (lower left), and MHCII$^+$ (lower right) in CD11b$^+$/CD11c$^+$ dendritic cells in the draining lymph nodes were analyzed by flow cytometry. **(B, C)** Representative flow cytometry plots and bar graphs of **(B)** CD4+ or **(C)** CD8+ cells releasing IFN-γ (upper panel) and TNF-α (lower panel) in the draining lymph nodes after restimulation with the Ag85B protein for 72 h. **(D)** Cytokine expression levels in the supernatant from lymph nodes restimulated with the Ag85B protein for 72 h were measured by ELISA. The results show the levels of IFN-γ, TNF-α, IL-12p40, and IL-10. The asterisk above the bar indicates statistical significance compared with PBS-MNPs, and the asterisk with a line indicates statistical significance compared with the indicated group. Statistical analysis: One-way ANOVA with Tukey's multiple comparison test, *P < 0.05, **P < 0.01 and ***P < 0.001.

such as IFN-γ, TNF-α, and IL-12p40, secreted by splenocytes, are also indicators of the cell-mediated immune response and were increased in the splenocytes from the BCG/MP group on day 3 after Ag85B restimulation, while similar levels of IL-10 were detected in all groups (Figure 5E). These trends were also observed when splenocytes were restimulated with H37Ra lysates, and the abundance of H37Ra-specific IgG subsets and the activation of T cells were increased (Supplementary Figure 3). Collectively, these results demonstrate that the BCG prime-boost strategy with Mpg-MNP elicits an improved Th1-biased immune response in a virulent *M. tuberculosis* infection model, suggesting that Mpg-MNP provides enhanced vaccine efficacy as a BCG vaccine booster.

Discussion

BCG is the only TB vaccine administered worldwide that can reduce the incidence of childhood TB (30). Although BCG vaccination is highly recommended in most countries, TB remains a fatal infectious disease (31). Since BCG vaccination coverage was 85% in 2020 globally

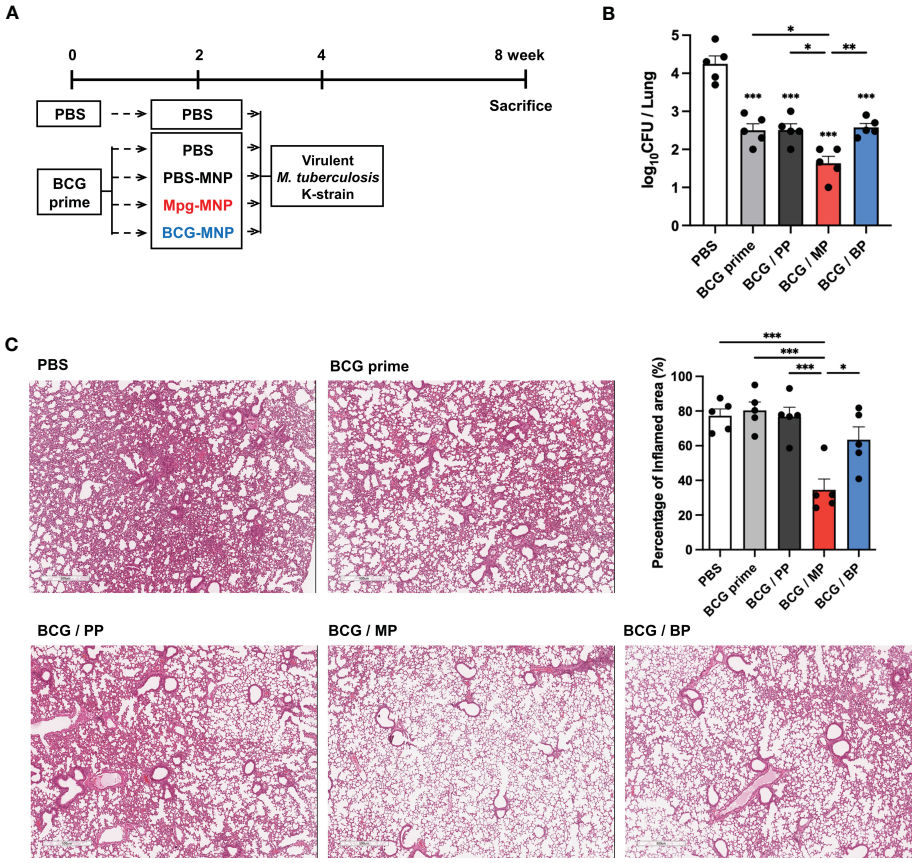

FIGURE 4
Protective efficacy of a BCG prime/Mpg-MNP boost protocol against virulent *M. tuberculosis in vivo*. **(A)** Schedule used to demonstrate the efficacy of the BCG prime/Mpg-MNP boost strategy against virulent *M. tuberculosis* K-strain challenge (BALB/c, female, n=5 per group). The PBS group was treated with PBS 2 times with a 2-week interval without BCG prime vaccination **(B)** The number of CFUs in the lungs. A representative image of H&E-stained lung lesions is presented in **(C)**. **(C)** The percentage of inflamed area was measured *via* lung histology (BCG prime; BCG prime only, BCG/PP; BCG prime/PBS-MNP boost, BCG/MP; BCG prime/Mpg-MNP boost, BCG/BP; BCG prime/BCG-MNP boost). Statistical analysis: One-way ANOVA with Tukey's multiple comparison test, *P < 0.05, **P < 0.01 and ***P < 0.001.

(32), the development of a new booster vaccine is mandatory to properly control TB in adults who have previously received the BCG vaccine. It has been proven that the sequential administration of vaccines using different antigens, the so-called heterologous prime-boost vaccine strategy, could be more effective for T-cell-based vaccines against *M. tuberculosis* than the repeated homologous prime-boost vaccine strategy (33). Indeed, *M. indicus pranii* has been shown to provide enhanced protection against *M. tuberculosis* as a BCG booster vaccine by increasing the frequency of multifunctional T cells (34). Based on this concept, we boosted the efficacy of BCG vaccination with Mpg-MNP to control tuberculosis infection by eliciting more enhanced T-cell immunity than BCG-only or BCG-MNP boost.

Microneedles have attracted attention as a promising transdermal immunization strategy (35). Several microneedle systems have been approved by the FDA or been investigated in clinical trials (36). However, most existing dissolving-type microneedles have been manufactured *via* a step-by-step micro-molding method using a three-dimensional (3D) mold and with the use of heat or ultraviolet (UV) light in the curing step (37). It is difficult to fill the mold cavity without drug loss, and such curing steps involve harsh conditions for biological drugs such as vaccines. In the DEN method, by dissolving the microneedle in each droplet, the drug can be loaded into the microneedle without loss of the drug, and the dose of the drug can be easily controlled by controlling the volume and concentration of the drug in the droplet. In addition, since the DEN method does not require molds, it is suitable for mass production and can achieve manufacture within 10 minutes. Following these perspectives, the DEN method provides additional advantages in terms of fabrication costs and the retention of drug biological activity. Consistent with the benefits of the DEN method, the fabrication of Mpg-MNPs showed superior market competitiveness.

Our previous study showed that Mpg is a temperature-sensitive vaccine candidate against tuberculosis, which proved to be safer and more effective in protecting against *M. tuberculosis* and *M. abscessus* in mouse model than BCG (12, 38). Mpg induces a shift in cytokine patterns and antibody production toward a Th1 phenotype and enhances the cytotoxic T-cell response by enhancing DC maturation. In addition, the feasibility of using Mpg as a vaccine vehicle expressing foreign antigens has also been proven in two independent studies (13, 14). Furthermore, live vaccines have shown powerful immunogenicity with induction of long-term immunity by inducing both humoral and cell-mediated immunity based on strong innate immune responses to

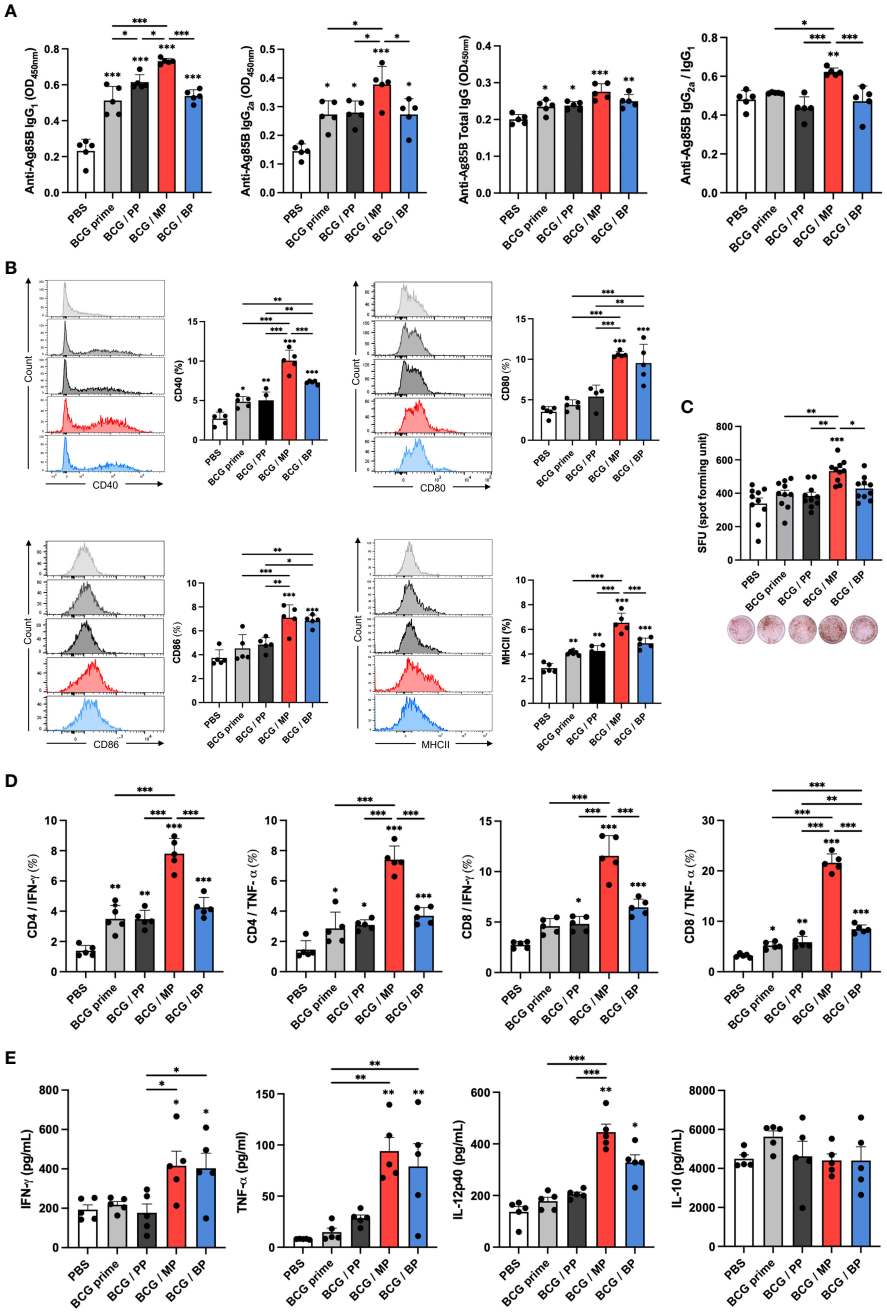

FIGURE 5
Induction of immune responses against virulent *M. tuberculosis* in splenocytes with a BCG prime/Mpg-MNP boost protocol. **(A)** The levels of IgG_1, IgG_{2a}, and total IgG against the Ag85B protein in the serum were measured by ELISA, and the ratio of IgG2a/IgG1 was determined by dividing the OD values of IgG2a by those of IgG1. **(B)** The graphs show the $CD40^+$ (upper left), $CD80^+$ (upper right), $CD86^+$ (lower left) and $MHCII^+$ (lower right) on $CD11b^+$ $CD11c^+$ dendritic cells among splenocytes. **(C)** The level of IFN-γ -secreting splenocytes restimulated with Ag85B peptides was measured by ELISPOT. The plots of bar graph show two biological replicate for each mouse. **(D)** The results of flow cytometry indicate the populations of IFN-γ - or TNF-α-releasing $CD4^+$ (left panel) and $CD8^+$ T cells (right panel) among splenocytes that were restimulated with the Ag85B protein for 72 h. **(E)** The bar graphs show the cytokine expression levels in the supernatant of splenocytes restimulated with the Ag85B protein for 72 h, as measured by ELISA. The results show the levels of IFN-γ, TNF-α, IL-12p40, and IL-10 (BCG prime; BCG prime only, BCG/PP; BCG prime/PBS-MNP boost, BCG/MP; BCG prime/Mpg-MNP boost, BCG/BP; BCG prime/BCG-MNP boost). Statistical analysis: One-way ANOVA with Tukey's multiple comparison test, *P < 0.05, **P < 0.01 and ***P < 0.001.

vital pathogen-associated molecular patterns (vita-PAMPs) (39). Several recent studies have illustrated that cyclic-di-adenosine monophosphate (c-di-AMP) or cyclic-di-guanosine monophosphate (c-di-GMP) produced by live gram-positive bacteria, including *Listeria* spp. and *Mycobacterium* spp., can induce DC activation *via* activation of the innate sensor stimulator of interferon genes (STING)-type 1 interferon (IFN-I) axis, highlighting the importance of maintaining microbial viability in live vaccine formulations (40, 41).

In this study, the high viability of Mpg on the MNPs indicates that Mpg is a more suitable strain for MNPs than BCG. To increase the viability of BCG during microneedle manufacturing, preservatives such as D-(+)-trehalose dihydrate should be added or BCG should be powdered for loading (22, 42). However, such preservatives could cause gastrointestinal discomfort and should be used with caution, especially in insulin users. Additionally, to prepare BCG powder, BCG should be lyophilized at -40°C, which requires more time, leading to reduced manufacturing efficiency. Based on the strong viability of Mpg, we aimed for a process without any preservatives or lyophilization process through the DEN method. Furthermore, Mpg has a faster optimal growth rate than BCG at 30°C, which provides great advantages for the mass production of Mpg-MNPs at low cost, illustrating the benefits of manufacturing. Considering these observations, the superiority of Mpg as a live vaccine makes it a suitable strain for MNP fabrication for tuberculosis protection.

The microneedle system mainly targets antigen-presenting cells in the skin, which can lead to systemic immunity by activating cellular immune responses in the skin-draining lymph nodes (43). In this study, we identified a large subset of MHCII+ langerin+ cells in the dermis, which are considered a subtype of not Langerhans cells but dermal langerin+ DCs (44–46). Langerin+ dermal DCs express langerin, a C-type lectin involved in the capture of antigens and antigen presentation to T cells, and play an essential role in cell-mediated and Th1 immune responses by migrating to the draining lymph nodes (47, 48). In addition, we detected a robust increase of Ki-67+ langerin+ cells, indicating that the inflammatory environment can induce local regeneration of DCs by renewal, enhancing their response to antigenic challenge and increasing migration to the draining lymph nodes (49, 50).Since the protective effect against *M. tuberculosis* relies on cell-mediated immunity, effector T cells play a pivotal role during *M. tuberculosis* infection, and it is important to boost the efficacy of BCG vaccination in protecting against tuberculosis by activating antigen-specific CD4+ and CD8+ T cells *via* migratory dermal DCs (51). Furthermore, langerin+ dermal DCs are known to play a pivotal role in lung immunity by inducing CD8+ T-cell-mediated immune responses (52). During influenza virus infection, although they have a low frequency among total dermal DCs, depletion of dermal langerin+ DCs impedes pathogen clearance and worsens lung infection (53). Therefore, compared to a single dose of BCG vaccination or BCG-MNP boost, a booster with Mpg-MNP vaccination after BCG priming can enhance the protective effect against *M. tuberculosis* by enhancing cell-mediated immunity *via* activation of Th1 immune responses by proliferating dermal langerin+ DCs. The successful transdermal delivery of live Mpg engages systemic immune responses against *M. tuberculosis* infection *via* activation of antigen-presenting cells, specifically MHCII+ langerin+ cells, migrating into the skin draining lymph nodes. Of note, the induction of cellular immune responses by Mpg-MNP boost has been shown to reduce the pulmonary bacterial burden and ameliorate lung pathology caused by infection with a virulent *M. tuberculosis* strain compared to those observed after BCG priming (Figure 6).

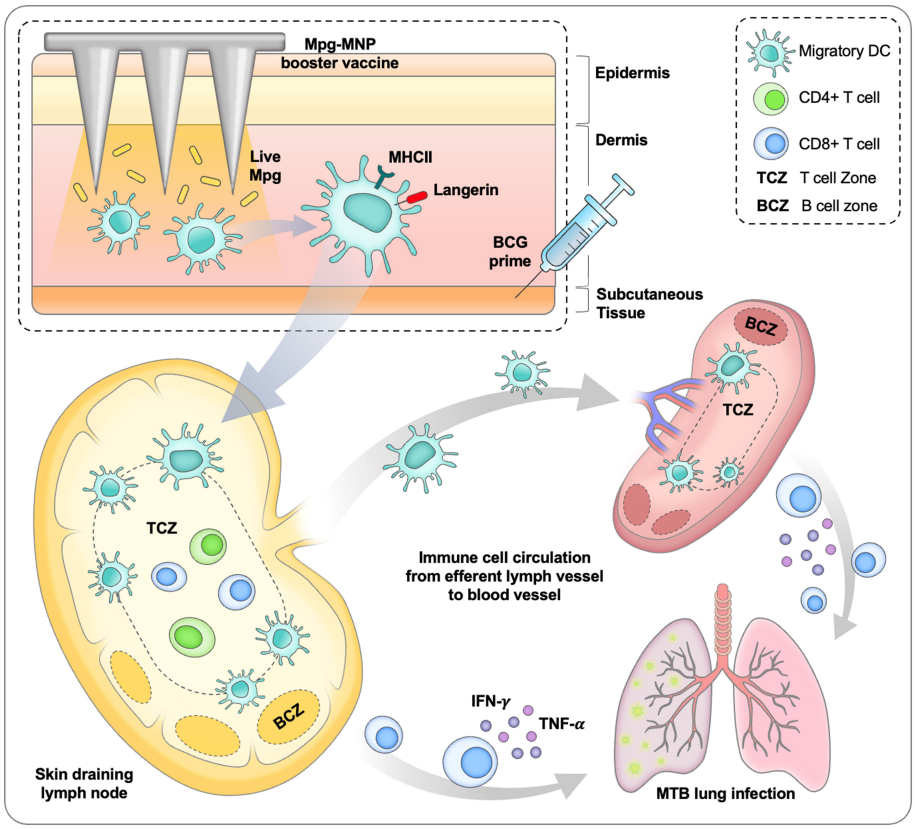

FIGURE 6
Schematic diagram about protective immune response induced by BCG prime/Mpg-MNP boost strategy.

In this study, we proposed to introduce Mpg-MNP to overcome the limitations of hypodermic injection through comparison with BCG-MNP and we demonstrated the superiority of Mpg-MNPs to induce local dermal immune system as an effective topical transdermal delivery strategy. On the other hand, due to the lack of delivery efficiency of MNP (Supplementary Figure 5A), MNP shows limitation of immune response induction compared to hypodermic injection (Supplementary Figure 5B). Since this is the first attempt to apply live mycobacterial-loaded MNP based on the DEN method, further technical optimizing processes will be necessary for MNPs to increase the delivery efficiency of the live Mpg.

In conclusion, our data showed that Mpg-MNP led to enhanced humoral and cell-mediated immune responses against tuberculosis antigens in the BCG prime-boost vaccination strategy, mainly due to enhanced abundance of MHCII+ langerin+ subsets in the dermis of a mouse model. Furthermore, booster vaccination with Mpg-MNP after BCG vaccination led to enhanced protection against infection with the hypervirulent *M. tuberculosis* K-strain in mice, suggesting the feasibility of the HA-based dissolving Mpg-MNP introduced in our study as a candidate for a booster tuberculosis vaccine.

Data availability statement

The original contributions presented in the study are included in the article/Supplementary Material. Further inquiries can be directed to the corresponding authors.

Ethics statement

The animal biosafety level-2 (BSL-2) experiments were approved by the Institutional Animal Care and Use Committee (IACUC; Approval No. SNU-210531-5) of the Institute of Laboratory Animal Resources of Seoul National University. The BSL-3 experiments were approved by the Institutional Animal Care and Use Committee of Seoul National University Hospital (SNUH-IACUC; Approval No. SNUH IACUC No. 19-0162-C1A1), and animals were maintained in a facility accredited by AAALAC International (#001169) in accordance with the Guide for the Care and Use of Laboratory Animals 8th edition, NRC (2010).

Author contributions

B-JK and M-HL designed the study and wrote the manuscript. M-HL designed *in vivo* experiments. M-HL and HS performed experiments and analyzed data. BK conceived the conceptualization. M-SL, JS and JJ provided MNPs. HK, DL and JO participated data analysis. B-JK and DJ supervised the study. The authors confirmed and approved the final manuscript. All authors contributed to the article and approved the submitted version.

Funding

The study was supported by Korea Health Industry Development Institute (KHIDI), funded by Ministry of Health &Welfare, Republic of Korea (Grant No. HV20C0147 and HI22C0312). The funder was not involved in the study design, data analysis and writing of the manuscript.

Conflict of interest

Authors M-SL, JS, JJ and DJ were employed by Raphas Co., Ltd.

The remaining authors declare that the research was conducted in the absence of any commercial or financial relationships that could be construed as a potential conflict of interest.

Publisher's note

All claims expressed in this article are solely those of the authors and do not necessarily represent those of their affiliated organizations, or those of the publisher, the editors and the reviewers. Any product that may be evaluated in this article, or claim that may be made by its manufacturer, is not guaranteed or endorsed by the publisher.

Supplementary material

The Supplementary Material for this article can be found online at: https://www.frontiersin.org/articles/10.3389/fimmu.2023.1178688/full#supplementary-material

References

1. Barberis I, Bragazzi NL, Galluzzo L, Martini M. The history of tuberculosis: from the first historical records to the isolation of koch's bacillus. *J Prev Med hygiene* (2017) 58(1):E9.

2. Zwerling A, Behr MA, Verma A, Brewer TF, Menzies D, Pai M. The BCG world atlas: a database of global BCG vaccination policies and practices. *PloS Med* (2011) 8(3): e1001012. doi: 10.1371/journal.pmed.1001012

3. Citro B, Soltan V, Malar J, Katlholo T, Smyth C, Sari AH, et al. Building the evidence for a rights-based, people-centered, gender-transformative tuberculosis response: an analysis of the stop TB partnership community, rights, and gender tuberculosis assessment. *Health Hum Rights* (2021) 23(2):253.

4. Shrivastava J, Shrivastava A. Scenario of tuberculosis in India. *J Lung Pulm Respir Res* (2021) 8(2):24–5. doi: 10.15406/jlprr.2021.08.00246

5. Rodrigues LC, Mangtani P, Abubakar I. How does the level of BCG vaccine protection against tuberculosis fall over time? *Bmj* (2011) 343. doi: 10.1136/bmj.d5974

6. Jirjees FJ, Bashi YHD, Al-Obaidi HJ. COVID-19 death and BCG vaccination programs worldwide. *Tuberculosis Respir Diseases* (2021) 84(1):13. doi: 10.4046/trd.2020.0063

7. Khademi F, Derakhshan M, Yousefi-Avarvand A, Tafaghodi M, Soleimanpour S. Multi-stage subunit vaccines against mycobacterium tuberculosis: an alternative to the

BCG vaccine or a BCG-prime boost? *Expert Rev Vaccines* (2018) 17(1):31–44. doi: 10.1080/14760584.2018.1406309

8. Nemes E, Geldenhuys H, Rozot V, Rutkowski KT, Ratangee F, Bilek N, et al. Prevention of m. tuberculosis infection with H4: IC31 vaccine or BCG revaccination. *New Engl J Med* (2018) 379(2):138–49. doi: 10.1056/NEJMoa1714021

9. Poyntz HC, Stylianou E, Griffiths KL, Marsay L, Checkley AM, McShane H. Non-tuberculous mycobacteria have diverse effects on BCG efficacy against mycobacterium tuberculosis. *Tuberculosis* (2014) 94(3):226–37. doi: 10.1016/j.tube.2013.12.006

10. Flaherty DK, Vesosky B, Beamer GL, Stromberg P, Turner J. Exposure to mycobacterium avium can modulate established immunity against mycobacterium tuberculosis infection generated by mycobacterium bovis BCG vaccination. *J leukocyte Biol* (2006) 80(6):1262–71. doi: 10.1189/jlb.0606407

11. von Reyn CF, Lahey T, Arbeit RD, Landry B, Kailani L, Adams LV, et al. Safety and immunogenicity of an inactivated whole cell tuberculosis vaccine booster in adults primed with BCG: a randomized, controlled trial of DAR-901. *PloS One* (2017) 12(5): e0175215. doi: 10.1371/journal.pone.0175215

12. Kim B-J, Kim B-R, Kook Y-H, Kim B-J. A temperature sensitive mycobacterium paragordonae induces enhanced protective immune responses against mycobacterial infections in the mouse model. *Sci Rep* (2017) 7(1):1–14. doi: 10.1038/s41598-017-15458-7

13. Kim B-J, Kim B-R, Kook Y-H, Kim B-J. Potential of recombinant mycobacterium paragordonae expressing HIV-1 gag as a prime vaccine for HIV-1 infection. *Sci Rep* (2019) 9(1):1–11. doi: 10.1038/s41598-019-51875-6

14. Kim B-J, Jeong H, Seo H, Lee M-H, Shin HM, Kim B-J. Recombinant mycobacterium paragordonae expressing SARS-CoV-2 receptor-binding domain as a vaccine candidate against SARS-CoV-2 infections. *Front Immunol* (2021) 12. doi: 10.3389/fimmu.2021.712274

15. Korkmaz E, Balmert SC, Carey CD, Erdos G, Falo LDJr. Emerging skin-targeted drug delivery strategies to engineer immunity: a focus on infectious diseases. *Expert Opin Drug Delivery* (2021) 18(2):151–67. doi: 10.1080/17425247.2021.1823964

16. Romani N, Thurnher M, Idoyaga J, Steinman RM, Flacher V. Targeting of antigens to skin dendritic cells: possibilities to enhance vaccine efficacy. *Immunol Cell Biol* (2010) 88(4):424–30. doi: 10.1038/icb.2010.39

17. Kim Y-C, Park J-H, Prausnitz MR. Microneedles for drug and vaccine delivery. *Advanced Drug delivery Rev* (2012) 64(14):1547–68. doi: 10.1016/j.addr.2012.04.005

18. Kang H, Zuo Z, Lin R, Yao M, Han Y, Han J. The most promising microneedle device: present and future of hyaluronic acid microneedle patch. *Drug Delivery* (2022) 29(1):3087–110. doi: 10.1080/10717544.2022.2125600

19. Du H, Liu P, Zhu J, Lan J, Li Y, Zhang L, et al. Hyaluronic acid-based dissolving microneedle patch loaded with methotrexate for improved treatment of psoriasis. *ACS Appl materials interfaces* (2019) 11(46):43588–98. doi: 10.1021/acsami.9b15668

20. Kim JD, Kim M, Yang H, Lee K, Jung H. Droplet-born air blowing: novel dissolving microneedle fabrication. *J Controlled release* (2013) 170(3):430–6. doi: 10.1016/j.jconrel.2013.05.026

21. Kim JH, Shin JU, Kim SH, Noh JY, Kim HR, Lee J, et al. Successful transdermal allergen delivery and allergen-specific immunotherapy using biodegradable microneedle patches. *Biomaterials* (2018) 150:38–48. doi: 10.1016/j.biomaterials.2017.10.013

22. Hiraishi Y, Nandakumar S, Choi S-O, Lee JW, Kim Y-C, Posey JE, et al. Bacillus calmette-guerin vaccination using a microneedle patch. *Vaccine* (2011) 29(14):2626–36. doi: 10.1016/j.vaccine.2011.01.042

23. Senna SG, Battilana J, Costa JC, Silva MG, Duarte RS, Fonseca LS, et al. Sequencing of hsp65 gene for identification of mycobacterium species isolated from environmental and clinical sources in Rio de Janeiro, Brazil. *J Clin Microbiol* (2008) 46 (11):3822–5. doi: 10.1128/JCM.00451-08

24. Pereira AC, Ramos B, Reis AC, Cunha MV. Non-tuberculous mycobacteria: molecular and physiological bases of virulence and adaptation to ecological niches. *Microorganisms* (2020) 8(9):1380. doi: 10.3390/microorganisms8091380

25. Stoitzner P, Tripp CH, Douillard P, Saeland S, Romani N. Migratory langerhans cells in mouse lymph nodes in steady state and inflammation. *J Invest Dermatol* (2005) 125(1):116–25. doi: 10.1111/j.0022-202X.2005.23757.x

26. Kissenpfennig A, Henri S, Dubois B, Laplace-Builhé C, Perrin P, Romani N, et al. Dynamics and function of langerhans cells *in vivo*: dermal dendritic cells colonize lymph node areasdistinct from slower migrating langerhans cells. *Immunity* (2005) 22 (5):643–54. doi: 10.1016/j.immuni.2005.04.004

27. Ghigo C, Mondor I, Jorquera A, Nowak J, Wienert S, Zahner SP, et al. Multicolor fate mapping of langerhans cell homeostasis. *J Exp Med* (2013) 210 (9):1657–64. doi: 10.1084/jem.20130403

28. Stoitzner P, Holzmann S, McLellan AD, Ivarsson L, Stössel H, Kapp M, et al. Visualization and characterization of migratory langerhans cells in murine skin and lymph nodes by antibodies against Langerin/CD207. *J Invest Dermatol* (2003) 120 (2):266–74. doi: 10.1046/j.1523-1747.2003.12042.x

29. Zeng G, Zhang G, Chen X. Th1 cytokines, true functional signatures for protective immunity against TB? *Cell Mol Immunol* (2018) 15(3):206–15. doi: 10.1038/cmi.2017.113

30. Trunz BB, Fine P, Dye C. Effect of BCG vaccination on childhood tuberculous meningitis and miliary tuberculosis worldwide: a meta-analysis and assessment of cost-effectiveness. *Lancet* (2006) 367(9517):1173–80. doi: 10.1016/S0140-6736(06)68507-3

31. Marciano BE, Huang C-Y, Joshi G, Rezaei N, Carvalho BC, Allwood Z, et al. BCG Vaccination in patients with severe combined immunodeficiency: complications, risks, and vaccination policies. *J Allergy Clin Immunol* (2014) 133(4):1134–41. doi: 10.1016/j.jaci.2014.02.028

32. Muhoza P, Danovaro-Holliday MC, Diallo MS, Murphy P, Sodha SV, Requejo JH, et al. Routine vaccination coverage–worldwide, 2020. *Morbidity Mortality Weekly Rep* (2021) 70(43):1495. doi: 10.15585/mmwr.mm7043a1

33. Palgen J-L, Feraoun Y, Dzangué-Tchoupou G, Joly C, Martinon F, Le Grand R, et al. Optimize prime/boost vaccine strategies: trained immunity as a new player in the game. *Front Immunol* (2021) 12:612747. doi: 10.3389/fimmu.2021.612747

34. Saqib M, Khatri R, Singh B, Gupta A, Kumar A, Bhaskar S. Mycobacterium indicus pranii as a booster vaccine enhances BCG induced immunity and confers higher protection in animal models of tuberculosis. *Tuberculosis* (2016) 101:164–73. doi: 10.1016/j.tube.2016.10.002

35. Wang M, Hu L, Xu C. Recent advances in the design of polymeric microneedles for transdermal drug delivery and biosensing. *Lab Chip* (2017) 17(8):1373–87. doi: 10.1039/C7LC00016B

36. Chen Y, Alba M, Tieu T, Tong Z, Minhas RS, Rudd D, et al. Engineering micro–nanomaterials for biomedical translation. *Advanced NanoBiomed Res* (2021) 1 (9):2100002. doi: 10.1002/anbr.202100002

37. Park J-H, Allen MG, Prausnitz MR. Biodegradable polymer microneedles: fabrication, mechanics and transdermal drug delivery. *J Controlled release* (2005) 104 (1):51–66. doi: 10.1016/j.jconrel.2005.02.002

38. Cha G-Y, Seo H, Oh J, Kim B-J, Kim B-J. Potential use of mycobacterium paragordonae for antimycobacterial drug screening systems. *J Microbiol* (2023) 61 (1):121–9. doi: 10.1007/s12275-022-00009-1

39. Blander JM, Barbet G. Exploiting vita-PAMPs in vaccines. *Curr Opin Pharmacol* (2018) 41:128–36. doi: 10.1016/j.coph.2018.05.012

40. Lee M-H, Kim B-R, Seo H, Oh JH, Kim HL, Kim B-J. Live mycobacterium paragordonae induces heterologous immunity of natural killer cells by eliciting type I interferons from dendritic cells *via* STING-dependent sensing of cyclic-di-GMP. *Microbes Infection* (2023) 105144. doi: 10.1016/j.micinf.2023.105144

41. Moretti J, Roy S, Bozec D, Martinez J, Chapman JR, Ueberheide B, et al. STING senses microbial viability to orchestrate stress-mediated autophagy of the endoplasmic reticulum. *Cell* (2017) 171(4):809–23.e13. doi: 10.1016/j.cell.2017.09.034

42. Chen F, Yan Q, Yu Y, Wu MX. BCG Vaccine powder-laden and dissolvable microneedle arrays for lesion-free vaccination. *J Controlled Release* (2017) 255:36–44. doi: 10.1016/j.jconrel.2017.03.397

43. Yu Y, Wang H, Guo B, Wang B, Wan Z, Zhang Y, et al. Microneedle-based two-step transdermal delivery of langerhans cell-targeting immunoliposomes induces a Th1-biased immune response. *Eur J Pharmaceutics Biopharmaceutics* (2022) 177:68–80. doi: 10.1016/j.ejpb.2022.06.004

44. Seneschal J, Jiang X, Kupper TS. Langerin+ dermal DC, but not langerhans cells, are required for effective CD8-mediated immune responses after skin scarification with vaccinia virus. *J Invest Dermatol* (2014) 134(3):686–94. doi: 10.1038/jid.2013.418

45. Clausen BE, Kel JM. Langerhans cells: critical regulators of skin immunity? *Immunol Cell Biol* (2010) 88(4):351–60. doi: 10.1038/icb.2010.40

46. Poulin LF, Henri S, de Bovis B, Devilard E, Kissenpfennig A, Malissen B. The dermis contains langerin+ dendritic cells that develop and function independently of epidermal langerhans cells. *J Exp Med* (2007) 204(13):3119–31. doi: 10.1084/jem.20071724

47. Valladeau J, Ravel O, Dezutter-Dambuyant C, Moore K, Kleijmeer M, Liu Y, et al. Langerin, a novel c-type lectin specific to langerhans cells, is an endocytic receptor that induces the formation of birbeck granules. *Immunity* (2000) 12(1):71–81. doi: 10.1016/S1074-7613(00)80160-0

48. Flacher V, Tripp CH, Mairhofer DG, Steinman RM, Stoitzner P, Idoyaga J, et al. Murine langerin+ dermal dendritic cells prime CD 8+ T cells while l angerhans cells induce cross-tolerance. *EMBO Mol Med* (2014) 6(9):1191–204. doi: 10.15252/emmm.201303283

49. Xue D, Tabib T, Morse C, Lafyatis R. Transcriptome landscape of myeloid cells in human skin reveals diversity, rare populations and putative DC progenitors. *J Dermatol sci* (2020) 97(1):41–9. doi: 10.1016/j.jdermsci.2019.11.012

50. Merad M, Manz MG, Karsunky H, Wagers A, Peters W, Charo I, et al. Langerhans cells renew in the skin throughout life under steady-state conditions. *Nat Immunol* (2002) 3(12):1135–41. doi: 10.1038/ni852

51. Li J, Zhan L, Qin C. The double-sided effects of mycobacterium bovis bacillus calmette–guérin vaccine. *NPJ Vaccines* (2021) 6(1):1–11. doi: 10.1038/s41541-020-00278-0

52. Merad M, Ginhoux F, Collin M. Origin, homeostasis and function of langerhans cells and other langerin-expressing dendritic cells. *Nat Rev Immunol* (2008) 8(12):935–47. doi: 10.1038/nri2455

53. GeurtsvanKessel CH, Willart MA, van Rijt LS, Muskens F, Kool M, Baas C, et al. Clearance of influenza virus from the lung depends on migratory langerin+ CD11b– but not plasmacytoid dendritic cells. *J Exp Med* (2008) 205(7):1621–34. doi: 10.1084/jem.20071365

frontiers | Frontiers in Immunology

TYPE Original Research
PUBLISHED 22 August 2023
DOI 10.3389/fimmu.2023.1200328

Check for updates

OPEN ACCESS

EDITED BY
Ernesto T. A. Marques,
University of Pittsburgh, United States

REVIEWED BY
Amit Kumar Jaiswal,
VIT University, India
Jiaqiang Wu,
Shandong Academy of Agricultural Sciences, China

*CORRESPONDENCE
Dinesh Kumar
drdinesh.fssai@gmail.com;
dinesh.k@fssai.gov.in
Subash Chandra Sonkar
drscsonkar@gmail.com

RECEIVED 04 April 2023
ACCEPTED 20 July 2023
PUBLISHED 22 August 2023

CITATION
Kumar D, Oberoi HS, Singh H, Shrivastav TG, Bhukya PL, Kumari M, Koner BC and Sonkar SC (2023) Development and optimization of an in-house heterologous ELISA for detection of prednisolone drug in enzyme conjugates using spacers. *Front. Immunol.* 14:1200328. doi: 10.3389/fimmu.2023.1200328

COPYRIGHT
© 2023 Kumar, Oberoi, Singh, Shrivastav, Bhukya, Kumari, Koner and Sonkar. This is an open-access article distributed under the terms of the Creative Commons Attribution License (CC BY). The use, distribution or reproduction in other forums is permitted, provided the original author(s) and the copyright owner(s) are credited and that the original publication in this journal is cited, in accordance with accepted academic practice. No use, distribution or reproduction is permitted which does not comply with these terms.

Development and optimization of an in-house heterologous ELISA for detection of prednisolone drug in enzyme conjugates using spacers

Dinesh Kumar[1,2]*, Harinder Singh Oberoi[2], Harpal Singh[3,4], Tulsidas G. Shrivastav[1], Prudhvi Lal Bhukya[5], Mansi Kumari[6], Bidhan Chandra Koner[7,8] and Subash Chandra Sonkar[7,9]*

[1]Department of Reproductive Biomedicine, National Institute of Health and Family Welfare (NIHFW), New Delhi, India, [2]Quality Assurance Division, Food Safety and Standards Authority of India (FSSAI), New Delhi, India, [3]Centre for Biomedical Engineering, Indian Institute of Technology Delhi (IIT-D), New Delhi, India, [4]Department of Biomedical Engineering, All India Institute of Medical Sciences Delhi (AIIMS-D), New Delhi, India, [5]Rodent Experimentation Facility, Indian Council of Medical Research (ICMR)-National Animal Resource Facility for Biomedical Research (Indian Council of Medical Research (ICMR)-NARFBR), Hyderabad, India, [6]Dr. D. Y. Patil Biotechnology and Bioinformatics Institute, Dr. D. Y. Patil Vidyapeeth, Pune, India, [7]Multidisciplinary Research Unit, Maulana Azad Medical College and Associated Hospital, New Delhi, India, [8]Department of Biochemistry, Maulana Azad Medical College and Associated Hospital, New Delhi, India, [9]Delhi School of Public Health, Institute of Eminence, University of Delhi, Delhi, India

The introduction of spacers in coating steroid protein complexes and/or enzyme conjugates or immunogens is known to exert an influence on the sensitivity of steroid enzyme immunoassays. We investigated the impact of different homobifunctional spacers, ranging in atomic length from 3 to 10, on the sensitivity and specificity of prednisolone (PSL) enzyme immunoassays. In this study, four homo-bifunctional spacers, namely, carbohydrazide (CH), adipic acid dihydrazide (ADH), ethylene diamine (EDA), and urea (U), were incorporated between PSL and horseradish peroxidase (HRP) for preparing the enzyme conjugate with an aim to improve the sensitivity of the assay without compromising assay specificity. The assays were developed using these enzymes conjugated with antibodies raised against the PSL-21-HS-BSA immunogen. The sensitivity of the PSL assays after insertion of a bridge in the enzyme conjugate was 1.22 ng/mL, 0.59 ng/mL, 0.48 ng/mL, and 0.018 ng/mL with ADH, CH, EDA, and urea as a spacer, respectively. Among the four combinations, the PSL-21-HS-BSA-antibody with PSL-21-HS-U-HRP-enzyme conjugate gave better sensitivity and less cross-reaction. The percent recovery of PSL from the exogenously spiked human serum pools was in the range of 88.32%-102.50%. The intra and inter-assay CV% was< 8.46%. The PSL concentration was estimated in the serum samples of patients on PSL treatment. The serum PSL values obtained by this method correlated well with the commercially available kit (r^2 = 0.98). The present study suggests that the nature of the spacer is related to assay sensitivity and not the spacer length.

KEYWORDS

heterologous ELISA, bridge/spacers, prednisolone, antibody, horseradish peroxidase, enzyme conjugates, spacers, immunogens

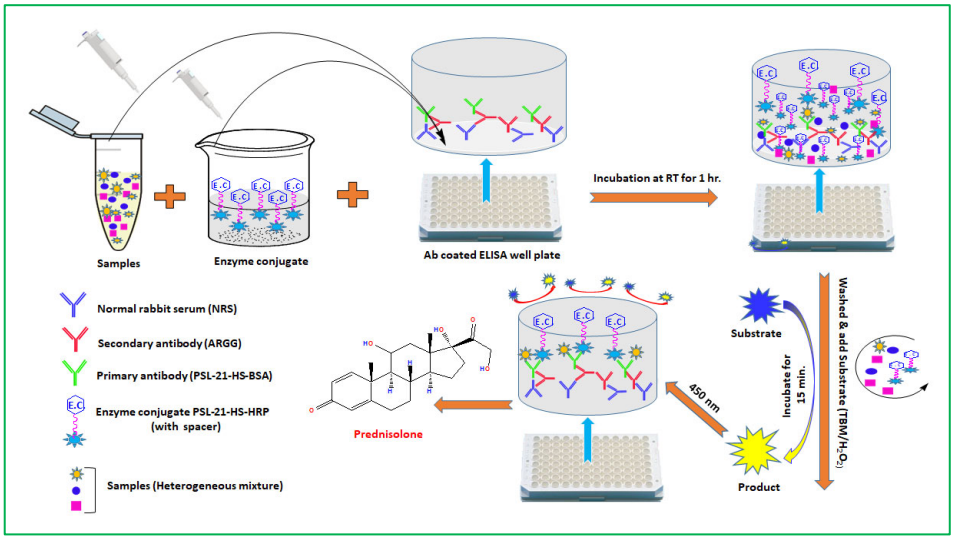

GRAPHICAL ABSTRACT

Highlights

- ❖ The spacer length is not significant as the spacer structure; it plays a remarkable role in improving the sensitivity of ELISA.
- ❖ The physicochemical nature of the bridge and steroid is determinant in defining the assay parameters.
- ❖ The in-house developed assay is simple, sensitive, direct, and convenient to use for prednisolone in serum.
- ❖ The procedure adopted for coating primary antibodies does not require affinity-purified antibodies.

1 Introduction

The PSL (1, 4-Pregnadiene-11β,17α,21-Triol-3, 20-Dione/1-Dehydrocortisol) is a synthetic analog of endogenous cortisol, with potent glucocorticoid and low mineralocorticoid activity, which makes it useful for the treatment and management of a broad range of autoimmune diseases (such as lupus, arthritis, and nephritis). It is also widely used in veterinary medicine, particularly to treat inflammatory diseases, shock, stress, circulatory collapse, and ketonemia, and to lower fever and reduce pain.

There is evidence that long-term exposure to low concentrations of glucocorticoid may increase negative toxic effects on public health, leading to diabetes and metabolic disorders. Prolonged use of therapy doses may cause depression, hypertension, weight loss, muscle atrophy, bone pain, increased susceptibility to infection, sleep disturbances, delayed wound healing, decreased sex hormone production, and a reduction in growth rates in children. Therefore, there is a growing demand for more sensitive, specific, rapid, and cost-effective methods for the determination of the low concentration of PSL residues in the samples.

Compared with physicochemical methods (HPLC, LC-MS/MS, GC-MS, etc.), enzyme-linked immunosorbent assay (ELISA) is rapid, simple, effective, and needs fewer or no sample preparation. ELISAs are presently the most used and successful technique for the immunologically-based detection of a wide variety of antigens. Its popularity has increased rapidly due to its high-throughput competencies, where it is capable of analyzing many samples in a relatively short period of time. It is not always easy to develop a specific and sensitive ELISA for a small molecule such as prednisolone, a synthetic steroid that is not naturally present in the body. One of the most important factors that determine the sensitivity and specificity is the combination of antibody and enzyme conjugate used in the assay (1–10).

The ELISAs for steroids (hapten) developed so far are either in a heterologous or homologous combination. The heterologous or homologous combinations of antibody and enzyme conjugate in steroid enzyme immunoassay (EIA) effects unlabeled steroid recognition which affects the sensitivity of the assay. In heterologous assays, the haptens used as antigens to produce the antibody are different from the haptens used for tagging the enzyme. In homologous immunoassays, the haptens are similar in

Abbreviations: PSL, Prednisolone; HS, hemisuccinate; BSA, bovine serum albumin; HRP, horseradish peroxidase; ADH, adipic acid dihydrazide; CH, carbohydrazide; EDA, ethylenediamine; U, urea; GABA, gamma amino butyric acid; 6ACA, 6-amino caproic acid; ODA, oxy diamine; BODA, bis-oxy diamine; NHS, N-hydroxysuccinimide; EDAC.HCl, 1-ethyl-3-(3-dimethylaminopropyl) carbodiimide hydrochloride; FAC, Freund's adjuvant complete; DMF, dimethyl formamide; TMB, tetramethylbenzidine; H_2O_2.U, hydrogen peroxide urea; MALDI-TOF, Matrix assisted laser desorption ionization-time of flight; ARASG, anti-rabbit anti-serum in goat.

both cases. It is often found that in a heterologous assay (11–17) certain differences, such as that of site, bridge, or antigen (steroid), exist between the steroid derivatives used for the preparation of the immunogen and enzyme conjugate, while the assay is more sensitive due to improved fitting of the steroid into the antibody binding pocket and reduced bridge recognition (12, 14, 17). However, the homologous combination does not provide satisfactory sensitivity, because the binding affinity of the labeled antigen to the antibody is higher than that of the antigen to be measured (18, 19). Few sensitive homologous assays for steroids have been developed (1–4, 20–29).

A remarkable improvement in the sensitivity of ELISA has been observed by various researchers using spacers between antigens and coupling protein when used as a coating antigen in the antigen immobilized format (14–17) or between antigen and enzyme when used as an enzyme conjugate in the antibody immobilized format (30, 31). It was demonstrated that in the antigen-immobilized format, varying the lengths of the spacer arm of the coating antigen had a significant effect on the sensitivity of ELISA (29, 32–36). A 19-atom linker, an oligoethylene glycol (OEG), was conjugated between progesterone and ovalbumin (OVA) and used as a coating antigen in the surface plasmon resonance (SPR) flow-through biosensor format. Its hydrophilic nature allows good projection of the antigen (progesterone) into the aqueous mobile phase (27–29, 32).

In the antibody-immobilized format, spacers have been coupled between steroid derivative and label protein to minimize the orthodox bridge recognition effects and to overcome steric constraints between the two high molecular weight proteins, i.e., the antibody and label (5–11, 14, 19, 20). Shrivastav et al. studied the differential behavior of spacers such as adipic acid dihydrazide (ADH), ethylenediamine (EDA), carbohydrazide (CH), urea (U), gamma amino butyric acid-ADH (GABA-ADH), and 6-amino caproic acid-ADH (6ACA-ADH) in the steroid-horseradish peroxidase (HRP) enzyme conjugate in the direct ELISA format. The study revealed that the use of a spacer between the steroid and enzyme in the enzyme conjugate increases the sensitivity and specificity of the assay. It has also been reported that the spacer length does not bear any correlation with the assay sensitivity in an ELISA of steroids (1, 5–11, 14, 19, 20). Further, the nature of the spacer (hydrophilic, hydrophobic, flexible, or rigid) is related to assay sensitivity and not to spacer length (5–11, 14, 33). This disparity in the behavior of spacers towards the sensitivity and specificity of assays might be due to the difference in the magnitude of overall forces of attraction between

the antibody and the enzyme conjugates (9). Sathe et al. coupled spacers (urea, ADH and oxy diamine (ODA), bis-oxy diamine (BODA)) between an organophosphorus pesticide and HRP and studied the effect of spacers on the sensitivity of the assay. The use of deliquescent spacers helped to increase the antibody binding signal and improve the sensitivity of the assay (28).

To the best of our knowledge, no reported studies exist on the development of ELISA for PSL using bridge heterology in enzyme conjugates. Also, the PSL derivatives of different bridge lengths are not available commercially to produce enzyme conjugate. It is not easy to synthesize novel hapten derivatives with different bridge lengths as it requires knowledge of synthesis, isolation, and purification of hapten derivatives. To overcome this, we first introduced spacers in the enzyme and purified the spacer-incorporated enzyme using simple dialysis or column chromatography. This spacer incorporated enzyme carboxyl derivative of PSL was coupled. We have incorporated four homobifunctional molecules, ADH (10 atomic length spacer), CH (5 atomic length spacer), EDA (4 atomic length spacer), and U (3 atomic length spacer) as spacers between PSL-21-HS and $-NH_2$ blocked HRP for preparation of the enzyme conjugates. The influence of these spacers on assay parameters such as sensitivity, ED_{50}, and specificity has been studied with respect to their length and physiochemical nature.

2 Methods

The experimental protocols were approved by the institutional animal ethics committee (IAEC) of the National Institute of Health and Family Welfare (NIHFW), New Delhi, India. All animal experiments were performed in accordance with the guidelines of the Committee for the Purpose of Control and Supervision of Experiments on Animals (CPCSEA), Government of India.

2.1 Materials

All solvents, chemicals, and salts used in the present study were of analytical grade and were used without prior purification. All steroids used for the conjugation and cross-reactivity were obtained from Steraloids, Inc. (Newport, RI, USA). Bovine serum albumin (BSA), N-hydroxysuccinimide (NHS), 1-ethyl-3-(3-dimethylaminopropyl) carbodiimide hydrochloride (EDAC.HCl), Freund's adjuvant complete (FAC), Dioxan, dimethyl formamide (DMF), Tetramethylbenzidine (TMB), Hydrogen peroxide urea (H_2O_2.U)/carbamide peroxide, ADH, EDA, CH, urea, and thimerosal were purchased from Sigma Chemical Company (St. Louis, MO, USA). Horseradish peroxidase was purchased from Bangalore Genei, Bangalore, India. An ELISA kit of prednisolone was purchased from Sincere Biotech Co. Ltd., Beijing, China. Microtitre plates were procured from Corning Life Sciences (Tewksbury, MA 01876, USA).

2.2 Instrumentation

Tecan Spectra micro-plate reader from Tecan Austria GmbH (5082 Grödig, Austria). A lyophilizer from Haryson (New Delhi, India) and a matrix-assisted laser desorption ionization-time of flight (MALDI-TOF) spectrometer from Bruker Daltonic, Germany.

2.3 Preparation of PSL-21-HS-BSA immunogen

PSL-21-HS was coupled to BSA by using N-hydroxysuccinimide mediated carbodiimide reaction (21). The plan of the chemical

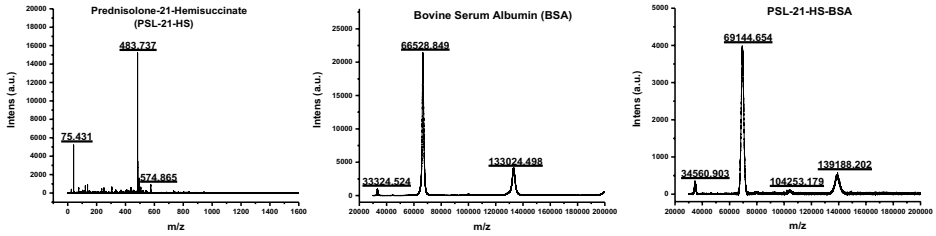

FIGURE 1
Mass spectra of PSL-21-HS, BSA, and PSL-21-HS-BSA by MALDI-TOF.

reaction is shown in Scheme 1. In brief, 200 µL of both DMF and dioxan, and 100 µL of distilled water containing 10 mg of NHS and 20 mg of EDAC.HCl were added to 5 mg of PSL-21-HS. The reaction mixture was mixed and kept at 4°C for activation overnight. Following the overnight activation, aqueous BSA solution (1 mg/0.5 mL) was added to the activated steroid reaction mixture and vortex-mixed and kept at 4°C overnight for the formation of an amide bond. The PSL-21-HS-BSA conjugate was dialyzed against distilled water for 3-4 changes at 4°C. The dialysate was frozen at -20°C, lyophilized, and stored at 4°C in aliquots of 1 mg for immunization.

2.4 Preparation of enzyme conjugate

All the conjugation reactions were carried out as previously described by an active ester method with modification (10).

2.5 Preparation of enzyme conjugates with spacer (PSL-21-HS-ADH-HRP, PSL-21-HS-CH-HRP, PSL-21-HS-EDA-HRP, and PSL-21-HS-U-HRP)

The enzyme conjugates with spacers were prepared as shown in Schemes 2 and 3 by an active ester method (7).

2.5.1 Coupling of spacers to HRP

As per Scheme 2, 5 mg of NHS-acetic acid was added to 10 mg of HRP per 1 mL of milli q water. The reaction mixture was vortex-mixed and kept overnight at 4°C to form an amide bond with the $-NH_2$ group of HRP that led to the formation of acetylated HRP (blocking of the $-NH_2$ group). Thereafter, the reaction mixture was extensively dialyzed against water. Carboxyl moieties of HRP were activated by the addition of 10 mg of NHS plus 20 mg of EDAC.HCl. The activated HRP was

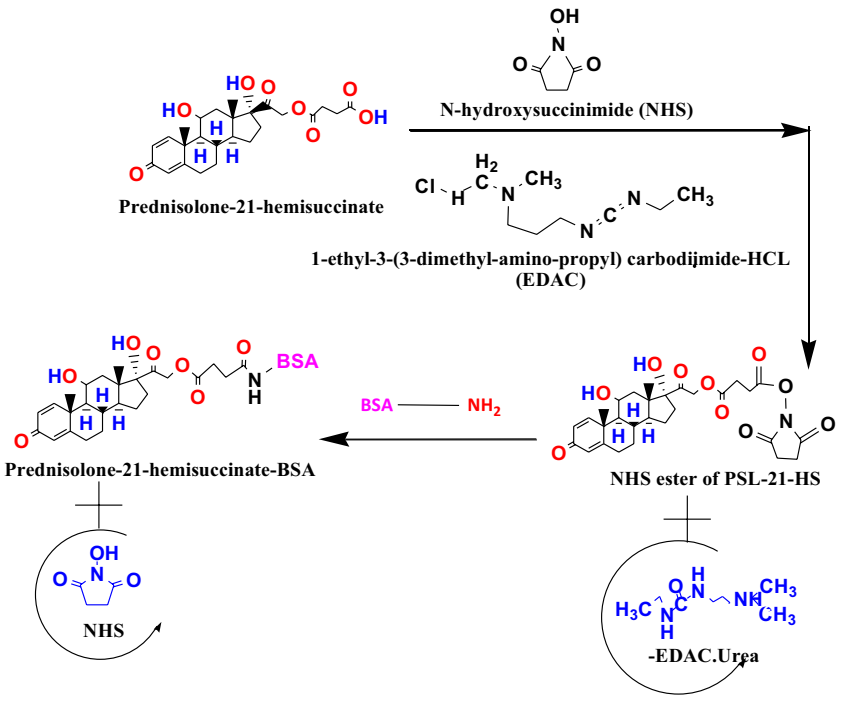

SCHEME 1
Conjugation of PSL-21-HS (a carboxylic derivative of prednisolone) to BSA.

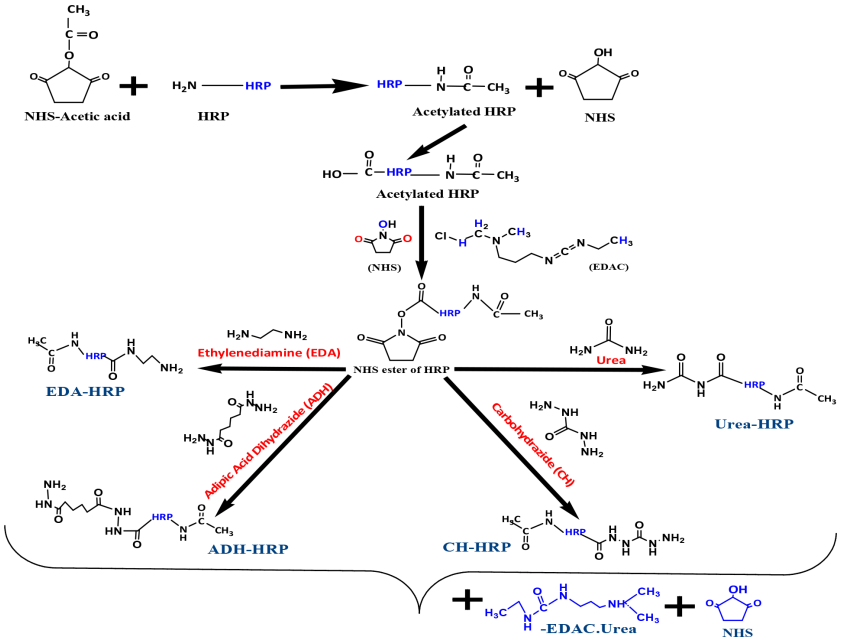

SCHEME 2
Blocking of the amino group and coupling of spacers (ADH, CH, EDA, and U) to HRP.

then divided into four equal portions; 10 mg each of ADH, CH, EDA, and urea was added to the respective activated HRP portion and kept overnight. After overnight incubation, the reaction mixture was extensively dialyzed against water.

2.5.1.1 Coupling of prednisolone to spacers containing HRP

As per Scheme 3, 200 µL each of dioxan and DMF and 100 µL of distilled water containing 10 mg NHS and 20 mg EDAC were added to 10 mg of PSL-21-HS; the reaction mixture was kept at 4°C for activation for 24 hours. The activated PSL-21-HS solution was divided into four equal parts, and each part was added to HRP-U, HRP-EDA, HRP-CH, and ADH-HRP, respectively, and kept for 24 hours at 4°C. Thereafter, each reaction mixture was passed separately through a G-25 column, formerly equilibrated with 10 mM PBS containing 0.01% thimerosal. The brown-colored fractions containing enzyme activity were pooled, and 1% of sucrose, ammonium sulfate, BSA, and an equal volume of ethylene glycol

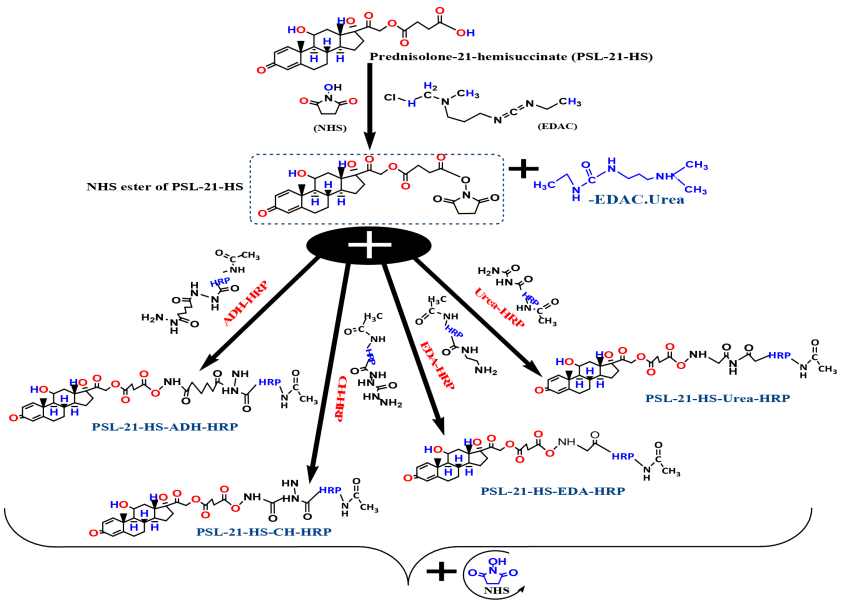

SCHEME 3
Coupling of prednisolone to spacer-HRP.

were added to them. The solution was kept at -30°C for future use (10).

2.6 Characterization of immunogen and enzyme conjugates by a matrix-assisted laser desorption ionization-time of flight spectrometer

Matrix-assisted laser desorption ionization mass spectrometry (MALDI-MS) has been effectively utilized for the molecular weight determination of various proteins with a claimed limit of 500 000 Da. The practical limit for the routine study of proteins is approximately 300 000 Da with a sensitivity in the low pmol range and an accuracy of up to ± 0.1%. Protein-hapten conjugates were characterized by employing MALDI-TOF. The mass of PSL, BSA, HRP, PSL-BSA, PSL-HRP, PSL-ADH-HRP, PSL-CH-HRP, PSL-EDA-HRP, and PSL-U-HRP were determined using a MALDI-TOF spectrometer. The 1 mg of sample/mL of distilled water was mixed with 1 mL of a matrix (3, 5-dimethoxy-4-hydroxycinnamic acid (Sinapinic acid) was prepared in 33% acetonitrile) in a 1:1 ratio (v/v), thereafter, 0.5 µL of 0.1% trifluoroacetic acid (TFA) was added. The samples were analyzed in linear mode with a 337 nm laser light at 30 kV and spectra for each sample were recorded at a threshold laser irradiance for 50 shots and the data obtained were analyzed using the software provided with the system (22, 30). Each spectrum contained at least two larger and shorter peaks and were in singly $(M+H)^+$ and doubly $(M+2H)^{2+}$ charged states. The molecular weight of each sample was calculated from the singly centroid $(M+H)^+$ peak. The number of haptens attached per molecule of protein was determined using the formula:

$$\text{Number of haptens} = \frac{[\text{conjugate molecular weight (MW)}] - [\text{Protein (BSA/HRP) MW}]}{(\text{hapten (PSL)} + \text{spacer MW})}$$

2.7 Immunization of rabbits and collection of antiserum

The polyclonal antibody was raised in New Zealand white rabbits against PSL-21-HS-BSA as per the procedure described elsewhere (20). Briefly, PSL-21-HS-BSA (1mg) was dissolved in 0.9% saline (0.5 mL) and emulsified with 0.5 mL of Freund's complete adjuvant. The prepared emulsion (250 µL) was injected intramuscularly in each limb of the rabbits. Primarily, the first five booster injections were prepared with Freund's complete adjuvant and given per week and were further followed by monthly booster injections prepared using Freund's incomplete adjuvant. Further, the rabbits were bled after 9-14 days after the booster dose injections. Blood was collected from the rabbits and after clotting, antiserum was separated by centrifugation at 1000 g for 15 min. The separated antiserum was collected and stored at -30°C.

2.8 Collection of normal rabbit serum and generation of anti-rabbit anti-serum in goat

For the collection of normal rabbit serum, blood was withdrawn from the non-immunized New Zealand white rabbits. After clotting, the blood was centrifuged at 2000 rpm for 10 min. The separated serum was collected and stored as NRS at -30°C until use. The anti-rabbit anti-serum was generated in goats (ARASG) by immunizing the immunoglobulin (IgG) of rabbits (1–3, 21). Further, the booster injection blood was collected from the goat and centrifuged after clotting. The obtained antiserum was collected and stored at -30°C for further use.

2.9 Coating of antibody to microtiter plates

The 96-well microtitre plates were coated using the immunobridge technique for primary antibody immobilization (11). Briefly, 250 µL of normal rabbit serum (NRS) diluted (1: 250) in water was dispensed into each well and incubated overnight at 37°C. Following incubation, the plate was washed 2-3 times using a washing solution (buffer E). To the NRS coated wells, 250 µL of 1:1000 diluted anti-rabbit anti-serums in goat (ARASG) was added and incubated for 5 hours at 37°C or overnight at 4°C. Thereafter the plate was washed carefully using a washing solution (buffer E). The raised antiserum against immunogen (PSL-21-HS-BSA) was serially diluted in antibody dilution buffer to 1:500, 1:1000, 1:2000, and 1:4000, and 150 µL was added per ARASG coated wells (single dilution per eight-well strip). For non-specific binding (NSB), 150 µL of antibody dilution buffer was added in a separate ARASG-coated eight-well strip and incubated for 2 hours at 37°C. The unabsorbed antibody was then decanted and the microtitre plate was washed with buffer E. Thereafter, 250 µL of buffer 'D' was added and kept at room temperature (RT) for 1 hour to block the unoccupied sites of the plate. The contents of the plate were decanted, packed, and stored at 4°C in zip-lock bags for further use and the plate was dried at RT.

2.9.1 Determination of optimal dilution of primary antibody and enzyme conjugates

To determine the amount of immobilized primary antibody and enzyme conjugates required to develop the assay, 100 µL of serially diluted (1:500, 1:1000, 1:2000, and 1:4000) enzyme conjugate in buffer B (PSL-21-HS-ADH-HRP, PSL-21-HS-CH-HRP, PSL-21-HS-EDA-HRP, or PSL-21-HS-U-HRP) was added in the above coated plates for respective assays (one dilution per two wells in vertical fashion). The plates were incubated at RT for 1 hour. Unbound contents were decanted and the plate was washed with buffer E. The bound enzyme activity was assessed by adding 100 µL of TMB/H_2O_2 substrate to each well followed by incubation at RT for 15 min. The reaction was stopped by the addition of 100 µL of 1 N HCl, and the color intensity was measured at 450 nm in a Tecan-spectra ELISA plate reader. The dilutions of antiserum and enzyme conjugate that showed maximum zero binding (optical density more than 2.5) and minimum

nonspecific binding (optical density less than 0.1) were selected for each combination for assay development.

2.9.2 Preparation of prednisolone standard

Eight PSL working standards (0.0, 0.62, 1.25, 2.5, 5.0, 10.0, 20.0, and 40.0 ng/mL) were prepared in stripped pooled serum. The stripping of steroids from the serum was carried out by adding activated charcoal at a concentration of 50 mg/mL to pooled serum, stirring for two hours at 45 °C, and centrifuging at 3000 x g to eliminate the charcoal, followed by filtration through 0.45 µM membrane filter. Thimerosal 0.01% was added as a preservative.

2.9.3 Preparation of recovery pools

Six recovery pools were prepared in the serum by spiking the serum with different known concentrations of prednisolone, viz., 0.0, 0.62, 2.5, 5.0, 15.0, and 25.0 ng/mL.

2.9.4 Standard displacement assay (assay procedure)

To the antibody-coated wells (PSL-21-HS-BSA-antibody), 100 µL of different concentrations of the standard were added in duplicate. Next, 100 µL of the working dilution of the enzyme conjugates (PSL-21-HS-ADH-HRP, PSL-21-HS-CH-HRP, PSL-21-HS-EDA-HRP, or PSL-21-HS-U-HRP) was added to all of the wells. The incubation, washing, and measurement of the bound enzyme activity were as described in section 2.9.2.

2.9.5 Measurement of serum prednisolone by commercial ELISA kit

Five working standards (0, 15, 30, 60, 120, and 240 pg/mL) were freshly prepared by serially diluting the stock standard with diluent. To the pre-coated wells, 10 µL of different concentrations of standards or samples were added followed by 40 µL of sample diluent and incubated for 30 min at 37 °C. Thereafter, the plate was washed thoroughly using washing solution and 50 µL of HRP-conjugate was added to all the wells except the blank well and incubated at 37°C for 30 min. The wells were washed again with a washing solution, and the bound enzyme activity was developed by adding 100 µL of TMB/H_2O_2 substrate to each well and incubating at 37°C for 15 min. The enzymatic reaction was stopped by adding 100 µL of stop solution, and the color intensity was measured at 450 nm in a Tecan-spectra ELISA plate reader (TECAN, Austria).

3 Data analysis

3.1 Preparation of the standard curve, determination of affinity constant, and sensitivity

The standard curve was plotted using GraphPad Prism 6.0 and Microsoft Excel software. The concentration was plotted on the X-axis (log scale) and the A/A0x100 on the Y-axis. The values of the unknown samples were calculated by an in-house–developed personal computer program written in QBASIC language using the logit–log linear regression method according to the method described elsewhere (5). The affinity constant of the PSL antibody for PSL was estimated by a Scatchard plot according to the method described elsewhere (10). The sensitivity of the developed method was determined according to the method described elsewhere (21, 32–41).

3.2 Goodness of fit

The goodness of fit was expressed as the estimated non-linear squared correlation coefficient (R^2) of the standard data. An R^2 value that approaches 1.0 is indicative of a precise fit for the data to the standard curve.

4 Results

4.1 Determination of hapten density by MALDI-TOF spectrometry

4.1.1 In immunogen

The molecular weights of PSL-21-HS, BSA, and PSL-21-HS-BSA were determined by MALDI-TOF and found to be 483.737 Kelo Dalton (KDa), 69144.654 KDa and 66528.848 KDa respectively as shown in Figure 1. The quantity of hapten (PSL) density was calculated by the formula given under section 2.6 and found to be 5.40 per molecule of BSA as shown in Table 1.

4.1.2 In enzyme conjugates

The molecular weights of HRP, PSL-21-HS, PSL-21-HS-ADH-HRP, PSL-21-HS-CH-HRP, PSL-21-HS-EDA-HRP, and PSL-21-HS-U-HRP were determined by MALDI-TOF and found to be 43348.001 KDa, 483.737 KDa, 50231.004 KDa, 49524.341 KDa, 46221.734 KDa, and 48962.172 KDa, respectively as shown in Figure 2. The quantity of hapten (PSL) density was calculated by the formula given in section 2.6 and found to be 10.46, 10.76, 5.28, and 10.32 per molecule of the PSL-21-HS-ADH-HRP, PSL-21-HS-CH-HRP, PSL-21-HS-EDA-HRP, and PSL-21-HS-U-HRP enzyme conjugates respectively. The observed mass, changes in mass, and the hapten density of enzyme conjugates are shown in Table 2.

4.2 Dose-response study

The dose-response studies of the four enzyme conjugates PSL-21-HS-ADH-HRP, PSL-21-HS-CH-HRP, PSL-21-HS-EDA-HRP, and PSL-21-HS-U-HRP were carried out with the antibody raised against PSL-21-HS-BSA. Figure 3 depicts the composite standard curves of the ELISA for prednisolone using the PSL-21-HS-BSA antibody with PSL-21-HS-HRP (with different length spacer) enzyme conjugates, where concentrations of PSL are plotted on the X axis and bound fraction (A/A0%) on the Y axis. The CVs for the A/A0 ratio of each standard ranged from 1.38% to 9.93% for the enzyme immunosorbent assays. Each value is a mean ± SD of eight assays (in duplicate). Thus, the standard curves achieved over several assays remained stable and

TABLE 1 Estimation of hapten density in immunogen.

Sample	Analyte MW (KDa)	Conjugate MW (KDa)	Change in mass (Conjugate MW – BSA MW)	Hapten density (Change in mass/hapten M.W.)
Prednisolone (PSL)-21-HS	483.737		-	-
Bovine Serum Albumin (BSA)	66528.848		–	–
PSL-21-HS-BSA	-	69144.654	2615.806	5.40

precise. The slope and intercept of the curves were calculated by logit–log transformation of standard curve data, the affinity constant of the PSL antibody for the PSL was estimated by a Scatchard plot, and the goodness of fit was the estimated non-linear squared correlation coefficient (R^2) of the standard data and is shown in Table 3.

4.3 Sensitivity

The lower detection limit of the PSL assay after insertion of the spacers in the enzyme conjugate was 1.22 ng/mL (ADH spacer), 0.59 ng/mL (CH spacer), 0.48 ng/mL (EDA spacer), and 0.018 ng/mL (urea spacer) and are shown in Table 3. Among the four combinations, the PSL-21-HS-BSA antibody and PSL-21-HS-U-HRP enzyme conjugate had better sensitivity.

4.4 Specificity

The specificity of the anti-PSL-21-HS-BSA-antiserum with PSL-21-HS-U-HRP, PSL-21-HS-EDA-HRP, PSL-21-HS-CH-HRP, and PSL-21-HS-ADH-HRP was estimated as the percentage of cross-reaction with commercially available 53 analogous steroids. Only 4 to 5 steroids showed cross-reaction and are shown in Table 4. Among the four combinations, the PSL-21-HS-BSA-antibody with the PSL-21-HS-U-HRP-enzyme conjugate had better sensitivity and less cross-reaction. The percentage of cross-reaction was calculated from the following formula:

$$\text{cross reaction} = \frac{\text{concentration of prednisolone, required for 50\% inhibition}}{\text{concentration of related steroid, required for 50\% inhibition}} \times 100$$

4.5 Selection of the best combination of antibody and enzyme conjugate

Since, among all four combinations, anti-PSL-21-HS-BSA and PSL-21-HS-U-HRP enzyme conjugate had better sensitivity, ED_{50}, affinity, and specificity thus, this combination was further studied for analytical variables such as recovery, precision, and correlation coefficient.

4.6 Recovery

The ability of an assay to accurately quantify PSL in serum was tested. Table 5 represents the percentage of recoveries of known amounts of PSL added to five aliquots of serum pools. After spiking,

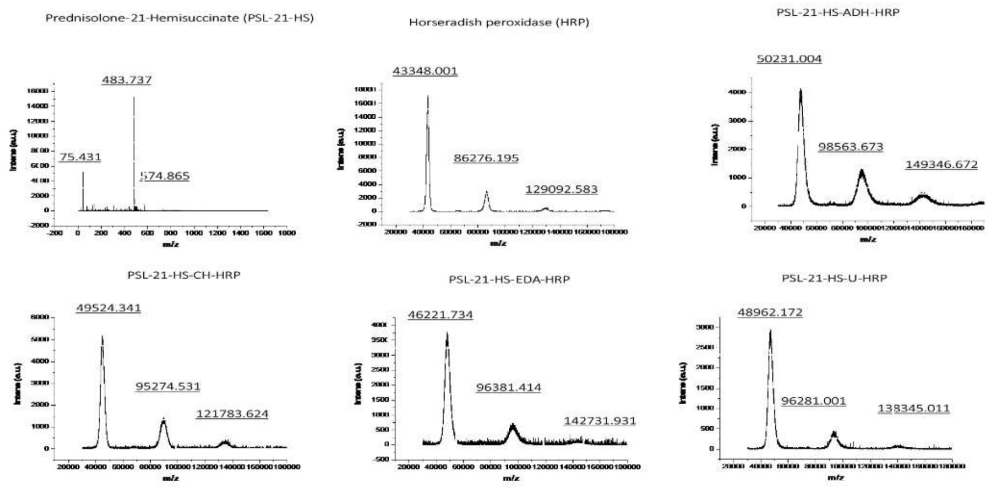

FIGURE 2
Mass spectra of PSL-21-HS, HRP and enzyme conjugate with spacers by MALDI-TOF.

10.3389/fimmu.2023.1200328

TABLE 2 Estimation of hapten density in enzyme conjugate.

Sample	Analyte MW	Conjugate MW (KDa)	Change in mass (conjugate MW – HRP MW)	Hapten density (change in mass/hapten +spacer M.W.)
Horseradish peroxidase (HRP)	43348.001 KDa			
Prednisolone-21-hemisuccinate (PSL-21-HS)	483.737 KDa			
Adipic acid dihydrazide (ADH)	174.2 g/mol			
PSL-21-HS-ADH-HRP	–	50231.004	6883.00	10.46
Carbohydrazide (CH)	90.09 g/mol			
PSL-21-HS-CH-HRP	–	49524.341	6176.34	10.76
Ethylenediamine (EDA)	60.10 g/mol			
PSL-21-HS-EDA-HRP	–	46221.734	2873.733	5.28
Urea (U)	60.06 g/mol			
PSL-21-HS-U-HRP	–	48962.172	5614.171	10.32

the concentration of PSL was measured and recovery was intended for each pool. The recovery ranged from 88.32 – 102.50%.

The percentage of recovery was calculated by using the formula: (C - B)/A * 100. Where A = a known amount of analyte, B = a base (B), and C = measuring the concentration.

4.7 Precision

The levels of precision are estimated by studying the intra-assay and inter-assay variations. Serum pools of very low, low, medium, high-medium, and high PSL concentrations were utilized for

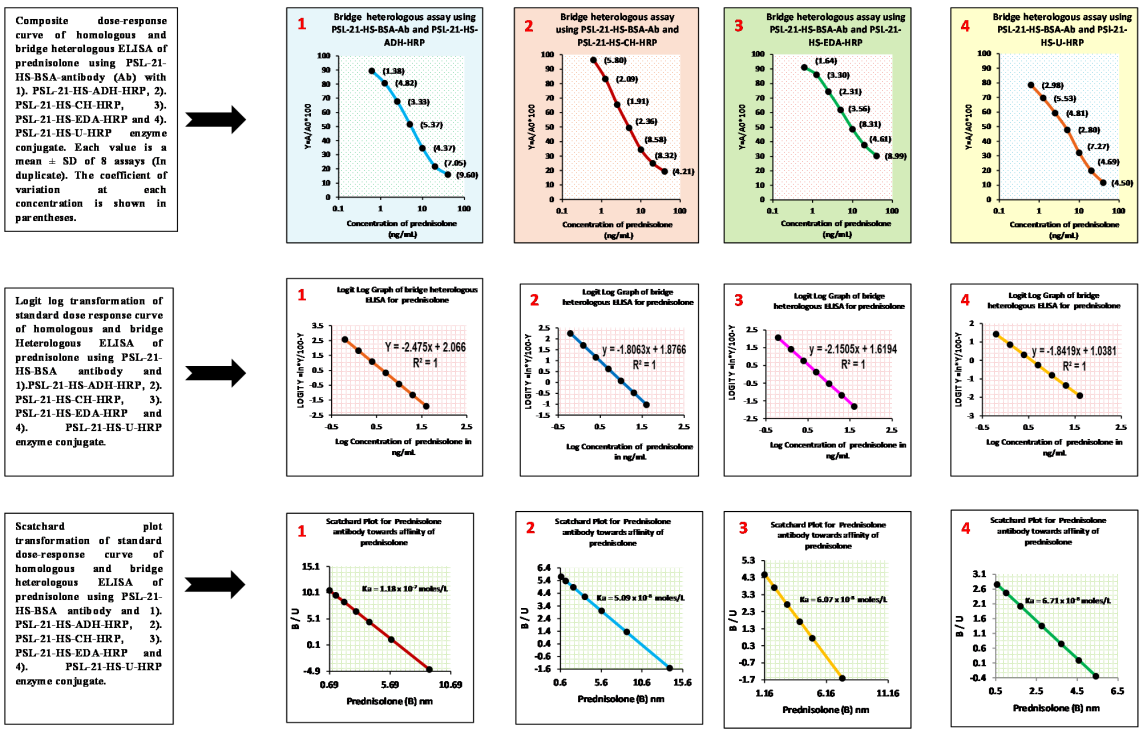

FIGURE 3
Composite dose-response, logit-log, and Scatchard plot curves of the homologous and bridge heterologous ELISA of prednisolone using PSL-21-HS-BSA antibody PSL-21-HS-HRP with (ADH, CH, EDA, and U) different length spacer–containing enzyme conjugates.

TABLE 3 Slope (m), intercept (c), sensitivity, affinity, ED_{50}, and R^2 of prednisolone assays, using PSL-21-HS-BSA-antibody and PSL-21-HS-HRP (with spacers) enzyme conjugates.

Assay combination of PSL-21-HS-BSA-antibody with	Slope (m) and intercept (c)		Sensitivity of the assay (ng/mL)	Affinity of the assay (mole/L)	ED_{50} (ng/mL)	R^2
	m	c				
PSL-21-HS-ADH-HRP Enzyme conjugate	-2.47	2.06	1.22	1.18×10^{-7}	6.79	0.9
PSL-21-HS-CH-HRP Enzyme conjugate	-1.80	1.87	0.59	5.07×10^{-8}	4.03	1.0
PSL-21-HS-EDA-HRP Enzyme conjugate	-2.15	1.61	0.48	4.71×10^{-8}	3.60	1.0
PSL-21-HS-U-HRP Enzyme conjugate	-1.84	1.03	0.018	5.09×10^{-8}	1.89	1.0

TABLE 4 Cross-reactivity of analogous steroids in bridge heterologous ELISA of PSL using the PSL-21-HS-BSA antibody and PSL-21-HS-HRP (with spacers) enzymes conjugate.

Steroid Measured	% Cross-reactions with PSL-21-HS-EDA-HRP	% Cross-reactions with PSL -21-HS-Urea-HRP	% Cross-reactions with PSL-21-HS-CH-HRP	% Cross-reactions with PSL-21-HS-ADH-HRP
C-27 Steroid				
Cholesterol	<0.025	<0.025	<0.025	<0.025
C-22 Steroid				
Danazol	<0.025	<0.025	<0.025	<0.025
C-21 Steroid				
Progesterone	4.7	1.65	2.21	9.46
5 α Dehydro Progesterone	<0.025	<0.025	<0.025	<0.025
5 β Dehydro Progesterone	<0.025	<0.025	<0.025	<0.025
17α 20β Dioh Progesterone	<0.025	<0.025	<0.025	<0.025
17α 20 α Dioh Progesterone	<0.025	<0.025	<0.025	<0.025
11α OH Progesterone	<0.025	<0.025	<0.025	<0.025
16-dehydroprogesterone	<0.025	<0.025	<0.025	<0.025
Medroxy Progesterone Acetate (MPA)	<0.025	<0.025	<0.025	<0.025
Pregnenolone	<0.025	<0.025	<0.025	<0.025
17α-OH progesterone	21.25	6	12.5	14
17α-OH pregnenolone	<0.025	<0.025	<0.025	<0.025
5 Pregnene 3 β 20 α diOL	<0.025	<0.025	<0.025	<0.025
5α Pregnane 3β, 20α diOL	<0.025	<0.025	<0.025	<0.025
5α Dihydropregnanolone	<0.025	<0.025	<0.025	<0.025
5β-pregnane-3,20-dione	<0.025	<0.025	<0.025	<0.025
Betamethosone	<0.025	<0.025	<0.025	<0.025
Pregnanediol	<0.025	<0.025	<0.025	<0.025
Cortisol	11.6	4.5	12.5	10.4

(Continued)

10.3389/fimmu.2023.1200328

TABLE 4 Continued

Steroid Measured	% Cross-reactions with PSL-21-HS-EDA-HRP	% Cross-reactions with PSL -21-HS-Urea-HRP	% Cross-reactions with PSL-21-HS-CH-HRP	% Cross-reactions with PSL-21-HS-ADH-HRP
5 α Dihydro Cortisol	<0.025	<0.025	<0.025	<0.025
5 β Dihydro Cortisol	<0.025	<0.025	<0.025	<0.025
Prednisolone	100	100	100	100
Prednisone	42	8	27	24
Aldosterone	<0.025	<0.025	<0.025	<0.025
Dexamethasone	<0.025	<0.025	<0.025	<0.025
Flutamide	<0.025	<0.025	<0.025	<0.025
Corticosterone	8.6	<0.025	7.48	4.44
5 α Dihydro Corticosterone	<0.025	<0.025	<0.025	<0.025
5 β Dihydro Corticosterone	<0.025	<0.025	<0.025	<0.025
Cortisone	<0.025	<0.025	<0.025	<0.025
5 α Dihydro Cortisone	<0.025	<0.025	<0.025	<0.025
5 β Dihydro Cortisone	<0.025	<0.025	<0.025	<0.025
Deoxycorticosterone (DOC)	<0.025	<0.025	<0.025	<0.025
C-19 Steroid				
Testosterone	<0.025	<0.025	<0.025	<0.025
6 Dehydro Testosterone	<0.025	<0.025	<0.025	<0.025
17 α Methyl Testosterone	<0.025	<0.025	<0.025	<0.025
11 Keto testosterone	<0.025	<0.025	<0.025	<0.025
Dihydrotestosterone (DHT)	<0.025	<0.025	<0.025	<0.025
Etiocholanolone	<0.025	<0.025	<0.025	<0.025
Dehydroepiandrosterone (DHEA)	<0.025	<0.025	<0.025	<0.025
Dehydroepiandrosterone Sulfate (DHEAS)	<0.025	<0.025	<0.025	<0.025
Dehydroisoandrosterone	<0.025	<0.025	<0.025	<0.025
Androstenedione	<0.025	<0.025	<0.025	<0.025
Androstanedione	<0.025	<0.025	<0.025	<0.025
Androsten 3 β, 17 β -Diol	<0.025	<0.025	<0.025	<0.025
Androstenediol	<0.025	<0.025	<0.025	<0.025
Mesterolone	<0.025	<0.025	<0.025	<0.025
Nandrolone	<0.025	<0.025	<0.025	<0.025
C-18 Steroid				
Estrone	<0.025	<0.025	<0.025	<0.025
Estrone 3-Glu (E_1 3G)	<0.025	<0.025	<0.025	<0.025
Estradiol	<0.025	<0.025	<0.025	<0.025
Estriol	<0.025	<0.025	<0.025	<0.025
2 Methoxy Estradiol	<0.025	<0.025	<0.025	<0.025

TABLE 5 Recovery of prednisolone from exogenously spiked human serum pools using the PSL-21-HS-BSA-antibody and PSL-21-HS-Urea-HRP-enzyme conjugate.

Human serum pools	Prednisolone added (ng/mL)	Prednisolone observed (ng/mL)	Prednisolone expected (ng/mL)	% Recovery
Pool A (Basal)	–	0.75	––	–
Pool B	0.62	1.21	1.37	88.32
Pool C	1.25	2.05	2.00	102.50
Pool D	5.0	5.55	5.75	98.26
Pool E	15.0	`15.50	15.75	98.41
Pool F	25.0	25.80	25.75	100.19

determining the level of imprecision in the assay by assessing the PSL in each pool eight times in the assay and in eight different assays. Table 6 depicts the intra and inter-assay coefficient of variations. The coefficient of variation (CVs) of five serum pools for intra and inter-assay variation (n=8 and N=8, replicate of each pool) was< 8.46%. The percentage of coefficient of variation is calculated as % CV = (SD/X) * 100 at a particular analyte level, where X = mean, SD = standard deviation, and CV = coefficient of variation.

The intra-assay coefficients of variation ranged from 2.50%–7.09% whereas, the inter-assay coefficients of variation ranged from 1.47%– 8.46%.

4.8 Correlation coefficient

The newly developed technique must yield results analogous to those of the already available conventional method. The correlation coefficient for values of PSL in serum samples (n = 103) measured by developed ELISA and ELISA kit of prednisolone purchased from Sincere Biotech Co. Ltd., Beijing, China was found to be $r^2 = 0.98$. The regression analysis was performed in which both X and Y were subject to measurement error. Figure 4 shows that the method fit a straight line to a two-dimensional data where both the variables, X and Y, are measured with errors that can accommodate differences in measurement error between the test and the reference method. The linear regression curve of the correlated data was plotted using Graph Pad Prism version 6.0 for Microsoft Windows (42–46).

4.9 Estimation of prednisolone in patients treated for different diseases

We determined the prednisolone concentration in human serum using samples from healthy volunteers (17 males and 11 females) and in human patients taking treatment with prednisolone through oral, local, or injection forms for chronic asthma (20 males and 5 females), rheumatoid arthritis (16 males and 11 females), and allergies (11 males and 12 females) with ages between 10 to 72 years. We followed all institutional guidelines and ethical approval as per the norm was taken before the initiation of the study (44–46). Samples values as determined by the developed ELISA are described in Table 7 and also presented in the form of a box and whisker diagram (plotted using Graph Pad Prism version 6.0 for Microsoft Windows), as shown in Figure 5.

5 Discussion

In the present study, we investigated the use of different spacers in enzyme conjugates to develop a sensitive and specific enzyme-linked immunosorbent assay (ELISA) for prednisolone. Four homobifunctional spacers, namely ADH, CH, EDA, and urea, were introduced between the PSL-21-HS carboxyl derivative of prednisolone and horseradish peroxidase (HRP) as the enzyme label. The influence of spacer length on the functional parameters of the prednisolone ELISA was examined. The terminal functional

TABLE 6 Inter and intra-assay coefficient of variation for the measurement of prednisolone in human serum pools using the PSL-21-HS-BSA-antibody and PSL-21-HS-U-HRP-enzyme conjugate.

Variation	Sample value (ng/mL) (mean ± S.D.)	Coefficient of variation (%)
Intra-assay *n* = 8	0.80 ± 0.02 1.41± 0.10 5.45 ± 0.21 15.72 ± 0.84 25.85 ± 0.94	2.50 7.09 3.85 5.34 3.63
Inter-assay *N*= 8	0.77 ± 0. 05 1.30 ± 0.11 14.92 ± 0.22 15.72 ± 0.44 26.02 ± 1.04	6.49 8.46 1.47 2.79 3.99

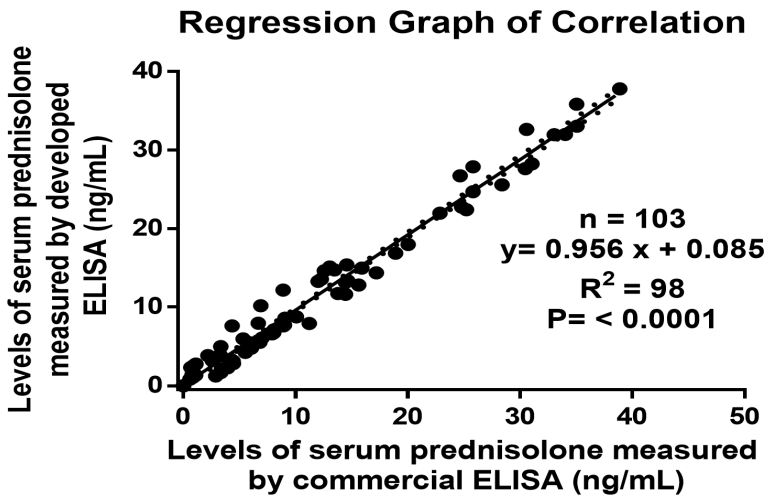

FIGURE 4
Regression graph of the correlation between the serums prednisolone concentrations as estimated by the developed ELISA and an established ELISA kit.

TABLE 7 Estimation of prednisolone by developed ELISA in human serum of healthy volunteers and patients taking treatment.

Variable	Healthy		Asthma		Rheumatic		Allergic	
Gender	Male	Female	Male	Female	Male	Female	Male	Female
No. of samples	17	11	20	5	16	11	11	12
Age	18-64		10 -72		40-62		16-60	
Prednisolone (mean ± SD) (ng/mL)	(0.00 ± 0.00)		(24.06 ± 8.09)		(8.17 ± 3.15)		(1.80 ± 1.24)	

groups of these spacers do not spontaneously react with the functional group of steroid/carrier protein/enzyme, and therefore, necessitate some bioconjugate reagent as an in-between to carry out the effective coupling of these spacers (10). Carbodiimide along with N-hydroxysuccinimide has been the optimal reagent for coupling steroid and proteins through spacers as they do not introduce any additional atoms in the conjugate.

The data of the present investigation revealed that the insertion of spacers in the enzyme conjugate affected the lower detection limit and ED50 of the PSL assay. The assays using ADH, CH, EDA, and

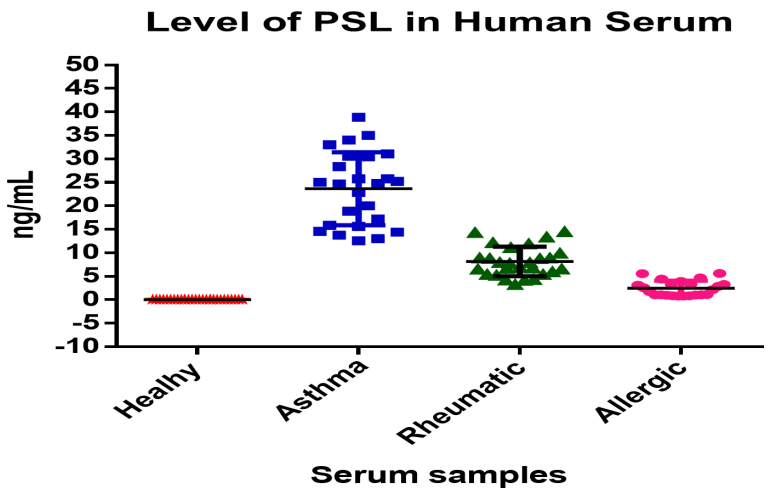

FIGURE 5
Box-and-Whisker diagram of level of prednisolone in human serum samples estimated by developed ELISA.

urea spacers exhibited sensitivities of 1.22 ng/mL, 0.59 ng/mL, 0.48 ng/mL, and 0.018 ng/mL, respectively. Among the different combinations, the PSL-21-HS-BSA antibody and PSL-21-HS-urea-HRP enzyme conjugate demonstrated the highest sensitivity and ED_{50}.

The rigid nature of the urea spacer, with its atomic length of three and non-aliphatic, hydrophilic properties, may have contributed to the enhanced sensitivity of the assay. This rigidity could have created a greater distance between the prednisolone moiety and the enzyme, reducing steric hindrance and allowing easier access for unlabeled prednisolone to bind to the antibody. The findings suggest that the nature of the spacer, rather than its length, is more relevant to assay sensitivity. Previous studies have also reported similar observations, highlighting the potential of hydrophilic and rigid spacers to improve assay sensitivity and specificity. It has also been previously reported that the spacer length does not bear any correlation with the assay sensitivity in ELISA (1–5, 11, 19, 20) as it does have an effect in some other immunoassays and auxiliary binding systems (9–11, 20). The use of a hydrophilic and rigid spacer possibly helped in projecting the hapten away from the enzyme, leading to an enhanced antibody binding signal and improved sensitivity of the assay (9–11, 14, 20).

Since the assay was based on superior sensitivity, ED50, affinity, and specificity, the combination of PSL-21-HS-BSA antibody and PSL-21-HS-urea-HRP enzyme conjugate was selected for further analysis. The recovery of PSL from exogenously spiked human serum pools ranged from 88.32% to 102.50%, and the intra-assay and inter-assay coefficients of variation were<8.46%. Additionally, the correlation coefficient between the developed ELISA and a commercially available kit for serum PSL measurement was found to be r^2 = 0.98 and the correlation coefficient for values of prednisolone in serum samples (n = 103).

The results of the present study were compared to the commercially validated accepted kit, the developed assay showed advantages such as simplicity, single-step immunoassay procedure, fewer washing steps, lower intra-assay and inter-assay variability, and the provision of recovery and cross-reactivity data.

To the best of our knowledge, this study is the first to compare the impact of different spacers in enzyme conjugates on the analytical variables of an ELISA for prednisolone. All the reagents used in the assay, including buffers, immunogen, antigen-enzyme conjugate, and antibody generation, were developed in-house.

6 Conclusions

In the present study, the introduction of different spacers in enzyme conjugates affected the sensitivity and specificity of the prednisolone ELISA. The rigid nature of the urea spacer demonstrated improved sensitivity and reduced steric hindrance. Due to this rigid nature of urea, it might have projected PSL moiety away from the enzyme which might have aided in keeping the bound antibody away from the enzyme, thereby reducing the inclusive attraction between enzyme and antibody simultaneously. The results highlight the importance of spacer properties in influencing assay performance and provide insights for the development of more sensitive and specific assays for prednisolone detection.

Data availability statement

The original contributions presented in the study are included in the article/Supplementary Material. Further inquiries can be directed to the corresponding authors.

Ethics statement

The experimental protocols were approved by the institutional animal ethics committee (IAEC) of the National Institute of Health and Family Welfare (NIHFW), New Delhi, India. All animal experiments were performed in accordance with the guidelines of Committee for the Purpose of Control and Supervision of Experiments on Animals (CPCSEA), Government of India. Written informed consent was obtained from the owners for the participation of their animals in this study.

Author contributions

DK, TS, HS, and SS conceived and designed the experiments; DK, SS, HO, MK, and PB carried out the experiments; DK, HS, TS, SS, and PB analyzed the data; DS, HS, BK, SS, and PB wrote and finalized the manuscript. All authors contributed to the article and approved the submitted version.

Funding

This study was supported by the National Institute of Health and Family Welfare (NIHFW), New Delhi, India.

Acknowledgments

We acknowledge the volunteers for providing their blood for prednisolone estimation, also thankful to Mr. Subodh Jain from the Indian Institute of Technology Delhi (IITD) for the MALDI-TOF study. The Multidisciplinary Research Unit, Maulana Azad Medical College and Associated Hospital, New Delhi are acknowledged for providing the required facilities for running the experiments.

Conflict of interest

The authors declare that the research was conducted in the absence of any commercial or financial relationships that could be construed as a potential conflict of interest.

Publisher's note

All claims expressed in this article are solely those of the authors and do not necessarily represent those of their affiliated organizations, or those of the publisher, the editors and the reviewers. Any product that may be evaluated in this article, or claim that may be made by its manufacturer, is not guaranteed or endorsed by the publisher.

References

1. Shrivastav TG, Chaube SK, Kariya KP, Kumari P, Singh R, Kumar D. Influence of different homologous and heterologous combinations of antibodies and enzyme conjugates of dehydroepiandrostosterone on the sensitivity and specificity of DHEA ELISA. *J Immunoassay Immunochem* (2011) 32:114–27. doi: 10.1080/15321819.2010.543221

2. Shrivastav TG, Chaube SK, Kariya KP, Bhanot S, Singh R, Kumar D. Development of heterologous enzyme linked immunosorbent assay for dehydroepiandrosterone in serum. *J Immunoassay Immunochem* (2010) 31:266–78. doi: 10.1080/15321819.2010.524857

3. Shrivastav TG, Chaube SK, Charu, Rangari K, Kariya KP, Singh R, Nagendra A. Enzyme linked immunosorbent assay for milk progesterone. *J Immunoassay Immunochem* (2010) 31:301–13. doi: 10.1080/15321819.2010.528734

4. Shrivastav TG, Chaube SK, Kariya KP, Kumar D, Singh R. Antigen heterologous enzyme linked immunosorbent assay for the measurement of DHEA in serum. *J Immunoassay Immunochem* (2011) 32:326–41. doi: 10.1080/15321819.2011.570117

5. Kumar D, Azad RMR, Oulkar D, Oberoi HS, Jacob S, Koner BC, et al. A quantification method for trace level of oxytocin in food matrices using LC-MS/MS. *Front Anal Sci* (2022) 2:1039606. doi: 10.3389/frans.2022.1039606

6. Kinneer K, Wortmann P, Cooper ZA, Dickinson NJ, Masterson L, Cailleau T, et al. Design and preclinical evaluation of a novel B7-H4-directed antibody-drug conjugate, AZD8205, alone and in combination with the PARP1-selective inhibitor AZD5305. *Clin Cancer Res* (2023) 29(6):1086–101. doi: 10.1158/1078-0432.CCR-22-2630

7. Weng W, Meng T, Zhao Q, Shen Y, Fu G, Shi J, et al. Antibody-exatecan conjugates with a novel self-immolative moiety overcome resistance in colon and lung cancer. *Cancer Discovery* (2023) 13(4):950–73. doi: 10.1158/2159-8290.CD-22-1368

8. Roas M, Vick B, Kasper MA, Able M, Polzer H, Gerlach M, et al. Targeting FLT3 with a new-generation antibody-drug conjugate in combination with kinase inhibitors for treatment of AML. *Blood* (2023) 141(9):1023–35. doi: 10.1182/blood.2021015246

9. Lai W, Zhao S, Lai Q, Zhou W, Wu M, Jiang X, et al. Design, synthesis, and bioevaluation of a novel hybrid molecular pyrrolobenzodiazepine-anthracenecarboxyimide as a payload for antibody-drug conjugate. *J Med Chem* (2022) 65(17):11679–702. doi: 10.1021/acs.jmedchem.2c00471

10. Zhou T, He G, Hu C, Wu K, Liu Y, Li J, et al. Development of a highly sensitive and specific monoclonal antibody-based ELISA coupled with immuno-affinity extraction for the detection of anticancer drug 5-fluorouracil in blood samples. *Talanta* (2022) 249:123655. doi: 10.1016/j.talanta.2022.123655

11. Shrivastav TG, Chaube SK, Kariya KP, Singh R, Kumar D, Pandit D, et al. Influence of different length linker containing DHEA-7-CMO-enzyme conjugates on sensitivity and specificity of DHEA-17-CMO-antibody. *J Immunoassay Immunochem* (2011) 32:269–83. doi: 10.1080/15321819.2011.560325

12. Basu A, Chaube SK, Kariya KP, Singh R, Kumar D, Pandit D, et al. The influence of spacer-containing enzyme conjugate on the sensitivity and specificity of enzyme immunoassays for hapten. *Clin Chim Acta* (2006) 366:287–92. doi: 10.1016/j.cca.2005.10.024

13. Hosoda H, Kobayashi N, Ishii N, Nambara T. Bridging phenomena in steroid immunoassays. The effect of bridge length on sensitivity in enzyme immunoassay. *Chem Pharm Bull (Tokyo)* (1986) 34:2105–11. doi: 10.1248/cpb.34.2105

14. Shrivastav TG, Chaube SK, Prasad PKV, Kariya KP, Kumar D. Heterologous enzyme linked immunosorbent assay for measurement of testosterone in serum. *J Immunoassay Immunochem* (2012) 33:252–68. doi: 10.1080/15321819.2011.638525

15. Nara S, Tripathi V, Chaube SK, Rangari K, Singh H, Kariya KP, et al. Influence of hydrophobic and hydrophilic spacer-containing enzyme conjugates on functional parameters of steroid immunoassay. *Anal Biochem* (2008) 373:18–25. doi: 10.1016/j.ab.2007.10.042

16. Shrivastav TG, Chaube SK, Kariya KP, Prasad PKV, Kumar D. Influence of different length spacers containing enzyme conjugate on functional parameters of progesterone ELISA. *J Immunoassay Immunochem* (2013) 34:94–108. doi: 10.1080/15321819.2012.686470

17. Shrivastav TG, Chaube SK, Kariya KP, Singh R, Kumar D, Jain P, et al. Influence of different length linker containing DHEA-7-cmo-enzyme conjugates on sensitivity and specificity of DHEA-3-hs-antibody. *J Immunoassay Immunochem* (2012) 33:1–17. doi: 10.1080/15321819.2011.591475

18. Hallaj S, Rasaee MJ, Haerian M, Paknejad M, Kashanian S, Rahbarizadeh F, et al. A heterologous enzyme linked immunosorbant assay of morphine using penicillinase as label. *Iran J Biotechnol* (2003) 1:239–46.

19. Tripathi V, Nara S, Chaube SK, Rangari K, Saroha A, Kariya KP, et al. Development of rapid and sensitive one-step direct enzyme linked immunosorbent assay for 17-alpha-OH-progesterone in serum. *J Immunoassay Immunochem* (2008) 29:117–27. doi: 10.1080/15321810801887599

20. Shrivastav TG. Incorporation of different bridge length linkers in enzyme and its use in the preparation of enzyme conjugates for immunoassay. *J Immunoassay Immunochem* (2004) 25:215–25. doi: 10.1081/IAS-200028007

21. Wang Y, Wang M, Zhou L, Geng X, Xu Z, Zhang H. Development of a competitive ELISA based on estrogen receptor and weak competitive molecule for the screening of potential estrogens in foods. *Food Chem* (2023) 401:134084. doi: 10.1016/j.foodchem.2022.134084

22. Yang JY, Zhang Y, Wang H, Xu ZL, Eremin SA, Shen YD, et al. Development of fluorescence polarisation immunoassay for carbofuran in food and environmental water samples. *Food Agric Immunol* (2015) 26:340–55. doi: 10.1080/09540105.2014.914890

23. Alhajj M, Zubair M, Farhana A. Enzyme linked immunosorbent assay. In: *StatPearls*. Treasure Island (FL: StatPearls Publishing (2023). Available at: https://www.ncbi.nlm.nih.gov/books/NBK555922/.

24. Zhang B, Lv S, Qiang Z, Guo M, Tan X, Li H, et al. Improved sensitivity and wide range detection of small analytes using a two-antigen-combined competitive immunoassay. *ACS Omega.* (2022) 7(51):48121–9. doi: 10.1021/acsomega.2c06126

25. ZHANG X, DONG X, ZHAO S, KE Y, WEN K, ZHANG S, et al. Synthesis of haptens and production of antibodies to bisphenol A. *Front Agr. Sci Eng.* (2017) 4 (3):366–372. doi: 10.15302/J-FASE-2017132

26. Zhang Q, Wang L, Ahn KC, Sun Q, Hu B, Wang J, et al. Hapten heterology for a specific and sensitive indirect enzyme-linked immunosorbent assay for organophosphorus insecticide fenthion. *Anal Chim Acta* (2007) 596:303–11. doi: 10.1016/j.aca.2007.06.009

27. Mitchell JS, Wu Y, Mitchell JS, Wu Y. Surface plasmon resonance biosensors for highly sensitive detection of small biomolecules. *Biosensors (Basel)* (2010). doi: 10.5772/7208

28. Sathe M, Srivastava S, Agrawal SK, Ghorpade R. Effect of spacer and the enzyme-linked immunosorbent assay. *Def Sci J* (2016) 66:471–8. doi: 10.14429/dsj.66.10700

29. Kumar D, Singh H, Shrivastava TG. Homologous ELISA for detection of prednisolone in human serum. *FoodAgric Immunol.* (2018) 29(1):369–85. doi: 10.1080/09540105.2017.1376184

30. Kim D, Herr AE. Protein immobilization techniques for microfluidic assays. *Biomicrofluidics* (2013) 7(4):41501. doi: 10.1063/1.4816934

31. Zhang B, Yu J, Liu C, Wang J, Han H, Zhang P, et al. Improving detection sensitivity by oriented bioconjugation of antibodies to quantum dots with a flexible spacer arm for immunoassay. *RSC Adv* (2016) 6:50119–27. doi: 10.1039/C6RA09279A

32. Rajesh K, Rana KV, Suri CR. Characterization of hapten-protein conjugates: antibody generation and immunoassay development for pesticides monitoring. *Bionanoscience* (2013) 3:137–44. doi: 10.1007/s12668-013-0083-8

33. Adamczyk M, Gebler JC, Mattingly PG. Characterization of protein-hapten conjugates. 2. Electrospray mass spectrometry of bovine serum albumin-hapten conjugates. *Bioconjug Chem* (1996) 7:475–81. doi: 10.1021/bc960035h

34. Moody MT, Ringel MM, Mathews CM, Midthun KM. Determination of cross-reactivity of contemporary cannabinoids with THC direct immunoassay (ELISA) in whole blood. *J Anal Toxicol* (2022) 46(8):844–51. doi: 10.1093/jat/bkac051

35. Colby JM, Patel PC, Fu DY, Rutherford NJ. Commonly used fluoroquinolones cross-react with urine drug screens for opiates, buprenorphine, and amphetamines. *Clin Biochem* (2019) 68:50–4. doi: 10.1016/j.clinbiochem.2019.04.009

36. Koirala N, McLennan G. Mathematical models for blood flow quantification in dialysis access using angiography: A comparative study. *Diagnostics (Basel).* (2021) 11 (10):1771. doi: 10.3390/diagnostics11101771

37. Garg S, Singh VK, Sonkar SC, Kelkar H, Singh S, Garg S, et al. Pattern of serum protein capillary electrophoretogram in SARS- CoV-2 infection. *Clin Chim Acta* (2022) 527:11–6. doi: 10.1016/j.cca.2022.01.003

38. Irungbam M, Chitkara A, Singh VK, Sonkar SC, Dubey A, Bansal A, et al. Evaluation of performance of detection of immunoglobulin G and immunoglobulin M antibody against spike protein of SARS-coV-2 by a rapid kit in a real-life hospital setting. *Front Microbiol* (2022) 13:802292. doi: 10.3389/fmicb.2022.802292

39. Dubey A, Kotnala G, Mandal TK, Sonkar SC, Singh VK, Guru SA, et al. Evidence of the presence of SARS-CoV-2 virus in atmospheric air and surfaces of a dedicated COVID hospital. *J Med Virol* (2021) 93(9):5339–49. doi: 10.1002/jmv.27029

40. Sonkar SC, Sachdev D, Mishra PK, Kumar A, Mittal P, Saluja D. A molecular-beacon-based asymmetric PCR assay for easy visualization of amplicons in the diagnosis of trichomoniasis. *Biosens Bioelectron.* (2016) 86:41–7. doi: 10.1016/j.bios.2016.06.025

41. Sonkar SC, Arora G, Wasnik K, Ali M, Mittal P, Saluja D. Improved management can be achieved by introducing additional parameters in the syndromic diagnosis of nonviral sexually transmitted infections at low-resource settings. *AJOG Glob Rep* (2021) 2(1):100037. doi: 10.1016/j.xagr.2021.100037

42. Sachdev D, Wasnik K, Patel AL, Sonkar SC, Desai P, Mania-Pramanik J, et al. Multi-centric validation of an in-house-developed beacon-based PCR diagnostic assay kit for Chlamydia and Neisseria and portable fluorescence detector. *J Med Microbiol* (2018) 67(9):1287–93. doi: 10.1099/jmm.0.000803

43. Sonkar SC, Wasnik K, Kumar A, Sharma V, Mittal P, Mishra PK, et al. Evaluating the utility of syndromic case management for three sexually transmitted infections in women visiting hospitals in Delhi, India. *Sci Rep* (2017) 7(1):1465. doi: 10.1038/s41598-017-01422-y

44. Sonkar SC, Wasnik K, Kumar A, Mittal P, Saluja D. Comparative analysis of syndromic and PCR-based diagnostic assay reveals misdiagnosis/overtreatment for trichomoniasis based on subjective judgment in symptomatic patients. *Infect Dis Poverty*. (2016) 5:42. doi: 10.1186/s40249-016-0133-x

45. Sonkar SC, Yadav S, Malla N, Dhanda RS, Khurana S, Bagga R, et al. Evaluation of DNA based techniques for the diagnosis of human vaginal trichomoniasis in North Indian population. *Br Microbiol Res J* (2016) 17(6):1–2. doi: 10.9734/BMRJ/2016/29557

46. Mishra PK, Sonkar SC, Raj SR, Chaudhry U, Saluja D. Functional analysis of hypothetical proteins of Chlamydia trachomatis: a bioinformatics based approach for prioritizing the targets. *J Comput Sci Syst Biol* (2013) 7(1):010–014. doi: 10.4172/jcsb.1000132

frontiers | Frontiers in Immunology

TYPE Original Research
PUBLISHED 15 December 2023
DOI 10.3389/fimmu.2023.1302891

Check for updates

OPEN ACCESS

EDITED BY
Ernesto T. A. Marques,
University of Pittsburgh, United States

REVIEWED BY
Mingbo Sun,
Sichuan Real & Best Biotech Co., Ltd., China
Maria-Jose Martinez-Bravo,
University College London, United Kingdom

*CORRESPONDENCE
Chaiwat Chuaychoosakoon
psu.chaiwat@gmail.com;
chaiwat.c@psu.ac.th

RECEIVED 27 September 2023
ACCEPTED 27 November 2023
PUBLISHED 15 December 2023

CITATION
Laohawiriyakamol T, Boonsri P, Phutphithak K, Niyomkarn T, Klabklay P and Chuaychoosakoon C (2023) Appropriate intradeltoid muscle needle penetration depth in vaccine administration: an MRI study in Thailand.
Front. Immunol. 14:1302891.
doi: 10.3389/fimmu.2023.1302891

COPYRIGHT
© 2023 Laohawiriyakamol, Boonsri, Phutphithak, Niyomkarn, Klabklay and Chuaychoosakoon. This is an open-access article distributed under the terms of the Creative Commons Attribution License (CC BY). The use, distribution or reproduction in other forums is permitted, provided the original author(s) and the copyright owner(s) are credited and that the original publication in this journal is cited, in accordance with accepted academic practice. No use, distribution or reproduction is permitted which does not comply with these terms.

Appropriate intradeltoid muscle needle penetration depth in vaccine administration: an MRI study in Thailand

Teeranan Laohawiriyakamol, Pattira Boonsri, Khetnathee Phutphithak, Thamonchanok Niyomkarn, Prapakorn Klabklay and Chaiwat Chuaychoosakoon*

Faculty of Medicine, Prince of Songkla University, Songkhla, Thailand

Objective: The objective of this study was to evaluate the appropriate vaccination needle penetration depth into the deltoid muscle to avoid injection-site complications from an inappropriate injection depth and/or injection site in the Thai population.

Methods: This was a retrospective study using axial proton density-weighted images of MRI shoulders at the level of 2 fingerbreadths below the acromion process to measure the combined thickness of the skin, subcutaneous fat pad and deltoid muscle to evaluate the percentage of injections into the deltoid muscle with various needle penetration depths.

Results: There were 509 MRI shoulder images of 222 males and 287 females (265 right shoulders and 244 left shoulders). The average body mass index and age were 24.54 $\pm$ 3.54 kg/m^2 and 64.81 $\pm$ 10.20 years, respectively. Using a needle penetration depth of 12.7 mm (0.5 inches) achieved 100% of injections into the deltoid muscle.

Conclusion: We recommend advancing the entire length of a 0.5-inch needle perpendicular to the skin at 2 fingerbreadths below the acromion process for adult intradeltoid vaccinations. This approach ensures optimal vaccine delivery and minimizes the risk of injection-related injuries.

KEYWORDS

deltoid, injection depth, subcutaneous, thickness, vaccination

Introduction

Vaccination stands as one of the most effective strategies in preventing the spread of infectious diseases. The precise administration of a vaccine requires careful attention to various factors, including the selection of an appropriate needle length to ensure accurate delivery of the vaccine at the intended site. Intramuscular vaccines, such as those for

hepatitis A, hepatitis B, rabies, influenza, diphtheria toxoid, and coronavirus-19 (COVID-19) show optimal efficacy when administered intramuscularly (1, 2), predominantly within the deltoid muscle. It has been observed that using a needle that is too short may inadvertently lead to subcutaneous administration of the vaccine (Figure 1), resulting in reduced vaccine efficacy, seropositivity, and antibody titers compared to an intramuscular injection (3). On the other hand, the use of a too-long needle may lead to inadvertent injection into the subdeltoid bursa (Figure 2), potentially causing bursitis (4). Thus, careful attention to needle length selection during vaccine administration is important to ensure proper intramuscular deposition of the vaccine, thereby enhancing vaccine effectiveness and minimizing the risk of adverse events associated with subcutaneous or bursal injections.

As per the Centers for Disease Control and Prevention (CDC) guidelines, the correct injection site is 2 or 3 fingerbreadths below the acromion process. However, utilizing 2-3 fingerbreadths below the acromion process with an excessively long needle may increase the likelihood of injecting into the subdeltoid bursa, as this bursa can extend more than 5 cm below the acromion process. Notably, research findings indicate that using a distance of 3 fingerbreadths (57.69 mm) (5) below the acromion process may pose a risk of iatrogenic axillary nerve injury. Some studies have reported the presence of the axillary nerve at a location 5 cm below the acromion process (6–10). In summary, an injection site located 3 fingerbreadths below the mid-acromion process, when using a needle of excessive length, carries a risk of both axillary nerve injury and subdeltoid bursitis. Conversely, utilizing an injection site located 2 fingerbreadths below the mid-acromion process only poses a risk of subdeltoid bursitis, making this measurement more suitable for vaccination administration. Healthcare practitioners should exercise caution and employ appropriate needle lengths to minimize the risk of complications while adhering to the recommended injection site guidelines.

To date, there are no studies which have comprehensively evaluated the thickness of the subcutaneous fat pad and the thickness from the skin to the subdeltoid fascia, providing guidance for determining the optimal needle penetration depth for intradeltoid muscle vaccination at the landmark of 2 fingerbreadths below the mid-acromion process. Thus, the objective of this study was to measure the thickness of the subcutaneous fat pad and the thickness from the skin to the subdeltoid fascia, aiming to establish an ideal needle penetration depth that would avoid both subcutaneous and subdeltoid bursa delivery of the injectant at the landmark of 2 fingerbreadths below the acromion process, and secondly, to assess the risk of vaccine injection into the subcutaneous fat pad or subdeltoid bursa for the Thai population when following the CDC guidelines. The study hypothesized that a needle penetration depth of 0.5 inches (12.7 mm) would successfully reach the deltoid muscle while avoiding passage into the subdeltoid bursa, effectively traversing both the skin and subcutaneous fat pad. Additionally, it was anticipated that following the CDC guidelines for vaccination may result in the use of a needle length that is too long in our Thai patients, potentially leading to injection into the subdeltoid bursa.

Methods

Study design, population, and place

This retrospective study was approved by the Institutional Review Board of the Faculty of Medicine of Prince of Songkla University. The requirement for informed consent from the study

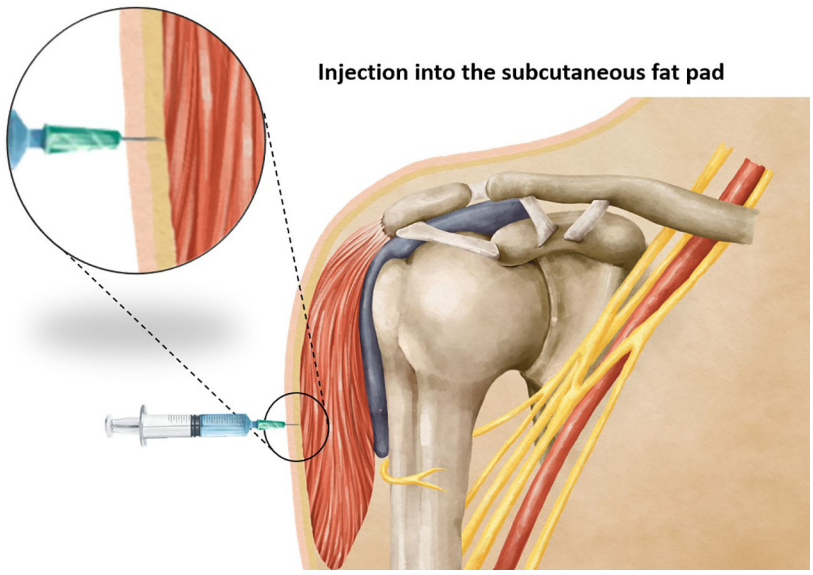

FIGURE 1
Showing an injection into the subcutaneous fat pad when using a too-short needle length.

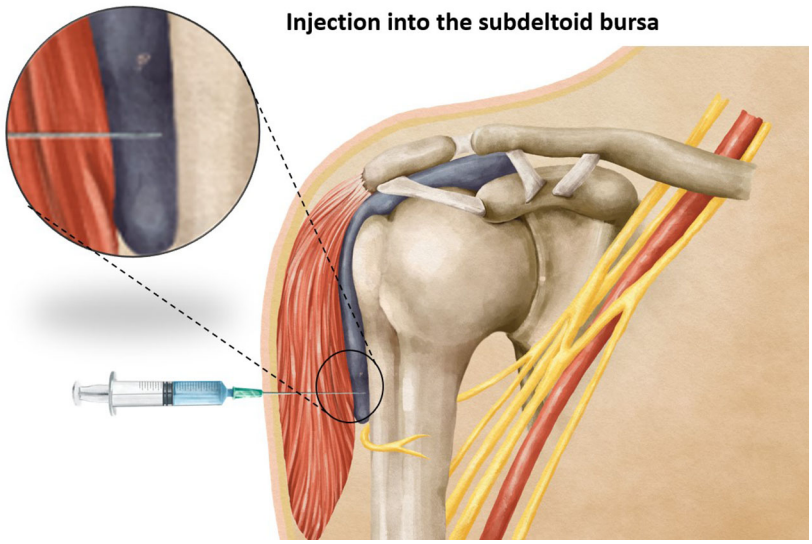

FIGURE 2
Showing an injection into the subdeltoid bursa when using a too-long needle length.

subjects was waived by the Institutional Review Board due to the retrospective study design (REC 65-293-11-1). MRI images were examined and certain measurements made to assess the thickness of the skin, subcutaneous fat pad and deltoid muscle, in order to determine an appropriate needle penetration depth.

This study was an anatomical study based on patient MRIs, therefore there was no public involvement, and no direct patient involvement.

The study included 600 MRIs which had been taken between January 1, 2012, and July 31, 2022, of which the MRIs of 91 patients who had had bone or soft tissue tumor, a fracture around the shoulder joint or a history of shoulder surgery, or were aged less than 18 years were excluded. All of the MRI images were anonymized, therefore the patients could not be contacted before or after the study.

To conduct the analysis, the MRI shoulder images were carefully selected and measured using a specialized Picture Archiving and Communication System (PACS) workstation. In our study, we simulated the vaccination conditions by selecting the injection site as 2 fingerbreadths below the mid-acromial process and administering the simulated injection perpendicular to the skin. This approach aimed to replicate the standard vaccination procedure for accurate and consistent results in our simulation.

For this investigation, MRI images that passed through the most anterolateral aspect of the acromion process, as depicted in Figure 3, were chosen as the coronal images. To identify the indicated site for an injection, a line of 2 fingerbreadths (39.19 mm) in length was drawn vertically downward along the skin surface, just below the inferior aspect of the acromion process. Axial proton density-weighted images at the level of the injection site were utilized for the measurements carried out in this study. The thickness of the subcutaneous fat pad and deltoid muscle measurements were obtained at designated distances from the center of the humeral head, as depicted in Figure 4. Each measurement was independently performed three times by an experienced musculoskeletal radiologist to ensure the accuracy and reliability of the findings.

The study's findings are presented through the use of descriptive statistics, specifically means ± standard deviations (SDs), and incidence ratios, which indicate the penetration into the intradeltoid muscle at different needle penetration depths. Statistical analysis was conducted utilizing the R program and the epicalc package (version 3.4.3, R Foundation for Statistical Computing, Austria). To compare the mean age, mean height, mean weight, mean body mass index (BMI), mean deltoid subcutaneous fat, and mean deltoid thickness from skin to subdeltoid fascia, t-tests were employed. The chi-square test of independence or Wilcoxon rank sum test was utilized to compare the incidence ratios of penetration into the intradeltoid muscle across various needle penetration depths. Pearson's correlation coefficient was used to assess correlations between the thickness of the deltoid subcutaneous fat pad, deltoid thickness from skin to subdeltoid fascia, deltoid muscle, and the participant's weight, height, and BMI for both men and women. Statistical significance was set at $P < 0.05$. Intraclass correlation coefficients were calculated to assess measurement reliability.

Results

509 MRI shoulder images of 222 males (123 right and 99 left shoulders) and 287 females (142 right and 145 left shoulders) were included in the study. The patient characteristics are shown in Table 1. Of the 509 MRI shoulders, 215 were diagnosed as rotator cuff pathology, 197 as combined rotator cuff pathology and adhesive capsulitis, 30 as osteoarthritis, 27 as adhesive capsulitis, 8 as labral pathology, 14 as combined rotator cuff and labral pathologies, 10 as combined rotator cuff and labral pathologies and adhesive capsulitis, and 8 as normal.

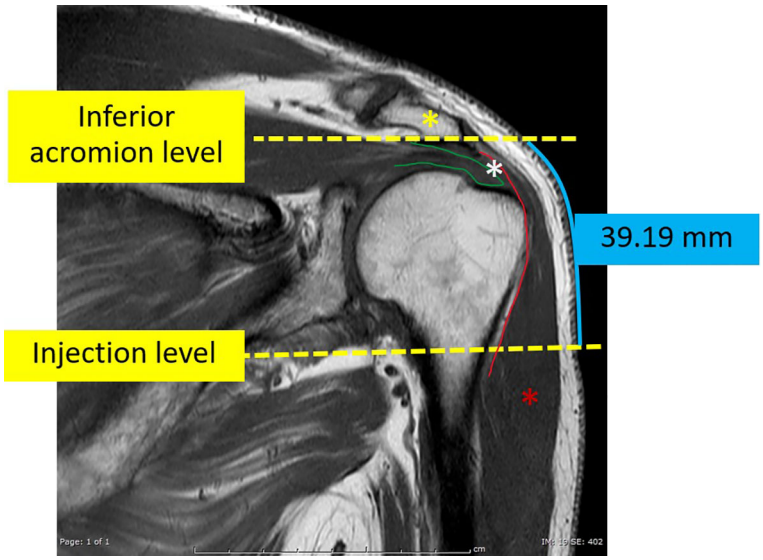

FIGURE 3
The coronal T1-weighted image of an MRI shoulder passing through the mid-acromial process (yellow asterisk) which was used as the reference coronal image. On this image, a vertical line, about 39.19 mm in length, was manually drawn vertically downwards from the level of the inferior aspect of the acromion process. The terminal point of this vertical line indicated the level of the simulated injection. The green line indicates the supraspinatus tendon. The red asterisk indicates the deltoid muscle. The red line indicates the subdeltoid fascia. The space between the deltoid and the acromial process and the underlying supraspinatus is the subacromial-subdeltoid bursa (white asterisk).

Demographic data and needle lengths

The clinical and demographic characteristics of the patients are shown in Table 1. Our study's findings demonstrated the outcomes of simulated vaccine administrations using different needle lengths. Notably, when using a 0.5-inch needle (12.7 mm), 100% of the simulated administrations successfully penetrated into the deltoid muscle without reaching the subdeltoid fascia (Figure 5). With a 1-inch needle (25.4 mm), 6 of 222 males and 17 of 287 females had needle penetration restricted to the deltoid muscle, while 216 of 222

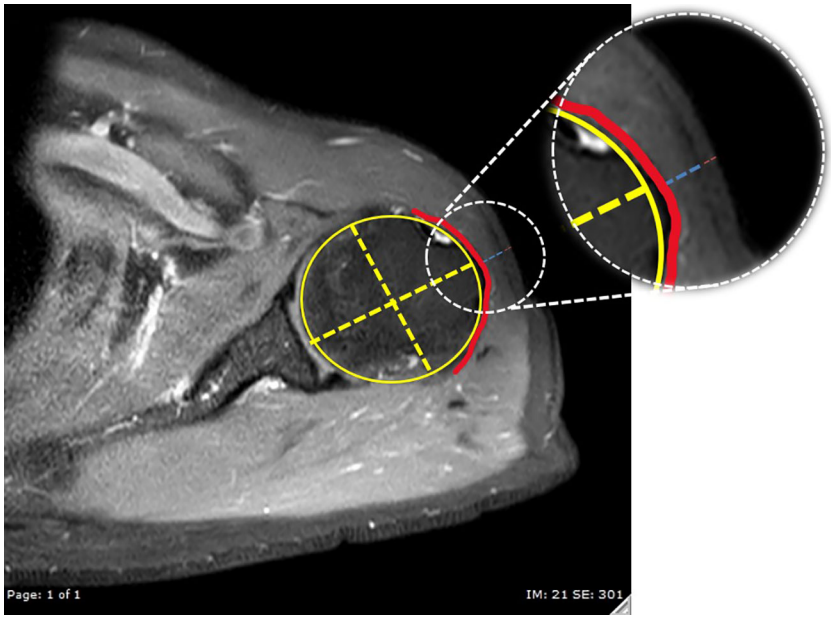

FIGURE 4
The reference axial proton density-weighted image with fat suppression at the injection level. A best-fit circle of the humeral head was created (yellow circle), then a line passing through the center of the humeral head (decussation of the yellow dashed lines) and perpendicular to the glenoid surface was used to indicate the direction for measurements of the thickness of the deltoid muscle (blue dashed line) and subcutaneous fat pad (red dashed line). The red line indicates the subdeltoid fascia.

10.3389/fimmu.2023.1302891

TABLE 1 Patient clinical and demographic characteristics.

Variable	Male (222)	Female (287)	P-value
Mean age in years (SD)	64 (11.1)	65.4 (9.4)	0.135
Mean height in cm (SD)	166.4 (6.2)	154.1 (6.6)	<0.001
Mean weight in kg (SD)	68.3 (10.1)	58 (9.2)	< 0.001
Mean BMI in kg/m^2 (SD)	24.6 (3.3)	24.5 (3.7)	0.64
Mean thickness of subcutaneous fat pad in mm (SD)	5.4 (1.7)	8 (2.2)	< 0.001
Mean thickness from skin to subdeltoid fascia in mm (SD)	17.8 (3.4)	19.4 (3.6)	< 0.001

males and 270 out of 287 females had penetration beyond the subdeltoid fascia. Employing a longer 1.5-inch needle (38.1 mm), all male and female participants had penetration beyond the subdeltoid fascia. The complete results of the spatial analysis of needle tip locations, conducted in accordance with the CDC guidelines, are displayed in Table 2.

Correlation of the thicknesses of the skin, subcutaneous fat pad and deltoid muscle with BMI

The analysis revealed a positive correlation between BMI and the thickness of the deltoid subcutaneous fat pad, and the total thickness from the skin to the subdeltoid fascia. Conversely, a negative correlation was observed between BMI and deltoid muscle thickness, as illustrated in Figures 6, 7. There was high intraobserver correlation with the correlation coefficients of all assessments greater than 0.986.

Discussion

This investigation was aimed at determining the most appropriate needle penetration depth for intradeltoid vaccination administration, seeking to achieve precise vaccine delivery within the deltoid muscle while mitigating the potential for overpenetration or injury to adjacent anatomical structures. Our study found that employing a 0.5-inch needle with a perpendicular insertion angle relative to the skin, guided by the reference point of two fingerbreadths below the mid-acromion process, yielded a 100% success rate in ensuring a vaccine injection accurately targeted the deltoid muscle (Figure 5). These observations hold significant implications for optimizing vaccination procedures and enhancing the safety and efficacy of intradeltoid administrations. Furthermore, by employing meticulous measurements and adherence to the recommended injection technique, healthcare practitioners can confidently administer vaccinations with enhanced precision and reduced risk of adverse events, thereby reinforcing the role of intradeltoid injections in contemporary vaccination practices.

According to the guidelines provided by the CDC on vaccine administration, the recommended injection site and needle length for intradeltoid vaccinations are as follows: The injection site should be 2-3 fingerbreadths below the mid-acromion process, aligned perpendicularly to the skin. However, in clinical practice, many medical professionals often follow a general rule of thumb and insert the needle 1-3 fingerbreadths below the acromion process. Unfortunately, this approach can lead to complications. Earlier reports have found that inserting the needle only 1 fingerbreadth below the acromion process resulted in cases of subacromial bursitis following the vaccination (4, 11). A case series of shoulder injuries related to vaccine administration (SIRVA) after a COVID-19 vaccination demonstrated the potential clinical consequences of

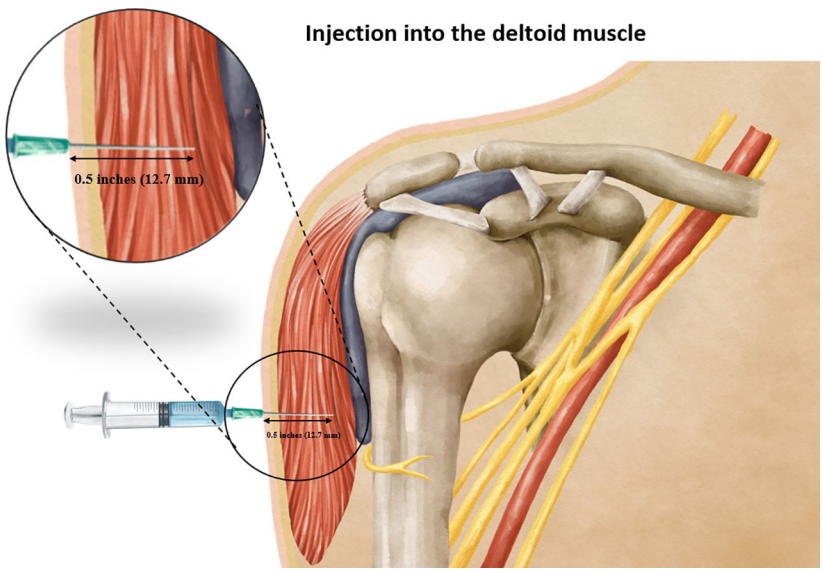

FIGURE 5
Showing the correct injection depth into the deltoid muscle when using an appropriate needle length.

10.3389/fimmu.2023.1302891

TABLE 2 Final needle tip position of different needle lengths in males and females.

Depth of needle penetration	Location of needle tip																	
	Males (n=222)								Females (n=287)									
	Weight less than 70 kg (147)			Weight between 70-118 kg (75)			Weight more than 118 kg (0)			Weight less than 70 kg (263)			Weight between 70-90 kg (22)			Weight more than 90 kg (2)		
	Subcutaneous fat pad	Deltoid muscle	Subdeltoid bursa	Subcutaneous fat pad	Deltoid muscle	Subdeltoid bursa	Subcutaneous fat pad	Deltoid muscle	Subdeltoid bursa	Subcutaneous fat pad	Deltoid muscle	Subdeltoid bursa	Subcutaneous fat pad	Deltoid muscle	Subdeltoid bursa	Subcutaneous fat pad	Deltoid muscle	Subdeltoid bursa
12.7 mm (0.5 inches)	0 (0%)	147 (100%)	0 (0%)	0 (0%)	75 (100%)	0 (0%)	–	–	–	0 (0%)	263 (100%)	0 (0%)	0 (0%)	22 (100%)	0 (0%)	0 (0%)	2 (100%)	0 (0%)
25.4 mm (1 inch)	0 (0%)	0 (0%)	147 (100%)	0 (0%)	6 (8%)	69 (92%)	–	–	–	0 (0%)	13 (4.94%)	250 (95.06%)	0 (0%)	4 (18.18%)	18 (81.82%)	0 (0%)	0 (0%)	2 (100%)
38.1 mm (1.5 inches)	0 (0%)	0 (0%)	147 (100%)	0 (0%)	0 (0%)	75 (100%)	–	–	–	0 (0%)	0 (0%)	263 (100%)	0 (0%)	0 (0%)	22 (100%)	0 (0%)	0 (0%)	2 (100%)

administering vaccines at a too-high injection site. Additionally, the series highlighted the challenge of differentiating these patients from those with pre-existing but undiagnosed septic arthritis of the shoulder (4). In one instance, a vaccinated patient received a combined therapy of intravenous antibiotics and an oral non-steroidal anti-inflammatory drug (NSAID) as an empirical treatment because septic arthritis could not be ruled out during the initial evaluation. Although the patient eventually experienced complete resolution of the bursitis, the unnecessary antibiotic exposure raised concerns about the development of antibiotic resistance. Another case reported by Mayer et al. (12) involved subacromial bursitis as a complication following a COVID-19 vaccine administration at a too-high location. The patient experienced acute severe pain, disrupted daily activities, and low-grade fever. By considering the patient's vaccination history, observing the needle injection mark indicating improper needle placement, and analyzing the clinical symptoms, the physician could diagnose SIRVA-related subacromial bursitis and offer available treatment options. Due to the patient's desire to return to work early, arthroscopic decompression was chosen. During the procedure, a large hemorrhagic bursitis of the subacromial bursa was visualized and decompressed using an arthroscopic shaver. In another case report, a more complicated subacromial bursitis resulted from a too-high injection site of a human papilloma (HPV) vaccine (13). The strong adjuvant in the HPV vaccine caused the bursitis to be unresponsive to corticosteroid injections, leading to chronic severe inflammation evident during arthroscopy. Consequently, the patient underwent an arthroscopic synovectomy with subacromial decompression as definitive treatment.

Caution must also be exercised at 3 fingerbreadths, or approximately 2 inches (5.08 cm), below the acromion process since the axillary nerve has been identified to be at risk of puncture injury with injections made at this location. For instance, Choi et al. (14) documented a case in which an intramuscular injection of a non-neurotoxic agent, hydroxyzine hydrochloride, led to an isolated paralysis of the middle head of the deltoid. Notably, the absence of pain or sensory deficit after the injection suggested a direct injury to the motor branch of the axillary nerve rather than an injectate-related chemical neuropathy, which would likely have resulted in a more widespread extent of injury. Similarly, another case report (15) highlighted the potential injury of the axillary nerve due to too-low needle insertions. Following injections of influenza, diphtheria, and tetanus vaccines, the patient experienced limited active ranges of shoulder motion in abduction and forward flexion, along with decreased muscle power in the corresponding muscle groups. Examination of voluntary forward flexion and abduction revealed an absence of contractility in the anterior and medial heads of the deltoid, both through observation and palpation. The affected dermatome also exhibited decreased sensation, corroborating the presence of an axillary nerve lesion. The diagnosis was confirmed through axonal regeneration patterns observed on nerve conduction studies (NCS). The preferred treatment approach involved physical rehabilitation, which resulted in complete clinical resolution at 11 months post-injury, with normal NCS patterns observed at 12 months.

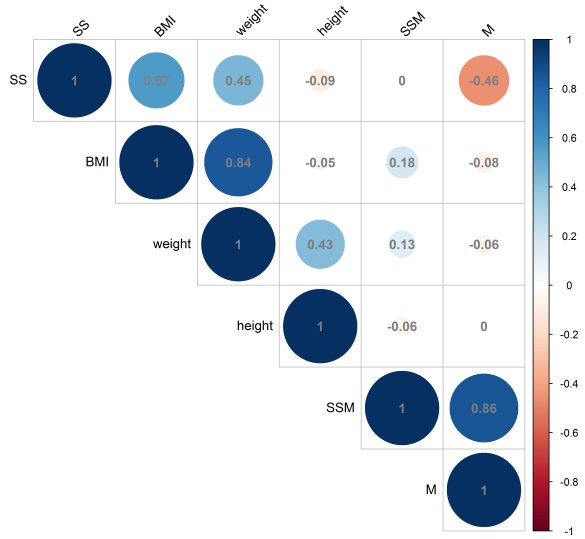

FIGURE 6
Correlations in male measurements between BMI (kg/m^2), weight (kg) and height (cm) and the thickness of the deltoid subcutaneous fat pad, deltoid muscle and skin to subdeltoid fascia (mm). (BMI, body mass index; SS, thickness of deltoid subcutaneous fat pad; M, thickness of deltoid muscle; SSM, thickness of skin to subdeltoid fascia).

Given these findings, administering vaccines in this region requires careful attention to minimize the risk of nerve injury and its associated potential complications. The precise selection of needle length is important in vaccination procedures. In accordance with the CDC guidelines, specific needle lengths are recommended based on an individual's weight. However, in our investigation concerning the application of these recommendations to our particular population and have identified various concerns regarding injection depth. Our simulation study, conducted based on the CDC guidelines for vaccine administration, yielded diverse outcomes based on different needle lengths among individuals with varying body weights. In subjects weighing less than 70 kilograms, employing a 1-inch needle resulted in complete penetration into the deltoid muscle in 0% of males and 4.94% of females. However, when simulating the use of a 1.5-inch needle in males weighing between 70 and 118 kilograms and females weighing between 70 and 90 kilograms, a 100% risk of injection into the subdeltoid bursa was observed. Moreover, in females weighing over 90 kilograms, the utilization of a 1.5-inch needle also led to a 100% risk of injection into the subdeltoid bursa. These findings unequivocally demonstrate that intradeltoid vaccinations adhering to the CDC guidelines carry a potential risk of subdeltoid bursitis attributable to the utilization of too-long needle lengths. It is thus necessary for healthcare practitioners to be mindful of individual body weights and employ appropriate needle lengths to minimize the risk of such complications.

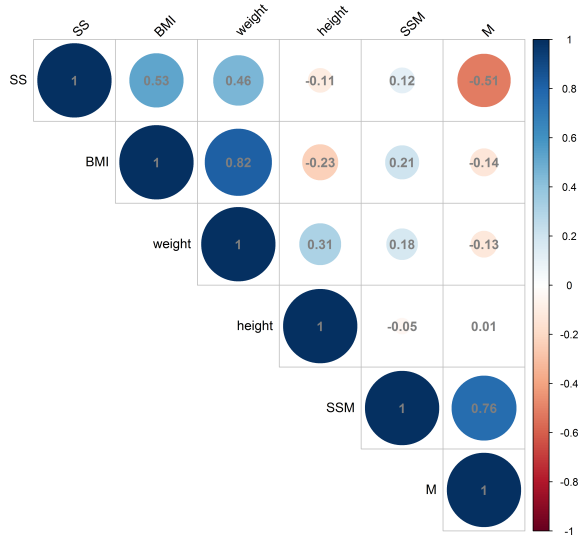

FIGURE 7
Correlations in female measurements between BMI (kg/m^2), weight (kg) and height (cm) and the thickness of the deltoid subcutaneous fat pad, deltoid muscle and skin to subdeltoid fascia (mm). (BMI, body mass index; SS, thickness of deltoid subcutaneous fat pad; M, thickness of deltoid muscle; SSM, thickness of skin to subdeltoid fascia).

While two fingerbreadths below the acromion process is the safest injection site to avoid axillary nerve injury, caution must also be exercised to prevent overpenetration and subdeltoid bursitis. Previous recommendations for full needle insertions in intramuscular vaccinations could lead to overpenetration in our study population. Conversely, a minimum 5-mm (1/5th inch) insertion depth, commonly recommended for intramuscular injections, may not be applicable to the Thai population, as it could result in vaccine delivery into the subcutaneous fat pad, leading to potential vaccination failure or local reactions. In terms of local reactions, various studies have reported higher complication rates in individuals who received a subcutaneous vaccination as opposed to those getting an intramuscular injection (1, 3, 16, 17). This should raise awareness of the importance of following the correct intramuscular injection technique as choosing an insufficient needle length will result in an increased possibility of a subcutaneous injection.

To address individual variability and optimize vaccination success, various measures for assessing the skin-to-deltoid muscle distance have been proposed, including age, body weight (18), and BMI (19, 20). In an ultrasound study of 386 patients, BMI was found to have a superior predictive value of the deltoid subcutaneous fat pad (DSFP) thickness (20). The study concluded that the appropriate needle depth was DSFP thickness + 7 mm, but which has the problem of being difficult to apply in a real-time vaccination setting. The previously mentioned study from Cook et al. (2006) (19) recommended a 25-mm needle for intramuscular injections in individuals with a BMI less than 35 kg/m$_2$ and a 32-mm needle for females with a BMI over 35 kg/m$_2$. These and other studies have various recommendations concerning appropriate needle length and injection site, which are often, however, somewhat contradictory, which may be attributed to differences in study populations, methodologies, or anatomical considerations. Clearly, optimal needle length for intramuscular injections can depend on multiple factors, including muscle mass, age, gender, and anatomical variations. Therefore, while our study suggests a

shorter needle length (0.5 inches of needle penetration depth), it must be considered within the broader context of existing guidelines and individualized patient care, taking into account variations in anatomy and clinical practice, to ensure safe and effective intramuscular injections in other populations..

Our study found positive correlations between BMI and the thickness of the deltoid subcutaneous fat pad and the thickness from skin to subdeltoid fascia, but a negative correlation between BMI and deltoid muscle thickness in both males and females. Our findings are similar to the findings of earlier studies, which found that body weight relative to height was positively associated with subcutaneous fat accumulation. Earlier studies have found that as BMI increased, there was a corresponding increase in subcutaneous fat content (21, 22). Conversely, a negative correlation has been found between BMI and the thickness of the deltoid muscle, indicating that as BMI rises, the proportion of lean muscle mass, including the deltoid muscle, tends to decrease. The results of our study suggest that individuals of both male and female genders may be at an increased risk of having injections administered into the deltoid subcutaneous fat pad when shorter needle lengths are employed. Conversely, the utilization of longer needle lengths may elevate the risk of injections into the subdeltoid bursa.

For clinical implementation, we recommend the utilization of a 0.5-inch needle, which should be inserted perpendicular to the skin at an injection site of 2 fingerbreadths below the mid-acromion process. Alternatively, a 1-inch needle can be employed, with the insertion depth limited to half its length. However, caution should be exercised when using the 1-inch needle, as accurately determining the midpoint for insertion is subjective and susceptible to error. By employing this technique, it can be ensured that the needle tip is correctly inserted within the deltoid muscle, leading to a heightened success rate of vaccinations with minimal complications. These recommendations are supported by both empirical evidence and extensive research in the field of vaccination techniques. As such, their incorporation into clinical practice is likely to yield superior outcomes and contribute to improved patient care and safety. However, doctors or practitioner nurses should be cautious concerning this recommendation in extremely thin or obese patients who may have body measurements outside the normal range. Another option to avoid intradeltoid vaccinations is to use a microneedle vaccination. Microneedles for vaccination offer a promising alternative to intradeltoid vaccination, potentially mitigating complications associated with inappropriate needle penetration depth. Unlike traditional intradeltoid injections, microneedles are designed to painlessly and consistently deliver vaccines into the epidermal and dermal layers of the skin. This approach capitalizes on the abundance of antigen-presenting cells and the dense network of capillaries within the skin, leading to efficient antigen uptake and activation of the immune system. By bypassing muscle tissue, microneedles eliminate the risk of suboptimal vaccine delivery into the deltoid muscle and associated complications such as pain or discomfort, and reduced efficacy. Furthermore, microneedles may offer a more controlled and precise vaccination process, minimizing variations in injection techniques, thereby reducing the likelihood of complications (23, 24). This innovative vaccination method has the potential to improve vaccination outcomes and patient experiences while also enhancing vaccine coverage and accessibility.

This study had several strengths, particularly in considering the practical applicability of the results to real-world vaccination scenarios. To ensure accurate measurements of deltoid muscle thickness, the researchers controlled the shoulder position during the MRI scans. Specifically, they opted for a relaxed adduction position with the patient's arm by their side, as this position was deemed more suitable compared to abduction, another common shoulder position used during vaccine administration. Abduction can lead to varying degrees of deltoid muscle contraction, making it challenging to standardize the procedure across different individuals. In mass vaccination sites, precise control of shoulder abduction degree becomes impractical, increasing the risk of errors and complications associated with improper needle penetration depths. Moreover, the researchers chose MRI over ultrasonography as the imaging modality. The MRIs provided detailed and high-resolution images of the soft tissue layers, allowing for accurate assessment of deltoid muscle thickness. Conversely, ultrasonography can result in compression effects due to the use of the ultrasound probe, potentially leading to misinterpretation of the thicknesses of the skin and subcutaneous layers. By employing these methodological considerations, the study aimed to enhance the relevance and practicality of its findings for real-world vaccination practices.

This study also had some limitations. Firstly, our findings were derived from a specific Thai population, and the variations in body fat distribution and deltoid muscle thickness observed in this study may not be applicable to populations outside of Southeast Asia. Consequently, caution should be exercised when extrapolating these results to other ethnicities and/or geographic regions. Secondly, our research design excluded individuals with extremely low or high BMI values. Therefore, the determination of appropriate needle lengths for these specific subpopulations cannot be ascertained with precision from the present study. Further investigations, specifically targeting individuals with extreme BMI values, are necessary to establish accurate recommendations for needle length in such cases. Such comprehensive investigations will provide a more nuanced understanding of vaccination techniques and contribute to enhanced clinical guidelines across a broader spectrum of individuals. Nonetheless, the present study's insights remain valuable within the context of the examined Thai population, facilitating informed decision-making for healthcare practitioners working with this specific demographic.

Conclusions

Our study demonstrates that using a 0.5-inch needle penetration depth perpendicular to the skin, at two fingerbreadths below the mid-acromion process is a safe and effective for intradeltoid vaccination. This technique ensures precise vaccine delivery into the deltoid muscle while minimizing the risk of overpenetration or injury to surrounding structures.

Adherence to the CDC guidelines for vaccination may lead to the use of a needle length that is too long, potentially resulting in injection into the subdeltoid bursa. Our findings highlight the importance of carefully selecting an appropriate needle length to avoid complications and ensure optimal vaccination outcomes.

Data availability statement

The original contributions presented in the study are included in the article/Supplementary Material. Further inquiries can be directed to the corresponding author.

Ethics statement

The study, involving humans, was approved by the Ethics Committee of the Faculty of Medicine of Prince of Songkla University. The study was conducted in accordance with the local legislation and institutional requirements. The Ethics Committee waived the requirement of written informed consent for participation from the participants or the participants' legal guardians/next of kin because this was a retrospective study.

Author contributions

TL: Conceptualization, Investigation, Methodology, Validation, Writing – review & editing. PB: Investigation, Methodology, Validation, Writing – review & editing. KP: Investigation, Methodology, Writing – review & editing. TN: Investigation, Methodology, Writing – review & editing. PK: Conceptualization, Supervision, Writing – review & editing. CC: Conceptualization, Formal Analysis, Methodology, Project administration, Writing – original draft, Writing – review & editing.

Funding

The authors declare that no financial support was received for the research, authorship, and/or publication of this article.

Conflict of interest

The authors declare that the research was conducted in the absence of any commercial or financial relationships that could be construed as a potential conflict of interest.

Publisher's note

All claims expressed in this article are solely those of the authors and do not necessarily represent those of their affiliated organizations, or those of the publisher, the editors and the reviewers. Any product that may be evaluated in this article, or claim that may be made by its manufacturer, is not guaranteed or endorsed by the publisher.

Supplementary material

The Supplementary Material for this article can be found online at: https://www.frontiersin.org/articles/10.3389/fimmu.2023.1302891/full#supplementary-material

References

1. Zuckerman JN. The importance of injecting vaccines into muscle. *Br Med J* (2000) 321:1237–8. doi: 10.1136/bmj.321.7271.1237

2. Ng JY. Inadvertent subcutaneous injection of COVID-19 vaccine. *Postgrad Med J* (2021) 97:400. doi: 10.1136/postgradmedj-2021-139870

3. Cook IF. Subcutaneous vaccine administration–an outmoded practice. *Hum Vaccin Immunother* (2021) 17:1329–41. doi: 10.1080/21645515.2020.1814094

4. Maliwankul K, Boonsri P, Klabklay P, Chuaychoosakoon C. Shoulder injury related to COVID-19 vaccine administration: A case series. *Vaccines (Basel)* (2022) 10 (4):588. doi: 10.3390/vaccines10040588

5. Jee SC, Yun MH. An anthropometric survey of Korean hand and hand shape types. *Int J Ind Ergon* (2016) 53:10–8. doi: 10.1016/j.ergon.2015.10.004

6. Vathana P, Chiarapattanakom P, Ratanalaka R, Vorasatit P. The relationship of the axillary nerve and the acromion. *J Med Assoc Thai* (1998) 81:953–7.

7. Cetik O, Uslu M, Acar HI, Comert A, Tekdemir I, Cift H Is there a safe area for the axillary nerve in the deltoid muscle? *J Bone Joint Surg American Volume* (2006) 88:2395–9. doi: 10.2106/00004623-200611000-00011

8. Kongcharoensombat W, Wattananon P. Risk of axillary nerve injury in standard anterolateral approach of shoulder: cadaveric study. *Malays Orthop J* (2018) 12:1–5. doi: 10.5704/MOJ.1811.001

9. Fox O, Lorentzos P, Farhat M, Kanawati A. The change in position of the axillary nerve with rotation of the arm. *Clin Anat* (2019) 32:268–71. doi: 10.1002/ca.23295

10. Chuaychoosakoon C, Suwannaphisit S. The relationship between arm abduction position and the risk of iatrogenic anterior branch of the axillary nerve injuries: A cadaveric study. *Orthop J Sports Med* (2021) 9:232596712110088. doi: 10.1177/23259671211008834

11. Bodor M, Montalvo E. Vaccination-related shoulder dysfunction. *Vaccine* (2007) 25:585–7. doi: 10.1016/j.vaccine.2006.08.034

12. Mayer EN, Gajewski CR, Bernthal NM, Jensen AR. Arthroscopic debridement for acute hemorrhagic subacromial bursitis following COVID-19 vaccine administration: A case report. *Shoulder Elbow* (2022) 15(5):527–33. doi: 10.1177/17585732221090821

13. Uchida S, Sakai A, Nakamura T. Subacromial bursitis following human papilloma virus vaccine misinjection. *Vaccine* (2012) 31:27–30. doi: 10.1016/j.vaccine.2012.10.075

14. Choi HR, Kondo S, Mishima S, Shimizu T, Hasegawa Y, Ida K, et al. Axillary nerve injury caused by intradeltoid muscular injection: a case report. *J Shoulder Elbow Surg* (2001) 10:493–5. doi: 10.1067/mse.2001.114682

15. Meirelles H, Rocha G, Filho M. Lesão do nervo axilar causada pela injeção intramuscular no deltóide: relato de caso Axillary nerve injury caused by deltoid muscle intramuscular injection: case report. *Rev Bras Ortop* (2004) 39(10):615–9.

16. Eliakim A, Swindt C, Zaldivar F, Casali P, Cooper DM. Reduced tetanus antibody titers in overweight children. *Autoimmunity* (2006) 39:137–41. doi: 10.1080/08916930600597326

17. Kearns C, Houghton C, Dickinson E, Hatter L, Bruce P, Krishnamoorthy S. What variables should inform needle length choice for deltoid intramuscular injection? *A Syst Rev BMJ Open* (2023) 13:e063530. doi: 10.1136/bmjopen-2022-063530

18. Poland GA, Borrud A, Jacobson RM, McDermott K, Wollan PC, Brakke D, et al. Determination of deltoid fat pad thickness implications for needle length in adult immunization. *JAMA* (1997) 277(21):1709–11. doi: 10.1001/jama.1997.03540450065037

19. Cook IF, Williamson M, Pond D. Definition of needle length required for intramuscular deltoid injection in elderly adults: An ultrasonographic study. *Vaccine* (2006) 24:937–40. doi: 10.1016/j.vaccine.2005.08.098

20. Sebro R, de la Garza-Ramos C. *Statistically based nomograms for the minimal needle length required to achieve intra-articular fluoroscopic-guided injections of the shoulder, hip, and knee*. PM and R (2022) 15(7):853–64. doi: 10.1002/pmrj.12864

21. Snijder MB, Visser M, Dekker JM, Goodpaster BH, Harris TB, Kritchevsky SB, et al. Low subcutaneous thigh fat is a risk factor for unfavourable glucose and lipid levels, independently of high abdominal fat. *Health ABC Study Diabetol* (2005) 48:301–8. doi: 10.1007/s00125-004-1637-7

22. Taksali SE, Caprio S, Dziura J, Dufour S, Calí AMG, Goodmand TR, et al. High visceral and low abdominal subcutaneous fat stores in the obese adolescent:A determinant of an adverse metabolic phenotype. *Diabetes* (2008) 57:367–71. doi: 10.2337/db07-0932

23. Prausnitz MR, Langer R. Transdermal drug delivery. *Nat Biotechnol* (2008) 26:1261–8. doi: 10.1038/nbt.1504

24. Kim YC, Park JH, Prausnitz MR. Microneedles for drug and vaccine delivery. *Adv Drug Delivery Rev* (2012) 64:1547–68. doi: 10.1016/j.addr.2012.04.005

frontiers | Frontiers in Immunology

TYPE Review
PUBLISHED 18 December 2023
DOI 10.3389/fimmu.2023.1281667

Check for updates

OPEN ACCESS

EDITED BY
P Bernard Fourie,
University of Pretoria, South Africa

REVIEWED BY
Eva Gizella Rakasz,
University of Wisconsin-Madison, United States
Henry Puerta-Guardo,
Universidad Autónoma de Yucatán, Mexico

*CORRESPONDENCE
Gustavo Cabral-Miranda
gcabral.miranda@usp.br;
gcabral.miranda@gmail.com

†These authors have contributed equally to this work and share first authorship

RECEIVED 22 August 2023
ACCEPTED 24 November 2023
PUBLISHED 18 December 2023

CITATION
Côrtes N, Lira A, Prates-Syed W, Dinis Silva J, Vuitika L, Cabral-Miranda W, Durães-Carvalho R, Balan A, Cabral-Marques O and Cabral-Miranda G (2023) Integrated control strategies for dengue, Zika, and Chikungunya virus infections.
Front. Immunol. 14:1281667.
doi: 10.3389/fimmu.2023.1281667

COPYRIGHT
© 2023 Côrtes, Lira, Prates-Syed, Dinis Silva, Vuitika, Cabral-Miranda, Durães-Carvalho, Balan, Cabral-Marques and Cabral-Miranda. This is an open-access article distributed under the terms of the Creative Commons Attribution License (CC BY). The use, distribution or reproduction in other forums is permitted, provided the original author(s) and the copyright owner(s) are credited and that the original publication in this journal is cited, in accordance with accepted academic practice. No use, distribution or reproduction is permitted which does not comply with these terms.

Integrated control strategies for dengue, Zika, and Chikungunya virus infections

Nelson Côrtes[1,2†], Aline Lira[1,2†], Wasim Prates-Syed[1,2], Jaqueline Dinis Silva[1,3], Larissa Vuitika[1], William Cabral-Miranda[4], Ricardo Durães-Carvalho[5], Andrea Balan[2,6], Otavio Cabral-Marques[1,3,7] and Gustavo Cabral-Miranda[1,2,3*]

[1]Department of Immunology, Institute of Biomedical Sciences, University of São Paulo, São Paulo, Brazil, [2]The Interunits Graduate Program in Biotechnology of the University of São Paulo, the Butantan Institute and the Technological Research Institute of the State of São Paulo, São Paulo, Brazil, [3]The Graduate Program in Pathophysiology and Toxicology, Department of Clinical and Toxicological Analyses, School of Pharmaceutical Sciences, University of São Paulo, São Paulo, Brazil, [4]Institute of Research and Education in Child Health (PENSI), São Paulo, Brazil, [5]São Paulo School of Medicine, Department of Microbiology, Immunology and Parasitology, Federal University of São Paulo, São Paulo, Brazil, [6]Applied Structural Biology Laboratory, Institute of Biomedical Sciences, University of São Paulo, São Paulo, Brazil, [7]Department of Medicine, Division of Molecular Medicine, University of São Paulo School of Medicine, São Paulo, Brazil

Arboviruses are a major threat to public health in tropical regions, encompassing over 534 distinct species, with 134 capable of causing diseases in humans. These viruses are transmitted through arthropod vectors that cause symptoms such as fever, headache, joint pains, and rash, in addition to more serious cases that can lead to death. Among the arboviruses, dengue virus stands out as the most prevalent, annually affecting approximately 16.2 million individuals solely in the Americas. Furthermore, the re-emergence of the Zika virus and the recurrent outbreaks of chikungunya in Africa, Asia, Europe, and the Americas, with one million cases reported annually, underscore the urgency of addressing this public health challenge. In this manuscript we discuss the epidemiology, viral structure, pathogenicity and integrated control strategies to combat arboviruses, and the most used tools, such as vaccines, monoclonal antibodies, treatment, etc., in addition to presenting future perspectives for the control of arboviruses. Currently, specific medications for treating arbovirus infections are lacking, and symptom management remains the primary approach. However, promising advancements have been made in certain treatments, such as Chloroquine, Niclosamide, and Isatin derivatives, which have demonstrated notable antiviral properties against these arboviruses *in vitro* and *in vivo* experiments. Additionally, various strategies within vector control approaches have shown significant promise in reducing arbovirus transmission rates. These encompass public education initiatives, targeted insecticide applications, and innovative approaches like manipulating mosquito bacterial symbionts, such as *Wolbachia*. In conclusion, combatting the global threat of arbovirus diseases needs a comprehensive approach integrating antiviral research, vaccination, and

10.3389/fimmu.2023.1281667

vector control. The continued efforts of research communities, alongside collaborative partnerships with public health authorities, are imperative to effectively address and mitigate the impact of these arboviral infections on public health worldwide.

KEYWORDS

arboviruses, tropical regions, climate change, dengue virus, Zika virus, Chikungunya virus, strategies control, public health

1 Introduction

The arbovirus (arthropod-borne viral) diseases have become serious public health problem with a wide geographic distribution, mainly in tropical regions (1), due to the presence of competent vectors (2). These infectious agents predominantly contain ribonucleic acid (RNA) as their genetic material, with an exception that is the *Asfarviridae* family, which have deoxyribonucleic acid (DNA) as their genetic material (3).

At the moment, there are more than 534 arboviruses identified, of which approximately 134 cause disease in humans (4). The families of arboviruses include *Flaviviridae*, *Togaviridae*, *Asfarviridae, Orthomyxoviridae, Reoviridae, Rhabdoviridae and Bunyaviridae* (5, 6). Most arboviruses are asymptomatic, but those of medical interest often cause symptoms (Figure 1) such as febrile illness, headache, muscle and joint pains. Rash may be present, as well as petechial rashes. In some cases, arboviruses can cause encephalitis, hemorrhagic fever, or polyarthralgia (6).

Dengue virus (DENV) is the most prevalent arbovirus worldwide, found in more than 100 tropical and subtropical countries (7). According to the World Health Organization (WHO), it affects approximately 16.2 million people annually only in the Americas, with more than 500 million people at risk of contracting the disease in this region. As reported by the Pan American Health Organization (PAHO), in 2022, more than 2.8 million cases were registered in the Americas, with 4,607 of them being serious cases that caused 1,292 deaths. It is estimated that half of the world's population is at risk of contracting the disease (8).

There are four genetically distinct serotypes of DENV that cause the dengue disease (9). However, in 2013, a fifth serotype was first detected in the blood of a patient in the state of Sarawak, Malaysia (10). In endemic countries, there can be co-circulation of more than one DENV serotype, as well as other arborviruses, all mainly transmitted by mosquitoes of the *Aedes* genus (11).

DENV-1 was first isolated in 1943 in Japan and later in 1945 in Hawaii. Since 1977, some countries in America have reported cases of DENV-1 (12–14). Over the years, new epidemics have emerged in several countries, leading to the reporting of other DENV serotypes. In 1944, DENV-2 was reported in Papua New Guinea and Indonesia, and in 1953 in Americas. In the 1970s, it started to spread to countries in Latin America, such as Puerto Rico and Brazil in 1984. DENV-3 and DENV-4 were first reported in 1953 in the Philippines and Thailand. The reports of DENV-3 in Brazil started around 2000s in Rio de Janeiro, and DENV-4 in 1981 (11, 14, 15).

The Zika virus (ZIKV) is another re-emerging flavivirus and human pathogen, that was first isolated in 1947 in the Zika forest in

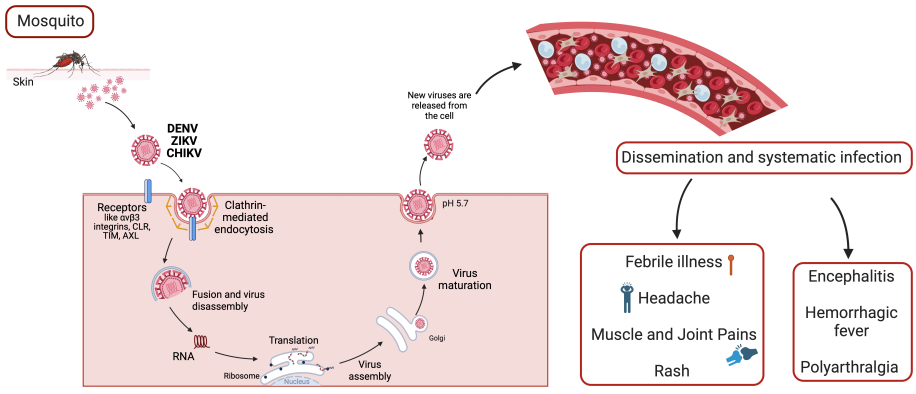

FIGURE 1
The arbovirus replication cycle and systematic infection. Arboviruses interact with multiple types of host attachment factors, including molecules that bind to the viral membrane or virion-associated N-linked carbohydrates. Virions are internalized by clathrin-dependent mechanisms that usurp host factors involved in the uptake of large macromolecules. Subsequently, viral RNA replication takes place, and infected cells migrate through skin into blood stream and lymphoid organs, such as lymph nodes, spleen, liver and brain. Host immune response, and each affected organ can trigger different sinptoms and pathologies.

Uganda (16). Although the ZIKV has many similarity with other flavivirus, such as DENV, the ZIKV has an highly variable region present in its envelope, located close to an important glycosylation site that contains the amino acid asparagine at position 154 (Asn154) which is associated with its virulence (17). Before 2007, it was identified as a virus that cause a mild feverish disease in a small number of humans in Africa and parts of Asia. However, ZIKV has since spread to several countries, and in 2014, it was introduced in Brazil and other regions in the Americas (6). Genomic and phylogenetic analysis of virus isolates indicated the presence of two distinct lineages, African and Asian, both originating in East Africa (18). In addition to viral transmission through the bite of the *Aedes* mosquitoes, there are other forms, such as transmission through infected blood transfusion, sexual, and maternal-fetal transmission (19) which makes it even more difficult to control.

The chikungunya virus (CHIKV) was initially identified in patient serum during an epidemic in 1952 in Tanzania, and in 1953, the virus was isolated from *Aedes* and *Culex* spp. mosquitoes (20, 21). Phylogenetic studies show that the circulating strains of CHIKV have a common ancestor that originated 500 years ago (22). Currently, there are four identified CHIKV lineages, namely the Asian (AL), West African (WA), East/Central/South African (ECSA), and Indian Ocean (IOL) lineages. Among these, two main strains, responsible for several epidemics in Brazil, are the ECSA and AL (23, 24).

The ECSA genomic sequences isolated from patients of the outbreak in 'La Reunion Island in the Indian Ocean' showed a mutation in 90% of the viral sequences of the structural protein E1, where there was an exchange of the amino acid alanine for valine in region 226 (A226V) (25, 26). This mutation allowed the adaptation of a new vector, *A. albopictus*, which is present in temperate regions, favoring outbreaks in Italy and France (25, 26). A seroprevalence analysis between the years 2000-2019 found that the ECSA strain is the most frequent (27).

Since the first record of CHIKV in 1950s, several epidemics have emerged in Africa, Asia, Europe, and the Americas. Nowdays, CHIKV has been found in more than 100 countries (28). According to the WHO, more than one million cases are reported annually only in the Americas, with most cases occuring in Brazil (29). In 2016, in the Caribbean and the Americas, 185,000 cases of CHIKV were reported, with more than 90% of cases in the Americas being in Brazil (29).

The geographic distribution (Figure 2) of each arbovirus is related to ecological parameters that define the transmission cycle. Some factors include patterns of vegetation, temperature, and typical precipitation, which influence the distribution of the arthropod vector and the vertebrate host necessary for the maintenance of the virus. Social, demographic and climate change, deforestation, population migration, and urbanization in recent years have also had a strong impact on arbovirus infections (30).

All these factors increase the possibility of human contact with vectors, contributing to the increasing transmission of viruses and the appearance of epidemics around the world. In recent decades, for example, the reemergence of arboviral infections has been observed in numerous countries (Figure 2). The reemergence of CHIKV in Asia, ZIKV outbreaks in the Americas, as well as West Nile virus (WNV) and Rift Valley fever virus (RVFV) outbreaks in Europe, are increasingly frequent (15, 31–33).

Therefore, control and prevention programs for arboviruses are essential, which must be based on the development of vaccines, treatment, vector control, and genomic surveillance programs based on tracking viruses using genomic sequence data as a cross-cutting activity (34). In this manuscript, we discuss the principal arboviruses, such as DENV, ZIKV and CHIKV, responsible for outbreaks in many countries. Furthermore, we address the perspectives of controlling these diseases.

2 Viral structure and morphogenesis

Flaviviruses like DENV and ZIKV have a spherical and small composition of viral particles (~50nm in diameter). They contain a 10-11 kb genome and an open reading frame (ORFs) that encodes three structural proteins: capsid (C), premembrane/membrane (prM/M), and envelope (E), as well as seven non-structural proteins (NS1, NS2A, NS2B, NS3, NS4A, NS4B, and NS5), as seen in the Figure 3. The structural and non-structural proteins are important for correct virion assembly, cell receptor binding, and viral replication (Figure 1) (12, 35). The E protein is an essential structure responsible for viral attachment and membrane fusion. It is composed by three domains (E-DI, E-DII, and E-DIII) linked to the viral membrane by a helical region and two antiparallel transmembrane segments. The E-DI is responsible for the structural organization of the envelope, while E-DII allows the fusion of the virus with the host cell membrane (36, 37), and the E-DIII is highlighted as the most neutralizing antibody site and allows the virus to bind to the cell receptor (38, 39). Therefore, the E-DIII has been used as the best candidate for vaccine development, as well as for treatment (40).

The viral capsid (C) is a small helical protein with surfaces that bind to viral nucleic acids or host lipids and directs the incorporation of the viral genome into the host cells (17). The M protein originates from the cleavage of the precursor protein prM (41) and it is essential for the maturation of virions. For example, in the immature virions, prM prevents structural changes in the E glycoprotein, which are essential for the correct folding, maturation, and assembly of E protein during replication (Figure 1) (42).

As illustrated in Figure 3, the alphaviruses like CHIKV form spherical particles (~70nm in diameter) with icosahedral symmetry in their capsids. The virions consist of a host-derived lipid bilayer that is enriched in cholesterol. The lipid envelope contains 240 copies of E1 and E2 heterodimers glycoproteins arranged in a trimeric format (80 copies) (43, 44). The genome consists of two ORFs that encode four nonstructural proteins (nsP1-nsP4) and six structural proteins (Capsid, E3, E2, 6K, E1).

Some receptors involved are the Mxra8, αVβ3 integrins, C-type lectin receptors (CLR), TIM, TAM, AXL and phosphatidylserine receptor families (T cell immunoglobulin and mucin domain) (45). Most of the *Arbovirus* enter the cells by clathrin-mediated endocytosis (12, 46, 47). In the case of flaviviruses, the viral

10.3389/fimmu.2023.1281667

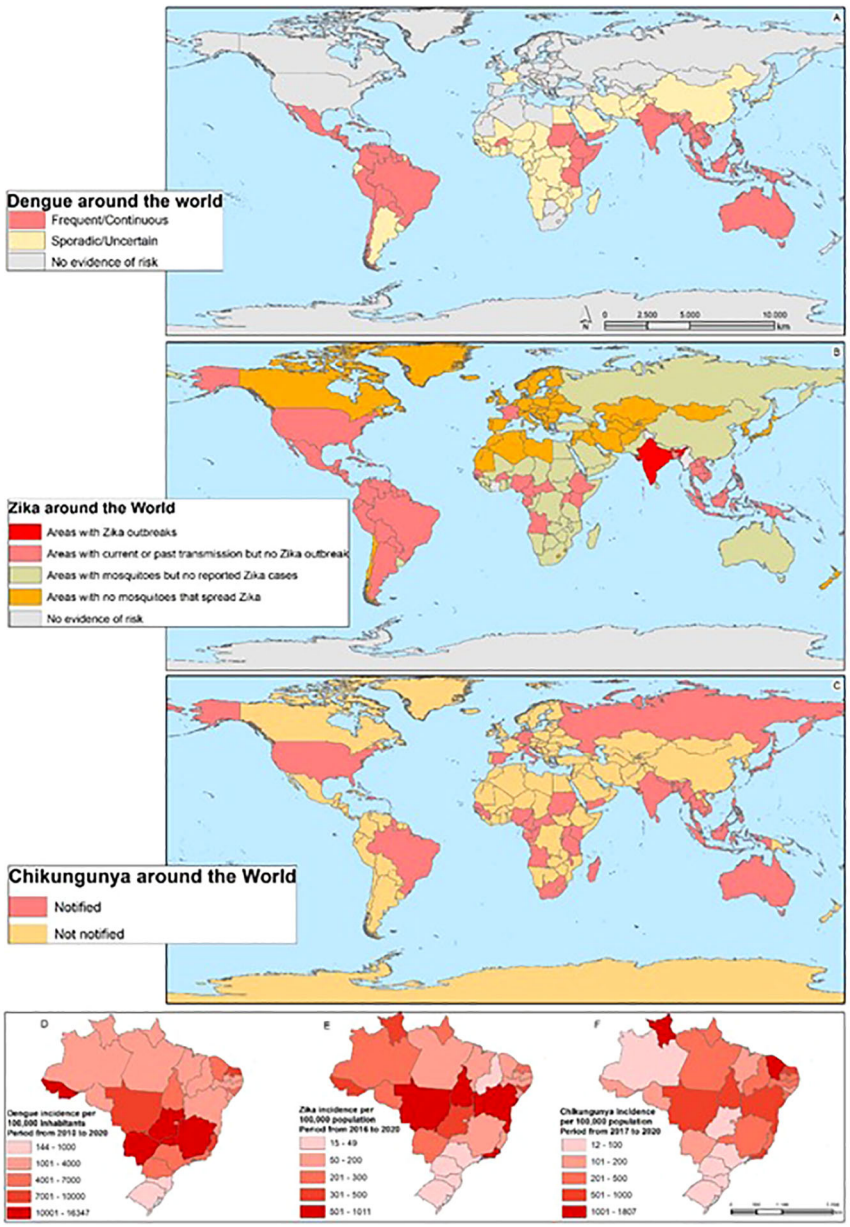

FIGURE 2
The Arbovirus DENV, ZIKV, and CHIKV distribution around the world: The map shows the areas with the distribution of the risk of DENV throughout the world **(A)**, the areas with the risk of ZIKV **(B)**, and the areas of the risk of CHIKV **(C)**. On **(D)**, the incidence of DENV is shown in the Brazilian states, **(E)** ZIKV, and **(F)** CHIKV.

polyprotein (NS2-NS3) undergoes cleavage in the endoplasmic reticulum (ER) by host proteases to produce functional proteins. The viral genome is synthesized within a viral capsid (C) and surrounded by a lipid bilayer containing two transmembrane proteins, envelope (E) and membrane (M). Subsequently, the particles are released from the ER (Figure 1) (35).

In the case of alphaviruses, the E1 glycoprotein fuses the viral envelope in the endosome, while E2 interacts with the cell receptor, triggering endocytosis. The E2 glycoprotein conjugates with E3 glycoprotein (pE2) inside the cell. pE2 undergoes maturation in the Golgi complex and releases E2 and E3. Cleavage of E3 is crucial for particle fusion. E3 aids in spicule folding and prevents premature glycoprotein activation. 6K is involved in virion formation and growth (43, 48, 49). Nonstructural proteins play essential roles in genome replication and transcription, as well as in protecting the replication complex and genomic RNA from protease degradation (38). These proteins are translated into two forms: P123, which is more abundant, and P1234, generated by reading the opal stop codon at the junction of nsP3 and nsP4. Following cleavage, these proteins give rise to four distinct proteins: nsP1, nsP2, nsP3, and nsP4. The nonstructural proteins actively participate in the replication of the viral genome (50–55).

After attachment to the host cells, mainly innate immune cells, such as dendritic cells, monocytes, and macrophages, by receptor-

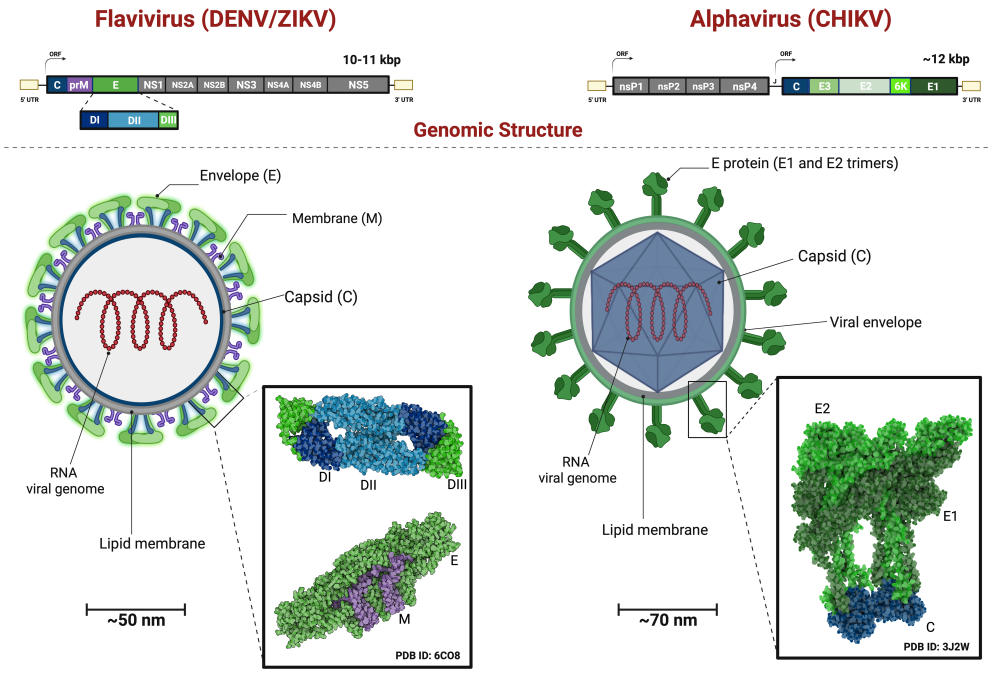

FIGURE 3
Genomic Organization and Viral Structure of Flavivirus and Alphavirus. Flavivirus comprise a single Open Reading Frame with the genes for the Structural Proteins followed by the Non-Structural Proteins transcribed and translated and the resulting polyprotein undergoes proteolytic processing. Alphavirusus are comprised of the genes for the Non-Structural Proteins followed by the Structural Proteins, transcribed from two distinct ORFs, and each resulting polyprotein undergoes further proteolytical processing. Flavivirus structure have a mature virions with capsid (C) and membrane (M) covered by 90 dimers of (E) proteins. The E proteins exhibit three domain: E-DI (dark blue), E-DII (light blue) and E-DIII (green) anchored to the viral membrane (purple). The Alphavirus virion have the envelope glycoproteins in a shape of 240 dr trimer of E1(dark green), E2 (light green) ancored in lipid membrane (M) and the capsid (C) protein (blue). Showing heterodimers interacting with capsid protein.

mediated endocytosis, the viral RNA replicates. Once infected, dendritic cells migrate to lymphoid organs, allowing replication and dissemination to other organs (Figure 1) (56).

3 Pathogenicity of arboviruses and host immune responses

The arbovirus infects resident skin cells, such as fibroblasts, macrophages, and dendritic cells, through the bite of an infected female *Aedes* spp. mosquito (57). Once the virus is transferred to the tissues, it initiates the pre-acute phase of infection, characterized by an inflammatory response, including increased permeability and chemokine release from resident cells. After viral replication (Figure 1), it systemically migrates through lymph nodes, joints, spleen, liver, brain and muscles (58–61). During the initial days of infection, high titres of the virus can be detected in the blood (62–65).

The innate immunity plays an important role in controlling arboviruses in the early stages of infection. As is well known, the viral RNA is a pathogen-associated molecular patterns (PAMP) recognized by pattern recognition receptors (PRRs), mainly Toll-like receptors (TLRs 3, 7 and 8), RIG-I like receptors (RLRs) and Nod-like receptors (NLRs) (66, 67). As with other viral infections, type I interferon (IFN-α and IFN-β) acts as the first line of defense against arboviruses. These interferons stimulate the expression of many genes that interupt the virus replication and proliferation (68, 69). The IFNs activate the cells through a signal transducer such as Janus kinase, which induces the transcription factor JAK-STAT to produce interferon regulatory factors (IRFs 3, 5 and 7) and interferon-stimulated genes (ISG), that block viral replication by triggering an antiviral state in both infected and uninfected cells (70–72). Secondary infections, however, are known to cause serious diseases, specifically after a heterotypic infection (73). It is believed that the phenomenon of antibody-dependent enhancement (ADE) may cause increased virulence and pathogenicity (74).

The ADE phenomenon occurs when non-neutralizing antibodies from a previous heterotypic infection create a virus-antibody complex that is phagocytosed by cells that are generally not infected, via Fcγ receptors and complement receptors present in permissive cell for ADE, such as dendritic cells, monocytes and macrophages (75). ADE is primarily mediated by the IgG antibody, and in some instances, by IgM (76). It is expected to result in an increase in viral uptake and, therefore, contribute to the replication, leading to an exacerbated immune response to the infection, and cytokine storm, with an upregulation of IL-6, TNF-α and IL-10, whereas IL-12 and IFN-γ is downregulated (77).

It is worth mentioning Vo et al. (78) that conducted a study to investigate the phenomenon of ADE in the context of the four DENV serotypes by assessing plasma samples from patients with confirmed DENV-2 infections. Initially, during the early stages of infection, no significant differences in ADE activity were observed

among the serotypes. However, intriguing distinctions emerged in later stages, specifically at 10 and 60 days post-infection confirmation. ADE activity was found to be notably higher against DENV-1 when compared to DENV-4 during these later time points. When analyzing the cumulative ADE activity by calculating the area under the curve (AUC), it was determined to be most pronounced against DENV-2, which happened to be the serotype responsible for the infection in the cohort under investigation (78).

Moreover, overall it is not new that DENV antibody avidity shifts from the previous infecting serotype to the current infecting serotype over time (79). Over time, there is a transition in the overall avidity of these antibodies, influenced by changing quantities and qualities. For example, the quantity of afucosylated Fc-IgG increases during convalescence compared to the acute phase of primary infections, potentially impacting the occurrence of ADE (80, 81). Additionally, antibody titers specific to DENV tend to decrease as time progresses, which may further contribute to the susceptibility to ADE (82, 83). This is of particular concern since antibodies targeting specific regions of viral proteins, such as the fusion loop of the envelope protein (E) and other surface proteins like (prM), have been identified as factors promoting ADE both in laboratory settings and animal models (84, 85). Structural aspects of the virus, including its maturation state, have also been found to influence ADE. Notably, severe cases of DENV infection can witness an increase in mortality rates of up to 20% (73).

Another important factor for pathogenicity is the NS1. This protein is found on the surface of infected cells and circulating viral particles in the host. The interaction of NS1 with cellular receptors and viral proteins contributes to viral replication, viable viral particles, viral persistence, and primarily the activation of immune system receptors, such as C3, C4, and C5 complement receptors, and even the membrane attack complex (86). TLR3, present in dendritic cells and macrophages, is activated via NS1, triggering the expression of antiviral factors. NS1 also activates TLR2 and TLR6 during DENV infection, increasing the production of proinflammatory cytokines like IL-6 and TNF-α (87). The recognition of NS1 by TLR4 causes the activation of peripheral blood mononuclear cells (PBMCs), leading to an increase in proinflammatory cytokines that induce endothelial tissue dysfunction (88). Studies using human endothelial cell cultures have shown that flavivirus NS1 can cause modulation and endothelial hyperpermeability in various tissues, favoring pathogenesis (89).

The most severe dengue clinical syndrome can manifest itself in the form of shock, including coagulation abnormalities, plasma leakage, and increased vascular fragility. Fluid loss due to increased capillary permeability leads to hypovolemic shock and multiorgan failure (90). Because the clinical diagnosis of these diseases is not specific (91), due to the wide spectrum of clinical manifestations and clinical overlap with other circulating arboviruses, molecular diagnostic techniques are necessary and are the most commonly used to confirm infection by some flavivirus at the beginning of symptoms (92, 93).

The presence of viral RNA in the amniotic fluid and placenta evidences the association of Congenital Zika Syndrome (SCZ) with neonatal complications, such as congenital microcephaly, optic neuropathy, congenital glaucoma, ventriculomegaly and lissencephaly (94, 95). Beyond neonatal complications, ZIKV infection in adults is related to Guillain Barré Syndrome (GBS), an autoimmune disease that attacks neural cells leading to gradual muscle weakness and even paralysis. Other complications such as arthralgia and cardiovascular problems have been reported; however, it is necessary to establish the exact connection (96, 97).

In the chronic phase, CHIKV propagation through the lymphatic, circulatory, and joint systems (98). The chronic-phase arthritis and the pro-inflammatory environment are associated, the persistence of viral RNA in macrophages, muscles and joints may favor persistent arthritis (99). Unlike other arboviruses, which show symptoms only in the acute infection phase, more than a third of CHIKV-caused infections are symptomatic and most patients experience joint pain years after the onset of the disease (100, 101).

4 Outlook on control strategies development

It is necessary to understand in detail the Arbovirus' biology, its relationship with the vectors, with the host and its history, so that is possible to develop integrated control strategies in an effective way, because multiple factors contribute to the emergence of arboviruses. For instance, population growth in areas with unplanned urbanization, climate changes, and viral genetic adaptation are significant contributors (30). Beyond their transmission between arthropods and humans, these viruses can infect a wide range of animal species, rendering complete eradication virtually impossible. Arbovirus infections exhibit diverse clinical presentations, ranging from mild to severe, and are categorized as either visceral or neurotropic, with some viruses displaying both characteristics (102, 103).

4.1 Vaccines

An effective vaccine against DENV must be able to induce a balanced response against all four DENV serotypes (104). However, its development is challenging due to the theoretical risk that an incomplete immunity generated by the vaccine could lead to increased pathogenesis upon subsequent natural infection, as discussed earlier with the ADE phenomenon.

Dengvaxia® (Sanofi Pasteur) is a live attenuated tetravalent vaccine containing chimeras of pre-structural membrane (prM) and envelope (E) genes from the four DENV types, combined with non-structural genes from the yellow fever vaccine strain 17D (dengue chimeric yellow fever – CYD) (105). It has been licensed in several American countries, including Mexico, Brazil, El Salvador, Costa Rica, Paraguay, Guatemala, and Peru (106). However, despite being licensed by ANVISA (The National Health Surveillance Agency) in 2015 (107), Dengvaxia® has raised numerous concerns in the scientific and health communities, particularly regarding its potential to predispose people with no prior DENV exposure to severe diseases. As a result, the vaccine is no longer considered a viable prevention tool, partly due to its high cost (106).

In the Philippines, immunizations with Dengvaxia® were suspended in 2017 after 14 vaccination-associated child deaths occurred (108). In Brazil, the vaccine was recommended for individuals aged 9 to 45 years old, with a documented history of prior laboratory-confirmed DENV infection (106). In the European Union and the United States, Dengvaxia® was also licensed for its use in people aged 9 or older living in DENV endemic areas, but limited to those who had experienced a previous DENV infection (109, 110). The Advisory Committee on Immunization Practices (ACIP) recommended in June 2021 Dengvaxia for routine use in children aged 9 to 16 years living in endemic areas with laboratory confirmation of previous DENV infection (111). Low acceptance of the vaccine is driven by concerns about an increased risk of severe dengue in vaccinated individuals without prior exposure to DENV.

Recently, the ANVISA approved the QDENGA® vaccine (TAK-003 – Takeda Pharma) to immunize individuals aged 4 - 60 years, without the need to confirm a previous infection, different from the Dengvaxia® vaccine. This vaccine, QDENGA®, is based on a live attenuated DENV-2 virus that serves as the genetic backbone for the four vaccine viruses, the chimeras (DENV-1, DENV-3, and DENV-4), which were generated by replacing the pre-membrane and envelope genes. The QDENGA® vaccine also received evaluation and a positive recommendation from the European Health Agency (EMA) under the "EU Medicines for all" program. Several clinical trials involving more than 20,000 subjects have demonstrated the vaccine's safety and efficacy against DENV disease (112–114).

Despite the success of vaccines already licensed for certain flaviviruses such as Yellow Fever Virus (YFV), and Japanese Encephalitis Virus (JEV), combating epidemics caused by emerging flaviviruses poses significant challenges. The primary challenge stems from the extensive cross-reactivity observed in flavivirus-immune sera. While neutralization assays help to understanding antibody responses to both homologous and heterologous viruses in convalescent sera, the use of sera from acute infected individuals has been limited (115, 116).

The detection of flavivirus infection using molecular assays is limited due to the transient nature of viremia, making them sensitive only for relatively short periods. To develop vaccines against flaviviruses, new platforms must be explored, underscoring the necessity for further studies on the biology, structure, and heterogeneity of vaccine antigens (117).

The accessibility to vaccines also remains a significant challenge even after their development. This issue is particularly evident in regions like South America and Africa, where vaccine shortages have led to a continuous circulation of Yellow Fever Virus (YFV), prompting research on vaccine economics (118). Furthermore, the availability of effective vaccines does not always guarantee the expected impact on global health. An illustrative example was observed during the SARS-CoV-2 pandemic, where in many areas, the acceptance of vaccination was lower than anticipated, necessitating the implementation of public policies to ensure access and raise awareness about the importance of this preventive measure.

High safety, immunogenicity, and efficacy are always essential prerequisites for a vaccine to be embraced by both the public and the scientific community. However, a crucial question remains unanswered: Will these DENV vaccines offer superior protection to individuals with no prior exposure to DENV infections? Ensuring a vaccine's effectiveness without the risk of sensitizing the population and exposing them to symptomatic or severe disease upon subsequent natural DENV infection is of utmost importance. Therefore, addressing these questions is imperative before we can consider using these vaccines as a significant tool in the prevention and control of dengue disease on a public scale.

Currently, no vaccines are available to prevent ZIKV and CHIKV infections. Nevertheless, several vaccine candidates are in the developmental pipeline (see Figure 4), with ongoing clinical trials. These vaccines utilize diverse technologies, encompassing live attenuated, inactivated virus, mRNA, DNA, recombinant, and VLP approaches.

4.2 Antivirals therapies

At the present, there are no specific therapy against arbovirus-causing infections, but some drugs are used to reduce symptoms (Table 1). Studies using "sofosbuvir" as an antiviral agent has been shown to inhibit ZIKV replication in hepatic and neural cell cultures, and also provided protection using animal model such as mice after being challenged with ZIKV (119). In another study, the antibiotic azithromycin was analyzed *in vitro* using glial cells, and it was capable to reduce viral proliferation (120). Even though these data are promising, it is known that the ideal drug against ZIKV should reduce viral load, symptoms, and prevent neurological complications in the fetus, what these experiments are far from achieving it (121, 122).

In the case of CHIKV, the treatment of arthralgia often involves the use of non-steroidal anti-inflammatory drugs, such as ribavirin and chloroquine. Additionally, the investigation of monoclonal antibodies as potential therapeutic agents has been explored (123–125). Passive transfer of immune serum protects against virus-induced lethality and studies in mice demonstrated a prophylactic efficacy when it is provided before or immediately after CHIKV challenge (124). Ribavirin has antiviral activity against several RNA viruses, and the authors (126, 127) suggest that it has a beneficial effect in relieving arthralgia and swelling associated with chronic arthralgia. Chloroquine is another treatment that has been shown to be effective as it inhibited CHIKV infection in cultured cells through endosomal acidification, thus interfering with the activation of Toll-like receptors (TLR), reducing inflammatory activity (128–130). Niclosamide, a medication used as an antiparasitic, was able to inhibit *in vitro* the entry of DENV, ZIKV, and CHIKV into the cells. This medication also interferes with endosomal acidification and inhibits membrane fusion (131, 132).

Isatin and its derivatives are heterocyclic organic compounds. They have broad applications in the pharmacological field, and several studies have pointed out their antiviral activities, such as spiropyrazolopyridone. Bin Zou and colleagues (133) used a viral infection model in mice with DENV and observed a reduction in

10.3389/fimmu.2023.1281667

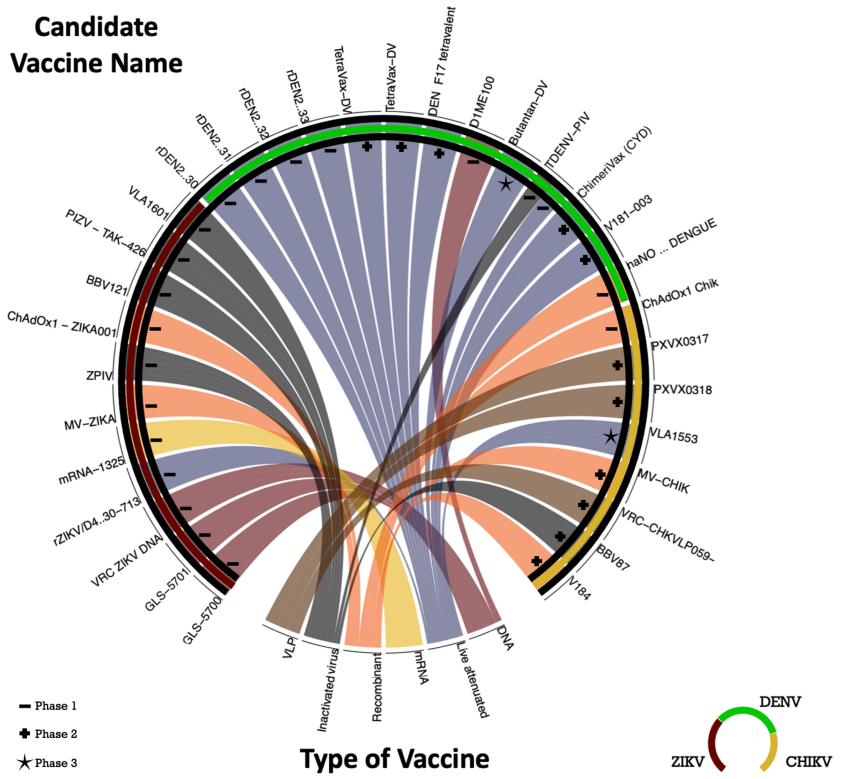

FIGURE 4
Chord Diagram with candidate vaccine in clinical trials to DENV, ZIKV and CHIKV. The chord diagram employed in this study depicts a central circle representing the target virus of the vaccines, including DENV (dark green), ZIKV (red), and CHIKV (yellow). The diverse segments of the circle are assigned to distinct vaccine development methodologies: 3 trials on VLP (brown), 5 trials on inactivated virus (gray), 6 trials on recombinant methods (orange), 1 mRNA trial (yellow), 12 trials on live attenuated (blue), and 1 trials involving DNA (red). The phases of the clinical trials are indicated by symbols: dash (Phase 1), plus (Phase 2), and star (Phase 3). The vaccines mentioned in the chord diagram are registered in the ClinicalTrials.gov - National Library of Medicine (U.S.) database.

viremia in the treated mice after oral administration of the drug. Another isatin derivative, 1-[(2-methylbenzimidazol-1-yl)methyl]-2-oxo-indolin-3-ylidene]-amino]thiourea (MBZM-N-IBT), demonstrated antiviral activity against CHIKV by inhibiting the nsP2 protease activity *in vitro* and *in vivo* experiments (134, 135).

Natural compounds belonging to the Flavonoid family, such as Delphinidin (D) and epigallocatechin gallate (EGCG), possess antioxidant activities, and according to recent studies, they also exhibit antiviral functions against some arboviruses, such as DENV, ZIKV, and CHIKV. Delphinidin likely acts during the interaction of viral proteins with receptors present in cells; this compound showed antiviral activity only during the early stages of viral infection tested *in vitro* (136). The EGCG was also able to inhibit CHIKV infection and attchament to cells, as shown by researchers (137) that transfected HEK cells with lentiviral vectors pseudotyped with CHIKV envelope proteins and subsequently added EGCG to assess antiviral effects.

4.3 Vector control strategies

Although there are several important studies in progress, the absence or limitation of effective therapies and vaccines makes the control of circulating mosquitoes vectors a commonly used strategy to combat arbovirus transmission. Vector control represents a viable approach to reduce the prevalence of these disease vectors (Table 1). Arboviruses are distributed worldwide, and their surveillance has become a crucial tool for detecting and controlling the circulation of viruses (138). Metatranscriptomics surveillance programs monitor and test mosquito populations for arboviruses, as demostrated by The Victorian Arbovirus Disease Control Program (VADCP) (139). Metatranscriptomics is a novel RNA sequencing approach used to analyze the RNA present in a sample. This technique aids in identifying viral mutations and even tracing the origin of cases. To achieve it, a complex bioinformatic analysis is required, as demonstrated in a study conducted in Australia (140). In this study, they analyzed the species of mosquitoes and the circulating virus to gain valuable insights into viral dynamics and transmission patterns.

Various methods targeting different stages of the mosquito life cycle can aid in controlling their population. Implementation of these strategies involves public education and raising awareness, encouraging measures like managing and preventing the deposition of eggs and larvae in water accumulations, tires, plant pots, and uncovered water tanks. Additionally, the application of insecticides to eliminate mosquito larvae and adults is crucial (141).

10.3389/fimmu.2023.1281667

TABLE 1 Possible antiviral targets and mosquito control strategies.

IMPLEMENTATION OF PREVENTIVE MEASURES	
Antiviral Proactiveness – Pre infection	
Strategy	Description
Metatranscriptomics surveillance	Monitors arboviruses in mosquitoes, mutations identification and transmission
Genetically modified mosquitoes	The mosquito's natural defense mechanisms allow new strategies for insect resistance to viruses
Mosquito bacterial microbiota	Promotes a reduction in the viral replication capacity of vectors.
Prophylaxis - post infection	
Name/Compound	Mode of action
Sofosbuvir	Inhibits viral replication **(ZIKV)**
Azithromycin	Inhibits viral replication **(ZIKV)**
Ribavirin	Antiviral activity **(CHIKV)**
Chloroquine	Antiviral activity **(CHIKV)**
Niclosamide	Antiviral activity **(DENV, ZIKV and CHIKV)**
Spiropyrazolopyridone	Antiviral activity **(DENV)**
1-[(2-methylbenzimidazol-1-yl) methyl]-2-oxo-indolin-3-ylidene]-amino] thiourea	Antiviral activity **(CHIKV)**
Delphinidin	Antiviral activity in early stages **(DENV and ZIKV)**
Epigallocatechin gallate	Inhibits infection and antiviral activity **(DENV and CHIKV)**

Furthermore, the incorporation of antiviral controls within mosquitoes has shown promise in preventing arbovirus transmission. Some recent studies have explored the use of genetically modified mosquitoes with antiviral genes that hinder viral replication (142).

Mosquitoes present a different defense system compared to mammals; they lack B and T lymphocytes, do not produce immunoglobulins, and do not develop specific antigen responses. However, they do exhibit defense mechanisms found in the innate immunity of mammals, such as Toll-like pathways, Janus kinase/signal transducer and activator of transcription (JAK/STAT), immune deficiency (IMD), and RNA interference (RNAi) pathways, which interfere with viral gene expression (143).

The Toll-like receptors (TLRs) bind to cytokine receptors like Spätzle, inducing signal transductions in the cytoplasm, where they interact with the myeloid differentiation primary response protein (MyD88)-Tube-Pelle complex, leading to the expression of B cell-dependent immune response-related NF-kB. The NF-kB expression can also be stimulated via IMD through the activation of peptidoglycan-recognition protein receptors PGPR-LC and PGPR-LG. Activation of the JAK/STAT pathway initiates the transcription of antiviral cytokines and growth factors.

Gene regulation is carried out by small non-coding RNAs, approximately 21-30 nucleotides long, classified as small interfering RNAs (siRNAs), microRNAs (miRNAs), and Piwi-associated interfering RNAs (piRNAs) (144, 145). siRNAs are double-stranded RNA molecules that target complementary messenger RNA (mRNA) sequences, subsequently degrading the gene and suppressing its function. miRNAs act in the post-transcriptional phase, repressing mRNA translation, while piRNAs regulate element transposition (144–147).

A better understanding of these insect modulation mechanisms aids in developing more efficient approaches for arbovirus control. This includes inhibiting specific genes to reduce virus transmission, enhancing insect resistance to the virus by using antimicrobial peptides, and even inhibiting viral replication in mosquitoes to prevent transmission.

Currently, a cutting-edge methodology for arbovirus control involves the manipulation of mosquito bacterial symbionts' microbiota. The composition of the bacterial community can vary among different mosquito species (141). One notable example is *Wolbachia pipiens*, an α-proteobacterium found in a few arthropod species, which has been extensively researched for insect population control. *Wolbachia* is present in various mosquito tissues, including the Malpighian tubules, muscles, head, glands, and reproductive organs (148). The technique employed to introduce *Wolbachia* into insects is termed Insect Lineage Infection by *Wolbachia*. This method entails inoculating *Wolbachia* bacteria into insect eggs during the embryonic stage, resulting in the establishment of a persistent infection in the cells.Its effective spread is attributed to its ability to induce cytoplasmic incompatibility (CI), where mating between uninfected females and *Wolbachia*-infected males results in eggs that fail to develop, leading to the production of only *Wolbachia*-infected offspring. Additionally, *Wolbachia* can cause reduction of vectorial capacity by decreasing the mosquito's lifespan (parthenogenesis) and inducing feminization. Moreover, *Wolbachia* inhibits virus replication within the mosquito and decreases saliva production, affecting feeding capacity during meals (149–151).

Research conducted in Brazil and Colombia has shown promising results in vector control, demonstrating that the release of modified *Aedes aegypti* mosquitoes containing *Wolbachia* led to the suppression of arbovirus transmission and replication. Consequently, *Wolbachia* has been proven capable of inhibiting the replication of DENV, ZIKV, and CHIKV (152–154). The use of *Wolbachia* as a vector control agent has been applied in several countries as part of programs aimed at eliminating arboviruses. One such example is the "Eliminate Dengue" project, an international program with the objective of controlling DENV circulation through *Wolbachia* infection in *Aedes aegypti* mosquitoes. This program has been implemented in countries such as Australia, Brazil, Indonesia, Vietnam, and Colombia, showing promising results in reducing DENV transmission rates. The initiative that combats the spread of arboviruses using *Wolbachia* is the "World Mosquito Program" (WMP). These prevention and control programs, which are based on the introduction of *Wolbachia* into insects, represent a promising and innovative approach (155).

5 Conclusion

The reemergence of arbovirus infections has been observed in several countries. Furthermore, the spread to new geographical areas is on the rise, underscoring the necessity for the implementation of effective control and prevention programs. These programs should be grounded in entomological surveillance activities and disease monitoring.

While specific pharmaceutical interventions for arbovirus infections remain elusive, we conclude that encouraging progress has been made with certain compounds, including Chloroquine, Niclosamide, and Isatin derivatives. These compounds have demonstrated substantial antiviral efficacy against these pathogens in both laboratory and animal studies.

It is crucial to implement strategic vector control measures to contain arbovirus transmission. These strategies encompass a range of interventions, as exemplified by the VADCP, along with educational campaigns to raise public awareness. Notably, advanced techniques like the manipulation of bacterial symbionts in mosquitoes, illustrated by the utilization of *Wolbachia* in *Aedes aegypti* mosquitoes, have shown remarkable success in suppressing the transmission of diseases like DENV across various nations, which holds potential such as pivotal component of integrated prevention strategy. By reducing vector competence, limiting viral replication, and influencing mosquito lifespan, *Wolbachia* contributes substantially to breaking the transmission cycle.

As we confront the complex challenges posed by arboviruses, it becomes evident that a holistic and collaborative approach is imperative. The integration of advancements in antiviral research, the development of effective vaccines, innovative vector control methodologies, and surveillance programs collectively fortify the global defense. This unified front not only prevents immediate outbreaks, but also lays the foundation for resilient and adaptative aproch to combat future arbovirus challegens.

Author contributions

NC: Conceptualization, Writing – original draft. AL: Conceptualization, Writing – original draft. WP: Writing – review & editing. JS: Writing – review & editing. LV: Writing – review & editing. WC: Writing – review & editing. AF: Writing – review & editing. OC: Writing – review & editing. GC: Writing – review & editing. RD: Writing – review & editing.

Funding

The author(s) declare financial support was received for the research, authorship, and/or publication of this article. The authors acknowledge the support provided by The São Paulo Research Foundation – FAPESP: GC-M: 2019/14526-0, 2020/04667-3; GC-M and NC: 2021/03508-1 (PhD Scholarship); GC-M and AL: 2021/03102-5 (PhD Scholarship); (FAPESP Young Investigator Program, 2021/03684-4, RD-C); (FAPESP grants: 2020/01688-0 and 2020/07069-0 to OC-M).

Conflict of interest

The authors declare that the research was conducted in the absence of any commercial or financial relationships that could be construed as a potential conflict of interest.

Publisher's note

All claims expressed in this article are solely those of the authors and do not necessarily represent those of their affiliated organizations, or those of the publisher, the editors and the reviewers. Any product that may be evaluated in this article, or claim that may be made by its manufacturer, is not guaranteed or endorsed by the publisher.

References

1. Lopes N. Características gerais e epidemiologia dos arbovírus emergentes no Brasil. *Rev Pan-Amaz Saude* (2014) 5:55–64. doi: 10.5123/S2176-62232014000300007

2. Braack L, Gouveia de Almeida AP, Cornel AJ, Swanepoel R, de Jager C. Mosquito-borne arboviruses of African origin: review of key viruses and vectors. *Parasit Vectors* (2018) 11:29. doi: 10.1186/s13071-017-2559-9

3. Kleiboeker SB, Scoles GA. Pathogenesis of African swine fever virus in Ornithodoros ticks. *Anim Health Res Rev* (2001) 2:121–8. doi: 10.1079/AHRR200133

4. Karabatsos N. Supplement to International Catalogue of Arboviruses including certain other viruses of vertebrates. *Am J Trop Med Hyg* (1978) 27:372–440. doi: 10.4269/ajtmh.1978.27.372

5. Weaver SC, Charlier C, Vasilakis N, Lecuit M. Zika, Chikungunya, and other emerging vector-borne viral diseases. *Annu Rev Med* (2018) 69:395–408. doi: 10.1146/annurev-med-050715-105122

6. Young PR. Arboviruses: A family on the move. *Adv Exp Med Biol* (2018) 1062:1–10. doi: 10.1007/978-981-10-8727-1_1

7. Brady OJ, Gething PW, Bhatt S, Messina JP, Brownstein JS, Hoen AG, et al. Refining the global spatial limits of dengue virus transmission by evidence-based consensus. *PLoS Negl Trop Dis* (2012) 6:e1760. doi: 10.1371/journal.pntd.0001760

8. PAHO. *Pan American Health Organization (PAHO) World Health Organization (WHO) Actualización epidemiológica semanal para dengue, chikunguña y zika en* (2022). Available at: https://www3.paho.org/data/index.php/en/ (Accessed 10/05).

9. Thomas SJ, Endy TP, Rothman AL. *Viral Infections Of Humans: Epidemiology and Control. Fifith edition*. Kaslow RA, Stanberry LR, Duc JWL, editors. New York, NY: Springer (2007).

10. Mustafa MS, Rasotgi V, Jain S, Gupta V. Discovery of fifth serotype of dengue virus (DENV-5): A new public health dilemma in dengue control. *Med J Armed Forces India* (2015) 71:67–70. doi: 10.1016/j.mjafi.2014.09.011

11. Messina JP, Brady OJ, Scott TW, Zou C, Pigott DM, Duda KA, et al. Global spread of dengue virus types: mapping the 70 year history. *Trends Microbiol* (2014) 22:138–46. doi: 10.1016/j.tim.2013.12.011

12. Laureti M, Narayanan D, Rodriguez-Andres J, Fazakerley JK, Kedzierski L. Flavivirus receptors: diversity, identity, and cell entry. *Front Immunol* (2018) 9:2180. doi: 10.3389/fimmu.2018.02180

13. HOTTA S. Experimental studies on dengue. I. Isolation, identification and modification of the virus. *J Infect Dis* (1952) 90:1–9. doi: 10.1093/infdis/90.1.1

14. Figueiredo LTM. Human urban arboviruses can infect wild animals and jump to sylvatic maintenance cycles in South America. *Front Cell Infect Microbiol* (2019) 9:259. doi: 10.3389/fcimb.2019.00259

15. Figueiredo LT. Emergent arboviruses in Brazil. *Rev Soc Bras Med Trop* (2007) 40:224–9. doi: 10.1590/s0037-86822007000200016

16. DICK GW, KITCHEN SF, HADDOW AJ. Zika virus. I. Isolations and serological specificity. *Trans R Soc Trop Med Hyg* (1952) 46:509–20. doi: 10.1016/0035-9203(52)90042-4

17. Sirohi D, Kuhn RJ. Zika virus structure, maturation, and receptors. *J Infect Dis* (2017) 216:S935–44. doi: 10.1093/infdis/jix515

18. Gatherer D, Kohl A. Zika virus: a previously slow pandemic spreads rapidly through the Americas. *J Gen Virol* (2016) 97:269–73. doi: 10.1099/jgv.0.000381

19. Hills SL, Russell K, Hennessey M, Williams C, Oster AM, Fischer M, et al. Transmission of Zika virus through sexual contact with travelers to areas of ongoing transmission - continental United States, 2016. *MMWR Morb Mortal Wkly Rep* (2016) 65:215–6. doi: 10.15585/mmwr.mm6508e2

20. ROSS RW. The Newala epidemic. III. The virus: isolation, pathogenic properties and relationship to the epidemic. *J Hyg (Lond)* (1956) 54:177–91. doi: 10.1017/s0022172400044442

21. Chevillon C, Briant L, Renaud F, Devaux C. The Chikungunya threat: an ecological and evolutionary perspective. *Trends Microbiol* (2008) 16:80–8. doi: 10.1016/j.tim.2007.12.003

22. Volk SM, Chen R, Tsetsarkin KA, Adams AP, Garcia TI, Sall AA, et al. Genome-scale phylogenetic analyses of chikungunya virus reveal independent emergences of recent epidemics and various evolutionary rates. *J Virol* (2010) 84:6497–504. doi: 10.1128/JVI.01603-09

23. Burt FJ, Chen W, Miner JJ, Lenschow DJ, Merits A, Schnettler E, et al. Chikungunya virus: an update on the biology and pathogenesis of this emerging pathogen. *Lancet Infect Dis* (2017) 17:e107–17. doi: 10.1016/S1473-3099(16)30385-1

24. Nunes MR, Faria NR, de Vasconcelos JM, Golding N, Kraemer MU, de Oliveira LF, et al. Emergence and potential for spread of Chikungunya virus in Brazil. *BMC Med* (2015) 13:102. doi: 10.1186/s12916-015-0348-x

25. Schuffenecker I, Iteman I, Michault A, Murri S, Frangeul L, Vaney MC, et al. Genome microevolution of chikungunya viruses causing the Indian Ocean outbreak. *PloS Med* (2006) 3:e263. doi: 10.1371/journal.pmed.0030263

26. Rezza G, Nicoletti L, Angelini R, Romi R, Finarelli AC, Panning M, et al. Infection with chikungunya virus in Italy: an outbreak in a temperate region. *Lancet* (2007) 370:1840–6. doi: 10.1016/S0140-6736(07)61779-6

27. Li Z, Wang J, Cheng X, Hu H, Guo C, Huang J, et al. The worldwide seroprevalence of DENV, CHIKV and ZIKV infection: A systematic review and meta-analysis. *PLoS Negl Trop Dis* (2021) 15:e0009337. doi: 10.1371/journal.pntd.0009337

28. Vairo F, Haider N, Kock R, Ntoumi F, Ippolito G, Zumla A. Chikungunya: epidemiology, pathogenesis, clinical features, management, and prevention. *Infect Dis Clin North Am* (2019) 33:1003–25. doi: 10.1016/j.idc.2019.08.006

29. WHO. World Health Organization. *A report about health. Chikungunya*. Available at: https://www.who.int/news-room/fact-sheets/detail/chikungunya (Accessed 16/05).

30. Gubler DJ. Human arbovirus infections worldwide. *Ann N Y Acad Sci* (2001) 951:13–24. doi: 10.1111/j.1749-6632.2001.tb02681.x

31. Schatzmayr HG. [Emerging and reemerging viral diseases]. *Cad Saude Publica* (2001) 17(Suppl):209–13. doi: 10.1590/S0102-311X2001000700031

32. Vorou RM, Papavassiliou VG, Tsiodras S. Emerging zoonoses and vector-borne infections affecting humans in Europe. *Epidemiol Infect* (2007) 135:1231–47. doi: 10.1017/S0950268807008527

33. Powers AM, Logue CH. Changing patterns of chikungunya virus: re-emergence of a zoonotic arbovirus. *J Gen Virol* (2007) 88:2363–77. doi: 10.1099/vir.0.82858-0

34. Gubler; J,D, Kuno G, Markoff L. *Flaviviruses; Field's Virology* Vol. 1. . Philadelphia: Lippincott Williams & Wilkins (2007) p. 1153–252.

35. Chong HY, Leow CY, Abdul Majeed AB, Leow CH. Flavivirus infection-A review of immunopathogenesis, immunological response, and immunodiagnosis. *Virus Res* (2019) 274:197770. doi: 10.1016/j.virusres.2019.197770

36. Dai L, Song J, Lu X, Deng YQ, Musyoki AM, Cheng H, et al. Structures of the Zika virus envelope protein and its complex with a flavivirus broadly protective antibody. *Cell Host Microbe* (2016) 19:696–704. doi: 10.1016/j.chom.2016.04.013

37. Ye Q, Liu ZY, Han JF, Jiang T, Li XF, Qin CF. Genomic characterization and phylogenetic analysis of Zika virus circulating in the Americas. *Infect Genet Evol* (2016) 43:43–9. doi: 10.1016/j.meegid.2016.05.004

38. Zhang Y, Zhang W, Ogata S, Clements D, Strauss JH, Baker TS, et al. Conformational changes of the flavivirus E glycoprotein. *Structure* (2004) 12:1607–18. doi: 10.1016/j.str.2004.06.019

39. Kostyuchenko VA, Lim EX, Zhang S, Fibriansah G, Ng TS, Ooi JS, et al. Structure of the thermally stable Zika virus. *Nature* (2016) 533:425–8. doi: 10.1038/nature17994

40. Barba-Spaeth G, Dejnirattisai W, Rouvinski A, Vaney MC, Medits I, Sharma A, et al. Structural basis of potent Zika-dengue virus antibody cross-neutralization. *Nature* (2016) 536:48–53. doi: 10.1038/nature18938

41. Mukhopadhyay S, Kuhn RJ, Rossmann MG. A structural perspective of the flavivirus life cycle. *Nat Rev Microbiol* (2005) 3:13–22. doi: 10.1038/nrmicro1067

42. Stiasny K, Kiermayr S, Heinz FX. Entry functions and antigenic structure of flavivirus envelope proteins. *Novartis Found Symp* (2006) 277:57–65; discussion 65-73, 251-253. doi: 10.1002/0470058005.ch5

43. Holmes AC, Basore K, Fremont DH, Diamond MS. A molecular understanding of alphavirus entry. *PLoS Pathog* (2020) 16:e1008876. doi: 10.1371/journal.ppat.1008876

44. Brown RS, Wan JJ, Kielian M. The alphavirus exit pathway: what we know and what we wish we knew. *Viruses* (2018) 10(2):89. doi: 10.3390/v10020089

45. Musso D, Gubler DJ. Zika virus. *Clin Microbiol Rev* (2016) 29:487–524. doi: 10.1128/CMR.00072-15

46. Cordero-Rivera CD, De Jesús-González LA, Osuna-Ramos JF, Palacios-Rápalo SN, Farfan-Morales CN, Reyes-Ruiz JM, et al. The importance of viral and cellular factors on flavivirus entry. *Curr Opin Virol* (2021) 49:164–75. doi: 10.1016/j.coviro.2021.05.001

47. Schnierle BS. Cellular attachment and entry factors for Chikungunya virus. *Viruses* (2019) 11(11):1078. doi: 10.3390/v11111078

48. Jose J, Snyder JE, Kuhn RJ. A structural and functional perspective of alphavirus replication and assembly. *Future Microbiol* (2009) 4:837–56. doi: 10.2217/fmb.09.59

49. Carey BD, Bakovic A, Callahan V, Narayanan A, Kehn-Hall K. New World alphavirus protein interactomes from a therapeutic perspective. *Antiviral Res* (2019) 163:125–39. doi: 10.1016/j.antiviral.2019.01.015

50. Rupp JC, Sokoloski KJ, Gebhart NN, Hardy RW. Alphavirus RNA synthesis and non-structural protein functions. *J Gen Virol* (2015) 96:2483–500. doi: 10.1099/jgv.0.000249

51. Ahola T, Kääriäinen L. Reaction in alphavirus mRNA capping: formation of a covalent complex of nonstructural protein nsP1 with 7-methyl-GMP. *Proc Natl Acad Sci USA* (1995) 92:507–11. doi: 10.1073/pnas.92.2.507

52. Peränen J, Rikkonen M, Liljeström P, Kääriäinen L. Nuclear localization of Semliki Forest virus-specific nonstructural protein nsP2. *J Virol* (1990) 64:1888–96. doi: 10.1128/JVI.64.5.1888-1896.1990

53. Rikkonen M, Peränen J, Kääriäinen L. ATPase and GTPase activities associated with Semliki Forest virus nonstructural protein nsP2. *J Virol* (1994) 68:5804–10. doi: 10.1128/JVI.68.9.5804-5810.1994

54. Wong KZ, Chu JJH. The interplay of viral and host factors in Chikungunya virus infection: targets for antiviral strategies. *Viruses* (2018) 10(6):294. doi: 10.3390/v10060294

55. Tomar S, Hardy RW, Smith JL, Kuhn RJ. Catalytic core of alphavirus nonstructural protein nsP4 possesses terminal adenylyltransferase activity. *J Virol* (2006) 80:9962–9. doi: 10.1128/JVI.01067-06

56. Briant L, Desprès P, Choumet V, Missé D. Role of skin immune cells on the host susceptibility to mosquito-borne viruses. *Virology* (2014) 464-465:26–32. doi: 10.1016/j.virol.2014.06.023

57. Suhrbier A, Jaffar-Bandjee MC, Gasque P. Arthritogenic alphaviruses–an overview. *Nat Rev Rheumatol* (2012) 8:420–9. doi: 10.1038/nrrheum.2012.64

58. Matusali G, Colavita F, Bordi L, Lalle E, Ippolito G, Capobianchi MR, et al. Tropism of the Chikungunya virus. *Viruses* (2019) 11(2):175. doi: 10.3390/v11020175

59. Schwartz O, Albert ML. Biology and pathogenesis of chikungunya virus. *Nat Rev Microbiol* (2010) 8:491–500. doi: 10.1038/nrmicro2368

60. Rohatgi A, Corbo JC, Monte K, Higgs S, Vanlandingham DL, Kardon G, et al. Infection of myofibers contributes to increased pathogenicity during infection with an epidemic strain of chikungunya virus. *J Virol* (2014) 88:2414–25. doi: 10.1128/JVI.02716-13

61. Ozden S, Huerre M, Riviere JP, Coffey LL, Afonso PV, Mouly V, et al. Human muscle satellite cells as targets of Chikungunya virus infection. *PLoS One* (2007) 2:e527. doi: 10.1371/journal.pone.0000527

62. Hiroki CH, Toller-Kawahisa JE, Fumagalli MJ, Colon DF, Figueiredo LTM, Fonseca BALD, et al. Neutrophil extracellular traps effectively control acute Chikungunya virus infection. *Front Immunol* (2019) 10:3108. doi: 10.3389/fimmu.2019.03108

63. Reddy V, Mani RS, Desai A, Ravi V. Correlation of plasma viral loads and presence of Chikungunya IgM antibodies with cytokine/chemokine levels during acute Chikungunya virus infection. *J Med Virol* (2014) 86:1393–401. doi: 10.1002/jmv.23875

64. Teng TS, Kam YW, Lee B, Hapuarachchi HC, Wimal A, Ng LC, et al. Systematic meta-analysis of immune signatures in patients with acute Chikungunya virus infection. *J Infect Dis* (2015) 211:1925–35. doi: 10.1093/infdis/jiv049

65. Silva LA, Dermody TS. Chikungunya virus: epidemiology, replication, disease mechanisms, and prospective intervention strategies. *J Clin Invest* (2017) 127:737–49. doi: 10.1172/JCI84417

66. Rudd PA, Wilson J, Gardner J, Larcher T, Babarit C, Le TT, et al. Interferon response factors 3 and 7 protect against Chikungunya virus hemorrhagic fever and shock. *J Virol* (2012) 86:9888–98. doi: 10.1128/JVI.00956-12

67. Ryman KD, Klimstra WB. Host responses to alphavirus infection. *Immunol Rev* (2008) 225:27–45. doi: 10.1111/j.1600-065X.2008.00670.x

68. Thurmond S, Wang B, Song J, Hai R. Suppression of type I interferon signaling by. *Viruses* (2018) 10(12):712. doi: 10.3390/v10120712

69. Makhluf H, Shresta S. Innate antiviral immunity against dengue virus. *Crit Rev Immunol* (2015) 35:253–60. doi: 10.1615/critrevimmunol.2015014251

70. Schoggins JW, Rice CM. Interferon-stimulated genes and their antiviral effector functions. *Curr Opin Virol* (2011) 1:519–25. doi: 10.1016/j.coviro.2011.10.008

71. Mamane Y, Heylbroeck C, Génin P, Algarté M, Servant MJ, LePage C, et al. Interferon regulatory factors: the next generation. *Gene* (1999) 237:1–14. doi: 10.1016/s0378-1119(99)00262-0

72. Fros JJ, Pijlman GP. Alphavirus infection: host cell shut-off and inhibition of antiviral responses. *Viruses* (2016) 8(6):166. doi: 10.3390/v8060166

73. Screaton G, Mongkolsapaya J, Yacoub S, Roberts C. New insights into the immunopathology and control of dengue virus infection. *Nat Rev Immunol* (2015) 15:745–59. doi: 10.1038/nri3916

74. Halstead SB. Observations related to pathogensis of dengue hemorrhagic fever. VI. Hypotheses and discussion. *Yale J Biol Med* (1970) 42:350–62.

75. Littaua R, Kurane I, Ennis FA. Human IgG Fc receptor II mediates antibody-dependent enhancement of dengue virus infection. *J Immunol* (1990) 144:3183–6. doi: 10.4049/jimmunol.144.8.3183

76. Cardosa MJ, Porterfield JS, Gordon S. Complement receptor mediates enhanced flavivirus replication in macrophages. *J Exp Med* (1983) 158:258–63. doi: 10.1084/jem.158.1.258

77. Chareonsirisuthigul T, Kalayanarooj S, Ubol S. Dengue virus (DENV) antibody-dependent enhancement of infection upregulates the production of anti-inflammatory cytokines, but suppresses anti-DENV free radical and pro-inflammatory cytokine production, in THP-1 cells. *J Gen Virol* (2007) 88:365–75. doi: 10.1099/vir.0.82537-0

78. Vo HTM, Upasani V, Auerswald H, Lay S, Sann S, Vanderlinden A, et al. Temporal patterns of functional anti-dengue antibodies in dengue infected individuals with different disease outcome or infection history. *Sci Rep* (2022) 12:17863. doi: 10.1038/s41598-022-21722-2

79. Puschnik A, Lau L, Cromwell EA, Balmaseda A, Zompi S, Harris E. Correlation between dengue-specific neutralizing antibodies and serum avidity in primary and secondary dengue virus 3 natural infections in humans. *PLoS Negl Trop Dis* (2013) 7: e2274. doi: 10.1371/journal.pntd.0002274

80. Bournazos S, Vo HTM, Duong V, Auerswald H, Ly S, Sakuntabhai A, et al. Antibody fucosylation predicts disease severity in secondary dengue infection. *Science* (2021) 372:1102–5. doi: 10.1126/science.abc7303

81. Thulin NK, Brewer RC, Sherwood R, Bournazos S, Edwards KG, Ramadoss NS, et al. Maternal anti-dengue igG fucosylation predicts susceptibility to dengue disease in infants. *Cell Rep* (2020) 31:107642. doi: 10.1016/j.celrep.2020.107642

82. Salje H, Cummings DAT, Rodriguez-Barraquer I, Katzelnick LC, Lessler J, Klungthong C, et al. Reconstruction of antibody dynamics and infection histories to evaluate dengue risk. *Nature* (2018) 557:719–23. doi: 10.1038/s41586-018-0157-4

83. Katzelnick LC, Gresh L, Halloran ME, Mercado JC, Kuan G, Gordon A, et al. Antibody-dependent enhancement of severe dengue disease in humans. *Science* (2017) 358:929–32. doi: 10.1126/science.aan6836

84. Dejnirattisai W, Jumnainsong A, Onsirisakul N, Fitton P, Vasanawathana S, Limpitikul W, et al. Cross-reacting antibodies enhance dengue virus infection in humans. *Science* (2010) 328:745–8. doi: 10.1126/science.1185181

85. Xu M, Zuest R, Velumani S, Tukijan F, Toh YX, Appanna R, et al. A potent neutralizing antibody with therapeutic potential against all four serotypes of dengue virus. *NPJ Vaccines* (2017) 2:2. doi: 10.1038/s41541-016-0003-3

86. Avirutnan P, Fuchs A, Hauhart RE, Somnuke P, Youn S, Diamond MS, et al. Antagonism of the complement component C4 by flavivirus nonstructural protein NS1. *J Exp Med* (2010) 207:793–806. doi: 10.1084/jem.20092545

87. Chen J, Ng MM, Chu JJ. Activation of TLR2 and TLR6 by dengue NS1 protein and its implications in the immunopathogenesis of dengue virus infection. *PloS Pathog* (2015) 11:e1005053. doi: 10.1371/journal.ppat.1005053

88. Modhiran N, Watterson D, Muller DA, Panetta AK, Sester DP, Liu L, et al. Dengue virus NS1 protein activates cells via Toll-like receptor 4 and disrupts endothelial cell monolayer integrity. *Sci Transl Med* (2015) 7:304ra142. doi: 10.1126/scitranslmed.aaa3863

89. Puerta-Guardo H, Glasner DR, Espinosa DA, Biering SB, Patana M, Ratnasiri K, et al. Flavivirus NS1 triggers tissue-specific vascular endothelial dysfunction reflecting disease tropism. *Cell Rep* (2019) 26:1598–1613.e1598. doi: 10.1016/j.celrep.2019.01.036

90. Pang X, Zhang R, Cheng G. Progress towards understanding the pathogenesis of dengue hemorrhagic fever. *Virol Sin* (2017) 32:16–22. doi: 10.1007/s12250-016-3855-9

91. Faye O, Dupressoir A, Weidmann M, Ndiaye M, Alpha Sall A. One-step RT-PCR for detection of Zika virus. *J Clin Virol* (2008) 43:96–101. doi: 10.1016/j.jcv.2008.05.005

92. Gourinat AC, O'Connor O, Calvez E, Goarant C, Dupont-Rouzeyrol M. Detection of Zika virus in urine. *Emerg Infect Dis* (2015) 21:84–6. doi: 10.3201/eid2101.140894

93. Plourde AR, Bloch EMA. Literature review of Zika virus. *Emerg Infect Dis* (2016) 22:1185–92. doi: 10.3201/eid2207.151990

94. de Araújo TVB, Rodrigues LC, de Alencar Ximenes RA, de Barros Miranda-Filho D, Montarroyos UR, de Melo APL, et al. Association between Zika virus infection and microcephaly in Brazil, January to May, 2016: preliminary report of a case-control study. *Lancet Infect Dis* (2016) 16:1356–63. doi: 10.1016/S1473-3099(16)30318-8

95. Baud D, Gubler DJ, Schaub B, Lanteri MC, Musso D. An update on Zika virus infection. *Lancet* (2017) 390:2099–109. doi: 10.1016/S0140-6736(17)31450-2

96. Edupuganti S, Natrajan MS, Rouphael N, Lai L, Xu Y, Feldhammer M, et al. Biphasic Zika illness with rash and joint pain. *Open Forum Infect Dis* (2017) 4:ofx133. doi: 10.1093/ofid/ofx133

97. Minhas AM, Nayab A, Iyer S, Narmeen M, Fatima K, Khan MS, et al. Association of Zika virus with myocarditis, heart failure, and arrhythmias: A literature review. *Cureus* (2017) 9:e1399. doi: 10.7759/cureus.1399

98. Baxter VK, Heise MT. Immunopathogenesis of alphaviruses. *Adv Virus Res* (2020) 107:315–82. doi: 10.1016/bs.aivir.2020.06.002

99. Paixão ES, Rodrigues LC, Costa MDCN, Itaparica M, Barreto F, Gérardin P, et al. Chikungunya chronic disease: a systematic review and meta-analysis. *Trans R Soc Trop Med Hyg* (2018) 112:301–16. doi: 10.1093/trstmh/try063

100. Erasmus JH, Rossi SL, Weaver SC. Development of vaccines for chikungunya fever. *J Infect Dis* (2016) 214:S488–96. doi: 10.1093/infdis/jiw271

101. Weaver SC, Lecuit M. Chikungunya virus and the global spread of a mosquito-borne disease. *N Engl J Med* (2015) 372:1231–9. doi: 10.1056/NEJMra1406035

102. Venter M. Assessing the zoonotic potential of arboviruses of African origin. *Curr Opin Virol* (2018) 28:74–84. doi: 10.1016/j.coviro.2017.11.004

103. Zhang W, Chen S, Mahalingam S, Wang M, Cheng A. An updated review of avian-origin Tembusu virus: a newly emerging avian Flavivirus. *J Gen Virol* (2017) 98:2413–20. doi: 10.1099/jgv.0.000908

104. Sabin AB, Schlesinger RW. Production of immunity to dengue with virus modified by propagation in mice. *Science* (1945) 101:640–2. doi: 10.1126/science.101.2634.640

105. Villar L, Dayan GH, Arredondo-García JL, Rivera DM, Cunha R, Deseda C, et al. Efficacy of a tetravalent dengue vaccine in children in Latin America. *N Engl J Med* (2015) 372:113–23. doi: 10.1056/NEJMoa1411037

106. World Health Organization. Dengue vaccine: WHO position paper – July 2016. *Wkly Epidemiol Rec* (2016) 91:349–64. doi: 10.1016/j.vaccine.2016.10.070

107. *Diário Oficial da União, B., DF, Brazil*. Available at: https://www.jusbrasil.com.br/diarios/106783857/dou-suplemento-secao-1-pg-4 (Accessed 28/05).

108. Reuters. *Philippines says anti-dengue vaccine may be connected to three deaths*. Available at: https://www.reuters.com/article/us-sanofidengue-Philippines/Philippines-says-anti-dengue-vaccine-may-beconnected-to-three-deaths-idUSKBN1FM0SP (Accessed 20/05).

109. European Medicines Agency. *Dengvaxia vaccine approved for prevention of dengue in Europe*. London, UK: European Medicine Agency (2018).

110. Administration, F.-U.F.a.D. *First FDA-approved vaccine for the prevention of dengue disease in endemic regions*. Swiftwater PA, USA: Sanofi Pasteur Inc. (2019).

111. Wong JM, Adams LE, Durbin AP, Muñoz-Jordán JL, Poehling KA, Sánchez-González LM, et al. Dengue: A growing problem with new interventions. *Pediatrics* (2022) 149(6). doi: 10.1542/peds.2021-055522

112. Biswal S, Reynales H, Saez-Llorens X, Lopez P, Borja-Tabora C, Kosalaraksa P, et al. Efficacy of a tetravalent dengue vaccine in healthy children and adolescents. *N Engl J Med* (2019) 381:2009–19. doi: 10.1056/NEJMoa1903869

113. Sáez-Llorens X, Tricou V, Yu D, Rivera L, Tuboi S, Garbes P, et al. Safety and immunogenicity of one versus two doses of Takeda's tetravalent dengue vaccine in children in Asia and Latin America: interim results from a phase 2, randomised, placebo-controlled study. *Lancet Infect Dis* (2017) 17:615–25. doi: 10.1016/S1473-3099(17)30166-4

114. Biswal S, Borja-Tabora C, Martinez Vargas L, Velásquez H, Theresa Alera M, Sierra V, et al. Efficacy of a tetravalent dengue vaccine in healthy children aged 4-16 years: a randomised, placebo-controlled, phase 3 trial. *Lancet* (2020) 395:1423–33. doi: 10.1016/S0140-6736(20)30414-1

115. Collins MH, McGowan E, Jadi R, Young E, Lopez CA, Baric RS, et al. Lack of durable cross-neutralizing antibodies against Zika virus from dengue virus infection. *Emerg Infect Dis* (2017) 23:773–81. doi: 10.3201/eid2305.161630

116. Montoya M, Collins M, Dejnirattisai W, Katzelnick LC, Puerta-Guardo H, Jadi R, et al. Longitudinal analysis of antibody cross-neutralization following Zika virus and dengue virus infection in asia and the Americas. *J Infect Dis* (2018) 218:536–45. doi: 10.1093/infdis/jiy164

117. Richner JM, Himansu S, Dowd KA, Butler SL, Salazar V, Fox JM, et al. Modified mRNA Vaccines Protect against Zika Virus Infection. *Cell* (2017) 169:176. doi: 10.1016/j.cell.2017.03.016

118. Casey RM, Harris JB, Ahuka-Mundeke S, Dixon MG, Kizito GM, Nsele PM, et al. Immunogenicity of fractional-dose vaccine during a yellow fever outbreak - final report. *N Engl J Med* (2019) 381:444–54. doi: 10.1056/NEJMoa1710430

119. Bullard-Feibelman KM, Govero J, Zhu Z, Salazar V, Veselinovic M, Diamond MS, et al. The FDA-approved drug sofosbuvir inhibits Zika virus infection. *Antiviral Res* (2017) 137:134–40. doi: 10.1016/j.antiviral.2016.11.023

120. Retallack H, Di Lullo E, Arias C, Knopp KA, Laurie MT, Sandoval-Espinosa C, et al. Zika virus cell tropism in the developing human brain and inhibition by azithromycin. *Proc Natl Acad Sci USA* (2016) 113:14408–13. doi: 10.1073/pnas.1618029113

121. Hamer DH, Wilson ME, Jean J, Chen LH. Epidemiology, prevention, and potential future treatments of sexually transmitted Zika virus infection. *Curr Infect Dis Rep* (2017) 19:16. doi: 10.1007/s11908-017-0571-z

122. McArthur MA. Zika virus: recent advances towards the development of vaccines and therapeutics. *Viruses* (2017) 9(6):143. doi: 10.3390/v9060143

123. Gardner J, Anraku I, Le TT, Larcher T, Major L, Roques P, et al. Chikungunya virus arthritis in adult wild-type mice. *J Virol* (2010) 84:8021–32. doi: 10.1128/JVI.02603-09

124. Couderc T, Khandoudi N, Grandadam M, Visse C, Gangneux N, Bagot S, et al. Prophylaxis and therapy for Chikungunya virus infection. *J Infect Dis* (2009) 200:516–23. doi: 10.1086/600381

125. Akahata W, Yang ZY, Andersen H, Sun S, Holdaway HA, Kong WP, et al. A virus-like particle vaccine for epidemic Chikungunya virus protects nonhuman primates against infection. *Nat Med* (2010) 16:334–8. doi: 10.1038/nm.2105

126. Smee DF, Alaghamandan HA, Kini GD, Robins RK. Antiviral activity and mode of action of ribavirin 5'-sulfamate against Semliki Forest virus. *Antiviral Res* (1988) 10:253–62. doi: 10.1016/0166-3542(88)90044-7

127. Sidwell RW, Smee DF. Viruses of the Bunya- and Togaviridae families: potential as bioterrorism agents and means of control. *Antiviral Res* (2003) 57:101–11. doi: 10.1016/s0166-3542(02)00203-6

128. Khan M, Santhosh SR, Tiwari M, Lakshmana Rao PV, Parida M. Assessment of in *vitro* prophylactic and therapeutic efficacy of chloroquine against Chikungunya virus in vero cells. *J Med Virol* (2010) 82:817–24. doi: 10.1002/jmv.21663

129. De Lamballerie X, Boisson V, Reynier JC, Enault S, Charrel RN, Flahault A, et al. On chikungunya acute infection and chloroquine treatment. *Vector Borne Zoonotic Dis* (2008) 8:837–9. doi: 10.1089/vbz.2008.0049

130. Ermann J, Bermas BL. The biology behind the new therapies for SLE. *Int J Clin Pract* (2007) 61:2113–9. doi: 10.1111/j.1742-1241.2007.01528.x

131. Wang YM, Lu JW, Lin CC, Chin YF, Wu TY, Lin LI, et al. Antiviral activities of niclosamide and nitazoxanide against chikungunya virus entry and transmission. *Antiviral Res* (2016) 135:81–90. doi: 10.1016/j.antiviral.2016.10.003

132. Kao JC, HuangFu WC, Tsai TT, Ho MR, Jhan MK, Shen TJ, et al. The antiparasitic drug niclosamide inhibits dengue virus infection by interfering with endosomal acidification independent of mTOR. *PloS Negl Trop Dis* (2018) 12: e0006715. doi: 10.1371/journal.pntd.0006715

133. Zou B, Chan WL, Ding M, Leong SY, Nilar S, Seah PG, et al. Lead optimization of spiropyrazolopyridones: a new and potent class of dengue virus inhibitors. *ACS Med Chem Lett* (2015) 6:344–8. doi: 10.1021/ml500521r

134. Mishra P, Kumar A, Mamidi P, Kumar S, Basantray I, Saswat T, et al. Inhibition of Chikungunya virus replication by 1-[(2-methylbenzimidazol-1-yl) methyl]-2-oxo-indolin-3-ylidene] amino] thiourea(MBZM-N-IBT). *Sci Rep* (2016) 6:20122. doi: 10.1038/srep20122

135. De S, Ghosh S, Keshry SS, Mahish C, Mohapatra C, Guru A, et al. MBZM-N-IBT, a novel small molecule, restricts Chikungunya virus infection by targeting nsP2 protease activity. *Antimicrob Agents Chemother* (2022) 66:e0046322. doi: 10.1128/aac.00463-22

136. Vázquez-Calvo Á, Jiménez de Oya N, Martín-Acebes MA, Garcia-Moruno E, Saiz JC. Antiviral properties of the natural polyphenols delphinidin and epigallocatechin gallate against the flaviviruses west nile virus, Zika virus, and dengue virus. *Front Microbiol* (2017) 8:1314. doi: 10.3389/fmicb.2017.01314

137. Weber C, Sliva K, von Rhein C, Kümmerer BM, Schnierle BS. The green tea catechin, epigallocatechin gallate inhibits chikungunya virus infection. *Antiviral Res* (2015) 113:1–3. doi: 10.1016/j.antiviral.2014.11.001

138. Kraemer MUG, Reiner RC, Brady OJ, Messina JP, Gilbert M, Pigott DM, et al. Past and future spread of the arbovirus vectors Aedes aEgypti and Aedes albopictus. *Nat Microbiol* (2019) 4:854–63. doi: 10.1038/s41564-019-0376-y

139. The Victorian Arbovirus Disease Control Program. Department of Natural Resources and Environment. Available at: https://www.betterhealth.vic.gov.au/mosquito-management-victoria (Accessed 07/24).

140. Batovska J, Mee PT, Sawbridge TI, Rodoni BC, Lynch SE. Enhanced arbovirus surveillance with high-throughput metatranscriptomic processing of field-collected mosquitoes. *Viruses* (2022) 14(12):2759. doi: 10.3390/v14122759

141. Schrieke H, Maignien L, Constancias F, Trigodet F, Chakloute S, Rakotoarivony I, et al. The mosquito microbiome includes habitat-specific but rare symbionts. *Comput Struct Biotechnol J* (2022) 20:410–20. doi: 10.1016/j.csbj.2021.12.019

142. Franz AW, Sanchez-Vargas I, Raban RR, Black WC, James AA, Olson KE. Fitness impact and stability of a transgene conferring resistance to dengue-2 virus following introgression into a genetically diverse Aedes aEgypti strain. *PLoS Negl Trop Dis* (2014) 8:e2833. doi: 10.1371/journal.pntd.0002833

143. Liu T, Xu Y, Wang X, Gu J, Yan G, Chen XG. Antiviral systems in vector mosquitoes. *Dev Comp Immunol* (2018) 83:34–43. doi: 10.1016/j.dci.2017.12.025

144. Tafesh-Edwards G, Kalukin A, Eleftherianos I. Zika virus induces sex-dependent metabolic changes in. *Front Immunol* (2022) 13:903860. doi: 10.3389/fimmu.2022.903860

145. Ding SW, Voinnet O. Antiviral immunity directed by small RNAs. *Cell* (2007) 130:413–26. doi: 10.1016/j.cell.2007.07.039

146. Zeng T, Jaffar S, Xu Y, Qi Y. The intestinal immune defense system in insects. *Int J Mol Sci* (2022) 23(23):15132. doi: 10.3390/ijms232315132

147. Sheehan G, Garvey A, Croke M, Kavanagh K. Innate humoral immune defences in mammals and insects: The same, with differences? *Virulence* (2018) 9:1625–39. doi: 10.1080/21505594.2018.1526531

148. Werren JH. Biology of wolbachia. *Annu Rev Entomol* (1997) 42:587–609. doi: 10.1146/annurev.ento.42.1.587

149. Frentiu FD, Robinson J, Young PR, McGraw EA, O'Neill SL. Wolbachia-mediated resistance to dengue virus infection and death at the cellular level. *PLoS One* (2010) 5:e13398. doi: 10.1371/journal.pone.0013398

150. Caragata EP, Dutra HL, Moreira LA. Inhibition of Zika virus by. *Microb Cell* (2016) 3:293–5. doi: 10.15698/mic2016.07.513

151. Wu M, Sun LV, Vamathevan J, Riegler M, Deboy R, Brownlie JC, et al. Phylogenomics of the reproductive parasite Wolbachia pipientis wMel: a streamlined genome overrun by mobile genetic elements. *PLoS Biol* (2004) 2:E69. doi: 10.1371/journal.pbio.0020069

152. Callaway E. Rio fights Zika with biggest release yet of bacteria-infected mosquitoes. *Nature* (2016) 539:17–8. doi: 10.1038/nature.2016.20878

153. Aliota MT, Peinado SA, Velez ID, Osorio JE. The wMel strain of Wolbachia Reduces Transmission of Zika virus by Aedes aEgypti. *Sci Rep* (2016) 6:28792. doi: 10.1038/srep28792

154. Dutra HL, Rocha MN, Dias FB, Mansur SB, Caragata EP, Moreira LA. Wolbachia blocks currently circulating zika virus isolates in Brazilian aedes aEgypti mosquitoes. *Cell Host Microbe* (2016) 19:771–4. doi: 10.1016/j.chom.2016.04.021

155. Monash Universit. World Mosquito Program. Available at: https://www.worldmosquitoprogram.org (Accessed 07/24).

Frontiers in Immunology

Explores novel approaches and diagnoses to treat immune disorders.

The official journal of the International Union of Immunological Societies (IUIS) and the most cited in its field, leading the way for research across basic, translational and clinical immunology.

Discover the latest Research Topics

See more →

Frontiers

Avenue du Tribunal-Fédéral 34
1005 Lausanne, Switzerland
frontiersin.org

Contact us

+41 (0)21 510 17 00
frontiersin.org/about/contact